MARTIN MARIETTA ENERGY SYSYEMS LIBRARIES

3 4456 0324068 7

ORNL/TM-11586

ornl

OAK RIDGE
NATIONAL
LABORATORY

MARTIN MARIETTA

Ceramic Technology for Advanced Heat Engines Project Semiannual Progress Report for October 1989 Through March 1990

OAK RIDGE NATIONAL LABORATORY
CENTRAL RESEARCH LIBRARY
CIRCULATION SECTION
4500N ROOM 175
LIBRARY LOAN COPY
DO NOT TRANSFER TO ANOTHER PERSON
If you wish someone else to see this report, send in name with report and the library will arrange a loan.

CERAMIC TECHNOLOGY FOR ADVANCED HEAT ENGINES

CERAMIC TECHNOLOGY PROJECT • DOE/ORNL •

OPERATED BY
MARTIN MARIETTA ENERGY SYSTEMS, INC.
FOR THE UNITED STATES
DEPARTMENT OF ENERGY

This report has been reproduced directly from the best available copy.

Available to DOE and DOE contractors from the Office of Scientific and Technical Information, P.O. Box 62, Oak Ridge, TN 37831; prices available from (615) 576-8401, FTS 626-8401.

Available to the public from the National Technical Information Service, U.S. Department of Commerce, 5285 Port Royal Rd., Springfield, VA 22161.
NTIS price codes—Printed Copy: A23 Microfiche A01

This report was prepared as an account of work sponsored by an agency of the United States Government. Neither the United States Government nor any agency thereof, nor any of their employees, makes any warranty, express or implied, or assumes any legal liability or responsibility for the accuracy, completeness, or usefulness of any information, apparatus, product, or process disclosed, or represents that its use would not infringe privately owned rights. Reference herein to any specific commercial product, process, or service by trade name, trademark, manufacturer, or otherwise, does not necessarily constitute or imply its endorsement, recommendation, or favoring by the United States Government or any agency thereof. The views and opinions of authors expressed herein do not necessarily state or reflect those of the United States Government or any agency thereof.

ORNL/TM-11586

Metals and Ceramics Division

CERAMIC TECHNOLOGY FOR ADVANCED HEAT ENGINES PROJECT
SEMIANNUAL PROGRESS REPORT FOR
OCTOBER 1989 THROUGH MARCH 1990

D. R. Johnson
Project Manager

Date Published: September 1990

NOTICE: This document contains information of a preliminary nature. It is subject to revision or correction and therefore does not represent a final report.

Prepared for
U.S. Department of Energy
Assistant Secretary for Conservation and Renewable Energy
Office of Transportation Technologies
Advanced Materials Development Program
EE 04 00 00 0

Prepared by the
OAK RIDGE NATIONAL LABORATORY
Oak Ridge, Tennessee 37831-6285
operated by
MARTIN MARIETTA ENERGY SYSTEMS, INC.
for the
U.S. DEPARTMENT OF ENERGY
under Contract DE-AC05-84OR21400

MARTIN MARIETTA ENERGY SYSTEMS LIBRARIES

3 4456 0324068 7

REPORTS PREVIOUSLY ISSUED

ORNL/TM-9325	Period March 1983-September 1983
ORNL/TM-9466	Period October 1983-March 1984
ORNL/TM-9497	Period April 1984-September 1984
ORNL/TM-9673	Period October 1984-March 1985
ORNL/TM-9947	Period April 1985-September 1985
ORNL/TM-10079	Period October 1985-March 1986
ORNL/TM-10308	Period April 1986-September 1986
ORNL/TM-10469	Period October 1986-March 1987
ORNL/TM-10705	Period April 1987-September 1987
ORNL/TM-10838	Period October 1987-March 1988
ORNL/TM-11116	Period April 1988-September 1988
ORNL/TM-11239	Period October 1988-March 1989
ORNL/TM-11489	Period April 1989-September 1989

Research sponsored by the U.S. Department of Energy, Assistant Secretary for Conservation and Renewable Energy, Office of Transportation Technologies, as part of the Ceramic Technology for Advanced Heat Engines Project of the Advanced Materials Development Program, under contract DE-AC05-84OR21400 with Martin Marietta Energy Systems, Inc.

CONTENTS

SUMMARY 1

0.0 PROJECT MANAGEMENT AND COORDINATION 3

1.0 MATERIALS AND PROCESSING 5

INTRODUCTION 5

1.1 MONOLITHICS 7

1.1.1 *Turbomilling of SiC Whiskers* (Southern Illinois University) 7

1.1.2 Silicon Nitride 18

Microwave Sintering of Silicon Nitride (ORNL) . . . 18

Silicon Nitride Milling Characterization (NIST) . . 30

1.1.4 Processing of Monolithics 36

Improved Processing (Norton) 36

Improved Processing (ORNL) 73

Improved Processing (GTE) 77

Processing Science for Si_3N_4 Ceramics (University of California) 106

1.2 CERAMIC COMPOSITES 110

1.2.2 Silicon Nitride Matrix 110

SiC-Whisker-Toughened Silicon Nitride (Garrett) . . 110

Silicon Nitride-Metal Carbide Composites (GTE) . . . 132

Fabrication of Si_3N_4/SiC Composites by Transient Liquid Phase Sintering (University of Michigan) . . 150

1.2.3 Oxide Matrix 161

Dispersion-Toughened Oxide Composites (ORNL) 161

Processing and Characterization of Transformation-Toughened Ceramics with Strength Retention to Elevated Temperatures (Ceramatec) 163

1.2.4 Silicate Matrix 174

Low Expansion Ceramics for Diesel Engine Applications (VPI) 174

1.3 THERMAL AND WEAR COATINGS 200

1.3.1 ZrO_2 Base Coatings 200

Advanced Coating Technology (ORNL) 200

Development of Adherent Ceramic Coatings to Reduce Contact Stress Damage of Ceramics (GTE) 204

Wear-Resistant Coatings (Caterpillar) 214

Development of Wear Resistant Ceramic Coatings for Diesel Engine Components (Cummins) 219

1.4 JOINING 238

1.4.1 Ceramic-Metal Joints 238

Joining of Ceramics for Heat Engine Applications (ORNL) 238

Analytical and Experimental Evaluation of Joining Silicon Nitride to Metal and Silicon Carbide to Metal for Advanced Heat Engine Applications (GTE) . 243

Analytical and Experimental Evaluation of Joining Ceramic Oxides to Ceramic Oxides and Ceramic Oxides to Metal for Advanced Heat Engine Applications (Battelle Columbus Laboratories) 255

Analytical and Experimental Evaluation of Joining Silicon Carbide to Silicon Carbide and Silicon Nitride to Silicon Nitride for Advanced Heat Engine Applications (Norton) 262

2.0 MATERIALS DESIGN METHODOLOGY 281

INTRODUCTION 281

2.1 MODELING 283

2.1.1 Modeling 283

Microstructural Modeling of Cracks (University of Tennessee) 283

2.2 CONTACT INTERFACES 286

2.2.1 Static Interfaces 286

Elastic Properties and Adherence of Thin Films and Coatings (University of Tennessee) 286

2.2.2 Dynamic Interfaces 288

Studies of Dynamic Contact of Ceramics and Alloys for Advanced Heat Engines (Battelle) 288

2.3 NEW CONCEPTS 298

Advanced Statistical Concepts of Fracture in Brittle Materials (GE) 298

3.0 DATA BASE AND LIFE PREDICTION 317

INTRODUCTION 317

3.1 STRUCTURAL QUALIFICATION 319

Microstructural Analysis of Structural Ceramics (NIST) 319

Microstructural Characterization (ORNL) 330

Project Data Base (ORNL) 344

3.2 TIME-DEPENDENT BEHAVIOR 347

Characterization of Transformation-Toughened Ceramics (AMTL) 347

Fracture Behavior of Toughened Ceramics (ORNL) . . . 352

Cyclic Fatigue of Toughened Ceramics (ORNL) 359

Rotor Data Base Generation (ORNL) 373

Toughened Ceramics Life Prediction (NASA-Lewis Research Center) 383

Life Prediction Methodology (Allison) 397

Life Prediction Methodology (GAPD) 402

3.3 ENVIRONMENTAL EFFECTS 412

Environmental Effects in Toughened Ceramics (University of Dayton) 412

Low Heat Rejection Diesel Coupon Tests (ORNL) . . . 438

3.4 FRACTURE MECHANICS 440

Testing and Evaluation of Advanced Ceramics at High Temperature in Uniaxial Tension (North Carolina A&T State University) 440

Standard Tensile Test Development (NIST) 447

3.5 NONDESTRUCTIVE EVALUATION DEVELOPMENT 453

Nondestructive Characterization (ORNL) 453

NDE Standards for Advanced Ceramics (ORNL) 461

X-Ray Computed Tomographic Imaging (ANL) 462

Nuclear Magnetic Resonance Imaging (ANL) 468

Powder Characterization (ORNL) 476

Spectroscopic Characterization (University of Wisconsin-Madison) 478

Surface Adsorption (Pennsylvania State University) . 487

Surface Thermodynamics (Rutgers University) 490

4.0 TECHNOLOGY TRANSFER 499

4.1 TECHNOLOGY TRANSFER 499

4.1.1 *Technology Transfer* (ORNL) 499

IEA Annex II Management (ORNL) 500

Standard Reference Materials (NIST) 504

CERAMIC TECHNOLOGY FOR ADVANCED HEAT ENGINES PROJECT SEMIANNUAL PROGRESS REPORT FOR OCTOBER 1989 THROUGH MARCH 1990

SUMMARY

The Ceramic Technology for Advanced Heat Engines Project was developed by the Department of Energy's Office of Transportation Systems (now the Office of Transportation Technologies, OTT) in Conservation and Renewable Energy. This project, part of the OTT's Advanced Materials Development Program, was developed to meet the ceramic technology requirements of the OTT's automotive technology programs.

Significant accomplishments in fabricating ceramic components for the Department of Energy (DOE), National Aeronautics and Space Administration (NASA), and Department of Defense (DoD) advanced heat engine programs have provided evidence that the operation of ceramic parts in high-temperature engine environments is feasible. However, these programs have also demonstrated that additional research is needed in materials and processing development, design methodology, and data base and life prediction before industry will have a sufficient technology base from which to produce reliable cost-effective ceramic engine components commercially.

An assessment of needs was completed, and a five-year project plan was developed with extensive input from private industry. The objective of the project is to develop the industrial technology base required for reliable ceramics for application in advanced automotive heat engines. The project approach includes determining the mechanisms controlling reliability, improving processes for fabricating existing ceramics, developing new materials with increased reliability, and testing these materials in simulated engine environments to confirm reliability. Although this is a generic materials project, the focus is on the structural ceramics for advanced gas turbine and diesel engines, ceramic bearings and attachments, and ceramic coatings for thermal barrier and wear applications in these engines. This advanced materials technology is being developed in parallel and close coordination with the ongoing DOE and industry proof-of-concept engine development programs. To facilitate the rapid transfer of this technology to U.S. industry, the major portion of the work is being done in the ceramic industry, with technological support from government laboratories, other industrial laboratories, and universities.

This project is managed by ORNL for the Office of Transportation Technologies and is closely coordinated with complementary ceramics tasks funded by other DOE offices, NASA, DoD, and industry. A joint DOE and NASA technical plan has been established, with DOE focus on automotive applications and NASA focus on aerospace applications. A common work breakdown structure (WBS) was developed to facilitate coordination. The work described in this report is organized according to the following WBS project elements:

0.0 Management and Coordination

1.0 Materials and Processing

- 1.1 Monolithics
- 1.2 Ceramic Composites
- 1.3 Thermal and Wear Coatings
- 1.4 Joining

2.1 Materials Design Methodology

- 2.1 Modeling
- 2.2 Contact Interfaces
- 2.3 New Concepts

3.0 Data Base and Life Prediction

- 3.1 Structural Qualification
- 3.2 Time-Dependent Behavior
- 3.3 Environmental Effects
- 3.4 Fracture Mechanics
- 3.5 NDE Development

4.0 Technology Transfer

This report includes contributions from all currently active project participants. The contributions are arranged according to the work breakdown structure outline.

0.0 PROJECT MANAGEMENT AND COORDINATION

D. R. Johnson
Oak Ridge National Laboratory

Objective/scope

This task includes the technical management of the project in accordance with the project plans and management plan approved by the Department of Energy (DOE) Oak Ridge Operations Office (ORO) and the Office of Transportation Technologies. This task includes preparation of annual field task proposals, initiation and management of subcontracts and interagency agreements, and management of ORNL technical tasks. Monthly management reports and bimonthly reports are provided to DOE; highlights and semiannual technical reports are provided to DOE and program participants. In addition, the program is coordinated with interfacing programs sponsored by other DOE offices and federal agencies, including the National Aeronautics and Space Administration (NASA) and the Department of Defense (DoD). This coordination is accomplished by participation in bimonthly DOE and NASA joint management meetings, annual interagency heat engine ceramics coordination meetings, DOE contractor coordination meetings, and DOE Energy Materials Coordinating Committee (EMaCC) meetings, as well as special coordination meetings.

1.0 MATERIALS AND PROCESSING

INTRODUCTION

This portion of the project is identified as project element 1.0 within the work breakdown structure (WBS). It contains four subelements: (1) Monolithics, (2) Ceramic Composites, (3) Thermal and Wear Coatings, and (4) Joining. Ceramic research conducted within the Monolithics subelement currently includes work activities on green state ceramic fabrication, characterization, and densification and on structural, mechanical, and physical properties of these ceramics. Research conducted within the Ceramic Composites subelement currently includes silicon nitride and oxide-based composites, which, in addition to the work activities cited for Monolithics, include fiber synthesis and characterization. Research conducted in the Thermal and Wear Coatings subelement is currently limited to oxide-base coatings and involves coating synthesis, characterization, and determination of the mechanical and physical properties of the coatings. Research conducted in the Joining subelement currently includes studies of processes to produce strong stable joints between zirconia ceramics and iron-base alloys, as well as Si_3N_4- and SiC-to-metal joints, and SiC-to-SiC and Si_3N_4-to-Si_3N_4 joints.

A major objective of the research in the Materials and Processing project element is to systematically advance the understanding of the relationships between ceramic raw materials such as powders and reactant gases, the processing variables involved in producing the ceramic materials, and the resultant microstructures and physical and mechanical properties of the ceramic materials. Success in meeting this objective will provide U.S. companies with new or improved ways for producing economical, highly reliable ceramic components for advanced heat engines.

1.1 MONOLITHICS

1.1.1 Silicon Carbide

Turbomilling of SiC Whiskers
D. E. Wittmer (Southern Illinois University)

Objective/Scope

The purpose of this work is to continue the investigation of the turbomilling process as a means of improved processing for SiC whisker-ceramic matrix composites and dispersion of matrix powders prior to composite processing.

Technical Progress

Phase II is divided into 4 major tasks:

Task 1. Beneficiation of SiC whiskers.
Task 2. Development of aspect ratio reduction parameters.
Task 3. Improved dispersion of particulate matrices.
Task 4. Final Report

Task 1. Beneficiation of SiC whiskers

During this reporting period, Task 1 was completed. Both coarse and fine whisker fractions were heat treated in $Ar/4\%H_2$ for 1 hour at 1400°C and then stored under vacuum for use later in Task 3. Spectrographic analyses showed that this heat treatment reduces the boron, silica and calcia content in the as-received whiskers. Reduction in these constituents should lead to better high-temperature properties.

Task 2. Development of aspect ratio reduction parameters

Work continued, during this reporting period, to determine the effects of turbomilling on the SiCw aspect ratio during turbomilling and processing of the whiskers alone and whisker/ceramic matrix composites for both Al_2O_3 and Si_3N_4 matrices. Direct optical measurements and measurements from SEM photomicrographs of AMI SiCW

processed by turbomilling have been compared to results obtained from an image analysis system. The results indicate a close agreement between lengths and aspect ratios measured directly by image analysis and indirectly from SEM photomicrographs. Direct optical measurements techniques appear more prone to operator error and eye fatigue.

In addition to the data obtained from the turbomilled AMI SiCW analyzed prior to addition to the matrix materials, volume fraction of whisker, particulate and matrix was determined for both Al_2O_3 and Si_3N_4 matrix hot-pressed composites. Both optical microscopy and scanning electron microscopy were utilized to make measurements of the SiCw diameters and lengths for 4 length ranges, L<4 μm, 4 μm<L<8 μm, 8 μm<L<16 μm, and L>16 μm. Volume fraction distributions of SiCw for each whisker length range, both excluding and including the particulate fraction, were calculated based on the average diameters and lengths for each range. The particulate was assumed spherical for all calculations. The results are given graphically in a series of bar charts (Fig. 1 through 6).

Fig. 1 shows the effect of turbomilling on the volume fraction of SiCw with and without the Al_2O_3 matrix, excluding the contribution due to the particulate fraction. For the SiCw alone, the aspect ratio distribution appears to decrease almost linearly from L>16 μm to L<4 μm. When the SiCw were added to the Al_2O_3 matrix in volume fractions of 20 and 30 vol.% (AR-20 and AR-30, where AR stands for American Matrix, Inc. SiCw in Reynolds RCHP-DBM matrix), the volume of high aspect ratio whiskers appear to be reduced considerably.

Fig. 2 is for the same whiskers and composites analyzed in Fig. 1, only now the particulate fraction has been taken into account in the calculation of the volume fractions. For the SiCw alone, the fine fraction is increased considerably. The effect of the addition of the whiskers to the matrix is seen to have an even greater effect, with a large increase in the volume of low aspect ratio whiskers (L<8 μm) and corresponding decrease in the volume of higher aspect ratio whiskers.

Fig. 3 shows a comparison of the SiCw data for the Al_2O_3 matrix composites both with and without the particulate fraction considered. When the particulate

Figure 1.

Effect of Turbomilling on Vol. Fraction of SiCw With and Without Al_2O_3 Matrix

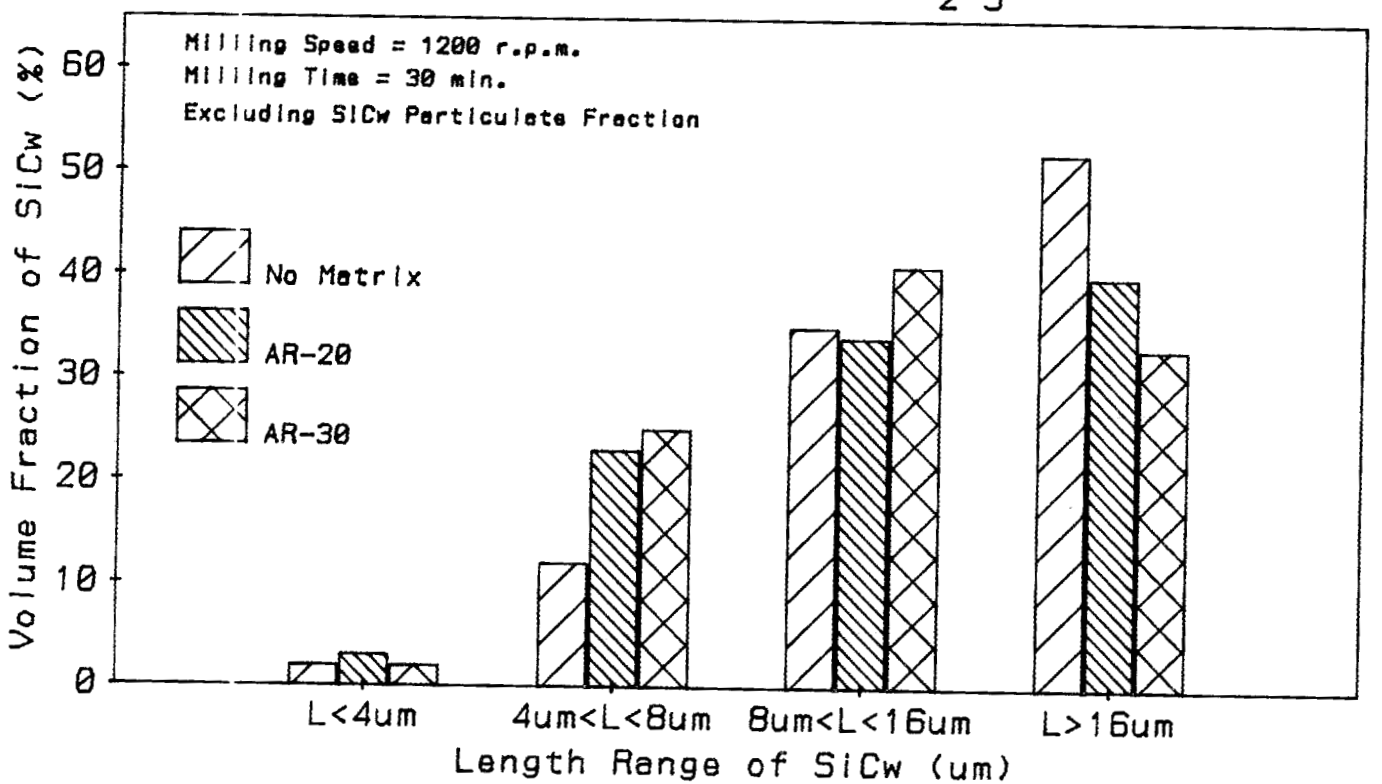

Figure 2.

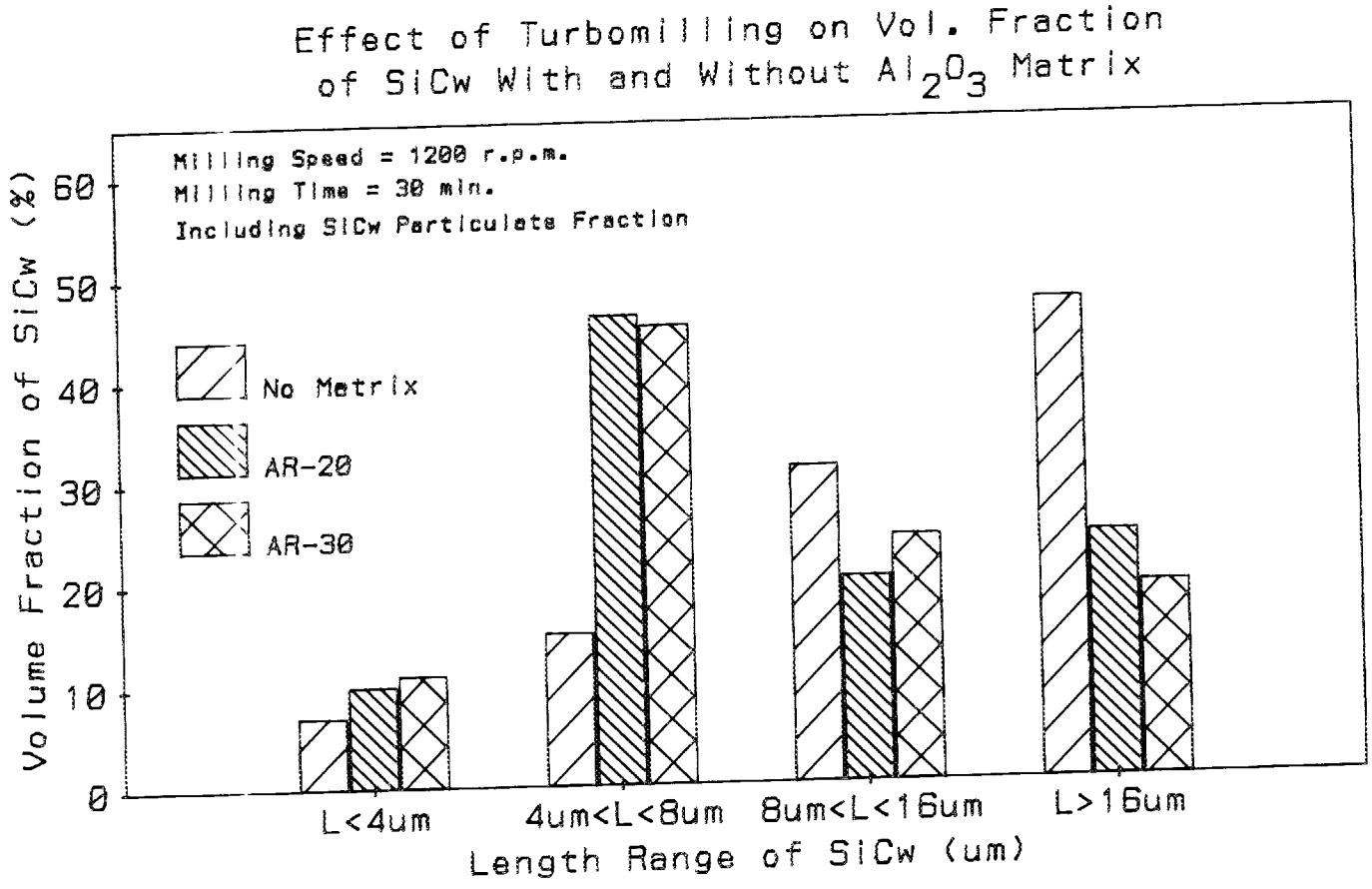
Effect of Turbomilling on Vol. Fraction
of SiCw With and Without Al_2O_3 Matrix
Milling Speed = 1200 r.p.m.
Milling Time = 30 min.
Including SiCw Particulate Fraction
No Metrix
AR-20
AR-30
Volume Fraction of SiCw (%)
0
10
20
30
40
50
60
L<4um
4um<L<8um
8um<L<16um
L>16um
Length Range of SiCw (um)

Figure 3.

Comparison of SiCw Data for Al_2O_3 Matrix With and Without Fraction of Particulate

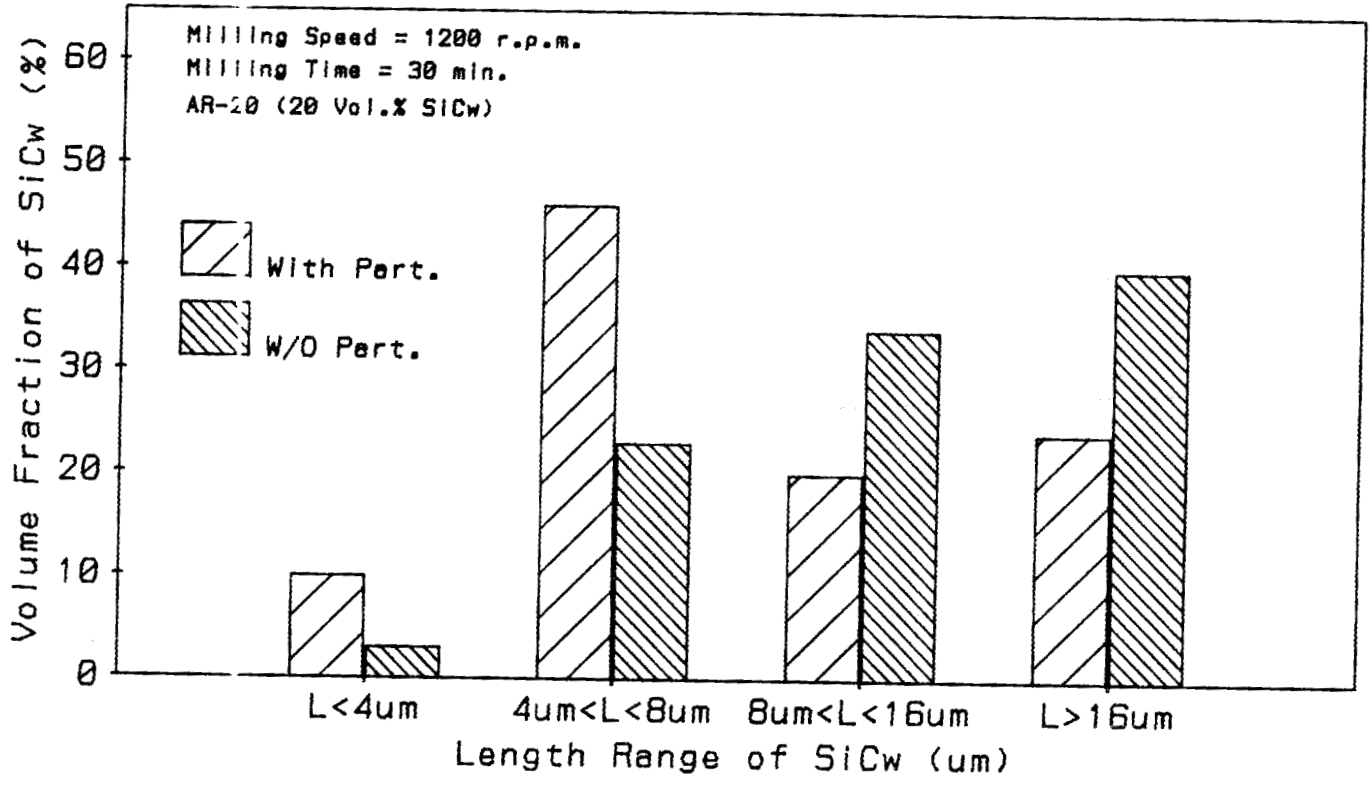

Figure 4.

Effect of Turbomilling on Vol. Fraction of SiCw With and Without Si_3N_4 Matrix

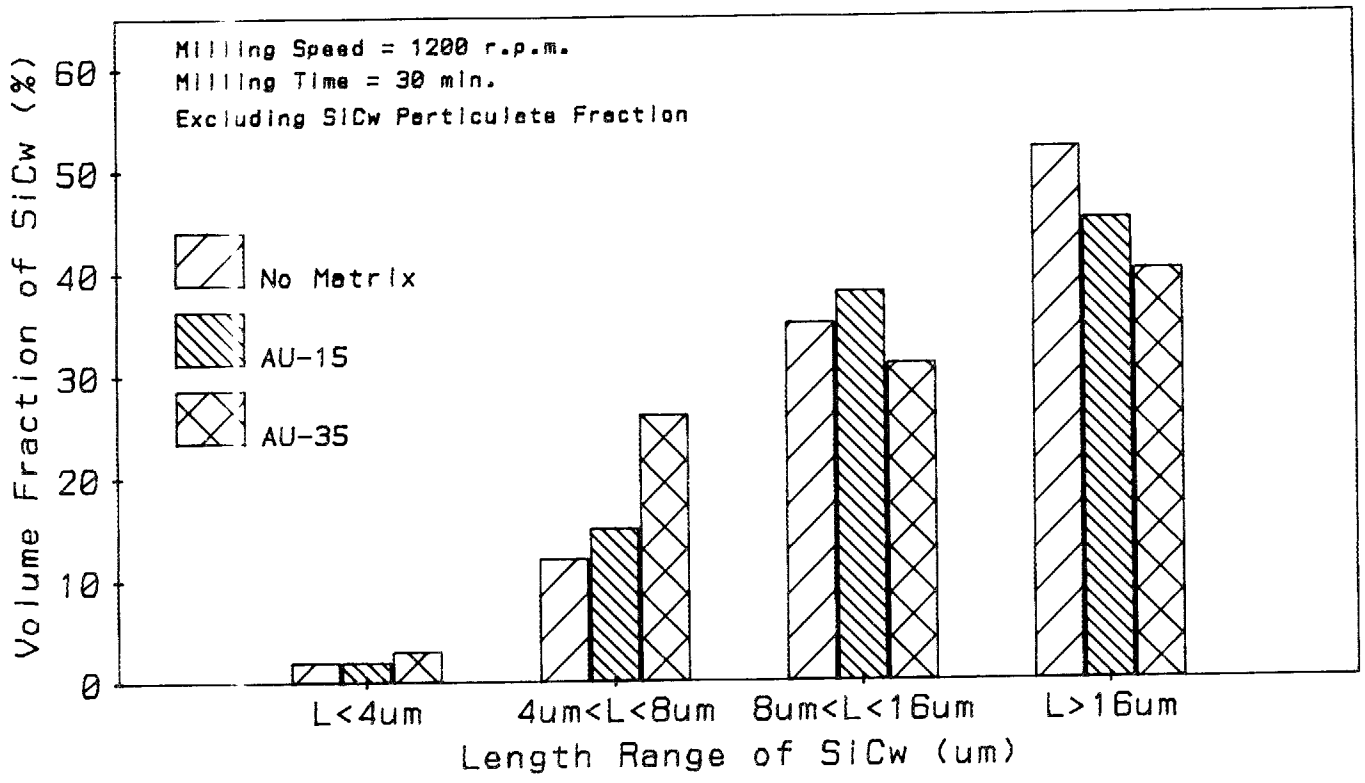

Figure 5.

Effect of Turbomilling on Vol. Fraction of SiCw With and Without Si_3N_4 Matrix

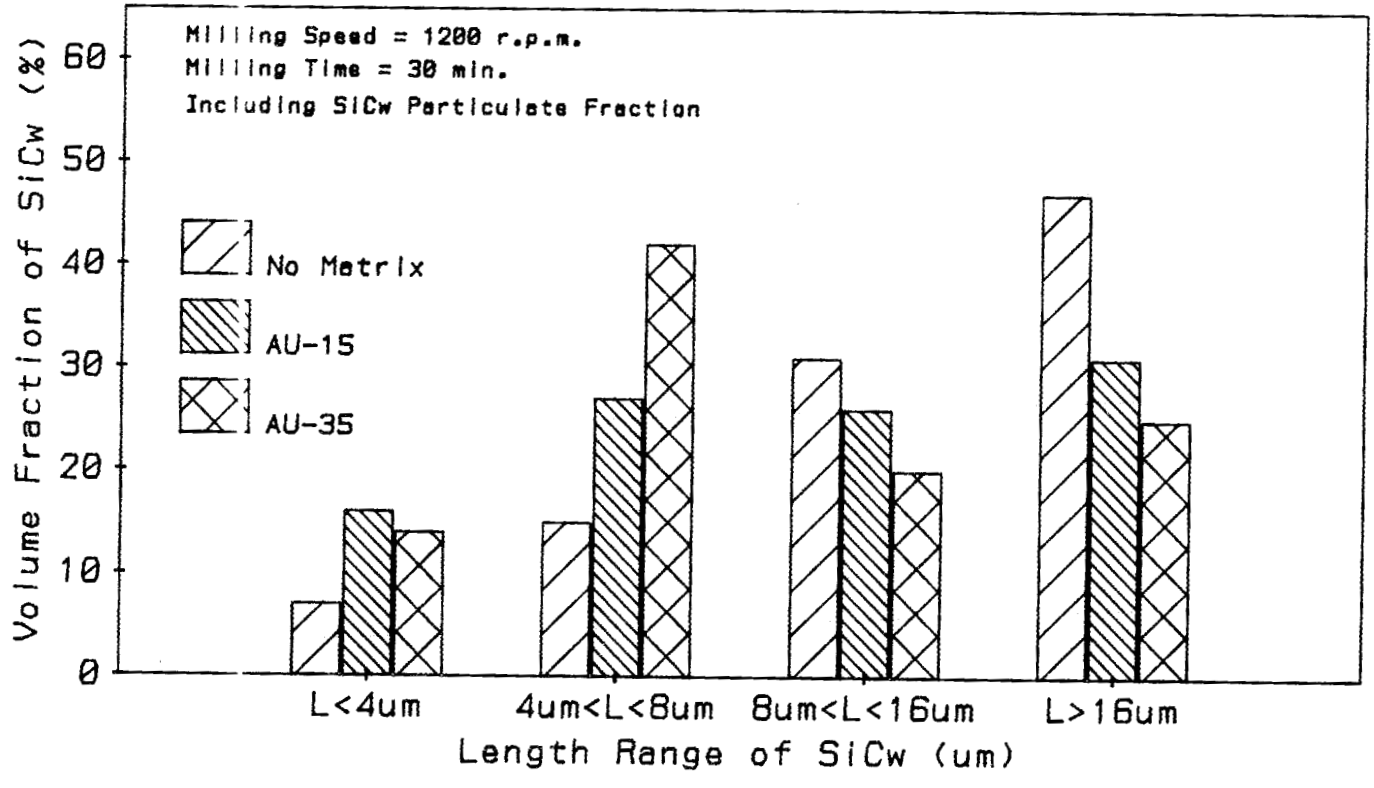

Figure 6.

Comparison of SiCw Data for Si_3N_4 Matrix
With and Without Fraction of Particulate

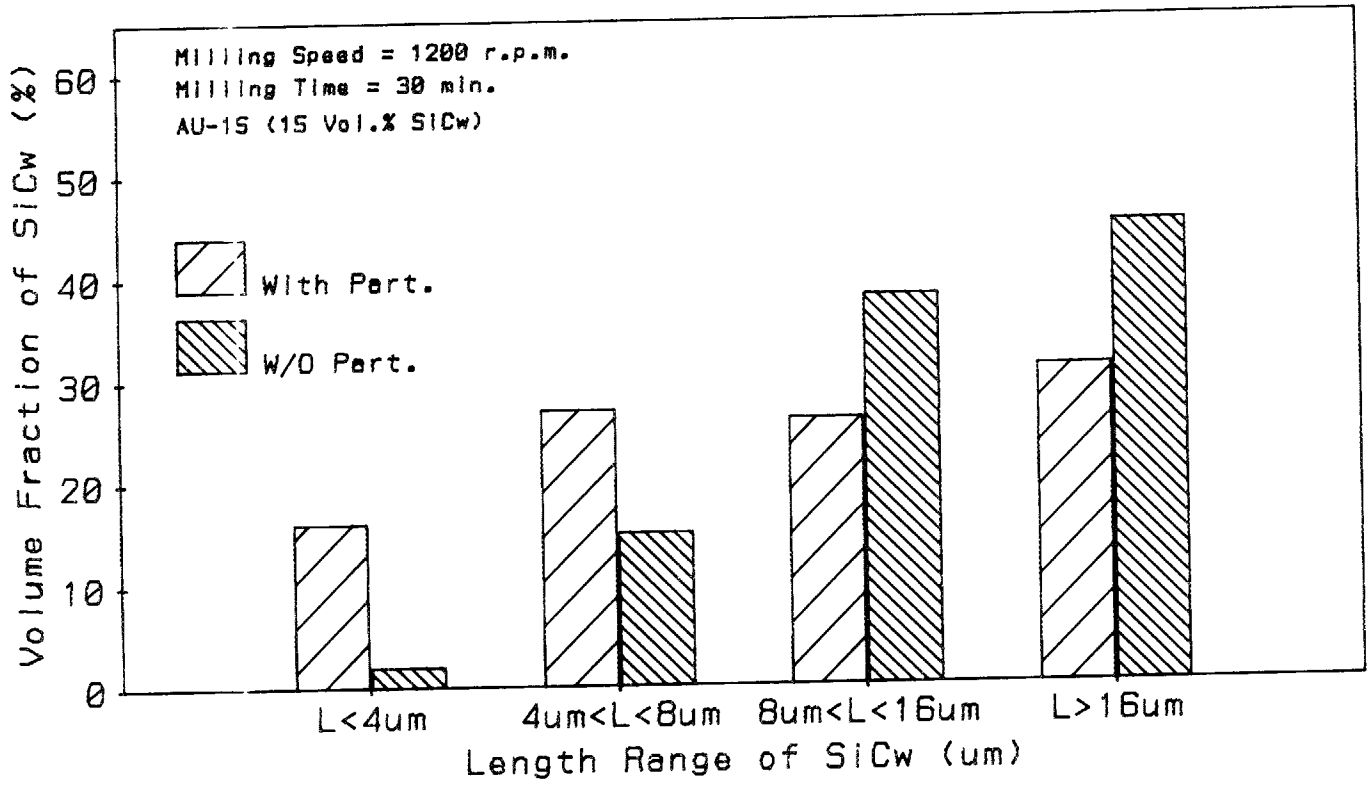

fraction is considered the volume of the SiC in the range of 4 μm<L<8 μm is almost double that shown when the particulate fraction is excluded from the calculations.

A similar behavior was observed for the Si_3N_4 matrix composites containing 15 and 35 vol.% SiCw (AU-15 and AU-35, where the AU stands for American Matrix, Inc. SiCw in UBE E-10 Si_3N_4). Fig. 4 shows the results where the particulate was excluded from the calculations, while Fig. 5 includes the particulate fraction. Fig. 6 shows a comparison of the SiCw data for the Si_3N_4 matrix composites both with and without the particulate fraction considered. When the particulate fraction is considered, the volume fraction of the SiCw is almost linear and equivalent for the 4 length ranges considered. The largest increase though is for the SiCw with L<4 μm.

From observations made during this Task, the following conclusions can be made:

- Processing of the SiCw in the Al_2O_3 and Si_3N_4 matrices appears to reduce the volume fraction of whiskers with L>8 μm and increase the particulate fraction for L<8 μm.

- The total volume of SiC in the composite is comprised of both SiCw and a substantial portion of SiC particulate.

- Removal of the particulate prior to composite processing would lead to higher SiCw volume per unit weight for any given composite formulation.

- Removal of the particulate should also lead to an enhancement in the strength and fracture toughness.

Presently work is continuing to develop techniques for the measurement of SiCw aspect ratio in situ during processing of SiCw/Si_3N_4 matrix composite slurry utilizing a Lasentech 150 Fiber Analyzer. This instrument is basically a scanning laser microscope that can be calibrated to measure whisker lengths in high solids loaded slurries.

Task 3. Improved dispersion of particulate matrices

During this reporting period, Task 3 was altered to focus on the effect of temperature, dispersant and pH on the flocculation/dispersion behavior of the Al_2O_3 and Si_3N_4 matrix materials to determine optimum conditions for turbomilling and pressure filtration of the monolithic matrix, prior to the addition of SiCW. Prior work indicated that turbomilling for 1-2 hours using PSZ media is sufficient to physically disperse and deagglomerate any of the matrix materials and wet screening through a 600 mesh sieve following turbomilling will remove the large particulate and any hard agglomerates remaining. However, the stability of the dispersion and control of the flocculation behavior, following turbomilling and screening, appear to greatly affect the success of subsequent processing.

Presently the 2 sources of Al_2O_3, 3 sources of Si_3N_4, and 2 sources of Y_2O_3 powders used for processing both Al_2O_3 and Si_3N_4 matrix composites are being analyzed for their flocculation/dispersion behavior as functions of pH, time and temperature. The results of this task should be of benefit to processing of monolithic ceramics, self-reinforcing ceramics, and whisker reinforced ceramics.

Status of Milestones

Phase II:

Task 1.	Beneficiation of SiC whiskers	Oct. '89 (Completed)
Task 2.	Development of aspect ratio reduction parameters.	July '90
Task 3.	Improved dispersion of matrices	Aug. '90
Task 4.	Final Report	Sept.'90

Presentations and Publications

D. E. Wittmer, W. Trimble, and T. Paulson, "Processing of Ceramic Matrix Composites by Turbomilling", Proceedings of the Vacuum Industries Symposium on High Temperature Materials, Boston, MA, Oct. 18-20, 1989.

D. E. Wittmer, "Processing of SiC_w Reinforced Ceramic Matrix Composites", Invited Seminar, University of Illinois at Urbana-Champaign, Urbana, IL, Oct. 12, 1989.

D. E. Wittmer and T. Paulson, "Effect of Turbomilling on Beneficiation and Aspect Ratio of SiCw" 14th Annual Conference on Composites and Advanced Ceramics Materials, Cocoa Beach, FL, Jan. 14-19, 1990.

T. Paulson and D. Wittmer, "Effect of Beneficiation on Aspect Ratio and Properties of $SiCw/Si_3N_4$ Composites", 92nd Annual Am. Ceram. Soc. Meeting Abstracts, Dallas, TX, April 22-26, 1990, pp. 74.

1.1.2 Silicon Nitride

Microwave Sintering of Silicon Nitride

T. N. Tiegs, H. D. Kimrey, Jr., J. O. Kiggans, Jr., and P. A. Menchhofer
(Oak Ridge National Laboratory)

Objective/scope

The objective of this research element is to identify those aspects of microwave processing of silicon nitride that might (1) accelerate densification, (2) permit sintering to high density with much lower levels of sintering aids, (3) lower the sintering temperature, or (4) produce unique microstructures. The investigation of microstructure development is being done on dense silicon nitride materials annealed in the microwave furnace. The sintering of silicon nitride involves two approaches. The first approach comprises heating of silicon nitride and sialon powder compositions in the 2.45- or 28-GHz units. The second approach deals with using reaction-bonded silicon nitride as the starting material and is done entirely in the 2.45-GHz microwave furnace.

Technical progress

Sintering of silicon nitride

As reported previously, Si_3N_4 is very difficult to heat uniformly by microwaves and produce crack-free specimens. Analysis of power curves for various Si_3N_4 compositions from successful and unsuccessful sintering runs showed that the heating is dependent on the heating rate and the amounts of additives. Unsuccessful sintering runs showed high initial power requirements and low efficiency. Examples of the temperature and power curves are shown in Figs. 1 through 4. In the analysis it was observed that a power relaxation occurs for the Si_3N_4-Y_2O_3-Al_2O_3 materials in the temperature range of 1200 to 1400°C. Reaction of the sintering aids to form a complex glass was observed in essentially all samples and is believed to be responsible for the coupling behavior (Fig. 5).

Previous results showed Si_3N_4-6% Y_2O_3-2% Al_2O_3 (with and without TiN and SiC additions) could be sintered in the 28-GHz microwave furnace to densities of 90 to 93% TD at 1750°C for 1 h. Compositions of Si_3N_4-12% Y_2O_3-4% Al_2O_3 (with and without the TiN, TiC, and SiC additions) were fabricated and fired in the 2.45-GHz and 28-GHz furnaces at 1750°C. Those results are summarized in Table 1. As shown, higher densities were achieved with microwave heating as compared to conventional firing. However, for the compositions with high sintering aid contents the difference is not very significant. Of major concern is the fact that we are still unable to obtain fully dense materials even with excessive amounts of sintering aids. Some of the problem may be with the starting Si_3N_4 powder used (Ube E10) which is difficult to pressureless sinter under 1 atm of nitrogen and with short holding times at temperature. Extending the firing times to 2 h improved the conventionally fired densities, but gave mixed results with the microwave-heated samples tested so far. Extending the time at temperature may have resulted in volatilization and weight loss problems which are exaggerated in the microwave system. Immediate plans will examine use of other Si_3N_4 starting powders (such as Ube E03 and Starck LC-12) and also develop alternate packing powder combinations to minimize weight losses during microwave sintering.

While the sintered densities achieved were not as high as desired, significant progress was made in the ability to produce crack-free specimens in the 2.45-GHz furnace. The initial results in that cavity, reported previously, were dismal. However, improvements in sample configuration and packing powder compositions have been made to permit more uniform heating.

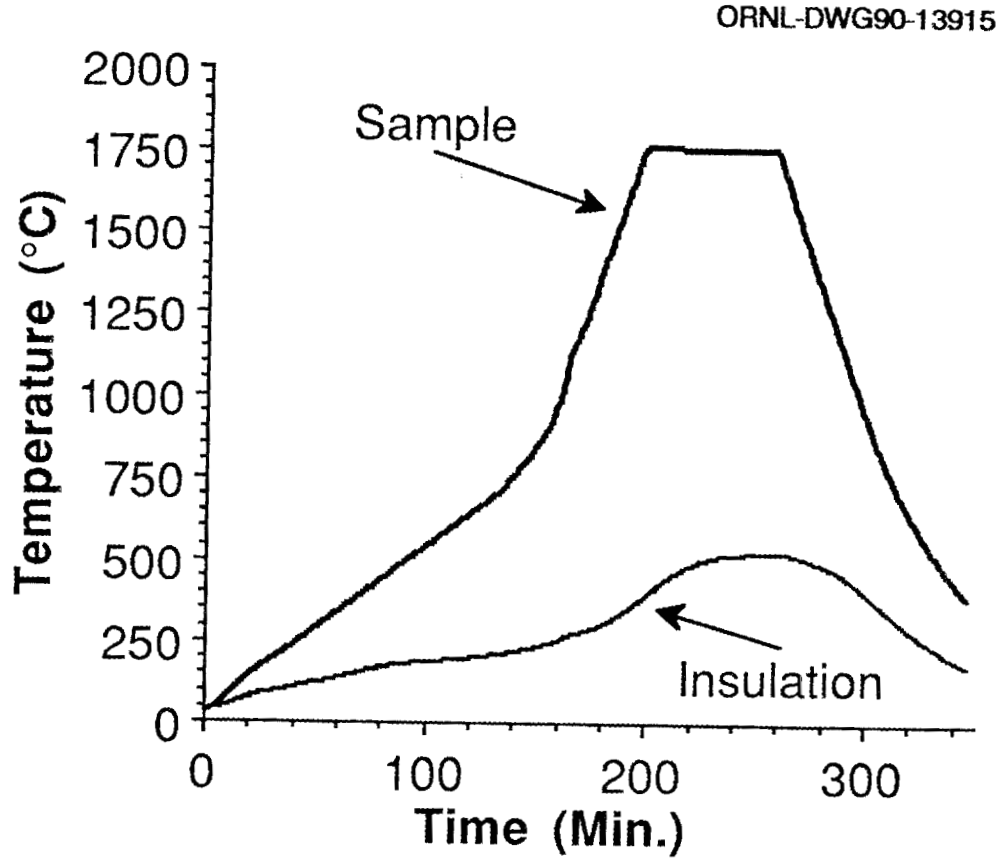

Fig. 1. Temperature profile in 2.45-GHz microwave furnace for sintering of Si_3N_4-6% Y_2O_3-2% Al_2O_3 which showed specimen cracking.

ORNL-DWG90-13916

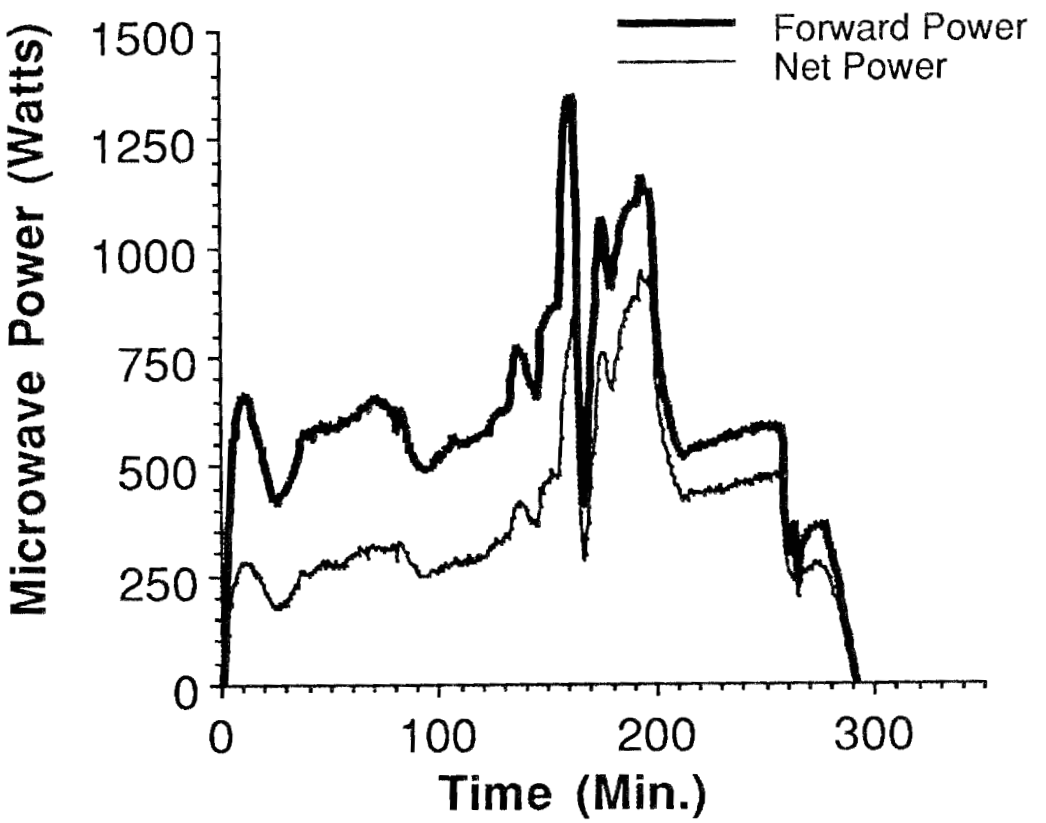

Fig. 2. Power curves in 2.45-GHz microwave furnace for sintering of Si_3N_4-6% Y_2O_3-2% Al_2O_3 showing high initial power requirements and low efficiency. Samples generally developed cracks.

ORNL-DWG90-13917

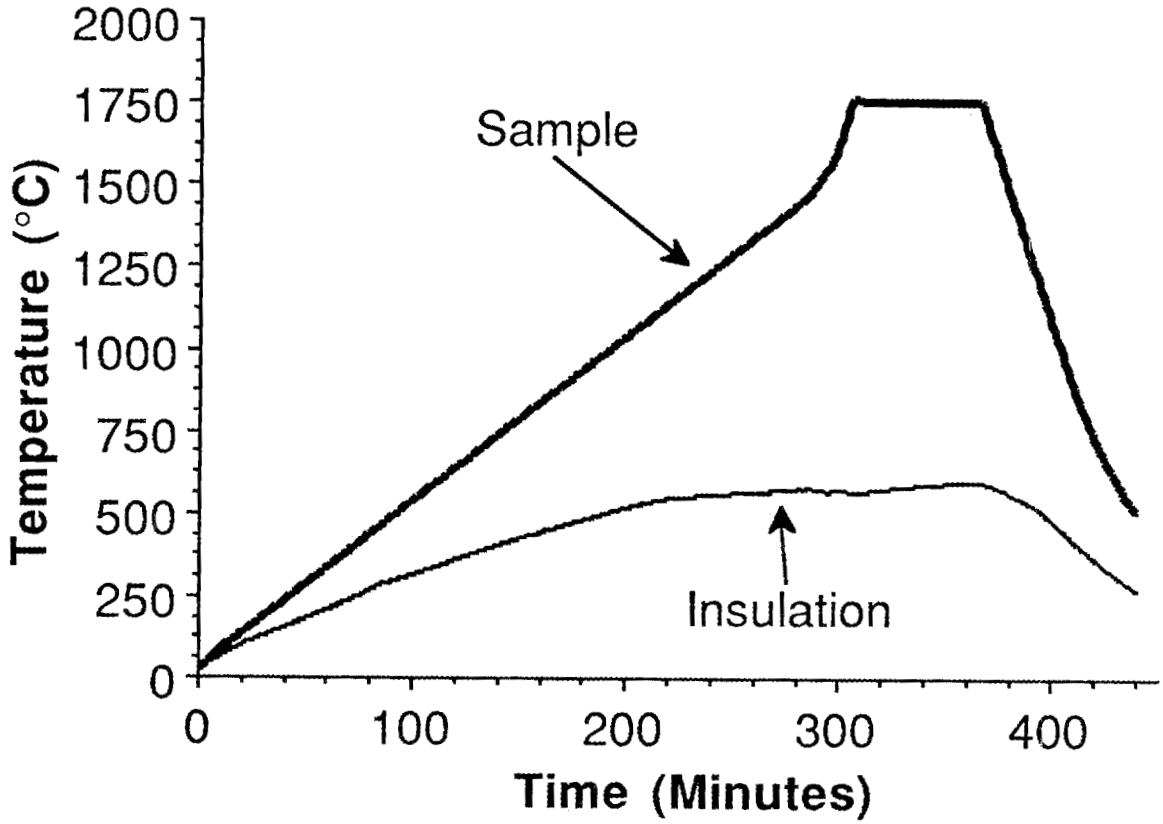

Fig. 3. Temperature curves in 2.45-GHz microwave furnace for sintering of Si_3N_4-12% Y_2O_3-4% Al_2O_3 samples that were generally crack free.

ORNL-DWG90-13918

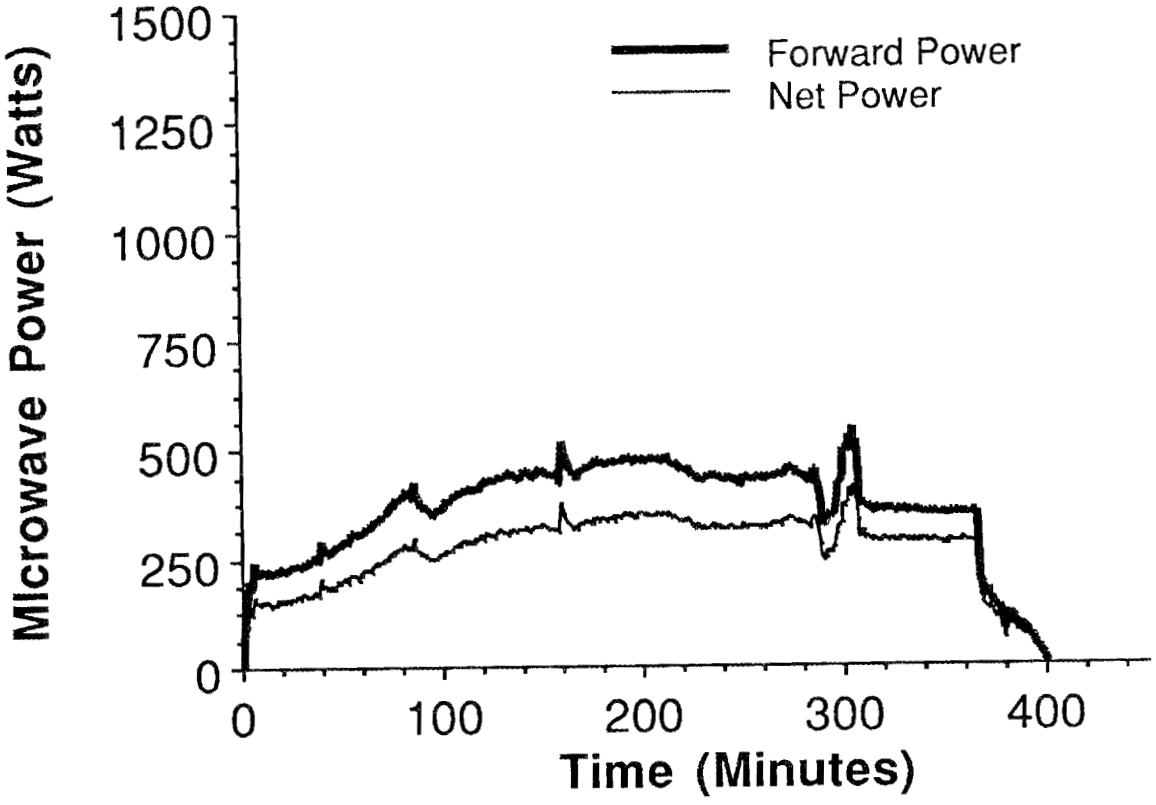

Fig. 4. Power curves in 2.45-GHz microwave furnace for sintering of Si_3N_4-12% Y_2O_3-4% Al_2O_3 showing lower initial power requirements and higher efficiency. The samples were crack free.

ORNL-DWG90-13919

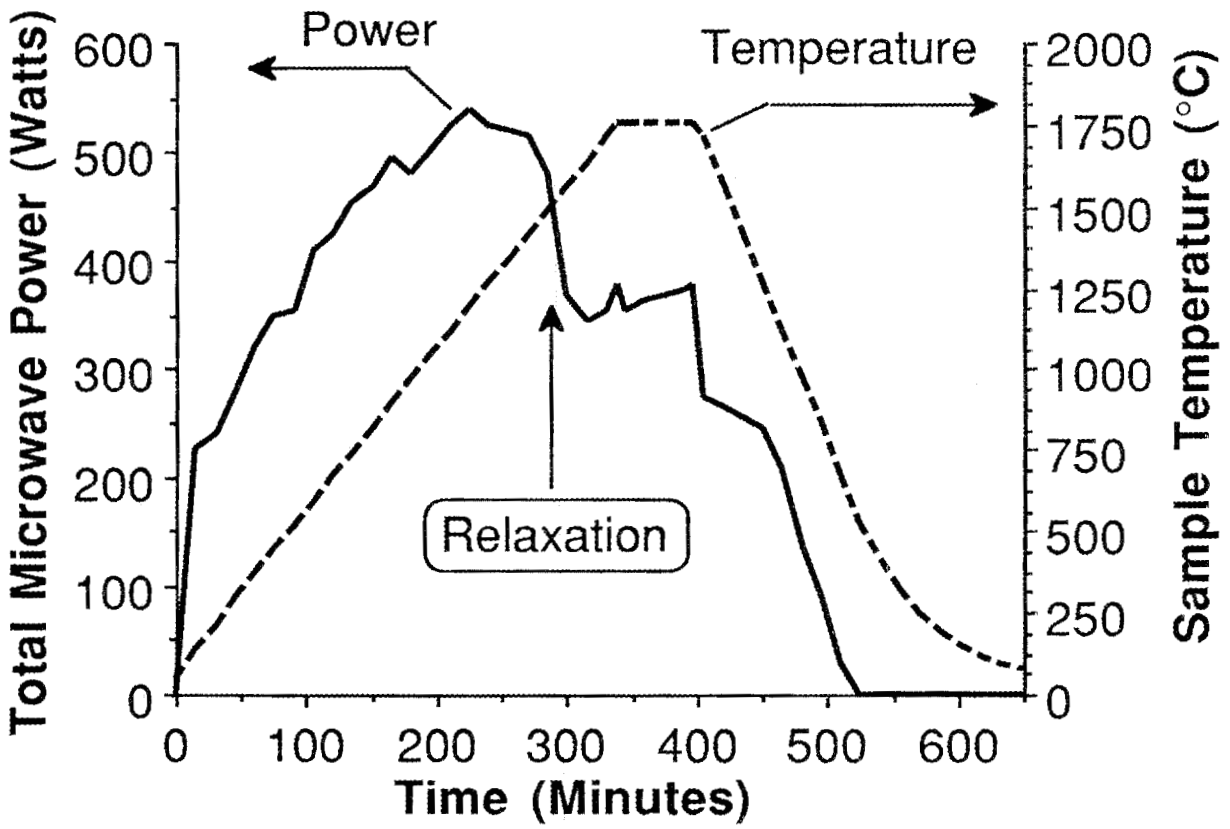

Fig. 5. Power and temperature profile for Si_3N_4-12% Y_2O_3-4% Al_2O_3 illustrating relaxation in temperature range of 1200 to 1400°C.

Table 1. Sintered densities of silicon nitride materials by conventional and microwave heating[a]

Composition	Conventional heated		Microwave heated		
	1 h	2 h	28 GHz 1 h	2.45 GHz 1 h	2.45 GHz 2 h
Si_3N_4-2% Al_2O_3-6% Y_2O_3	75.4	-	89.9	80-85	-
Si_3N_4-2% SiC-2% Al_2O_3-6% Y_2O_3	79.9	-	93.3	80-85	-
Si_3N_4-2% TiC-2% Al_2O_3-6% Y_2O_3	78.7	-	-	80-85	-
Si_3N_4-2% TiN-2% Al_2O_3-6% Y_2O_3	81.8	-	91.1	80-85	-
Si_3N_4-4% Al_2O_3-12% Y_2O_3	87.3	92.9	91.0	96.0	96.4
Si_3N_4-2% SiC-4% Al_2O_3-12% Y_2O_3	-	-	95.6	95.7	94.3
Si_3N_4-2% TiC-4% Al_2O_3-12% Y_2O_3	-	-	93.5	93.1	-
Si_3N_4-2% TiN-4% Al_2O_3-12% Y_2O_3	94.6	97.3	96.6	96.1	-

[a]All samples sintered at 1750°C for the times shown at 1 atm of nitrogen. Samples packed in excess Si_3N_4 powder with 2 % Y_2O_3.

Reaction-bonded silicon nitride (RBSN)

Previous results showed enhanced reaction rates for the nitridation of silicon in the 2.45-GHz microwave furnace as compared to conventional heating. While the nitridation was usually uniform, the center of the samples always contained some unreacted silicon that would experience melting in some cases. The sample sizes were typically 100 g of Si-6% Y_2O_3-2% Al_2O_3 with cross sections of ≤3.8 mm (1.5 in.). Such samples are rather thick in comparison to others in much of the nitridation experiments in the literature. To establish the parameters required to nitride samples of this size, a series of tests were done varying the heating rate, insulation configurations, and nitrogen gas additions.

The tests showed significant temperature gradients existed in the silicon parts that were most likely due to a nonuniform microwave field in that location of the cavity. Modification of the insulation configuration, using a slower heating rate (0.2-1°C/min), and making the nitrogen additions at elevated temperatures resulted in uniform nitridation of the Si-6% Y_2O_3-2% Al_2O_3 samples and weight gains that corresponded to ≥95% reaction of the initial silicon. However, the full cycle times went from ~22 to 36 h for the current sample size. It is anticipated that the cycle time can be significantly reduced by use of specimens with smaller cross sections, but for the near term the larger sample size will be used.

Microstructure development

As reported previously, an annealing study was performed to investigate microstructural development of silicon nitride in a microwave furnace. Samples of Si_3N_4-4% Y_2O_3 and Si_3N_4-6% Y_2O_3-2% Al_2O_3 were hot-pressed to full density and annealed both by microwave and conventional heating at 1200, 1400, and 1500°C for times of 10 and 20 h.

Initial results showed increased elastic modulus and enhanced grain growth for the microwave-sintered samples. The changes in grain structure are shown in Fig. 6. However, it was also noted that the microwave-annealed specimens had higher weight losses as shown in Fig. 7. Apparently, the microwaves couple to the grain-boundary phases and cause the greater weight losses by volatilization of the glass phase. There is also an effect on the fracture toughness, as shown in Figs. 8 and 9. As shown, the fracture toughness is apparently degraded by the microwave annealing, which is believed to be a result of changes in the intergranular bonding caused by the loss of grain boundary phases. Further tests will seek to minimize the weight losses and the grain-boundary phase degradation.

New microwave furnace construction

A new microwave furnace was constructed and is currently being tested under manual control. Test loads have been heated and controller adjustments are being performed. The furnace will operate at 2.45 GHz with up to 12 kW of power and have more than double the volumetric capacity of the previous cavity. These additional features will significantly increase the capabilities over the current furnace. Of most importance will be the improved uniformity of the microwave field.

Publications

T. N. Tiegs, J. O. Kiggans, Jr., and H. D. Kimrey, Jr., "Microwave Processing of Si_3N_4," to be published in proceedings of Materials Research Society Spring 1990 Meeting, San Francisco, CA.

Status of milestones

Milestone 112402 was completed.

M23322 M23231

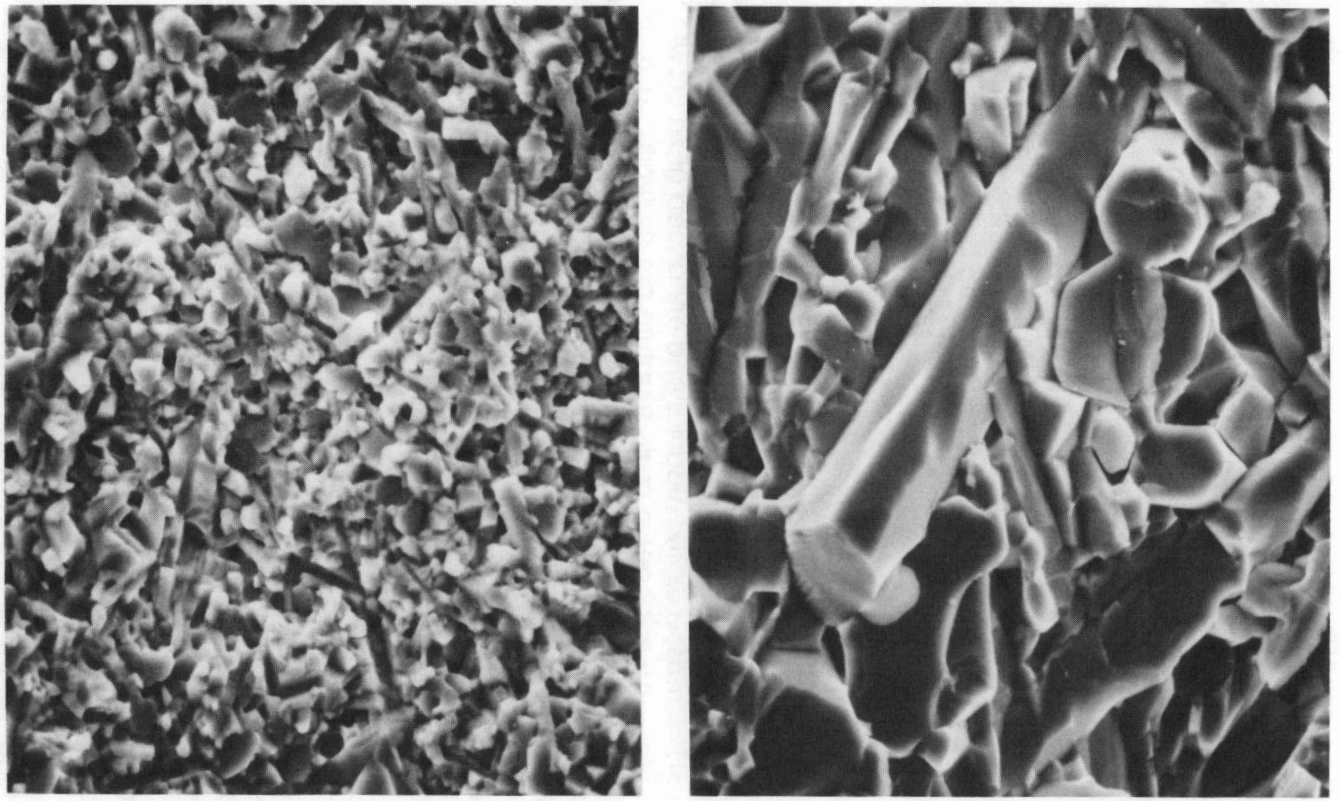

Fig. 6. Fracture surfaces of Si_3N_4-6% Y_2O_3-2% Al_2O_3. (*a*) After conventional annealing at 1400°C for 20 h; (*b*) after microwave annealing at 1400°C for 20 h.

ORNL-DWG90-13920

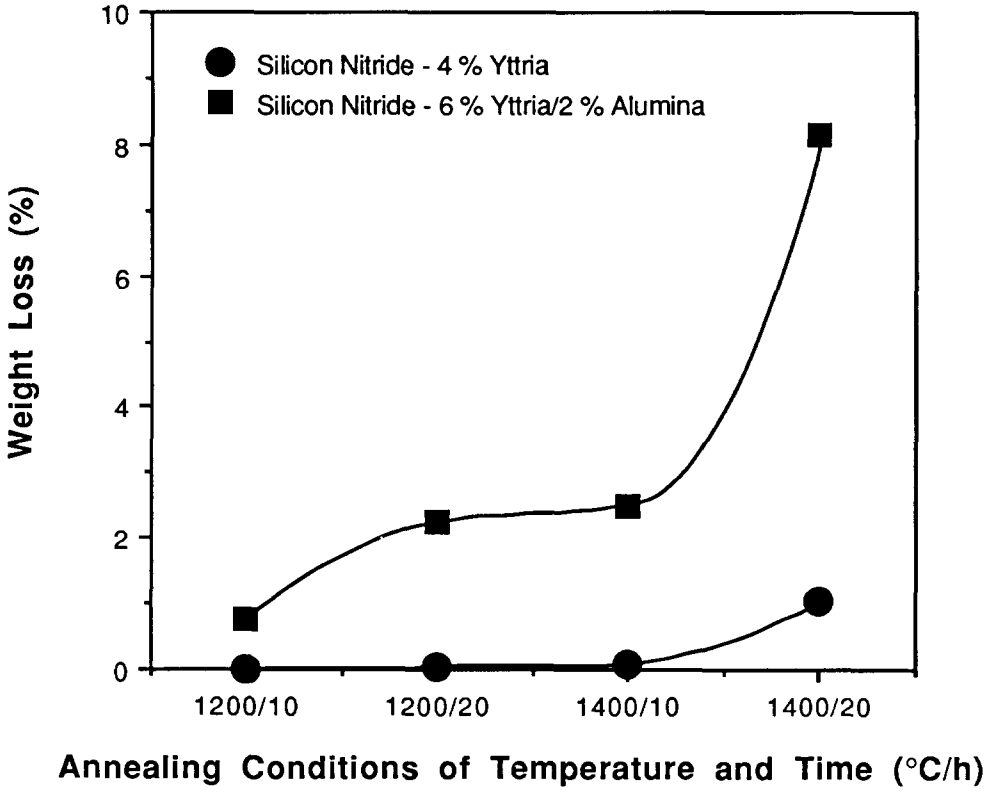

Fig. 7. Weight losses for Si_3N_4-6% Y_2O_3-2% Al_2O_3 during microwave annealing. Conventional heating counterparts showed weight losses <0.5 wt % for all heating conditions.

ORNL-DWG90-13921

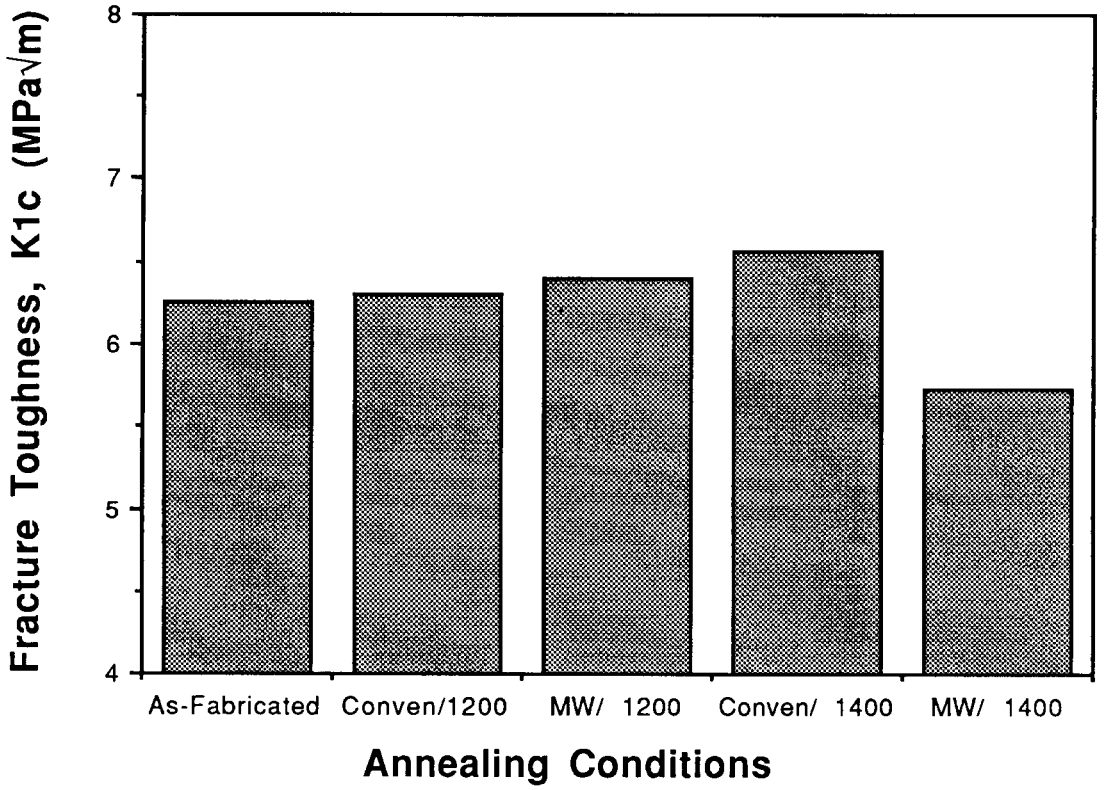

Fig. 8. Fracture toughness of microwave versus conventional annealed Si_3N_4-4% Y_2O_3. Samples were hot pressed to full density prior to annealing.

ORNL-DWG90-13922

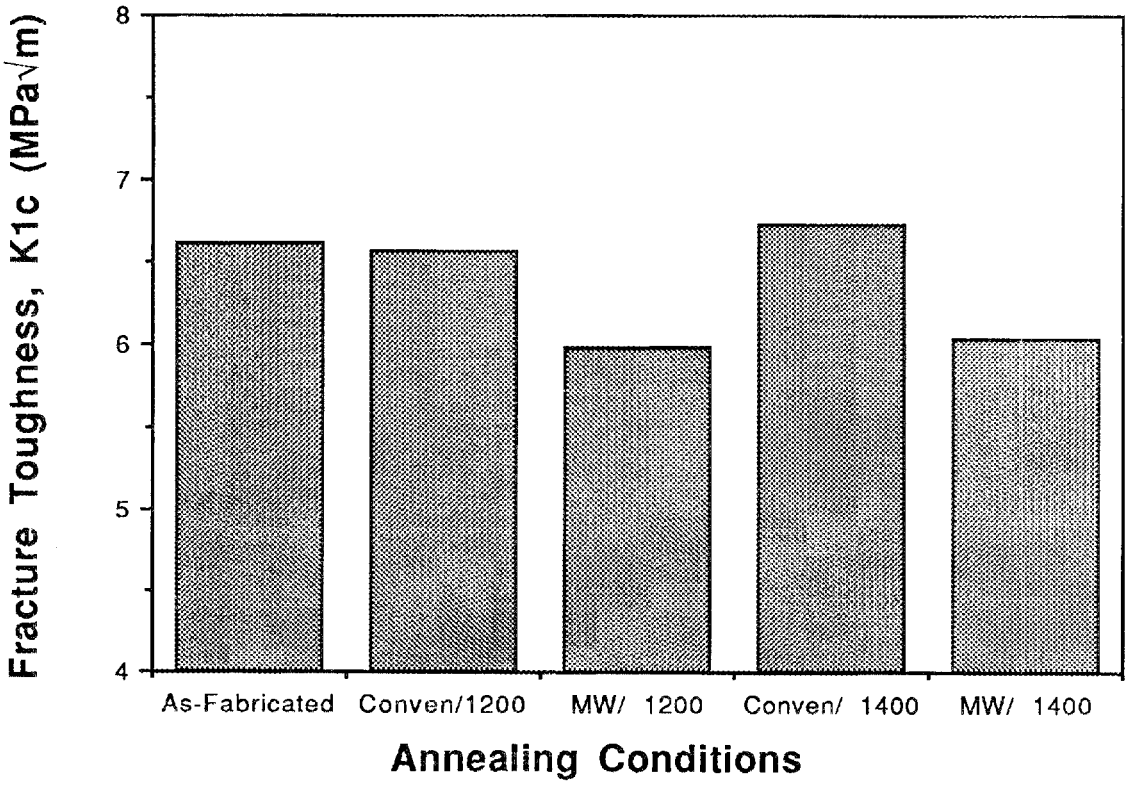

Fig. 9. Fracture toughness of microwave versus conventional annealed Si_3N_4-6% Y_2O_3-2% Al_2O_3. Samples were hot pressed to full density prior to annealing.

Silicon Nitride Milling Characterization

S. G. Malghan, L. H. S. Lum and D. Minor
(National Institute of Standards and Technology)

Objective/Scope

Ceramics have been successfully employed in engines on a demonstration basis. The successful manufacture and use of ceramics in advanced engines depends on the development of reliable materials that will withstand high, rapidly varying thermal stress loads. Improvement in the starting ceramic powders is a critical factor in achieving reliable ceramic materials for engine applications. Milling of powders is an integral unit operation in the manufacture of silicon nitride components for advanced energy applications. The production and use of these powders require the use of efficient milling techniques and understanding of characteristics of the milled powders in a given environment. High energy attrition milling appears to offer significant advantages over conventional tumbling and attrition mills.

The objectives of this project are to: (1) develop fundamental understanding of surface chemical changes taking place when silicon nitride powder is attrition milled in aqueous environment, and (2) demonstrate the use of high energy attrition milling for silicon nitride powder processing, by developing measurement techniques and data on the effect of milling variables on the resulting powder. This study will provide data and models for effective application of high energy attrition milling to industrial processing of silicon nitride powder. It also will provide recommended procedures for physical and surface chemical characterization of powders and slurries involved in the milling process.

Technical Progress

During the past six months, significant progress has been made in terms of characterization of milling kinetics as a function of milling variables, influence of milling liquid and surface chemistry of milled powders.

Milling Kinetics. The kinetics of milling a 50/50 mixture of Ube's[1] SNE-3 and SNE-5 powders under a variety of milling conditions was studied as a function of particle size distribution and specific

[1] Certain commerical equipment, instruments and materials may be identified in this report in order to adequately specify the experimental procedure. Such identification does not imply recommendation or endorsement by the National Institute of Standards and Technology, nor does it imply that the materials or equipment identifies are necessarily the best available for the purpose.

surface area. Figure 1 shows that increase of specific surface area is a linear function of milling time. However, the rate of evolution of specific surface area is a strong function of rotor speed and feed flow rate. The power input to the mill is a direct function of cube of rotor speed. As a result the rotor speed is expected to have the maximum effect on the milling kinetics. When the rotor speed was increased from 2000 to 2600 rpm at the feed flow rate of 4 ml/sec, a significant increase in the surface area was achieved. Under the conditions of 4 ml/sec flowrate and 2600 rpm rotor speed, the specific area of the feed can be doubled from 4 m^2/g to 8 m^2/g in 60 minutes.

The particle size distributions (PSD) of the milled powders follow the same trend as that of the specific surface area. However, at different milling periods, different milling mechanisms appear to dominate. Initially, deagglomeration appears to be the primary mechanism of milling. This is demonstrated in Fig. 2 for the 60 min. milling data, in which the coarsest size of the particles are broken. As the milling continues, though deagglomeration is continuing, more fines are being produced. This is an indication of shear forces being dominant under these conditions, in relation to compression forces. To promote breakage of larger particles, both suspension rheology and milling speed will be modified in the next stage tests.

Influence of Milling Liquid. Isopropyl alcohol (IPA) was used in place of water as a milling fluid. The solids loading of the feed slurry could not be increased beyond 22% v/v when IPA was used. As the solids loading in the slurry increased from 12% to 22% by volume, the milling rate decreased significantly. This type of decrease in the milling rate is related to the increased concentration of agglomerates in relation to the number of media contacts. For comparison, the specific surface area of the powder milled in aqueous environment under the same feed rate and rotor speed is shown in Figure 3. Though the kinetics of milling in water are slower than that in the IPA, the effective milling rate in terms of powder surface area per unit volume (taking into account increased solids loading) is higher for the aqueous suspension.

Surface Chemistry of Milled Powders. Surface chemistry of the milled powders was examined by the measurement of oxygen concentration, acoustophoretic mobility and electron spectroscopy for chemical analysis (ESCA). These data indicate that oxygen content of the milled powders is related to the amount of attrition of the powders in the mill. Higher the feed rate, higher the oxygen content of the milled powders to achieve the same specific surface area. The acoustophoretic mobility data indicated that higher surface area of the powder resulted in a lower pH_{iep}. These results indicate the formation of a thicker oxide surface on the powders milled for longer periods of time.

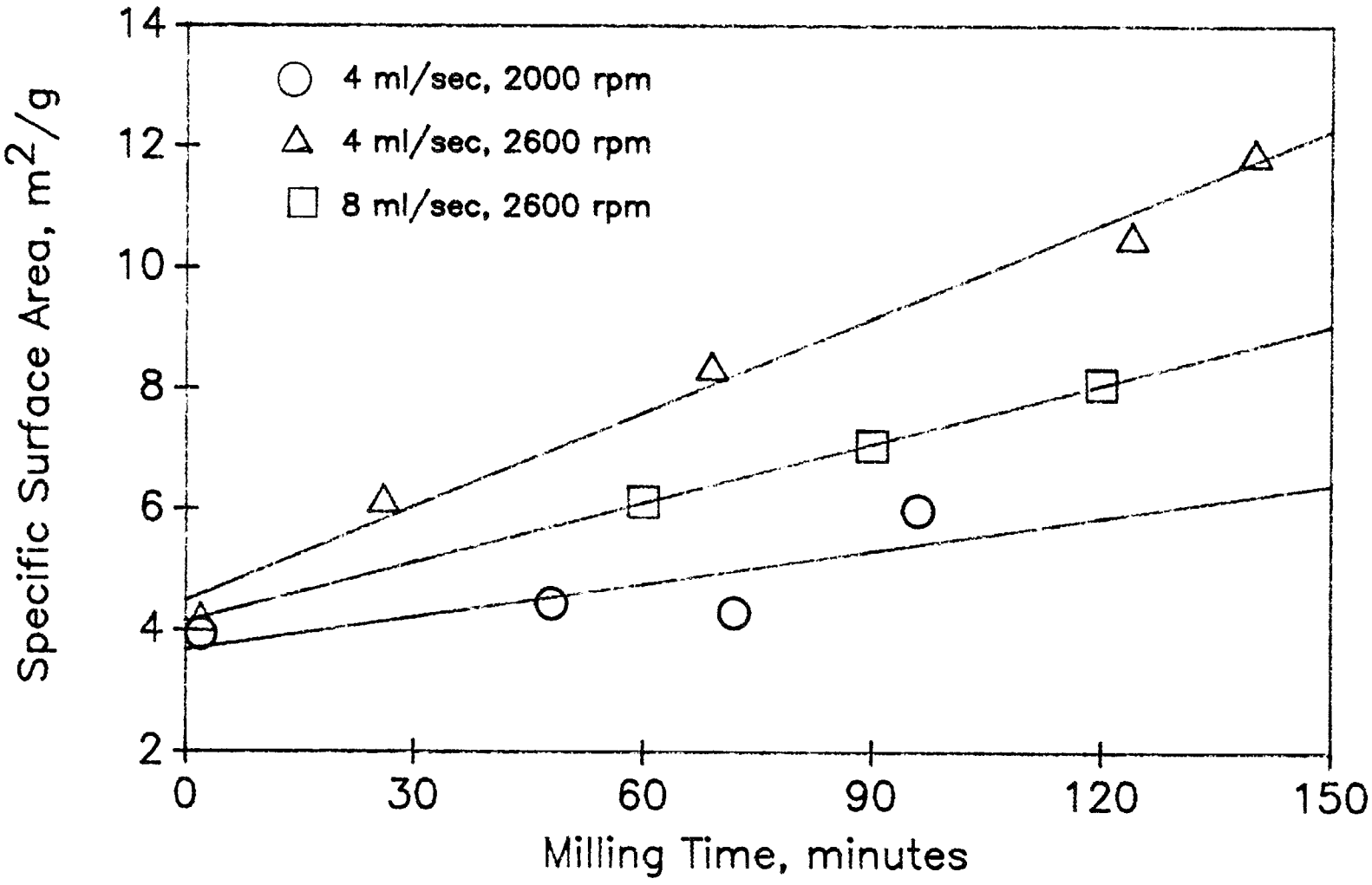

Figure 1. Comparison of specific surface area of milled powders as a function of milling time. Milling was conducted using water as solvent at two different feed flow rates and rotor speeds.

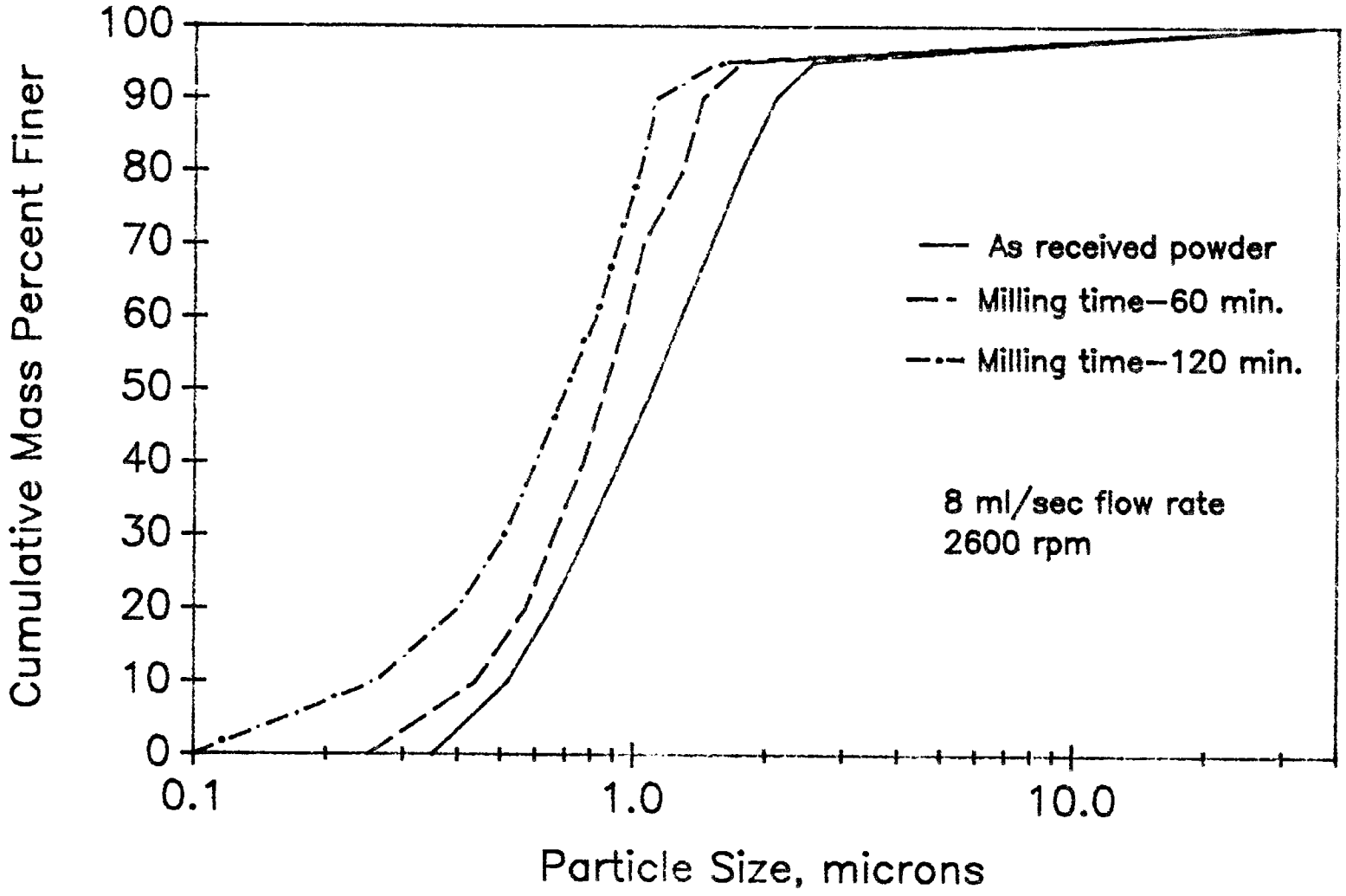

Figure 2. Comparison of particle size distribution of powders milled at 60 and 120 min. at one set of milling conditions in water.

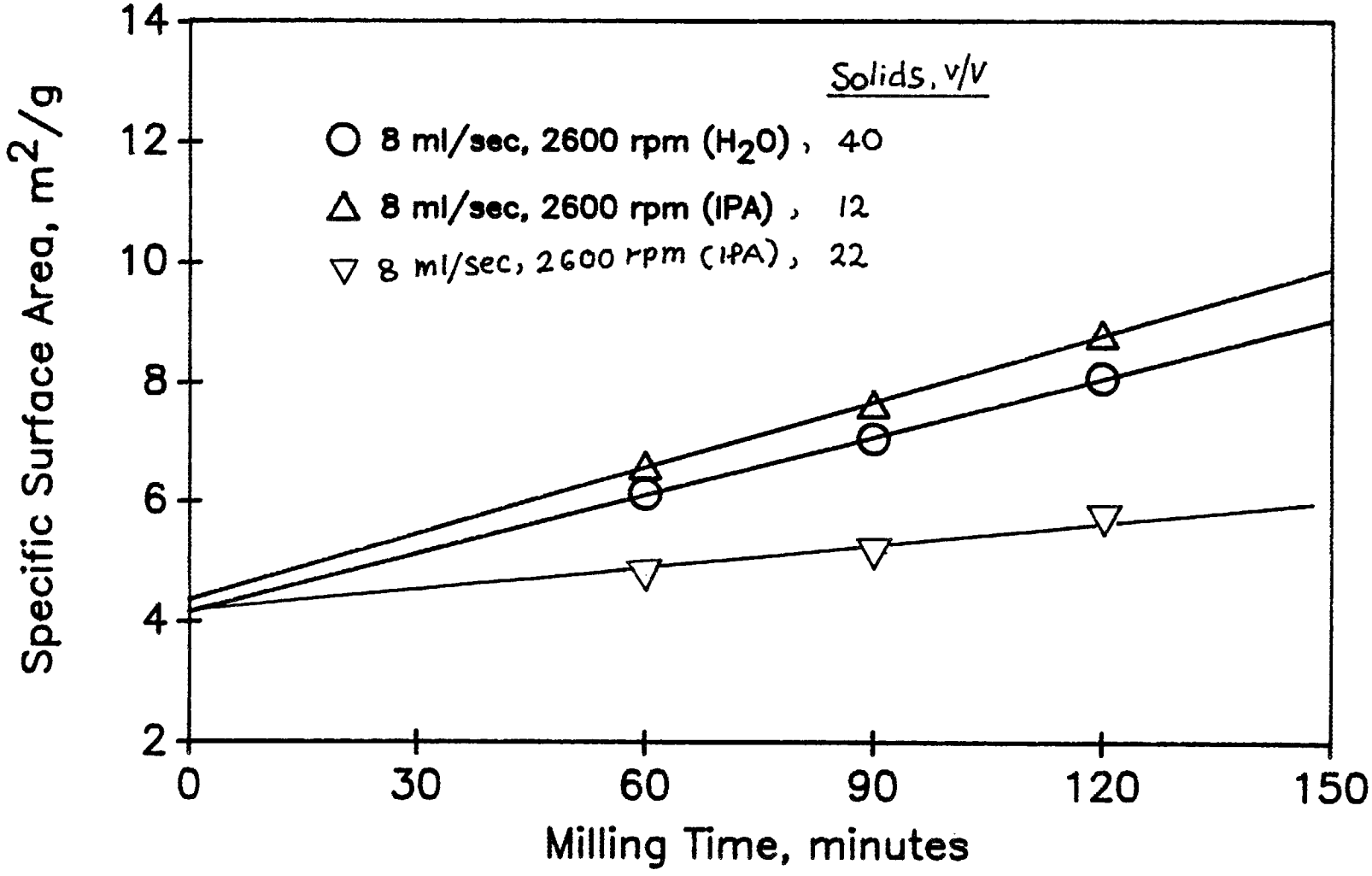

Figure 3. Comparison of specific surface area of milled powders as a function of milling time. Milling was conducted at the same feed flow rate and rotor speed using isopropyl alcohol and water as solvents.

Status of Milestones

On target.

Publications

1. S. G. Malghan and L.-H. Lum, "Factors Affecting Interface Properties of Silicon Nitride Powders in Aqueous Environment" Accepted for publication in Powder Processing III, Ed. G. L. Messing, ACerS, February 1990.

1.1.4 Processing of Monolithics

Improved Processing

V. K. Pujari, K. E. Amin, P. H. Tewari, C. A. Willkens, N. I. Paille,
G. A. Rossi, R. D. Creehan, M. R. Foley, and L. C. Sales (Norton Company)

Objective/scope

The goals of the program are to develop and demonstrate significant improvements in processing methods, process controls, and nondestructive evaluation (NDE) which can be commercially implemented to produce high-reliability silicon nitride components for advanced heat engine applications at temperatures to 1370°C. Achievement of this goal shall be sought by:

- The use of silicon nitride - 4% yttria composition which is consolidated by glass encapsulated HIP'ing.
- The generation of baseline data from an initial process route involving injection molding.
- Fabrication of tensile test bars by colloidal techniques - injection molding and colloidal consolidation.
- Identification of (critical) flaw populations through NDE and fractographic analysis.
- Correlation of measured tensile strength with flaw populations and process parameters.
- Minimization of these flaws through innovative improvements in process methods and controls.

The quantitative program goals are: 1) mean RT tensile strength of 900 MPa and Weibull modulus of 20, 2) mean 1370°C fast fracture tensile strength of 500 MPa, and 3) mean 1230°C tensile stress rupture life of 100 hours at 350 MPa.

Technical progress

The technical progress against the major tasks is described. The major tasks are: 1) Material Selection and Characterization; 2) Material Processing and Process Control; 3) Development and Application of NDE; 4) Property Testing and Microstructural Evaluation; 5) Reporting; 6) Quality Assurance.

In this period development efforts in the individual unit operations (sub tasks) leading to the total process are described. Where found suitable, fractional factorial design experiments based upon the Taguchi method were conducted to optimize a particular unit operation. No attempt was made at this stage to link various unit operations for the sake of total process optimization.

TASK 1

Material Selection and Characterization

The procedure for characterizing starting powder and additives along with all the processed material at each unit operation (as shown in Figure 1 of a previous bimonthly report[1] has been established and is being implemented.

A broad spectrum of analytical tools has been used for characterization of the materials used in the program.

The powder analysis basically has two segments; 1) chemical analysis: chemistry of the powder, powder impurities, analysis of the additives used for different processes; 2) physical analysis: particle size distribution, surface, morphology, phases, etc.

Apart from these analyses of the powders, scanning transmission microscopy, SEM and TEM, has been routinely used where needed.

X-ray photoelectron spectroscopy and Auger analysis has also been used on powders to study their surface chemistry.

Colloidal characterization has been done by Pen Kem 7000 acoustophoretic technique which not only determines the charge on the particles but also assesses the role of impurities and their extent on the powder surface.

Rheological measurements on the slurry have been performed by Bohlin rheometer model VOR and constant stress rheometer C.S. These two units combined are powerful enough to analyze slurries completely in viscometry, oscillatory and relaxation tests. Injection molding compound is fully characterized rheologically using capillary rheometer.

Oxygen Analysis Oxygen content in the silicon nitride powder is analyzed by LECO method. The oxygen in samples combines with carbon at high temperature to produce CO which is analyzed by infra-red detection.

The water content in the as-received powders is determined by the Karl Fisher method and is generally below 0.1%.

The oxygen in the powder after yttria precipitation on the surface is a combination of oxygen generated during milling, the original oxygen in the powder, moisture content of the powder and the colloidally precipitated Y_2O_3. Therefore, two values of the oxygen is determined: 1) from the powder after controlled drying, which contains the contributions from all the sources discussed above; and 2) after calcining the powder at high temperature in N_2.

Thermal Gravimetric analysis of yttrium salt showed that the material has $6H_2O$ molecules as specified. It decomposes to Y_2O_3 at ~700°C with a 70% weight loss. Also, the TGA for $Y(OH)_3$ showed that the full conversion to Y_2O_3 occurs between 800°C and 900°C with a 35% weight loss. Therefore, the calcination of $Y(OH)_3$ to a 1000°C is needed to give a corresponding oxygen for Y_2O_3. However, the oxidation of Si_3N_4 needs to be minimized. Various calcination treatments in vacuum and/or nitrogen to 800°C have consistently shown additional oxygen pick up.

The final value of the oxygen on the presintered bar as well as on the MOR bars after HIP'ing and machining have also been determined using LECO analysis. For these determinations, the bar is crushed to small pieces, while taking precautions that no contamination or oxidation occurs in the bar while crushing. These pieces (50-60 mg) are used for the LECO analysis.

Analysis of Metallic Species

The metallic species were extracted by acid digestion of the powder. The powder is digested first in sodium hydroxide. The fused material is then dissolved in hydrochloric acid. The yttrium analysis is performed on this solution by atomic absorption (AA) techniques.

The dissolved solution is also analyzed by inductively coupled plasma (ICP) technique. The choice of the equipment depends on the sensitivity of the determination of the element.

For yttrium both AA and ICP is used; however, ICP gives a better sensitivity for the yttrium species.

We have also determined yttrium by x-ray fluorescence (XFS). We will continue to use ICP and AA for yttrium in solutions but for solids MOR bars XFS is being evaluated and compared with the AA and ICP after digestion of the bars. The data base being generated will establish the reproducibility and ease of many of these techniques.

Emission spectroscopy technique has been used to analyze metallic impurities in the powder. For aluminum, zirconium and iron, this technique is exclusively used, although the analysis is applicable to B, Ni, Cu, V, Na, Cr, Ca, Ti, Mg, and Li also.

The anionic species in the powder is being analyzed by ion chromatography. The material is digested and the solution is analyzed for anionic species.

Injection molding binders have been characterized for thermal conductivity, specific heat, glass transition temperature and pressure-volume-temperature (p-v-t) correlation. These properties have also been used for the FEM (finite element method) analysis of the injection molding process. DSC and Gel Permeation Chromatography techniques were also utilized to characterize the virgin binder and the molding compound for Q.C purposes.

Particle Size and Surface Area of the Powder

Both the surface area and the particle size distribution of the powders have been routinely measured to assess the extent of milling of Si_3N_4 powders, while simultaneously measuring the oxygen content.

The particle size distribution has been determined routinely by two techniques: 1) sedigraph; 2) microtrac. These two instruments combined give a reasonable picture of the size distribution of the particles. We measure d_{10}, d_{50}, and d_{100} for a general comparison from batch to batch.

The surface area is determined by BET gas adsorption using N_2 as the gas. These two combined measurements give a reasonable state of the milled powder along with the oxygen values.

TASK 2

Material Processing and Process Control

i) Powder Processing

Effort in this unit operation includes comminution of powder blends and addition of yttria (4w%) in aqueous suspensions using a solution precipitation technique. The procedure for aqueous milling is being developed in a vibratory mill. After solution precipitation of yttria, the slurry is rinsed and concentrated to be used for colloidal consolidation or dried to powder for test tiles and injection molding. The powder is CIP'ed into rectangular tiles and subsequently HIP'ed to achieve near theoretical density. MOR bars, 3mm x 4mm x 50mm,

are machined out of tiles in order to evaluate the room and high temperature mechanical properties of this powder.

Procedures have been implemented in the class 10,000 hardwall clean room to minimize the risk of contamination. A closed process stream has been implemented throughout powder processing to further minimize the risk of contamination. Sampling and process control features are being introduced, such as sampling ports on the mill and automatic pH control for solution precipitation.

The entire aqueous milling process has been scaled up to provide large batch sizes, meeting the goal that was required for a single iteration (30kg). Three large powder batches have been supplied to enable full scale casting and injection molding studies using water milled powder. Media wear has been extremely low with the in-house fabricated media. The iron level has been very low throughout powder processing, partly due to the high purity media used.

Powder was processed on schedule using single batch sizes. This material showed promising MOR fast fracture data at room temperature and 1370°C and also Weibull modulus (see Task 4). Fracture origins have been almost entirely surface flaws. Final properties of the scaleup (4X) batches (W008, W009) were also promising. Further improvements are being sought by addressing the yttrium distribution, as discussed below, and by further optimizing materials of construction.

The effect of solids content, milling time and batch size on particle size distribution is being studied. Conditions were established that produced a particle size distribution similar to the baseline alcohol milled powder in both single and 4X scaleup batches. Packing density was acceptable for both casting and injection molding. Refinement of the fines (less than 0.2 micron) has been difficult due to the accuracy of the Sedigraph 5100 in this range. A Colter N4 equipment is being evaluated. The precipitated oxygen (with 4% Y_2O_3) is still higher than expected when compared to the as-milled oxygen value. This discrepancy is thought to result from the heat treatment used prior to Leco oxygen measurement.

The yttrium distribution for single batch size was extremely uniform as observed using SEM/EDXA. However, on scale-up from 1X to 5X, large regions rich in yttria were observed. These regions were attributed to the mixing conditions in the precipitation reactor not scaling properly. Actions have been taken to address this problem and improvements are now evident.

A water co-milled (Si_3N_4/Y_2O_3) batch (C001) was produced to separate the effects of water milling and precipitation of the sintering aid on total oxygen pickup. Co-milled powder showed no

additional oxygen pickup as observed with the Y_2O_3 precipitated powder. Segregation during storage occurred, which made casting results ambiguous. The fast fracture properties of powder made from this process were promising.

ii) Colloidal Consolidation

Two key steps in the colloidal consolidation process, i.e. slip formulation and tensile bar forming are being developed simultaneously:

a. Slip Formulation

The objective of these experiments is to develop an aqueous suspension of silicon nitride containing 50-70 w/o solids for centrifugal/pressure casting of crack free NSF (Net Shape Formed) specimens. This requires development of suitable dispersant-binder system(s). Slips were developed using both alcohol milled (baseline) and water milled powders.

Using baseline alcohol milled (Si_3N_4 + 4% Y_2O_3) powder, various slips containing 60-70 w/o solids were pressure cast (into 76 mm dia. x 13 mm thick discs) at 0.1 MPa using colloid presses. The time required for visible cracks to develop during drying in air under ambient conditions was monitored for these discs.

Based on these experiments, several binder systems were identified which produced crack-free green discs.

Slip development to cast water milled Si_3N_4 + 4% colloidally precipitated Y_2O_3 was also carried out. An excellent dispersant for alcohol milled (Si_3N_4 + 4% Y_2O_3) powder was found to be ineffective for the water milled powder. Therefore, an alternate surfactant was identified for the water milled systems. However, cast pieces invariably showed cracking after drying. This is suspected to be caused by segregation of the suspension due to the lower solids loading in the suspension and/or segregation caused by excessive longer casting time. Since the cracking and fluffiness (low packing dense) of the green specimens (made from water milled Si_3N_4 + 4% colloidally precipitated Y_2O_3) is tentatively attributed to low solid loading caused by the hydroxide surface of the particles in suspension, it is of interest to develop a water-milled suspension with "non-hydroxide" yttria. A suspension was developed by water milling of Si_3N_4 and then mixing 4% Y_2O_3 suspension.

This "mixed" system was evaluated for casting. Specimens (discs 76 mm dia., 13 mm thickness) pressure cast at 0.1 MPa, remained in one piece after drying. However, some surface cracks

developed during drying. These surface cracks may be attributed to segregation caused by low (25 w/o) solids suspension. Glossy upper surface of these specimens corroborate the segregation hypothesis. It is anticipated that crack free specimens could be cast using higher solids loading in the suspension.

Crack free discs cast from 1) aqueous suspensions of alcohol milled powders and 2) "mixed suspensions" obtained by blending Y_2O_3 powder with water milled Si_3N_4 suspension were analyzed by mercury porosimetry. Analysis of the best discs of the two series has shown that the bulk density is about 57-58% of theoretical for all discs, even though the solids loading of the suspensions was very different, i.e. about 25% for "mixed" and 75% for alcohol milled. Slight differences in bulk density (between 2 and 7%) were measured between top and bottom of the same disc and are believed to be caused by particle segregation during casting as a result of the low solids loading.

In the case of water milled Si_3N_4 with 4 w/o colloidally precipitated Y_2O_3 [$Y(OH)_3$] as mentioned previously the cracking problem in the cast discs was found to be mainly due to the low solids content suspension used in the casting experiments. Therefore, a novel technique was developed to prepare suspensions containing greater than 70 w/o solids and discs were pressure cast using several binder systems. Virtually all discs were uncracked after drying, and had a density of 58% of theoretical, with a standard deviation of 1.2% (24 discs).

Several pressure cast discs were also analyzed by mercury porosimetry for Y_2O_3 concentration and by SEM for possible particle segregation during casting. The samples submitted for porosimetry were cast from slurries containing no binder and binders B3, B5 (previously used), B11 and B12 and were fired in air at 600°C. The porosimetry results are shown in Table 1.

The data of Table 1 shows that the highest packing density was obtained without binder and that aging of the suspension resulted in lower density. No significant differences were found among binders, except for B11, which gave a relatively low bulk density. Y_2O_3 concentration was analyzed by AA on selected discs on top and bottom portions. Maximum differences found were 3%.

The SEM photographs did not show any significant particle segregation.

b. Tensile Bar Casting

Those suspensions which rendered crack free discs (as described in section (a)) were used for tensile bar casting.

Both pressure casting and centrifugal casting techniques were employed to fabricate tensile bars. Furthermore, three

different tensile bar shapes, i.e. NSF, bow-tie and straight cylinder were cast to examine the effect of geometry on the cracking pattern. For both casting techniques higher solids loading (>65 w%) was necessary to achieve crack free bars. With lower solids loading suspensions severe cracking was experienced. Preliminary results from the two casting techniques are described below.

Pressure Casting

A limited number of NSF specimens were cast crack free using suspensions with and without binder additions. A limited number of water soluble binders or emulsions screened so far did not show any improvement over unbinderized suspension. Green densities in the range 1.8 to 1.95 gm/cc (58 to 60% T.D.) were measured in the cast bars.

Using alcohol milled powder suspensions tensile bars with the three different shapes were cast at 0.1 MPa pressure using plaster of Paris molds. In most cases, a longitudinal crack was observed immediately after removal of the part from the mold. In some cases, cracks developed only after a few days of drying in air under ambient conditions. Prior to drying, these bars were held in a sealed plastic bag to complete the strain recovery process. For these slip formulations no cracking was observed due to the strain recovery process as mentioned in Reference 2. It must be emphasized that these slip formulations in cast discs (using colloid press) did not show any cracking problem under identical drying conditions.

Tensile bars cast from mixed suspension (obtained by blending Y_2O_3 powder with water milled silicon nitride suspensions) did not show any longitudinal cracks as observed in the case of alcohol milled powder. However, some shrinkage related radial cracking was noticed. Further results using this suspension will be reported in future reports.

A new batch with water milled powder and precipitated $Y(OH)_3$ was prepared, with a solids loading greater than 70 w/o.

NSF tensile bars were pressure cast using no binder and binders B5, together with two new binders, B13 and B14. Rheological properties of the four suspensions were measured, and the results are under evaluation.

Table 2 shows the number of bars that survived after casting, drying and firing.

As shown in Table 2, best results were obtained without binder. Binder B13 was the best of the three used.

Table 3 shows the results of mercury porosimetry performed on pieces taken from gauge section and shank of NSF bar prefired

at 600°C/1hr in air. Binder B5 has given the highest bulk density and smallest pore size, but unfortunately no bars survived after drying.

Centrifugal Casting (CC)

Similar to pressure casting, crack free bars were made using suspensions without binder additions. However, centrifugally cast bars showed poor strength near the gate causing eventual breakage. This was observed both in the porous and non-porous mold castings. Due to this inconsistency, no further effort was devoted to centrifugal casting experiments.

iii) Injection Molding (IM)

The three sub-steps in the injection molding process (mold design, molding process optimization, and dewaxing) have been addressed concurrently. To date all of the experimental work has been carried out using the alcohol milled powder with the exception of Batch D, the initial test batch using water milled powder. The purpose of this is two-fold, to establish the baseline mechanical properties using the Initial Process Route (IPR) and to develop the information necessary for mold design, molding, and dewaxing of tensile bar shapes.

a) Mold Design

In order to optimize the mold design, two techniques were used. The first was experimental including experimental design and analysis of the molded parts using both the destructive and non-destructive methods. A second task was conducted in parallel to the experimental work which involved finite element modeling (FEM) of the mold filling process. This made it possible to evaluate changes in the mold design without having to make changes in the actual hardware. A total of three different gate designs were evaluated experimentally which are designated as "G1", "G2", and "G3" as shown in Figure 1. A sub variation of G2 was also evaluated which differed only in depth. The experimental work provided both information on initial conditions necessary for the FEM work, and later, confirmation of the results generated by the modelling.

Experimental

The experimental work was carried out using an aluminum tool with a single tensile bar cavity. The original design, G1,

used a double runner design gated into the buttonhead area of the part. This was an unbalanced runner design to avoid weld lines in the gage area of the bar. This design resulted in excessive void formation and was dropped from subsequent evaluations. The second design, G2, was a single end gate design. This resulted in a reduction or elimination in voids within the part. A third modification of the mold was made to allow the use of an edge or fan gate to feed the material into the middle of the part. Tests of this design also yielded good parts based on reduction of voids. This design was designated G3.

Factorial experimental designs were utilized in order to evaluate both mold design as well as molding parameters. Figure 2 comparing the two gate designs, G2 and G3, shows that there is little difference between the two designs based on voids. Both gate designs are capable of molding tensile bars of similar quality and indicate that some other factor, such as residual stress or ease of molding, should determine the choice of gate design.

Finite Element Modeling

The finite element modeling required of two steps; first, materials characterization and then the modeling. The materials characterization determined the density, specific heat,thermal conductivity, rheology and pressure-volume-temperature behavior of the ceramic molding compound. The rheological properties are shown in Figure 3. Table 4 summarizes the remaining thermal and physical properties of the material. The following comments from the analytical laboratory were made concerning the material: 1) The rheology was typical for highly filled polymers with a tendency to level off at high shear rates. 2) The DSC curve showed multiple transitions reflecting the different polymers present. 3) The thermal conductivity was high because of the high ceramic content and 4) The PVT measurements did not record any noticeable transitions because of the low polymer content.

The above information was then used, along with the initial molding parameters determined experimentally, to conduct the computer simulations for mold filling and packing. The two gate designs G2 and G3 were modeled in varying sizes. Preliminary analysis indicated that the end gate should give better results based on a more uniform distribution of shear rates during filling of the part. The edge gate showed a tendency for the gate to freeze off in certain areas resulting in a split flow of material, resulting in the possibility for air entrapment during the filling. Further analysis confirmed that the end gate, with

the proper speed profile, would yield a nearly consistent melt front velocity, illustrated in Figure 4, and a more consistent bulk temperature throughout the part. These, along with other factors, should lead to a part with minimal stresses in the as-molded part.

This information, combined with the experimental design work done earlier as well as practical considerations, resulted in the final design for the molding tool now in use.

b) Molding Process Optimization

A total of five molding batches were prepared including one, weighing 24 Kg, which was used to mold the base line NSF bars by the initial process route. One of the other four batches, Batch D, used the water milled powder. All of the batches except the last, Batch E, were molded using the smaller tensile bar mold. Batch E was molded using the new two cavity tool. Each cavity produces an NSF bar which is 1.84 times the volume of the original small bar.

Experimental design was used to evaluate the effects of both the tool design, as mentioned earlier, and the molding parameters on the quality of the parts. The measures of part quality include weight, dimensions,and runout, or out of roundness. In addition, the parts were checked using microfocus X-ray which is discussed in Task 3 section of this report. These measurements are being used to generate preliminary SPC information.

Batch A was used to evaluate gate designs G1 and G2 as well as several molding parameters. As a result of this experiment, gate G1 was dropped and it was determined that injection speed and barrel temperature were the most important settings. Figure 5 shows the affect of these settings on part weight.

Batch B was used to evaluate gate design G3. During this experiment, it was determined that the changeover position during molding had a significant effect on part weight. NDE results later confirmed that there was a reduction in defects.

Molding Batch C was used to compare gate designs G2 and G3. The analysis showed that there was little difference between the two gate designs, as noted earlier, and that the barrel temperature and injection pressure profiles are significant. This is shown by the contour plot in Figure 6 which indicates an area of temperatures and pressures yielding the fewest defects.

The water milled powder was used to prepare Batch D. This was used with gate G2 to confirm the results of the preceding experiments and to investigate another mold design feature,

sprue size or mold opening. From this experiment it was learned that the molding parameters used were satisfactory and the sprue size could be reduced, thereby saving material.

Batch E was the large batch used to mold the initial process route (IPR) NSF bars. The new two cavity tool was used along with operating parameters developed during the preceding experiments and the FEM work. The molding proceeded with no problems and all samples have been weighed and measured and should prove sufficient to provide for testing and deliverables. As reported earlier, the variation in weights and lengths is 0.2% and 0.3% respectively for the more than 200 samples checked.

c) Dewaxing

Dewaxing procedures were developed using a combination of time, temperature, pressures, and atmospheres which resulted in a yield of approximately 85% for the smaller NSF bar. Initial results for the larger NSF bar gave considerably lower yields, but the latest modifications in the dewax cycle and setting procedures have resulted in yields approaching those obtained with the smaller bars. Dewaxed full sized bars have been submitted for further processing.

iv) HIP Densification

During this period two principal tasks were carried out. Evaluation of water-milled silicon nitride compositions required several qualification runs where test tiles from water-milled powders were CIP'ed and densified by a Norton proprietary HIP'ing process. Concurrently, an experimental evaluation of fixturing approaches to eliminate part warpage during HIP'ing was conducted with both CIP'ed and injection molded tensile rods. Both densified tiles and tensile rods were submitted for testing.

Water-Milled Powder Qualification Runs

In comparing the HIP'ing behavior of alcohol-milled silicon nitride-yttria compositions with water-milled compositions, the results to date indicate that water-milled materials, when milled to the same powder specification as alcohol-milled materials, do not achieve the density of alcohol-milled materials when processed with the same HIP schedule. Typical densities for alcohol-milled material would be 3.23 g/cm^3 while water-milled materials are 3.22 g/cm^3 on average. The reason for

this density difference has not been confirmed to data although it can be attributed to different levels of oxygen and/or yttria content in the aqueous milled powder. Mechanical properties of these two powders are reported in Task 4.

As with water-milled materials, injection-molded samples, which had been fabricated from alcohol-milled powders, produce lower densities than observed with CIP'ed, alcohol-milled materials. On average, injection-molded samples had densities of 3.21 g/cm^3 compared with 3.23 g/cm^3 for CIP'ed, alcohol-milled samples.

HIP Fixturing Experiments

In Table 5, preliminary results of tensile rod warpage (measured as rod runout due to bowing) are provided for the HIP fixturing experiments. Results for tensile rods which were machined from CIP'ed blanks as well as rods which were injection molded to net shape are presented. Note that the runout on green tensile rods is reported along with HIP'ed sample data since green rod runout varies dramatically with the CIP'ed and injection molded samples. While green machined CIP'ed rods have reasonably good tolerances (< 0.010"), green injection molded samples tend to have widely variable tolerances (0.004" - 0.070") due to warpage which occurs during handling after molding. Recently with better fixturing procedure the upper limit of molded part tolerance has been reduced to less than 0.030".

As indicated by the results provided in Table 5, rigid fixturing designs are fairly successful at eliminating warpage of tensile rods during HIP'ing.

As shown in Table 5, the results for flexible fixturing designs are obviously inferior for both machined CIP'ed rods as well as injection molded rods where runout is increased dramatically and exceeds the maximum runout observed in green tensile rods.

v) Machining

Based upon the machining study at various machine shops, Norton Northboro Advanced Ceramics Machine Shop has been selected to perform final machining of tensile bars. This decision was based on such issues as quality of the machined parts, production control, cost and delivery schedules.

vi) Process Control and Optimization

a. SCHEDULING: Schedules for the first two (2) iterations, Initial Process Route, and the Water-milled/ Colloidal consolidation Route have been drawn-up, and are currently under way. Disregarding a couple of operations that required rescheduling (due to power/equipment maintenance), these have been on time. One area that could necessitate additional modifications to the schedule has been yield. This has as yet not been a problem, but based on information obtained from the first iteration, the second iteration incorporates provision for lower yields.

b. SPC: SPC charts have been set-up for performance variables of unit operations that are thought to be critical to the overall process. An impediment in this area has been the inability to set specifications on certain unit operations, as some of these were still under development, and it was not known apriori what would be "good" limits. A related problem has been the identification of appropriate tests, and sample preparation schemes to obtain performance data. Based on the best knowledge to-date, an SOP has been implemented which guides unit operations, and the sampling, and sample preparation required for monitoring the process. The examples of the SPC charts shown in Figure 7 are a product of this effort.

c. EXPERIMENTAL DESIGN: Experiments are currently being carried out in the areas of molding, casting, and densification (and are covered in detail in those sections). An issue currently under study is the incorporation of data obtained from Non Destructive Evaluation, into a form effective for manipulation by statistical methods. A potential benefit from this study would be the ability to predict which pieces could fail due to inherent flaws, and corrective measures that would be taken to reduce and/or correct these before incurring additional processing costs. This could also be helpful in increasing the yield of the process, by re-working flawed material.

TASK 3

Development and Application of NDE

In-house NDE:

Technique development:

a. Film digitization capability for defect quantification: The hardware/software setup was established inhouse with guidance of Argonne National Laboratory (ANL). The most useful features of such software has been contrast enhancement using grey level stretch/slide and threshold operations and the use of non-convolution filters and edge enhancement filters. A composite of frame averaging and edge enhancement appears to provide appropriate images for defect sizing and counting.

An example of such defect quantification module (Image Measure/IP-IM5100) is shown in Figure 8 for a Si_3N_4 reference sample with seeded 200 μm Fe inclusions (made inhouse). By adjusting the grey level threshold of a digitally enhanced image at selected areas on the sample radiograph defects were counted and quantified (length, width, etc.). The units of the statistics data shown in the diagram are unnormalized.

Alternate software module and densitometry/fluorometry (IM4100) are also being evaluated to explore the feasibility of quantifying material density gradients from optical density variations in radiographs.

ANL has developed a dual field image analysis computer program which we hope to acquire soon to compare and evaluate NDE images obtained using different techniques (radiography, NMRImaging and ultrasonics).

b. Reference Samples: Si_3N_4 rods with known seeded inclusions and simulated voids using PMMA beads of different sizes were fabricated for evaluating the detection sensitivity of the various NDE techniques employed in the program. Si_3N_4 powder was mixed with various weight percentages of such seeds (precalculated to give a known total defect number per sample). The mix was then CIP'ed into rods, some kept for study on green ceramics, others were presintered and then machined into tensile samples. Some of those samples were then HIP'ed to full density. Between each processing step, microfocus film radiographs were obtained on the samples. An example of microfocus radiography detection sensitivity data on the CIP'ed samples is shown in Table 6. It may be noticed that the use of film digitization

technique helps improve reliability of detection (compare columns for manual versus digitized data).

Other Si_3N_4 samples were CIP'ed at different pressures ranging from 5 to 30 KSI for density gradient study. The rod densities varied from 1.660 to 1.878 g/cc. Manual microfocus radiography film density measurements done using a densitometer do not show a correlation with the rod density. Further evaluation is underway.

c. Microfocus Radiography: This work is still in the early stages. Experiments with a variety of target materials, film sensitivity, exposure conditions, filters, and mating surfaces are being conducted to offset the thickness gradient. A Panasonic high resolution CCD camera (768 X 493 lines, 0.5 loux screen illumination) was acquired for improved real time imaging. This camera does not suffer from target depletion, a problem encountered with Plumicon type cameras. A converted Dage camera (x-ray sensitive vedicon with a 1-inch CSI screen) was installed to achieve high magnifications.

d. Dye Penetrant: A number of tensile samples were indented at various loads ranging from 1 to 30 Kgf to generate cracks with known lengths for fluorescent detection sensitivity and optimization study.

Processing Iterations:

Microfocus film radiography evaluation was conducted on the as-molded tensile rods of first iteration. The average flaw indications per sample was around two which represents a significant improvement over past molding experiments. The majority of flaws are voids located either in the shank or the buttonhead section of the rod; some inclusions were detected. The average void size is > 500 μm and the inclusions around 200 to 500 μm.

Previously it was reported in earlier molding experiments that those rods which did not survive during binder removal/ handling/presintering had a larger void size distribution, as molded, than those which survived. Based on this, flaw parameterization analysis reported previously will be modified to include a weighting factor that accounts for survivability at subsequent processing steps. A software program was written for the parameterization computations. This work will be integrated with the strength separation/flaw maps work to be conducted soon with Prof. KJakus of the University of Massachusetts.

Subcontractors/Consultants:

a. Precision Acoustic Devices (PAD): PAD started on ultrasonic development work on November 27, 1989. They have been concentrating on system manufacturing (Task 2A under Technique Development of Subcontract ACS936555) which includes building the rotating scanning stage, test fixtures and transducer mounting fixtures to handle round tensile samples on the CCS 3000 scanning system. A cantilevered scan arm was designed and installed as well as a tilting mechanism for surface wave imaging.

Acoustic transmission measurements were made on a Norton-supplied tensile bar in the molded state. Because this material had not been tested acoustically, there was uncertainty as to the value of its properties, particularly attenuation. PAD found that at 5 MHz, attenuation was sufficiently low that a through transmission signal was easily obtained through the length of the sample. This may allow conducting velocity measurements across the samples at frequencies as high as 20 to 50 MHz, yielding measurement accuracy considerably better than 1%. The velocity and impedance obtained for this sample were 2.3 mm/sec and 5.3 MR, respectively.

Design specifications for 20, 30, 50, and 100 MHz contact and immersion transducers were completed, and orders have been placed for parts. Silicon nitride wedges were made by Norton Co. and delivered to PAD for shear wave transducers (mating surfaces) and transducer fabrication has begun. The rotating stage and time of flight electronics are under construction. Other equipment was purchased including a Panametrics pulser-receiver and scanner parts. Pulser/T-R switch modules with 50 and 100 MHZ capacity were constructed.

b. Argonne National Lab.: The subcontract with ANL has been awarded (contract No. 85093) and work was scheduled to commence early April, 1990.

TASK 4

Property Testing and Microstructural Evaluation

i) Tensile Testing of Green Specimens

Fixtures for tensile testing green (as-molded) and presintered NSF bars have been designed and built. Eighteen as-injection molded NSF specimens have been tested with an average strength of 3.3 ± 1.5 MPa. Sixteen specimens failed in the gauge

section and two failed in the shank region between gauge and buttonhead.

ii) Tensile Testing of Dense Specimens

Procedures for tensile testing at room temperature (R.T.) and elevated temperature have been established. Tests were performed on NT154 silicon nitride cylindrical buttonhead specimen at three gauge diameters. The R.T. strength data is summarized in Table 7 and the 1370°C data is in Table 8. Optical fractography of the R.T. specimens show 35 of 37 specimens failed at the surface while the 1370°C specimens all failed from bulk flaws. Also approximately 20% of the R.T. specimens failed at the gauge/transition region. Finite element modelling indicates a stress rise at this location.

iii) Comparison of Alcohol and Aqueous Milled Powders

Mechanical properties of the two powders were compared using four point bend MOR bars (Mils Std. 1942 (MR) B). Thorough chemical analyses were performed (see Task 1 and 2) on aqueous milled powder at each stage of the processing. Physical and chemical properties of the alcohol milled powder and resulting mechanical properties used in this comparison were those developed in ATTAP program (for NT154 material) by Norton/TRW.

As shown in Table 9, RT and 1370°C fast fracture (FF) strengths measured from several batches of aqueous milled powder are consistently above 900 MPa and comparable to those of alcohol milled powder. The stress rupture lives at 1230°C/350 MPa (test condition defined in this program) also consistently meets and exceeds 100 hour as required in this program. However, the stress rupture life data for alcohol milled powder have been generated (by Norton/TRW for NT154 material) at 1370°C/300 MPa as required in the ATTAP program. Consequently, most of the stress rupture testing for aqueous milled powder was also performed under ATTAP conditions. Whereas baseline alcohol milled powder consistently achieves 200 hours stress rupture life (data provided by Norton/TRW), the aqueous milled powder shows greater scatter in the data. On seven aqueous milled powder batches, approximately 40% of the bars were found to survive 200 hours stress rupture life. This anomaly could be attributed to, as mentioned in Task 1 and Section (i) Task 2, relatively high variation in yttria distribution (standard deviation of 0.3 vs. 0.03 for alcohol milled powder) and 20% higher oxygen content in the aqueous milled powder as compared

to alcohol milled variations. These variations seem to be processing related and hence suggest further process improvement needs which is consistent with the scope of this program.

It is therefore being recommended that aqueous milling of powder be continued during the remainder of the first stage of the program with emphasis on process improvements and/or modifications to existing approach while generating a tensile strength database for the two forming techniques, eg. injection molding and colloidal consolidation.

References

1. Bimonthly Technical Progress, August-September 1989, Subcontract No.-86X-5B182C.

2. F. F. Lange and K. T. Miller, "Pressure Filtration: Consolidation Kinetics and Mechanics," Am. Cer. Soc. Bull., 66[10], 1498-1504 (1987).

Status of Milestones

All milestones are on schedule.

Publications

Vimal K. Pujari presented a paper entitled, "Powder Characteristics and Its Effects on the Binder Removal Process," at a poster session of the Third International conference on Ceramic Processing Science, February 4-7, 1990, San Diego, California.

Table 1 Mercury porosimetry results of pressure cast discs with and without binders

SAMPLE	TIV	MPD	TPA	BD	SD	%TD
NB≠-T	0.216	107	15.53	1.90	3.21	59
NB≠-C	0.206	110	12.76	1.89	3.09	59
NB≠-B	0.202	110	10.67	2.66	5.76	
NB*-T	0.252	127	15.91	1.74	1.74	54
NB*-C	0.254	127	16.74	1.76	3.19	55
NB*-B	0.271	127	22.25	1.72	3.21	54
B5-C	0.222	115	14.22	1.85	3.14	58
B11-C	0.240	128	12.32	1.77	3.09	55
B3-C	0.228	110	18.19	1.86	3.23	58
B12-C	0.237	123	16.39	1.82	3.20	57
	0.237	0.054	17.47	1.82	3.19	57
	0.252	0.058	17.29	1.79	3.26	56

NOTE: NB = No Binder; T = top; C = Center; B = Bottom;
* = Aged Slurry (8 days)
≠ = Unaged Slurry
TIV = Total Intrusion Volume (cm^2/g)
MPD = Median Pore Diameter (nm)
TPA = Total Pore Area (m^2/g)
%TD = Percent of Theoretical Density
BD = Bulk Density (g/cm^3)
SD = Skeletal Density (gm/cm^3)

Table 2 Number of tensile bars that survived after casting, drying and firing

Bars Cast	Binder Used	# Broken in Mold	# Broken in Drying	# Broken in Firing	# Survived Firing
10	no bind.	6	1	0	3
10	B5	2	7 + 1*	0	0
10	B13	1	2	5	2
10	B14	3	4 + 1*	2	0

Note: * broken in handling. All samples dried in controlled humidity oven. Firing done in air at 600°C/1hr. It is suspected that 100°C/hr heating rate during air firing may have been too fast and caused cracking in bars made using binders.

Table 3 Mercury porosimetry results for tensile bars with and without binders

Sample	TIV	MPD	TPA	BD	SD	%TD
NB-G	0.235	111	15.06	1.80	3.14	56
NB-S	0.238	110	15.73	1.82	3.20	57
B13-G	0.233	112	14.65	1.82	3.16	57
B13-S	0.237	110	16.15	1.83	3.22	57
B14-G	0.236	115	13.17	1.78	3.07	55
B14-S	0.240	113	17.14	1.81	3.21	56
B5-G	0.209	104	14.69	1.90	3.14	59
B5-S	0.203	105	12.93	1.93	3.17	60

Note: NB = No Binder
G = Gauge Section
S = Shank
TIV = Total Intrusion Volume (cm^3/g)
MPD = Median Pore Diameter (nm)
TPA = Total Pore Area (m^2/g)
BD = Bulk Density (g/cm^3)
SD = Skeletal Density (g/cm^3)
%TD = Percent of Theoretical Density

Table 4 Material property summary

Density - Instrument: Capillary Rheometer (melt)

State	Temperature °C	Density g/cc
solid	23	2.287

Specific Heat - Instrument: DSC

State	Temperature °C	Specific Heat J/g°c
solid	80	1.14
melt	100	1.191
		Tg 92°C

Thermal Conductivity - Instrument: K-System

State	Temperature °C	Press Bar	Thermal Cond. w/m°k
melt	90	0	0.35

Table 5 Runout measurements for initial HIP fixturing experiments (inches)

Sample Type	Green Rod	As-HIP'ed Runout with Fixturing	
		Rigid	Flexible
Injection Molded			
Max.	± 0.070	± 0.009	± 0.080
Min.	± 0.004	± 0.003	± 0.000
Typical	± 0.015	± 0.006	± 0.030
Machined-CIP			
Max.	± 0.010	± 0.009	± 0.032
Min.	± 0.002	± 0.002	± 0.029
Typical	± 0.005	± 0.004	± 0.027

Table 6– Microfocus Film Radiography Detection Data for Fe Inclusions (Green Samples)

Size of Inclusion (um)	% Thickness Sensitivity	# of Seeded Defects	Average# of Detected Defects		Point Estimate of POD	
			Manual	Digitized	Manual	Digitized
200	1.2	620	490	381	0.79	0.61
100	0.6	509	357	121	0.70	0.24
50	0.3	400	0	72	0.0	0.18
20	0.15	---	0	0	0.0	0.00

TABLE 7 TENSILE STRENGTH DATA FOR NT154 AT ROOM TEMPERATURE

GAUGE DIAMETER (MM)	4.5	5.5	6.35
AVERAGE STRENGTH (MPA)	715.6	685.1	710.6
STANDARD DEVIATION (MPA)	83.0	76.4	76.7
WEIBULL MODULUS	9.3	8.2	9.6
# OF SPECIMENS	12	12	13

Table 8 Tensile Strength Data for NT154 at 1370°C

Gauge Diameter (mm)	4.5	5.5	6.35
Ave. Strength (MPa)	430.6	427.8	449.0
# of Specimens	2	2	3

TABLE 9 COMPARISONS OF MECHANICAL PROPERTIES RESULTING FROM AQUEOUS AND ALCOHOL MILLED POWDERS

BATCH	STRENGTH (MPA) M = WEIBULL MODULUS				Fracture Toughness	Vickers Hardness
	Room Temp.		1370°C		MPa $m^{1/2}$	(GPa)
	σ_f	m	σ_f	m		
SWM04-CO	790	7.8	610	16	---	---
SWM04-CC	624	8.8	549	28	---	---
W005	950	10.4	576	18.2	6.06	16.0
W006	931	8.3	603	11.9	5.97	16.1
W007	903	10.5	525	--	6.10	16.2
W008	1000	14.4	555	--	5.98	16.1
W009	999	12.0	584	28	6.40	---
C001	1027	17.3	556	21.3	6.42	---
NT154	896	19	579	11	4.7-5.5	15.9

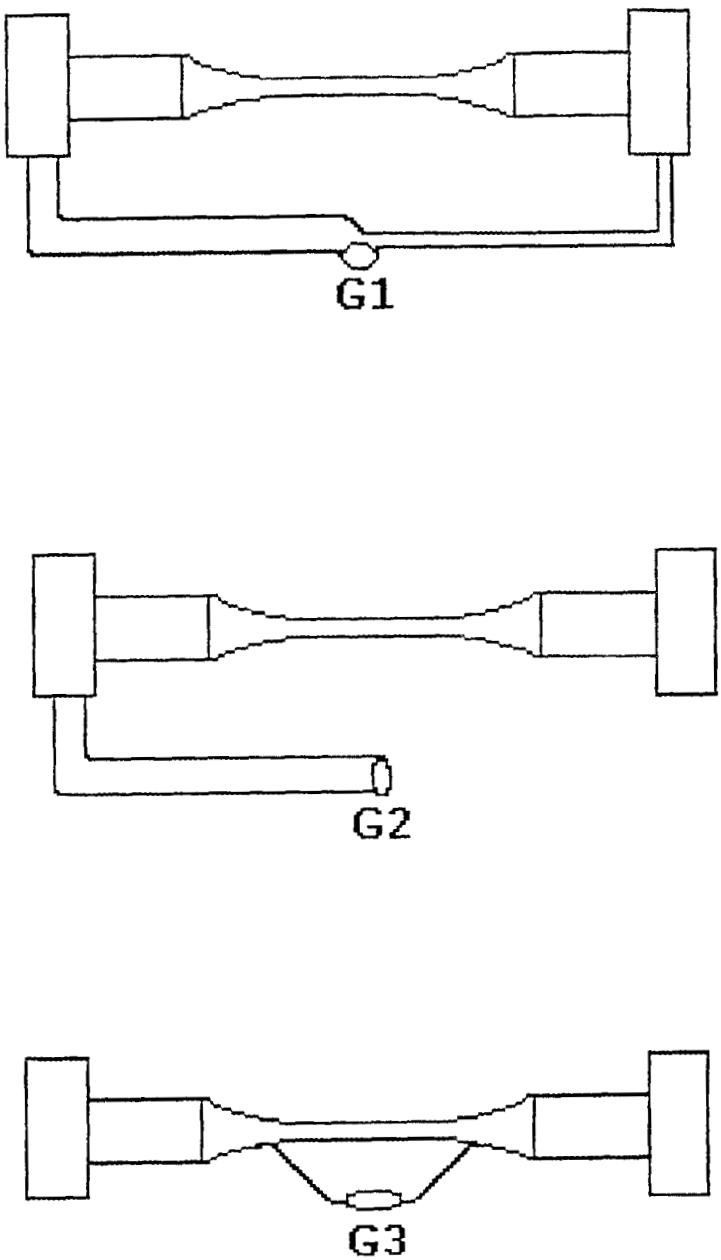

Figure 1 Gate design for tensile bar mold
(G1) Double Gated
(G2) Single Gated
(G3) Fan Gate

Analysis of variance

Source of variation	Sum of Squares	d.f.	Mean square	F-ratio	Sig. level
Between Gate designs	423014	1	423013.56	.490	.4934*
Within Gate designs	66458767	77	863100.86		
Total (corrected)	66881780	78			

* A significance level of >.10 indicates no difference in Gate designs

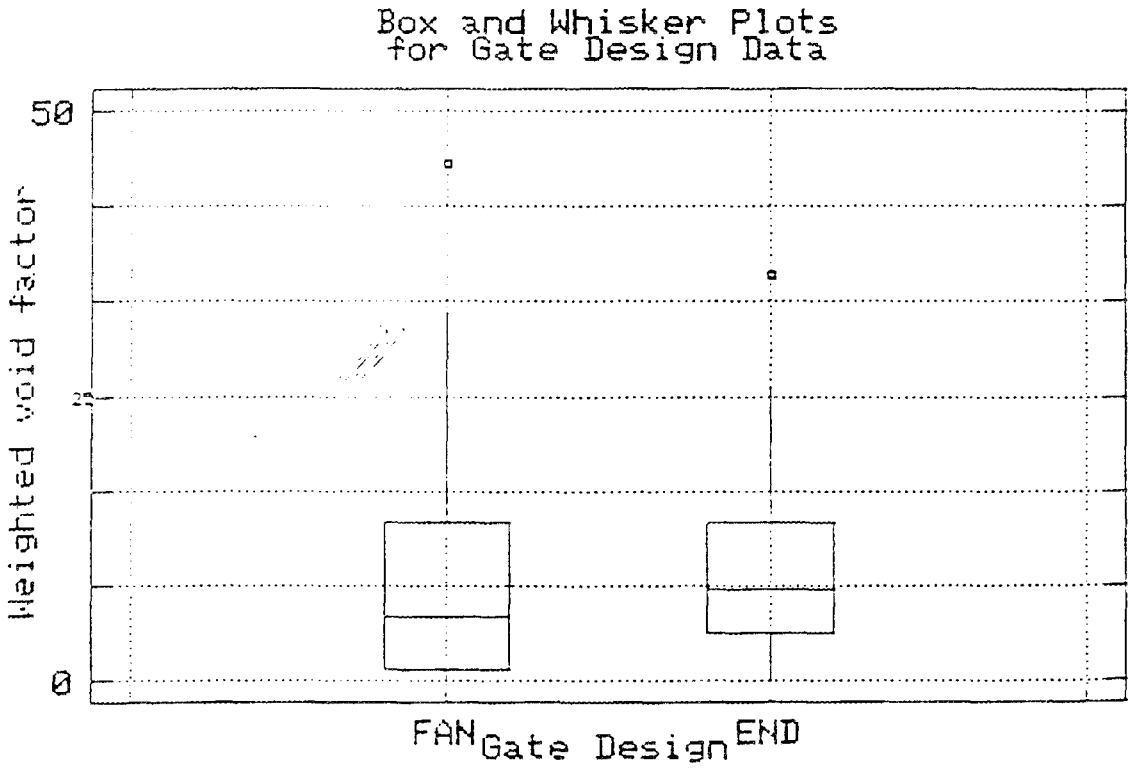

Figure 2 Voids in molded part for the fan gate and end gated molds

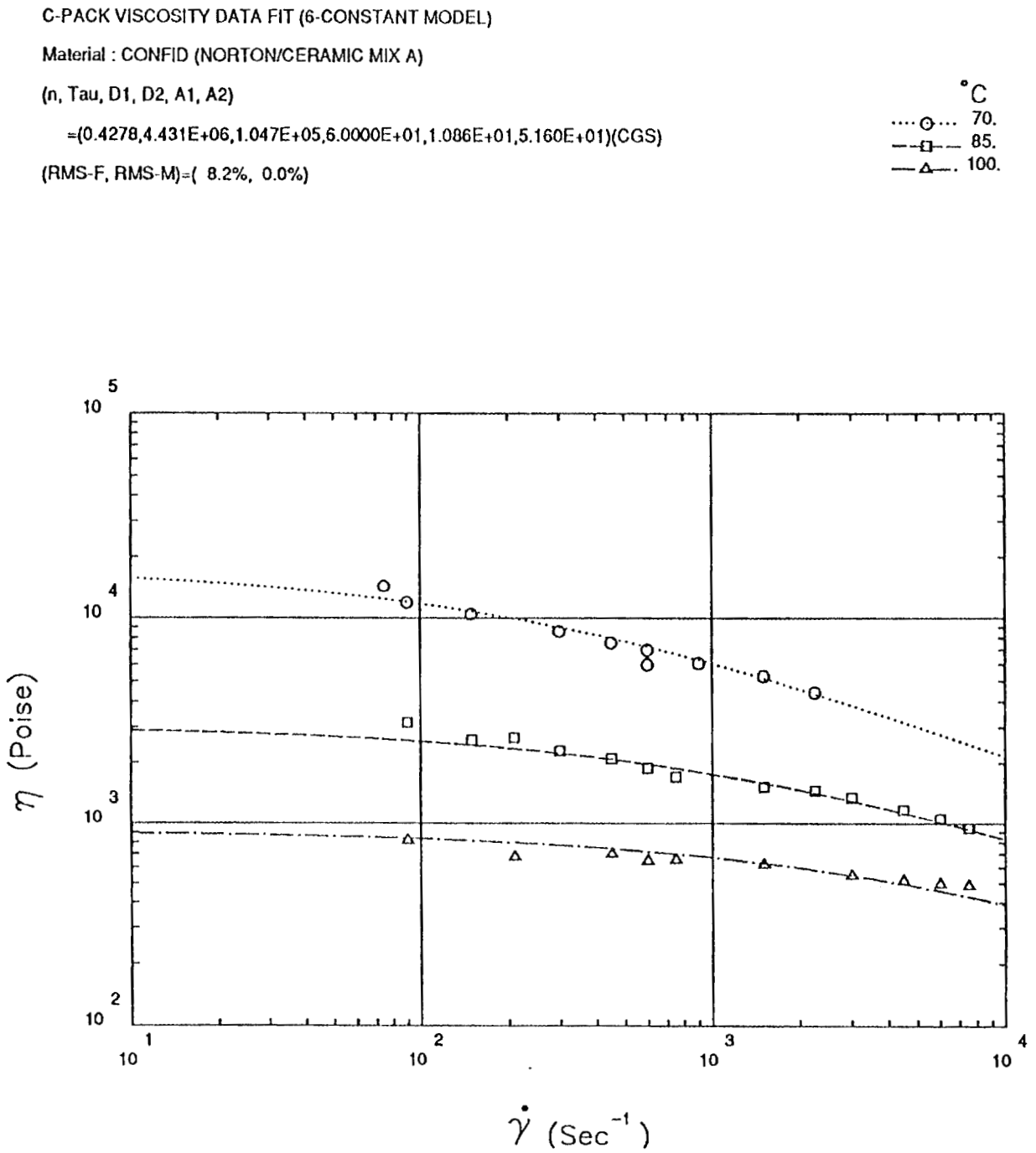

Figure 3 Rheological properties of injection molding compound

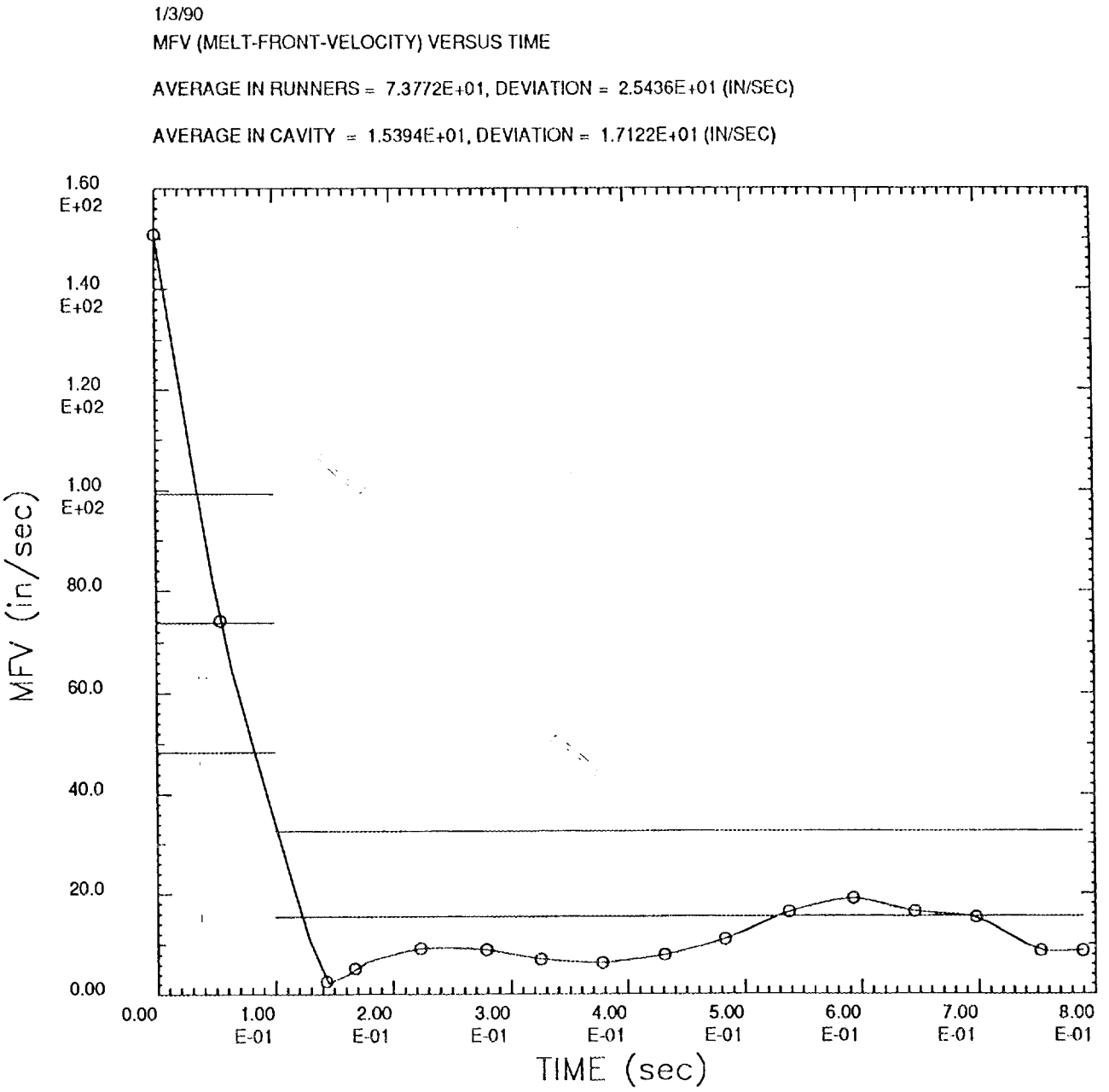

Figure 4 Melt front velocity in the end gated mold

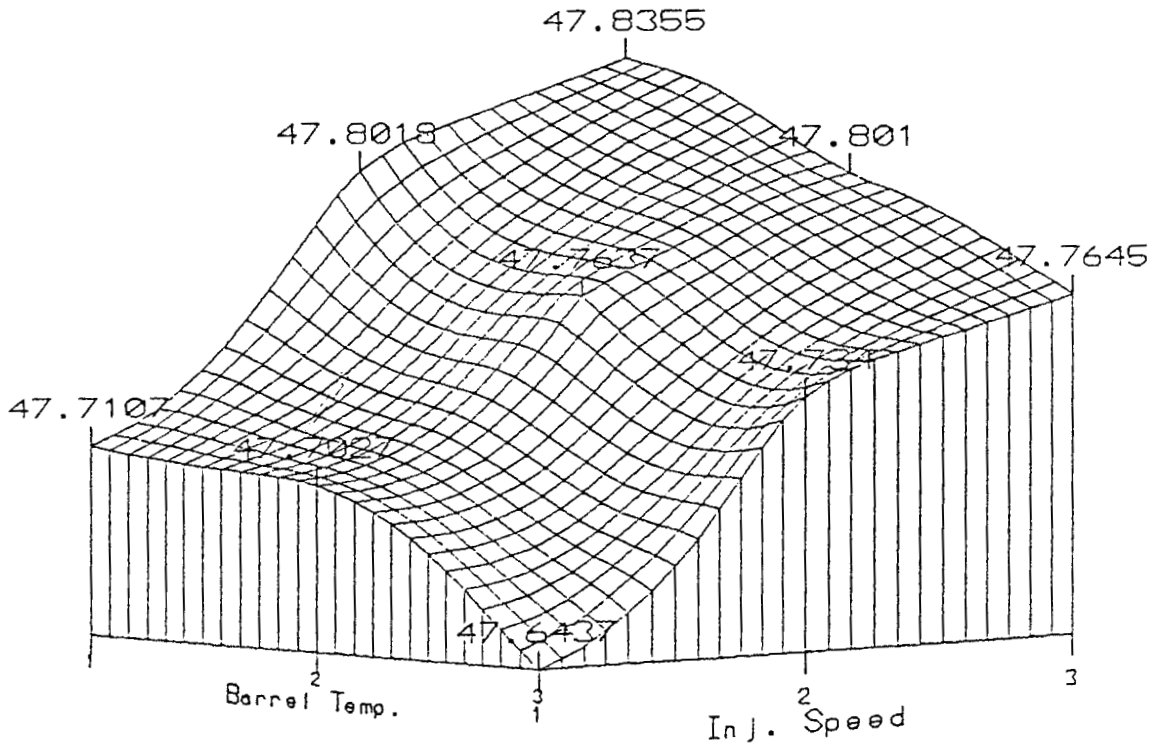

Figure 5 Weight of injection molded NSF bars as a function of Barrel Temperature and Injection Speed

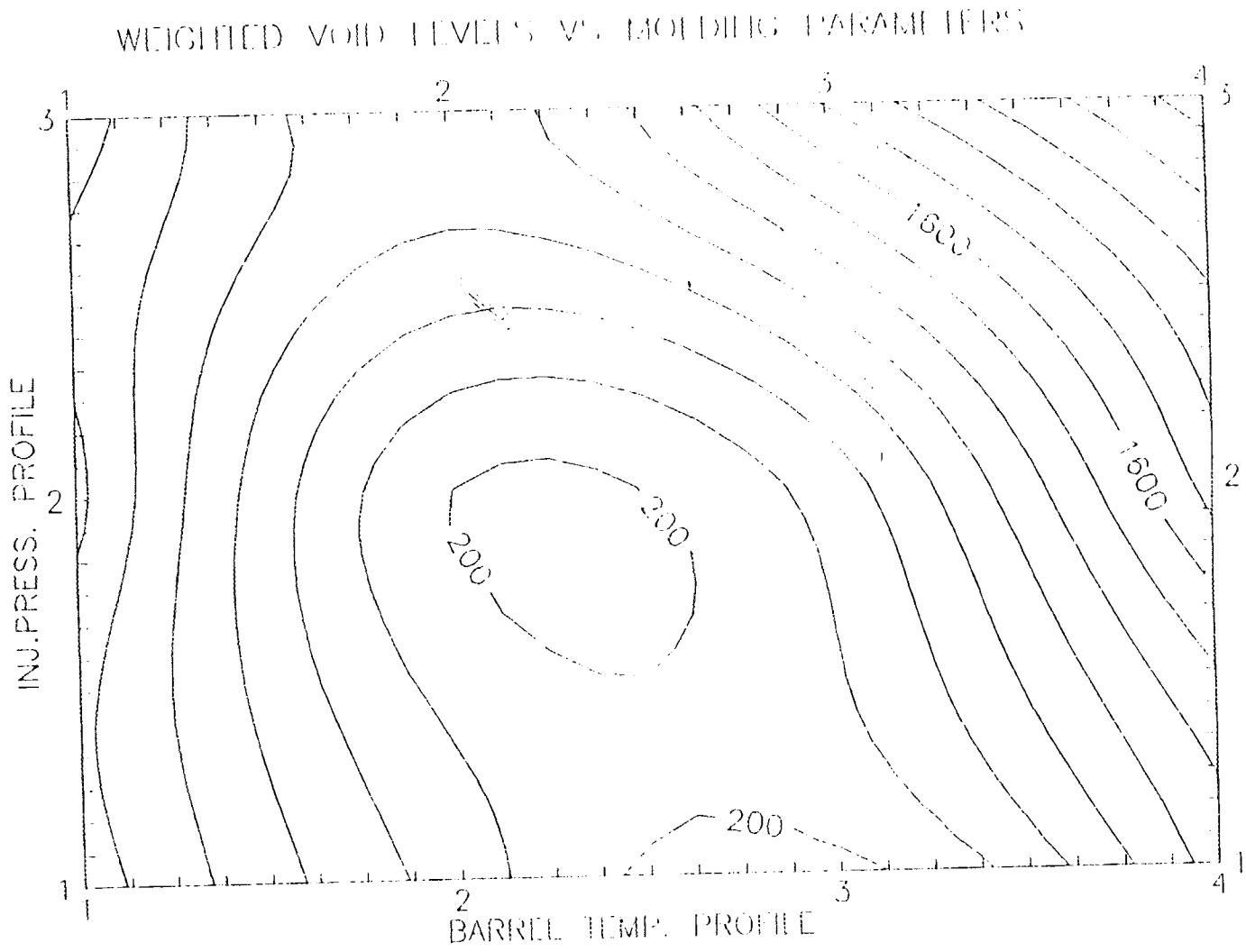

Figure 6 Contour plots showing effects of injection pressure and barrel temperature on void formation

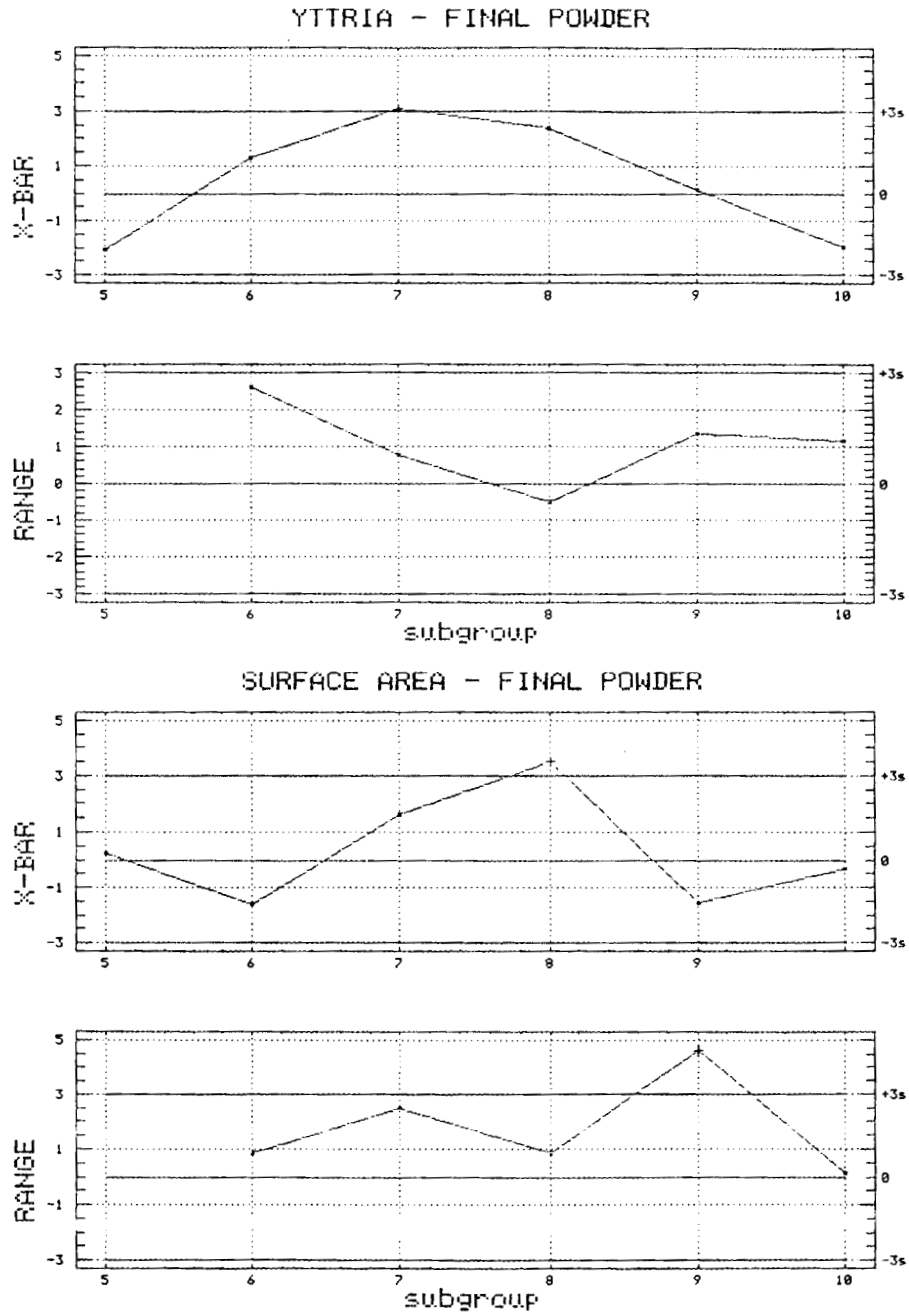

Figure 7(a) SPC charts showing yttria and surface area variations in the milled powders

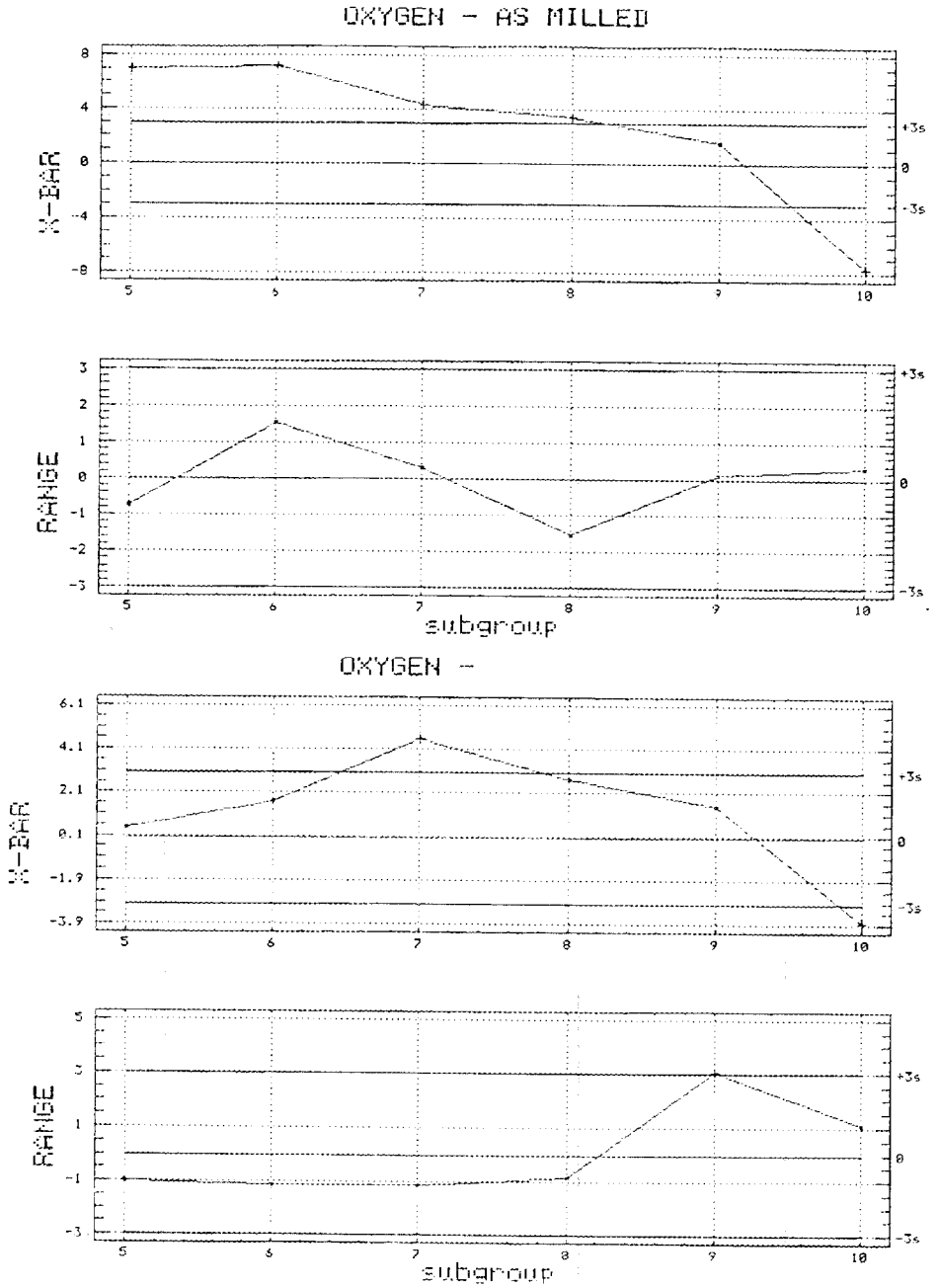

Figure 7(b) SPC charts showing oxygen variation in as-milled and Y_2O_3 precipitated powder

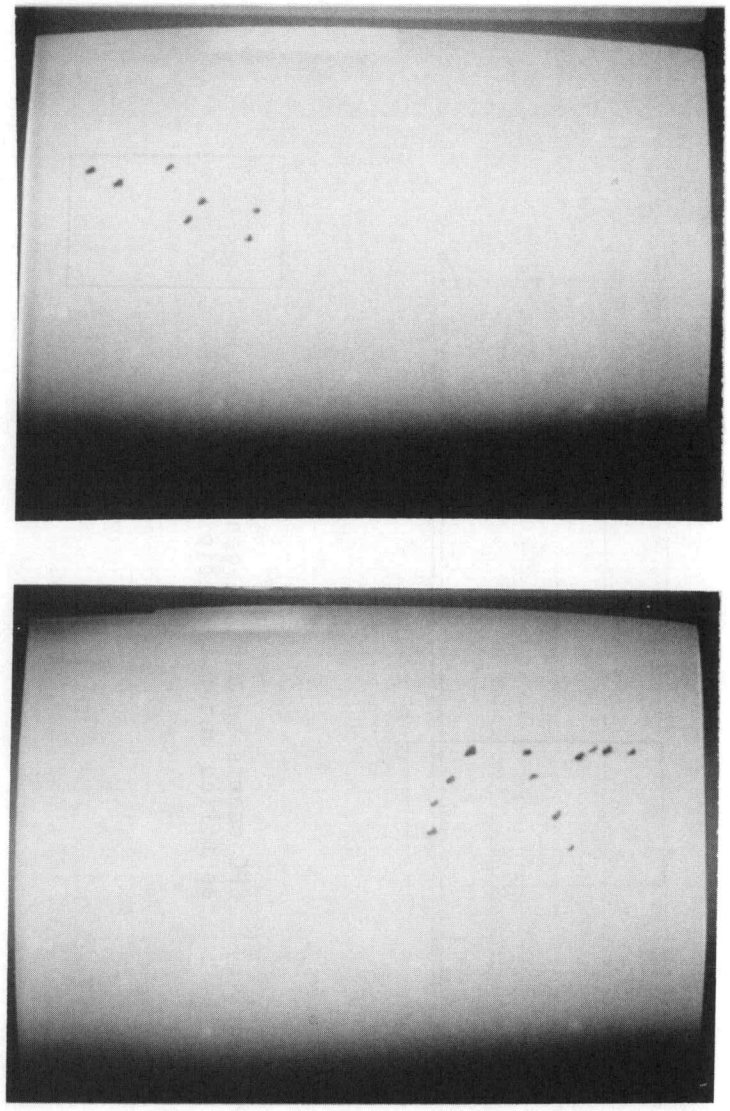

ImageMeasure/IP: Counting and Sizing DATE/TIME: 04-03-1990/08:41:15
FILE: C:SI3N4FE
DESCRIPT: si3n4 with 200 um fe seeds frame ave. plus edge enhanced
OWNER: K.E. Amin, Norton Co., USER:

Equation: Y = -1.184465 + .9728301 * X

Correlation Coefficient: 0.9537
Explained variance: 90.95

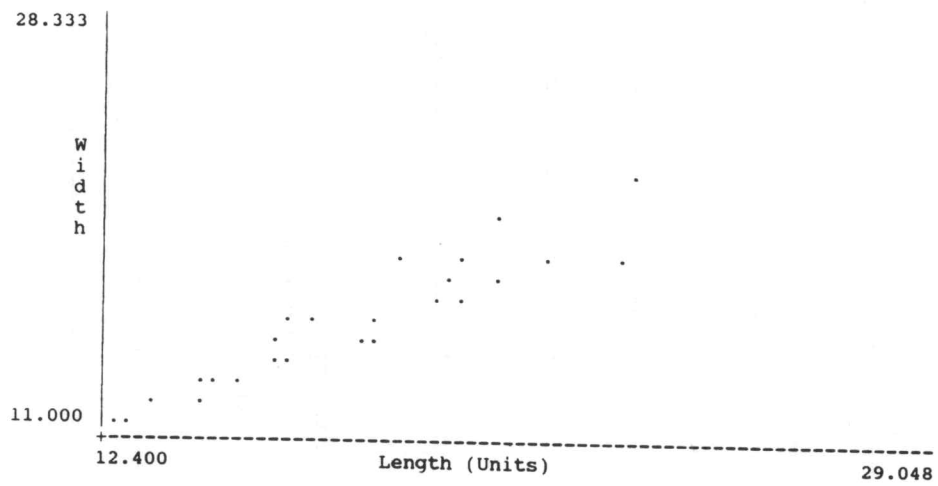

Figure 8- An example of sizing and counting of defects (Fe inclusions) in a Si3N4 rod.

Improved Processing

R. L. Beatty, R. A. Strehlow, and O. O. Omatete (Oak Ridge National Laboratory)

Objective/scope

The purpose of this task is to determine and develop the reliability of selected advanced ceramic processing methods. This task is to be conducted on a scale that will permit the potential for manufacturing use of candidate processes to be evaluated.

Technical progress

I. Silicon nitride gelcasting and sintering

Attempts continued to fabricate silicon nitride by the gelcasting method. Several commercial powders were tested: Denka 9-S and 9-FW; Starck S, S-1, LC10, and LC12-SX; and UBE - E03 and E10 silicon nitride powders. Approximately 12 successful castings were made at loadings of 45 to 50 vol %.

Casting runs were also made using fine-grained Vesuvius AA sialon powder. This material was dried, debindered, and sintered to a density of 3.13 g/cm^3 (the range of values for four specimens was 0.005 g/cm^3). This is 97.5% of the theoretical density for this composition and more than 99% of the hot-pressed density according to manufacturer's data.

Sintering schedules for the various formulations being studied are to be examined using pressed pellets made of the same powder and composition as the test castings. (The compositions for pelletizing are ball-milled in i-propanol with poly-vinyl alcohol, die pressed in 1.27-cm (0.5-in.), 1.000-g pellets, and debindered to provide the test specimens.)

Installation was completed of a specially designed controlled atmosphere furnace obtained for silicon nitride sintering. The furnace was successfully tested to 2300°C and to 1900°C at the full design nitrogen pressure of 0.2 MPa (2 atm). Two graphite crucibles were siliconized in preparation for sintering studies. A second furnace designed for 10 MPa (100 atm) operation was acquired and is being installed.

II. Drying studies

A controlled humidity, ambient temperature drying cabinet was built that permits control from approximately 40 to 95% relative humidity. Although the drying procedure has not been optimized for any of our test formulations, data are being developed using a separate gravimetric system that permits drying under controlled humidity-temperature conditions. The design conditions of the experimental system include a temperature range of 20 to 40° C and relative humidity from 70 to 95%. We believe this covers the range of greatest interest for drying of gelcast parts.

The drying schedule that is being used now for our plate specimens is 3 days at room temperature and 92% relative humidity, followed by accelerated drying to finish. Initial data suggest that 1 or 2 days would be sufficient for the early stage drying.

III. Machining and testing of tensile test specimens

The experimental method for this program is to measure the uniaxial tensile strength of product ceramics as the dependent variable with selected processing variables serving as the independent ones. A slicing machine for specimen preparation was obtained. The first six of a series of alumina plates were cut into tensile test specimens.

Two sets of specimens were tested. The specimen design is that of a 5.5-mm-square cross section bar with chamfered edges and a gage length of approximately 40 mm. The first processing variable examined was the extent of de-airing.

Air is introduced during mixing of the suspension. If air is not removed adequately, small bubbles may be entrained that are expected to lead to strength impairment. Two levels of de-airing were examined for these specimens.

The tensile strengths of the specimens are shown in Figs. 1 and 2. It is evident that the de-aired specimen has a higher strength. Using an estimate for K_{Ic} of 4 MPa-m$^{1/2}$ the critical flaw sizes were estimated. For these two sets the average estimated flaw size decreased from 0.2 to 0.08 mm. These values correspond to the observed void size in the inadequately de-aired specimens and to the measured agglomerate size in the well-deaired series. For continuing studies, milled slips are being investigated.

IV. Environmental, safety, and health studies

A series of experiments was conducted to verify the neutralization procedure used for wastes containing monomeric acrylamide. The procedure is based on the addition of sodium bisulfite to the carbon-carbon double bond of acrylamide in the presence of peroxide:

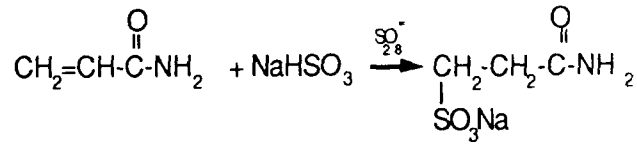

The resulting sulfonic acid is not considered hazardous. Three series of samples were examined with the two reagents separately and mixed. Reagents were added over a 2-h period. The resulting solutions were analyzed rapidly by Analytical Division personnel at the close of the period. The data are shown in Fig. 3.

The rate of the reaction was found to be high, reducing the concentration of test samples from 7000 to less than 10 ppm in 0.5 h. This level is deemed satisfactory for neutralization of waste and spills.

V. Cooperative research agreement

A cooperative research agreement has been concluded with Garrett Ceramic Components Division of Allied-Signal Aerospace Company. The purpose of the research is to determine the applicability of the gelcasting technique to Garrett's silicon nitride components.

Status of milestones

On schedule.

Publications and Presentations

None.

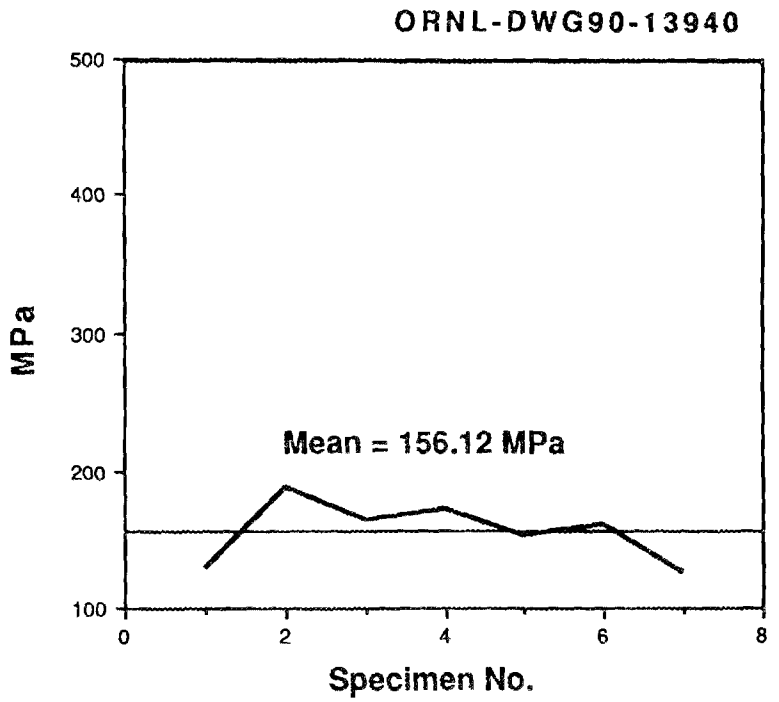

Fig. 1. Tensile strengths of alumina specimens that were not well de-aired.

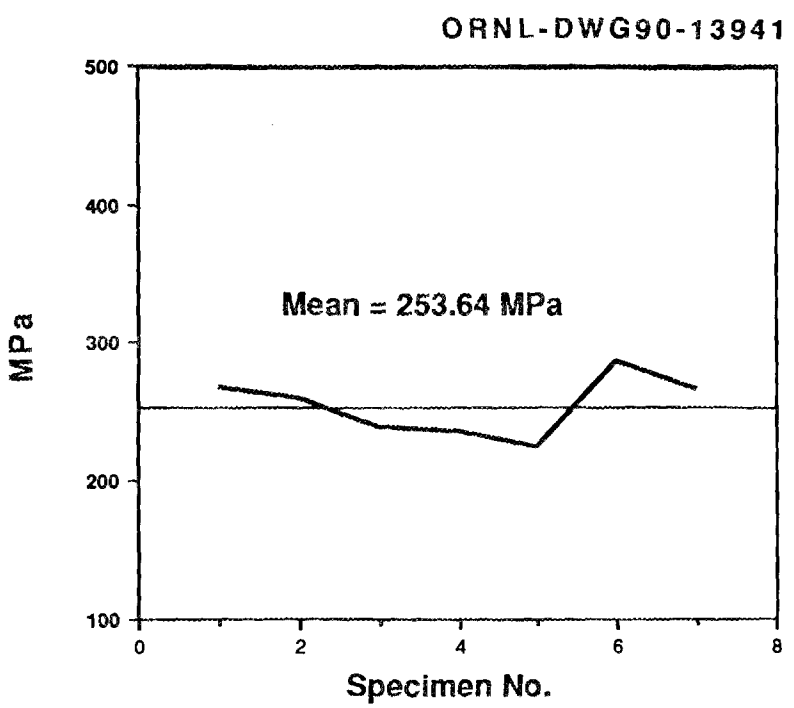

Fig. 2. Tensile strengths of alumina specimens that were well de-aired.

ORNL-DWG90-13942

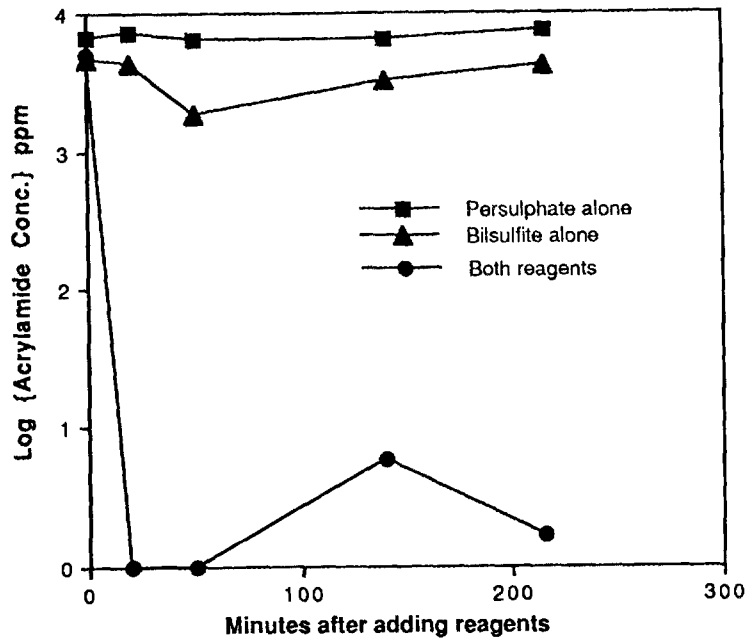

Fig. 3. Acrylamide remaining after addition of sodium metabisulfite and ammonium persulfate solutions separately and mixed.

Improved Processing

A. E. Pasto and S. Natansohn (GTE Laboratories Incorporated)

Objective/Scope

The overall project objective is to develop and demonstrate a process for reproducibly fabricating (by injection molding and HIPing) a series of tensile specimens of PY6 silicon nitride with the following properties:

Average tensile strength of 900 MPa at 25°C
Average tensile strength of 500 MPa at 1370°C
Weibull modulus of 20 in both instances.

This will be accomplished by determining the source(s) of failure-causing defects, and modifying and controlling the manufacturing process to minimize their occurrence. All potential sources of defects will be evaluated, from raw materials through individual powder processing and densification steps and finally through machining and surface finishing of the test specimen.

Technical Highlights

Task 1 - Material Selection and Characterization

CHARACTERIZATION OF SILICON NITRIDE:

The silicon nitride powder chosen for establishing the baseline properties of the process is from UBE Industries, Ltd., (Tokyo, Japan), designated by GTE as "UBE-B". The baseline lot of powder (200 kg) was received. This lot (designated lot #0) consists of four 50 kg drums. The powder to be used in the lot-to-lot reproducibility study was also received. It consists of five separate 20 kg samples taken from each of five separate 200 kg lots (numbers 1 through 5).

The baseline materials were riffled to obtain representative samples for analysis and characterized. Seven samples were submitted for each characterization technique except for the detemination of Si and N which was based on three samples only.

The vendor also provided five bags containing powder samples taken at random from this lot in a routine procedure used in the plant to collect material for analytical and archival

needs. Samples were taken from each of these containers and characterized by selected analytical techniques to obtain a comparison between the results of the evaluation of riffled and unriffled samples. The data obtained in this evaluation are presented in Table 1; the following is a brief discussion of the results.

The x-ray diffraction patterns of all powders are quite similar; the only positively identified crystalline phase is alpha-silicon nitride which is present in the amount of at least 95%. There is an indication of the presence of beta-silicon nitride in amounts not exceeding 5%.

Silicon was determined by a classical analytical technique in which the initial dissolution of the sample was achieved by alkali salt fusion. The results are typical for silicon nitride powders and confirm the applicability of this technique to the quantitative determination of silicon in silicon nitride.

Nitrogen was initially determined by the inert gas fusion technique but the results were poor. The measurement was therefore repeated by the classical Kjeldahl method which provided data not only far more consistent with the silicon nitride composition but also more precise. The former technique does not seem appropriate for high nitrogen concentration.

Both oxygen and carbon were determined by the inert gas fusion method which is quite useful in measuring small amounts of these elements. The data show no difference in the average oxygen content of the riffled vs. the unriffled samples. The carbon content is typical of the silicon nitride powders prepared by the vendor's method.

The concentration of impurities in the powder was determined by Glow Discharge-Mass Spectrometry (GD-MS). Only those impurities exceeding a concentration of 1 ppm by weight are listed. The impurity levels are within the specifications for this material except for chlorine which is present at about twice the concentration generally found in this powder. A comparison of the data for riffled and unriffled samples shows that, at least within the accuracy and precision of this analytical technique, there is no difference in the contaminant levels.

The surface composition of the powder was determined by X-ray photoelectron spectrometry (XPS). In addition to the expected major constituents of the powder (silicon, nitrogen, and oxygen), carbon and fluorine are also present on the surface. Chlorine, iron, calcium and aluminum, although present in greater amounts than fluorine in the bulk sample, were not detected on the surface in measurable quantities.

The photoelectron spectra of O 1s and C 1s binding energies have complex structures (Fig. 1) indicating more than one chemical bonding structure for these atoms. A curve fitting technique has been applied to resolve these spectra in an attempt to identify the chemical nature of the binding energies; this effort is continuing.

The concentration of the elements was calculated from the measured integrated intensities of all detected lines. The atomic concentration of Si and O implies that the oxygenated species on the surface are primarily silicon oxynitride, in which the atomic ratio of Si:O is 2:1, rather than silicon dioxide (1:2 ratio) but the latter compound is probably present as well. The photoelectron energy spectrum of carbon is even more complex, possibly stemming from the presence of fluorine. This element has been detected unambigously in powders supplied by this vendor and, while its bulk concentration in this lot is very low (< 4 ppm), it is clearly present on the surface. This aspect is under investigation.

The soluble Si was obtained by treating the silicon nitride powder with an HF solution for a fixed time period and analyzing the Si content of the aqueous filtrate. It was found in earlier extensive investigations that the amount of the dissolved Si reaches a maximum value, characteristic of a powder, which does not increase upon continued acid treatment, even at higher acid concentrations and/or higher temperatures. This indicates the presence of a discrete, HF-soluble, oxygenated layer on the surface of the silicon nitride powder particles. Once this layer is removed, there is no dissolution of the underlying silicon nitride substrate by HF solutions.

The average amount of dissolved Si is the same for both the set of riffled and unriffled samples but the measurement precision of the former determination is much better. The improved sampling inherent in the riffling process manifests itself only in analytical techniques capable of good precision, of which this is one. The amount of dissolved Si can be used to calculate the surface oxygen content. This calculation is based on the generally plausible assumption that the oxygenated surface layer consists of equal molecular amounts of silicon oxynitride and silicon dioxide, i.e. that the atomic ratio of Si to O in this layer is one. Using this assumption, the amount of surface oxygen in this powder is 0.26 w/o, that is 22% of the total oxygen in the powder is located on its surface.

There is also an observed difference in the specific surface area of the riffled versus unriffled powders, not only in the improved precision of the former but also in the average value of the parameter. There is a 90-95% probability, based on the limited database, that this difference is statistically valid and if so, it would imply that samples obtained by riffling result in a different value of a material parameter or, alternately, that some particle reduction occurred in the riffling process. The independently determined particle size distribution (PSD) also provides a different value for the median particle diameter of the two sample sets, consistent with their respective surface areas. The powders are not strongly agglomerated as evidenced by the value of the equivalent spherical diameter calculated from the specific surface area which is comparable to that obtained from the PSD determination. This is also demonstrated by the SEM photograph of the powder (Fig. 2.).

Characterization of the five silicon nitride powder lots acquired to establish lot-to-lot reproducibility has been completed. Three of these lots were selected, based on the uniformity of their properties, for use in the program and their remainder, i.e., 180 kg of each for a total of 540 kg of powder, is being purchased. The data obtained in this evaluation as well as in that of the baseline powder lot (lot #0) are summarized in the tables below.

The characteristics of the six silicon nitride powder lots are presented in Table 2. The x-ray diffraction patterns of all powders are quite similar; the only positively identified crystalline phase is alpha-silicon nitride which is present in the amount of at least 95%. There is an indication of the presence of beta-silicon nitride in amounts not exceeding 5%.

The specific surface areas of the powders are comparable and statistically indistinguishable. The same comment applies to the particle size distribution as expressed in the median particle diameter. A possible exception is the somewhat higher value for the lot #0 powder but this is probably indicative of agglomeration rather than primary particle size.

Measurable differences are observed in the total oxygen content of the six powders. The oxygen concentration of the baseline material is lower than that of lots 1 and 2 but higher than that of the other three powders; the latter three powder lots have identical values of many of the parameters measured. The determination of the soluble silicon also identifies a difference between two sets of powders; the powders #0, 1 and 2 having a common value with lots # 3, 4, and 5 having a lower amount of silicon dissolved under identical conditions. Silicon solubility is an independent parameter and the measurement results corroborate the finding that there are subtle differences in the properties of these two sets of materials.

A spectrophotometric technique for the determination of ammonia, known as the indophenol blue method, has been adapted for use in the analysis of the silicon nitride surfaces. The data show that the amount of dissolved nitrogen is comparable in all samples; however, because of the different Si solubility, the molar ratio of Si:N shows a differentiation between sample groups. These molar ratios are high; a value of 3.0 implies that the dissolved layer consists of 4 moles of silica and 1 mole of silicon oxynitride or 9 moles of silica and 1 mole of silicon nitride or any combination thereof. This also indicates that the oxygen concentration on the surface is greater than the amount which was calculated assuming, as cited in the literature, that the surface layer consists of equimolar fractions of silica and silicon oxynitride. In spite of the clearly established differences in the surface composition of the powders, the isoelectric point of all samples is the same.

The impurity content of the six powder lots is listed in Table 3. Only elements whose concentration exceeds 1 ppm (by weight) are reported. Within the limits of the analytical

technique used, there are no differences in the impurity levels among the powders, and they are acceptable levels for these powders.

The flexural strength of PY6 ceramics made by hot-pressing of these six material lots was measured in an attempt to identify correlations between powder and ceramic properties. Results of four-point bend testing are summarized in Table 4, which also includes data obtained in an evaluation of an early lot (#EL) of this material. Samples made from the baseline powder lot (#0) were broken both at 1370°C and 1400°C. The data show some variation in flexural strength of the ceramics made from the various material lots but it is likely that this is caused by uncontrolled processing factors rather than differences in powder properties. One manifestation of this effect is the room temperature data for the two billets made from lot #1; they show a rather large difference in average flexural strength but the standard deviation of the lower strength sample is much larger so that the two values are statistically equivalent.

As a result of these studies, powder lots #3, 4 and 5 were selected for use in this program. This decision was based on the fact that all the measured properties of these powder lots were virtually identical and that the flexural strength of ceramics made from them was comparable to that of ceramics made from the other lots. Uniformity of powder properties is thought to be essential because it will provide a base against which the effects of future process and/or powder modifications can be clearly assessed. Selection of these powders for use in the program constitutes accomplishment of Milestone #114301.

CHARACTERIZATION OF YTTRIA:

The yttria to be used in the project is Molycorp's Grade 1600. A total of 55 kg of this powder was received. The entire powder lot was riffled and samples were submitted for evaluation of the material's properties. The results are summarized in Table 5 and briefly discussed below.

The X-ray diffraction pattern of the powder showed cubic yttrium oxide with a trace of impurity, either an yttrium hydroxide or carbonate. The determination of the surface atomic composition by X-ray photoelectron spectroscopy showed the O 1s peak as an unresolved doublet, probably because of its presence in both oxide and hydroxide or hydrate bonding configuration. Application of curve fitting procedures to the binding energy spectrum permitted its resolution into an "oxide" (Binding energy: 535.4 0.2 eV) and "hydroxide" (Binding energy: 537.9 0.2 eV) bands as shown in Fig. 3. The surface composition was then determined from the integrated intensities of the detected peaks.

The data show that there are about equal atomic amounts of oxygen as the oxide or hydroxide species on the powder surface. Yttria is the dominant form, however, as indicated by the Y concentration which at 36.7 a/o is close to the theoretical value of 40 a/o for stoichiometric yttrium oxide. The concentration of carbon is too low to be detectable as a crystallographic impurity. The presence of hydroxide on the surface is not unusual in

yttria materials and can be reduced or eliminated by treatment at elevated temperatures. This is indicated by the loss on ignition of about 0.7% and also observed by the decreased intensity of the "hydroxide" band in the XPS spectra.

The specific surface area of the powder is typical for these materials. The median particle size diameter is large for a powder of this surface area indicating considerable agglomeration. The equivalent spherical diameter calculated from the specific surface area value is 0.17 micrometers, about a factor of 20 smaller than determined directly.

The concentrations of impurities, as determined by GD-MS, are comparable to those measured in silicon nitride and present no concern for the intended application. It is interesting to note that the concentration of Cl and F (which is not detected) in this material is far lower than that in the silicon nitride powder indicating that it is not a measurement artifact.

Task 2 - Material Processing and Process Control

This task has two major thrusts: the first is to develop and apply appropriate techniques for controlling the injection molding/HIPing processes for the chosen silicon nitride composition and shapes through statistical process control (SPC) so as to minimize the occurrence of defects. The second thrust is to improve each individual process step and incorporate these improvements into the overall process. The task is divided into several subtasks detailed below.

BASELINE PROCESS:

A simplified dogbone tensile specimen having near-net-shape gage section has been designed for use in the initial ten months of the program, prior to establishment of a near-net-shape buttonhead sample. A drawing of the specimen after HIP densification is shown in Figure 4, with the outline of the final buttonhead specimen to be cut from it shown inside. Using this configuration, a preliminary injection molding tool was designed and procured. In keeping with a desire to allow careful process control, the tool allows control of cavity temperature, incorporating several optional cooling/heating arrangements within it. Measurements of cavity pressure and temperature can be made at both ends of the specimen during molding. The design depicted results in a HIPed specimen requiring removal of approximately 1mm thickness by grinding to form the final tensile rod.

A similar tool for the ASCERA tensile test sample configuration was purchased and made operational.

Preparation of the first PY6 material for the baseline properties demonstration was initiated. The silicon nitride and yttria powders were batched in SWECO mills to make up approximately 20 kg total batches. These were then milled and discharged. Three

batches, utilizing material randomly sampled (i.e.- not riffled), were prepared, with about 63 kg total PY6 resulting. These batches were compounded with the binders in sub-batches of approximately 10 kg each. Other, separate PY6 batches were milled, utilizing materials which were riffled from the main lot of material, to allow determination of the effect of riffling on material performance.

These compounded PY6 batches were injection molded into ASCERA- and dogbone-style tensile rods. Both molds were found to exhibit moderate to severe flashing of the mix, and were consequently returned to the mold-maker for rework. This situation was repeated twice, until the mold yielded parts with minimal flash. Table 6 lists the number of components fabricated from each of the three baseline lots. These components are undergoing NDE evaluation prior to burnout and densification.

Chand-Kare Technical Ceramics, Worcester, MA has been selected to provide the final grinding of buttonhead tensile specimens for the program.

STATISTICAL EXPERIMENTATION:

The subcontract with American Supplier Institute, who will be providing support in the areas of statistical experimentation (especially with Taguchi techniques) and statistical process control, has been signed. A meeting has been set at GTE Laboratories for 10 - 11 April to initiate activities on this effort.

DATABASE DEVELOPMENT:

A prototype database for tracking materials and operations in this program has been designed using Double Helix relational database software for the Macintosh from Odesta Corp., Northbrook, Ill. In the present version, data are stored in 26 files, and linkage between the files is effected using codes unique to each file. The codes identify each material, formulation, batch, method, specimen, test, and analysis. To minimize operator error, much of the coding is done automatically or with the use of defaulted values. Although the software is fully relational, the ceramic process is hierarchical in nature. Therefore, an hierarchical overlayer has been impressed on the database structure to greatly increase the ease and speed of data retrieval at a small sacrifice in the ease with which the database structure can be modified.

The first stage of the design process was completed with a successful test of the prototype structure using dummy data. In the second design stage, entry and output forms are currently being custom designed for each operation in the process. This is essentially a process of mutual accommodation and fine tuning of the database to personal preferences and to actual operations, and some minor structural modifications have already been made. Real data, relating to powder inventory and chemical and physical powder analysis, have been entered into the database to aid in this effort.

The final stage of database design will consist of putting the program on a four station

Appleshare network and enlarging that to approximately eight stations for convenient operation. A more detailed description of the database structure and operation will be presented at the completion of the second design stage.

LIQUID PROCESSING:

An investigation of liquid processing procedures was begun according to the flow diagram illustrated in Figure 5.

The Si_3N_4 and Y_2O_3 raw materials of the PY6 composition were first assessed for the presence of coarse material not detectable in conventional particle size analysis by Sedigraph X-ray sedimentation or Microtrac light scattering techniques. These powders were independently suspended in 2-propanol by milling, then screened through stainless steel screens down to approximately 20 μm aperture. A vacuum was applied to the screens and the slurry agitated manually to prevent blinding of the mesh and assist the process. Only a very small amount (less than 0.1 gm) of coarse fraction was retained on the screens from processing of 10 kgms of Si_3N_4 and 0.6 kgms of Y_2O_3; this will be studied by SEM.

A preliminary investigation of several processing variables was then conducted to compare the following:

Type of milling
Screening
Milling medium
Surface Area of Y_2O_3

Powders milled in solvents were either dried in trays using a forced air explosion proof dryer or in a rotary evaporator. Dried cakes were then granulated by screening through an 80 mesh nylon screen.

Studies of powder processing effects on properties are in progress via isopressing/HIPing, hot-pressing, and injection molding.

MOLDING IMPROVEMENTS:

A portion of this task has the objective to develop and construct a combined compounder/molder under subcontract. Expected improvements to the process are in the areas of contamination reduction, entrapped air reduction and superior integrity of large cross section molded parts. This task is being completed in two stages; firstly a feasibility evaluation using an existing (Mk. 1) compounder/molder to highlight design factors, and secondly the construction and demonstration of a full-scale compounder/molder (Mk. 2) customized for silicon nitride ceramics.

A redesign of the standard(Mk.1) injection unit barrel and was completed prior to the beginning of this program. The redesign, which included the construction of associated hardware, improves temperature control and reliability of operation of the Mk. 1 Molder. The reactivation of this molder involved reassembly, debugging and test molding using polyethylene.

A tool was selected for use in completing preliminary molding tests. The tool produces a center, sprue gated disk approximately 4 inches in diameter and 5/16 inches thick. The thickness of the disk can be increased as desired to evaluate large cross section parts. It is fitted with a transducer for the measurement of cavity pressure.

The prototype (Mk. 1) compounder/molder was operated using PY6 material with the center-gated disk mold. The number of parts produced was limited to approximately twenty due to operating difficulties described below. The results are considered positive in that the Mk. 1 machine functioned to provide good quality molded parts. The PY6 material flowed easily, without bleeding, through the complex path between compounder and molder. Several cool downs and restarts were accomplished without difficulty. The parts showed a clear and significant reduction of "fold lines". These trials were successful in that moldings were produced and difficulties specific to the PY6 material have been identified. Several problems were encountered involving the flow of the abrasive materials creating excessive wear. Solutions to these problems appeared to include redesign of critical wear areas, incorporation of more wear-resistant materials, and better control of temperatures to prevent the mix from losing viscosity.

A tentative design for the Mk. 2 compounding and injection unit was devised. Initial discussions concentrated on how best to ensure rheologically consistent compounding. It is presently assumed that continuous operation of the twin screw extruder is required for this condition. A design comprising two injection units was accordingly considered. This would allow continuous operation of the twin screw extruder through the filling of the one of the injection units during the injection of the other injection unit. These and other design issues were discussed at a meeting between GTE Laboratories and its subcontractor on December 27, 1989.

A second conceptual design was then been formulated for the Mk. 2 compounder/molder, and a plan and schedule for its procurement and construction formulated. The plan allows for the program to proceed as scheduled with delivery of the completed Mk. 2 molder to GTEL in April 1991. A detailed review of the design has been scheduled for April 3, 1990 at GTEL. The Mk. 2 compounder/molder will be assembled from the following:

•A 200 ton HPM injection molder base with toggle clamp. A 220 ton hydraulic clamp unit was also considered. The toggle clamp unit is expected to be less costly by approximately

10%.

•A twin screw extruder. This compounder will have standard temperature control system. The drive unit will be selected to provide sufficient powder for GTE's compounder needs and sufficient output for up to a 300 cc shot within required cycle times.
Manufacturers have been identified for these components.

FINISHING STUDIES:

An annealing study has been initiated to evaluate optimum annealing conditions for machined PY6. The object of this experiment is to determine what occurs in the annealing process (healing of machine damage, crack blunting, etc) and what effect this process has upon the mechanical properties of machined samples. The temperature range to be examined is 1000 to 1400°C, since previous testing has shown this treatment to yield improved mechanical strength.

Task 3 - Development and Application of NDE Methods

ULTRASONIC TESTING SYSTEM:

An ultrasonic inspection system was specified for nondestructive evaluation of ceramics. Several meetings with a preferred vendor (Panametrics Inc., Waltham, Ma) resulted in preparation of a final quotation for the system. The system will provide GTEL with four major capabilities:

1) High resolution pulse-echo imaging of subsurface structures
2) Time-of-flight scanning for mapping density gradients
3) Surface wave (Rayleigh wave) inspection of flat specimens
4) Surface wave (Rayleigh wave) inspection of cylindrical specimens.

Experience has shown that pulse-echo imaging and density mapping are extremely valuable for characterizing the homogeneity of ceramic specimens. Surface wave inspection complements radiographic methods, providing enhanced detectability of surface and near-surface flaws. The most novel attribute of the system is the capability of performing surface inspection of cylindrical specimens. To meet this requirement, an additional rotational stage will be incorporated in the specimen manipulator, and software for motion control and image reconstruction will be developed. Surface wave inspection will allow for direct NDE of tensile specimens.

Dr. Ron Roberts of the Ames NDE Center at Iowa State University is the selected subcontractor on ultrasonics for this program. An engineering review of our new system was conducted at Panametrics on 3/20/90 in conjunction with Iowa State and GTE

Laboratories ultrasonic NDE personnel. Development of the custom designed ultrasonic system has progressed well ahead of schedule with several required capabilities fully demonstrated during the review. The delivery time for the ultrasonic system is 9 months. In the interim, the quotation allows for both toll testing at Panametrics and rental of a standard Hy-scan system.

Image quality indicators (IQIs) were fabricated for use in development and acceptance testing of the ultrasonic inspection system. Silicon nitride test bars (3.5x4.5x50 mm) with known internal voids, characterized by microfocus radiography, are being utilized to benchmark the pulse-echo imaging capability.

Alumina slabs approximately 75x75x10 mm which have been ultrasonically mapped for relative density gradients will be used to test time-of-flight scanning. Density variations across the slabs span the range of 0.1 to 1.0 percent.

Silicon nitride specimens with laser-machined simulated voids are being used for assessing surface wave imaging. Flat test bars (1.27x2.54x25.4 mm) have been prepared with a single 10, 20, 50, and 100 mm void having an aspect ratio of one machined into their surfaces. Two cylindrical ASEA style tensile rods (6 mm diameter, 120 mm long) have been laser-machined with multiple voids approximately 10, 20, 50, and 100 mm in width and depth.

The images shown in Figure 6 were obtained by surface wave (Rayleigh wave) inspection of 4 silicon nitride modulus of rupture test bars with laser-machined simulated voids. The technique utilized a focused 50 MHz transducer designed to produce a radial surface wave. Centrally positioned surface voids of 100, 50, and 20 micrometers were readily detected. One bar (shown on bottom) had a 10 micrometer surface void, indicated by a marker pen, which would probably not have been detected. Longitudinal grinding marks were also apparent.

A major technical hurdle anticipated in the ultrasonic system development did not materialize when surface wave imaging was successfully applied to inspect cylindrical tensile rods (6-mm in diameter). A novel rotational stage was incorporated in the prototype specimen manipulator. Software for manipulator control, data acquisition, and image reconstruction was developed concurrently. The technical requirements included:

1) maintaining the footprint of the focused 50 MHz transducer to ensure it is small in comparison with the radius of curvature of the tensile rod
2) assuring orthogonality of the transducer with respect to the specimen
3) concentrically rotating the specimen and precisely preserving the transducer to specimen spacing during the longitudinal scan
4) reliably gating on the surface wave signal.

Surface wave imaging was performed on an ASCERA style tensile rod, 6-mm in diameter and 120-mm long, containing laser-machined simulated voids. The tensile rod was rotated 360 degrees in 2-degree increments and scanned longitudinally. An optical image of the tensile rod at low and high magnification and a representative surface wave image are shown in Figure 7. Initial experiments detected voids 50 micrometers in size and larger.

High resolution C-scan images of silicon nitride test bars revealed all the naturally-occurring internal voids previously detected and characterized with microfocus radiography (voids nominally 50 micrometers or greater in size). The C-scans were produced via pulse-echo imaging using a 50 MHz transducer.

The ultrasonic system is being integrated by Panametric's Automation Division, Ithaca, NY. The full-scale precision manipulator and enhanced software should be available for testing at Panametrics in June 1990.

SURFACE PROFILOMETRY:

A non-contact laser surface profilometer which allows for precise characterization of surface profile has been purchased from Rodenstock Precision Optics. Profiles of microscopic surface terrain over spans of up to 60mm are achievable at a scan rate of 30 mm/min. The laser beam allows surface height resolution on the order of one micron. In initial tests with the system, both longitudinal and radial profile scanning were successfully performed on cylindrical tensile test specimens. Radial scanning is possible because the footprint of the focused solid state laser (0.8 μm) is small compared to the radius of curvature of the specimen.

Results were acquired from the gage section of an ASCERA-style zirconia tensile specimen. The specimen was a right circular cylinder with a 6-mm diameter that was cylindrically ground and lapped. Digital filtering was utilized to remove the curvature from the radial direction surface trace. It was observed that the surface roughness (R_a) was greater in the longitudinal scan, where radial grinding marks from cylindrical machining were profiled.

The surface profilometer software calculates numerous parameters from the surface roughness profile. As the Advanced Processing Program continues, the research effort will be focused on determining which of these roughness parameters or additional spectral analysis (max peak/unit distance, fractal dimension, etc.) are predictive of mechanical behavior, and relating them to fabrication variables.

Scans of precision ground and lapped silicon nitride tensile specimens have revealed steep-sided 'valleys' as deep as 20 μm in the surface profiles. These valleys would be critical flaws at the stress levels required (900 MPa at room temperature). A representative profile is shown in Figure 8.

Traditionally, lapping of tensile specimens is employed to reduce surface roughness;

however, surface profiles have shown that, while lapping is operative in minimizing peaks, it is not necessarily affecting valleys. Aggressive lapping with coarse diamond pastes (e.g. 30 micron) may exacerbate the problem by causing pullouts. Optical micrographs of tensile specimens machined in this way have revealed pitting of the surface. Presently, this NDE information is being used to modify the machining procedures. Investigation of the cause-and-effect of surface roughness will continue as the baseline process tensile specimens become available.

IN-PROCESS NDE:

Microfocus film radiography was employed to nondestructively evaluate as-received and milled powders for the baseline process. Samples of the as-received powder showed no indications of high density inclusions. This result was consistent with Task 1 powder characterization which quantified iron contamination as less than 50 ppm.

Three samples of milled PY6 powder were taken from each of the baseline batches and radiographed in uniform plastic vials. Batch-to-batch differences in the radiographic density of the samples were apparent. Variation in the yttria content of the PY6 was suspected; however, wet chemical analysis showed the powder stoichiometry was correct. Modeling of the X-ray attenuation, based on mass attenuation coefficients of the constituent elements, indicated that the change in radiographic density measured (0.54 change in the worst case) could be explained by a 0.35% variation in yttria percentage or a 3.5% variation in bulk (packing) density.

X-ray attenuation is an order of magnitude more sensitive to variation in yttria content than to changes in bulk density. Bulk density is not controlled precisely in the milled state. Therefore, monitoring yttria content and distribution with radiography will be investigated in the as-molded and densified states, where bulk density is controlled more exactly. Radiography of vials packed to different tap-densities in a controlled experiment confirmed the attenuation modeling results and indicated that the difference in radiographic density observed was due to variation in packing density of the powder.

Microfocus radiography of milled powders readily detected agglomerates, which were determined to be relatively rigid. The radiograph shown in Figure 9 exhibits the agglomerates in one batch. The agglomerates are imaged as low radiographic density areas (high X-ray attenuation). Wet chemical analysis showed that agglomerates from the milled powders were stoichiometric PY6, and not yttria rich. The method of densification aid addition to the mill was changed for the next batch and the agglomerates were absent. The efficacy of microfocus radiography as a monitoring tool for powder quality, requiring little or no sample preparation, will be investigated as the program continues.

OPTIMIZATION OF DEFECT DETECTABILITY:

Image quality indicators (IQIs) are being fabricated to assess defect detectability limits of the various NDE methods in use. In the past, the use of flat IQIs containing laser-machined simulated voids was beneficial in evaluating and optimizing microfocus radiography for NDE of ceramics. Cylindrical IQIs are now being prepared to determine the detectability of flaws in ceramic tensile test specimens.

Resonetics Inc. of Nashua, NH has successfully machined simulated voids in silicon nitride specimens with an Excimer laser. Two longitudinally ground and lapped tensile specimens have been provided to them with plans for machining 100 each of 10, 20, 50, and 100 mm voids. One of these IQIs was provided to Panametrics, Inc. for use in development of their surface wave technique for ultrasonic inspection of cylindrical specimens.

A theoretical analysis of x-ray image contrast was developed to help explain empirically-observed behavior in microfocus x-ray projection radiography of silicon nitride components. This involved the relationships among film contrast, x-ray attenuation coefficient, object thickness, projective magnification, accelerating potential, film exposure characteristics, and x-ray scattering. The analysis showed that an accelerating potential can always be found that maximizes image contrast, and that the optimum accelerating potential depends in part on the degree of image magnification employed. Simply stated, for magnification greater than 3 or 4, the optimum condition for film is $\mu x=k$, where k is the film gradient, μ is the linear attenuation coefficient, and x is the nominal thickness of the part under inspection. Because x and k are known for a given test, μ can be determined explicitly. Then, the accelerating potential is chosen from tables relating attenuation coefficient of materials to accelerating potential. This predicted maximum contrast property has not been found in standard NDE or radiography texts, but it has been observed qualitatively in real-time and film radiographic studies.

In order to quantitatively validate the theory, a test was performed with a silicon nitride step wedge. A set of exposure conditions (accelerating potential, beam current, exposure time) was arbitrarily chosen to produce a given film density on the projection image (10X magnification) of the thin portion of the step wedge. Contrast was determined by measuring the difference between the film densities in the thin and thick regions. The accelerating potential was then changed in increments of 5 kilovolts, requiring concomitant changes in beam current and/or exposure time to produce the same film density in the thin section. The density difference was again measured. Additional data were obtained to generate a plot of film density difference as a function of accelerating potential. The results are displayed in the Figure 10, which clearly shows a contrast maximum occurring at 30 kilovolts for this example. The asymmetric nature of the curve shows that image contrast decreases much more rapidly for accelerating potential below the optimum than for kilovoltage above the optimum. With this information, accelerating potential can be

chosen a priori to realize maximum contrast in the detection of defects in silicon nitride tensile test specimens. It has also been shown that the maximum contrast condition corresponds directly with previous probability of detection studies, which have taken weeks to perform (the test described here required two days and twenty-two separate film exposures).

Task 4 - Property Testing and Microstructural Evaluation

Tensile testing of ceramic rods with the ASCERA tensile test system has generated valuable data and practical experience for the mechanical testing requirements of this program. In evaluating the ASCERA system, mechanical failure of 10 ground and lapped zirconia rods was achieved, with fractures originating primarily at internal defects. It was shown that for machined specimens, rod-piston eccentricity contributed negligibly to directly measured fracture strength, indicating that bending moments were minimal. However, the adhesive bond for three rods failed before sufficient stress was realized to fracture the rods. The stress at which the bonds released was less than the stress at which other rods fractured, revealing a repeatability problem. It was determined that the allowable stress of the adhesive must be improved to make it sufficient to break the strongest tensile rods of silicon nitride.

To resolve this problem, experiments are were begun to determine the cause of the bond failure. The rod-to-piston clearance has been changed to meet the exact thickness specified by the adhesive manufacturer. An etching technique was developed for increasing the surface area of the ends of the tensile specimen. Redesign of the pistons and modification of the specimen chamber has been employed to allow larger gripping area for a longer specimen. The allowable stress increases with increasing surface area of the adhesive bond and surface area increases linearly with an increase in length of the tensile specimen. The three tensile rods which slipped from their associated pistons before fracture were successfully tested to failure when the adhesive joint conditions were modified. Of the modifications cited, increasing the rod-piston clearance was determined to be the critical factor limiting adhesive bond strength.

Redesign of the pistons and ASEA specimen chamber has been completed to accommodate the larger gripping area of a longer specimen. Prototype pistons (long) and spacers required to modify the specimen chamber have been fabricated. Analysis shows that the system should exceed the 900 MPa requirement based on the strength of the adhesive bond specified by the manufacturer and increased allowable stress afforded by the modified test configuration.

On Sept. 20, a visit was made to the HTML, and on Oct 16 a visit was made to UDRI for the purpose of preliminary buttonhead specimen tensile testing trials. Sixteen specimens were tested at the HTML and an additional four samples were tested at

UDRI.(The specimens used are described below). Fifteen of the twenty samples failed either at the buttonhead or the transition area of the sample. The data from these tests were considered preliminary but it was felt that an effort was required to identify and understand the critical factors that relate to buttonhead failures. Consequently, follow-up testing was pursued in-house.

During November '89, an Instron Supergrip system for tensile testing was received and installed on an Instron Model 1332 servohydraulic test machine. This setup has been made operational for manual tensile testing. An Instron upgrade allowing computer controlled testing and data acquisition has been purchased. Computers have been acquired for the purpose of Instron control and strain gauge readout and are now being outfitted for these purposes.

Five tensile tests were run on samples of injection molded PY6 made prior to program commencement from UBE Si_3N_4. The objectives of these tests were to: 1) verify operation of the tensile tester, 2) understand the problem of buttonhead failures recently experienced by GTE samples at ORNL and UDRI, and 3) provide the GTEL machine shop with immediate feedback on their tensile sample and copper collet machining techniques(see below). All 5 samples failed either in the gage section or at the beginning of the gage to shank transition. All tests were run in a worst case scenario, with neither the specimens nor the collets being annealed. One sample failed from an inclusion that was obvious to the unaided eye. Sample strengths are reported in Table 7. These test results indicate that the samples and collets machined by the GTEL shop are acceptable with respect to avoidance of buttonhead failures.

The GTE Labs shop is using its longitudinal grinding attachment on a Weldon CNC grinder to provide samples to ORNL- print specifications. These are being ground from injection-molded and HIPed rods of various vintages, which were prepared with several types of silicon nitride powder outside of the Advanced Processing Program. Several of these samples, along with samples ground by four private shops, were taken to the HTML and UDRI as noted above for tensile testing. The GTEL shop reviewed the grinding process and found a need to improve the radius at the button head. The problem was determined to be a curvature inconsistency from one side of the grinding wheel to the other. Consequently, a new, plated, 400 grit diamond wheel was purchased to correct this problem. The data in Table 7 were derived from specimens ground to the exact dimensions specified with this new wheel.

The copper collets provided with the Instron tensile test system were examined for shape and dimensional accuracy. Based on these examinations, the GTEL shop made several experimental sets of collets with a tighter inside and outside diameter specification. Buttonhead failures were noted when the three copper collets were not evenly inserted into the grip/specimen interface. When these factors were brought under control, gage section

failures predominated, with failure originating from internal defects, usually metallic inclusions.

Status of Milestones

Selection of the silicon nitride and yttria powders for use in the program constitutes the accomplishment of Milestone #114301. The test specimen geometry and test procedure are considered satisfactory for the accomplishment of the program. This completes milestone #114319. Overall execution of the remainder of the program is on schedule.

Publications

None.

References

None.

Table 1. Summary of Silicon Nitride Powder Characterization Data

	Average of Seven Riffled Samples	Average of Five Vendor Samples
Phase Content (XRD)	a-Si_3N_4 (<5% ß-Si_3N_4)	a-Si_3N_4
Si (w/o)	58.67±0.16	—
N(w/o) (Leco)	42.5±0.8	—
(Kjehdahl)	38.4±0.2	
O(w/o)	1.15±0.04	1.14±0.03
C(w/o)	0.16±0.01	—
Impurities (ppm) by GD-MS		
F	3.8±0.6	1.9±0.4
Na	6.8±1.7	3.9±1.8
Mg	3.1±3.4	1.0±0.2
Al	11.0±4.6	21.0±30.0
Cl	194.0±26.0	217.0±23.0
Ca	22.0±3.8	27.0±11.0
Cr	8.3±2.6	3.4±0.1
Fe	52.0±14.0	58.0±63.0
Ni	3.1±0.4	6.2±1.8
Cu	24.0±6.3	16.0±2.4
Surface Composition - XPS		
Si(a/o)	34.5±3.1	—
N(a/o)	31.9±1.6	—
O(a/o)	20.3±1.3	—
C(a/o)	12.3±2.6	—
F(a/o)	1.1±0.1	—
HF-soluble Si (mg/g)	4.61±0.13	4.40±0.34
HF-soluble (mmol/m^2)	0.026	0.025
Surface oxygen (w/o)	0.26	0.24
Surface oxygen as fraction of total oxygen (%)	22.0	21.0
Specific surface area (m^2/g)	7.79±0.14	7.54±0.25
PSD, d_v 0.5 (µm)	0.49±0.01	0.58±0.01
d_{calc} (µm)	0.24	0.25

Table 2. Characteristics of Silicon Nitride Powders

Lot No.	0	1	2	3	4	5
XRD:	Alpha phase is the only crystalline phase positively detected, beta phase possible.					
Surface area						
(m^2/g)	7.54±0.25	8.08±0.25	8.05±0.19	7.83±0.32	7.49±0.23	7.77±0.24
PSD						
d_{50} (μm):	0.58±0.01	0.50±0.03	0.51±0.03	0.52±0.01	0.52±0.02	0.54±0.02
O(w/o):	1.14±0.03	1.29±0.02	1.24±0.03	1.07±0.01	1.04±0.02	1.06±0.01
(mg/m^2):	1.51	1.59	1.54	1.37	1.39	1.36
Sol. Si						
(mg/g):	4.40±0.34	4.67±0.18	4.35±0.79	3.54±0.14	3.62±0.14	3.59±0.09
($mmol/m^2$):	0.021	0.021	0.019	0.016	0.017	0.016
Sol. NH_3						
(mg/g):	0.65±0.10	0.61±0.05	0.78±0.13	0.73±0.05	0.73±0.01	0.74±0.08
($mmol/m^2$):	0.0051	0.0044	0.0057	0.0055	0.0057	0.0056
Molar ratio						
Si:N :	4.1	4.6	3.4	2.9	3.0	3.0
Surface O						
(w/o):	0.24	0.36	0.24	0.19	0.20	0.20
(% of total):	21	28	19	18	19	19
Isoelectric Point:	6.5	6.5	6.4	6.6	6.5	6.6

Table 3. Impurities in Silicon Nitride Powders(ppm*)

Lot No.	0	1	2	3	4	5
F	1.9±0.4	2.2±1.0	2.7±1.2	2.8±0.6	2.3±0.3	2.9±0.3
Na	3.9±1.8	23±15	5.4±1.9	1±0.4	3.7±1.1	5.1±4.5
Mg	1.0±0.2	1.1±0.6	1.4±0.5	2.4±2.3	2.3±2.4	1.8±0.8
Al	21±30	7.5±4.8	8.0±3.4	8.7±3.9	8.9±3.5	33±60
Cl	220±23	140±29	90±75	220±37	220±24	200±15
Cl (NAA)**		93±9				
Ca	27±11	23±11	25±5.1	37±29	24±4.5	25±6.7
Cr	3.4±0.1	4.5±0.2	4.1±0.2	4.0±0.4	3.9±0.1	4.2±0.5
Fe	58±63	37±1.3	37±10	33±1.2	35±4.7	33±0.7
Ni	6.2±1.8	4.2±0.3	3.7±0.6	3.2±0.6	3.3±0.2	3.5±0.3
Cu	16±1.8	15±7.0	13±10	25±23	12±3.5	17±6.1

* Measured by glow discharge mass spectrometry, except ** by neutron activation analysis.

Table 4. Comparison of Flexural Strength of PY-6 Ceramics Made from Different Silicon Nitride Powder Lots

Lot No.	Billet #	Flexural Strength (MPa) at 25°	1200°C	1370°C	1400°C
EL		1030	770	-	570
0	1	1020±100	-	550±30	510±20
	2	1050± 60	-	560±50	460±25
1	1	930±140	670±25	515±35	-
	2	1080±55	710±25	560±40	-
2		920±115	700±35	550±16	-
3		905±95	635±70	560±6	-
4		845±160	680±25	500±10	-
5		935±75	585±63	540±25	-

Table 5. Summary of Yttria Powder Characterization Data

ITEM	RESULT
XRD	Cubic Y_2O_3 (trace of impurity)
XPS	
Yttrium	36.7±0.2 a/o
Oxygen (as oxide)	30.1±0.9 a/o
Oxygen (as hydroxide)	31.5±0.8 a/o
Carbon	1.8±0.3 a/o
LOI	0.67 w/o
SSA	10.9±0.2 m^2/g
D(V, 0.5)	3.5±0.3 μm
Impurities (ppm)	

Na	14.0±5.0	Cr	17.0±10.0
Al	5.0±3.0	Fe	54.0±35.0
Si	55.0±15.0	Ni	9.0±5.0
Cl	22.0±9.0	Cu	31.0±22.0
Ca	6.0±2.0	La	59.0±90.0
Ti	15.0±18.0		

Table 6. Baseline PY6 Tensile Rods Fabricated

PY6 Batch #	# ASCERA Rods	# Dogbone Rods
900223	30	19
900327	69	19
900330	10	24

Table 7. Tensile Test Results

Sample ID	Gauge Section Surface Grind[a]	Tensile Strength (MPa)
#32	320	797
#31	320(P)	691
#41	400(P)	711
#181	220(P)	547
#171	220	703

[a] Wheel grit size used during final grinding step. (P) means polished.

Figure 1. X-ray photoelectron spectrum of species on baseline silicon nitride.
a) Oxygen 1s b) Carbon 1s

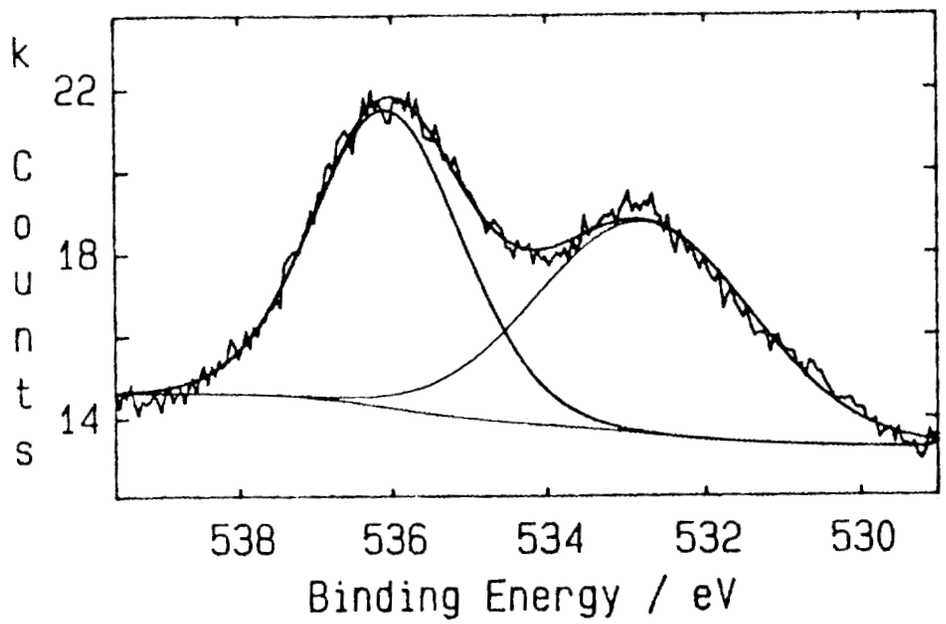

(a)

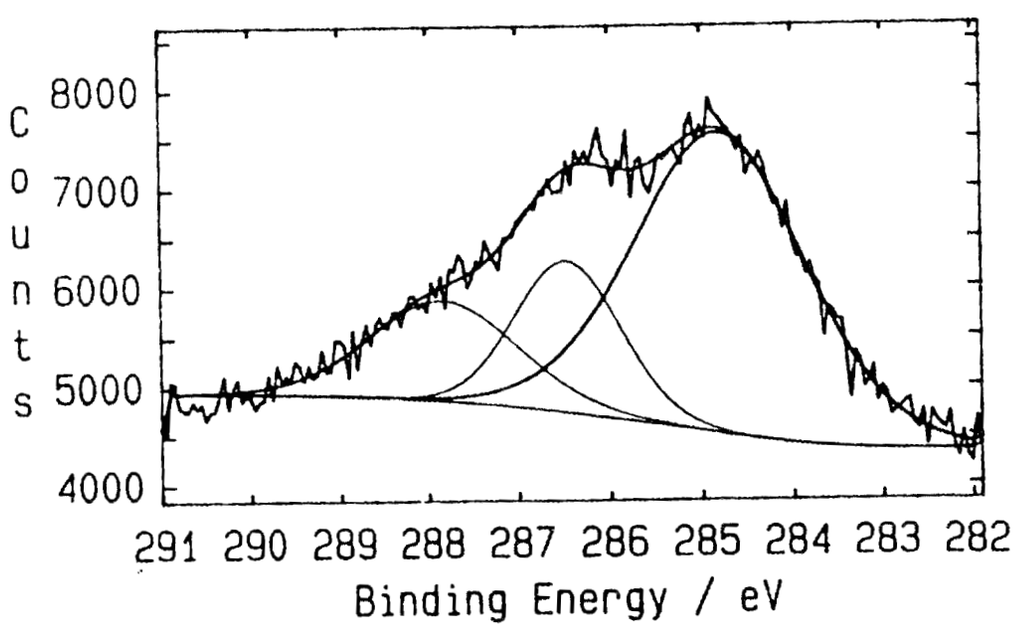

(b)

Figure 2. SEM micrograph of baseline silicon nitride powder.

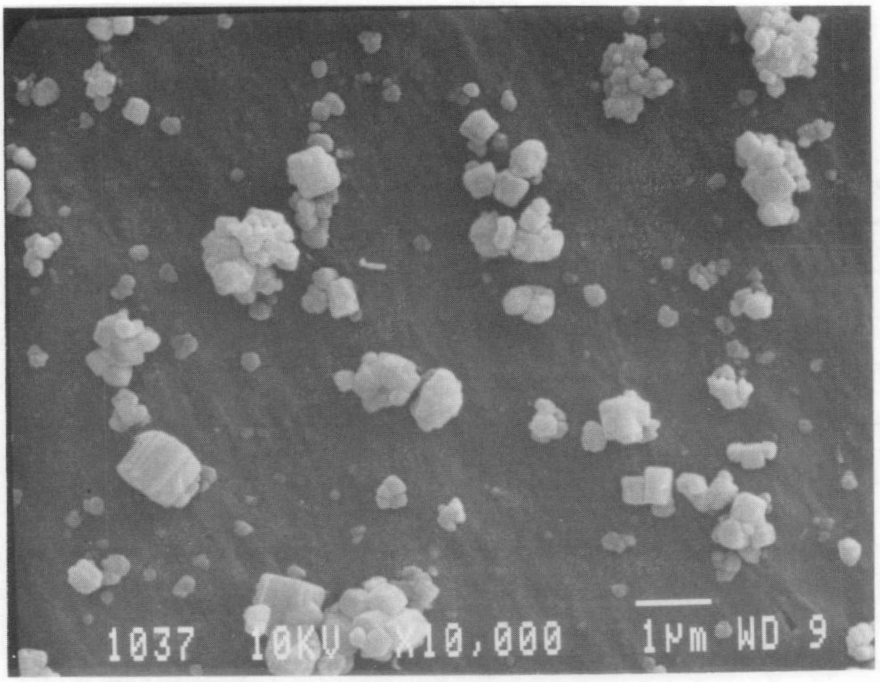

Figure 3. X-ray photoelectron spectrum of oxygen 1s on baseline yttria powder.
(Oxide binding energy: 535.4 eV,
hydroxide binding energy: 537.9 eV)

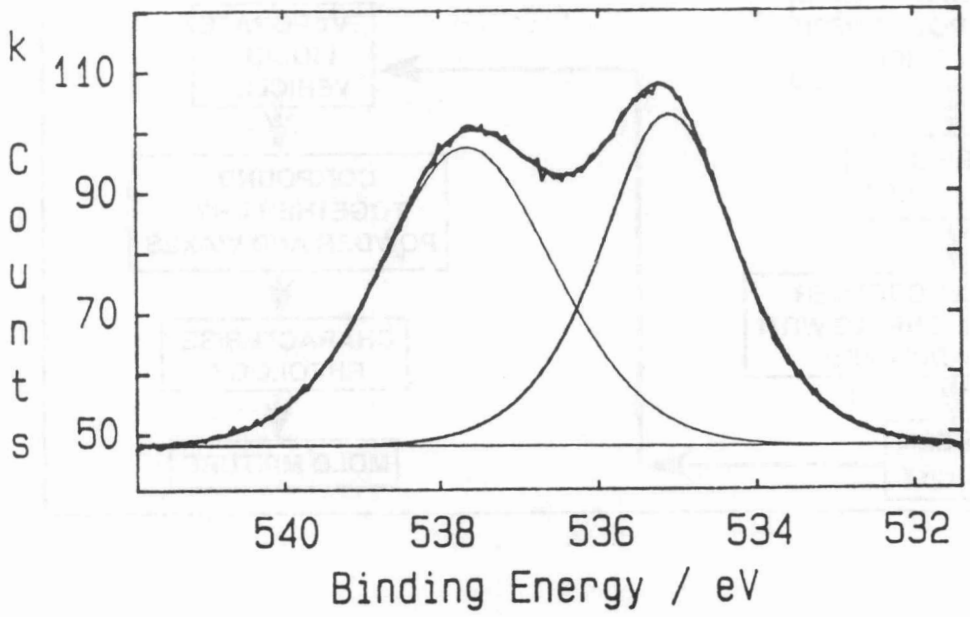

Figure 4. Sketches of buttonhead tensile specimen fabrication shapes.

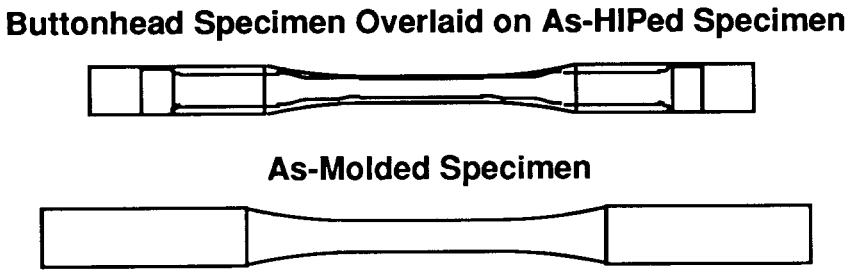

Figure 5. Flow diagram for liquid milling process.

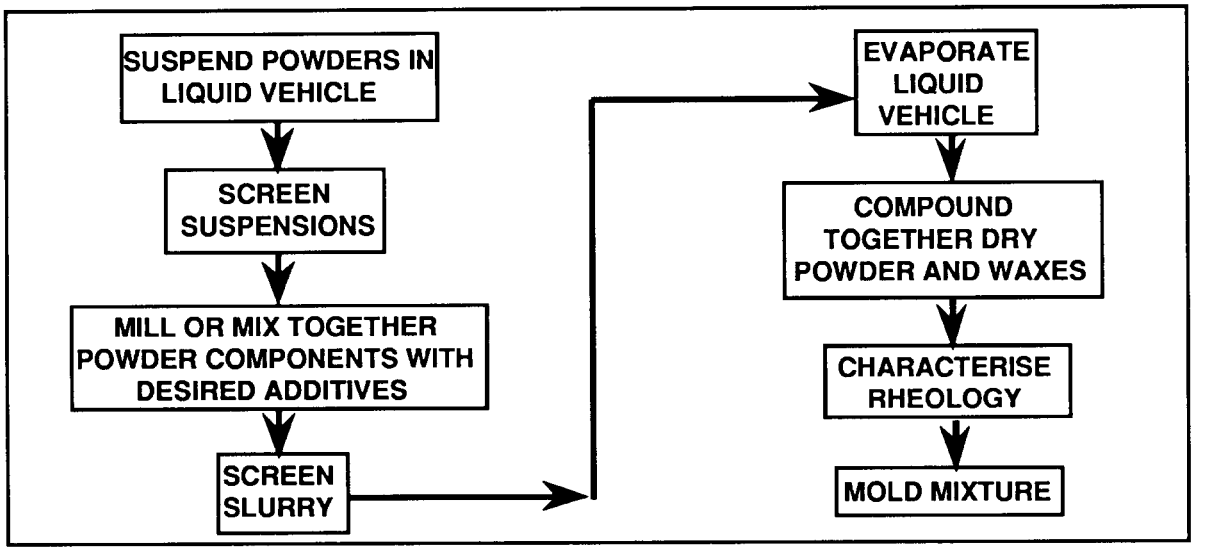

Figure 6. Ultrasonic Inspection of a Cylindrical Tensile Specimen. Optical image of the tensile rod at low (top) and high (middle) magnification. Surface wave image (bottom) revealed voids. Note, that the optical and ultrasonic images are reversed.

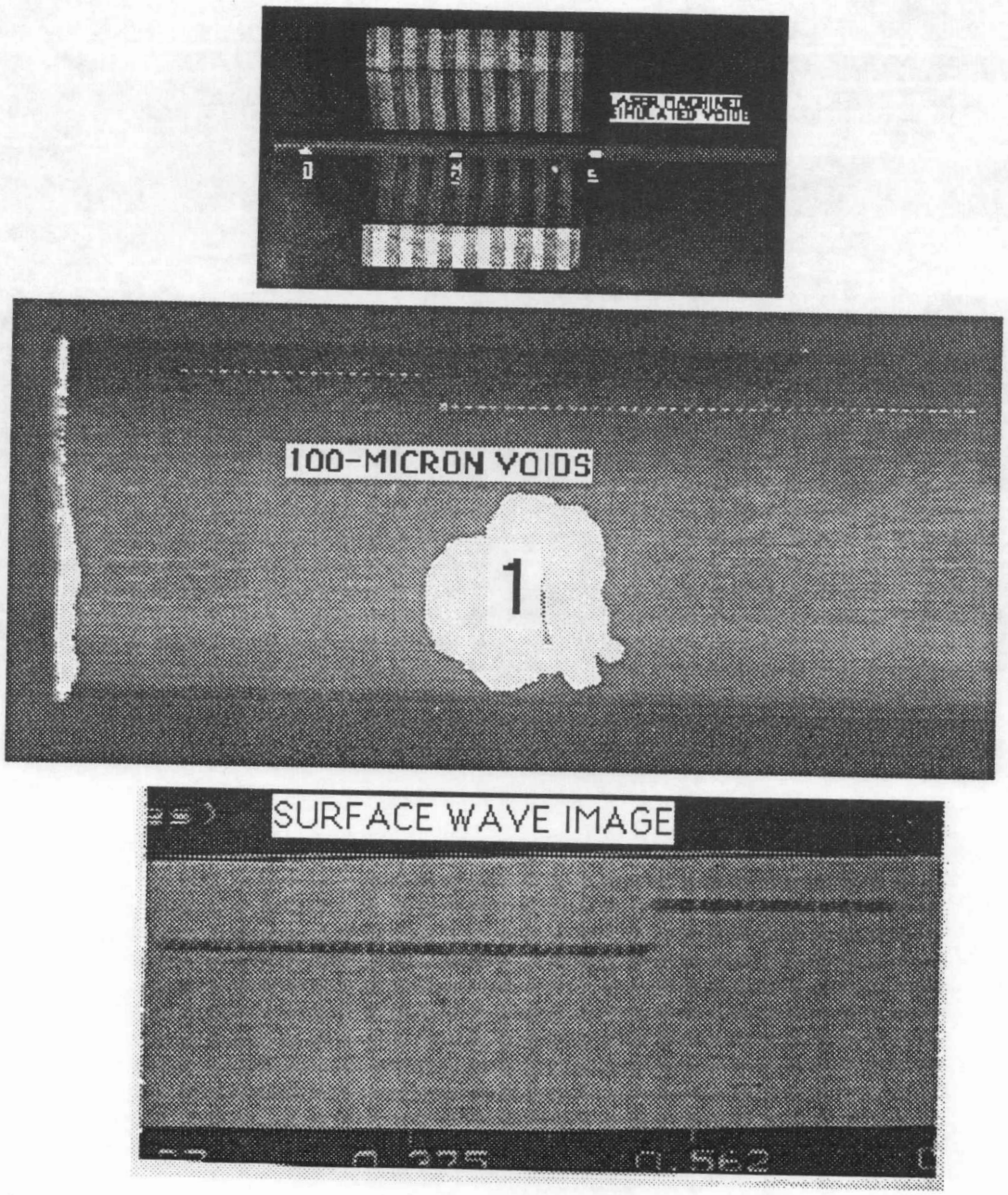

Figure 7. Surface Wave Image. The images shown were obtained by surface wave inspection of 4 silicon nitride modulus of rupture test bars. Centrally positioned surface voids of 100, 50, and 20 micrometers were readily detected.

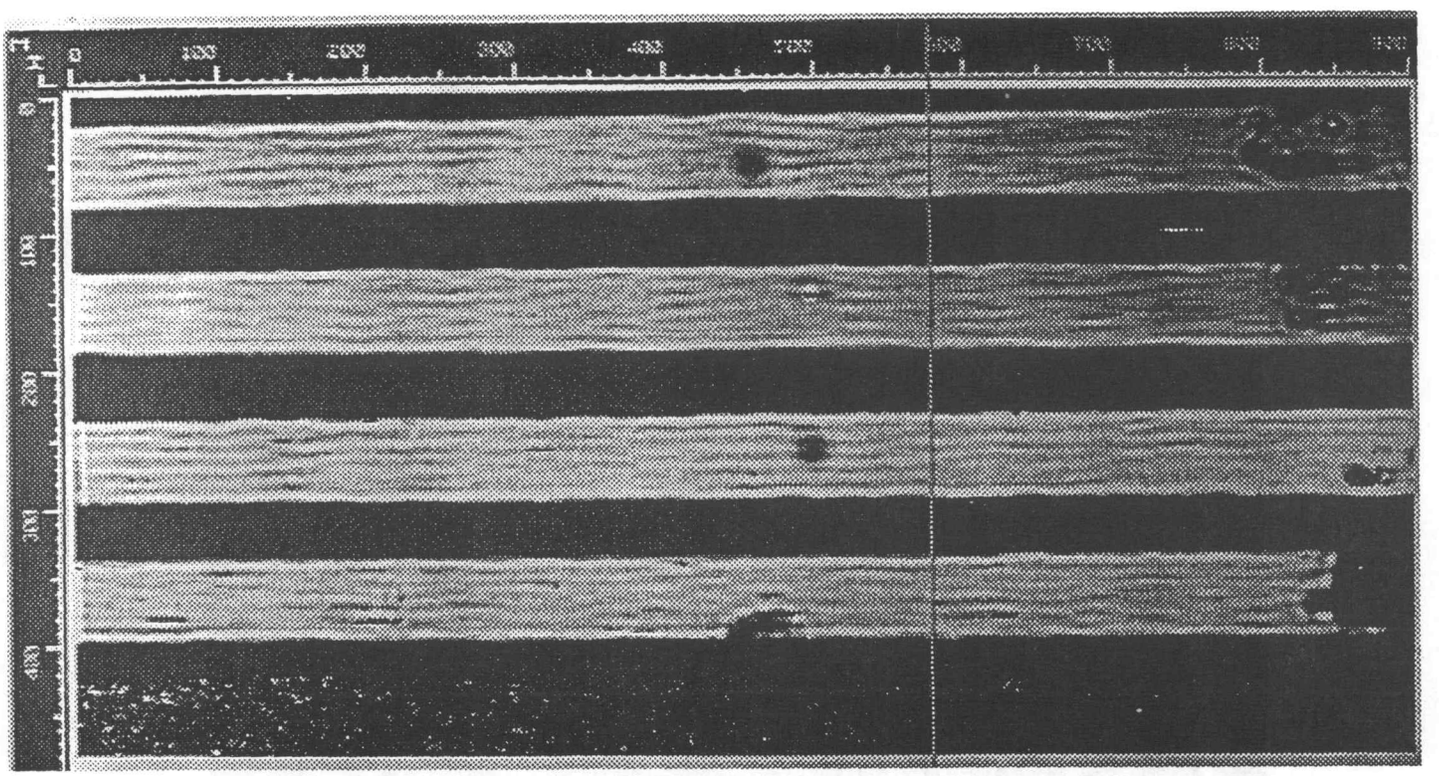

Figure 8. Laser surface profilometry scan. The gage section profile of a precision ground and lapped tensile specimen shows that relatively large valleys persist.

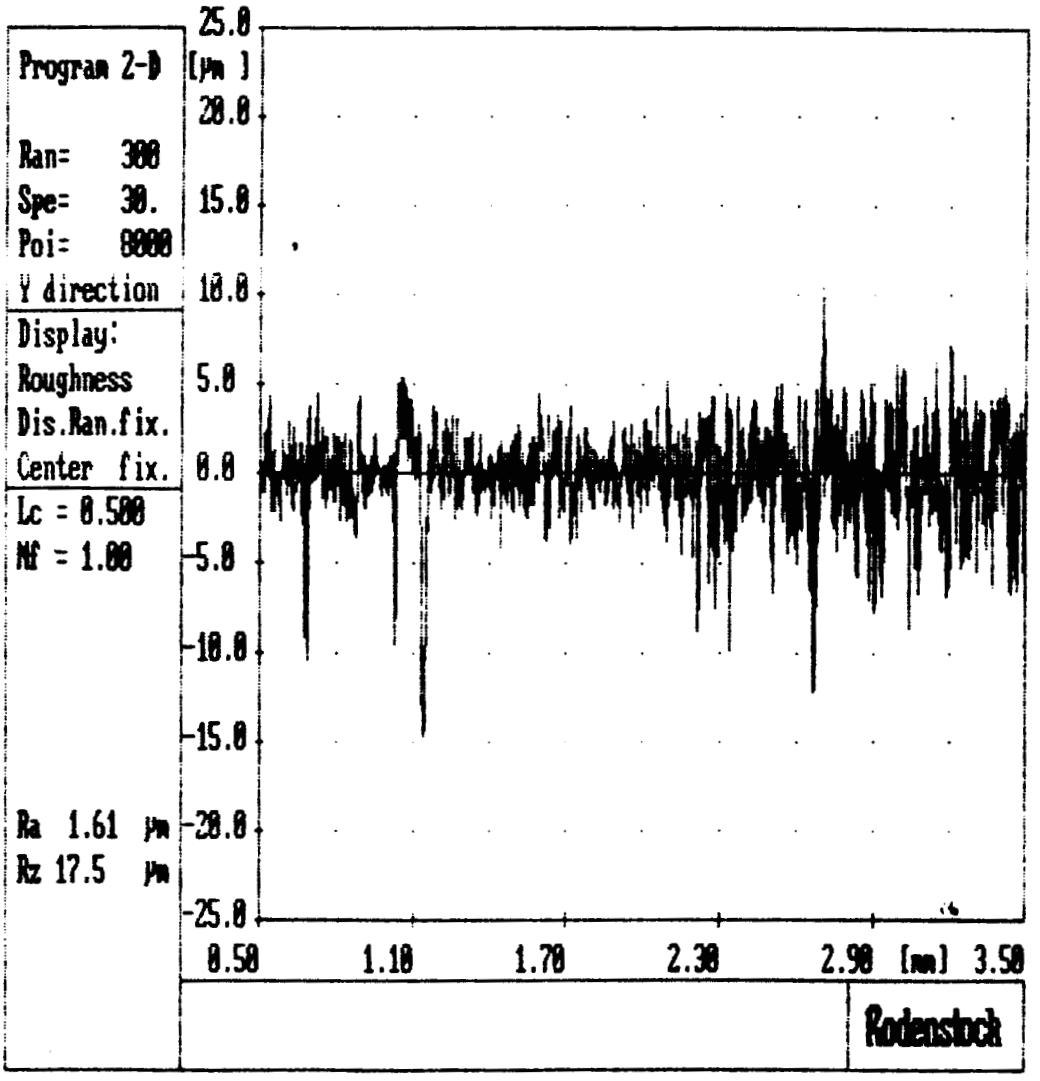

Figure 9. Microfocus Radiography of Milled Powders. Radiography showed agglomerates in batch 800-006. The method of densification aid addition to the mill was changed for batch 800-007 and the agglomerates were absent.

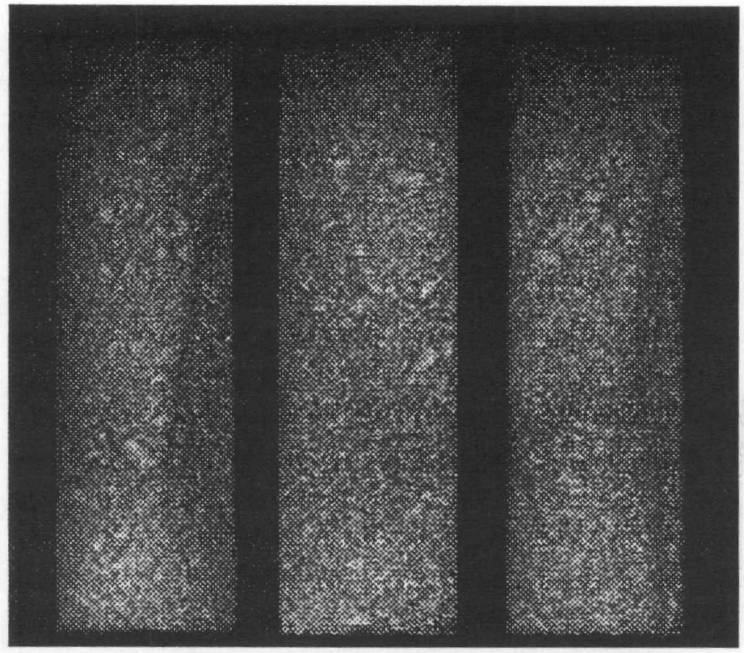

800-006

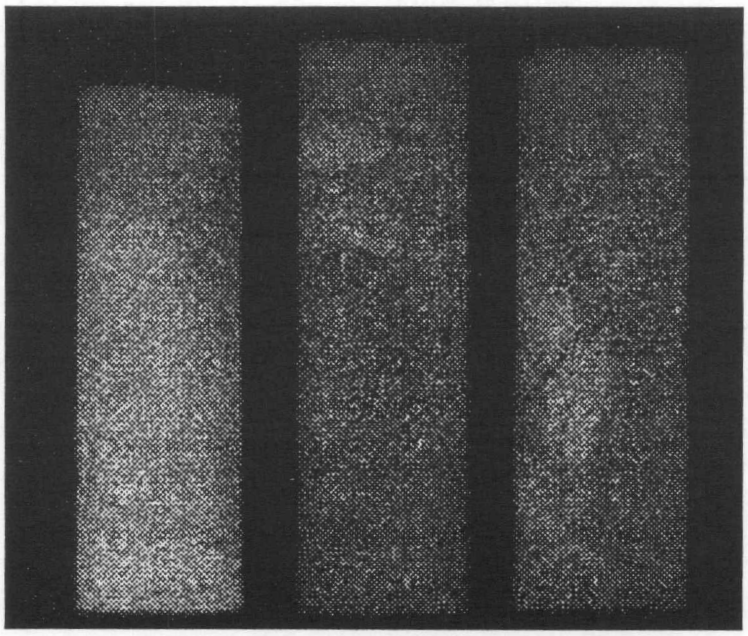

800-007

Figure 10. Plot of Film Density Versus Accelerating Potential.
Results clearly show a contrast maximum occurring at 30 kilovolts for this example. The asymmetric nature of the curve shows that image contrast decreases much more rapidly for accelerating potential below the optimum than for kilovoltage above the optimum.

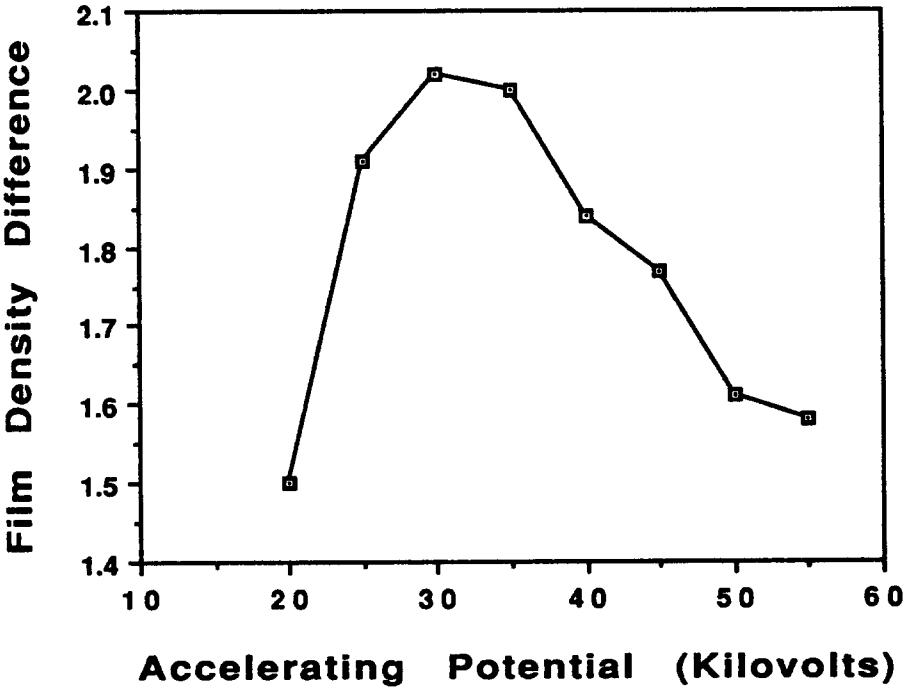

Processing Science for Si_3N_4 Ceramics F.F. Lange, D.S. Pearson
(University of California, Santa Barbara)

Objective/scope.

We are trying to increase the understanding of the role of interparticle forces in the processing of ceramics. The effects of electrolyte addition and pH changes on the rheological properties of dispersions, the kinetics of pressure filtration, and the mechanical properties and microstructure of the resulting bodies will be compared to each other and to existing models of interparticle forces (*i.e.* DLVO theory).

Technical progress.

The effects of the addition of salt to a slurry made by Norton Co. has been examined rheologically and by pressure filtration. The mechanical properties of several green pellets were also measured. KCl was added (0.125M, 0.25M, 0.625M on a liquid basis) to the Norton slurry diluted to 20vol% solids. A portion of each was allowed to sediment, while another portion was examined by pressure filtration on a MTS mechanical testing apparatus (MTS). Attempts were made to examine slurries using the Rheometrics RMS-800 (RMS) using cone and plate geometry (0.04% angle, 50mm diameter), but the torques generated were below the transducer's range (<1g-cm).

Pressure filtration follows Darcy's law:

$$J = k P / \mu X \qquad (1)$$

where J is the fluid flux (dX/dt), P is the filtration pressure, X is the displacement, and μ is the fluid viscosity.

$$k = f_s / (f_c - f_s) * k_p \qquad (2)$$

where f_s is the volume fraction particles in the slurry, f_c is the volume fraction particles in the consolidated body, and k_p is the

permeability of the consolidated layer (dependent on the size and number of percolation channels in the layer).

We used two modes of filtration in separate experiments: constant pressure and constant displacement. The results of these are shown in figure 1. The data is plotted as *ln(P/J) vs. ln(X)* to permit comparison of the two data sets. The two curves for the 0.125M sample are very similar to each other indicating that the pressure is not important for these samples. The various salt concentrations showed that pressing rate increased with increasing salt content.

The mechanical properties of samples produced by pressure filtration were examined using the MTS in axial compression and the RMS in torsion. In the MTS, the samples were found to flow slightly to relieve the applied pressure, and the elastic modulus was found to increase with increasing strain. In the RMS, the platens slipped on the pellet surface preventing good measurements, although a lower bound on the torsion modulus can be estimated from the small displacement data. Work is underway to increase the friction between the platen and the samples.

Status of milestones.

114401	Survey rheological characteristics of slurries produced under a variety of pH / electrolyte conditions. Develop methodologies for characterization of slurry rheological properties and green body mechanical properties.	1 Oct 90
114402	Status report on testing procedures and preliminary results.	1 Nov 90
114403	Determine effect of pH / electrolyte conditions on green body properties including processing rates, mechanical properties, and density.	1 Oct 91
114404	Status report on green body properties and processing relationships.	1 Nov 91
114405	Explore other means to modify interparticle interactions (polymers such as PVA).	1 Apr 92
114406	Status report on polymer effects	1 May 92

114407	Examine flaw populations in sintered bodies.	1 Oct 92
114408	Final report on colloidal processing	1 Nov 92

Publications.

None.

References.

(1) F.F. Lange and K.T. Miller, "Pressure Filtration: Consolidation Kinetics and Mechanics," American Ceramic Society Bulletin 66, p1498 (1987).

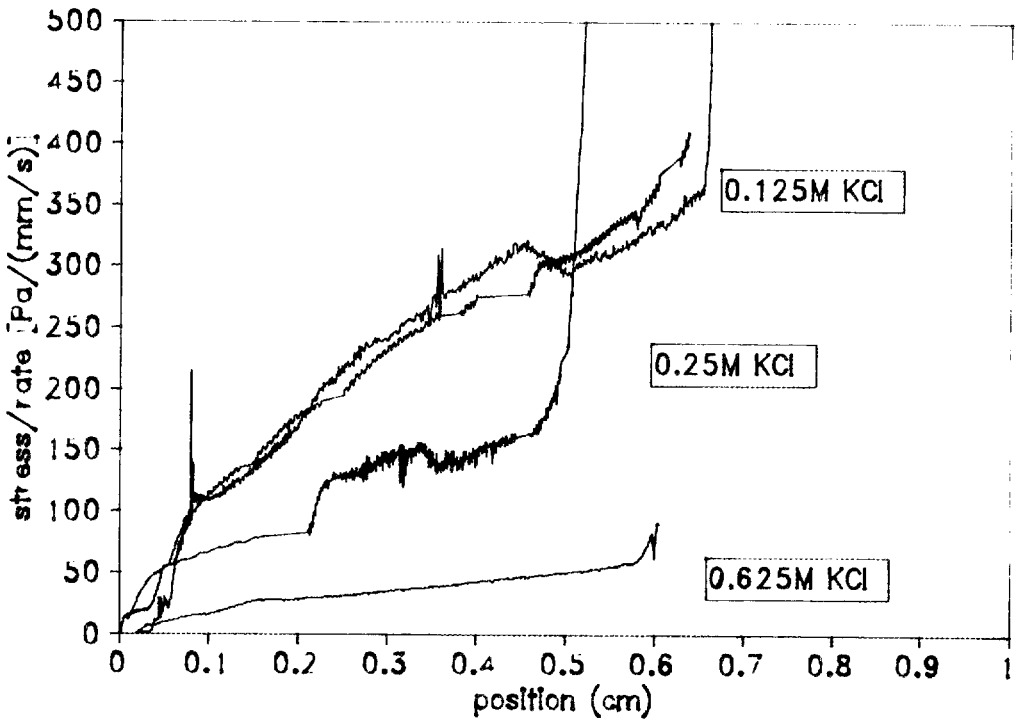

Figure 1. Pressure filtration data plotted as P/J (= Xμ/k) so a lower slope is indicative of a more permeable particle compact. Note that the top two curves represent the same slurry filtered at constant pressure and constant rate, while the lower two curves are constant rate filtration of the higher salt samples.

1.2 CERAMIC COMPOSITES

1.2.2 Silicon Nitride Matrix

SiC-Whisker-Toughened Silicon Nitride

H. Yeh, E. Solidum (Garrett Ceramic Components),
K. Karasek, G. Stranford and D. Yuhas (Allied-Signal Research and 22 Technology),
S. Bradley (UOP Research Center), and
J. Schienle (Garrett Auxiliary Power Div.)

OBJECTIVE/SCOPE

The objective of this program (Phase II) is to maximize the toughness in a high strength, high temperature SiC whisker/Si_3N_4 matrix material system that can be formed to shape by slip casting and densified by a method amenable to complex shape mass production. The ASEA glass encapsulation hot isostatic pressing (HIP) technique shall be used for densification throughout the program.

The program is divided into seven technical tasks with multiple iterations of process development and evaluation. Parametric studies shall be conducted to optimize processing steps developed in the Phase I effort, guided by established analytical and NDE techniques. The seven technical tasks are: Task 1 -Selection of SiC whiskers, Task 2 - Baseline Casting Process, Task 3-Parametric Densification Study, Task 4 - Effect of Specimen Size and Shape, Task 5 - On-Going Evaluation of Alternate Whisker, Task 6 -Nanometer Deposition of Sintering Aids, and Task 7 - In Process Characterization and Process Control During Drying of Cast Ceramic Parts.

The technical effort was initiated in June 1988. Task 1 was completed in January 1989. Based on the results, HF-etched American Matrix Inc. SiC whisker was selected for use for Tasks 2 -4. Task 2 was initiated in February 1989 and was completed in June 1989. Task 3 effort was initiated in July 1989, and is still in progress. Task 4 is scheduled to start in July 1990.

Tasks 5, 6 and 7 tasks were added onto this contract to supplement the mainline activities. These efforts were initiated in August 1989, and are still in progress.

TECHNICAL HIGHLIGHTS

TASK 1 - Selection of Whisker

All technical efforts had been completed and the results were summarized in Semi-Annual report October 1988 - March 1989.

TASK 2 - Baseline Casting Process

All technical efforts had been completed and the results were reported in the April-September 1989 Semi-Annual report. In summary, four iterations were conducted to optimize the green forming process for composites containing 10, 20, 30 and 40 wt% SiC whiskers, respectively. In these four iterations, the Si_3N_4 powder, prior to blending with SiC whiskers, contained the standard GN-10 sintering aids concentration. The optimized process, 4th iteration, was then used to fabricate another set of four composites (10, 20, 30 and 40 wt% SiC whiskers), in which the sintering aids concentrations in the Si_3N_4 powder were increased with SiC whisker loading to maintain a constant ratio between sintering aids and the sum of Si_3N_4 and SiC whisker. This set of composites are referred as 5th iteration samples. The purpose of the 5th iteration samples was to determine the effect of sinter aids concentration on the structure/properties of densified composites, when compared with the 4th iteration samples. The 4th and 5th iteration green composites, a total of eight varieties, plus a monolithic GN-10 were to be densified under Task 3.A - statistical matrix to determine the effect of HIP parameters.

TASK 3 - Parametric Densification Study

Three subtasks (A, B, and C) shall be conducted to evaluate the effects of key densification parameters on microstructures/properties of Si_3N_4/SiC(w) composites. The samples containing 10 to 40 wt% whiskers and two levels of sintering aids fabricated under Task 2 iterations 4 and 5 shall be densified by a HIP matrix (five runs), resulting in forty (40) different composites. A baseline monolithic GN-10 green sample shall also be included in each HIP run as a reference. Based on these results, three composites shall be refabricated for a more detailed characterization under Subtask B. Out of these three, the composite showing the best properties shall be refabricated in a larger quantity for a comprehensive characterization under subtask C. Only Subtask A was conducted during this reporting period.

A) Statistical Matrix

A HIP matrix consisting of Garrett Ceramic Component's baseline HIP cycle (T_2 $^oC/t_2$ hr) and three less severe conditions (T_2 $^oC/t_1$ hr, T_1 $^oC/t_2$ hr and T_1 $^oC/t_1$ hr) were conducted during the last semi-annual reporting period, where T_1 is less than T_2, t_1 less than t_2. In each HIP run, a baseline monolithic GN-10, four 4th iterations and four 5th iteration green samples were included according to plan. Due to large HIP furnace capacity, the 3rd iteration samples were also included to provide potential supplemental data. Based on the results, the fifth HIP run was designed and is in the process of being HIP'ed.

The less severe conditions selected in the first four HIP runs were intended to explore lower HIP process boundaries to produce weaker interfacial bonds. The HIP'ed samples showed a range of densities (reported in the last Semi-Annual report), consistent with the expected effects of HIP parameters, whisker content and sintering aid level. Additional analyses were conducted during this reporting period, and the results are presented below:

o Optical Metallography

Table I summarizes the results. Whisker agglomerates ranging from 50 to 300 microns in diameter were observed in all composites. The whisker loading and matrix composition did not appear to influence the size of the agglomerates. This suggests that the whiskers used contained hard agglomerates which were not broken up during green processing. Figure 1 shows an example of whisker agglomerates and the associated porosity in a 20 percent SiC whisker composites (4th iteration, T2 $^{o}C/t_2$ hr). Fine matrix porosity (5 to 10 microns) is also evident.

The degree of porosity was consistent with the measured densities, which were influenced by whisker loading, and HIP temperatures and times (i.e., more porosity was observed for higher whisker loadings, lower HIP temperatures and shorter HIP cycle durations). Whisker agglomerates in composites HIP'ed at highest-temperature/longest-duration HIP parameters in this study ($T_2{}^{o}C/t_2$ hr) are filled with the Si_3N_4 matrix, while those in composites HIP'ed under the lowest-temperature/shortest-duration conditions ($T_1{}^{o}C/t_1$ hr) are very porous.

The non-agglomerated whiskers in areas away from the agglomerates tended to be randomly oriented for iteration 4 composites (Figures 2 and 3). However, preferred orientation normal to the casting direction was observed in most composites fabricated under iteration 5 as illustrated in Figures 4 and 5.

All composites exhibited a 1 to 2 millimeter surface layer which was a lighter shade of green compared to the bulk of the composite (typically dark green). Under reflected light microscopy, no microstructural features associated with the shade differences were observed. However, the composite surface was heavily microcracked to a depth of 0.25 to 0.5 millimeter (Figure 6), which is less than the overall thickness of the reaction layer. The surface damage may be a result of the ASEA glass encapsulant removal process.

As a result of the whisker agglomerates observed in the 4th and 5th iteration samples, polished sections of selected iteration 3 samples, which were HIP'ed along with 4th and 5th iteration composites in the four HIP runs, were prepared for optical microscopy to examine the degree of whisker dispersion in the composites. Neither whisker agglomerates nor preferred orientations were observed in the

TABLE I METALLOGRAPHY RESULTS FOR TASK 3A COMPOSITES

Billet No.	% SiC	HIP Cycle (°C/hr)	Iteration	Density (g/cc)	Preferred Orientation	Comments
190-3	10	T1/t1	4	3.29	No	
185-3	20	T1/t1	4	3.17	No	high porosity
228-3	30	T1/t1	4	3/17	Slight	high porosity
193-4	40	T1/t1	4	3.01	?	very high porosity
190-4	10	T1/t2	4	3.29	No	
185-4	20	T1/t2	4	3.27	No	
228-4	30	T1/t2	4	3.21	Yes	areas of high porosity
193-3	40	T1/t2	4	3.05	?	very high porosity
222-4	10	T2/t1	4	3.3	No	
226-4	20	T2/t1	4	3.38	No	
188-4	30	T2/t1	4	3.26	No	less quantity of large pores due to better SiC distribution
226-3	20	T2/t2	4		No	some whiskers agglomerates filled with matrix
223-4	40	T2/t2	4	3.24	No	highest density microstructure of 40% SiC composites
196-3	10	T1/t1	5	3.3	Yes	less quantity of small pores than most
211-3	20	T1/t1	5	3.3	Yes	
201-2	30	T1/t1	5	3.21	Yes	high porosity
202-2	40	T1/t1	5	3.26	Slight	high porosity
196-4	10	T1/t2	5	3.3	Yes	less quantity of small pores than most
211-4	20	T1/t2	5	3.3	No	
201-3	30	T1/t2	5	3.29	Yes	less quantity of small pores than most 30% SiC composites
202-4	40	T1/t2	5	3.29	Yes	high porosity
214-4	10	T2/t1	5	3.3	Slight	
199-4	20	T2/t1	5	3.29	Yes	
205-4	30	T2/t1	5	3.3	Yes	
214-3	10	T2/t2	5	3.31	No	some whiskers agglomerates filled with matrix
199-3	20	T2/t2	5	3.3	Yes	
205-3	30	T2/t2	5	3.3	Yes	more fine pores than typical
208-3	40	T2/t2	5	3.29	Yes	

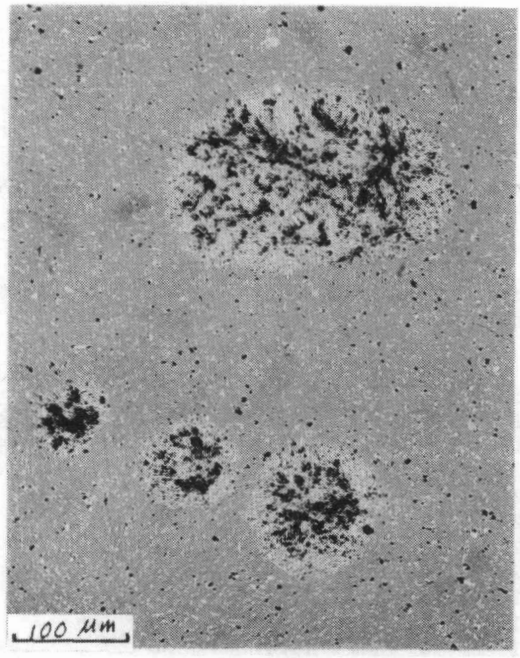

Figure 1 - An example of whisker agglomerates and the associated large pore clusters present in composites (Bullet No. 222-4)

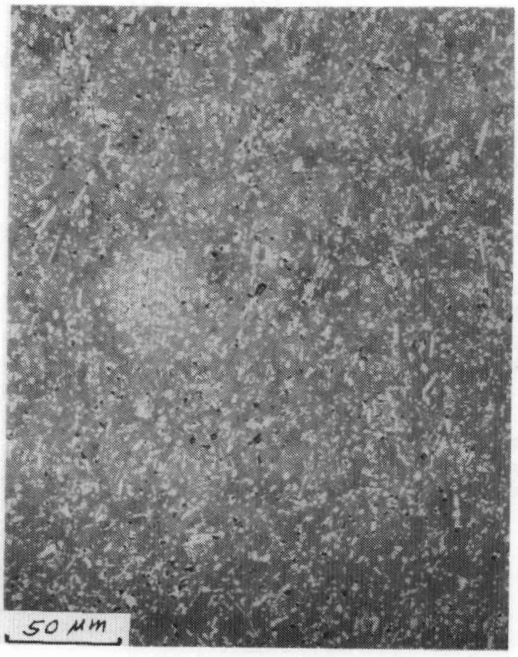

(parallel to casting direction)

(perpendicular to casting direction)

Figure 2 - Random whisker orientation in iteration 4 20 wt% SiC_w composite HIP'ed at T_2 $^oC/t_2$ hr

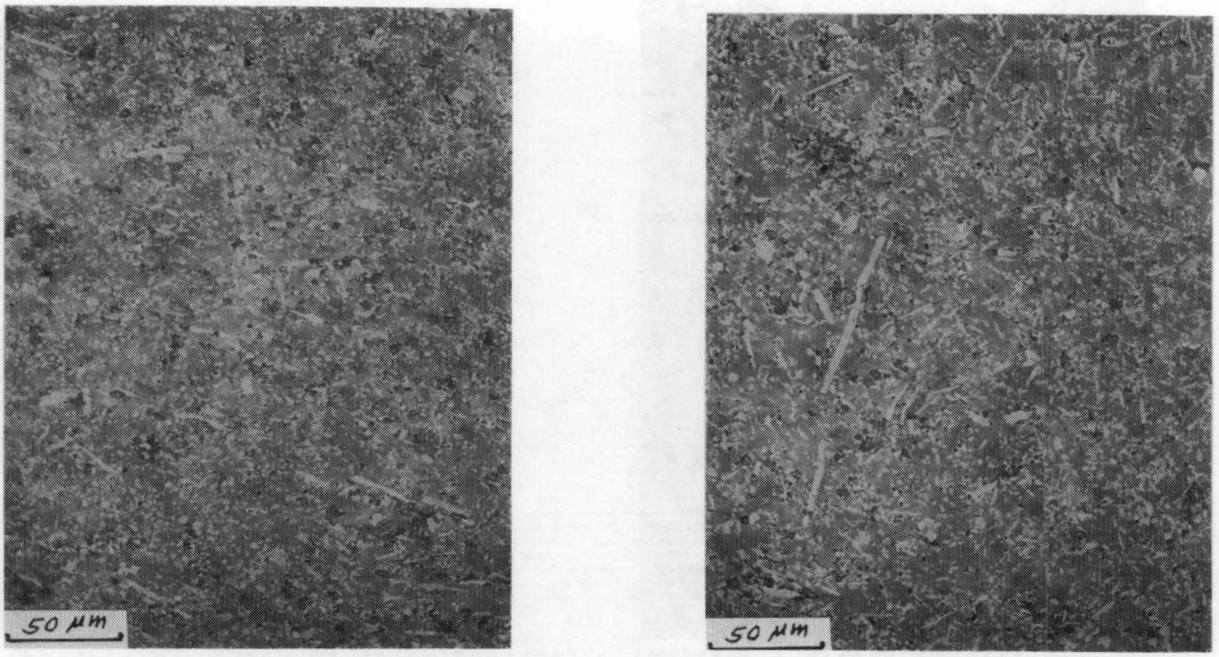

(Parallel to casting direction) (Perpendicular to casting direction)

Figure 3 - Random whisker orientation in iteration 4 30 wt % SiC_w composite HIP'ed at T_1 $^oC/t_1$ hr

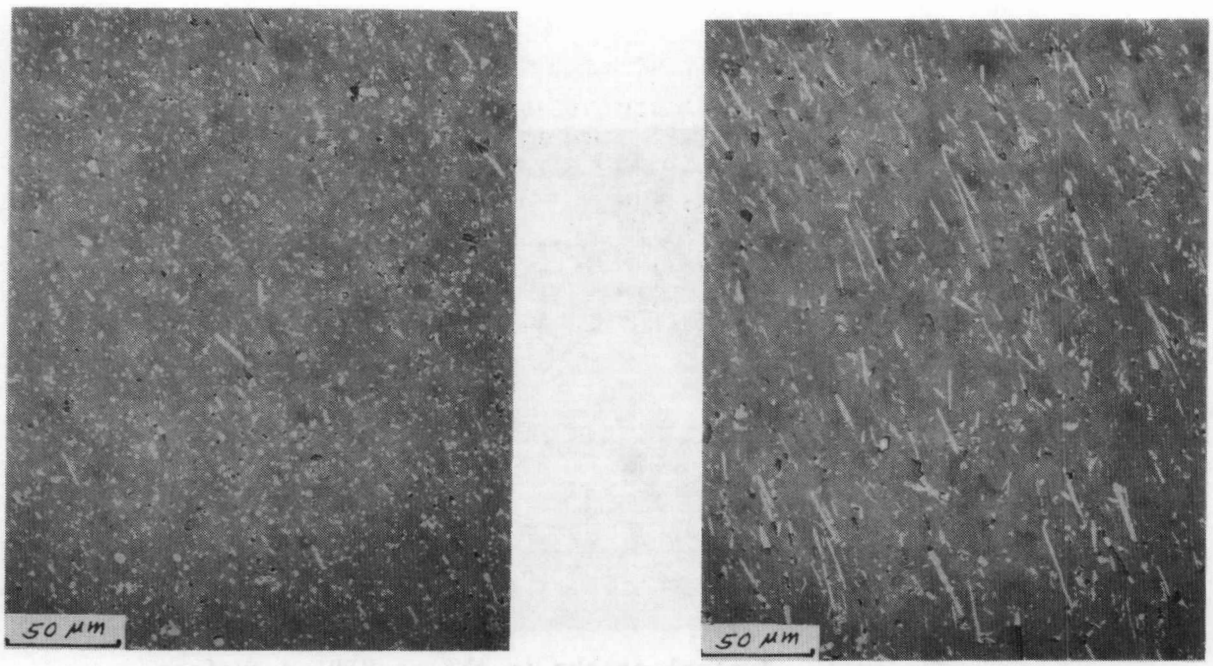

(Parallel to casting direction) (perpendicular to casting direction)

Figure 4 - Preferred whisker orientation in iteration 5 10 wt % SiC_w composite HIP'e at T_1 $^oC/t_1$ hr

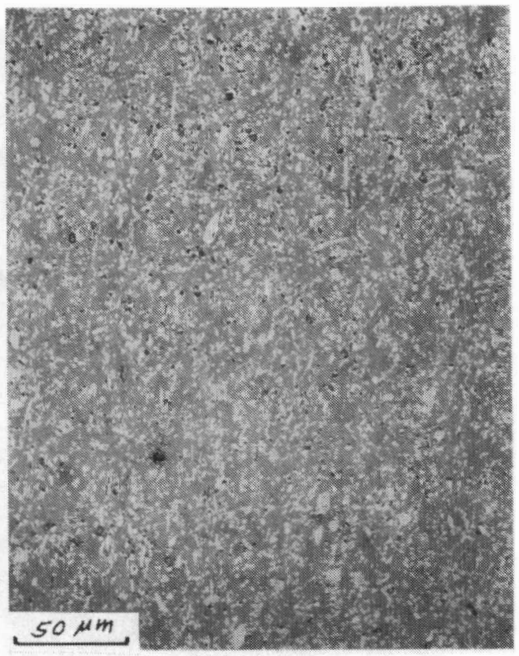

(parallel to castin direction)

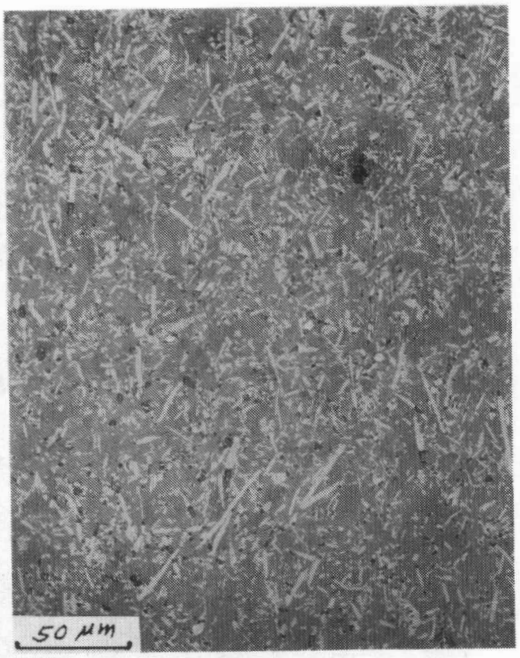

(perpendicular to casting direction)

Figure 5 - Preferred whisker orientation in iteration 5
30 % SiC_w composite HIP'ed at T_2 $^oC/t_2$ hr

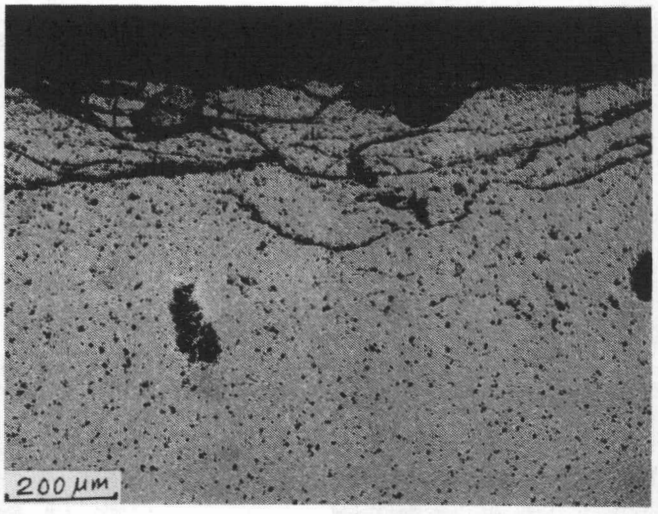

Figure 6 - Typical cracks in the as HIP'ed surface
layer of composite billets

composites.

Iteration 3 samples were mixed by wet ball milling, while 4th and 5th iteration samples were mixed by liquid state tumbling. Examinations of selected composite powder and green casting samples under Task 2 led to the conclusions that the liquid state tumbling technique resulted in non-agglomerated structure and was judged to produce less damage to the whiskers. For this reason iteration four procedures was chosen as optimum over iteration 3 to produce 5th iteration samples. In addition, after HIP'ing, high degree of cracking were observed on iteration 3 samples, but not on iterations 4 and 5 samples. Consequently, the HIP'ed iteration 3 samples were not evaluated initially.

o Elastic Moduli

The Young's modulus, shear modulus, and Poisson's ratio were measured for the samples of the first four HIP runs by an ultrasonic technique. Data and results are given in Table II. Measurements were made in two or three orthogonal directions, although this was not possible for some samples due to irregularities in sample dimensions. The moduli of several of the Iteration No. 4 samples HIP'ed at $T_1{}^oC$ appear to be low. This often correlates with low density. No obvious trend was observed.

o STEM and X-Ray Diffraction Analysis

Initial STEM examinations were made on the monolithic samples and Iteration No. 5 composites containing 30% SiC whiskers. The density of the monolithic sample HIP'ed at $T_1{}^oC/t_1$ hr is somewhat low at 3.21 g/cm^3 (97% full density), and the initial STEM results reflect this. A large number of small regions are present which lack grain boundary phase. The grain boundary phases are also chemically inhomogeneous. The monolithic sample HIP'ed at $T_1{}^oC/t_2$ hr also exhibited high porosity but the grain boundary phases became more homogeneous when the sintering time was increased. Both samples exhibited preferred whisker orientation.

X-ray diffraction indicated that the monolithic samples HIP'ed at $T_1{}^oC$ (for either t_1 or t_2 hr) had significant amounts of α-Si_3N_4. This indicates that the Si_3N_4 has not completely sintered. The monolithic sample HIP'ed at $T_2{}^oC$ for t_2 hours showed a small amount of α-Si_3N_4. Thus, the problem is reduced at $T_2{}^oC$, but it is still there to some extent. Similar results were seen in the 30% composites, although the amount of α-Si_3N_4 in the $T_2{}^oC/t_2$ hr composite was greater than that seen in the monolithic sample.

o Fracture Toughness

Fracture toughness and hardness values of monolithic GN-10 and the Iteration No. 5 composites were measured by an indentation technique[‡,*].

---

‡ A.G. Evans, "Fracture Toughness: The Role of Indentation Techniques"; pp. 112-35 in Fracture Mechanics Applied to Brittle Materials. (Edited by S.W. Freiman. Am. Soc. Test. Mater. Spec. Tech. Publ. 678, 1978.

* J.P. Singh, K.C. Goretta, D.S. Kupperman, and J.L. Routbort, "Fracture Toughness and Strength of SiC-Whisker-Reinforced Si_3N_4 Composites," Adv. Ceram. Mater., 3 [4] 357-60 (1988).

Table II

Ultrasonic Modulus Data*

SAMPLE ID (HIP °C/Hr)	Wt.% SiC_w	D Density (g/cm^3)	G_{13} Shear Modulus GPa	E_{33} Youngs Modulus GPa	ν Poissons Ratio
Monolithic GN-10					
195-3-1	0	3.310	132.46	338.65	0.28
(T_1C/t_1Hr)			128.93	324.24	0.26
195-3-2	0	3.310	122.68	312.97	0.28
(T_1C/t_1Hr)			127.87	322.65	0.26
			129.95	326.71	0.26
195-3a-1	0	3.300	116.93	301.76	0.29
(T_1C/t_2Hr)			121.79	309.57	0.27
195-4a-1	0	3.300	115.71	297.46	0.29
(T_2C/t_1Hr)			123.46	313.05	0.27
			111.80	291.01	0.30
195-4a-2	0	3.300	137.79	341.49	0.24
(T_2C/t_1Hr)			122.26	310.30	0.27
			134.11	322.45	0.20
195-4-1	0	3.300	132.53	330.54	0.25
(T_2C/t_2Hr)			114.86	295.94	0.29
			125.79	318.54	0.27
Iteration #4 Composites					
190-3-3	10	3.290	129.74	324.07	0.25
(T_1C/t_1Hr)			127.36	324.24	0.27
185-3-1	20	3.170	118.51	295.03	0.24
(T_1C/t_1H)			124.01	306.12	0.23
228-3-2	30	3.170	124.11	308.81	0.24
(T_1C/t_1Hr)			125.60	317.74	0.26
			135.03	326.90	0.21
193-3-2	40	3.010	113.75	270.78	0.19
(T_1C/t_1Hr)			126.25	294.57	0.17

* Measurements were made on each sample in two or three orthogonal directions resulting in two or three modulus data per sample.

SAMPLE ID (HIP $^{o}C/Hr$)	Wt.% SiC_w	D Density (g/cm^3)	G_{13} Shear Modulus GPa	E_{33} Youngs Modulus GPa	v Poissons Ratio
190-4-3	10	3.290	122.86	312.76	0.27
(T_1C/t_2Hr)			132.05	337.59	0.28
185-4-2	20	3.270	120.85	309.92	0.28
(T_1C/t_2Hr)					
228-4-2	30	3.210	133.63	329.19	0.23
(T_1C/t_2Hr)			139.54	343.49	0.23
			130.52	324.47	0.24
193-4-1	40	3.050	111.46	266.46	0.20
(T_1C/t_2Hr)			112.78	273.35	0.21
222-4-2	10	3.300	129.85	328.09	0.26
(T_2C/t_1Hr)			129.40	328.69	0.27
			128.97	324.58	0.26
226-4-2	20	3.280	132.76	331.15	0.25
(T_2C/t_1Hr)			133.66	334.60	0.25
			132.72	327.71	0.23
188-4-1	30	3.260	136.54	339.29	0.24
(T_2C/t_1Hr)			140.00	346.26	0.24
233-4-2	40	3.240	146.24	357.73	0.22
(T_2C/t_2Hr)			158.97	368.60	0.16
<u>Iteration #5 Composites</u>					
196-3-1	10	3.300	131.25	327.19	0.25
(T_1C/t_1Hr)					
211-3-1	20	3.300	130.60	326.12	0.25
(T_1C/t_1Hr)			137.88	337.64	0.22
201-2-2	30	3.210	118.83	291.31	0.23
(T_1C/t_1Hr)			135.08	322.17	0.19
202-3-3	40	3.260	134.91	325.27	0.21
(T_1C/t_1Hr)			134.35	329.09	0.22

SAMPLE ID (HIP ^{o}C/Hr)	We.% SiC_w	D Density (g/cm^3)	G_{13} Shear Modulus GPa	E_{33} Youngs Modulus GPa	v Poissons Ratio
196-4-1 (T_1C/t_2Hr)	10	3.300	139.98	353.24	0.26
			136.46	339.09	0.24
			131.28	330.55	0.26
211-4-1 (T_1C/t_2Hr)	20	3.300	126.41	318.85	0.26
			129.77	323.69	0.25
201-3-1 (T_1C/t_2Hr)	30	3.290	137.29	339.90	0.24
			136.21	336.94	0.24
202-4-1 (T_1C/t_2Hr)	40	3.290	198.60	425.77	0.07
			147.21	359.46	0.22
214-4-1 (T_2C/t_1Hr)	10	3.300	128.96	324.30	0.26
			131.40	329.51	0.25
			131.76	331.02	0.26
199-4-3 (T_2C/t_1Hr)	20	3.290	132.23	330.38	0.25
			131.38	328.10	0.25
205-4-1 (T_2C/t_1Hr)	30	3.300	129.46	326.05	0.26
			141.90	342.06	0.21
214-3-2 (T_2C/t_2Hr)	10	3.310	123.89	314.61	0.27
			129.72	326.83	0.26
			128.06	323.31	0.26
199-3-2 (T_2C/t_2Hr)	20	3.300	128.71	321.74	0.25
			130.37	327.71	0.26
			133.06	329.41	0.24
205-3-1 (T_2C/t_2Hr)	30	3.300	132.65	327.73	0.24
208-3-2 (T_2C/t_2Hr)	40	3.290	140.23	345.24	0.23

The results are given in Table III. It appears that the monolithic samples HIP'ed at T_1°C have lower fracture toughnesses than those HIP'ed at T_2°C. No toughness improvements are seen over the monolithic samples HIP'ed at T_2°C. Among the composites, higher density samples appear to exhibit slightly higher toughness.

Table III. Fracture Toughness and Hardness for Monolithic GN-10 and Iteration 5 Composite Samples

SiC(w) Vol %	T_1°C/t_1 h	T_1°C/t_2 h	T_2°C/t_1 h	T_2°C/t_2 h
	Fracture Toughness by Indentation Technique ($MPa\text{-}m^{1/2}$)			
0%	4.2+/-0.3	6.1+/-0.4	6.9+/-0.5	7.0+/-0.4
10%	-	6.9+/þ2.0	-	-
20%	5.4+/-0.4	6.5+/-0.2	6.1+/-0.3	6.9+/-0.5
30%	6.3+/-1.0	6.1+/-0.2	6.2+/-0.4	6.3+/-0.2
40%	-	5.2+/-0.6	-	6.5+/-0.4
		Hardness (GPa)		
0%	17.2+/-0.2	15.4+/-0.3	15.4+/-0.2	14.4+/-0.3
10%	-	17.0+/-4.9	-	-
20%	16.9+/-0.6	16.5+/-0.4	17.2+/-0.5	15.6+/-0.3
30%	14.6+/-0.3	16.2+/-0.4	16.6+/-0.4	15.9+/-þ0.3
40%	17.0+/-0.1	17.8+/-0.7	-16.0+/-0.5	

As explained under Optical Metallography section earlier, selected 3rd iteration composite samples were prepared to observe

whisker dispersion. Fracture toughness was measured on these samples. Two different orientations were measured for each composition and HIP-temperature combination. The results are reported in Table IV along with the corresponding data from the Iteration 5 samples. Overall, the 3rd iteration composites showed a slightly higher toughness than the 5th iteration.

Table IV. Fracture Toughness as a Function of HIP Parameters and SiC Whisker Content for Iterations 3 and 5.

Sample # *	HIP Parameters T^oC/tH	SiC%	Iteration 3 KIC MPa $m^{1/2}$	+/-	Iteration 5 KIC MPa $m^{1/2}$	+/-
#177-3 V	T_2/t_1	20%	6.3	0.5	6.1	0.3
#177-3 H	T_2/t_1	20%	5.9	0.3		
#177-4 V	T_2/t_2	20%	8	0.9	6.9	0.5
#177-4 H	T_2/t_2	20%	6.3	0.2		
#184-3 V	T_2/t_1	30%	7	0.5	6.2	0.4
#184-3 H	T_2/t_1	30%	6.7	0.3		
#184-4 H	T_2/t_2	30%	6.6	0.6	6.3	0.2
#184-4 V	T_2/t_2	30%	6.5	0.7		

* Fiber Orientation: V=vertical; H=horizontal

o Fifth HIP Run

The above results suggest an overall trend that higher HIP temperature, longer holding time result in higher density, fuller reaction (less alpha-Si_3N_4 phase) and slightly higher toughness. Based on this observation, a slightly higher temperature (T_3 ^oC) is selected for the 5th HIP run. In order to avoid too strong a bond formed between the whiskers and the matrix, the holding time t_2 is used. The composite samples included in this run was mixed by the wet milling procedure and the slips were prepared using an improved procedure based on the NASA/GAPD/ATTAP program at Garrett Ceramics.

TASK 5 - On-Going Evaluation of Alternate Whiskers

The objective of this Task is to stay abreast of the whiskers with improved properties which may become available during the course of this program.

Keramont Grade 9A, Tokai TWS-100, Tokai TWS-400, and Kobe Steel Grade AT SiC whiskers were analyzed by XPS. The Keramont whiskers exhibited a significant amount of surface SiO_2. They also had Fe, Na, Mg, P, and Ca impurities as well as polymeric carbon. The two

Tokai whisker sets and the Kobe Steel whisker set all had low surface oxygen levels (12 to 15 at.%). The surface impurity levels of the Tokai whiskers were quite low, while the Kobe Steel whiskers exhibited small amounts of Ca, F, and Na.

Three more sets of whiskers were examined by STEM. The Kobe Steel A'T whiskers had diameters in the range of 0.5 to 2.5 microns. Lengths ranged from 10 to 125 microns with most shorter than 40 microns. Some Cr inclusions were observed. Debris level was low, but higher than that seen in ACMC whiskers. These whiskers were considered to be very promising although it is unclear whether Kobe Steel will continue to market them. The Tokai TWS-100 MOD whiskers were fairly similar to Tokai whiskers we have examined before. They are generally quite distorted and twisted. In contrast, the Tokai TWS-400 whiskers are a major improvement. The diameters are larger than other Tokai whiskers - 0.5 to 1.5 micron. Lengths range from 10 to 50 microns. Most important, the whiskers do not exhibit many of the distortions that are so typical of Tokai whiskers. The amount of debris is fairly low -more than in the ACMC whiskers, but less than in the Kobe A'T whiskers. Some Co-Fe inclusions were seen.

Bulk impurity contents of Keramont 9A, Tokai Carbon TWS-100 and TWS-400, and Kobe Steel AT whiskers were measured by neutron activation at Texas A&M University. The results are given in Table V.

The Keramont sample exhibits the highest oxygen content, which is consistent with the high surface oxygen level presented in the last report. The Fe level is quite high, which could catalyze degradation reactions. In short, the Keramont sample requires significant cleaning. The other samples have relatively low impurity levels, although the Co and Fe are noticeable in the Tokai TWS-400 and Kobe Steel AT whiskers, respectively.

The Advanced Ceramic Technologies AT1 whiskers are quite straight. Their average lengths and diameters are among the smallest we've seen. A small amount of debris was present. X-ray photoelectron spectroscopy (XPS) revealed a surface which is very clean (i.e., very low impurity level) and has a very low oxygen content.

Task 6 - Nanometer Deposition of Sintering Aids

The objective of this Task is to develop nanometer deposition of the sintering aids through solution chemistry to promote grain boundary homogeneity resulting in improved high temperature properties and enhanced sinterability of GN-10, the matrix material of this program. The technology developed can be applied to a future GN-10 Si_3N_4 based composite effort.

Table V. Bulk Chemistry of Alternate SiC Whiskers by neutron Activation.

	Keramont 9A	Tokai Carbon TWS-100	Tokai Carbon TWS 400	Kobe Steel AT
O (%)	3.0	0.6	0.5	0.5
N (%)	2.2	3.9	1.1	1.6
F (%)	0.54	<0.05	<0.05	0.13
Cl (ppm)	150	40	40	40
Co (ppm)	0.4	0.4	2700	2.6
Cr (ppm)	7.3	21	62	720
Mg (ppm)	20	10	<10	60
Na (ppm)	480	25	24	52
Ni (ppm)	<10	<50	<150	<150

Approaches

Silicon nitride powders coated with GN-10 sintering aids were prepared using the following methods: precipitation (two approaches), spray drying, polymerization (two approaches), and evaporation of a solution containing carboxylates. Samples were calcined in air to form the desired phases. Sintering aid levels were confirmed by inductively coupled plasma-atomic emission spectroscopy. Samples were dissolved in a mixture of HF and HCl using a Parr bomb for analysis. Target GN-10 sintering aid levels were achieved within the accuracy of the technique (+/-0.25%).

Powder Characterization

Electronic amplitude measurements were performed to evaluate the surface chemistry of the coated powders. Low zeta potentials were observed when electrostatic charge was used to disperse the experimental powders. Stable dispersions were achieved by adding low levels of polyelectrolyte. The results suggested that the experimental powders can be processed using typical slip casting procedures.

To evaluate the uniformity of the sintering aids deposited on the Si_3N_4 particles in the experimental samples, XPS elemental analysis was performed on these powder samples as well as a control (GN-10 Si_3N_4 powder prepared by a baseline milling procedure). The results are listed in Table VI. XPS is a surface technique which only detects elements within approximately an 80 angstrom thick layer. The decrease in the Si and N signals would suggest an increase in amount of sintering aids deposited on the Si_3N_4 particles.

Table VI

X-RAY PHOTOELECTRON
SPECTROMETRY ELEMENTAL ANALYSIS RESULTS (AT %)

	Si	N_2	Sintering Aid Components 1	Sintering Aid Components 2	O_2
Control*	28.4%	28.3%	4.2%	4.1%	28.2%
Evaporation	19.0%	11.1%	12.8%	3.5%	41.6%
Polym 1	24.9%	19.4%	6.%	2.4%	36.4%
Precip 1	28.3%	15.3%	4.6%	2.0%	41.6%
Precip 2	34.4%	19.8%	0.9%	0.4%	40.4%
Spray Drying	23.1%	15.4%	8.8%	4.9%	42.0%
Polym 2	28.8%	27.4%	4.4%	3.1%	30.0%

(Balance of Signal is carbon and, in some cases, minor amounts of sodium)

* GN-10 Si_3N_4 powder prepared by ball milling

The lowest silicon and nitrogen signals were observed for the following three samples: evaporation, spray drying, and polymerization 1. Powders prepared by these three procedures also have the highest signals for sintering aid component 1, which is the major component. This correlation suggests that evaporation, polymerization 1, and spray drying yield the most uniform dispersion of sintering aids. Backscattered electron images of samples with higher silicon signals by XPS have numerous bright spots which correspond to the heavier sintering aid elements. Samples with higher sintering aid component 1 signals by XPS exhibit little sintering aid segregation in the backscattered electron images.

Densification

Experimental and control samples were gas pressure sintered at 1800°, 1900°, and 1975°C. The control sample is a GN-10 powder prepared by ball milling. Green and sintered densities are summarized Table VII.

Table VII. Gas Pressure Sintering Results

	1800°C/1 h 2500 psi		1900°C/.33 h 1500 psi		1975°C 2 h 450 psi; 2 h 900 psi	
	Green Density g/cc	Sintered Density g/cc	Green Density g/cc	Sintered Density g/cc	Green Density g/cc	Sintered Density g/cc
Control*	1.94	2.24	1.96	2.32	1.93	2.67
Polym 1	1.80	2.14	1.76	2.16	1.75	2.44
Precip 1	1.67	2.02	1.68	2.11	1.70	2.37
Precip 2	1.76	2.06	1.73	2.12	1.74	2.38
Polym 2	1.76	2.09	1.77	2.16	1.74	2.45
Evaporation	1.77	2.11	1.76	2.17	1.76	2.43
Spray Dried	1.69	2.01	1.67	2.07	1.67	2.31

*GN-10 Si_3N_4 prepared by all milling

The 1800° and 1900°C samples were packed in silicon nitride powder during sintering while the 1975°C samples were placed on a thin layer of BN. Even after sintering at 1975°C the samples were poorly densified. At all temperatures, the control samples reached higher final densities than the experimental samples. However, the higher density for the control sample seems to be a function of green density since a linear regression exists between the sintered density as the green density for all the samples densified at a particular temperature.

Cold isostatic pressing increases the green densities of the experimental samples while having little effect on the control samples. After isostatic pressing, the green densities of the experimental samples were between 1.80 and 1.91 g/cc while the control was 1.98 g/cc. Agglomerate formation during sintering aid deposition probably accounts for the lower green densities in the uniaxially pressed experimental samples. Effects of green density on sintered density will be confirmed by gas pressure sintering the isostatically pressed samples.

Experimental and control samples were glass encapsulated and hot isostatically pressed at T_2°C and 20,000 psi. Compacts were prepared by uniaxial pressing at 20,000 psi. Green and sintered densities are summarized Table VIII.

Table VIII. Green and HIP'ed Densities for GN-10 Compacts with the Sintering Aids Deposited by Various Methods.

	Green Density g/cc	HIP'ed* Density g/cc
Control	1.93	3.25
Polym. 1	1.74	3.21
Precip. 1	1.71	3.18
Precip. 2	1.71	3.21
Polym. 2	1.82	3.13
Evaporation	1.74	3.23

* HIP'ed at $T_2{}^{o}C/t_2$ hr

Similar final densities were achieved for all samples suggesting that method of sintering aid deposition does not affect densification for these HIP parameters. However, grain boundary chemistry may be different. Microstructure and grain boundary uniformity of these samples will be examined using STEM.

Phase analysis by x-ray diffraction was performed on control and experimental samples that were glass encapsulation HIP'ed at $T_2{}^{o}C$. All samples were greater than 95% density. Beta and alpha silicon nitride were the major phases.

Five hundred gram batches will be prepared with three different sintering aid levels using spray drying and polymerization 1.

TASK 7 - In Process Characterization and Control During Drying of Cast Ceramic Parts

The objective of this task is to determine the efficacy of ultrasonic methods for the real-time, on-line process control of the drying of green ceramics fabricated by aqueous slip casting, the shape forming method used throughout this program. The technique developed can be applied to slip cast whisker reinforced Si_3N_4 composites in a future effort for eliminating potential drying cracks.

Introduction

Initial work was focussed in four areas 1) Baseline properties of green ceramics 2) Ultrasonic coupling method investigations 3) Facilities development 4) Automated measurement methods.

Ultimate success of this task is dependent on developing reliable methods for coupling sound into and out of the friable green ceramics. Methods must be found which will not damage components, are sufficiently stable to permit continuous monitoring, and have low insertion loss. All work to date has been done using pulse-echo ultrasound in the frequency range 1. to 10. Megahertz. Green GN-10 slip cast samples, approximately 15 mm thick, were used in the initial studies.

Experimental

Ultrasonic instrumentation for the drying studies was the Matec MBS 8000. This system was chosen because it has a large dynamic range, 100 db, high precision for both velocity and attenuation measurements and the potential of being fully automated. Currently both velocity and attenuation measurements can automatically be made. Several experiments are being conducted to evaluate the stability and precision of the automated system.

Reliability and precision of the measurements were assessed. For a test set-up sample, we use an aluminum block was used which circumvents time dependent property changes associated with the drying of the green ceramics. Using this test sample the following parameters were varied to determine their effect on transit time measurements:

a) Gatewidth
b) Gate position
c) Receiver Gain
d) Number of Samples Averaged
e) Relative Run Time
f) Pulsewidth
g) Filter Setting

Optimal setting as found for each of these parameters. Measurement precision of a few parts in ten thousand was achieved. Experiments were conducted using both the reflection mode as well as the thru-transmission mode.

In order to conduct drying studies a humidity chamber has been designed, instrumented, and assembled. Access ports are available for continuous monitoring of temperature, humidity, and ultrasonics.

Modifications are needed to allow monitoring multiple sensors and conducting experiments over several hours. Alternate ultrasonic

processing schemes using a high speed digitizer are being tried. Several signal processing schemes were also explored which may enable us to measure moisture gradients.

Several coupling methods were explored. A high-viscosity, organic couplant was found to work best. This couplant, with the consistency of molasses, permits measurement of both longitudinal and shear waves. It exhibited the lowest insertion loss of all the methods tried. Other methods explored include pressure contact, plastic interlayers, and high viscosity water-based couplants. The organic couplant was stable for several hours with minimal contact pressure and leaves minimal residue.

Results

Using the organic couplant, baseline properties of the green ceramic plates were determined. Results were obtained on two green ceramic plates (#352-1 and 2). The moisture content of these materials was unknown, however the dry, powder-like character of the surface and their propensity for moisture absorption suggest low water content. The compressional wave velocity ranged from 1.50 to 1.56 km/sec. The attenuation at 10 megahertz was surprisingly low - -three reverberations were observed in the dry samples. This suggests that penetration of several inches of material is possible.

The shear wave properties at a lower frequency were also quite good. Several reverberant echoes were observed at 2.25 megahertz. The shear wave velocity for a dry casting with bulk density of 1.97 g/cc ranged from .99 to 1.02 km/sec.

In an attempt to estimate the change in properties with moisture content, ultrasonic velocities were measured in a small segment of sample #352-2 before and after saturation with water. At 10 megahertz attenuation in the green sample increased more than 40 db. This was sufficient to preclude a wet compressional wave velocity measurement. The shear wave properties also showed large changes. The shear wave velocity went from 1.018 km/sec for the dry sample to 0.913 km/sec for the saturated sample. This change is viewed as large in light of the expectations of measuring velocity to a precision of a few tenths of a per cent. Shear wave attenuation was 30 db higher in the saturated sample.

These experiments must be repeated in such a way as to separate potential coupling problems from the effects of moisture. However the large magnitude of the changes is viewed as encouraging.

When ultrasonic velocity was monitored for drying times of several hours it was found that the signals became unstable after a few hours. The SWC couplant (water-based organic) was found to be unsatisfactory. Stability of a non-water based couplant will be

evaluated. Long term stability in couplant stability is essential because the drying cycle may be a few days.

Preliminary experiments have shown that polyvinylidene fluoride (PVDF) transducers are sufficiently sensitive to act as ultrasound receivers in the megahertz range. Because of their small size and their ability to conform to curved surfaces, they have the potential for monitoring complex shapes.

A series of polyvinylidene fluoride (PVDF) piezoelectric transducers were fabricated. Thick and thin PVDF materials have been investigated for transducer production. Thinner films were superior because they conform better to the surface of the samples. After initial evaluation, the PVDF transducers will be used to conduct drying studies.

Experiments to date have been carried out by taking the dried green plates, saturating them with water, and monitoring property variations as a function of time. The next step is to start monitoring freshly cast test plates.

STATUS OF MILESTONES

All milestones are on schedule.

PROBLEMS ENCOUNTERED

None

PUBLICATIONS

K. R. Karasek, S. A. Bradley, J. T. Donner, H. C. Yeh, J. L. Schienle, and H. T. Fang, "Characterization of Silicon Carbide Whiskers," J. Am. Ceram. Soc., 72 (10) 1907-13 (1989).

Silicon Nitride-Metal Carbide Composites - S.T. Buljan (GTE)

Objective/scope

The objective of the proposed effort is to study the effect of sintering aids on microstructure and properties of Si_3N_4-SiC(w) composites and utilize the results obtained to design and synthesize an advanced composite of improved properties. It is also an objective of this effort to refine forming and consolidation processes and develop technology for prototype part fabrication.

Technical progress

Microstructural Design

Efforts to microstructurally tailor silicon nitride ceramics to improve high temperature mechanical properties focused on heat treating as a means of modifying the intergranular glass phase through devitrification. Monolithic and composite (30 v/o SiC whiskers) materials were prepared with either Y_2O_3-Al_2O_3 or MgO-Al_2O_3 sintering aids. Baseline materials were hot pressed (1800°C34.4 MPa/400 min.), while heat treated bodies were prepared by incorporating a post-densification annealing step (1200°C/240 min.) in the schedule. Since MgO-fluxed materials were observed to exhibit relatively poor engineering properties (lower strength at room and elevated temperature and extensive nonlinear behavior in mechanical testing at 1200°C), the focus has been on Y_2O_3-containing silicon nitride ceramics based on AY6 (6.0 w/o Y_2O_3 + 1.5 Al_2O_3 + Bal. Si_3N_4). The heat-treating step was confirmed by TEM techniques to produce extensive devitrification of the intergranular glass phase in Y_2O_3-containing bodies. While this change in intergranular phase produced a reduction in room temperature fracture toughness and strength, a 25% increase in modulus of rupture and a 20% increase in yield strength at 1400°C were realized. Thus the desired improvement in fast fracture mechanical properties in the operating range of engine applications was realized.

The low strain rate properties of the devitrified Y_2O_3-containing silicon nitride have also been evaluated via four-point creep at 1200°C and found to be identical to those of the standard hot-pressed materials. For example, at 1200°C and at imposed stress of 207 MPa, the steady state strain rate of hot-pressed AY6 was $3.6 \times 10^{-9} sec^{-1}$, while that of devitrified AY6 was $3.3 \times 10^{-9} sec^{-1}$. This result is attributed to in-situ devitrification of the hot-pressed material during stage 1 creep before steady state (linear) creep is observed.

The effect of post annealing is to set the microstructure of the Y_2O_3-containing silicon nitride materials to that which would be obtained after >100 hours' exposure at elevated temperature.

Determination of the morphology, crystallography, and crystal chemistry of the intergranular second phase in heat-treated ceramic materials (AY6, AY6/30 v/o SiC, and AY6/30 v/o Si_3N_4, were continued. These studies were carried out both at GTEL and the HTML of ORNL.

Bright-field images taken of monolithic and composite (30 v/o SiC whisker) ceramics consistently showed amorphous intergranular material at silicon nitride grain triple points (Figures 1 and 2) in the as-hot-pressed materials. No evidence for devitrification of the intergranular glass was observed in the investigated materials in the hot-pressed condition.

In contrast, significant crystallization of the intergranular glass was observed in all of the heat-treated samples. In most cases, the crystallized region did not extend through the complete volume of the triple points; the devitrified phase appeared to have formed in the interior of the glass and to have grown toward Si_3N_4 grain boundaries (Figure 3), where the amorphous phase can still be observed at the grain boundaries.

A preliminary study of the interface structure between adjoining Si_3N_4 grains, as well as between Si_3N_4 and the intergranular second phase, was carried out. A lattice image of two adjoining Si_3N_4 grains with a thin (~0.5-2 nm) amorphous interlayer is shown in Figure 4. The interface between a Si_3N_4 grain and the crystallized intergranular phase can also be seen in Figure 3. In this case lattice fringe patterns extending from each of the phases directly up to the interface boundary indicate complete devitrification. Electron diffraction patterns were taken from a number of locations. In general, the patterns taken from the heat-treated monolith and composite materials were very similar, which suggests the presence of a single type of crystalline material.

Convergent beam electron diffraction patterns taken from several of these phases exhibit diffuse HOLZ rings which are known to arise due to the presence of strain. The observation of this strain is consistent with the twin lamelae observed in the bright-field images of the devitrified pockets. These were readily imaged under high-resolution conditions (Figure 5). In comparison, such diffuse HOLZ rings were not observed in defect-free regions of silicon nitride grains; in contrast, very sharp Kikuchi line patterns were obtained.

Compositional analysis of the intergranular pockets was performed by acquiring EDX spectral data from thirty (30) regions from each of the heat-treated specimens (listed above). The data were analyzed by calculating the ratio of the Y_L and Si_K integrated peak intensities. The amorphous intergranular phase of hot pressed AY6 yielded a consistent Y_L/Si_K value of ~0.84 and an Al_K/Si_K of ~0.18; these areas were found to contain Y, Si, O, and relatively high Al concentrations. In contrast, samples of heat-treated AY6 showed crystallized phases containing Y, Si, O, and relatively low levels of Al. The Y_L/Si_K ratios were not consistent, implying that some stoichiometric fluctuation in these second phases may be present. Similar results were obtained from the data taken at the triple points in the AY6 + 30 v/o Si_3N_4 sample. The only crystalline phase resulting from devitrification in the SiC-containing specimen was an Al-free yttrium silicate.

The diffraction patterns taken from the heat-treated AY6 monolith and the admixed materials were very similar. It is expected that by using computer-simulated electron patterns of both the Si_3N_4 matrix and (four) known Y-Si-O phases, it will be possible to determine the precise crystal structure of this phase and the character of observed lamelar (twin) substructures. A number of interfaces between SiC whiskers and the intergranular phase were imaged. In general, no significant amount of amorphous phase was observed along these interfaces.

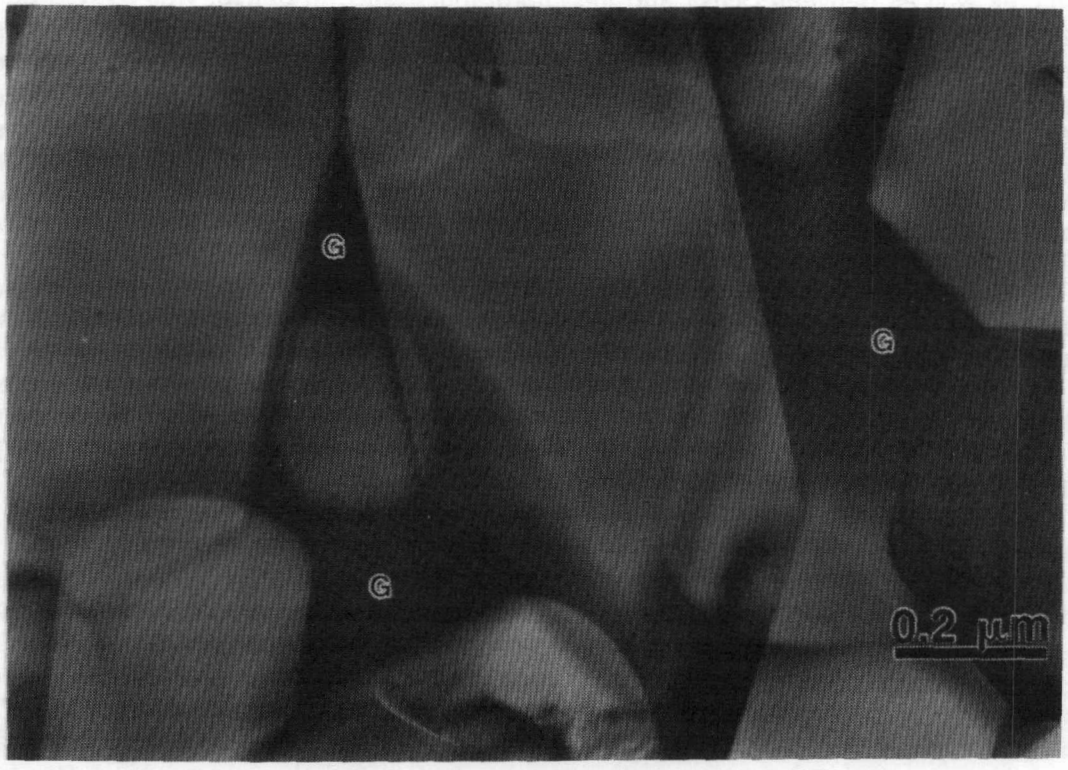

Figure 1: General morphology of hot pressed silicon nitride (Y_2O_3 and Al_2O_3) sintering aids (glass phase: "G")

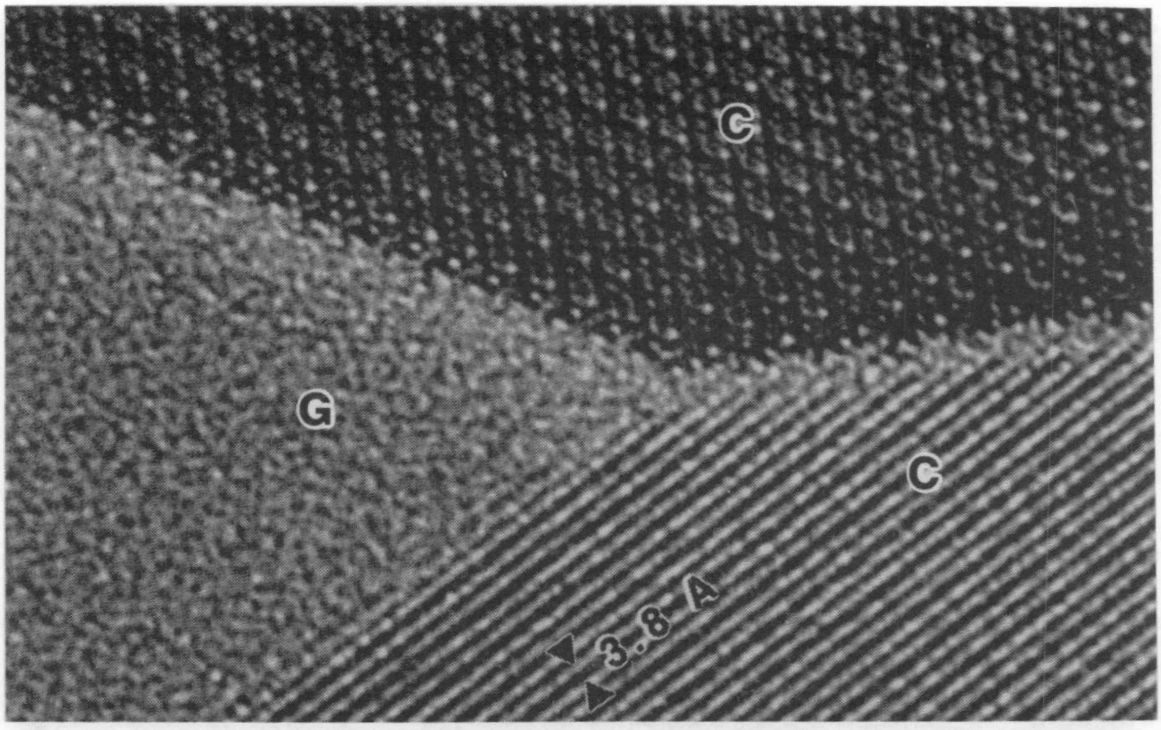

Figure 2: HRTEM image of triple-point junction showing two Si_3N_4 crystals (C), and an amorphous glass phase (G)

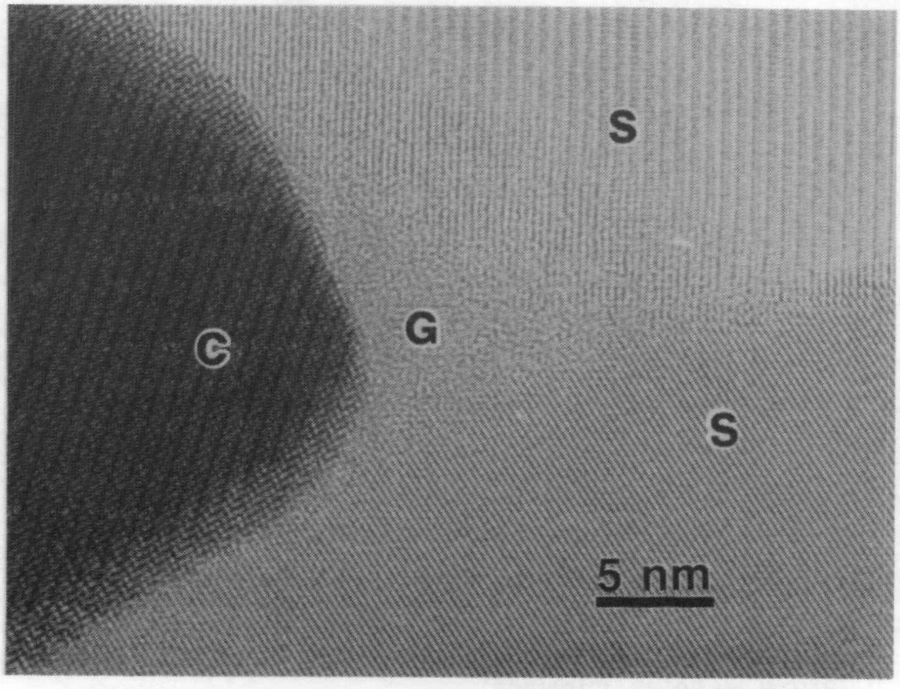

Figure 3: HRTEM image of heat-treated AY6/30 %v SiC triple-point junction. (Si_3N_4 crystals (S), crystallized intergranular phase (C), amorphous glass (G), arrow points to Si_3N_4-crystallized intergranular phase interface).

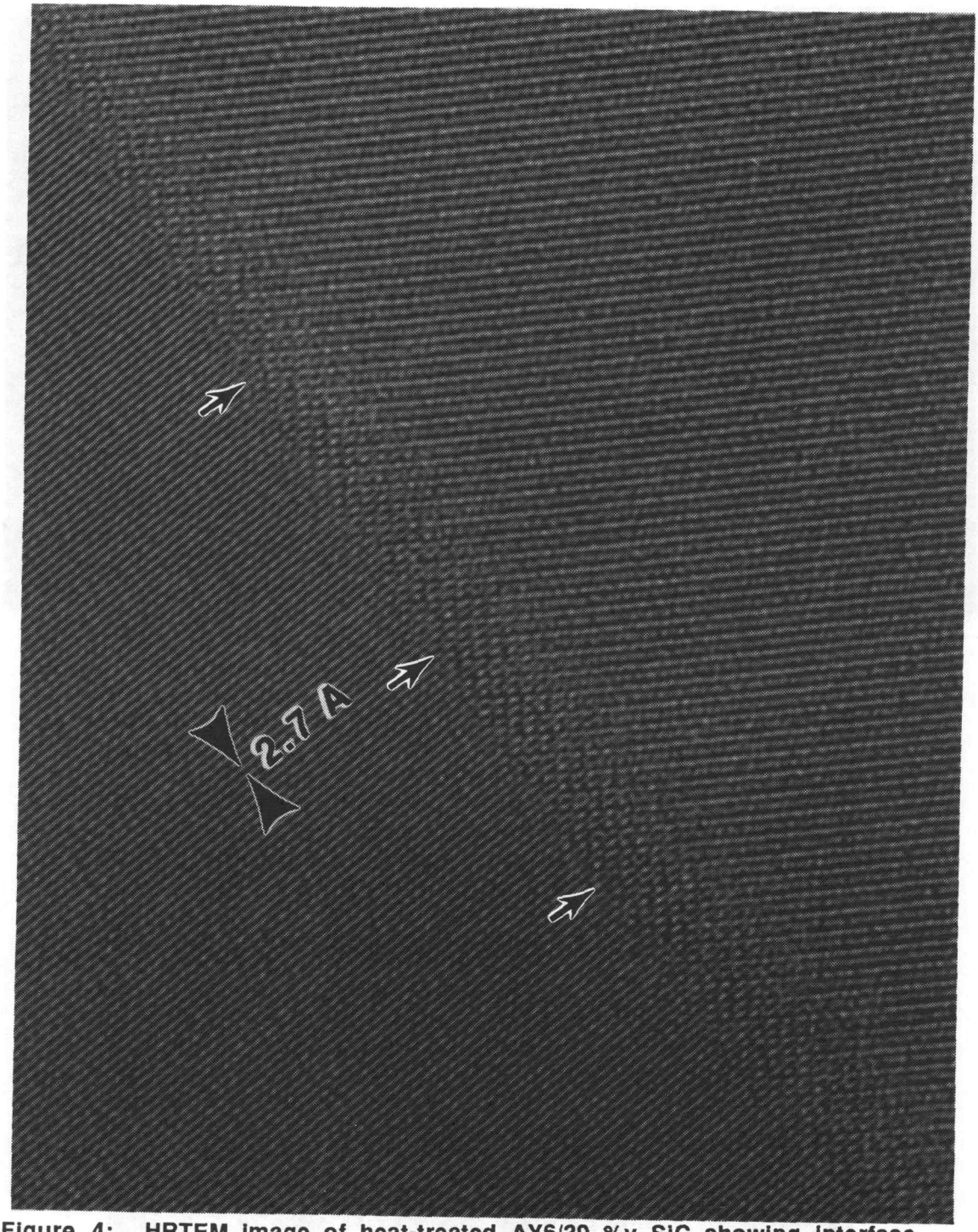

Figure 4: HRTEM image of heat-treated AY6/30 %v SiC showing interface between two Si_3N_4 grains with a thin amorphous glass interlayer. (arrow denotes interface)

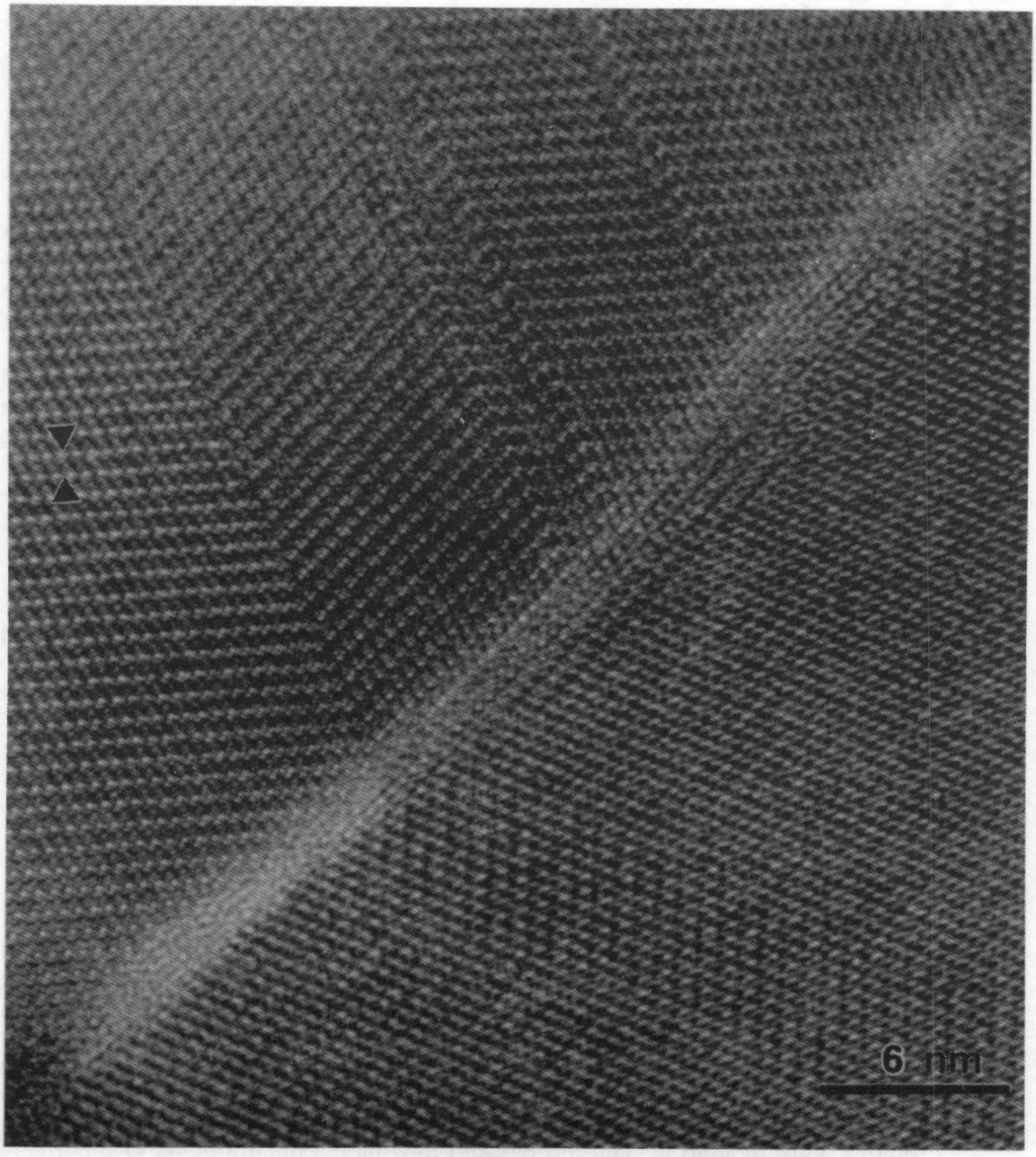

Figure 5: HRTEM of heat-treated AY6 crystallized intergranular phase showing the presence of twin lamelae

As has been noted during the course of this study, the addition of SiC(w) leads to a change in both composition and volume of intergranular glass phase produced during consolidation. For instance, an AY6 composition prepared from UBE E10 Si_3N_4 (having an oxygen content of 1.37 w/o) contains 8.6 v/o oxides having approximate composition of 24.2 w/o Si_3N_4 + 60.6 w/o Y_2O_3 + 15.2 w/o Al_2O_3 based on only the oxides, while an AY6 30 v/o SiC(w) (1.2 w/o oxygen) composite prepared with the same Si_3N_4 has 7.0 v/o oxides with a composition 30.7 w/o SiO_2 + 55.4 w/o Y_2O_3 + 13.9 w/o Al_2O_3. These results are calculated from the added Y_2O_3 and Al_2O_3 and the relative amounts of SiO_2 in both the Si_3N_4 and SiC, assuming the oxygen content is primarily SiO_2 and not adsorbed oxygen. As illustrated in the SiO_2, Y_2O_3, Al_2O_3 phase diagram (Figure 6), changes in composition of the glass such as these would affect the softening temperature and other properties of the glass phase as well as the formation of phases produced by the devitrification. The figure shows the relative position for most of the Si_3N_4-based compositions containing Y_2O_3 examined during these studies.

To further examine the effect of relative amount of glass phase and composition on composite properties, an AY6 30 v/o SiC(w) material having the same v/o and composition of oxide additives as AY6 was prepared. The material was hot pressed at the same temperature and time as the standard composite and the properties were measured and compared to both AY6 and AY6 30 v/o SiC(w) composite. Additional composites were also prepared by the same hot pressing schedule and heat treated to crystallize the grain boundary phase to determine if the increase in v/o and composition of the glass phase affects the mechanical properties of the resulting composite material. The densification of the composite material with the adjusted glass is enhanced compared to that of the standard material as illustrated in Figure 7. This increase in densification rate is due to the increase in glass content. Measurement of the mechanical properties (Table 1) shows an improvement in both fracture toughness and strength when compared to the standard composite and an AY6 having the same v/o and composition of glass. The additional heat treatment for this composition shows essentially the same room and elevated temperature properties as the non-heat treated material.

Process for Near Net Shape Part Fabrication

Investigations of near-net-shape fabrication of injection-molded AY6+30 v/o SiC(w) composite material have concentrated on mold modifications. The CATE blade mold mold modifications were designed to control the alignment of the whiskers along the blade surfaces in an effort to decrease the warpage produced during densification. To better understand the material parameters which may affect the whisker alignment during molding, materials were prepared at constant solids loading having both a high viscosity (~100 kilopoise) and low viscosity (~2 kilopoise). These changes were accomplished with only a slight modification to the binder used.

Blades were molded in both the old and new mold configurations to determine the flow effects on the fill of the mold. AY6 powder having a very low viscosity (~1/2 kilopoise) was used for these trials. Short shots showed that the mold modification produced the desired plug flow along the blade section with only a slightly faster flow being observed in the thicker cross section of the blade. Molding of the low viscosity AY6 +30 SiC whisker material produced a similar flow pattern during molding. Increasing the viscosity to 100 kilopoise caused a change in the flow pattern with the thin section of the airfoil filling last.

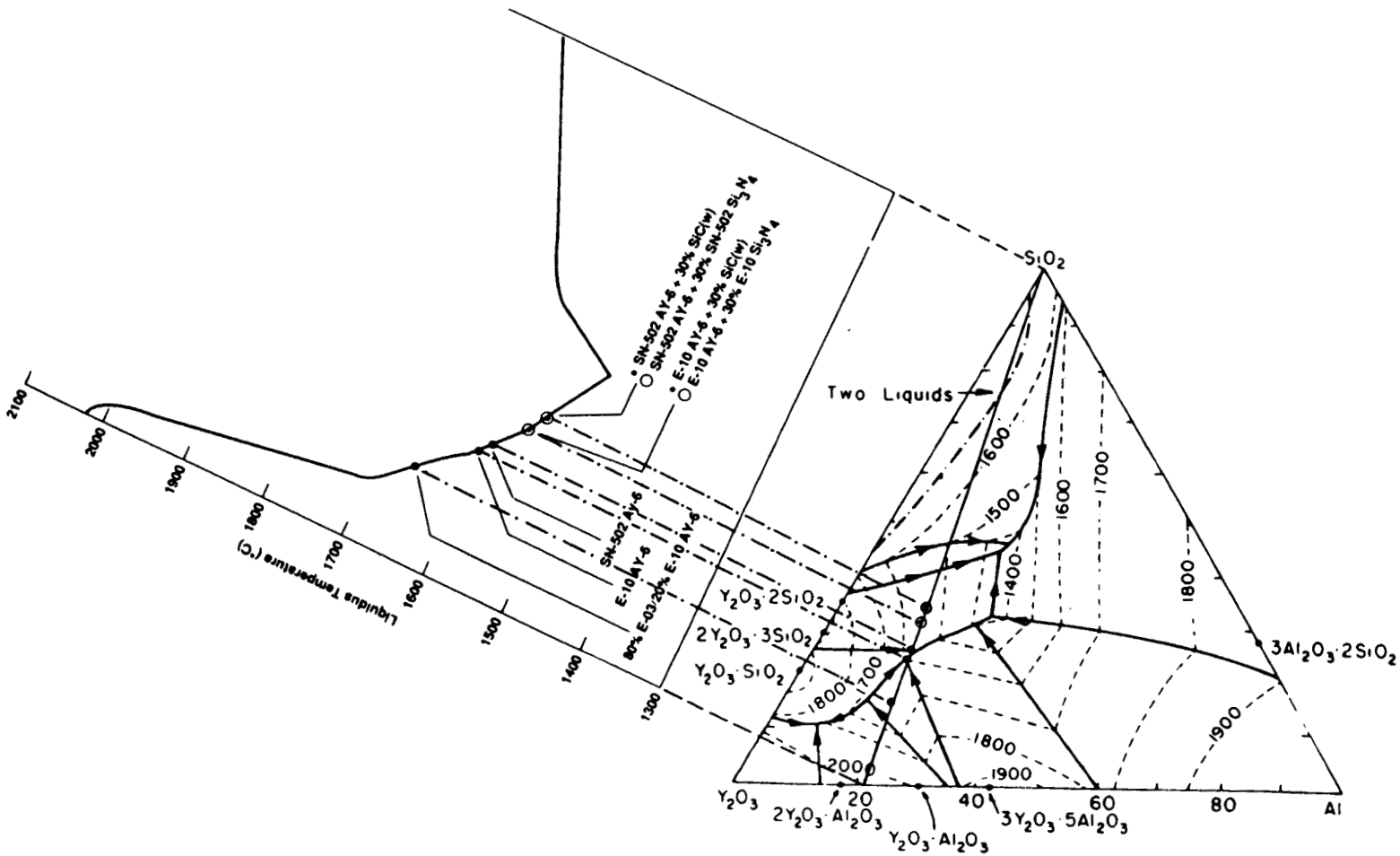

Figure 6: Phase diagram for SiO_2, Y_2O_3, Al_2O_3 composition with approximate liquidus temperature for Si_3N_4-based materials used in course of study

Ref. Fig. 2586-System Al_2O_3, Y_2O_3, SiO_2 - Phase Diagrams for Ceramists 1969 Supplement

I.A. Bondar and F. Ya. Goya Khor, Izv, Akad, Nauk SSR, Ser. Khim, 7, 1325 (1963).

Table 1: Properties of Various Si_3N_4-Based Compositions Prepared from UBE E10 Si_3N_4 Hot Pressed at 1800°C for Various Times

Material	HP Time	K_{IC} (MPa·m$^{1/2}$)	MOR (MPa) Test Temperature(°C) 25	1400
Std. AY6 (Sint. Aid=2.4 w/o SiO_2 +6.0 w/o Y_2O_3+1.5 w/o Al_2O_3)	100	7.0±0.1	1016±36	331±9
	400	7.4±0.1	981±44	361±3
Std. AY6 + 30 v/o SiC(w) (Sint. Aid=2.3 w/o SiO_2+4.3 w/o Y_2O_3+1.1 w/o Al_2O_3)	400	8.0±0.1	994±73	350±3
AY6 + 30 v/o SiC(w) Adjusted Glass (Sint. Aid=2.4 w/o SiO_2+6.0 w/o Y_2O_3+1.5 w/o Al_2O_3)	400	8.4±0.2	1083±113	369±12
	400 (+1200°C for 240 min. heat treatment)	8.6±0.2	1087±91	350±25

A number of blades were molded in both the old and new mold configurations from the whisker materials having both high and low viscosity. Blades were carried through the binder burnout stage and densified by hot isostatic pressing.

Comparison of blades prepared from the AY6 composition using either gate configuration showed little difference in distortion. Compared to the AY6 blades, some distortion appears to be present in all the composite blades. Figure 8 shows the distortion of the composite blade as prepared at the beginning of the second phase of this program using the original process flow sheet. This blade was prepared with an injection molding mix having low solids loading gated from the base of the blade and shows severe distortion in both the platform section and along the blade end. Using process changes, which were determined earlier in the second phase of the program through work with simple bar configuration, such as binder modification for increased solids loading, gating modifications and changes in the HIP cycle, reduced distortion can be achieved. Figure 9 compares the distortion for composite blades prepared from a low viscosity, high solids loading mix with an AY6 blade. As can be seen, there is a decrease in the overall warpage for either gating configuration of the blade for this material compared to the composite blade of Figure 8. The major improvements were observed for composite blades prepared from the high viscosity, high solids loading mix (Figure 10). Based on these preliminary observations, the least warpage is observed for the blades prepared from the high viscosity mix, high solids loading molded from the tip.

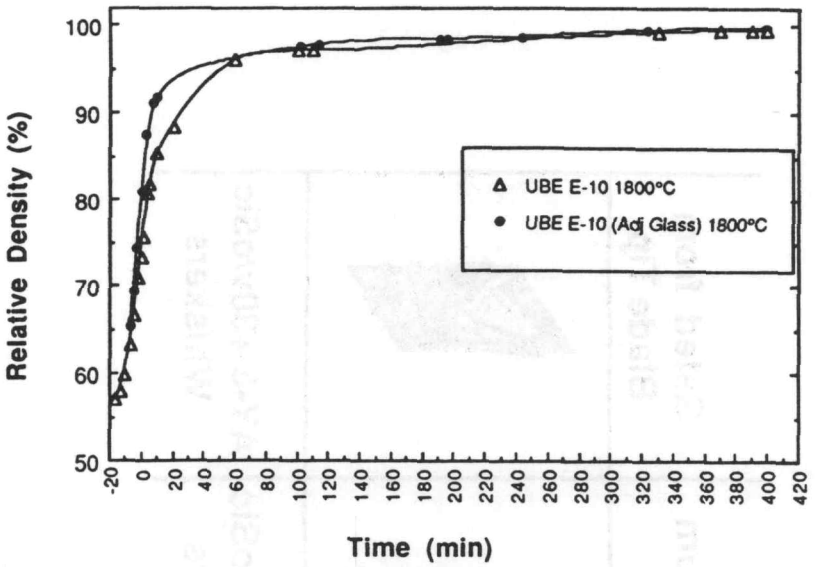

Figure 7: Densification curves for AY6 + 30 v/o SiC(w) composites prepared from UBE E10. Composite with adjusted glass has higher volumes of glass of same composition as AY6. (Negative time represents time before 1800°C is reached.)

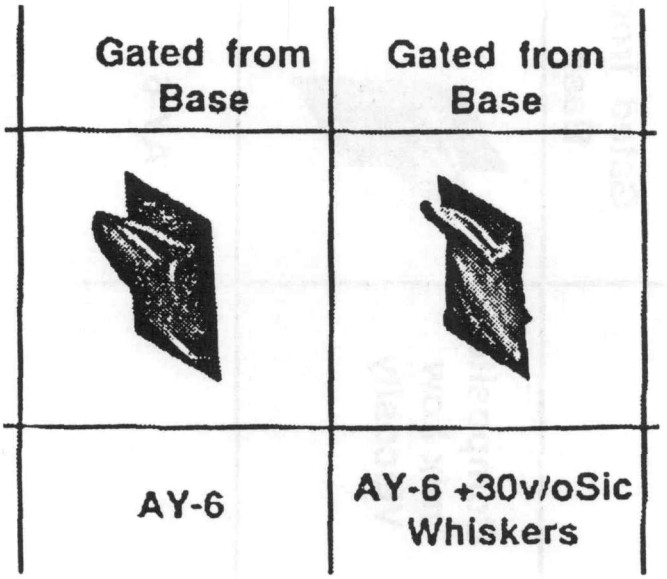

Figure 8: View from above the blades showing maximum distortion of the composite blade prepared from low solids loading mix compared to AY6 composition for same gating configuration

	Gated from Base	Gated from Base	Gated from Blade Tip
Composite mix Low Viscosity			
	AY-6	AY-6 +30v/oSic Whiskers	AY-6 +30v/oSic Whiskers

Figure 9: View from above the blades showing distortion of composite blades as a result of increased solids loadings, gate configuration and low viscosity mix

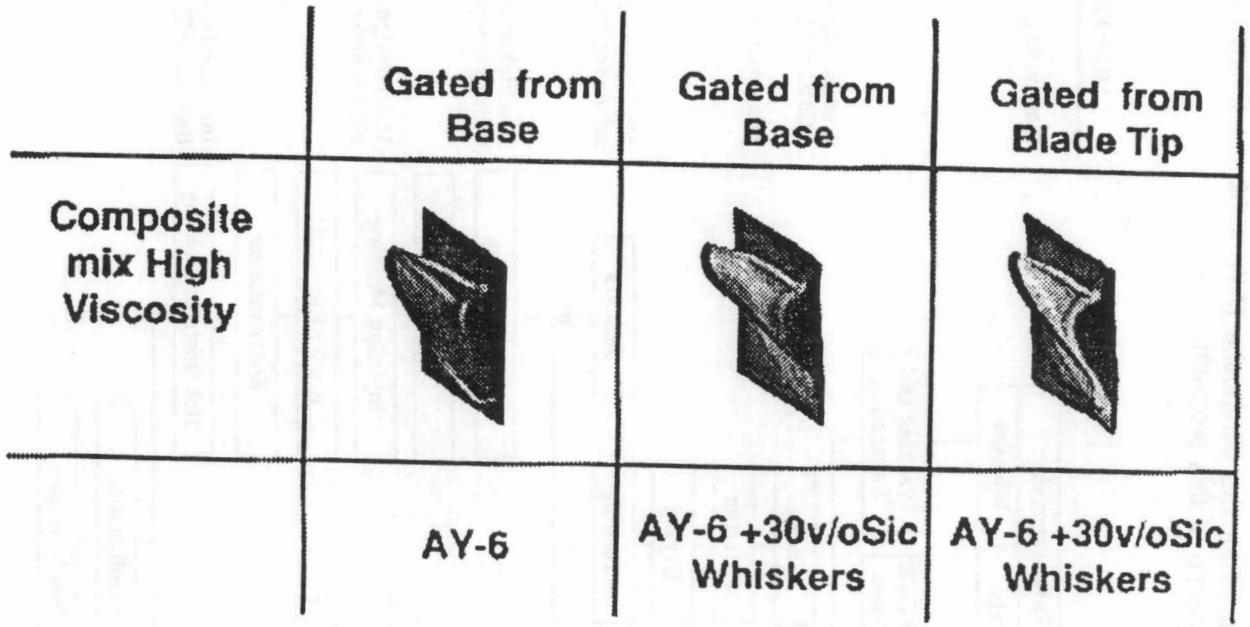

Figure 10: View from above the blades showing reduced distortion of composite blades as a result of increased solids loadings, gate configuration and high viscosity mix

The visual observations noted above for relative degrees of airfoil distortion were confirmed quantitatively using a coordinate measuring machine to trace the airfoil convex side contour at two heights from the platform.

As was stated previously, the composite blades shown above incorporate modifications from the original process flow sheet. These modifications are detailed in Figure 11 and are based on the findings leading to improved shape fabrication and mechanical property values for the composite (AY6 + 30 v/o SiC[w]) materials determined during the course of this program.

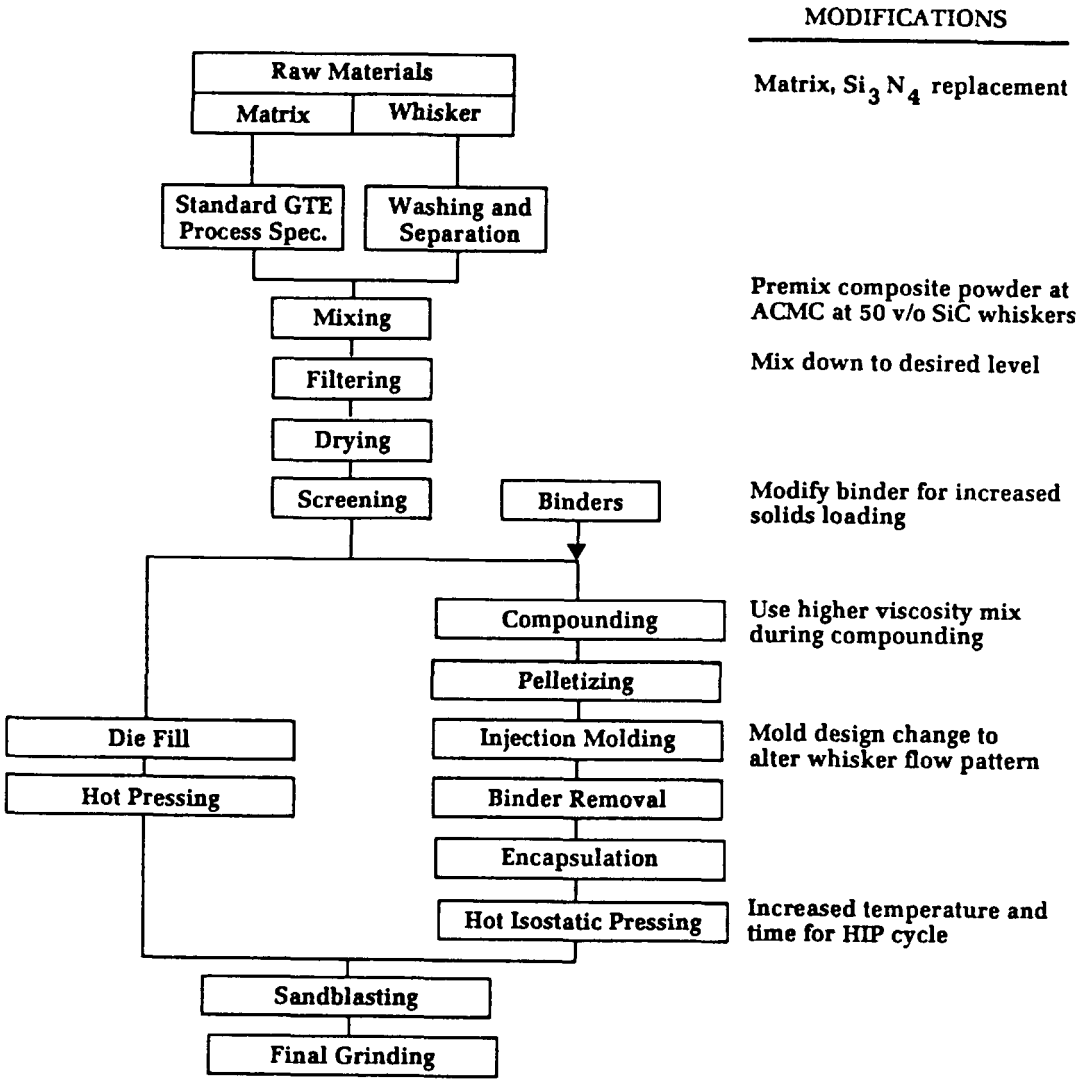

Figure 11: Process flow sheet with modifications leading to reduced distortion of injection-molded and HIPed AY6 + 30 v/o SiC whisker composite material

Modulus of Rupture Test Methodology

Resolution of modulus of rupture test methodology has been completed. Initial testing was conducted with hot-pressed AY6-Si_3N_4 with a fixture whose spans and load point size correspond to MIL-Std-1942 (MR) configuration B (quarter point loading with outer span=40 mm and load point dia.=4.5 mm) and compared to MOR values obtained using the standard GTEL fixture (outer span=22.9 mm, inner span=10.2 mm, load point dia.=6.1 mm). Room temperature MOR was measured at a crosshead speed of 4.95 mm/min corresponding to calculated strain rates of 5.7×10^{-3} min^{-1} and 7.4×10^{-3} min^{-1} for the MIL-Std and GTEL fixtures, respectively.

The results (Table 2) indicate that the average strength is reduced by 13% when the larger MIL-Std-B size bend bar compares to the GTEL standard..

Table 2: Comparison of MIL-Std-B and GTEL Four-Point Modulus of Rupture (Hot-Pressed AY6)

Fixture	Sample Size (mm)	MOR* (MPa)	2-Parameter Weibull Modulus	Effective Volume (mm^3)
MIL-Std-B	3.4x4.0x45.0	870 ± 89	11.7	10.2
GTEL-Std	1.3x2.5x25.0	1001±72	16.5	1.1

*Average of 20 samples

Since the configuration B bend bar size is large compared to hot-pressed plates normally densified to screen materials, MIL-Std-1942 (MR) configuration A (quarter point loading with outer span=20 mm and load point diameter=2.25 mm) was also evaluated. The crosshead speed in this instance was 0.25 mm/min., which is the closest approximation to the specified 0.20 mm/min. of which the testing machine is capable. Configuration A was compared to the GTEL standard using isopressed and HIPed AY6. The results (Table 3) show that the two test configurations yield statistically equivalent results.

Table 3: Comparison of GTEL Standard and MIL-Std-1942 (MR) Configuration A Modulus of Rupture

Fixture	Sample Size (mm)	MOR* (MPa)	2-Parameter Weibull Modulus
MIL-Std-A	1.5x2.0x25.0	1029 ± 130	7.9
GTEL-Std.	1.3x2.5x25.0	1049 ± 163	6.7

*Average of 20 samples

Summary

The objectives of the program "Dispersion-Toughened Silicon Nitride" carried out within the scope of the Ceramic Technology for Advanced Heat Engines (CTAHE) program are to develop an advanced toughened silicon nitride composite and a process for near net shape part fabrication. The work on this program was initiated in 1985.

The initial phase of the program has considered particulate and whisker-reinforced composites and examined the effect of TiC and SiC dispersoids on fracture toughness of Si_3N_4. The best results were obtained with whisker reinforcements. silicon carbide whisker-reinforced Si_3N_4 was selected for further development. Conducted research has identified fundamental microstructure-property relationships as well as processing parameters required to produce dense composites of simultaneously improved fracture toughness and strength.[1] A predictive model that relates microstructure-fracture toughness dependence developed and scrutinized in the course of these studies has shown that the fracture toughness of polycrystalline ceramics could be affected by changes of grain size and shape as well as strength of intergranular bond. Accordingly, it was shown that a deflection/debonding mechanism could utilize Si_3N_4 whiskers to toughen Si_3N_4 body.[2] Si_3N_4-SiC composites offer a number of distinct advantages over "monolith." One advantage, in addition to their improved thermal shock and wear resistance, due particularly to improved conductivity and hardness, is their tailorability with respect to high temperature properties. While the toughness of silicon nitride monolith can be raised by grain or, for that matter, whisker growth in situ, the required low surface tension and viscosity of liquid needed to promote such growth will tend to result in a material of reduced high temperature strength. It was therefore considered that in the heat engine applications, Si_3N_4-SiC whisker composites have, due to their higher hardness thermal conductivity, thermal shock and wear resistance, a definite advantage and warrant further development. In the current program (Phase II), 1987-1989, the properties were further improved to achieve nearly two times higher fracture toughness and concurrently improved elevated temperature (1400°C) strength of the composite. These improvements were obtained through optimization of processing and modifications of composite phase assembly, primarily intergranular phase (Figure 12).

Development of the process for near net part fabrication which concentrated on injection molding has demonstrated the feasibility of this forming method and produced hot isostatically pressed materials with properties equaling those of hot pressed laboratory specimens. At this point in time, the process has been brought to a level where development should more appropriately shift toward upscaled production of parts in a program such as ATTAP that also provides application testing. This technology was transferred and incorporated into the ATTAP program at GTE Laboratories, where it has been applied in injection modeling of ATTAP rotors (Figure 13).

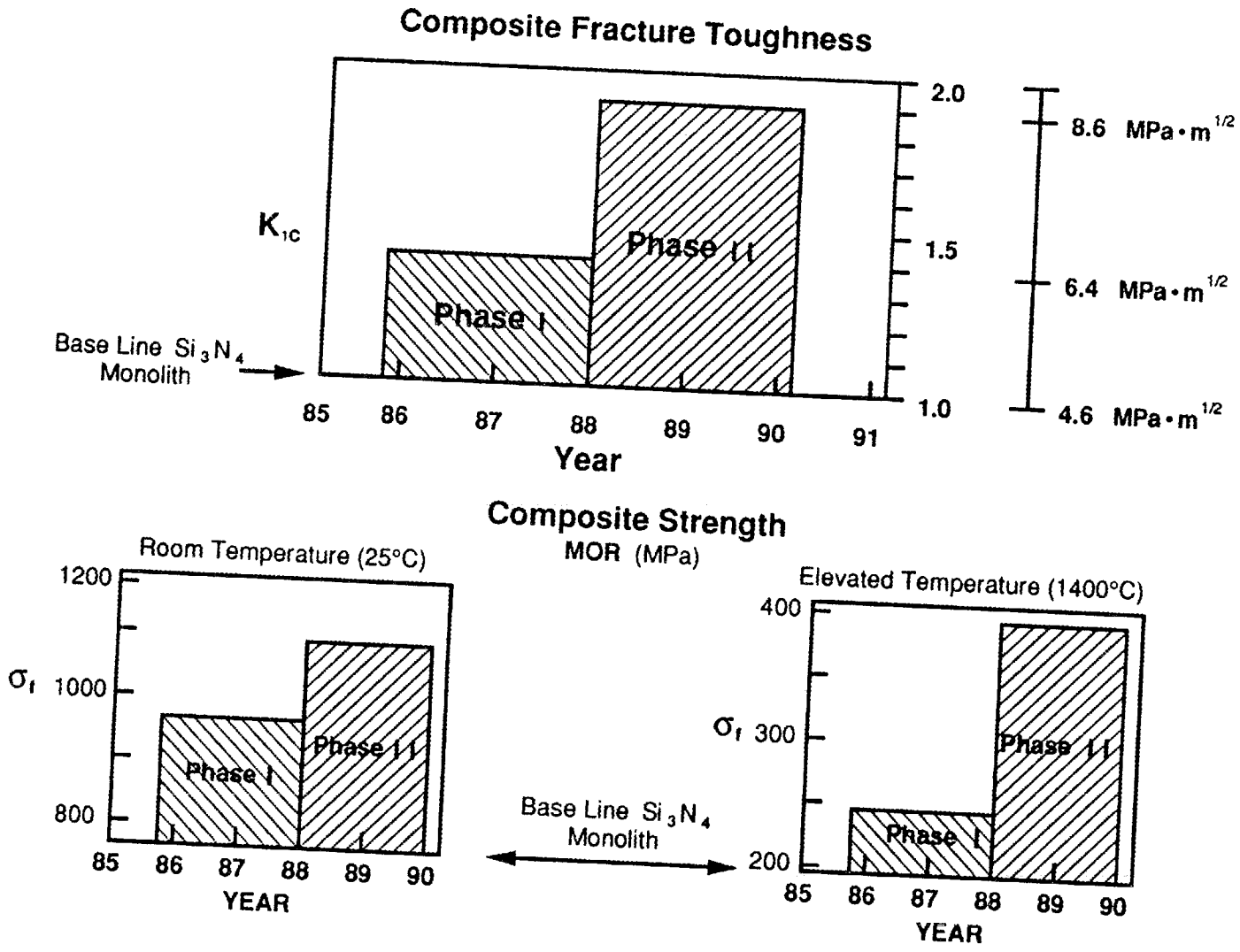

Figure 12: Development of dispersoid-toughened silicon nitride (Si_3N_4 + 30 v/o SiC whisker)

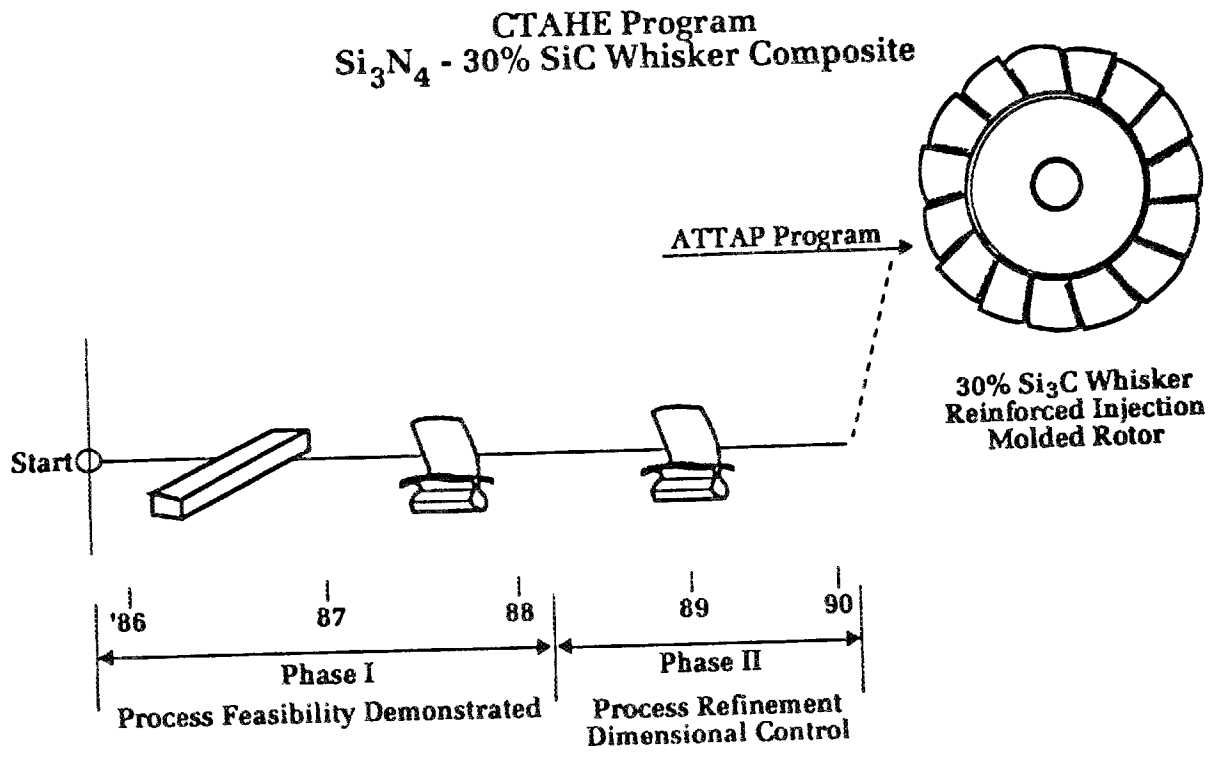

Figure 13: Development of a process for complex near net shape part fabrication (Si_3N_4 - 30 v/o SiC whisker composite--Forming: injection molding; Densification: hot isostatic pressing)

Status of milestones

The execution of the program has been completed: A draft of the final report was prepared and submitted to ORNL for review.

Milestone Schedule

122301	Complete analysis of candidate silicon nitride powders and silicon carbide whiskers for fabrication of whisker-toughened silicon nitride composites; choose the reference materials for the GTE composite development program.	May 31, 1988	Completed
122302	Complete use tests, select best materials, and submit a draft of an open literature publication.	Dec. 31, 1988	Completed
122303	Evaluate effects of sintering aids and process variables on composite properties. Select optimum systems and submit a draft of an open literature publication.	Oct. 31, 1989	Completed
122304	Complete process optimization and generate process flow sheet.	Dec. 31, 1989	Completed
122305	Submit final draft report to ORNL.	Jan. 31, 1990 Mar. 31, 1990	Delayed Completed

Publications

"Tensile Creep of SiC Whisker-Reinforced Silicon Nitride" by B.J. Hockey, S.M. Wiederhorn, and W. Liu (NIST) and J.G. Baldoni and S.T. Buljan (GTEL), *Proc. 27th Auto. Tech. Dev. CCM*, P-230, 251-257 (1990).

"Creep and Crack Growth Resistance of Silicon Nitride Composites," *Ceramic and Components for Engines*, Ed. V.J. Tennery, The American Ceramic Society, Inc., Columbus, OH, 786-795 (1989).

"Tensile Creep of Whisker-Reinforced Silicon Nitride," B.J. Hockey, S.M. Wiederhorn, W. Liu (NIST), J.G. Baldoni and S.T. Buljan (GTEL), *J. Mat. Sci.* (to be published).

References

1. S.T. Buljan, J.G. Baldoni, M.L. Huckabee, "Si_3N_4-SiC Composites," *Bull. Amer. Cer. Soc.* 66(2), 347-352 (1987).

2. S.T. Buljan, J.G. Baldoni, M.L. Huckabee, G. Zilberstein, "Microstructure and Fracture toughness of Si_3N_4 Composites," *Whisker and Fiber-Toughened Ceramics*, Eds. R.A. Bradley, E.E. Clark, D.C. Larsen, and J.O. Steigler, ASM International, 113-123, (1988).

Fabrication of Si_3N_4/SiC Composites by Transient Liquid Phase Sintering

S. D. Nunn and T. Y. Tien (The University of Michigan)

Objective/Scope

The goal of this project is to obtain dense silicon nitride composites containing silicon carbide whiskers by transient liquid phase sintering. The systems SiAlON, SiAlON-Garnet ($Y_3Al_5O_{12}$) and SiAlON-Cordierite ($Mg_2Al_4Si_5O_{18}$) were selected for this study. An additional system, SiAlON-N-phase ($MgAl_2Si_4O_6N_4$), was later added to the study. Mixtures of the starting materials form a sufficient amount of liquid to aid densification at the sintering temperatures. After sintering, the amorphous intergranular phase can be crystallized by heat treatment.

Technical Highlights

1.0 INTRODUCTION

The models proposed for describing the toughening of a ceramic matrix by whisker reinforcement emphasize the importance of four principal mechanisms in increasing the fracture energy of the composite material:[1-4]

1. Crack deflection along and around the whiskers which increases the fracture surface area.

2. Debonding of the whisker from the matrix which absorbs energy in fracturing the interface.

3. Bridging of the crack by whiskers which stores elastic strain energy in the unfractured whisker.

4. Pull-out of the whiskers in the crack wake which absorbs energy in overcoming the interfacial friction.

All of these mechanisms can be directly coupled to a dependence on the properties of the whisker/matrix interface, particularly in terms of the bond strength and the interfacial stress state. The ability to predict and control the interfacial properties would enhance the ability to engineer the microstructure of these composites.

One possible method of varying the stress state at the whisker/matrix interface is by incorporating an interfacial phase with a thermal expansion coefficient which either matches (low stress) or is significantly different from (high stress) that of the matrix and reinforcing phases.[3,5] A high tensile stress at the interface would reduce the bond strength between the whiskers and the matrix, and should result in enhanced debonding and pull-out, thus increasing fracture toughness.

The sintering aids used to help densify SiC whisker reinforced Si_3N_4 are believed to form a continuous intergranular layer. Two sintering aids were selected for evaluation, YAG ($Y_3Al_5O_{12}$) and N-phase[6] ($MgAl_2Si_4O_6N_4$). The thermal expansion coefficient of Si_3N_4 is $3.0 \times 10^{-6}/°C$, while that of SiC is $4.5 \times 10^{-6}/°C$. N-phase has a thermal expansion coefficient of about $2.6 \times 10^{-6}/°C$, slightly less than that of Si_3N_4, while YAG has a much larger thermal expansion coefficient, $8.0 \times 10^{-6}/°C$. The difference in thermal expansion coefficient between the two sintering aids should allow evaluation of

the possibility of modifying the stress state at the whisker/matrix interface. Composites with an N-phase intergranular phase should have a low-stress or stress-free interface after cooling from the crystallization temperature, while the YAG-containing composites should develop significant tensile stresses at the interface upon cooling. This variation in stress state should result in differences in the measured fracture toughness, between composites made with the two different sintering aids and between the as-fired (glassy interface) and the heat treated (crystalline interface) composites.

2.0 Experimental

SiC whisker reinforced Si_3N_4 composite compositions and test samples were prepared to compare the effects on mechanical properties of varying the properties of the intergranular phase. The compositions of the samples which were evaluated are given in Table 1. Two liquid phase sintering aids were used, N-phase ($MgAl_2Si_4O_6N_4$) and YAG ($Y_3Al_5O_{12}$). Both have been found to be effective sintering aids for pressureless sintering of SiC whisker reinforced Si_3N_4 and both phases have been crystallized by heat treatment after sintering.[6] The amount of sintering aid addition in sample Y1 was 12 vol.%, in samples Y2 and Y3 6 vol.%. The corresponding N-phase samples contained the same equivalent percent of the anionic species. It had been found in previous studies of pressureless sintering that comparable densities were achieved for different sintering aid additives by using the same atomic percent oxygen in the composition.[7] Two different matrix compositions were also evaluated, β-Si_3N_4 and β_{13}-SiAlON (Si_5AlON_7). All of the compositions contained approximately 20 vol.% SiC whiskers.

2.1 Processing

The details of the processing procedure were descibed in a previous report.[8] The matrix and sintering aid powders were attrition milled for three hours using isopropyl alcohol and alumina media. The whiskers, which had been dispersed using an ultrasonic shear homogenizer, were then added to the attriton mill and blended with the powders for one hour. The resulting slurry was oven dried. A mortar and pestle was used to break up the dried cake. The powders were then hot pressed at 1700°C under a static nitrogen pressure of about 0.07 MPa (10 psi). Consolidation by hot pressing rather than pressureless sintering was used to minimize variations in the microstructures (such as density and grain size) which could also have an effect on the mechanical properties. A portion of the samples were subsequently heat treated at 1350°C for 20-22 hours in a mildly flowing nitrogen atmosphere to crystallize the grain boundary phase.

2.2 Property Measurement

The density of the hot pressed samples was measured using Archimedes method. The elastic modulus was measured using an acoustic pulse-echo apparatus.

Four-point bend test specimens measuring 42 x 3 x 2.25 mm were machined from the hot pressed samples to evaluate the room temperature fracture strength and fracture toughness. The edges of the bars were chamfered and the tensile surface was final-ground using 6 μm diamond media before being polished to Linde B. Fracture strength and fracture toughness were measured in four-point bending. The four-point bend test fixture was fully articulated, and had an outer span of 30 mm and an inner span of 15 mm. A universal testing machine was used to fracture the test bars at a strain rate of 1 x 10^{-4}/sec. The strain rate, $\dot{\varepsilon}$, was calculated using the following relationship:

$$\dot{\varepsilon} = 6ds/L_1^2$$

where d is the thickness of the test bar, s is the crosshead speed, and L is the outer span of the test fixture. The fracture strength, σ, was calculated from the following equation:

$$\sigma = 3P_1(L_1 - L_2)/(2bd^2)$$

where P_1 is the load at fracture, L_2 is the inner span of the test fixture, and b is the width of the test bar.

The controlled surface flaw method was used for the fracture toughness determination. A Vicker's diamond point indent which was oriented orthogonally to the test bar was made at the midpoint of the inner span on the tensile surface. An indentation load of either 15 or 25 kg was used. The critical stress intensity factor, K_{Ic}, was then calculated after fracture using Chantickul's equation:[9]

$$K_{Ic} = 0.59(E/H)^{1/8}(\sigma P_2^{1/3})^{3/4}$$

where E is Young's modulus, H is the hardness, and P_2 is the indentation load. The critical strain energy release rate, $\mathcal{G}_{Ic}$, was also calculated and is given by:

$$\mathcal{G}_{Ic} = K_{Ic}^2/E.$$

3.0 Results and Discussion

The x-ray diffraction patterns of the samples are shown in Fig. 1. Analysis of the patterns showed that N-phase and YAG had been crystallized after annealing in the β_{13}-SiAlON compositions (Y1, Y2, N1 and N2). The β-Si_3N_4 - YAG composition (Y3) showed some retained α-Si_3N_4 and a small amount of $Y_2Si_2O_7$, but no YAG. The β-Si_3N_4 - N-phase sample (N3) showed considerable α-Si_3N_4 and no evidence of crystallization of the sintering aid.

The property measurement results are summarized in Table 2. Samples which received a crystallization heat treatment are indicated by an "A" in the sample code designation. The measured densities of the hot pressed samples were between 98 and 100% of the calculated theoretical density. Young's modulus was between 284 and 330 GPa, increasing with lower sintering aid content and after heat treatment. The hardness varied from 16.06 to 18.43 GPa and showed a similar dependence on sintering aid content and heat treatment.

The results of the fracture strength and fracture toughness measurements are shown graphically in Figures 2 and 3. The fracture strength values (Fig. 2) were quite uniform for all of the as-fired composites at about 800 MPa and always decreased after heat treatment. The decrease varied from 11 to 35% and shows a clear dependence on the amount of sintering aid in the composition, the greater the sintering aid content the greater the loss. The β_{13}-SiAlON - N-phase compositions show the greatest percent change in strength after heat treatment with losses of 30 - 35%. The fracture toughness values which ranged from 3.11 to 5.44 MPa$\sqrt{m}$ (Fig. 3) show a similar dependence on the heat treatment and the amount of sintering aid. The toughness decreases after heat treatment and with increasing sintering aid content. The toughness

also appears to depend on the matrix phase composition, the β-Si_3N_4 compositions have a higher toughness than the β_{13}-SiAlON compositions.

Examination of the fracture surfaces indicates that samples with the higher fracture toughness values show a predominantly intergranular fracture mode with clear evidence of crack deflection and subsurface fracture of bridging whiskers. The low toughness samples showed a transgranular fracture mode with little crack deflection. Examples of the fracture surfaces are shown in Fig. 4.

The differences in toughness between the as-fired YAG and N-phase samples are consistent with the predicted differences in the thermal expansion mismatch strains at the whisker/matrix interfaces in the composites. The subsequent loss of toughness after heat treatment may be due to the formation of strong interfacial bonds after the long-term thermal exposure. Additional analysis is currently underway to identify the specific mechanisms which control the composite properties.

4.0 Conclusions

The mechanical properties of 20 vol.% SiC whisker reinforced Si_3N_4 composites which contain sintering aid additives which have widely different thermal expansion coefficients show a clear variation which depends on the sintering aid and the heat treatment after hot pressing. The results for the as-hot-pressed samples are consistent with the predicted thermal expansion mismatch strains at the whisker/matrix interface. A loss in both fracture strength and fracture toughness is observed after heat treatment, and may be due to the formation of strong interfacial bonds which inhibit crack deflection and whisker pullout.

Status of Milestones

On schedule.

Communications/Visits/Travel

None.

Problems Encountered

None.

Publications

None.

References

[1] G. C. Wei and P. F. Becher, "Development of SiC-Whisker-Reinforced Ceramics," *Am. Ceram. Soc Bull.*, **64** [2] 298-304 (1985).

[2] A. G. Evans and D. B. Marshall, "The Mechanical Performance of Fiber Reinforced Ceramic Matrix Composites," *Mat. Res. Soc. Symp. Proc.*, Vol. 120 (1988) p. 213-246.

[3] P. F. Becher, C. H. Hsueh, P. Angelini, and T. N. Tiegs, "Toughening Behavior in Whisker-Reinforced Ceramic Matrix Composites," *J. Am. Ceram. Soc.*, **71** [12] 1050-61 (1988).

[4] G. H. Campbell, M. Rühle, B. J. Dalgleish and A. G. Evans, "Whisker Toughening: A Comparison Between Aluminum Oxide and Silicon Nitride Toughened with Silicon Carbide," *J. Am. Ceram. Soc.*, **73** [3] 521-30 (1990).

[5] C. H. Hsueh, P. F. Becher and P. Angelini, "Effects of Interfacial Films on Thermal Stresses in Whisker-Reinforced Ceramics," *J. Am. Ceram. Soc.*, **71** [11] 929-33 (1988).

[6] S. D. Nunn and T. Y. Tien, "Fabrication of Si_3N_4/SiC Composites by Transient Liquid Phase Sintering," Semi-annual report submitted to ORNL under Contract No. SC-19X-SA125C, October, 1989.

[7] S. D. Nunn and T. Y. Tien, "Pressureless Sintering of Si_3N_4/SiC Whisker Composites," Semi-annual report submitted to ORNL under Contract No. SC-19X-SA125C, October, 1988.

[8] S. D. Nunn and T. Y. Tien, "Pressureless Sintering of Si_3N_4/SiC Whisker Composites," Semi-annual report submitted to ORNL under Contract No. SC-19X-SA125C, April, 1988.

[9] P. Chantickul et al., "A Critical Evaluation of Indentation Techniques for Measuring Fracture Toughness: II, Strength Method," *J. Am. Ceram. Soc.*, **64** [9] 539-543 (1981).

Table 1. Composition of 20 vol.% SiC whisker reinforced Si3N4 composites.†

Sample	Matrix	Sintering Aid*	Equivalent Percent					
			Cation			Anion		
			Si	Al	Y or Mg	C	O	N
Y1	Si5AlON7	Y3Al5O12	82.80	14.04	3.17	24.40	14.28	61.32
Y2	Si5AlON7	Y3Al5O12	86.48	11.96	1.56	24.03	10.40	65.57
Y3	Si3N4	Y3Al5O12	96.07	2.46	1.48	22.75	5.29	71.96
N1	Si5AlON7	MgAl2Si4O6N4	86.35	17.09	1.55	24.40	14.28	61.32
N2	Si5AlON7	MgAl2Si4O6N4	88.23	11.01	0.77	24.03	10.40	65.57
N3	Si3N4	MgAl2Si4O6N4	97.33	2.00	0.67	22.75	5.29	71.96

†Si3N4 - UBE Industries, Inc., UBE-E10, Lot A710672
AlN - H. C. Starck, Grade A Lot S-8584B
Al2O3 - Malakoff Industries, Inc., RC-HP DBM Lot BM-2194
MgO - Mallenkrodt, MgCO3(5942) Lot KATJ, Calcined at 1000 C
Y2O3 - Morton Thiokol, Inc., 87829 Lot I17G
SiC Whiskers - Tateho Chemical Industries, SCW#1-S Lot 245

*Composition Y1 contains 12 vol.% YAG sintering aid, Y2 and Y3 contain 6 vol.%. The corresponding N compositions were formulated to contain the same equivalent percent of the anionic species.

Table 2. Properties of 20 vol.% SiC whisker reinforced Si3N4 composites hot pressed at 1700 C.

Sample*	Density	Young's Modulus	Hardness**	Fracture Strength	Fracture Toughness	
					KIc	$\mathcal{G}Ic$
	gm/cc (%T.D.)	GPa	GPa	MPa	MPa$\sqrt{m}$	J/m^2
Y1	3.27 (98%)	290	16.06±.44 (16)	832±153 (3)	4.92±.23 (8)	83.8±7.8
Y1A	3.27 (98%)	300	16.26±.46 (8)	631±2 (2)	3.32±.15 (4)	36.9±3.3
Y2	3.23 (99%)	305	16.93±.34 (24)	832±43 (6)	4.75±.15 (12)	73.9±4.5
Y2A	3.24 (100%)	314	17.65±.52 (20)	715±113 (3)	3.81±.18 (12)	46.3±4.5
Y3	3.24 (99%)	323	17.16±.37 (33)	820±95 (6)	5.44±.10 (6)	91.5±3.3
Y3A	3.23 (98%)	327	17.73±.51 (16)	717±45 (3)	5.37±.13 (8)	88.3±4.5
N1	3.11 (100%)	284	15.55±.26 (14)	777±4 (2)	3.82±.29 (8)	51.7±7.7
N1A	3.07 (99%)	287	15.65±.68 (8)	503±19 (3)	3.11±.22 (4)	33.9±4.8
N2	3.14 (100%)	304	17.37±.49 (40)	837±73 (3)	3.56±.24 (12)	41.8±5.4
N2A	3.14 (100%)	307	18.05±.33 (20)	589±145 (3)	3.33±.28 (12)	36.3±6.2
N3	3.16 (100%)	326	18.43±.51 (22)	821±170 (3)	4.65±.33 (4)	66.5±9.7
N3A	3.16 (100%)	330	18.27±.45 (16)	726±118 (3)	4.20±.44 (8)	53.9±11.1

*Samples marked with an A were heat treated at 1350 C for 20-22 hours after hot pressing.
**The numbers in parentheses indicate the number of data points.

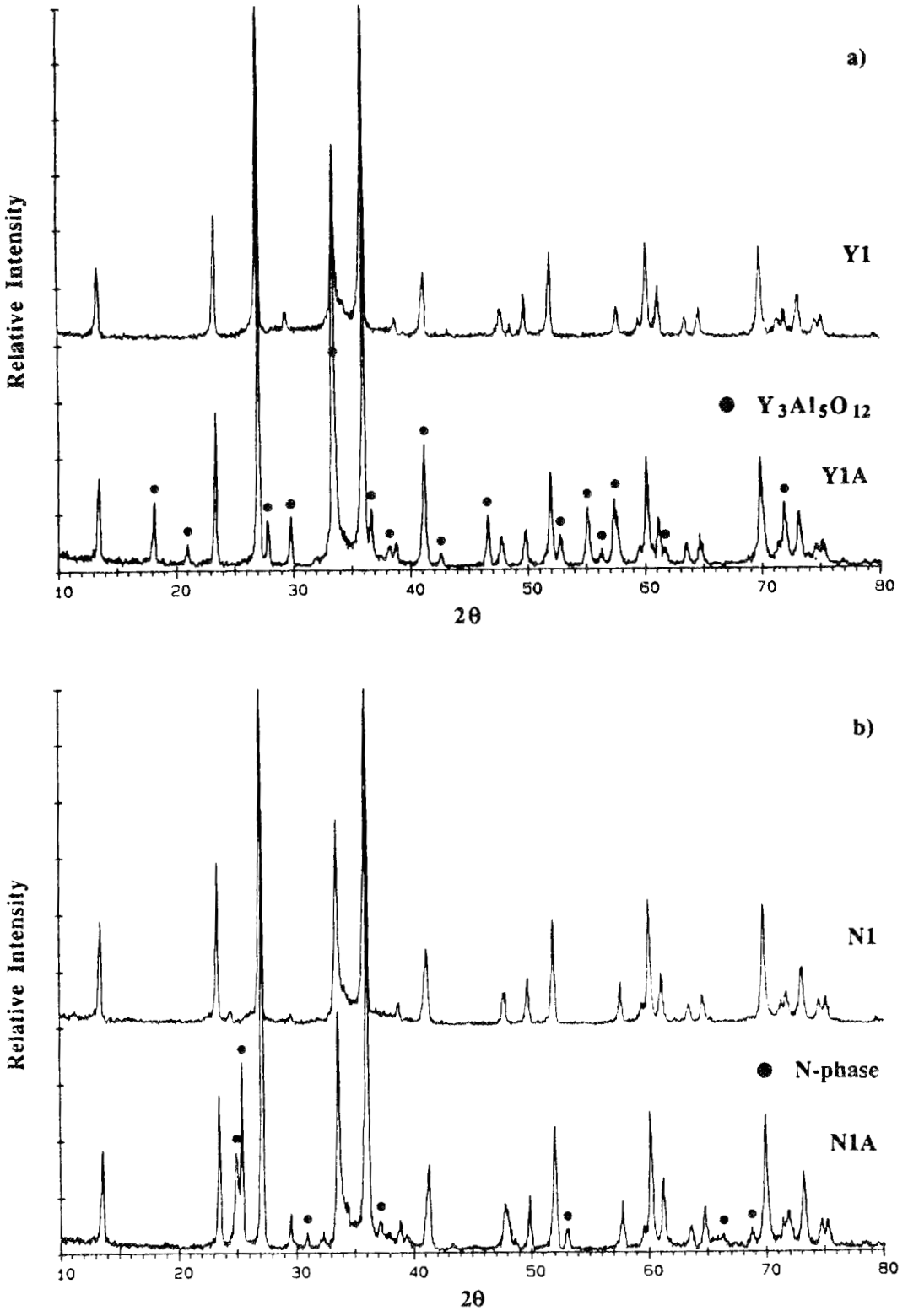

Figure 1. X-ray diffraction patterns of 20 vol.% SiC whisker reinforced Si_3N_4 composites containing different sintering aids in the as-fired condition (Yx or Nx) and after heat treatment (xxA). The principal peaks are due to β-Si_3N_4. The β-SiC peak is seen at 60° 2θ. Peaks due to the secondary phases are identified in the patterns. a) Y1 and Y1A, b) N1 and N1A.

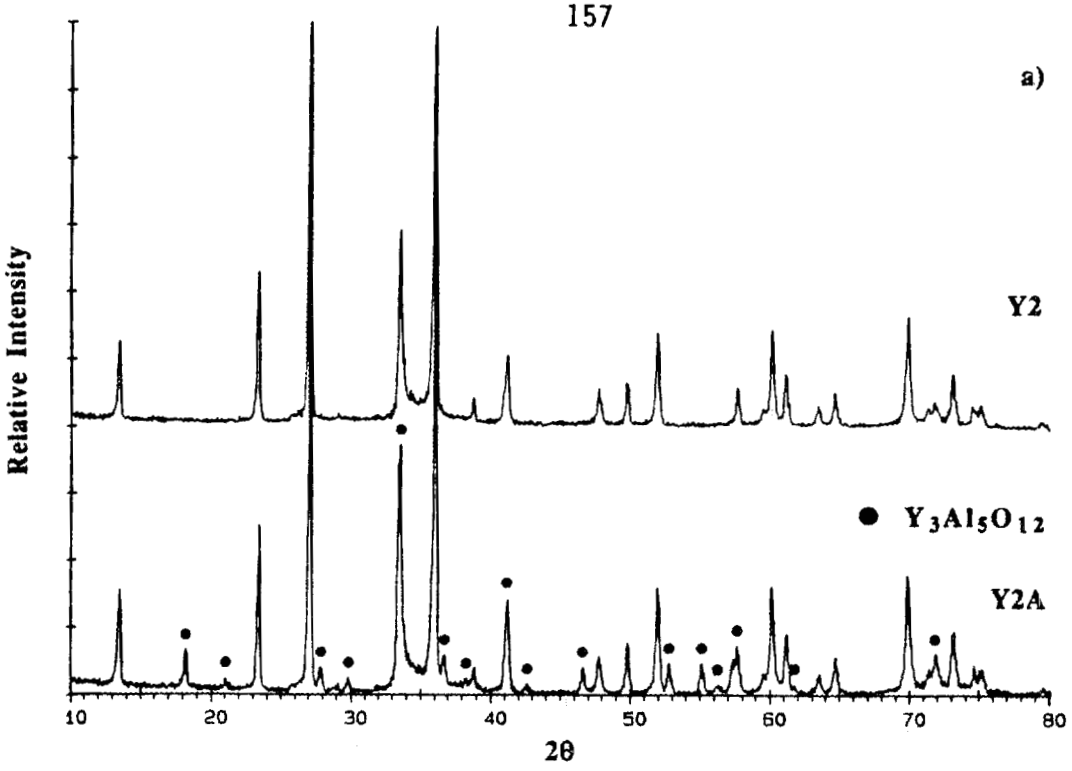

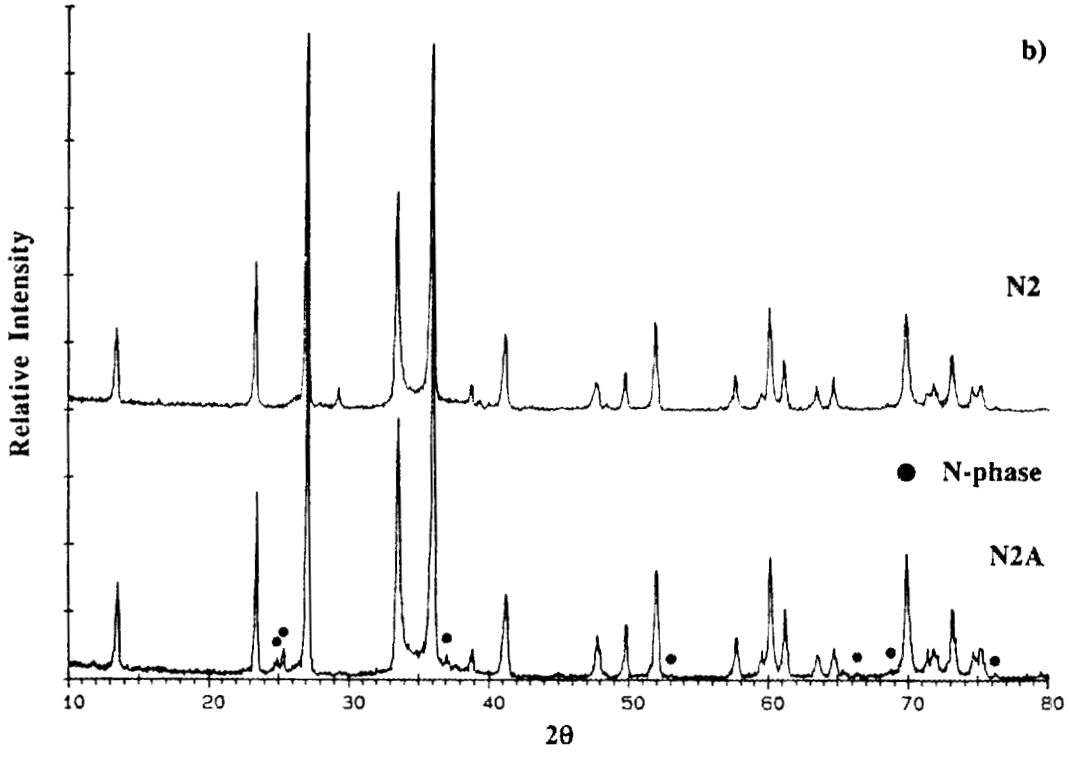

Figure 1(cont.). X-ray diffraction patterns of 20 vol.% SiC whisker reinforced Si_3N_4 composites containing different sintering aids in the as-fired condition (Yx or Nx) and after heat treatment (xxA). The principal peaks are due to β-Si_3N_4. The β-SiC peak is seen at 60° 2θ. Peaks due to the secondary phases are identified in the patterns. c) Y2 and Y2A, d) N2 and N2A.

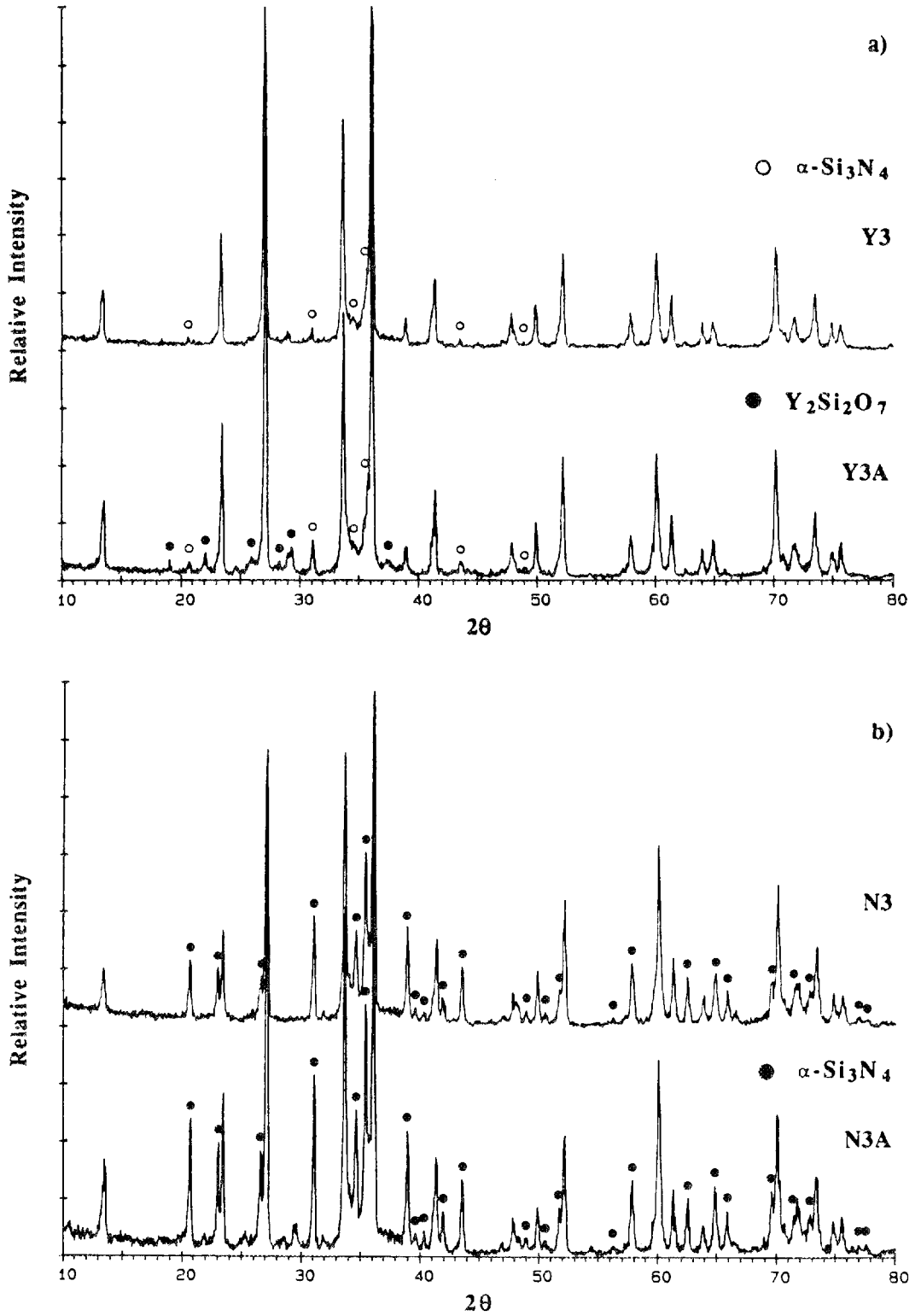

Figure 1(cont). X-ray diffraction patterns of 20 vol.% SiC whisker reinforced Si_3N_4 composites containing different sintering aids in the as-fired condition (Yx or Nx) and after heat treatment (xxA). The principal peaks are due to β-Si_3N_4. The β-SiC peak is seen at 60° 2θ. Peaks due to the secondary phases are identified in the patterns. e) Y3 and Y3A, f) N3 and N3A.

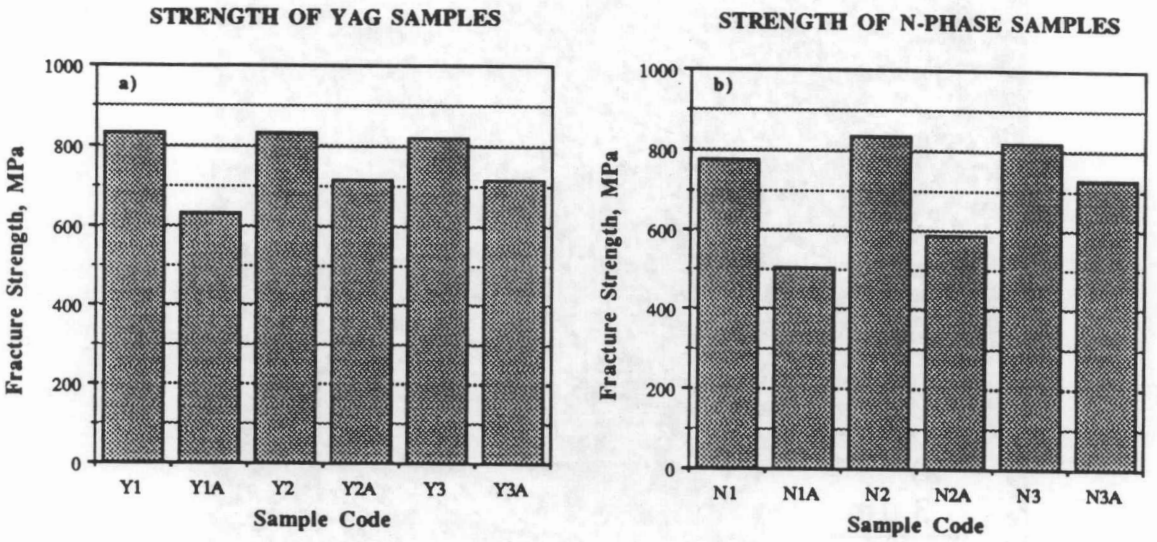

Figure 2. Fracture strength of 20 vol.% SiC whisker reinforced Si_3N_4 composites containing different sintering aids measured in 4-point bending at room temperature in the as-fired condition (Yx or Nx) and after heat treatment (xxA). a) YAG, b) N-phase.

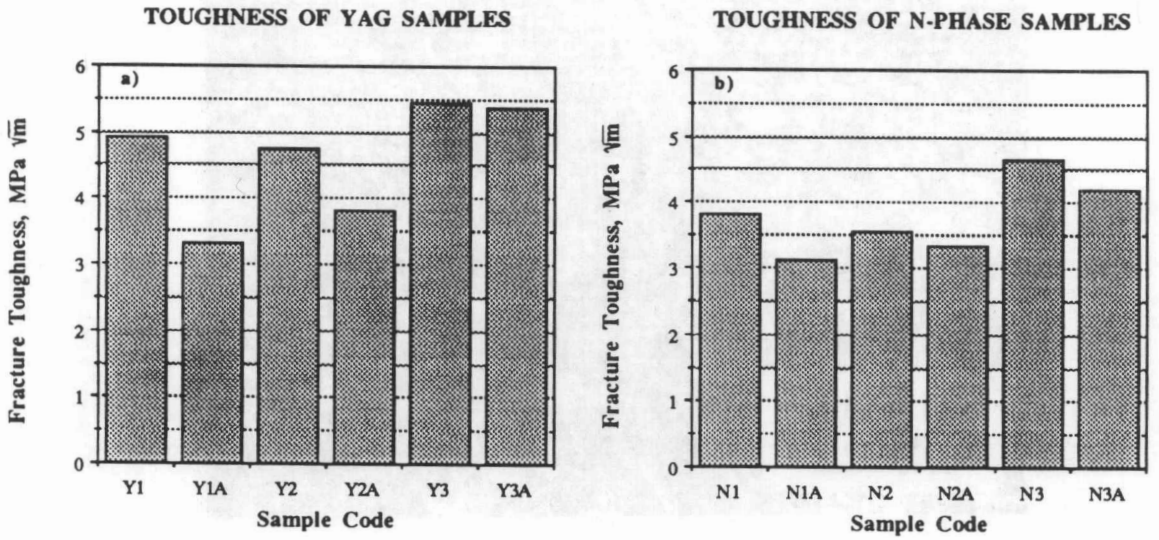

Figure 3. Fracture toughness of 20 vol.% SiC whisker reinforced Si_3N_4 composites containing different sintering aids measured in 4-point bending at room temperature in the as-fired condition (Yx or Nx) and after heat treatment (xxA). a) YAG, b) N-phase.

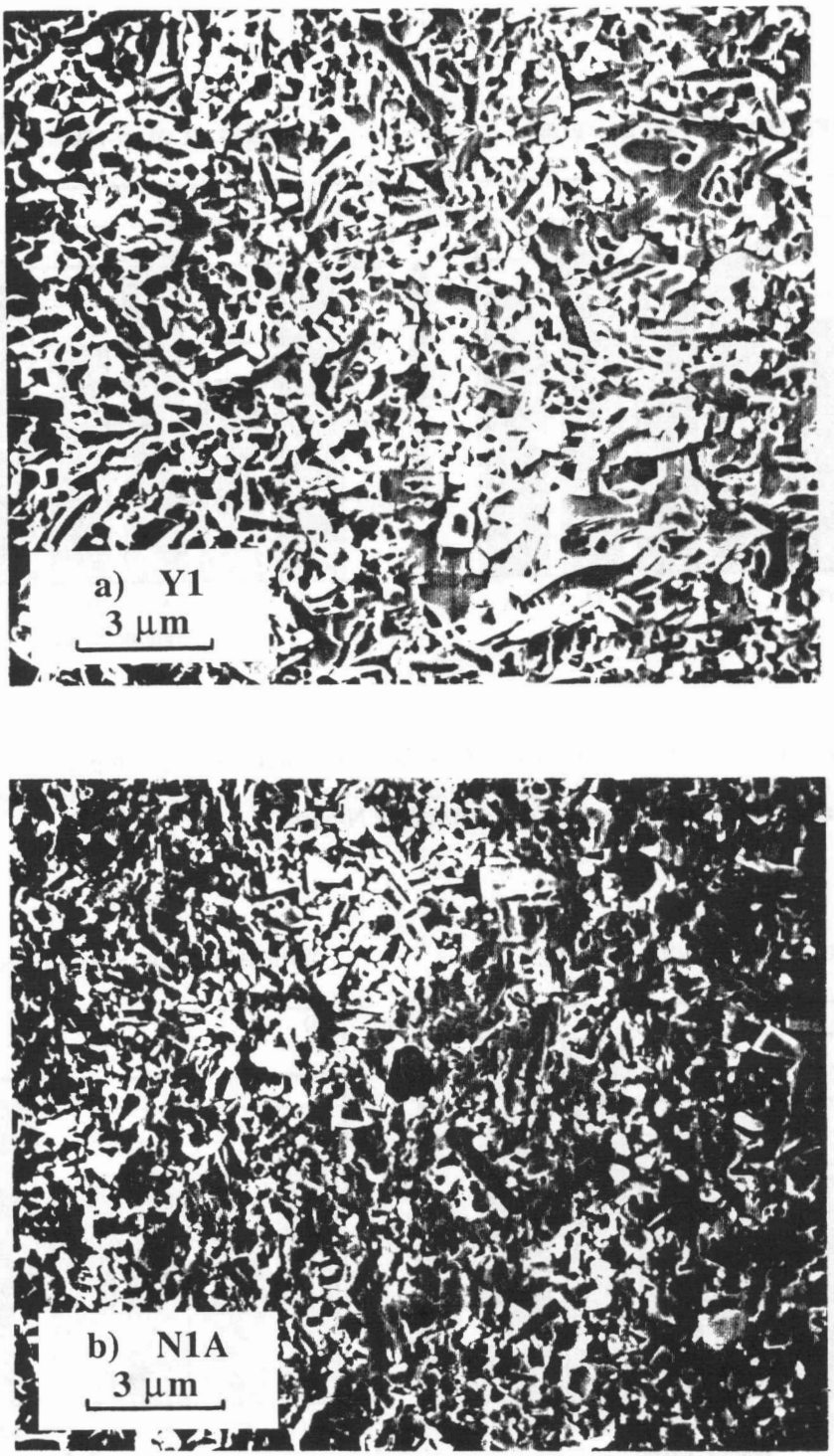

Figure 4. Fracture surface of a) sample Y1 showing primarily intergranular fracture and b) sample N1A showing primarily transgranular fracture. Sample Y1 had a higher fracture toughness than sample N1A.

1.2.3 Oxide Matrix

Dispersion-Toughened Oxide Composites

T. N. Tiegs, W. H. Elliott, and P. A. Menchhofer (Oak Ridge National Laboratory)

Objective/scope

This work involves development and characterization of SiC whisker-reinforced ceramic composites for improved mechanical performance. To date, most of the work has dealt with alumina as the matrix because it was deemed a promising material for initial study. However, an effort in SiC whisker reinforced-silicon nitride and sialon is in progress. In addition, studies of whisker-growth processes were initiated to improve the mechanical properties of SiC whiskers by reducing their flaw sizes. In-situ acicular grain growth is also being investigated to improve fracture toughness of silicon nitride materials.

Technical progress

Hot-pressed silicon nitride and sialon-SiC whisker composites

Results reported previously for the silicon nitride and sialon composites showed that impurities (mainly SiO_2) associated with the SiC whiskers have a detrimental effect on the high-temperature strength. The magnitude of the degradation is a function of the type of whisker (which dictates the impurity content), the total whisker content, the sintering aid type, and the sintering aid content. The SiO_2 is believed to react with the sintering aids and change the composition of the intergranular glass phase.

Based on those results, an additional series of samples has been fabricated to investigate techniques to control the intergranular glass phase, and tests are currently in progress. The different compositions fabricated are shown in Table 1. The parameters being investigated include methods to benificiate the SiC whiskers (to reduce the impurity levels), modification of intergranular glass-phase composition, and crystallization of the grain-boundary phases. High-temperature strength will be performed at 1200 to 1400°C.

It has been well known that silicon nitride materials can be encouraged to grow elongated grain microstructures. Significant toughening can be obtained in this manner and processing of the materials is simplified in comparison to whisker-toughened composites. An initial series of silicon nitride materials, as shown in Table 2, is currently being fabricated to assess the role of grain microstructure on fracture toughness. The compositions will give a range of microstructures and grain sizes.

Status of milestones

Milestone 123109, "Identify flaws in SiC whiskers and assess their effect on strength, submit progress report," is completed. Results are reported in the paper entitled "Identification and Development of Optimum Silicon Carbide Whiskers For Silicon Nitride Matrix Composites," by Terry N. Tiegs, Larry F. Allard, Paul F. Becher, and Matt K. Ferber.

Publications

"Identification and Development of Optimum Silicon Carbide Whiskers For Silicon Nitride Matrix Composites," by Terry N. Tiegs, Larry F. Allard, Paul F. Becher and Matt K. Ferber; submitted for publication in proceedings of Automotive Technology Contractors' Coordination Meeting, October 23-26, 1989, Dearborn, MI.

Table 1. Test matrix for silicon nitride and sialon composites at elevated temperature

Matrix composition	Sintering aid content (vol %)	SiC whisker	
		Content	Type[a]
Si_3N_4	6% Y_2O_3-2% Al_2O_3	None	---
$Si_{4.5}Al_{1.5}O_{1.5}N_{6.5}$	2% YAG	None	---
Si_3N_4	6% Y_2O_3-2% Al_2O_3	20	AMI[b]
$Si_{4.5}Al_{1.5}O_{1.5}N_{6.5}$	2% YAG	20	AMI[b]
Si_3N_4	GN-10 Type	20	AMI[b]
Si_3N_4	6% Y_2O_3	20	AMI[b]
$Si_{4.5}Al_{1.5}O_{1.5}N_{6.5}$	GN-10 Type	20	AMI[b]
$Si_{4.5}Al_{1.5}O_{1.5}N_{6.5}$	0.5% YAG	20	AMI[b]
Si_3N_4	6% Y_2O_3-2% Al_2O_3	20	AMI[c]
Si_3N_4	6% Y_2O_3-2% Al_2O_3	10	AMI[c]
Si_3N_4	6% Y_2O_3-2% Al_2O_3	30	AMI[c]
Si_3N_4	6% Y_2O_3-2% Al_2O_3	20	Tokai Carbon[c]
Si_3N_4	6% Y_2O_3-2% Al_2O_3	20	Tokai Carbon[c,d]
Si_3N_4	6% Y_2O_3-2% Al_2O_3	20	ACMC[c]
Si_3N_4	6% Y_2O_3-2% Al_2O_3	20	ACT[c]

[a]AMI is American Matrix, Inc.; ACMC is Advanced Composites Materials Corp.; ACT is Advanced Ceramic Technology.

[b]Acid-leached to remove excess silica.

[c]To be used for intergranular glass crystallization tests.

[d]Coated with approximately 25-Å carbon.

Table 2. Test matrix of silicon nitride materials to assess role of grain microstructure on fracture toughness

Composition	Comments
Si_3N_4-6% Y_2O_3-2% Al_2O_3	20% ß-Si_3N_4
Si_3N_4-6% Y_2O_3-2% Al_2O_3	40% ß-Si_3N_4
Si_3N_4-GN-10 additives	Alternate glass phase
Si_3N_4-8% La_2O_3	Alternate glass phase
Si_3N_4-3% Y_2O_3-4% La_2O_3-2% Al_2O_3	Alternate glass phase
Si_3N_4-3% AlN-2% Y_2O_3	a' - ß' Composite
Si_3N_4-6% AlN-4% Y_2O_3	a' - ß' Composite
Si_3N_4-10% AlN-6% Y_2O_3	a' - ß' Composite

Processing and Characterization of Transformation Toughened Ceramics with Strength Retention to Elevated Temperatures

R.A. Cutler and C. B. Brinkpeter (Ceramatec, Inc.),
A.V. Virkar and D.K. Shetty (University of Utah)

Objective/Scope

Previous work[1] has shown that it is possible to increase the strength of Al_2O_3-ZrO_2 ceramics by incorporating transformation-induced residual stresses in sintered specimens consisting of three layers. The outer layers contained Al_2O_3 and unstabilized ZrO_2, while the central layer contained Al_2O_3 and partially stabilized ZrO_2. When cooled from the sintering temperature, some of the zirconia in the outer layers transformed to the monoclinic form while zirconia in the central layer was retained in the tetragonal polymorph. The transformation of zirconia in the outer layers led to the establishment of surface compressive stresses and balancing tensile stresses in the bulk. In theory, the residual stress will not decrease with temperature until the monoclinic to tetragonal transformation temperature is reached since monoclinic and tetragonal ZrO_2 polymorphs have nearly the same coefficients of thermal expansion.

During the first two years of ORNL funding it was demonstrated that 1) three layer composites could be made with retention of compressive surface stresses to temperatures of 750°C[2,3]; 2) residual stresses could be detected by strength testing[2,3], strain gauge measurements[4], characterization of monoclinic content by x-ray diffraction[2], or indentation/strength measurements[5]; 3) the three layer composites have excellent damage resistance[5]; and 4) significant (300-400 MPa) residual compressive stress which is not transformation-induced can be introduced by grinding monolithic Al_2O_3-15 vol. % ZrO_2(3.0 mol. % Y_2O_3).

The objectives of the present two year subcontract are 1) to increase the use temperature of three-layer composites by substituting HfO_2 for ZrO_2, 2) develop aqueous and nonaqueous slip casting techniques for three layer composites in order to obtain better layer uniformity and to maximize residual compressive stress by optimizing the outer layer thickness, 3) superimpose temperature stresses on transformation-induced stresses in three layer composites, and 4) demonstrate improved thermal shock resistance and damage resistance in optimized composites.

Technical Progress

Thermal Shock Testing

Monolithic and "three-layer" Al_2O_3-15 vol. % ZrO_2 rods approximately 6.5 mm in diameter by 150 mm long were slip cast using a 35 vol. % solids loading in water. Solid cylinders

were cast instead of plates (which were subsequently cut into bars) in order to form a layer of high compressive stress over as much of the surface as possible. The "three-layer" rods consisted of an outer case of Al_2O_3-15 vol. % ZrO_2 and an inner core of Al_2O_3-15 vol. % ZrO_2(3 mol. % Y_2O_3). The outer layer thickness was controlled by the length of time the unstabilized zirconia slip was left in the mold. The green rods were air dried and then sintered at 1585°C for 30 minutes. They were subsequently HIPed at 1550°C for 30 minutes using 200 MPa applied Ar overpressure. The densified rods were cut into lengths of ≈45 mm and then surface ground circumferentially using a 1000 grit (≈10 μm) diamond wheel to obtain cylinders approximately 4.5 mm in diameter. The ground cylinders were testing in three-point bending using a span of 32 mm at a crosshead speed of 0.5 mm/minute. Samples were heated to various temperatures and held for 15 to 30 minutes before quenching in ice water (0°C).

The strength data are displayed in Table 1 and Figure 1 for monolithic outer, inner and "three-layer" rods. The "as-sintered" strengths were similar to those reported previously for bars in four-point bending. This is most likely due to the circumferential grinding in the case of rods and longitudinal grinding in the case of bars. The inner layer rods had a ΔT of slightly less than 300°C, the outer layer rods had a ΔT of ≈325 and the "three-layer" rods had a ΔT of ≈425. The exposed ends of the "three-layer" rods were the regions most susceptible to thermal shock and totally encapsulated rods would likely have resulted in a higher T for this material. Individual "three-layer" rods had strengths greater than 1200 MPa at temperatures up to 425°C. Since thermal shock under severe cooling conditions generally initiates from the outer surface of monolithic components, the increase in thermal shock resistance of the three-layer rods over the outer layer rods is of interest. This increase of 100°C can be compared with what would be expected for the strength improvement due to the surface compressive layer.

The compressive stress, σ_c, in the outer case and the balancing tensile stress, σ_t, in the inner core can be easily calculated assuming a square-wave stress distribution. These stresses are given by

$$\sigma_c = -(A_2/A)E\Delta\epsilon_o/(1-v) \quad (1)$$

and

$$\sigma_t = (A_1/A)E\Delta\epsilon_o/(1-v) \quad (2)$$

where A is the cross-sectional area of the rods, E is Young's modulus, $\Delta\epsilon_o$ is the unconstrained strain in the outer layer from the transformation of ZrO_2, v is Poisson's ratio and the subscripts 1 and 2 refer to the case and the core, respectively. The outer case thickness was approximately 0.375 mm or 1/12 the diameter of the rods. Taking values of 4.86×10^{-6} m^2, 1.10×10^{-5} m^2 and 1.59×10^{-5} m^2 for A_1, A_2, and A, respectively, E of 340 GPa, $\Delta\epsilon_o$ of 1.47×10^{-3}[3] and Poisson's ratio of 0.25 results in a compressive residual stress of -463 MPa in the case and a residual tensile stress of 204 MPa in the core. The calculated compressive stress is in fair

Table 1
Thermal Shock Data

ΔT (°C)[a]	Room Temperature Bend Strength (MPa) Outer[b]	Inner[c]	Three-Layer[d]
0	830±27	1185±109	1206±36
199	839	1167	1166
297	781	305	1303
343	178	104	---
400	145	73	953
424	---	---	694
454	---	---	354
502	---	---	6

a. Temperature change between sample temperature and 0°C quench temperature.
b. Monolithic Al_2O_3-15 vol. % ZrO_2.
c. Monolithic Al_2O_3-15 vol. % ZrO_2(3 mol. % Y_2O_3).
d. Outer layer 1/12 the diameter of the rod.

agreement with the increase in room temperature strength between the outer (830±27 MPa) and the "three-layer" (1206±36 MPa) rods of 376 MPa.

Based on the early work of Hasselman[6,7] it is possible to explain the improved thermal shock resistance of the Al_2O_3-

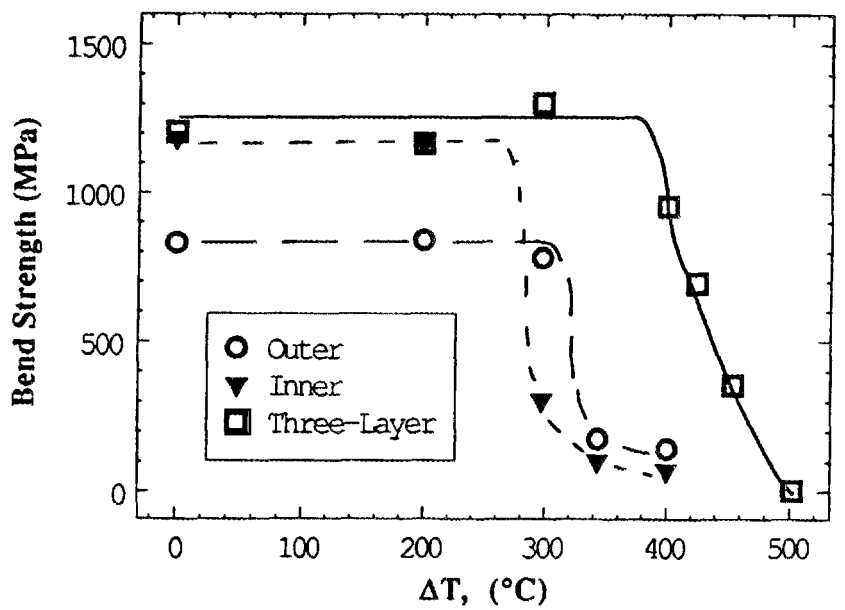

Figure 1. Thermal shock behavior of monolithic and "three-layer" Al_2O_3-15 vol. % ZrO_2 quenched in ice water. Layered rods with surface compressive stress of ≈400 MPa have critical ΔT 100°C higher than monolithic rods.

15 vol. % ZrO_2 ceramics having substantial compressive surface stresses as compared to the monolithic ceramics of similar composition, modulus and thermal expansion. The expected increase in ΔT, the critical temperature difference to which the rods are subjected in order to initiate crack growth and decrease strength, for a material with compressive residual stress is given by

$$\Delta T = \Delta T^{o} + [\sigma_c(1-v)/\alpha E]f(k/ha) \quad (3)$$

where ΔT^{o} is the temperature differential in the absence of residual stress given by $[\sigma_f(1-v)/\alpha E]f(k/ah)$ where σ_f is the unquenched strength, α is linear coefficient of thermal expansion, k is the thermal conductivity, h is the surface heat-transfer coefficient and a is the characteristic heat transfer length. The work of Becher et al.[8] investigating the effect of sample size on the thermal shock resistance of ceramics shows the need to take the Biot modulus (ah/k) into account in calculating ΔT. The Biot modulus was taken as 9 assuming h=10 $W/cm^2 °C$ and k=0.25 W/cm°C. This suggests that for the severe thermal shock conditions of ice water, as compared to boiling water, the effect of Biot modulus on ΔT for 4.5 mm diameter rods will be small[9] so that f(k/ha) will be near unity. Based on Equation (3), the predicted increase in ΔT for the "three-layer" rods is 123°C using the calculated compressive stress, or 100°C using the room temperature strength differential between outer and "three-layer" rods. It is seen from the experimental data ($\Delta T \approx 100°C$) that there is excellent agreement between the predicted and observed increase in thermal shock resistance for the "three-layer" material. The reason for the low values for ΔT (300-425°C) measured in the present study in contrast to the high values (ΔT > 800°C) reported by Becher[10] for monolithic Al_2O_3-ZrO_2 composites is believed to be due to the more vigorous quench of the ice water as compared to boiling water and to the difference in sample thickness between the two studies.

The improved thermal shock resistance of the three-layer composites agrees with predictions based on compressive surface stress of ≈400 MPa. These results show that residual compressive stress of substantial depth in layered composites not only increases strength, apparent toughness and damage resistance, but also makes the materials more resistant to thermal shock.

Indentation/Strength Testing

Indentation/strength testing of slip cast monolithic and three-layer Al_2O_3-15 vol. % ZrO_2 was performed in order to determine their response in comparison to the dry pressed bars tested previously[5]. The main differences between the dry pressed and the slip cast bars were the improved strength of all three slip cast materials and the increased uniformity of the outer layer thickness in the three-layer slip cast bars[11]. In addition, the thickness of the outer layers of slip cast three-layer bars was ≈250 μm in comparison to dry pressed bars with outer layer thickness of ≈375 μm.

A standard (136°) Vickers indenter was adapted to a universal testing machine and the bars were indented at a constant crosshead speed (0.05 mm/min) to the selected maximum load, held 10 seconds, and unloaded. A drop of dry mineral oil was placed at the site of the indentation before loading to minimize postindenation subcritical crack growth from moisture. Strengths of the indented specimens were assessed in four-point bending (40 mm support span and 20 mm loading span). Fractography was used to verify that the fracture had initiated from the indent. Five to seven bars of each composition (monolithic outer, monolithic inner, and three-layer) were indented at loads of 16, 37, 64, 126, 297 and 1000 N.

The indentation response of the slip cast materials are shown in Figures 2 and 3. Based on superposition of stress it can be easily shown[5] that the fracture strength, σ_f, expected for three-layer composites which have been indented at load P is given by

$$\sigma_f = \frac{CK_{Ic}^{4/3}}{(E/H)^{1/6}P^{1/3}} + \frac{\Delta\epsilon_o E d_2}{(1-v)d} \qquad (4)$$

where C is a constant equal to 2.02[5], K_{Ic} is fracture toughness, $\Delta\epsilon_o$ is the unconstrained strain in the outer layers from the transformation of ZrO_2, E is Young's modulus, d_2 is the inner layer thickness, H is hardness, v is Poisson's ratio and d is the thickness of the bar. According to Equation (4), a plot of σ_f vs $P^{-1/3}$ should yield a straight line with a slope related to K_{Ic} and an intercept giving the compressive residual stress, σ_c. Taking values of E=340 GPa, H=17 GPa, linear regression of the data for monolithic specimens gave slopes corresponding to K_{Ic} values of 5.35 and 5.03 $MPa \cdot m^{1/2}$ for outer and inner materials, respectively. Both materials had intercepts near zero, showing that they were free of residual stress (see Figure 2). A linear regression of the data for the three-layer composites gave a slope corresponding to a fracture toughness of 5.75 $MPa \cdot m^{1/2}$, similar to the monolithic materials, as predicted previously[5]. It is interesting to note, however, that there was very little decrease in strength at high indentation loads (greater than 125 N) suggesting that the three-layer material has even better damage resistance than predicted by Equation (4). The intercept from the linear regression gave a value of 588 MPa for the compressive stress. This value of σ_c is higher than the difference in strength of 497 MPa when comparing the unindented bars (see Figure 3). These data confirm the superior damage resistance of materials made using the three-layer concept and show that improved resistance to contact damage can be expected for ceramic components made using this technique.

Indentation/strength measurements demonstrated the excellent damage tolerance of three-layer Al_2O_3-15 vol. % ZrO_2 composites. In order to show the practical extension of this technology, totally encapsulated ≈5 mm diameter rods were fabricated by slip casting such that pits on the order of 50-

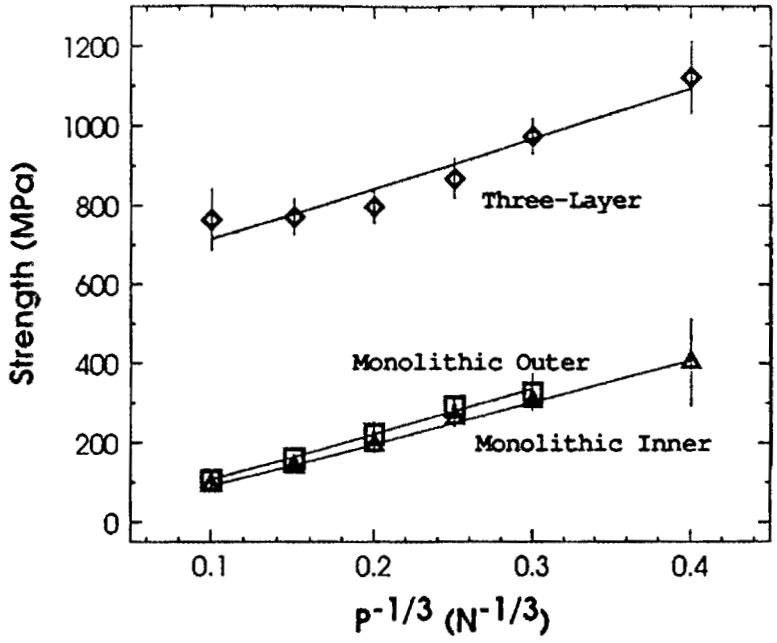

Figure 2. Fracture stress (σ_f) versus inverse cube root load ($P^{-1/3}$) plots for the slip cast three-layer and monolithic ceramics.

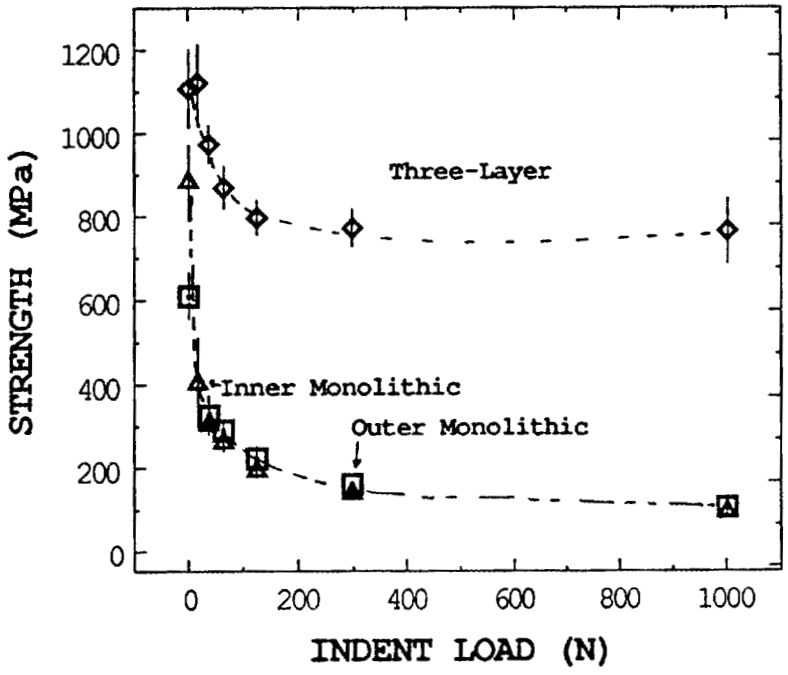

Figure 3. Indentation load dependence of fracture stress for the slip cast three-layer and the monolithic ceramics.

250 μm were prevalent on the surface but were rarely present in the bulk. The outer layer of the rods was ≈425 μm thick and surface compressive stress was on the order of 400 MPa. The strength (5 rods broken in 4-point bending using an inner span of 20 mm and an outer span of 40 mm) of the "as-HIPed" material was 908±116 MPa, as compared to strength of 1,211 ±123 MPa for three-layer rods which were ground to a 30μm surface finish. In contrast, monolithic outer layer rods had strength of 476±84 MPa in the "as-HIPed" state and 830±27 MPa in the ground state. The change in strength between the "three-layer" and "monolithic outer layer" materials was improved at larger flaw sizes. This means that as long as the outer layer thickness of the "three-layer" composite is sufficiently larger than the surface flaws, that strength improvement consistent with the indentation/strength data can be expected in components. In order to further explore the use of three-layer composites, monolithic and three-layer composite cam followers are being fabricated for automotive tests.

X-ray Measurement of Compressive Stress

Previously, it was shown that substantial compressive stress could be introduced into Al_2O_3-15 vol. % ZrO_2 ceramics during grinding[12]. Research by Johnson-Walls, et al.[13] suggested that the depth of compressive layer associated with the machined surface in Si_3N_4 was ≈10 μm. Dry pressed samples of Al_2O_3-15vol. % ZrO_2, Al_2O_3, and ZrO_2 (see Table 2) were sent to Dr. David Marshall at Rockwell International for surface stress analysis using x-rays[13]. Dr. Michael R. James performed the CuKα x-ray analysis using (416) and (620) planes for Al_2O_3 and ZrO_2, respectively. When using CrKα radiation, (1.1.10) and (331) planes were used for Al_2O_3 and ZrO_2, respectively. In Al_2O_3, the respective penetration depths for Cu and Cr radiation are 32 and 10 μm (i.e., 67% of the diffracted radiation comes from a depth less than these values (87 and 27 μm for 95% return)). Thus, the difference in residual stress between the two radiations represents the gradient of residual stress with depth. The penetration depths are slightly less for ZrO_2 (or ZrO_2 containing materials) since Zr is approximately three times more absorbent than Al.

The measured compressive residual stresses are shown in Table 3. Surprisingly, the inner monolithic material which showed a large strength increase with grinding, despite no observable transformation, also showed low residual stress and low dependence of residual stress on depth of penetration. Further work is needed to explain the significant strengthening which occurs upon grinding the inner layer material. The outer layer and three-layer (the outer layer of the three-layer sample was the surface exposed to radiation) materials showed significantly higher residual stresses at shallower penetration and were strongly influenced by grinding. The 98 MPa compressive stress for Al_2O_3 using CrKα

Table 2
Strength and % Monoclinic ZrO_2 of Samples
for XRD Stress Analysis

Composition	% m-ZrO_2 s[1]	g[2]	f[3]	Strength (MPa) unground[4]	ground[5]
Al_2O_3-15^V/oZrO_2(3 mol.%Y_2O_3)	<1	<1	<1	485±34	926±78
Al_2O_3-15^V/oZrO_2	83.1	85.6	88.5	389±23	650±59
Three-layer Al_2O_3-15^V/oZrO_2	--[6]	--	--	679±56	879±51
ZrO_2(3 mol. % Y_2O_3)	<1	1.9	24.8	677±63	998±73
Al_2O_3	--	--	--	308±30	434±64

1. Sintered surface.
2. Ground surface.
3. Fractured surface.
4. Chamfered by hand before HIPing with no other grinding.
5. Machine ground (220 grit wheel at a down feed of 2.5 μm/pass before spark out) after HIPing.
6. Not determined.

radiation compares with 125-145 MPa as reported by Lange, et al.[14]. ZrO_2(3 mol. % Y_2O_3) showed a strong dependence of residual stress on depth, with residual stress which correlated well with the observed strength increase. There was no overall correlation of compressive stress with strength increase for the materials tested. The residual stress difference between three-layer and outer layer Al_2O_3-ZrO_2 as determined by x-ray diffraction and strength measurements were both on the order of 300 MPa, verifying the substantial residual stress created by the stress-induced transformation in the three-layer composites.

Substitution of HfO_2 for ZrO_2

The monoclinic --> tetragonal transformation temperature is significantly increased for HfO_2 as compared to ZrO_2. A solid solution of HfO_2·50 mol. % ZrO_2 was made by milling and subsequently calcining unstabilized powders at 1700°C. The calcined powder was x-rayed (to make sure that a solid solution had formed) and reground before mixing with Al_2O_3 to make a Al_2O_3-15 vol. % HfO_2·ZrO_2. This powder was used as the

Table 3
Residual Stress Determined at Rockwell International
by X-ray Analysis

Composition	Residual Stress (MPa) CuKα Radiation unground	ground	CrKα Radiation unground	ground
Al_2O_3-15^V/oZrO_2(3 mol.%Y_2O_3)	-131	-203	-173	-261
Al_2O_3-15^V/oZrO_2	-131	-256	-267	-822
Three-layer	-486	-711	-570	-1106
ZrO_2(3 mol. % Y_2O_3)	-44	-15	-81	-271
Al_2O_3	-136	-135	-101	-199

outer layers to make a three-layer composite with the inner layer composition being Al_2O_3-15 vol. % ZrO_2(3 mol. % Y_2O_3). The room temperature strength of the composite was 947±164 MPa (5 bars). The strength at 1000°C was 523±23 MPa. This strength is not improved over the 577±48 MPa strength measured at 1000°C for three-layer Al_2O_3-15 vol. % ZrO_2 composites. While the concept of improving the high temperature strength of three-layer Al_2O_3-ZrO_2 composites by substituting HfO_2 for ZrO_2 is sound, improved HfO_2 or $HfO_2 \cdot ZrO_2$ powders will be required before this concept is realized in practice.

Reproducibility and Reliability

The reproducibility of making high strength three-layer composites strengthened by both transformation-induced and temperature-induced stresses[15] was demonstrated. Room temperature strength tests on three-layer composites with outer layers of Al_2O_3-15 vol. % ZrO_2 and an inner layer of ZrO_2(3 mol. % Y_2O_3)-40 vol. % Al_2O_3 resulted in strength of 1,257±74 MPa (16 bars) in comparison to the value of 1,244±103 (7 bars) reported previously[7]. The Weibull modulus of the most recent three-layer composites was 20.1 (see Figure 4), indicating the high reliability predicted for composites with compressive surface stresses[2,3].

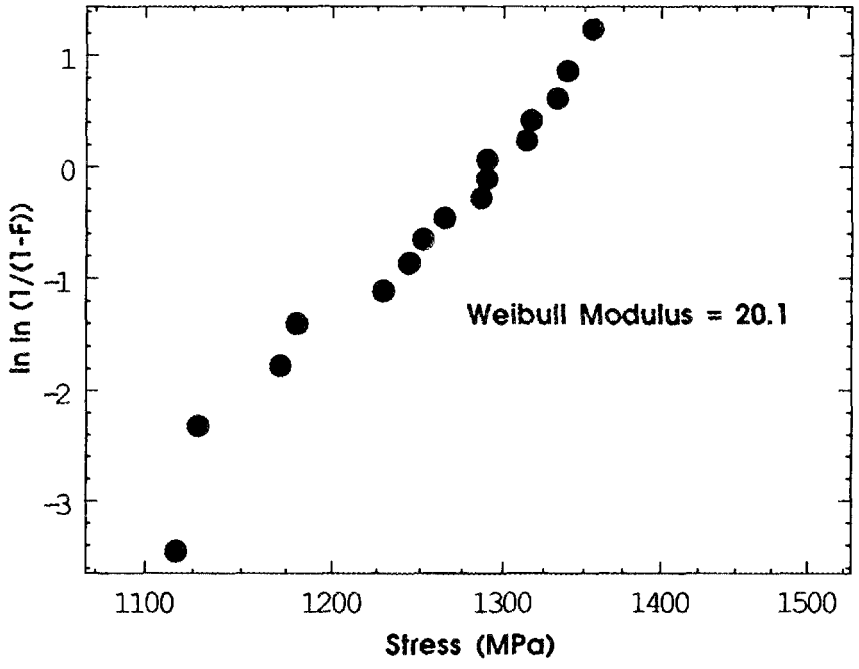

Figure 4. Weibull plot of ln ln (1/(1-F)), where F is the probability of failure, as a function of ln fracture stress for three-layer composites with temperature and transformation-induced stresses. The outer layers of the three-layer composites consist of Al_2O_3-15 vol. % ZrO_2 and the inner layer is ZrO_2(3 mol. % Y_2O_3)-40 vol. % Al_2O_3.

Status of Milestones

All milestones are on schedule.

Publications

A manuscript entitled "Transformation-Toughened Ceramics with Strength Retention to High Temperatures" by R. A. Cutler, C. B. Brinkpeter, S. L. Bruner, D. W. Prouse, A. V. Virkar and D. K. Shetty was submitted to SAE for their Proceedings of the 1989 Twenty-Seventh Automotive Technology Development Contractors' Coordination Meeting held October 23-26, 1989 in Dearborn, MI.

References

1. A. V. Virkar, J. L. Huang, and R. A. Cutler, "Strengthening of Oxide Ceramics by Transformation Induced Stresses," J. Am. Ceram. Soc., 70 [3] 164-170 (1987).

2. R. A. Cutler, J. J. Hansen, A. V. Virkar, D. K. Shetty, and R. C. Winterton, "Strength Improvement in Transformation Toughened Ceramics using Compressive Residual Surface Stresses," Advanced Structural Ceramics Vol. 78, ed. by P.F. Becher, M. V. Swain, and S. Somiya (Materials Research Society, Pittsburgh, PA, 155-163, 1987).

3. R. A. Cutler, J. D. Bright, A. V. Virkar, and D. K. Shetty, "Strength Improvement in Transformation-Toughened Alumina by Selective Phase Transformation," J. Am. Ceram. Soc., 70 [10] 714-18 (1987).

4. A. V. Virkar, J. F. Jue, J. J. Hansen and R. A. Cutler, "Measurement of Residual Stresses in Oxide-ZrO_2 Three-Layer Composites," J. Am. Ceram. Soc., 71[3] C-148-C-151 (1988).

5. J. J. Hansen, R. A. Cutler, D. K. Shetty and A. V. Virkar, "Indentation Fracture Response and Damage Resistance of Al_2O_3-ZrO_2 Composites Strengthened by Transformation-Induced Residual Stresses" J. Am. Ceram. Soc., 71[12] C-501-C-505 (1988).

6. D. P. H. Hasselman, "Unified Theory of Thermal Shock Fracture Initiation and Crack Propagation in Brittle Ceramics," J. Am. Ceram. Soc., 52[11] 600-04 (1969).

7. D. P. H. Hasselman, "Figures of Merit for the Thermal Stress Resistance of High-Temperature Brittle Materials," Ceramurgia Int. 4[4] 147-50 (1978).

8. P. F. Becher, D. Lewis, K. R. Carman and A. C. Gonzalez, "Thermal Shock Resistance of Ceramics: Size and Geometry Effects in Quench Tests," Am. Ceram. Soc. Bull., 59[5] 542-48 (1980).

9. P. F. Becher, "Effect of Water Bath Temperature on the Thermal Shock of Al_2O_3," J. Am. Ceram. Soc., 64[1] C-17-C-18 (1981).

10. P. F. Becher, "Transient Thermal Stress Behavior in ZrO_2-Toughened Al_2O_3," J. Am. Ceram. Soc., 64[1] 37-39 (1981).References

11. R. A. Cutler, C. B. Brinkpeter, S. L. Bruner, D. W. Prouse, A. V. Virkar and D. K. Shetty, "Processing and Characterization of Transformation Toughened Ceramics with Strength Retention to Elevated Temperatures," Bimonthly ORNL/CF-89/307 pp. 135-142 (ORNL, Oak Ridge, TN 1989).

12. R. A. Cutler, S. L. Bruner, D. W. Prouse, A. V. Virkar and D. K. Shetty, "Processing and Characterization of Transformation Toughened Ceramics with Strength Retention to Elevated Temperatures," Semiannual ORNL/TM-11116 pp. 118-124 (ORNL, Oak Ridge, TN 1988).

13. D. Johnson-Walls, A. G. Evans, D. B. Marshall and M. R. James, Residual Stresses in Machined Ceramic Surfaces," J. Am. Ceram. Soc., 69[1] 44-47 (1986).

14. F. F. Lange, M. R. James, and D. J. Green, "Determination of Residual Surface Stresses Caused by Grinding in Polycrystalline Al_2O_3," J. Am. Ceram. Soc., 66[2] C-16-C-17 (1983).

15. R. A. Cutler, C. B. Brinkpeter, S. L. Bruner, D. W. Prouse, A. V. Virkar and D. K. Shetty, "Processing and Characterization of Transformation Toughened Ceramics with Strength Retention to Elevated Temperatures," Bimonthly ORNL/CF-89/252 pp. 151-154 (ORNL, Oak Ridge, TN 1989).

1.2.4 Silicate Matrix

Low Expansion Ceramics for Diesel Engine Applications (VPI)
D.A.Hirschfeld and J.J.Brown (Center for Advanced Ceramic Materials
Virginia Polytechnic Institute and State University)

Objective/Scope

Optimize the chemistry, properties, and processing of selected low thermal expansion compositions based on the zircon (NZP) and the ß-eucryptite-$AlPO_4$ systems. The major long-term goal is to develop an economical, isotropic, ultra-low thermal expansion ceramic material capable of having stable properties above 1200°C.

Technical Highlights

Zircon (NZP) System

To produce NZP materials having higher density, techniques to synthesize more reactive powders were investigated. Sol-gel processes were developed to make $(Ca,Mg)Zr_4(PO_4)_6$, $(Ca,Ba)Zr_4(PO_4)_6$ (CBZP), and $(Rb,Cs)Zr_4(PO_4)_6$ (RCZP). Utilizing the sol-gel method, powders having a particle size as small as 20 nm were produced yielding compacts with densities 94% theoretical after cold pressing and sintering. Two different sol-gel processes were used to make $(Ca,Mg)Zr_4(PO_4)_6$ with the starting materials $Ca(NO_3)_2$, $Mg(NO_3)_2$, $ZrO(NO_3)_2$, and $NH_4H_2PO_4$.

In Process 1, zirconium solution is first added to a selected stoichiometric mix of calcium and magnesium nitrate, then phosphate solution is added drop by drop. The solutions are stirred constantly throughout the entire process. NH_4OH is then added to adjust the pH to 8-9, forming a homogeneous gel. The gel is stir dried at 40-60°C, oven dried at 110°C, and heat treated to form an ultra-fine $(Ca,Mg)Zr_4(PO_4)_6$ powder. In Process 2, the three nitrates are mixed. Then while constantly stirring the mixture, the hydroxide and phosphate are added alternately drop by drop, maintaining a pH of 7. This solution is heated at 60-80°C, forming a dry-gel, then heat treated at 600-700°C, forming a fine $(Ca,Mg)Zr_4(PO_4)_6$ powder. The technique used to make CBZP and RCZP is similar to Process 1.

The thermal stability, thermal expansion, and thermal conductivity of $CaZr_4(PO_4)_6$ and its limited solid solution with $MgZr_4(PO_4)_6$ were investigated. Samples for testing were prepared by either solid-state reaction or a sol-gel method (Process 1).

The thermal stability of $(Ca,Mg)Zr_4(PO_4)_6$ was examined by heating samples for long periods of time in air at high temperatures. Powder samples prepared by solid-state reaction were heated in Pt crucibles for 45 h at 1450°C. X-ray diffraction (XRD) analysis of the heated samples revealed that the $MgZr_4(PO_4)_6$ decomposed almost entirely into $Zr_2P_2O_9$ when heated at temperatures above 1100°C. These results were consistent with the significant weight loss observed and confirmed in recently published literature.[1] Samples with compositions that contained Mg in amounts greater than 50 mole% exhibited similar decompositions. However, as the Ca concentration increased, the formation of $Zr_2P_2O_9$ decreased. For samples with greater than 50 mole% Ca, XRD patterns showed little or no $Zr_2P_2O_9$ formation, indicating stable compositions up to 1450°C. A weight loss analysis of samples with greater Ca concentrations will be investigated in the future.

To better understand the axial expansion characteristics of compositions in the $CaZr_4(PO_4)_6$-$MgZr_4(PO_4)_6$ system, high temperature XRD was used to determine lattice parameter fluctuations upon heating. Powder samples were made by solid-state reaction methods. The compositions $CaZr_4(PO_4)_6$, $(Ca_{0.8},Mg_{0.2})Zr_4(PO_4)_6$, and $(Ca_{0.7},Mg_{0.3})Zr_4(PO_4)_6$ were selected for analysis. Samples were mixed with a pure Pt powder (for use as an internal standard) and scanned with a Scintag θ–θ fully-automated diffractometer equipped with a hot stage. Each sample was scanned over the 2θ range of 10° to 80°, allowing the collection of approximately 60 peaks per run. Six runs/scans were conducted for each sample at room temperature, 250°C, 500°C, 750°C, and 1000°C. Diffraction data for each run were stored on the Scintag's micro-vax system for data analysis. Diffraction patterns for all samples appeared to be structurally similar to that of the $CaZr_4(PO_4)_6$ end member. Thus, all of the patterns were refined based on this end member crystal structure which is characterized by the space group $R\bar{3}C$. Corrections for background, internal standard, and asymmetric peak shapes were performed. Samples were indexed relative to a hexagonal basis to yield **a** and **c** parameters.

The results of the high temperature diffraction analyses are shown in Figure 1. The **a** and **c** expansion behavior is anisotropic upon heating. The **c** parameter expands while the **a** parameter contracts. This behavior is consistent with many other NZP-type materials as well as with a structural model depicting NZP thermal expansion devised by Lenain.[2] It is important to note that as the concentration of Mg increases the anisotropy decreases. The **c** parameter expands less and the **a** parameter contracts somewhat less, which should improve the thermal shock resistance of the materials. For compositions

with Mg concentrations greater than 30 mole%, it is expected that the anisotropy will decrease further. Such samples will be examined in the near future. It should be noted that the room temperature lattice parameters determined for $CaZr_4(PO_4)_6$ were in excellent agreement with those of its NBS card.

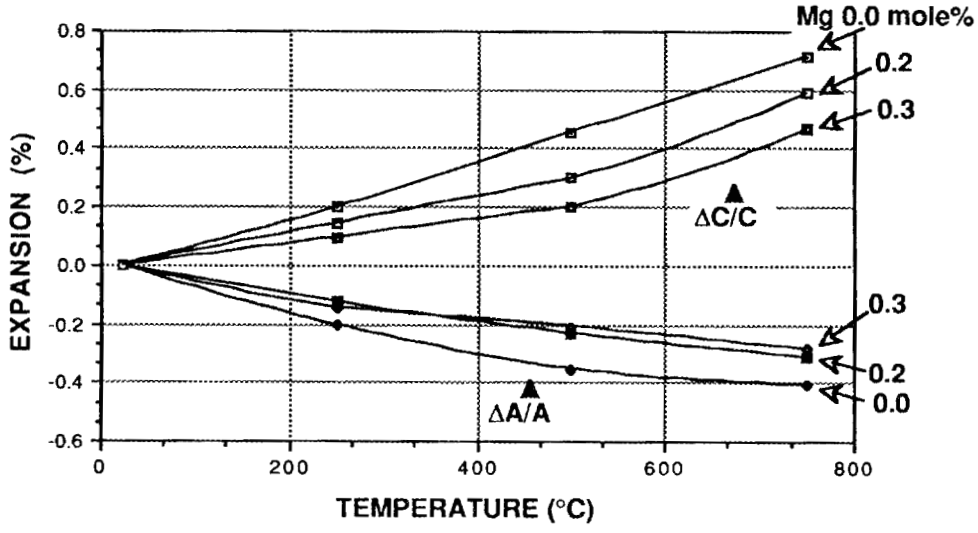

Figure 1. Axial expansion of $(Ca_{1-x},Mg_x)Zr_4(PO_4)_6$

Axial expansion was plotted as a function of temperature for both the **a** and **c** parameters. From this data, average axial thermal expansion values were determined for each composition, and used to compute the bulk coefficient of thermal expansion (CTE) values shown in Table 1.

Table 1. Calculated bulk CTE values for $(Ca_{1-x},Mg_x)Zr_4(PO_4)_6$ samples

Composition	CTE ($\times 10^{-7}$/°C)
$CaZr_4(PO_4)_6$	-4.4
$(Ca_{0.8},Mg_{0.2})Zr_4(PO_4)_6$	-0.74
$(Ca_{0.7},Mg_{0.3})Zr_4(PO_4)_6$	-4.46

The thermal conductivity of samples with composition $(Ca_{1-x},Mg_x)Zr_4(PO_4)_6$ where x= 0.2 and 0.5 was investigated using a laser flash thermal diffusivity apparatus and a differential scanning calorimeter (DSC) at the HTML facility, Oak Ridge National Laboratory. Thermal conductivity was determined by the product of the thermal diffusivity, specific heat, and bulk density of each sample. Samples were made by sol-gel Process 1.

Multiple DSC runs were made to determine the heat capacity of compositions where x = 0.0, 0.1, 0.2, 0.3, 0.4, and 0.5. Samples were evaluated relative to an empty Pt pan and the system was calibrated with a sapphire standard. Because the variation in specific heat values between each NZP composition was not significant, the combined mean values of specific heat from all compositions are shown in Figure 2. It is believed that the specific heat values presented are representative of the range of compositions being studied.

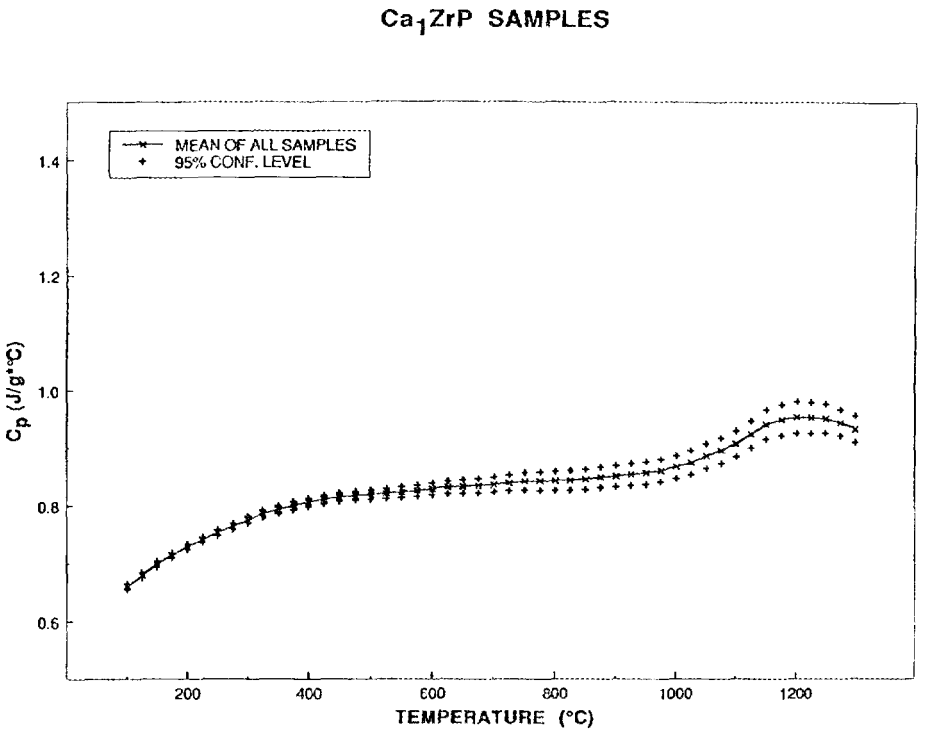

Figure 2. Specific heat of $(Ca_{1-x},Mg_x)Zr_4(PO_4)_6$ as a function of temperature

Thermal diffusivity was determined for samples where x = 0.2 and 0.5. Acceptable values of thermal diffusivity at temperatures below 600°C were difficult to obtain, likely owing to the very low thermal diffusivity of the samples and the resultant nonlinear heat flow. Measured bulk densities of the samples were approximately 80% theoretical.

The thermal conductivities of the two samples, plotted in Figure 3, are very low at temperatures around 1000°C. As the Mg concentration increases, the thermal conductivity becomes lower. Low thermal conductivity coupled with low thermal expansion suggest that these compositions are resistant to thermal shock. The thermal conductivity of these compositions is noticeably lower than those of ZrO_2, a common thermal barrier material. More samples are currently being evaluated and the effects of composition and density on thermal conductivity will be further established.

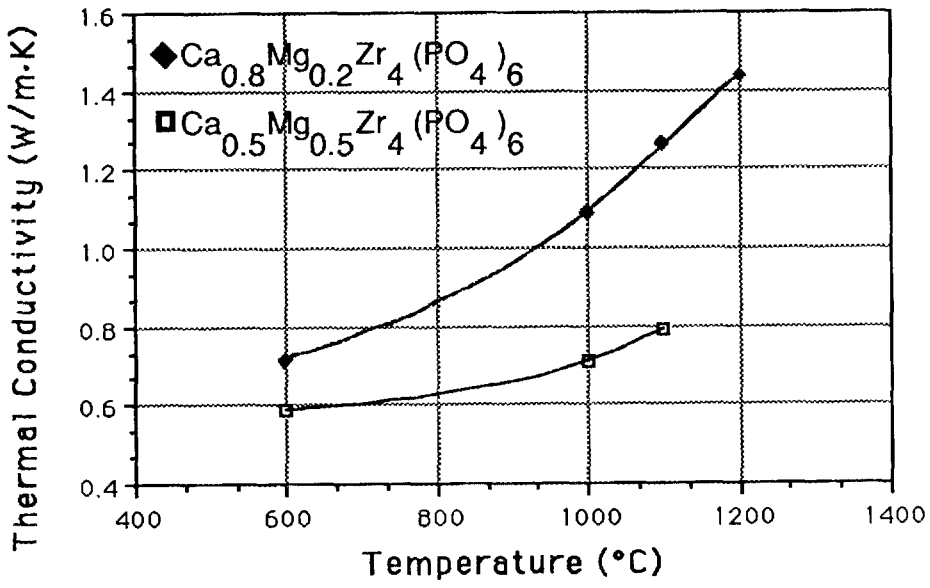

Figure 3. Thermal conductivities of $(Ca,Mg)Zr_4(PO_4)_6$ compositions

For RCZP, it was shown previously that the thermal expansion (measured using a Netzsch dual-rod differential dilatometer) was non-linear with increasing temperature. The effect of the sintering process on this non-linearity was studied by controlling the heating and cooling rates of the compositions $(Rb_{1-x},Cs_x)Zr_2(PO_4)_3$ (x = 0.0-1.0 by 0.1 increments). It was found that the non-linear expansion is not affected by rapid heating or cooling. No direct correlation between the grain size and the non-linear expansion was observed for samples prepared by the sol-gel processes.

During the past six months, the high temperature phase stability of RCZP was examined. The effect of long term, high temperature heat treatments on compositions $(Rb_{1-x},Cs_x)Zr_2(PO_4)_3$ (x = 0.0 to 1.0 by 0.1 increments) was studied after heating samples at 1000°C for 2 h, at 1200°C for 3 d, and finally at 1250°C

for 4 d. After the heat treatments, the samples were examined using XRD. The compositions where x = 0.4, 0.9, and 1.0 showed considerable instability, which was manifested by the presence of either $Zr_2P_2O_9$ or an unidentified phase. The remaining compositions showed no decomposition, but contained secondary phases ZrO_2 and ZrP_2O_7. Other samples heat treated at 1000°C for 3 h and then at 1200°C for 72 h showed no signs of decomposition, indicating that heating at 1250°C caused decomposition in samples where x = 0.4, 0.9, 1.0. The mechanism for the decomposition is still under study.

The phase stability of the RCZP system was also studied using a weight loss scheme in which samples were weighed after each repeated heating period. Compositions $(Rb_{1-x},Cs_x)Zr_2(PO_4)_3$ (x = 0.0, 0.5, 1.0) were tested. The heat treatment schedule consisted of a 3-h period at 1000°C followed by ten 4-h periods at 1250°C. Sample weight and XRD data were obtained after each heating period to determine the weight loss and phase change as functions of heating time. The Rb composition (x = 0.0) exhibited better stability than Cs-containing samples with a weight retention of 94.74%. The Cs-containing compositions exhibited weight retention of approximately 91%. Further investigations of weight loss at various temperatures are in progress.

Ceramic Composites

To reduce the porosity of ceramic composites based on the NZP system, a matrix of single phase $(Ca_{0.6},Mg_{0.4})Zr_4(PO_4)_6$ (CMZP) was prepared using sol-gel Process 1. The amorphous CMZP formed had a mean particle size of 20 nm. After calcining the amorphous powder, a single phase crystalline CMZP was obtained which is stable to 1500°C. To quantify the porosity present, it was necessary to determine the theoretical density. The calculated theoretical densities of CMZP and CBZP were 3.177 g/cm^3 and 3.264 g/cm^3, respectively, based on the theoretical density of $CaZr_4(PO_4)_6$ (3.20 g/cm^3) calculated by Limaye et al.[3]

The effects of sintering temperature and time on the thermal expansion behavior and microstructure of CMZP were investigated. As illustrated in Figure 4, with an increase in sintering temperature, the thermal expansion of CMZP changed from positive to negative. As the sintering temperature increases, the grain size of CMZP increases and the relationship between grain size and bulk CTE of CMZP is illustrated in Figure 5. By increasing the sintering temperature from 1150°C to 1300°C (sintering time = 24 h), the grain size increased from 2 μm to 30 μm and the CTE changed from a positive value (33.4×10^{-7}/°C) to a negative value (-21.1×10^{-7}/°C). Similarly, as shown in Figure 6, an increase in grain size was observed with the longer sintering time (sintering temperature = 1235°C) while the CTE decreased indicating that near zero CTE may be achieved with a sintering time of 75 h.

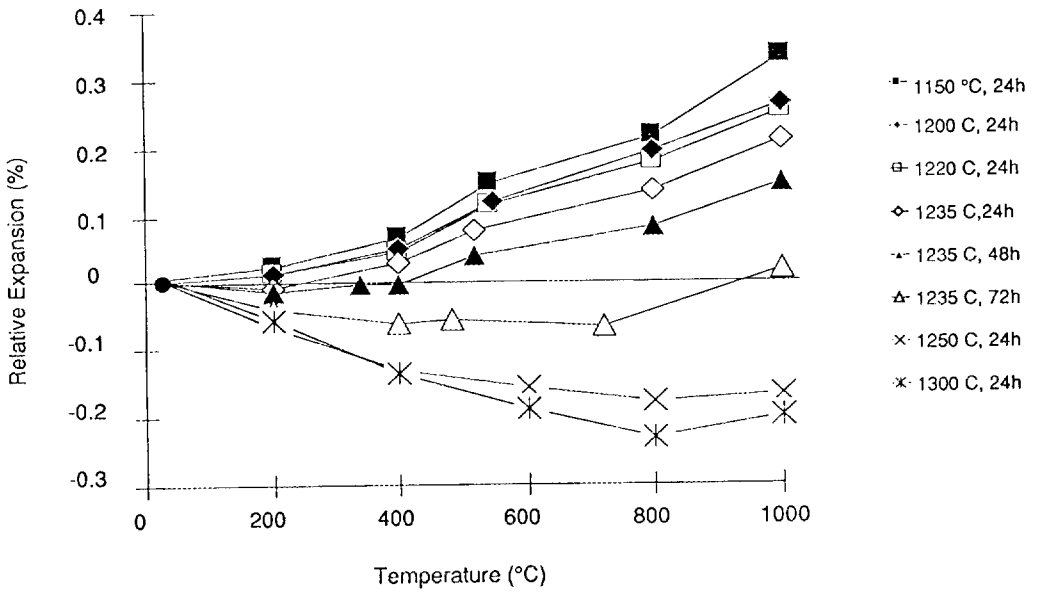

Figure 4. Expansion of CMZP as a function of sintering temperature and time

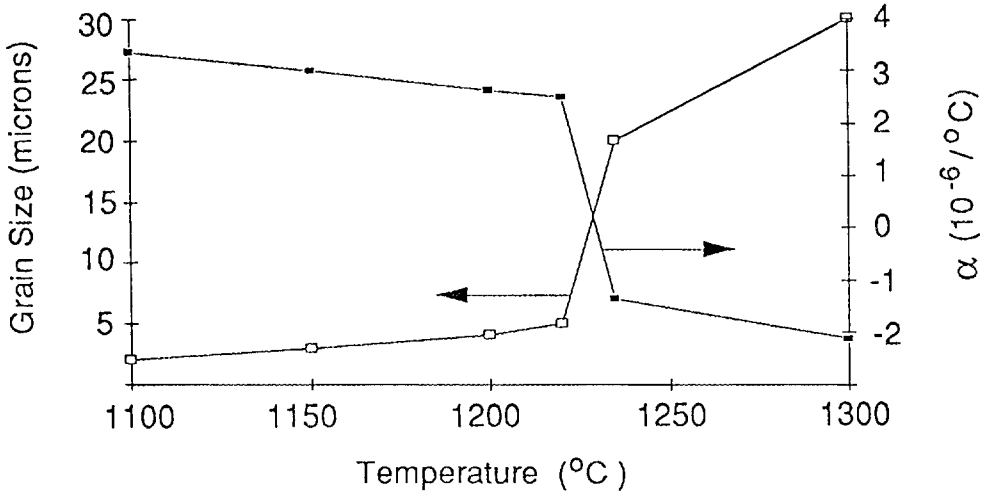

Figure 5. Effect of sintering temperature on grain size and CTE of CMZP

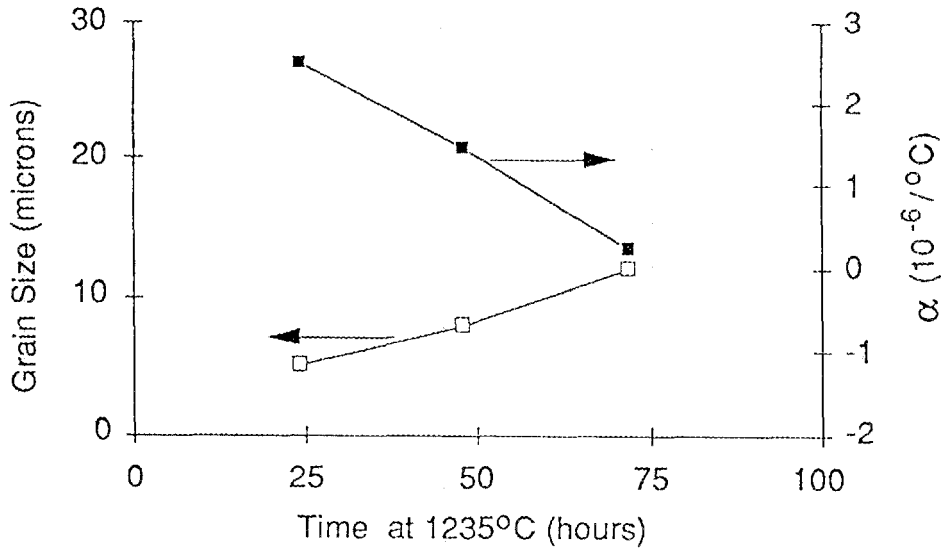

Figure 6. Effect of sintering time on grain size of CMZP

The observed relationship between sintering conditions and CTE can be explained through changes in the microstructure. When sintered at relatively low temperatures, the grain size of CMZP is smaller than a critical size[4] (G_{cr}) and microcracking does not occur during cooling. The bulk CTE of CMZP reflects mainly the contributions of the **c** axis expansion and results in a positive bulk thermal expansion. As sintering temperature increases, the grain size becomes larger. Once the grain size is equal to or larger than G_{cr}, microcracks form in the bulk during cooling. Because the compressive strength of a ceramic is much greater than the tensile strength, the microcracks are prone to form on the grain boundaries perpendicular to **c**-axis. Upon reheating, the CMZP contracts along **a**-axis, and the expansion along **c**-axis is absorbed by the microcracks, resulting in an overall negative thermal expansion. As soon as the microcracks are closed by the expansion along **c**-axis, the negative thermal expansion will change into positive expansion.

In Figure 7, SEM micrographs of CMZP show the change in grain size with sintering time and temperature. Microcracking due to excessive grain growth at high sintering temperatures is also observed. Examination of the grain boundaries by transmission electron microscopy (TEM) revealed only small amounts of amorphous phase present in specimens having a small grain size ($< G_{cr}$).

a)

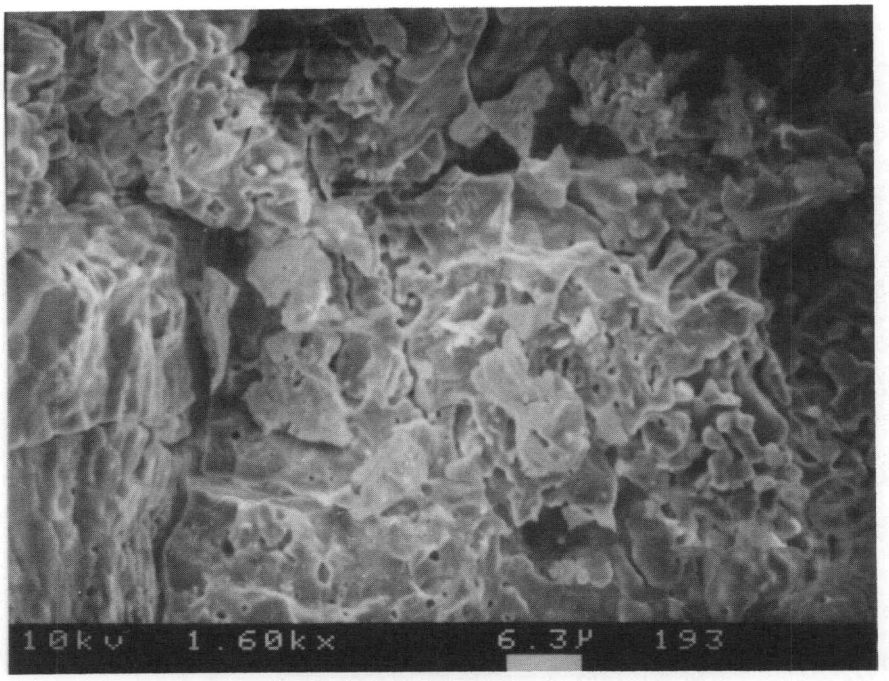

b)

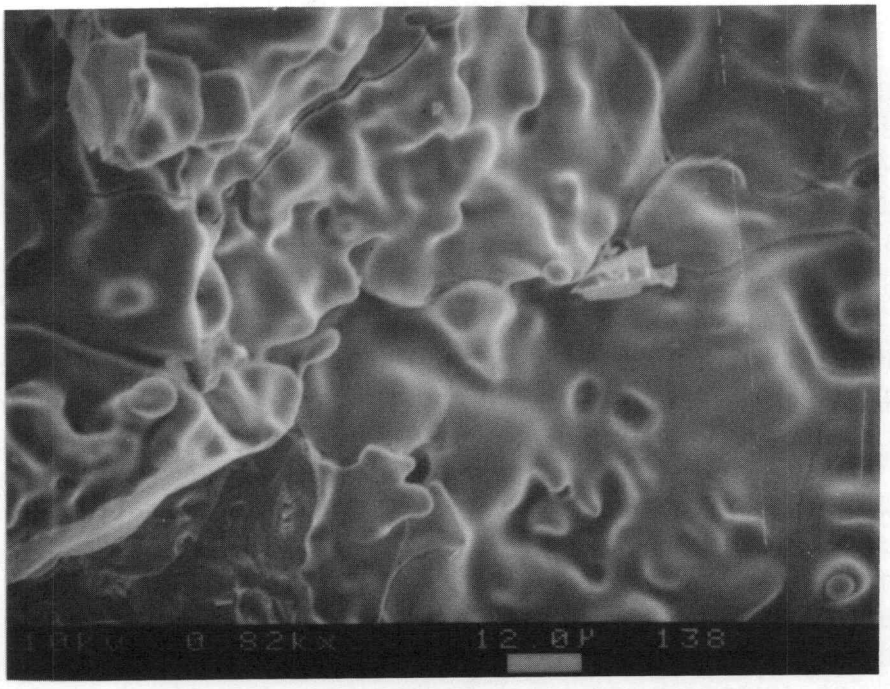

Figure 7. Micrographs of CMZP sintered at:
a) 1235°C for 24 h
b) 1300°C for 24 h

The effects of aging heat treatments on the bulk CTE of CMZP were examined, and the data in Table 2 indicate that: (1) aging generally lowers the bulk CTE; (2) a double aging treatment (900°C and 1200°C for 100 h) affects the CTE more than a single treatment (900°C for 100 h); and (3) the sample sintered at 1235°C for 72 h is unaffected by aging. It is also noted that the hot pressed (HP) sample exhibited a significant increase in expansion hysteresis after the double aging treatment. Examinations of the specimens using SEM and TEM reveal a slight increase in grain size and either the formation or the growth of microcracks at grain boundaries after aging treatments. It is noted that the effects of heat aging on microstructure and bulk thermal expansion behavior in the 1235°C, 72 h sample were significantly less than in other samples, suggesting a saturation in the number and size of microcracks with the particular heat treatment.

Table 2. Effect of aging on bulk CTE of CMZP

Sample Preparation Conditions (temp, time)	Average CTE (30-1000°C) ($\times 10^{-7}$/°C)		
	No Aging	900°C 100h	+1200°C 100h
1150°C, 24 h	30.2	28.4	7.8
1200°C, 24 h	27.0	25.1	11.9
1220°C, 24 h	26.2	20.0	8.4
1235°C, 24 h	21.8	19.0	7.4
1235°C, 72 h	1.0	-1.0	-0.6
1250°C, 24 h	-16.7	-13.7	-18.7
1300°C, 24 h	-21.6	-23.5	-32.4
1200°C, HP	32.7	29.0	21.4

The processing techniques developed for monolithic CMZP were applied to composites of CMZP and chopped NICALON-SiC fibers. The bulk CTE of a hot-pressed CMZP composite containing 5 vol % fibers was 33.7 x 10^{-7}/°C, near that of hot-pressed monolithic CMZP (see Table 2). However, following a heat aging treatment at 1235°C for 72 h, the CTE of the hot-pressed CMZP composite was -0.9 x 10^{-7}/°C. An investigation of the effect of heat aging on the CTE of fiber-reinforced composites is underway.

As an additional study, $(Ca_{0.8},Ba_{0.2})Zr_4(PO_4)_6$ ceramics were evaluated for their potential as low thermal expansion matrix materials. When made using a sol-gel technique (Process 1), a bulk density of 76% theoretical was achieved after sintering at 1350°C for 24 h. As shown in Table 3, the effects of sintering temperature and time on the bulk thermal expansions of CBZP and CMZP ceramics were similar. The effect of aging at 1350°C on the bulk thermal expansion of this sample (in Table 3) appears to be negligible. The CTE values for the sample sintered at 1350° for 72 h in different temperature ranges are presented in Table 4, and show considerable variation with temperature.

Table 3. Effect of sintering on CTE of CBZP

Sintering Treatment (temperature, time)	Average CTE (30-1000°C) ($x10^{-7}$°C)
1250°C, 24 h	2.25
1350°C, 48 h	5.4
1350°C, 72 h	3.2

Table 4. CTE values in different temperature ranges for CBZP sintered at 1350°C for 72 h

Temperature Range (°C)	CTE ($x10^{-7}$/°C)
30 - 200	-13.3
200 - 400	-1.5
400 - 600	6.0
600 - 800	9.2
800 - 1000	13.3

Densification

To reduce porosity of CMZP and CMZP composites, these materials were hot pressed using an Alfred Ceramics Hot Press (Model No. RH-1512) with an alumina die set having a diameter of 50.8 mm. The powders synthesized by sol-gel Process 1 were used as starting materials. For making composites, the fibers were added at the final stage of sol-gel reaction to ensure homogeneity of the mixture. Specimens for thermal expansion, density, hardness, toughness, and strength measurements were cut from the hot-pressed discs. Evaluations of these specimens are in progress.

A monolithic CMZP disc with a density of 97% theoretical was prepared by hot-pressing the sol-gel powders at 1200 °C, 10 MPa for 3 h, followed by aging at 1200°C for 24 h.

A composite disc of CMZP powder with 5 vol% chopped NICALON-SiC fibers was prepared by hot-pressing at 1200°C with about 14 MPa pressure for 8 h. The disc had a diameter of approximately 50 mm and an average thickness of 3 mm. The density at the center of the disc was approximately 97% theoretical, while near the edge, the density was 90% theoretical. Pressureless sintering an identical composition at 1200-1250 °C for 24 h resulted in densities of 66-70% theoretical.

Lightweight Ceramics

Because $CaZr_4P_6O_{24}$ (CaZP) has very low thermal conductivity as well as a low CTE, it is an ideal candidate for insulation and filtration. To produce a lightweight ceramic, polymer foam and polymer powder techniques have been developed to form ceramics with a wide range of pore sizes.

Lightweight ceramics formed using the polymer foam method are made by either saturating or coating a polymer foam (e.g., SiF, a flexible porous cellular plastic) with a ceramic slurry. The slurry is made of deionized water, 10-20 vol% NZP (CaZP powder with particle sizes of 30 μm or 50 nm), 5-25 wt% binder (based on the weight of ceramic powder), and 0.1-5 wt% ZnO. The slurry is thixotropic, that is, it has a lower viscosity when flowing than when stationary. A polymer foam with an appropriate pore size is completely immersed in the slurry. To produce a saturated foam, it is placed directly into a furnace and heated at a rate of 180-250°C/h to 1200-1300°C and held for 24 h to form a ceramic with both open and closed-cell pores. To produce a coated foam, the slurry saturated foam is squeezed to remove excess slurry before heat treatment. The lightweight ceramic thus produced has open cells.

The fracture surface morphology of ceramics formed by the polymer foam technique is dependent on the method used to synthesize the ceramic powders. Figure 8 shows the fracture surface of a slurry saturated foam made from powders synthesized by solid-state reaction having a particle size of 30-50 μm.

This ceramic foam has cell walls with a rough surface and an average wall thickness of 85 μm. The pores (about 250 μm in diameter) are arranged in a regular array, interconnecting to form a three-dimensional network, similar to the structure of the original polymer foam. A slurry saturated foam made with powders synthesized using sol-gel Process 2 with a particle size of 45 nm is shown in Figure 9. In this case, the pores have a diameter of 150 μm arranged randomly at an average spacing of 30 μm. The fracture surface of this ceramic foam appears to be smooth, with very few holes in the broken struts (ceramic portions connecting pores). Holes are present in the struts of the foamed ceramic made from the powders derived by solid-state reaction. The holes occur during pyrolysis of polymer foam during firing and may weaken the ceramic.[5,6,7] Although the slurry used to produce both foams contained 15 vol% CaZP powder, closer particle packing is obtained with the sol-gel derived powder than with the coarser powder. Also, the fine sol-gel-derived powder has a greater reactivity and mobility at elevated temperatures, resulting in a denser fired foam product having smaller pore size.

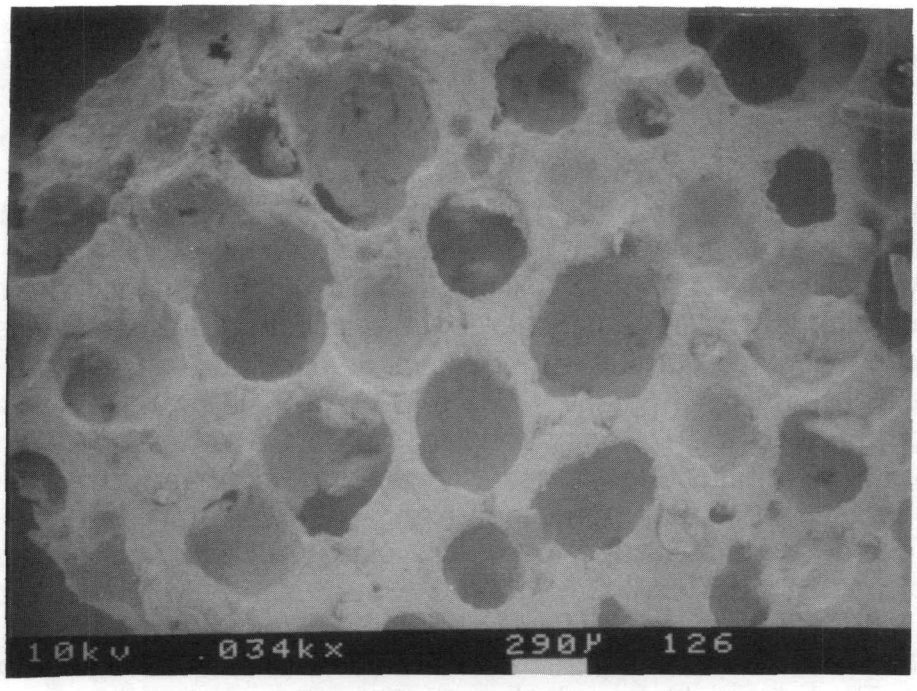

Figure 8. Fracture surface of lightweight CaZP ceramic made by the saturated polymer foam method using coarse powders

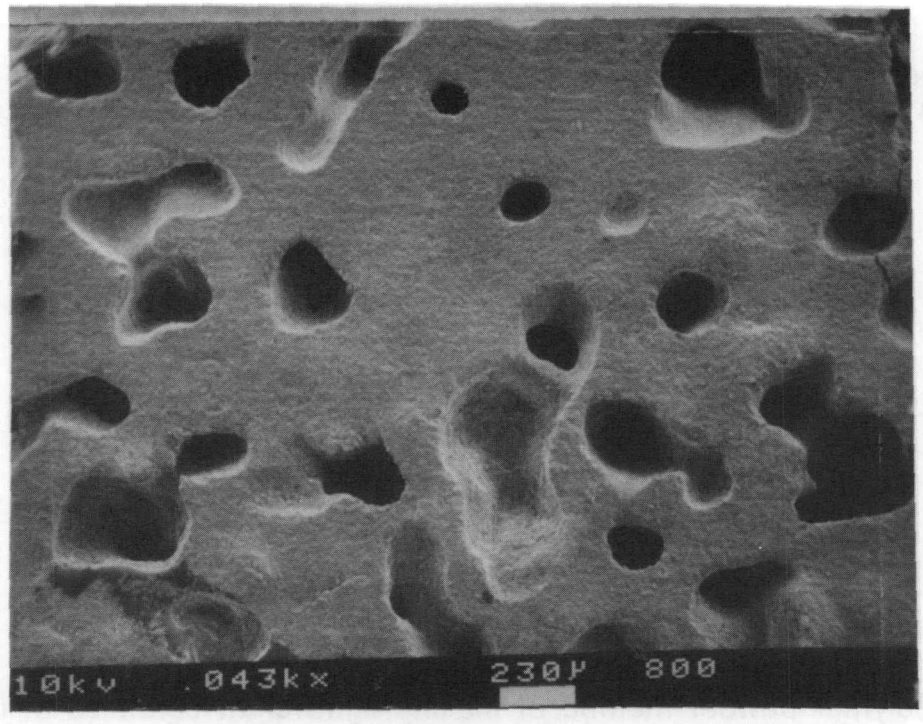

Figure 9. Fracture surface of lightweight CaZP ceramic made by the saturated polymer foam method using fine powders

The expansion behavior of lightweight CaZP ceramics formed using the slurry saturated method with sol-gel powders was determined as a function of relative density. It was observed that the CTE of lightweight CaZP is similar to that of dense CaZP, indicating that the structural form and porosity do not significantly affect the expansion behavior. As shown in Table 5, no significant difference was found in CTE of a lightweight CaZP ceramic after 15 quenches from 1250°C to water at 25°C. (The lightweight ceramic was a slurry saturated foam using sol-gel-derived powders with 0.1 wt% ZnO.) These results indicate that the lightweight NZP ceramics should exhibit good thermal shock resistance similar to that of dense NZP ceramics.

Table 5. Effect of thermal shock on the CTE of a slurry saturated lightweight CaZP

Number of Quenches from 1250°C to 25°C	Average CTE ($x10^{-6}$/°C) 30-1000°C	30-700°C	700-1000°C
1	-2.07	-1.94	-2.36
2	-2.16	-1.96	-2.27
3	-2.33	-2.32	-2.36
4	-2.24	-2.31	-2.06
5	-2.09	-2.15	-1.93
6	-2.12	-1.94	-1.92
7	-1.87	-1.93	-1.74
9	-2.10	-2.31	-1.98
10	-1.78	-2.44	-2.12
13	-2.24	-2.36	-2.31
15	-2.31	-2.90	-1.52

The polymer powder method of making lightweight ceramics utilizes an easily dispersed, high-melting point polymer powder to make a primarily closed cell material. Poly(vinyl chloride) (PVC) and poly (tetrafluoroethylene) are the polymer powders used in this study. A mixture of ceramic powder (CaZP synthesized by solid-state reaction), 5-25 wt% polymer powder, 0.1-5 wt% ZnO, and a few drops of cellulose ether solution was pressed in a stainless-steel die, then fired at 1200-1300°C for 24 h. The pore size of a lightweight ceramic produced by this method is dependent on the particle size of the polymer powder used during synthesis. The fracture surface of a sample synthesized using 10 wt% PVC powder having a particle size of 30 μm is shown in Figure 10. The specimen has a combination of both closed and open-cell pores approximately 30 μm in diameter.

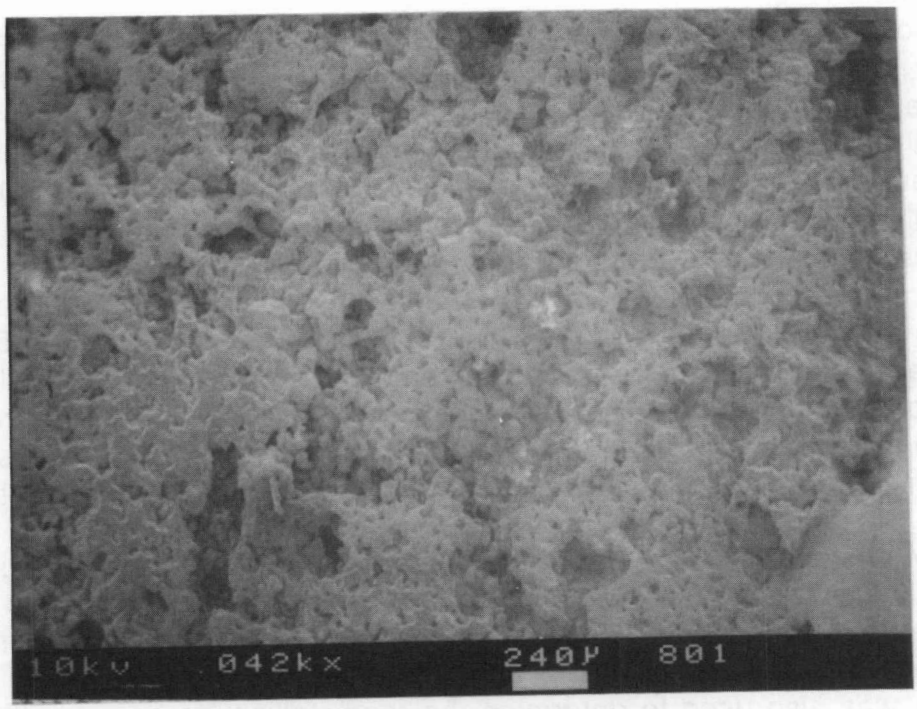

Figure 10. Fracture surface of lightweight CaZP ceramic made by the polymer powder method

ß-Eucryptite-$AlPO_4$ System

Before experimental studies to optimize the recrystallization heat treatment of modified ß-eucryptite could begin, it was necessary to reproducibly form pure solid-solution ß-eucryptite. The first step taken was to determine the weight loss factor necessary for each raw material to obtain the correct composition of final product. For modified ß-eucryptite ($Li_{0.41}Mg_{0.035}AlP_{0.52}Si_{0.48}O_4$), firing the exact batch amounts of raw materials at 1150°C for 100 h resulted in the formation of the modified ß-eucryptite phase and 10% free alumina as a secondary phase.

The free alumina phase also appeared when the modified ß-eucryptite powders were amorphous.

To obtain a pure modified ß-eucryptite glass product, the amounts of $Al(OH)_3 \cdot nH_2O$ and silicic acid determined from the calculated batch amounts were reduced during the solid-state reaction stage by 14 wt% and 5.6 wt%, respectively. Glass formation resulted following a heat treatment of this powder together with 4-8 wt% of ZrO_2 as a nucleation agent for 4 h at 1610°C with a heating rate of 30°C/min. Clear glass rods were drawn in air from molten glass and crystalline phases were not detected by XRD.

The nucleation behavior of the modified ß-eucryptite was determined by heating the glass rods (4 wt % ZrO_2) at 650°C, 700°C, 720°C, and 750°C for 2 h. These temperatures were chosen based on differential thermal analysis (DTA) of the glass using a Perkin Elmer model DTA 1700. Discs approximately 0.3 mm thick were sliced from each heat treated rod using a diamond saw, then mechanically thinned, dimpled, and ion-milled to examine the nucleation using TEM.

TEM photographs of the glass samples at the selected temperatures show uniformly distributed nuclei with size of 10-20 nm. The sample soaked at 750°C exhibited considerable growth of the nuclei. It was determined that maximum nucleation occurs between 720°C and 730°C.

DTA was also used to determine the recrystallization heat treatment. The DTA curve of the recrystallized glass shows a strong exothermic peak at 780°C, corresponding to the recrystallization process in the glass. In accordance with the DTA data, the glass samples were heated from room temperature to one of the following temperatures, 800°C, 900°C, and 1000°C with a heating rate of 10°C/min, then held at temperature for 5 to 48 h. XRD phase identification data after each heat treatment are listed in Table 6. The modified ß-eucryptite glass appears to pass through a series of crystalline states before reaching equilibrium. At 800°C, modified ß-eucryptite and $AlPO_4$ appear as the major phases and as the heating time increases, $AlPO_4$ peaks get smaller but can not be ignored. When the glass is heated at 900°C-1000°C, the modified ß-eucryptite phase appears as the equilibrium phase with trace amounts of $AlPO_4$. Therefore, in accordance with the nucleation and recrystallization studies, the glass samples were soaked at 720°C for 2 h and at 950°C for 1 h with steady heating and cooling rates of 6°C/h.

Table 6. Recrystallized phases present in modified ß-eucryptite following heat treatment

Heat Treatment Temp	Time	Major Phase	Minor Phase
800°C	10 h	$AlPO_4$, unknown	ß-eucryptite
800°C	24 h	ß-eucryptite, $AlPO_4$,	unknown
800°C	50 h	ß-eucryptite, $AlPO_4$,	unknown
900°C	5 h	ß-eucryptite	$AlPO_4$
900°C	10 h	ß-eucryptite	$AlPO_4$
1000°C	5 h	ß-eucryptite	$AlPO_4$
1000°C	10 h	ß-eucryptite	$AlPO_4$

Characterization of the recrystallized samples was conducted using SEM.A dense recrystallized glass with a grain size of less than 5 µm was produced; however, microcracks are present due to the thermal expansion mismatch between the parent glass and the recrystallized phase. Because microcracks inhibit mechanical property development, modifications to the processing technique are required. Several techniques are now under investigation, including one using ß-eucryptite powder made by a sol-gel process.

Sol-gel processing produces finer, more reactive powders which facilitate densification. Precursors for preparation of the modified ß-eucryptite powders include $Al(NO_3)\cdot 9H_2O$, $Si(OC_2H_5)_4$, $(C_2H_5O)P(O)$, $(CH_3CO_2)Li\cdot 2H_2O$, and $MgCO_3$. The precursors are dissolved in water or ethanol. Because the hydrolysis rate of silicon alkoxide is much slower than that of phosphorus alkoxide, $Si(OC_2H_5)_4$ was prehydrolized with water, then other precursors and water were added while stirring to form a homogeneous gel. The pH values of the solution were controlled by titrating NH_4OH. The dried gels were fired at 900°C and 1000°C for 24 h each. Results of XRD analyses of the phases present in the samples after firing (Table 7) indicate that modified ß-eucryptite powders may be obtained when the pH of the solution is higher than 5.5.

Table 7. Phases present after heat treatment of modified ß-eucryptite formed by sol-gel synthesis

Temp.(°C)	pH	Major Phase	Minor Phase
900	3	SiO_2, ß-eucryptite	Al_2O_3, unknown
	4	ß-eucryptite	SiO_2, Al_2O_3, unknown
	5.5	ß-eucryptite	SiO_2, Al_2O_3, unknown
1000	3	ß-eucryptite	SiO_2, unknown
	4	ß-eucryptite	SiO_2, unknown
	5.5	ß-eucryptite	unknown

During this period, investigations were conducted on the corrosion of recrystallized modified ß-eucryptite by HCl. The glass-ceramic was formed by recrystallizing glass rods at 1000°C for 1 h. The glass rods contained 4 wt% Zr_2O as a nucleating agent. Microcracks were present in the samples used for the corrosion studies which enhanced the corrosion rate by providing more exposed area.

Corrosion tests were conducted by placing rods of recrystallized modified ß-eucryptite in an aqueous 36% HCl solution (N = 12.1) at room temperature. The CTE was determined before and after exposure to the HCl solution for various times. It should be noted that each specimen experienced a thermal cycle from room temperature to 1000°C during each thermal expansion analysis. Before corrosion, bulk CTE of samples ranged from -7×10^{-7}/°C to -10×10^{-7}/°C (30-1000°C). After 20 min in HCl, the bulk CTE decreased to -33×10^{-7}/°C and then stabilized around -23×10^{-7}/°C for approximately 90 minutes (Figure 11). SEM analysis of the samples revealed a thin surface layer (0.1 mm) of corroded ß-eucryptite.

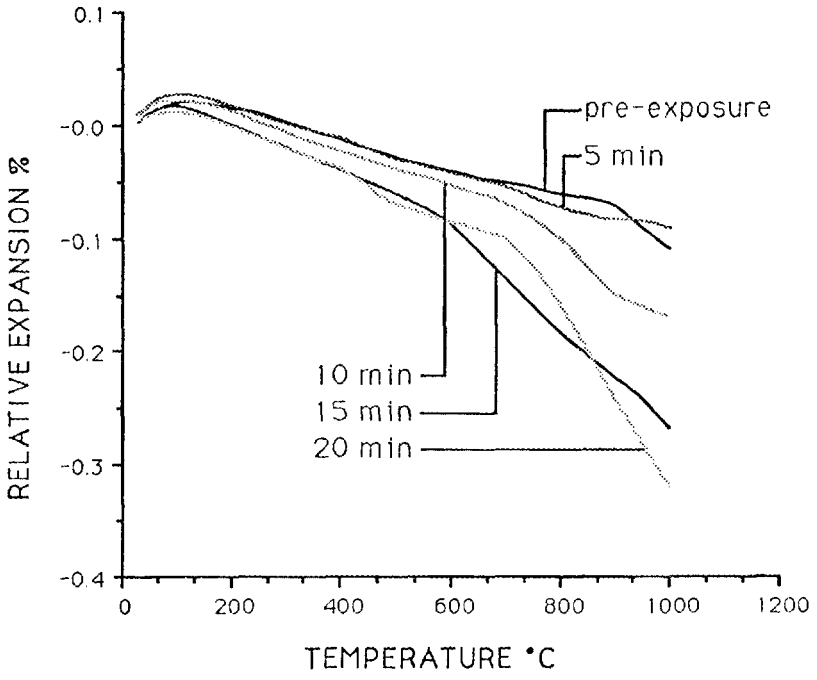

Pre-exposure:	$\alpha = -7.4 \times 10^{-7}/°C$
After 5 minutes in HCl:	$\alpha = -10.4 \times 10^{-7}/°C$
After 10 minutes in HCl:	$\alpha = -18.3 \times 10^{-7}/°C$
After 15 minutes in HCl:	$\alpha = -28.1 \times 10^{-7}/°C$
After 20 minutes in HCl:	$\alpha = -33.3 \times 10^{-7}/°C$

Figure 11. Expansion of modified ß-eucryptite before and after exposure to HCl solution (N = 12.1) at 20°C

Because the chemistry plays an important role in the corrosion process, it was necessary to determine the homogeneity of the rods prior to corrosion. Elemental mapping using energy dispersive X-ray analysis (EDX) was performed on non-corroded samples of recrystallized ß-eucryptite. No change in composition was detected from the edge of the sample to the center, nor in composition of the grain boundaries.

Other corrosion tests were conducted at 100°C in the HCl solution (N = 12.1). Post exposure evaluations of test specimens showed a change in CTE of $-7.40 \times 10^{-7}/°C$ to $-36.0 \times 10^{-7}/°C$ (Figure 12) after 1 h exposure. Severe corrosion of the sample surface to a depth of 0.3mm was observed.

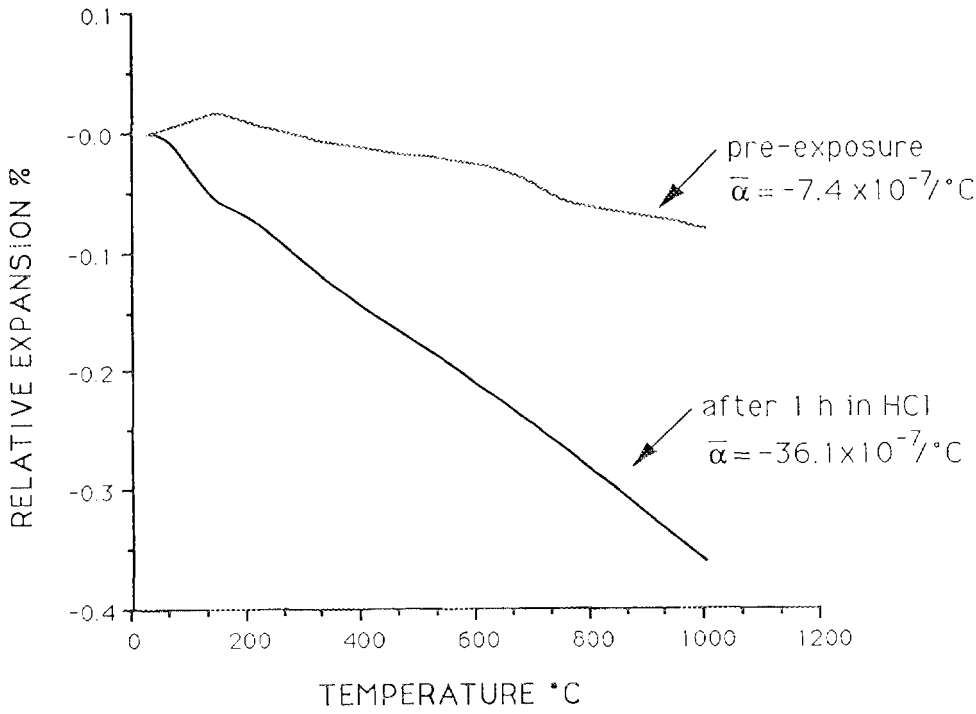

Figure 12. Effect of HCl exposure at 100°C on the expansion of ß-eucryptite

Experiments were conducted to determine the effects of thermal cycling during corrosion tests in which specimens were cycled seven times from 30-1000°C while monitoring expansion behavior. Test results showed little difference in the CTE between the first and the second thermal cycles (-7 $\times 10^{-7}$/°C to -9$\times 10^{-7}$/°C), probably due to recrystallization which occurred during the first thermal cycle. The CTE stabilized at -9$\times 10^{-7}$/°C for the next 6 thermal cycles indicating that thermal cycling should not contribute to the corrosion process.

Corroded modified ß-eucryptite samples examined using EDX at 80 µm intervals from the corroded surface to the non-corroded center exhibited aluminum and phosphorus losses of approximately 75% from the specimen surfaces. No change was observed in the amounts of silicon and zirconium throughout the specimen (ZrO_2 was used as a nucleating agent) suggesting that $AlPO_4$ is the first component to be leached by the HCl solution.

Comparisons made in the EDX analyses of samples corroded at 20°C and at 100°C for various durations (10 min - 1 h) indicated that corrosion at 100°C

was much more severe. Aluminum, phosphorus, and magnesium were removed, while silicon and zirconium remained in the specimens after exposure at either temperature. After 30 min exposure at 100°C, the composition of the corroded area stabilized although the thickness of the corroded layer continued to increase.

SEM analysis indicated that corrosion begins at the grain boundaries (grain size between 10 and 15 μm), and progresses through the grain. Corrosion transformed the dense and non-porous glass-ceramic into a very porous material with a collapsed structure. The advancement of the corrosion is shown in Figure 13, where the ß-eucryptite specimen is completely corroded at the exposed surface and proceeds gradually along the grain boundaries and microcracks toward the interior of the specimen.

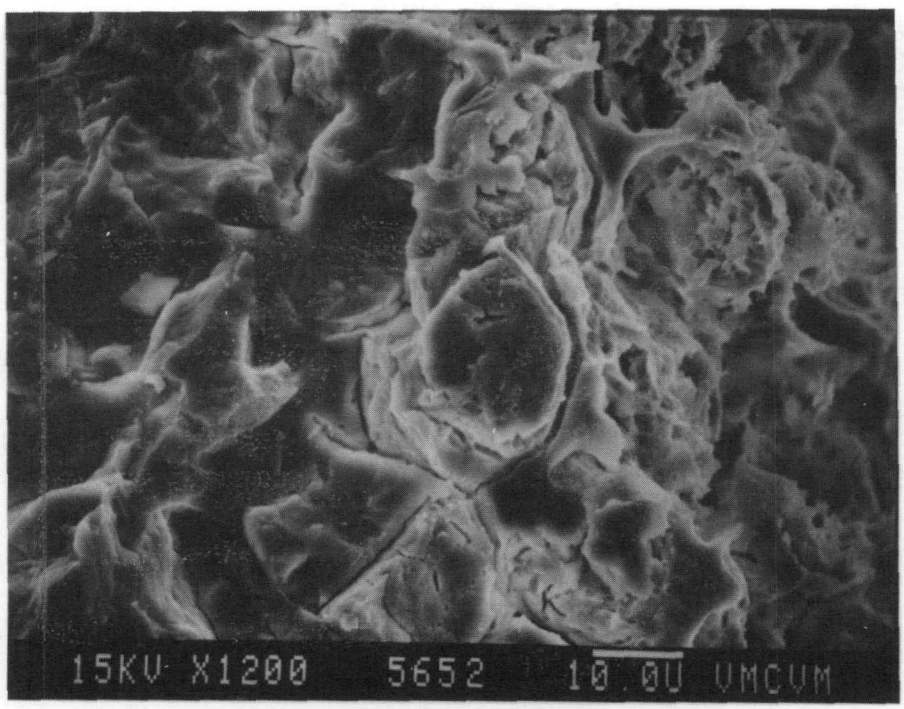

Figure 13. Corrosion of modified ß-eucryptite specimen after 20-min exposure to HCl solution at 100°C (exposed surface on right)

Status of Milestones

All milestones are on schedule except 2.4.1a which was delayed due to the difficulty in the GTE subcontract. Table 8 contains the key to major milestones and Figure 14 the milstones status chart.

Publications

Three patent disclosures have been submitted to Virginia Tech Intellectual Properties for evaluation:
1. Low Expansion and Low Thermal Conductivity Ceramic Materials ((Ca,Mg)NZP)
2. Synthesis and Sintering of Fine and Ultra-Fine Grain NZP Ceramics
3. Manufacture of Lightweight NZP Ceramics

The following presentations were made at the Steering Committee Meeting for the Center for Advanced Ceramic Materials, Virginia Tech, Blacksburg, VA, April 6, 1990:
1. "Processing and Properties of (Ca,Mg)NZP Ceramics" by T. Sun
2. "NZP Lightweight Ceramics" by D. Liu
3. "High Temperature NZP Ceramic Composites" by D. Hirschfeld

Posters on the following topics were prepared for display at the Steering Committee Meeting: NZP Ceramic Composites, ß-Cristobalite, Recrystallization and Corrosion of ß-eucryptite, Lightweight NZP Ceramics, and Thermal Properties of (Ca,Mg)NZP.

The following papers were presented at the American Ceramic Society 92nd Annual Meeting, Dallas, TX , April 21-26, 1990:
1. "Characterization of the Thermal Expansion of $CaZr_4(PO_4)_6$ and its Limited Solid Solution with $MgZr_4(PO_4)_6$ " by S. Van Aken, R. Swanson, J. Kim, and J. Brown.
2. "Thermal Expansion of Modified ß-Eucryptite Compositions" by Y. Yang and J. Brown.
3. "Structural Evolution and Stabilization Mechanism of ß-Cristobalite from Gel Precursors" by T. Sun and J. Brown.

References

1. A. S. Kazakos-Kijowski, et al., "Synthesis, Crystal Data, and Thermal Stability of Magnesium Zirconium Phosphate," Mat. Res. Bul., 23 1177-84 (1988).

2. G. E. Lenain, et al., "Structural Model for Thermal Expansion in $MZr_2P_3O_{12}$ (M=Li, Na, K, Rb, Cs)," J. Mat. Sci., 22 (1) 17-22 (1987).

3. S. Y. Limaye, D. K. Agrawal and H. A. McKinstry, "Synthesis and Thermal Expansion of $MZr_4P_6O_{24}$ (M = Mg, Ca, Sr, Ba)," J. Am. Ceram. Soc., 70 (10) C232-236 (1987).

4. J. J. Cleveland and R. C. Bradt, "Grain Size/Microcracking Relations for Pseudobrookite Oxides," J. Am. Ceram. Soc., 61 (11-12) 478-81 (1978).

5. M.F. Ashby, "The Mechanical Properties of Cellular Solids," Metall. Trans. A, 14A 1755-69 (1983).

6. H. Hagimara and D.J. Green, "Elastic Behavior of Open-Cell Alumina," J. Am. Ceram. Soc., 70 (11) 811-815 (1987).

7. F.F. Lange and K.T. Miller, "Open-Cell, Low-Density Ceramics Fabricated from Reticulated Polymer Substrates," Adv.Ceram. Mat. 2 (4) 827-31 (1987).

Figure 14 Status of milestones

	1989					1990						
Milestone	N	D	J	F	M	A	M	J	J	A	S	O
2.4.1a												
2.4.1b												
2.4.2a												
2.4.3a												
2.4.3b												
2.4.4a												
2.4.5a												
2.4.5b												

*
B
O
O
O
O
O
O
O

* On, Ahead of, or Behind Schedule

Table 8. Key to major milestones (WBS Elements)
(subtasks refer to calendar year 1990 milestones)

VPI	2.4.1	Property Optimization by Hot Isostatic Pressing (July 31, 1992)
	2.4.1a	Repeat VPI Studies Using HIP Densification (May 31, 1990)
	2.4.1b	Develop Powder Manufacturing and Shaping of Preliminary NZP Composition (Oct. 31, 1990)
VPI	2.4.2	Optimization of Compositions (March 31, 1991)
	2.4.2a	Complete Thermochemical Characterization of (Ca,Mg)NZP Compositions (July 31, 1990)
VPI	2.4.3	Riber Reinforced Composites (July 31, 1992)
	2.4.3a	Develop Composite Processing Techniques (Dec. 31, 1990)
	2.4.3b	Develop Techniques to Characterize Fiber/Matrix Interface (Dec. 31, 1990)
VPI	2.4.4	Lightweight Insulation (Sept. 31, 1991)
	2.4.4a	Develop Techniques for Making Insulation (July 31, 1990)
VPI	2.4.5	Recrystallized ß-Eucryptite Glasses (March 31, 1991)
	2.4.5a	Optimize Recrystallization Technique (July 31, 1990)
	2.4.5b	Develop Corrosion Test(s) for Recrystallized Glasses (July 31, 1990)

1.3 THERMAL AND WEAR COATINGS

1.3.1 ZrO_2 Base Coatings

Advanced Coating Technology

B. W. Sheldon, J. C. McLaughlin, and D. P. Stinton (Oak Ridge National Laboratory)

Objective/scope

Sodium corrosion of silicon carbide and silicon nitride components in gas turbine engines is a potentially serious problem. The outer surfaces of SiC and Si_3N_4 parts oxidize at high temperatures to form an SiO_2 layer which inhibits further oxidation. However, sodium which is present in high-temperature combustion atmospheres reacts with the SiO_2 layer, such that it is no longer protective. Previous studies performed by J. I. Federer of ORNL indicate that Al_2O_3 is much more resistant to sodium corrosion than this native SiO_2. This suggests the use of an alumina (α-Al_2O_3, etc.) coating to provide both oxidation and sodium resistance; however, sodium is likely to undergo some reaction with a pure alumina coating, such that the α or other alumina phases are converted to a sodium aluminate phase such as ß-alumina ($Na_2O \cdot 11\ Al_2O_3$). This type of transformation may cause an α pure alumina coating to fail. The objective of this task is to develop a coating that will protect the underlying SiC or Si_3N_4 from sodium corrosion and provide simultaneous oxidation protection. To evaluate the behavior of both α- and ß-aluminas in sodium-containing atmospheres, the corrosion resistance of hot-pressed samples of both materials will first be evaluated. A chemical vapor deposition (CVD) process will be developed for the application of the appropriate alumina coatings. The effect of the combustion environment upon coating characteristics such as microstructure, strength, adherence, and other properties will then be evaluated.

Technical progress

Hot-pressed β/β'' alumina samples were produced from high purity α-Al_2O_3 powder that was ball milled with 17.2 wt % Na_2CO_3 powder. This mixture was then calcined in argon at 1250°C for 1 h, and hot pressed under vacuum at 1600°C for 20 min. X-ray diffraction showed that these samples consisted of ß-Al_2O_3 and ß"-Al_2O_3. Samples of α-Al_2O_3 were produced from the same powder, under the same conditions, without the addition of sodium carbonate, and without the calcining step.

Corrosion tests on these samples were conducted by Federer. The samples were exposed to a combustion atmosphere composed of 7600 cm^3/min air and 685 cm^3/min methane. Two different exposures were conducted with different sodium contents: one with about 0.002 g/min Na_2CO_3 (110 ppm Na), and one with about 0.0006 g/min Na_2CO_3 (30 ppm Na). In each run, the samples were exposed for 200 h. Each pair of samples (one α and one ß,ß") was held at a different temperature by positioning them at different parts of the furnace. The measured temperatures were 965, 1130, or 1205°C. The surface composition of these samples was determined by X-ray diffraction; these results are summarized in Tables 1 and 2.

Table 1. Near-surface phase composition after exposure for 200 h

Temperature (°C)	30 ppm Na		110 ppm Na	
	Primary	Secondary	Primary	Secondary
		Hot-pressed α-alumina		
1205	ß-aluminas	α-alumina	α-alumina	ß-aluminas
1130	α-alumina	ß-aluminas	ß-aluminas	α-alumina
965	α-alumina	$NaAlO_2$ Na_2CO_3	α-alumina	$NaAlO_2$ Na_2CO_3
		Hot-pressed ß/ß"-aluminas		
1205	ß-aluminas	none	ß-aluminas	none
1130	ß-aluminas	none	ß-aluminas	none
965	ß-aluminas	$NaAlO_2$ Na_2CO_3	ß-aluminas	$NaAlO_2$ Na_2CO_3

Table 2. Relative X-ray diffraction intensities for β" and β phases[a]

Reference samples

Hot-pressed β-aluminas: 0.53

Powder from hot-pressed β-aluminas: 0.41

Samples exposed to the simulated combustion atmospheres

Temperature (°C)	Hot-pressed α-alumina		Hot-pressed ß/ß"-aluminas	
	30 ppm Na	110 ppm Na	30 ppm Na	110 ppm Na
1205	-	-	0.46	0.45
1130	-	0.48	0.47	0.44

[a]The quantity in this table is the ratio of the integrated intensities of the ß peak and the ß" peak, based on measurements which were made at low angle, with a scan rate of 0.1°/min.

At 1130°C and 1205°C, the surface of the α-alumina samples was converted to β/β" aluminas at both sodium concentrations. Comparing these four samples, the relative intensity of the β/β" patterns was the weakest for the sample with the most severe exposure (110 ppm Na at 1205°C). This apparent contradiction was supported by transmission electron microscopy observations, where β- and β"-alumina were not seen on ion-thinned transverse sections of this sample, compared to the distinct β/β"-alumina layers that were observed for both of the samples that were exposed to 30 ppm Na, and for the sample exposed to 110 ppm Na at 1130°C. The likely explanation for this behavior is that a thicker β/β"-alumina layer formed on the sample at 1205°C with 110 ppm Na, and that this layer spalled off of the sample because of the difference in thermal expansion coefficients or because of the volume expansion associated with the reaction.

At 965°C, β- and β"-aluminas were not observed on the hot-pressed α-alumina samples. In the furnace used for the sodium exposures, these low-temperature samples were located downstream from the samples exposed at 1130 and 1205°C. With this reactor configuration, the sodium carbonate and sodium aluminate phases that were observed suggest that sodium carbonate condensed onto these samples as the gases cooled. The sodium aluminate phase that formed at 965°C has a much higher sodium content than the β and β" phases that were observed at the higher temperatures. A likely explanation for the presence of this sodium aluminate phase is that it formed by a direct reaction between the α-alumina substrate and the sodium carbonate which condensed onto it. This represents a second possible corrosion mechanism, in addition to the direct gas-solid reaction which apparently formed the β and β" phases at higher temperatures. The absence of β- and β"-aluminas at 965°C indicates that this gas-solid reaction does not cause appreciable formation of these phases at this lower temperature.

The results shown in Table 2 indicate that the relative amounts of the β and β" phases are relatively constant during the exposures at both sodium concentrations, and at 1130 and 1205°C. This indicates that the β/β" composition is relatively stable under the conditions tested. However, the apparent spalling observed on the high-sodium, high-temperature α-alumina sample indicates that a β/β"-alumina coating may still fail. A serious concern is that the rapid diffusion of sodium through a β/β"-alumina coating will lead to a subsurface corrosion problem.

These initial results with hot-pressed samples indicate that phase transformations in high-temperature corrosive atmospheres are potentially complex. A better understanding of the phase chemistry under these conditions may be important in determining the performance of alumina-based coating systems, and of monolithic alumina or alumina matrix composites.

The other primary effort of this task is to form an alumina-based coating by CVD. The most common way to produce alumina by CVD is to use $AlCl_3$; however, β- and β"-aluminas can not be produced in this way because the $AlCl_3$ will react with a sodium source to produce NaCl. Therefore, trimethyl-aluminum (TMA) is being used as an aluminum source. Our efforts to date have focused on depositing alumina from TMA and oxygen. During the previous period, crystalline alumina was deposited at 720°C. However, powder formation (i.e., homogeneous nucleation) and the coating uniformity were difficult to control in this system.

During this period, a redesigned cold-wall CVD system was constructed and tested. The initial results indicate that the expected results of faster deposition and reduced powder formation have been achieved; however, only amorphous material has been produced at temperatures up to 775°C.

Several more experiments at this temperature will be carried out; if crystalline material is not produced, then two alternatives will be explored:

1. An RF generator which is currently available will be installed to obtain a cold-wall system with a higher substrate temperature.

2. The amorphous coatings will be annealed at higher temperatures to induce crystallization.

Currently, some small alterations on the cold-wall reactor are being made to evaporate NaOH in the CVD system. With this modification, the deposition of sodium aluminate coatings will be investigated.

Status of milestones

The March 1990 milestone to evaluate the corrosion resistance of bulk α- and ß-alumina samples was completed.

Development of Adherent Ceramic Coatings to Reduce Contact Stress Damage of Ceramics
- H. E. Rebenne and J. H. Selverian (GTE Laboratories Incorporated)

Objective/scope

The objective of this program is to develop oxidation-resistant, high toughness, adherent coatings for silicon based ceramics. These coatings will be deposited on reaction bonded Si_3N_4 (RBSN), sintered SiC (SSC), and HIP'ed Si_3N_4 (HSN) and used in an advanced gas turbine engine. A chemical vapor deposition (CVD) process will be used to deposit the coatings. These coatings will be designed to provide the best mix of mechanical, thermal, and chemical properties.

Technical progress

Oxidation Testing of the Coating

During Phase I, the oxidation resistance of the coating in static air was studied. The coating was found to be oxidation resistant for up to 500 hours at 1000°C, but not at 1200°C or 1375°C. The cause of failure is being studied in Phase II. The procedure for oxidation testing was given in the June, 1989 Bimonthly Progress Report.

Thus far, 500 hour tests on uncoated, AlN-coated, Al_2O_3+ZrO_2/AlN-coated, and Al_2O_3/AlN-coated substrates have been completed at 1100°C, 1200°C, and 1275°C. The latter coating was evaluated to eliminate the effect of ZrO_2, which is believed to be detrimental to the coating's oxidation resistance. This is due to the high diffusivity of oxygen in ZrO_2 and to the fact that ZrO_2 undergoes a phase transformation with a 10% volume change at ≈1200°C. It should be noted that the original coating design included ZrO_2 only to provide toughness and a low coefficient of friction. In addition to RBSN, SSC, and HSN, single crystal sapphire was also used as a substrate material in the tests to provide a baseline for interpreting the results. Since it is chemically inert to the coating, the effects of chemical reactions between the coating and substrate are not present in this system. Post-oxidation testing consisting of x-ray diffraction to identify phase changes and scanning electron microscopy to identify porosity, cracking, and regions of thin coating, has also been done. The time-dependence of the coating phase changes was monitored by x-ray diffraction using the single crystal sapphire samples. The RBSN, SSC, and HSN samples were analyzed for phase changes only at the end of the 500 hour test. The x-ray diffraction results are listed in Tables 1 and 2.

All coating configurations showed poor oxidation resistance on each substrate and at each temperature. In particular, no coating configuration gave complete protection of the substrate for the full 500 hours. When AlN was the only coating layer, it completely oxidized to α-Al_2O_3 during the first two hours of testing. This was indicated by weight gain and confirmed by the x-ray diffraction analysis of coated single crystal sapphire samples (see Table 1). This is expected based on the oxidation behavior of AlN reported in the literature[1,2,3]. The conversion of AlN to Al_2O_3 is accompanied by a 1.9% volume expansion, which in this system may be catastrophic to the coating since it could result in crack formation. When the coating consisted of the Al_2O_3+ZrO_2

Table 1: Phases identified by x-ray diffraction after oxidation in static air. Samples were AlN-coated, Al_2O_3+ZrO_2/AlN-coated, and Al_2O_3/AlN-coated single crystal sapphire. Phases associated with substrate reflections are not listed.

Oxidation Time, hours	Oxidation Temperature, °C		
	1100	1200	1275
AlN-coated			
2	α-Al_2O_3	α-Al_2O_3	α-Al_2O_3
8	α-Al_2O_3(?)*	α-Al_2O_3	α-Al_2O_3
30	α-Al_2O_3	α-Al_2O_3	α-Al_2O_3
125	α-Al_2O_3	α-Al_2O_3	α-Al_2O_3
500	α-Al_2O_3	-----	α-Al_2O_3
Al_2O_3+ZrO_2/AlN-coated			
2	-----	α-Al_2O_3	α-Al_2O_3, ZrO_2
8	-----	α-Al_2O_3, ZrO_2	α-Al_2O_3, ZrO_2
30	-----	α-Al_2O_3, ZrO_2	α-Al_2O_3, ZrO_2
125	-----	α-Al_2O_3, ZrO_2	α-Al_2O_3, ZrO_2
500	-----	α-Al_2O_3, ZrO_2	-----
Al_2O_3/AlN-coated			
2	-----	α-Al_2O_3, AlN	α-Al_2O_3, AlN
8	-----	α-Al_2O_3, AlN	α-Al_2O_3, AlN
30	-----	α-Al_2O_3, AlN	α-Al_2O_3, AlN
125	-----	α-Al_2O_3	α-Al_2O_3
500	-----	α-Al_2O_3	-----

* The question mark denotes uncertainty.

composite layer and AlN, all of the AlN was still converted to α-Al_2O_3, indicating that oxygen diffused through the Al_2O_3+ZrO_2 layer. The reasons for this could include the rapid diffusion of oxygen through ZrO_2, cracking in the Al_2O_3+ZrO_2 layer due to the transformation of ZrO_2 from the monoclinic to the tetragonal phase, and/or regions of very thin coating. It was not possible to distinguish between these failure modes by examining the samples after oxidation testing, since the coating was severely damaged and pieces of it had flaked off. When the coating consisted of a pure Al_2O_3 layer and AlN, the coating remained oxidation-resistant during the first 30 hours of testing, as indicated by the presence of AlN at 30 hours in the x-ray diffraction analysis of single crystal sapphire samples (see Table 1). This indicates that pure Al_2O_3 provides adequate protection for a period of time, which is apparently due to the very slow rate of oxygen diffusion through Al_2O_3 at these temperatures. For example, diffusion

calculations were performed which indicated that the oxygen concentration due to diffusion at a depth of 0.5 μm below the surface, a temperature of 1200°C, and a time of 500 hours should be $<10^{-4}$ atomic percent. Additional calculations were done for times up to 8000 hours, depths up to 1.5 μm, and temperatures up to 1500°C, and the results were reported in the October, 1989 Bimonthly Progress Report. It is thought that the reason for the failure between 30 and 125 hours of testing was diffusion of oxygen through very thin regions of the Al_2O_3 coating. Achieving coating thickness uniformity has been difficult due to the design of the reactor used in this program.

Table 2: Phases identified by x-ray diffraction after 500 hours of oxidation in static air. Samples were AlN-coated, Al_2O_3+ZrO_2/AlN-coated, and Al_2O_3/AlN-coated RBSN, SSC, and HSN. Phases associated with substrate reflections are not listed.

Sample	Oxidation Temperature, °C		
	1100	1200	1275
AlN-coated			
RBSN	α-Al_2O_3	α-Al_2O_3	α-Al_2O_3
SSC	α-Al_2O_3	α-Al_2O_3	α-Al_2O_3
HSN	α-Al_2O_3	α-Al_2O_3	AlN
Al_2O_3+ZrO_2/AlN-coated			
RBSN	- - - - -	α-Al_2O_3, ZrO_2	α-Al_2O_3, ZrO_2
SSC	- - - - -	α-Al_2O_3, ZrO_2	α-Al_2O_3, AlN, ZrO_2(?)
HSN	- - - - -	α-Al_2O_3, ZrO_2, AlN	ZrO_2, AlN(?), AlON(?)
Al_2O_3/AlN-coated			
RBSN	- - - - -	α-Al_2O_3, AlN	α-Al_2O_3, AlN, AlON(?)
SSC	- - - - -	α-Al_2O_3, AlN	α-Al_2O_3, AlN
HSN	- - - - -	α-Al_2O_3, AlN(?), AlON(?)	α-Al_2O_3, AlN(?), AlON(?)

* The question mark denotes uncertainty.

Results obtained on the RBSN, SSC, and HSN samples were similar to those obtained on the single crystal sapphire samples. In particular, the AlN layer was fully oxidized to α-Al_2O_3 when it was the only coating layer. The presence of AlN in the AlN-coated HSN sample tested for 500 hours at 1275°C is possibly due to AlN formation in

the substrate. This could occur due to chemical reaction between the Si_3N_4 and the Al_2O_3 that is added as a sintering aid. Thermodynamic modeling of HSN done during Phase I of the program showed that the Al_2O_3 could react with Si_3N_4 to form AlN in the substrate, and that this reaction is enhanced in the presence of the gaseous mixture used to deposit the AlN coating. When a sample contained ZrO_2 in the outer coating layer, the AlN phase was not detected after 500 hours of oxidation testing, suggesting that the AlN layer had completely oxidized. Notice that for the Al_2O_3+ZrO_2/AlN-coated SSC sample tested at 1275°C, the presence of ZrO_2 was questionable and AlN was found to be present (see Table 2). The presence of AlN in the Al_2O_3+ZrO_2/AlN-coated HSN samples would appear to contradict the results obtained for the other substrates unless the AlN is present in the substrate, as explained above. As with the results obtained on the single crystal sapphire samples, the pure Al_2O_3 coating over AlN appears to protect the sample from oxidation, even for 500 hours. The longer protection time obtained with the RBSN, SSC, and HSN substrates as compared to the sapphire substrates is probably due to thicker coatings on the silicon nitride and silicon carbide materials. Since all substrates were coated for the same length of time, this indicates that the AlN deposition rate is different on the different materials.

As discussed above, one possible cause of coating failure during oxidation is regions of very thin coating. A second possible cause of coating failure is porosity. Due to inability to control the coating morphology during the CVD process, as-grown coatings display a variety of crystallite sizes and shapes. These range from cauliflower-shaped clusters of grains to faceted grains. Examples of the two extremes in morphology are shown in Fig. 1. Examination of the cauliflower-shaped clusters shows the presence of large gaps between clusters. Due to the thinness of the oxide layer of the coating (typically less than 2 μm), these gaps could penetrate to the AlN layer. An attempt was made to determine if the AlN layer was exposed. This was done by taking nitrogen maps on the surfaces of two coated samples using an electron microprobe analyzer. Neither sample gave a nitrogen signal, suggesting that the Al_2O_3+ZrO_2 coating was continuous. However, the sensitivity of the microprobe to nitrogen was ≈3 weight per cent and the detection limit for gaps in the Al_2O_3+ZrO_2 coating was ≈1 μm; i.e., only gaps larger than 1 μm could be detected.

A third possible cause of coating failure is cracking of the coating during heating to the test temperature. This could occur as a result of phase transformation of ZrO_2 from the monoclinic to the tetragonal phase, or as a result of thermal mismatch. The coating is deposited at 975°C, and examination of as-deposited coatings has shown that they are crack-free. (The deposition temperature is limited to 1000°C by the materials of construction of the reactor.) In order to test this possibility, a series of samples was annealed in vacuum (10^{-7} torr) for 10 minutes after coating and examined in the SEM for cracks. Each sample was examined over the entire surface, including the faces and the edges. Table 3 lists the coating configurations that were tested and the anneal temperatures used. A set of samples was also oxidized in air at 1275°C for 10 minutes and then examined for cracks. These tests showed that the samples exposed to 1275°C, whether in vacuum or air, had cracks. In contrast, the as-coated samples and those exposed to 1000°C did not have cracks. Furthermore, the cracks observed on the samples treated at 1275°C were indicative of tensile cracks, which is expected since the thermal expansion coefficient of the coating is higher than that of the substrate. A typical crack is shown in Fig. 2. In order to further investigate the effect of residual stress on coating durability, attempts to measure the residual stress using the radius of curvature method will be made. No results from this effort are available yet.

The oxidation test plan included determination of kinetic parameters from the weight gain data. However, despite the large number of samples tested (3 samples of each coating configuration on each substrate at each temperature for a total of 36 on each substrate), kinetic parameters could not be reliably calculated due to scatter in the weight gain data.

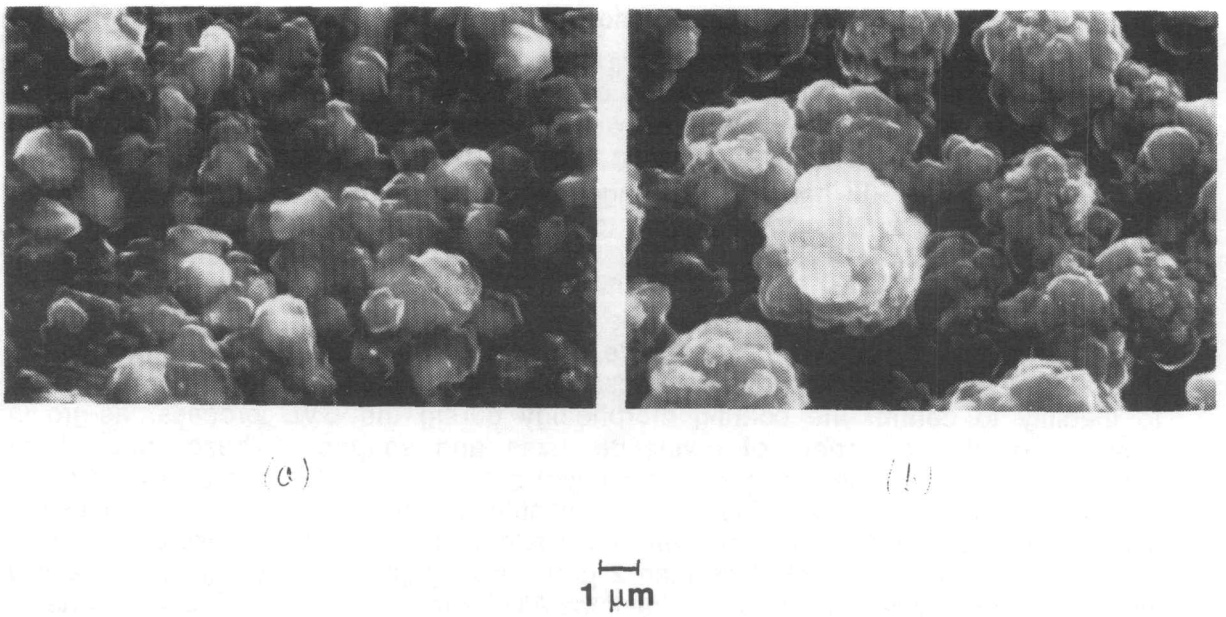

Figure 1. SEM photomicrographs showing the two main types of surface morphologies of the coating: a) coating on HSN with faceted morphology; b) coating on HSN with cauliflower morphology.

Dave Stinton and Brian Sheldon of Oak Ridge National Laboratory visited GTE Laboratories on March 7, 1990 to review the status of the program. The oxidation test results were shown to them, and we discussed future action. It was agreed that depositing the coating at a higher temperature should be tried. This should give a faster deposition rate and hence a thicker coating. In addition, it might reduce the residual stress in the coating at high temperatures. We are currently modifying the CVD process to deposit the coating at 1275°C in a new CVD reactor that was recently built at GTE Laboratories. We also discussed getting a three month, no-cost extension to give additional time to solve the oxidation problem. A formal request for the extension was made the following week. This extension is reflected in the milestone list at the end of the report.

Table 3. Summary of tests done to determine if cracking occurs in the coating due to thermal expansion mismatch. The sample designations are as follows: "C/A/HSN" and "C/A/SSC" denote the Al_2O_3+ZrO_2/AlN coating on HSN and SSC, respectively; "A/A/HSN" and "A/A/SSC" denote the Al_2O_3/AlN coating on HSN and SSC, respectively.

Sample	As-coated	Annealed at 1000°C	Annealed at 1275°C	Oxidized at 1275°C
C/A/HSN	no cracks	no cracks	cracks on edge	- - - - -
A/A/HSN	no cracks, porous-looking edge	- - - - -	- - - - -	separation between crystallites, spalling
C/A/SSC	separation between crystallites on face and edge	one small crack on face	large amount of cracking on face and edge	- - - - -
A/A/SSC	no cracks, porous-looking on edge	- - - - -	- - - - -	small cracks, separation between crystallites

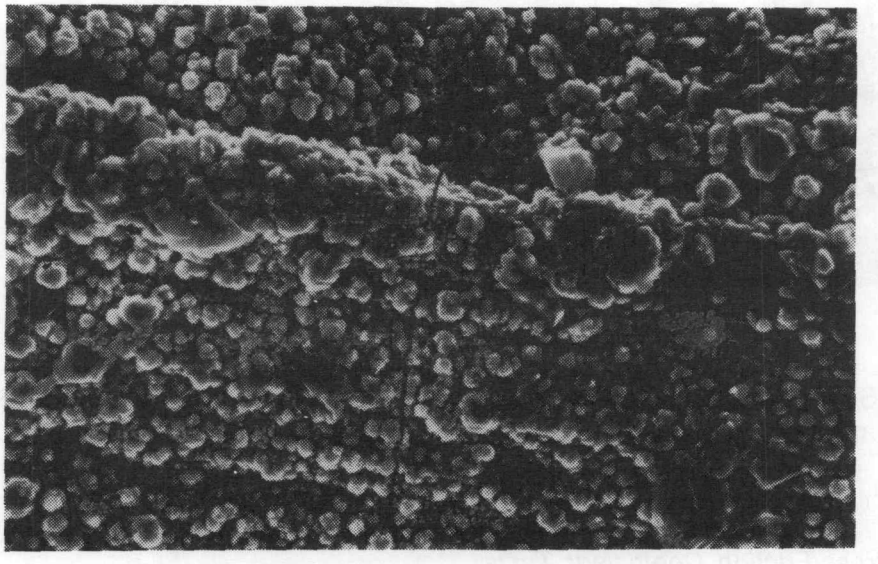

Figure 2. SEM photomicrograph of an Al_2O_3+ZrO_2/AlN coating on HSN after a 10 minute vacuum anneal at 1275°C.

Coating Morphology

A study was done to determine if the coating morphology and/or deposition rate could be modified to give a more fine-grained, uniform crystallite size or to give a thicker coating so that the possibility of porosity or very thin coating would be reduced. This study involved adding various gases to the inlet gas mixture that would act as catalysts for coating nucleation or growth. For example, Al_2O_3 is typically deposited at GTE Laboratories from a mixture of $AlCl_3$, CO_2, H_2, and Ar. Deposition runs were done using this mixture plus either H_2S, CH_4, or H_2S+CH_4. When H_2S was added, the coating was ≈50% thicker for a given run time, but the surface grains were larger and more discontinuous. This suggests that the nucleation rate was unaltered, but that the growth rate of stable nuclei was increased. Figure 3 shows an Al_2O_3-coated SSC sample prepared with H_2S. Addition of CH_4 gave no change in coating thickness, but a surface morphology that appeared to be even more porous than that obtained with H_2S (see Fig. 4). Addition of H_2S plus CH_4 gave similar results to addition of H_2S alone. These effects are not understood. Since they did not result in improved coating morphology, the study was discontinued.

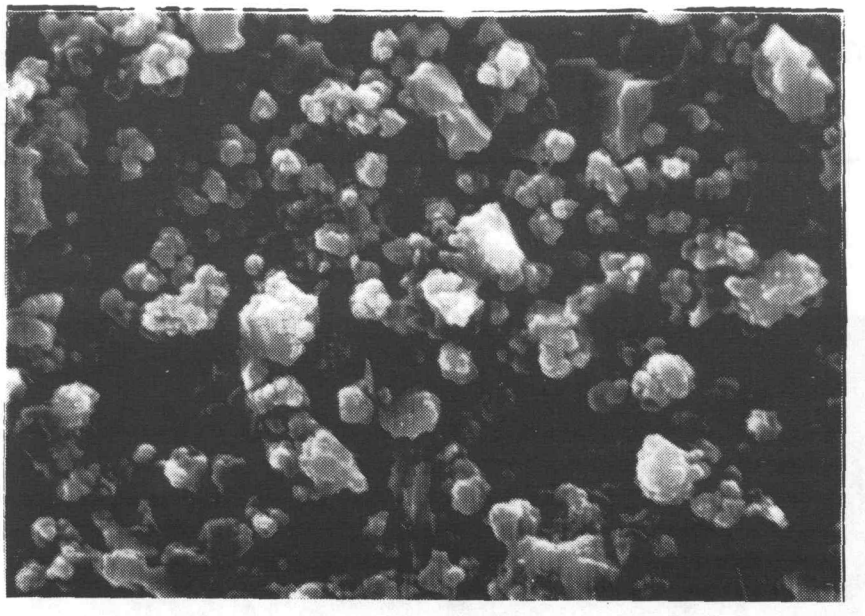

Figure 3. SEM photomicrograph of an Al_2O_3 coating on SSC deposited with H_2S added to the inlet gas mixture. Notice the large gaps between crystallites.

Contact Stress/Friction Coefficient Tests

Pins and disks for the milestone "Feasibility study of measuring friction coefficient and contact stress damage using conventional pin-on-disk or ball-on-disk

wear tests" were fabricated and polished to a 1 μm surface finish. This study will measure the friction coefficient and wear resistance behavior of both coated and uncoated material. Uncoated substrates are being included to provide a baseline for interpreting results obtained on coated materials. The tests are being done using the pin-on-disk apparatus illustrated in Fig. 5. Notice that the tip of the pin is spherical, which gives similar results to those obtained in a ball-on-disk test. Due to the sensitivity of measured values of friction and wear properties to the test conditions, and to the general problem of obtaining reproducible results in tribological studies, the test procedure chosen for this study is based upon the conditions used for the VAMAS round-robin on wear test methods[4]. This procedure is currently being used by a large number of laboratories, including GTE Laboratories and Oak Ridge National Laboratory. Initially, measurements on both uncoated and coated material will be done at room temperature. The measurements will then be repeated at a high temperature. The highest temperature that can be reached with the present apparatus is 800°C.

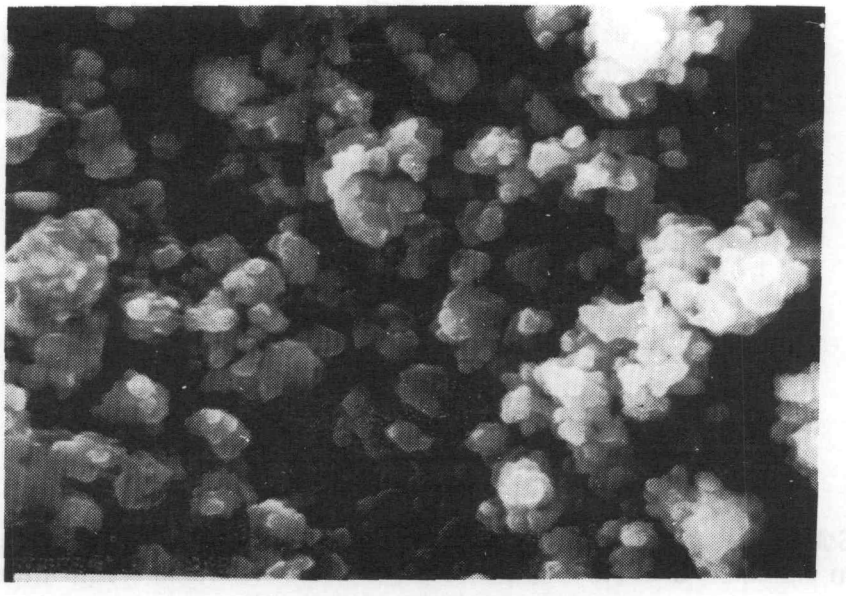

Figure 4. SEM photomicrograph of an Al_2O_3 coating on SSC deposited with CH_4 added to the inlet gas mixture. Notice the larger gaps between crystallites compared to Fig. 3.

Thus far, self-mated pin-on-disk sliding wear tests have been carried out with RBSN, HSN, and SSC materials. The tests were performed at a velocity of 0.1 m/s with a 1 kg static load in air at room temperature and a total sliding distance of 1000 meters. Table 4 summarizes the friction results obtained. The breakaway friction coefficients were measured prior to wear testing on surfaces polished to a 1 μm finish. The values reported for the kinetic friction coefficients are the steady state values obtained after 500 meters of sliding. The microstructure, fracture surface, and reactions at the wear interface are currently being studied to provide more insight into the wear behavior of these ceramics.

Table 4. Breakaway and kinetic friction coefficients for uncoated RBSN, HSN, and SSC.

Pin	Disk	μ_B	μ_K
RBSN	RBSN	0.1	0.5 - 0.8
HSN	HSN	0.3	0.8
SSC	SSC	0.1	0.3

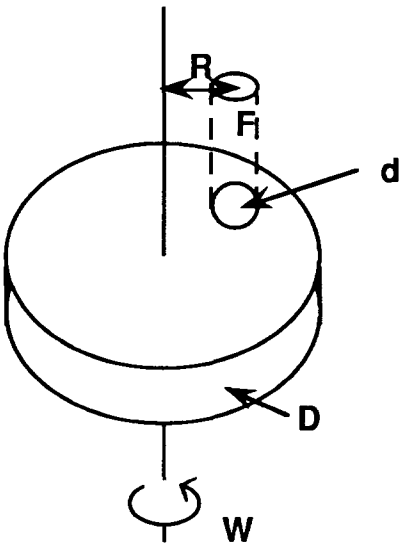

Figure 5. Schematic of pin-on-disk wear test system. F is the normal force on the pin, d is the pin diameter, D is the disk diameter, R is the wear track radius, and W is the rotation velocity of the disk.

Status of Milestones

Milestone	Due	Status
Microstructural evaluation of the Al_2O_3+ZrO_2 composite layer.	12/89	Completed
Studies of first generation coating configuration to determine cause of failure during oxidation tests at 1200°C and 1375°C.	03/90	Completed
Modification of coating configuration to	09/90	On schedule

improve oxidation resistance at ≥1200°C. Develop CVD process and coat samples for testing the following modifications: a) add Al_2O_3 layer between AlN and Al_2O_3+ZrO_2 composite layer; b) increase thickness of Al_2O_3+ZrO_2 composite layer to 10μm.		
Feasibility study of measuring friction coefficient and contact stress damage using conventional pin-on-disk or ball-on-disk wear tests.	12/90	On schedule
Performance tests of modified coating configuration including: i) 500 hour oxidation ii) thermal shock, and iii) flexure strength. Each test will be done on coated and uncoated samples. All tests will be conducted at room temperature, 1000°C, 1200°C, and 1375°C.	03/91	On schedule
Test feasibility of coating a commercial part or equivalent.	06/91	On schedule
Submit draft of final report covering Phase II results.	09/91	On schedule

Publications

None.

References

1. A. D. Katnani and K. I. Papathomas, "Kinetics and Initial Stages of Oxidation of Aluminum Nitride: Thermogravimetric Analysis and X-ray Photoelectron Spectroscopy Study", *J. Vac. Sci. Technol. A*, 5(4), 1335 (1987).

2. V. A. Lavrenko and A. F. Alexeev, "Oxidation of Sintered AlN," *Cer. Intl.*, 9(3), 80 (1983).

3. P. Boch, J. C. Glandus, J. Jarrige, J. P. Lecompte, and J. Mexmain, "Sintering, Oxidation and Mechanical Properties of Hot Pressed Aluminum Nitride," *Cer. Intl.*, 8(1), 34 (1982).

4. A. W. Ruff and S. Jahanmir, "Measurements of Tribological Behavior of Advanced Materials: Summary of U.S. Results on VAMAS Round-Robin No. 2," NISTIR 89-4170, U.S. Dept. of Commerce, Gaithersburg, MD, 1989.

Wear Resistant Coatings

C. D. Weiss (Caterpillar, Inc.)

Objective/Scope

The goal of this technical program is to develop wear-resistant coatings for piston ring and cylinder liner components for low heat-loss diesel engines.

Wear resistant coatings will be applied to metallic substrates using plasma spraying, vapor deposition (CVD/PVD), and enameling coating processes. First, the adherence of each coating for each coating process to metallic substrate will be optimized. Methods which can be used for improving the adherence of these coatings include development of unique substrate preparation methods before application of the coating, grading the coating composition to match thermal expansion, compositional changes, laser or electron beam fusing and/or optimization of coating thickness. Once the adherence of each coating system is optimized, each coating will be screened for friction and wear under lubricated conditions. Coatings which show promise after this initial screening will be further optimized to meet the friction and wear requirements. Then the optimized coating systems will be fully characterized for adherence, oxidation resistance, uniformity, thermal shock resistance, as well as friction and wear.

Selection of the most promising coatings and coating processes will be made after the characterization task. Criteria for selection will include not only performance (i.e., wear, adhesion, friction coefficient, thermal shock resistance and thermal stability) but manufacturability/cost factors as well. Using these criteria, a coating system having acceptable cost/benefit relationships will be selected.

Technical progress

Using the preliminary pin-on-disk testing of the ten candidate plasma spray, five chemical or physical vapor deposited, and the enamel coatings selected in Task 1 as a guide, a plasma sprayed chrome oxide-silica as well as a plasma sprayed high carbon iron-Mo composite were selected as potential candidates for both cylinder liner and piston ring wear resistant coatings. Also identified as potential wear resistant piston ring coatings were the plasma sprayed, self-lubricating PS 212 and the mid-temperature chemical vapor deposited Ti(C,N). Finally, a chemical vapor deposited chrome nitride was identified as a potential wear resistant cylinder liner coating.

Further screening of these selected coatings was accomplished using the Hohman A-6 friction and wear test machine. The following material pairs were evaluated on the Hohman A-6, lubricated, at 350°C:

1. Plasma sprayed high carbon iron-Mo composite rub shoes against a chemical vapor deposited CrN disk,

2. Plasma sprayed chrome oxide-silica composite rub shoes against a chemical vapor deposited CrN disk,

3. Plasma sprayed PS 212 rub shoes against chemical vapor deposited CrN disk,

4. Mid-temperature chemical vapor deposited Ti(C,N) rub shoes against a chemical vapor deposited CrN disk,

5. Plasma sprayed high carbon iron-Mo composite rub shoes against a plasma sprayed chrome oxide-silica disk,

6. Plasma sprayed chrome oxide-silica rub shoes against a plasma sprayed chrome oxide-silica disk,

7. Plasma sprayed PS 212 rub shoes against plasma sprayed chrome oxide-silica disk,

8. Mid-temperature chemical vapor deposited Ti(C,N) rub shoes against a plasma sprayed chrome oxide-silica disk.

The results of this Hohman A-6 friction and wear testing are contained in Tables 1 and 2.

Wear testing plasma sprayed chrome oxide-silica, plasma sprayed PS 212 or mid-temperature CVD Ti(C,N) rub shoes against a CVD CrN disk at 350°C, lubricated, produced very high friction coefficients (0.17-0.21). The high friction coefficients caused high CrN wear rates and for this reason, only one of these material pairs was tested for over 30 minutes before the wear track had completely worn through the 2 to 3 micron thick CrN coating.

The combination of plasma sprayed high carbon iron-Mo rub shoes running against CVD CrN disks produced mixed results. In two of the tests, this material pair recorded low friction coefficients and low shoe wear and medium-to-low disk wear. High disk wear was recorded during the two other tests with this material pair. Scanning electron photomicrographs of the surfaces of the CrN disks revealed that the CrN coating was not uniformly applied to the surface each disk. The disks which exhibited low friction and wear rates all had dense, uniformly applied CrN coatings. On the other hand, uncoated regions were observed on the CrN disks which exhibited the high wear.

The friction and wear testing showed that when a dense, uniform CrN coating is achieved, the material pair of high carbon iron-Mo running against CrN will meet both the friction and wear rate goals of this program. However, the CrN coating was applied to only 2-3 micron thickness. The longest test

time recorded for this material pair was 680 minutes before a wear track was completely worn through the coating. Thus, a 2-3 micron thick CrN will not meet a 10,000 hour durability goal. Additional CrN specimens, coated with a modified CVD process to produce denser, more uniform coatings will be obtained. These specimens will also have a 5 micron thick CrN coating. These specimens will be used to obtain a wear curve for the CrN. This wear curve will be used to determine the minimum CrN coating thickness required to meet the 10,000 hour durability goal.

Table 2 contains the results of wear testing the plasma sprayed high carbon iron-Mo, chrome oxide-silica composite, PS 212 and the mid-temperature CVD Ti(C,N) rub shoes against plasma sprayed chrome oxide-silica composite disks. Testing chrome oxide-silica or the Ti(C,N) shoes against the chrome oxide-silica disks produced high friction coefficients and medium-to-high disk wear. Again the reason for the high disk wear was the high friction coefficient. Low friction coefficients, and low shoe wear along with low-to-medium disk wear was recorded when running PS 212 shoes against a chrome oxide-silica disk.

Excellent results were obtained running high carbon iron-Mo rub shoes against the chrome oxide-silica disk. One test recorded both low friction and low disk and shoe wear and this test ran for 1455 minutes before the wear track wore through the chrome oxide-silica coating on the disk. This material pair met the program goals with respect to both friction and wear. Additional testing will be performed on this material pair to more completely define the wear curve.

Work on Task 1A was initiated. The purpose of this task is to develop enameling and sol-gel techniques for application of an adherent, wear resistant, glassy coating for cylinder liner applications. Enameling techniques will involve slurry spraying a glass frit onto cast iron, drying the coating to remove the water, and then firing at temperatures up to 800°C to melt and bond the enamel coating to the cast iron. Sol-gel techniques also use water-based solutions. These solutions will be sprayed onto the cast iron, dried and cured at 350°C. The 350°C curing temperature should minimize distortion of the cylinder liner.

The approach used in Task 1A differs from the previous enamel development program in that solid lubricants will be incorporated into the glassy phase composition to first reduce the coefficient of friction values of the glassy phase below 0.02. Once the coefficient of friction is optimized, wear particles will be added to the composition, if needed, to improve the wear properties of the coating.

The work performed in Task 1A first centered around developing robotic spray parameters for both the enamel and sol-gel compositions. Enamel and sol-gel coatings have been

successfully sprayed using robotic techniques onto 25X25 mm coupons. A successful drying and firing cycle has been developed for the enamel composition. Difficulties were encountered in obtaining a drying cycle for the sol-gel coating which would consistently produce a crack and blister free coating.

Four Falex disks were slurry sprayed with the enamel composition. These specimens will be used to obtain pin-on-disk baseline wear and friction data for the enamel composition. The enamel will be evaluated running against both ceramic and metallic counterfaces.

Table 1
Hohman A-6 Friction and Wear Test Results
Chemical Vapor Deposited Chrome Nitride Disks

Shoes	Test Time (minutes)	Coeff. of Friction	Wear Shoe	Wear Disk
Plasma sprayed high carbon iron-Mo	680	0.14	low	med
	425	0.1-.16	low	low
	<5	0.11	low	high
	<5	0.20	low	high
Plasma sprayed PS 212	120	0.21	low	high
	12	---	low	high
Plasma sprayed chrome oxide-silica	13	0.17	med.	high
	14	0.20	low	high
Mid-temperature chemical vapor deposited Ti(C,N)	11	0.17	med.	high
	30	---	low	high

Table 2
Hohman A-6 Friction and Wear Test Results
Plasma Sprayed Chrome Oxide-Silica Composite Disks

Shoe	Test Time (minutes)	Coeff. of Friction	Wear Shoe	Wear Disk
Plasma sprayed high carbon iron-Mo	370	0.18	low	med.
	1455	0.01-.1	low	low
Plasma sprayed chrome oxide-silica composite	120	0.17	low	med.
Plasma sprayed PS 212	480	0.04	low	low-med
Mid-temperature chemical vapor deposited Ti(C,N)	120	0.19	low	high

Status of milestones

MS1 Manufacture of 400 adherence specimens--complete
MS2 Manufacture friction and wear test specimens--complete
MS3 Identify a minimum of 12 adherent coating systems--complete
MS4 Identify 12 coating systems for friction and wear optimization--complete
MS6 Manufacture simulated engine component specimens--complete

Publications

M. H. Haselkorn, "Wear Resistant Ceramic Coatings for Diesel Engine Components", was presented at the 27th Automotive Technology Development Contractors' Coordination Meeting, October 24, 1989, Dearborn, Mi.

Development of Wear Resistant Ceramic Coatings for Diesel Engine Components

M.G.S. Naylor
Cummins Engine Company, Inc.

Objective/Scope

The objective of this program is to develop advanced wear resistant coatings for in-cylinder components for future, low heat rejection diesel engines. Coatings and substrates (for piston rings and cylinder liners) are to be developed to meet the following requirements:

1. low wear (as measured in laboratory rig tests at ambient temperature and 350°C). Wear coefficients in the range $5x10^{-12}$ to $5x10^{-11}$ $mm^3/mm/N$ are targeted (at 350°C).
2. low friction coefficients when tested under boundary lubricated conditions (target 0.1) and unlubricated conditions (target 0.2) at ambient temperature and 350°C.
3. good thermal shock resistance.
4. high adherence and compatibility with substrate materials up to 650°C
5. high uniformity and reproducibility

Technical Progress

Overview of Coating Development

Table 1 lists the wear coatings which have been under evaluation to this point in the program. Wear testing has been completed for almost all the air plasma sprayed (APS) chromium oxides, some of the high velocity oxy-fuel (HVOF) thermal sprayed materials and the slurry-sprayed silica-chromia-alumina (SCA). Microstructural characterization has been completed for all the coatings which have been wear tested.

Bond strengths have been measured for the APS chromium oxides, and a study of the effects of various spray parameters (powder composition, powder feed gas, powder feed rate, spray velocity and gun/nozzle selection) has been completed (see previous reports). Property measurements (microhardness, tensile strength and elastic modulus at room temperature and 320°C, thermal expansion coefficient from 25 - 540°C, and thermal diffusivity) and microstructural characterization of the UTRC coatings have been completed.

Attempts have been made to produce hard, dense boron carbide coatings by air plasma and low pressure plasma spray (LPPS) processes, but all techniques have so far proved unsuccessful.

A program has been initiated at Northwestern University Basic Industry Research Laboratory (BIRL) to develop laser processing techniques for ceramic and cermet coatings, and to develop APS and HVOF techniques for spraying a variety of chromium oxide and molybdenum metal based systems.

Coating	*Substrate*	*Supplier*
PLASMA SPRAYED		
APS UCAR Cr_2O_3	HK40 Stainless	APS Materials
APS Metco 106FP Cr_2O_3 - 2% SiO_2 - 2% other oxides	422 Stainless	UTRC
APS Metco 136 Cr_2O_3 - 5% SiO_2 - 3% TiO_2 (A)	HK40 Stainless	APS Materials
APS Metco 136 Cr_2O_3 - 5% SiO_2 - 3% TiO_2 (B)	HK40 Stainless	Boyd Machine
APS Cr_2O_3 - 15% Al_2O_3 - 4% SiO_2 - 3% TiO_2	HK40 Stainless	APS Materials
APS Cr_2O_3 - 33% Stellite 6 - 3% SiO_2 - 2% TiO_2	HK40 Stainless	APS Materials
APS Cr_2O_3 - 8% SiO_2 - 3% TiO_2	HK40 Stainless	APS Materials
APS Metco 143 ZrO_2 - 18% TiO_2 - 10% Y_2O_3	422 Stainless	UTRC
APS Armacor M	HK40 Stainless	APS Materials
APS Armacor T	HK40 Stainless	APS Materials
VPS Boron Carbide	HK40 Stainless	APS Materials
APS Cr_2O_3 and Cr_2O_3 - 50% Al_2O_3	422 Stainless	BIRL
APS Mo-Ni and Mo-MoO_2	422 Stainless	BIRL
HIGH VELOCITY		
WC - 12% Co	HK40 Stainless	Boyd Machine
Cr_3C_2-WC-NiCrCo	HK40 Stainless	Boyd Machine
Diamalloy 3007 Cr_3C_2-NiCr	422 Stainless	UTRC
Diamalloy 2001 NiCrBSi	422 Stainless	UTRC
Cr_2O_3 and Cr_2O_3 - 50% Al_2O_3	422 Stainless	BIRL
Mo-Ni and Mo-MoO_2	422 Stainless	BIRL
SLURRY-SPRAYED		
SiO_2 - Cr_2O_3 - Al_2O_3	Pearlitic Grey Cast Iron	Cummins
ION NITRIDED	Type 1 Niresist H13 Tool Steel	Cummins

Table 1. Ring and liner coating materials under evaluation.

Coating Development at UTRC, East Hartford CT

Thermal and mechanical property measurements of High Velocity Oxy-Fuel (HVOF) sprayed Cr_3C_2-NiCr and NiCrBSi coatings and advanced plasma sprayed zirconia-titania-yttria (ZTY) coatings have been completed (Figures 1 to 6). Properties were measured on free-standing coating materials sprayed to 0.1 inch thickness and removed from the substrate. Attempts were also made to produce thick chromium oxide coatings for evaluation, with no success.

All three materials, plus a plasma sprayed Cr_2O_3, have been deposited onto test substrates (422 stainless steel) and submitted to Cummins for finish grinding and wear evaluation. The same coatings were also sprayed to 0.010 in. thickness onto four sets of Chevrolet automobile piston rings to demonstrate the feasibility of applying the above coating procedures to piston

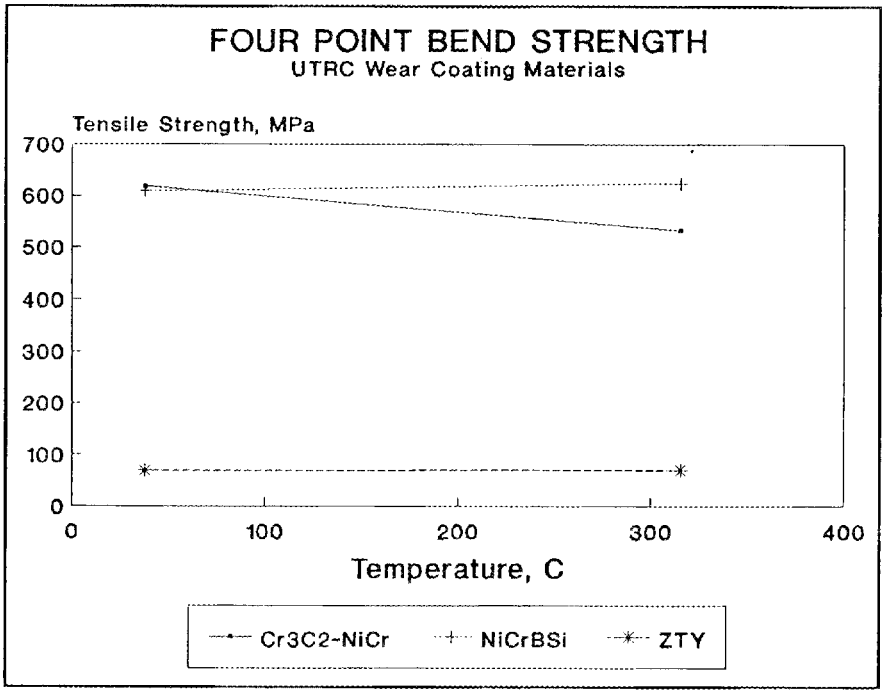

Figure 1. *Variation of four point bend strength with temperature for UTRC coatings.*

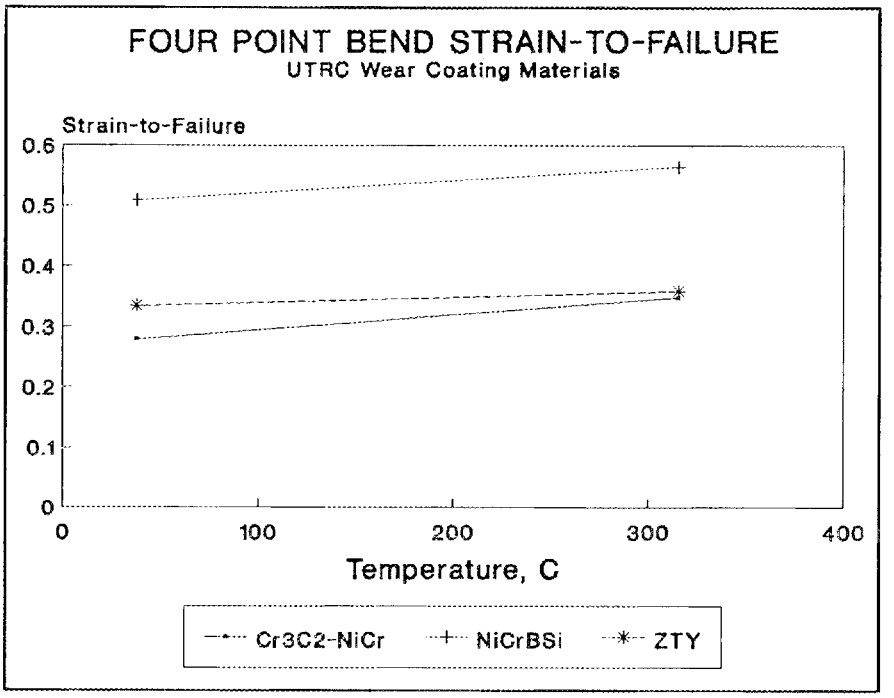

Figure 2. *Variation of strain-to-failure with temperature for UTRC coatings.*

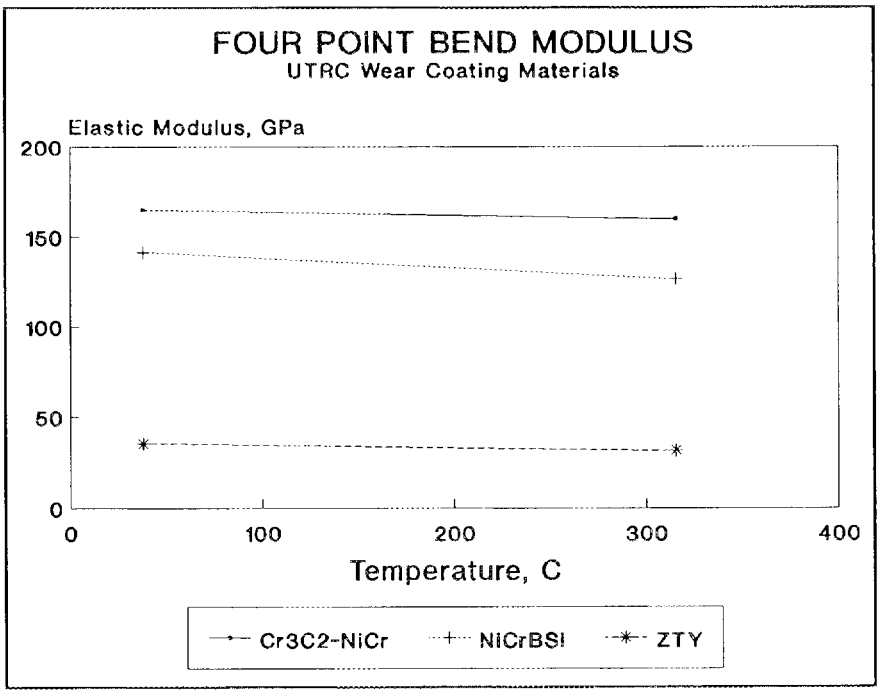

Figure 3. *Variation of four point bend modulus with temperature for UTRC coatings.*

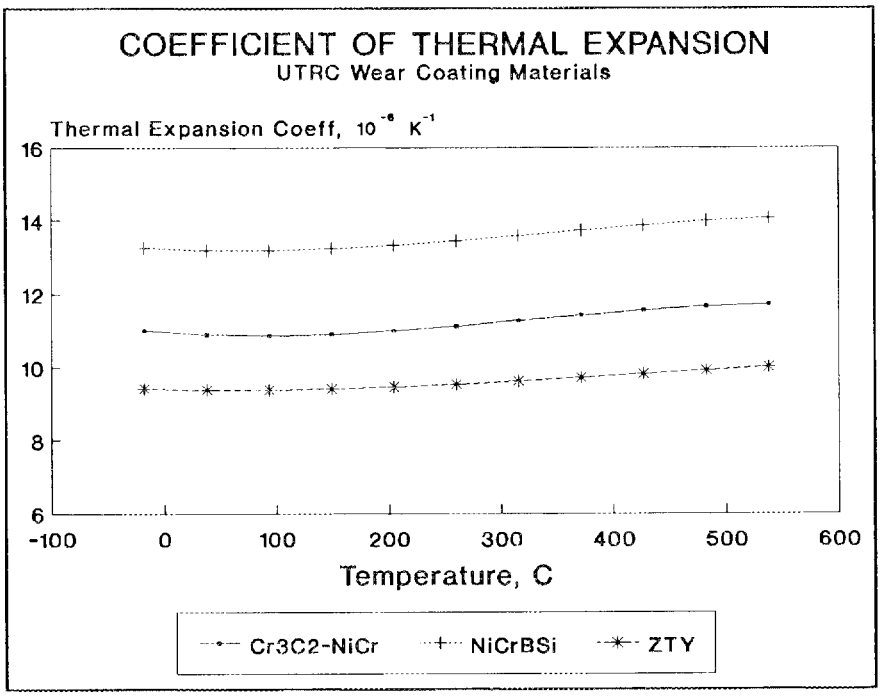

Figure 4. *Variation of thermal expansion with temperature for UTRC coatings.*

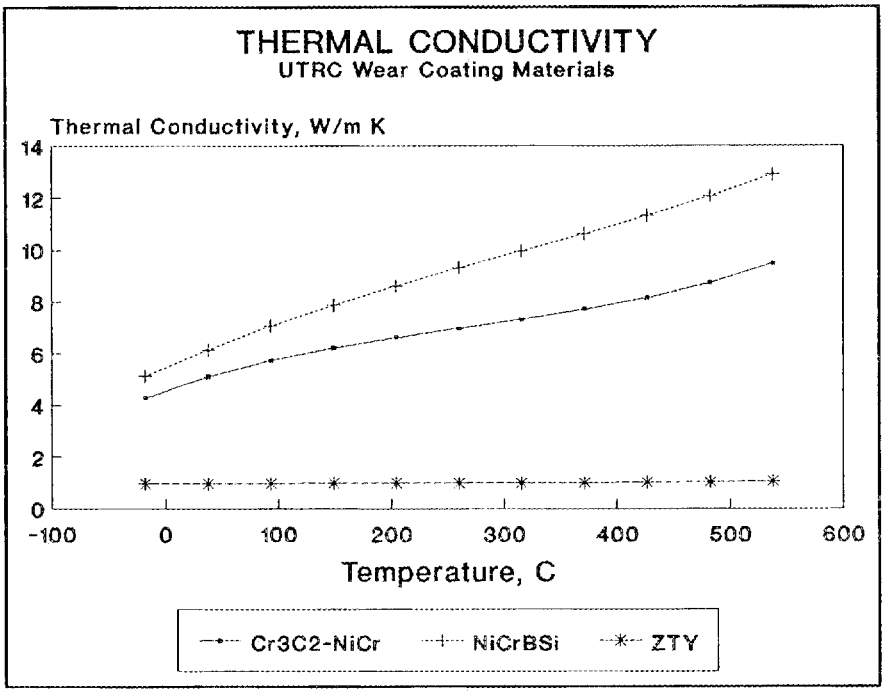

Figure 5. *Variation of thermal conductivity with temperature for UTRC coatings.*

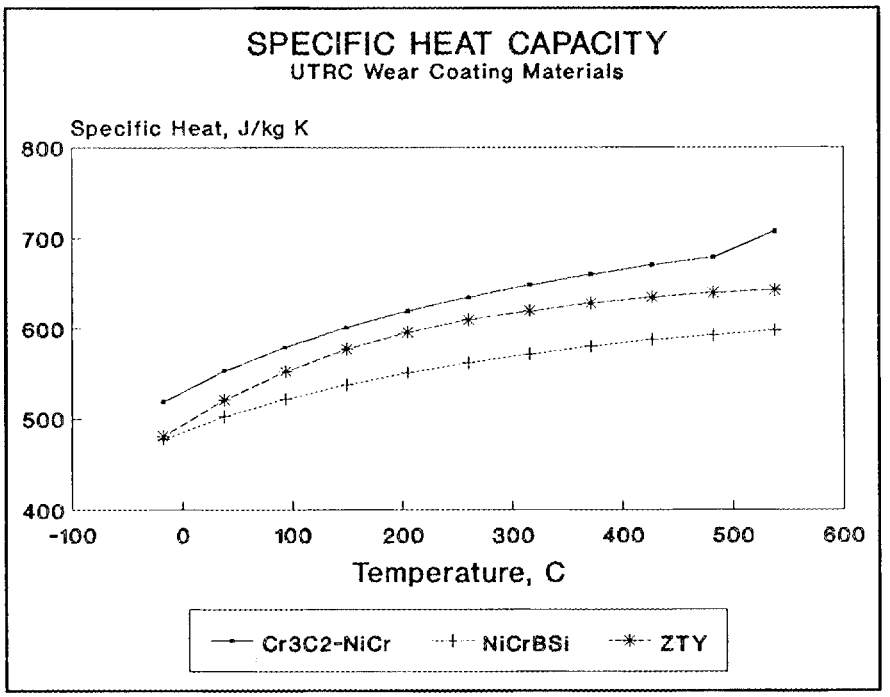

Figure 6. *Variation of specific heat capacity with temperature for UTRC coatings.*

ring geometries. The HVOF samples were ground to a surface finish of 15 - 16 microinches RA, and exhibited no cracking or chipping. The surface finish of the plasma sprayed ceramic materials was in the range 18 - 22 microinches RA after grinding. Approximately 9% of the ZTY and 4% of the Cr_2O_3 samples were found to have cracked or chipped to some degree during grinding, ranging from complete de-bond to small corner chips. Bonding of the ceramic materials to the substrate (422 stainless steel) was generally poor, as revealed by light microscopy of the interface, but may be improved by the use of a bond coat (none was used for these samples). The HVOF coatings exhibited excellent bonding with no bond coat. Coating microstructures have been characterized by light microscopy and scanning electron microscopy (SEM), as described below.

The Cr_3C_2-NiCr material was found to comprise an even distribution of fine (approximately 8 μm diameter) chromium carbide particles in a NiCr matrix, with little carbide solutionizing and very low porosity levels (Figure 7).

The NiCrBSi material showed greater porosity levels, primarily due to incorporation of a substantial number of unmelted powder particles (figure 8). Porosity/pullout occurred within the unmelted particles and at the interface between unmelted and melted material. The microstructure showed an extremely fine dispersion of sub-micron sized low atomic number particles (presumably carbides or borides) in a metallic matrix.

The ZTY material was less porous than many chromium oxide materials, but showed a "brick wall" type of crack distribution (Figure 9). A small amount of unmelted powder was present in the coating, associated with large pores. The backscattered electron signal from this material showed substantial variations in atomic number contrast from splat to splat. A series of 10gf Knoop microhardness indentations showed an extreme variation in hardness (from 390 to 1180 $kgfmm^{-2}$) across the microstructure. This variation is not thought to have been caused solely by interactions with cracks/pores, but may reflect a high degree of compositional inhomogeneity and/or the presence of amorphous material within the coating. This will be investigated further by means of energy dispersive X-ray spectrometry and X-ray diffraction.

The chromium oxide material showed high porosity levels (approximately 20%) with a large amount of "inter-splat" cracking/voiding (Figure 10). Again, the "brick wall" crack/void distribution morphology was evident.

Coating Development at APS Materials, Dayton OH

APS Materials have completed a Phase 1 effort to develop air plasma sprayed chromium oxide coatings. All the candidate materials have been delivered to Cummins, and wear evaluations are largely complete (see previous reports). Additional coatings tested during this reporting period included the Cr_2O_3 - 8% SiO_2 - 3% TiO_2 and Cr_2O_3 - 33% Stellite 6 materials. The Cr_2O_3 - 8% SiO_2 - 3% TiO_2 microstructure was similar to the Metco 136 Cr_2O_3 studied previously, and contained fewer microcracks than the UTRC material described above (Figure 11). The Cr_2O_3 - 33% Stellite 6 material contained discrete splats of Cr_2O_3 and Stellite 6, both phases having been melted in the plasma. Bonding between the two phases appeared to be good, with very little inter-splat cracking/voiding in this material (Figure 12).

Work is in progress to produce WC-Co coatings from the same powder by three different spray processes: air plasma, low pressure plasma and high velocity oxy-fuel ("Jetkote" system). The objective is to characterize microstructures and obtain correlations with wear test results, and to determine the optimum process for piston ring applications. Previous testing of a WC - 12% Co "Jetkote" material (from a different supplier) showed excellent wear results, including low wear of pearlitic grey iron liner counterfaces, but the coating was not well bonded to the substrate and was subject to high temperature cracking.

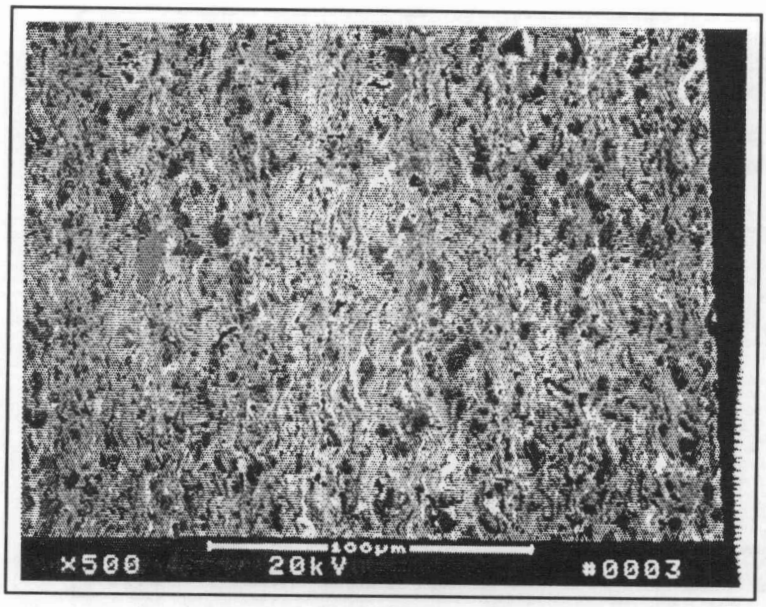

Figure 7. *Microstructure of HVOF Cr_3C_2-NiCr coating.*

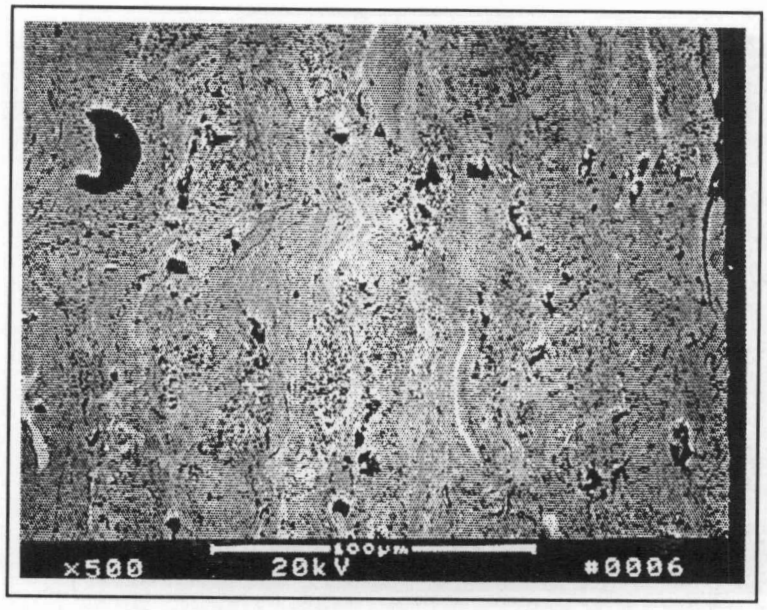

Figure 8. *Microstructure of HVOF NiCrBSi coating.*

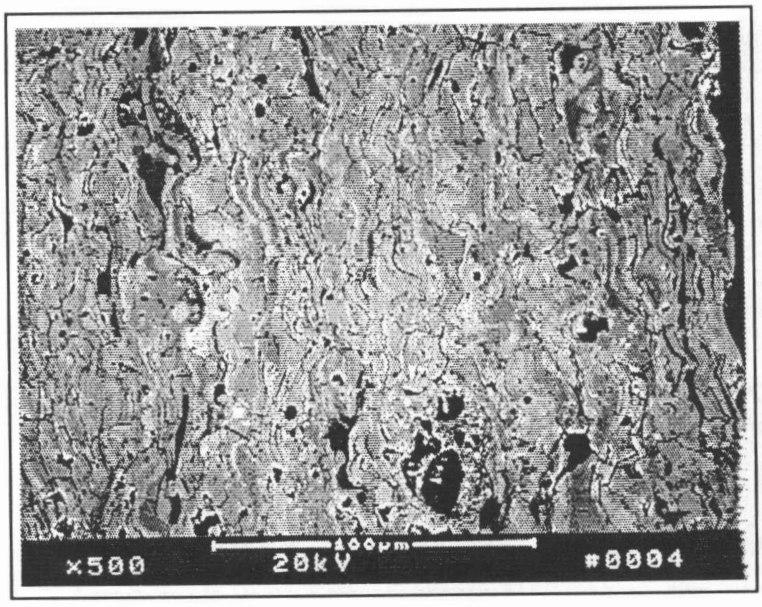

Figure 9. *Microstructure of APS ZrO_2 - TiO_2 - Y_2O_3 coating.*

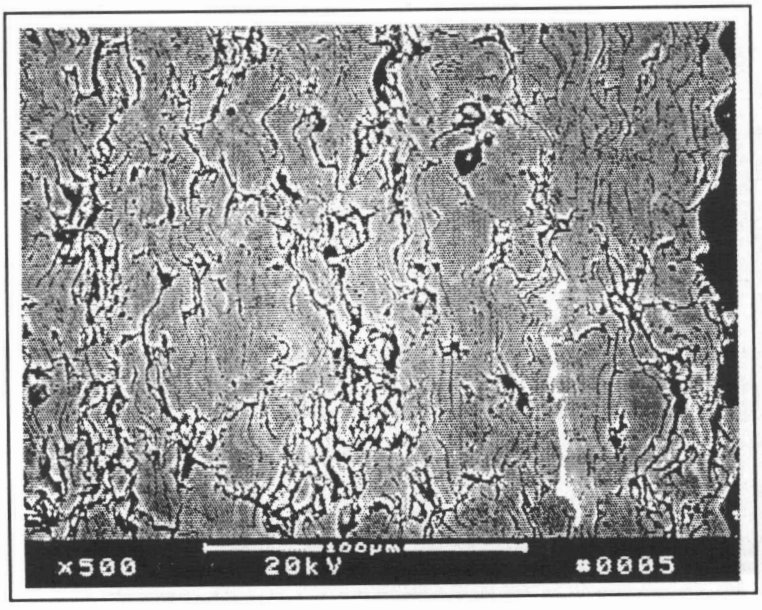

Figure 10. *Microstructure of UTRC Cr_2O_3 coating.*

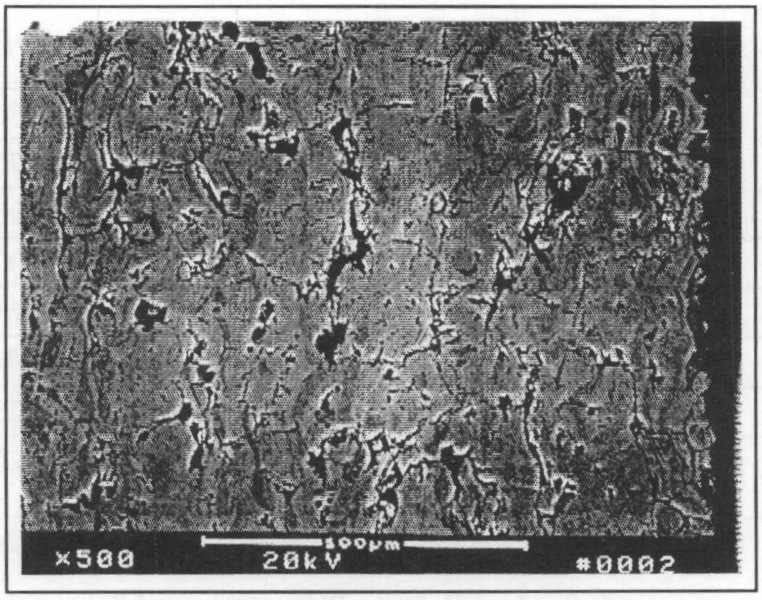

Figure 11. Microstructure of APS Cr_2O_3 - 8% SiO_2 - 3% TiO_2 coating.

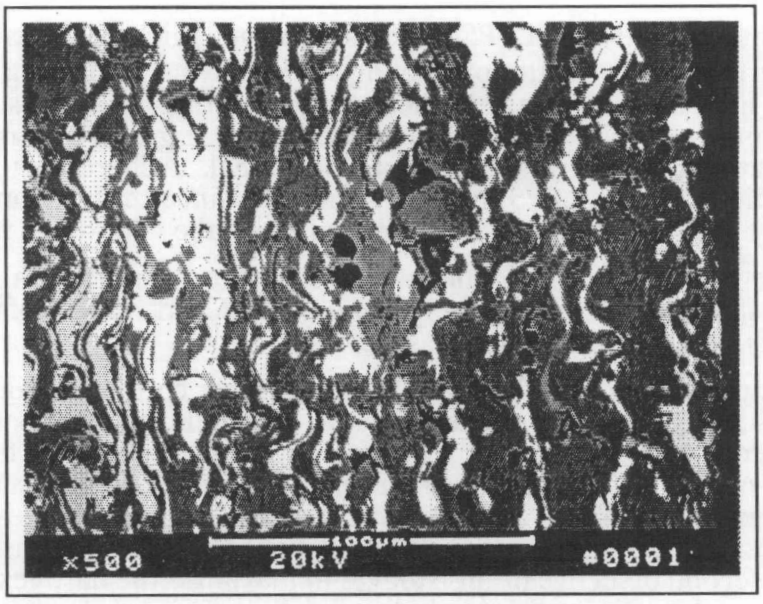

Figure 12. Microstructure of APS Cr_2O_3 - 33% Stellite 6 coating.

Test	Pressure Torr	Arc CFH	Mix CFH	Powder CFH	Hopper RPM	Volts	Amps	Anode
1	20	140	80-He	25	6	48	1550	115
2	20	120	12-H2	25	2	51	1475	115
3	280	120	80-He	25	2	44	1600	115
4	10	120	60-He	25	2	44	1600	115
5	10	120	80-He	20	2	46	1625	114
6	20	120	15-H2	20	4.6	48	1500	114
7	50	120	15-H2	25	3	46	1525	093
8	20	120	80-He 15-H2	25	2	52	1525	093

Table 2. Plasma spray parameters for Low Pressure Plasma Sprayed Boron Carbide tests. For each test, 4 coupons were placed at distances of 10, 19, 28 and 34 inches. No deposition occurred at any setting.
The 115 and 093 anodes are 20° rear injection; the 114 is a straight injection anode.

One difficulty encountered with the LPPS process was that thick coatings (greater than approximately 150 μm) tended to shatter on cooling after spraying, indicating high substrate temperatures and/or high residual stress in the coating. In this case, the substrate was a castable austenitic stainless steel (HK40), which would have a greater thermal expansion mismatch with the coating than 422 martensitic stainless steel. Adherence to the substrate was found to be excellent for the LPPS material, however, since tensile bond strengths in excess of 9500 psi were measured for coatings which survived the cool-down process.

Extensive efforts have been made to produce ultra-hard boron carbide coatings using low pressure and inert gas shrouded air plasma spray techniques. A wide variety of test conditions were utilized (Table 2), but no deposition occurred.

Two grades of Ferrotic powders, "CM" (45% TiC with a high chromium tool steel matrix phase) and "CS-40" (45% TiC with a martensitic stainless steel matrix phase) have been procured, and work is underway to establish the optimum spray parameters for these materials. A third material, "HT-6A" (35% TiC in an age-hardenable nickel base matrix) has also been ordered. The Ferrotic materials contain very smooth, rounded carbide particles, which should reduce the abrasiveness of the coating when sliding against pearlitic grey cast iron cylinder liner counterfaces. A second objective of this study is to maximize the hardness of the matrix phase, in order to reduce the relief polish (carbide particles protruding from a softer matrix) invariably generated with a cemented carbide during sliding wear. This will be attempted by heat treatment (including laser processing) of the coating and by plasma spray processes (e.g. low pressure spraying) which maximize carbon retention in the (steel) matrix phase.

Test Schedule for Each Coating:
Fresh CE/SF 15W40 mineral oil based lubricant at 200°C **Fresh** CE/SF 15W40 mineral oil based lubricant at 350°C **Engine-tested** CE/SF 15W40 mineral oil based lubricant at 200°C **Unlubricated**, 200°C
Test Conditions:
225 N on a 7.5 mm wide sample (30 N/mm) "Ring" sample has cylindrical radius of curvature of 50 mm "Liner" sample is flat 20 Hz frequency 5 mm stroke Lubricated tests: 6 hrs with 1 drop oil every 10 seconds Unlubricated tests: 10 - 30 minutes.

Table 3. Wear test conditions.

Coating Development at Northwestern University Basic Industry Research Laboratory (BIRL)

422 substrate materials have been shipped to BIRL for coating development. Four coatings will be sprayed by both air plasma and HVOF methods: chromium oxide, 50% chromium oxide - 50% aluminium oxide (solid solution), Mo-Ni and Mo-MoO_2. Coating parameters are to be optimized and microstructures characterized. Following this, laser processing techniques will be developed for selected coating systems (including candidates from the work at UTRC and APS Materials). For ceramic coatings, laser glazing provides the opportunity to produce smoother, denser, more homogeneous surface layers with compressive surface stresses. For metallic and cermet systems, laser processing is a method of increasing hardness or causing non-equilibrium reactions to occur which may create novel microstructures.

The first phase of effort, optimizing APS processes for the four coatings mentioned above, has been completed, and samples for wear testing have been sprayed. Microstructural characterization of the coatings is underway.

Wear Testing

Wear tests have been performed on a wide variety of piston ring/cylinder liner coating combinations, using a Cameron Plint wear tester. The test conditions, which were chosen to represent the ring:liner engine environment close to the top ring reversal position, are detailed in Table 3. Wear tests were performed using a fresh commercial CE/SF quality 15W40 mineral oil based lubricant at two temperatures, and with the same oil taken from an engine test which produced severe oil degradation, to simulate the chemical environment of the engine more closely. In addition, tests were run with no lubrication, in order to rank the sliding wear properties of the different materials under "scuffing" conditions. A material with good scuff resistance is desirable in case of temporary loss of oil film in the engine (on start-up or under temporary conditions of extreme hot running, for example). Under the loading conditions at top ring reversal, it is extremely unlikely that sufficiently low wear rates can be obtained with any coating for extended engine operation without lubrication.

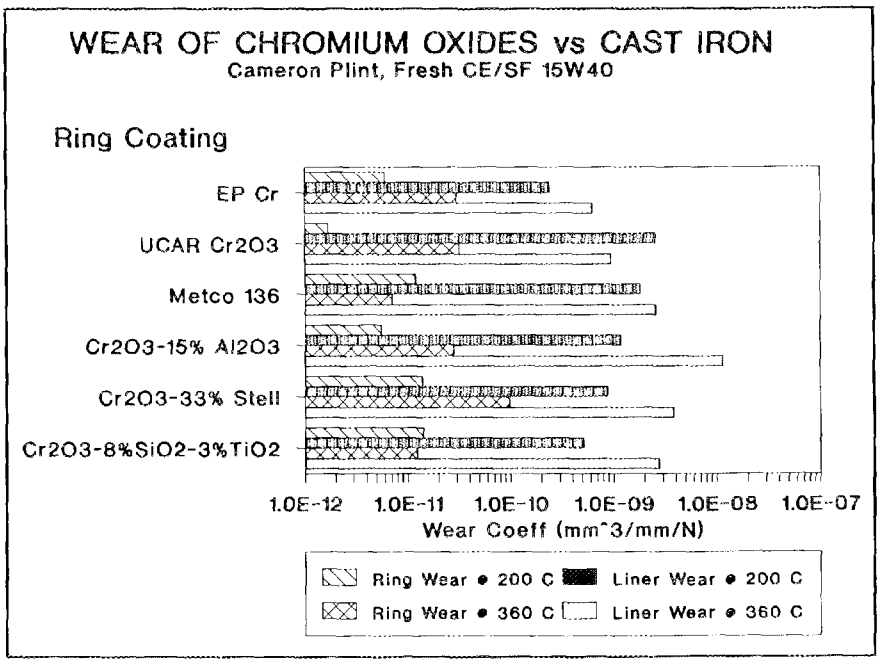

Figure 13. *Wear comparison of APS chromium oxide coatings and electroplated chromium sliding against grey iron liners at 200 and 350°C, lubricated with fresh CE/SF 15W40 oil.*

APS Chromium Oxide Ring Coatings vs Pearlitic Grey Cast Iron Liners

A variety of chromium oxide based materials has been evaluated with the conventional grey iron liner counterface (Figure 13). In most cases, ring wear was lower than for electroplated chromium, but liner wear was higher. The increase in liner wear is thought to have been caused by abrasion by rough edges in the coating. Before-test surface roughness values for the coatings were in the range 0.25 - 0.5 μm (measured parallel to the sliding direction, i.e. parallel to the grinding marks on the machined surface). Within experimental scatter, all the chromium oxides showed similar wear coefficients in the fresh oil tests (Figure 13).

Wear tests using degraded, heavily soot-loaded oil from an engine test showed a considerable increase in ring and liner wear rates compared to tests in fresh oil for the conventional electroplated chromium/grey iron system (Figure 14). By comparison, the chromium oxide/cast iron tests generally showed little effect of lubricant soot (Figure 14), which suggests that the advantages of using chromium oxide ring coatings over the conventional ring material becomes more pronounced as the oil degrades in the engine.

Chromium oxide wear data for unlubricated tests against grey iron liners are shown in Figure 15. The Cr_2O_3 - 33% Stellite 6 material showed the lowest wear coefficient in these tests, the other materials having wear coefficients equal to or greater than electroplated chromium. Liner wear rates were almost independent of ring material for these tests. Wear mechanisms identified for this type of test include oxidation and abrasion of the liner, formation of thick iron oxide transfer layers on the ring coating and inter-splat fracture in the coatings. The effect of the Stellite 6 phase in reducing wear of chromium oxide coatings is under investigation.

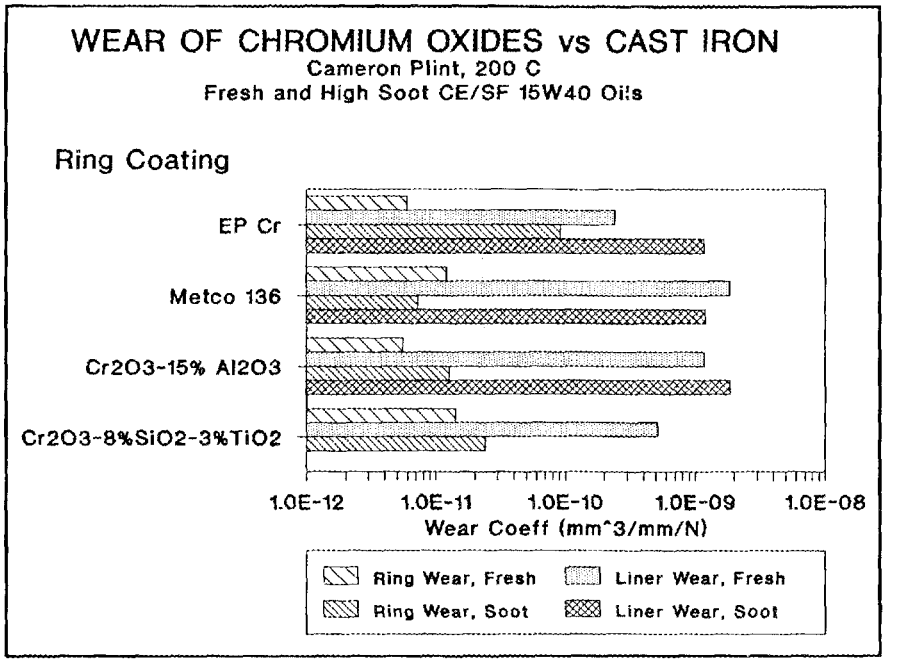

Figure 14. *Wear comparison of APS chromium oxide coatings and electroplated chromium sliding against grey iron liners at 200°C, lubricated with high soot CE/SF 15W40 oil.*

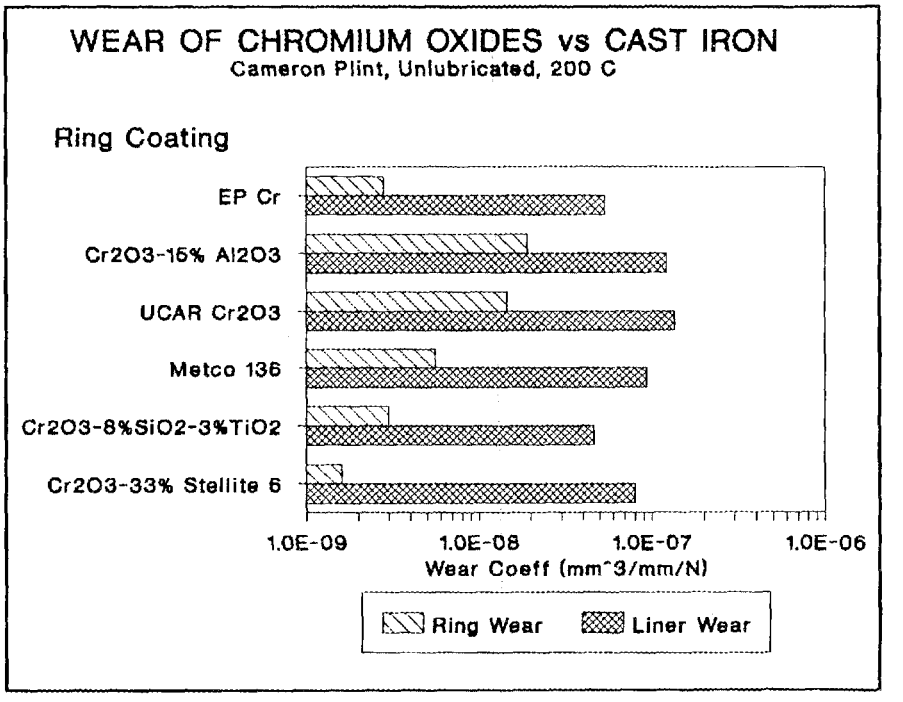

Figure 15. *Wear comparison of APS chromium oxide coatings and electroplated chromium sliding against grey iron liners at 200°C with no lubricant.*

Summary of Wear Results for All Coatings

Results for fresh oil (200°C), fresh oil (350°C), high-soot oil (200°C) and unlubricated (200°C) wear tests are shown in Figures 16, 17, 18 and 19 respectively. For reference, microhardness values for each coating are listed in Table 4.

In fresh oil (Figures 16 and 17), the wear ranking of the coatings was the same at both test temperatures, with approximately two orders of magnitude difference between the best (a HVOF WC - 12% Co) and the worst (APS ZrO_2 - TiO_2 - Y_2O_3). For these comparisons, Cr_2O_3 wear coefficients were obtained by taking the mean of all the Cr_2O_3-based materials evaluated. Of the materials tested, the cemented carbides appeared to have the best wear properties.

The high soot oil tests were conducted with a 4.5% soot oil from an engine test, until supplies of this oil were exhausted, when a 3.3% soot oil was used. Various tests established that the two oils gave similar wear coefficients. Comparing Figures 16 and 18, the high soot oils were found to cause a dramatic increase in wear of the metallic materials investigated (electroplated chromium and Armacor M, a proprietary iron-based material). Ceramic and cermet materials were found to be relatively inert to high soot concentrations. Again, the HVOF WC - Co had the lowest wear rate of the materials tested.

Unlubricated tests again showed very low wear rates for the HVOF WC-Co, although the grey iron liner material was severely abraded due to coating fracture (Figure 19). The Armacor M material showed much better wear properties in comparison to electroplated chromium and Cr_2O_3 in the dry tests.

Selection of coatings for engine components should be made after determining which properties are most important for the application (e.g. high temperature lubricated wear resistance, scuff resistance, resistance to degraded oils, etc.) and after assessing the relative importance of each surface. For example, maintaining low liner wear rates might be considered as important as low ring face wear in some applications.

Characterization of Wear Surfaces

Characterization of wear surfaces for some of the materials tested during the current reporting period is described below. Wear morphologies for many of the Cr_2O_3-based materials and the HVOF WC-Co coating have been characterized in previous reports.

The wear surface of a Cr_2O_3 - 8% SiO_2 - 3% TiO_2 coating tested against grey iron with fresh oil at 350°C is shown in Figure 20. Large areas of the surface were covered with flat, shallow pits. Since the area fraction of the pits was greater than the area fraction of porosity, this is thought to be evidence for inter-splat debond/fracture. The Cr_2O_3 - 33% Stellite 6 material showed less evidence of debond, but in this material the Stellite phase (lighter imaging in the SEM) was smeared across the wear track and, from the appearance of the wear surface, must have supported a large fraction of the bearing load (Figure 21).

The ZTY material, which had very high wear coefficients in lubricated tests, showed a microscopically rough wear surface with evidence of splat de-bonding and fracture (Figure 22).

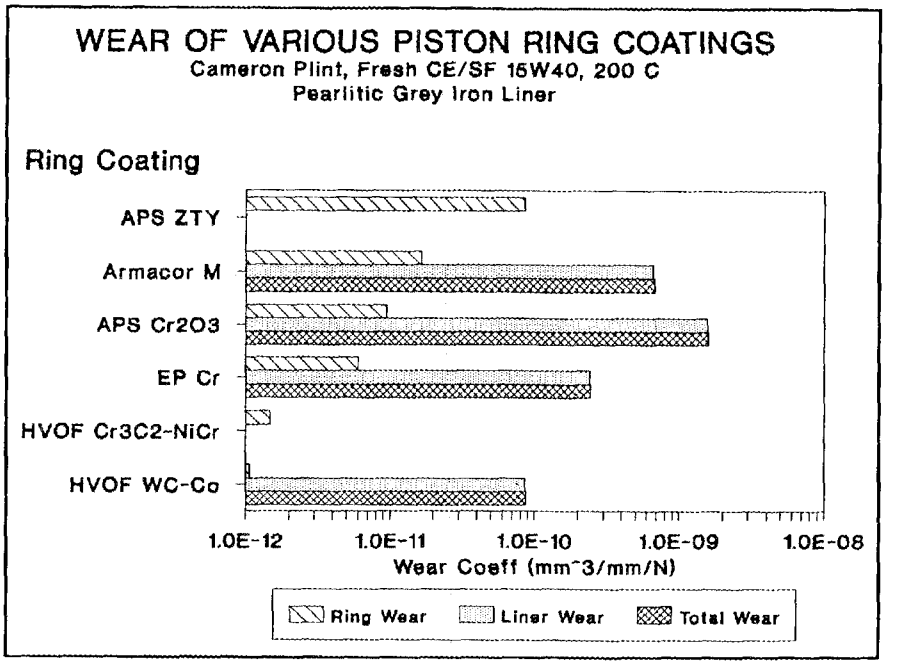

Figure 16. *Wear comparison of various ring/liner combinations at 200°C in fresh CE/SF 15W40 oil.*

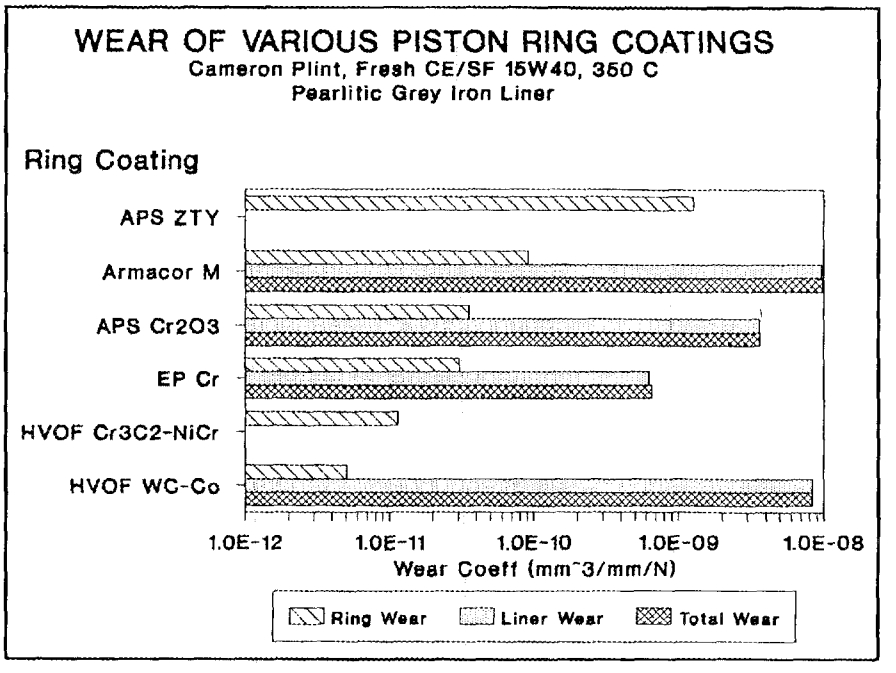

Figure 17. *Wear comparison of various ring/liner combinations at 350°C in fresh CE/SF 15W40 oil.*

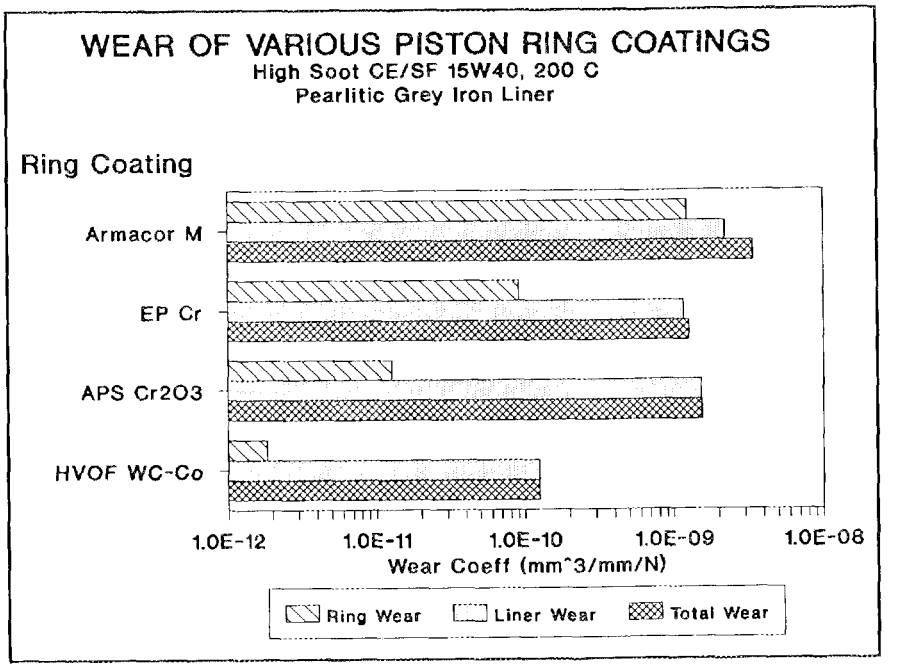

Figure 18. *Wear comparison of various ring/liner combinations at 200°C in fresh and engine-tested CE/SF 15W40 oils.*

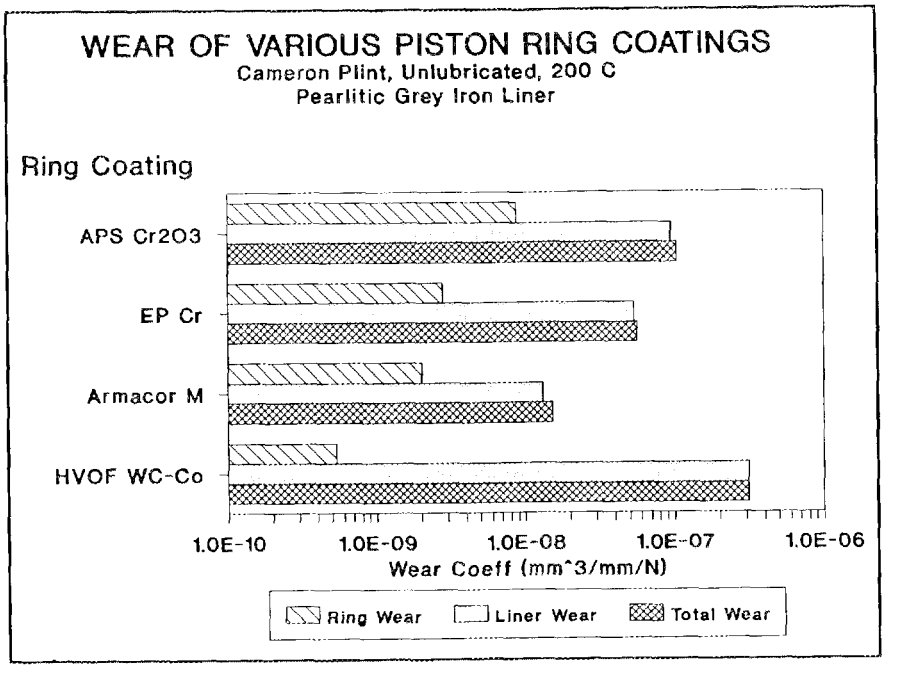

Figure 19. *Wear comparison of various ring/liner combinations at 200°C without lubrication.*

Coating	*Knoop Hardness at indicated load ($kgfmm^{-2}$)*	*Load (gf)*
APS UCAR Cr_2O_3	830	100
APS Metco 136 Cr_2O_3	960	100
APS Cr_2O_3 - 15% Al_2O_3	1260	100
APS Cr_2O_3 - 8% SiO_2 - 3% TiO_2	1020	100
APS Cr_2O_3 - 33% Stellite 6	1250 (Cr_2O_3) 440 (Stellite)	10
APS Armacor M	760	100
HVOF WC - 12% Co	1120	100
HVOF Cr_3C_2-NiCr	990	100
HVOF NiCrBSi	810	100
UTRC ZTY	690	10
UTRC Cr_2O_3	870	100

Table 4. *Microhardness of coatings.*

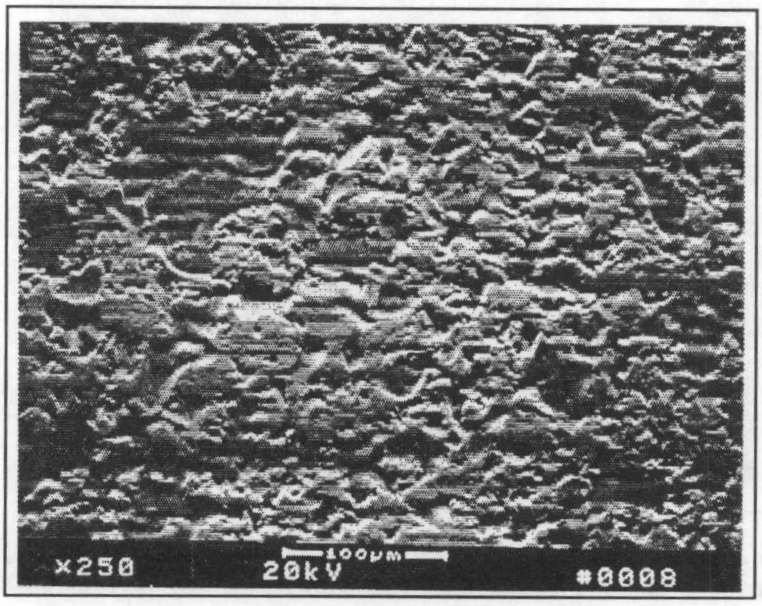

Figure 20. *Wear surface of APS Cr_2O_3 - 8% SiO_2 - 3% TiO_2 after sliding against grey cast iron liner for 6 hours at 350°C with fresh CE/SF 15W40 lubricant.*

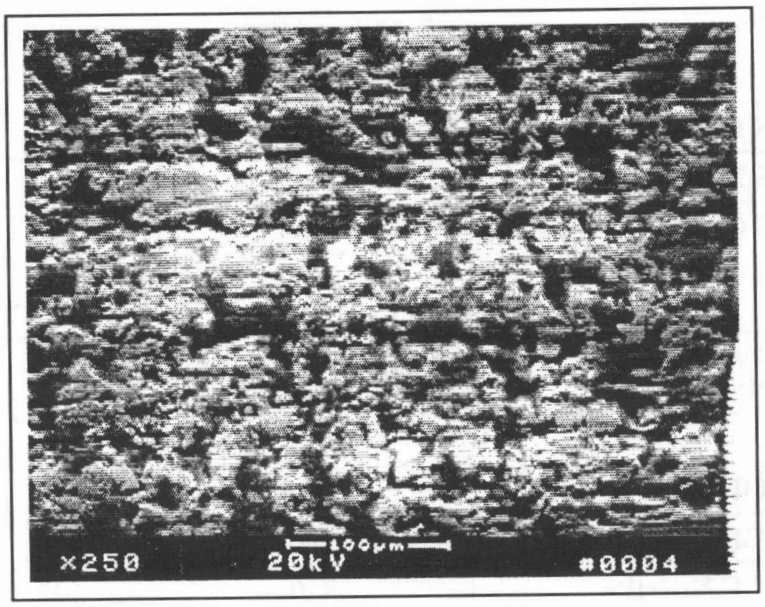

Figure 21. *Wear surface of APS Cr_2O_3 - 33% Stellite 6 after sliding against grey cast iron liner for 6 hours at 350°C with fresh CE/SF 15W40 lubricant.*

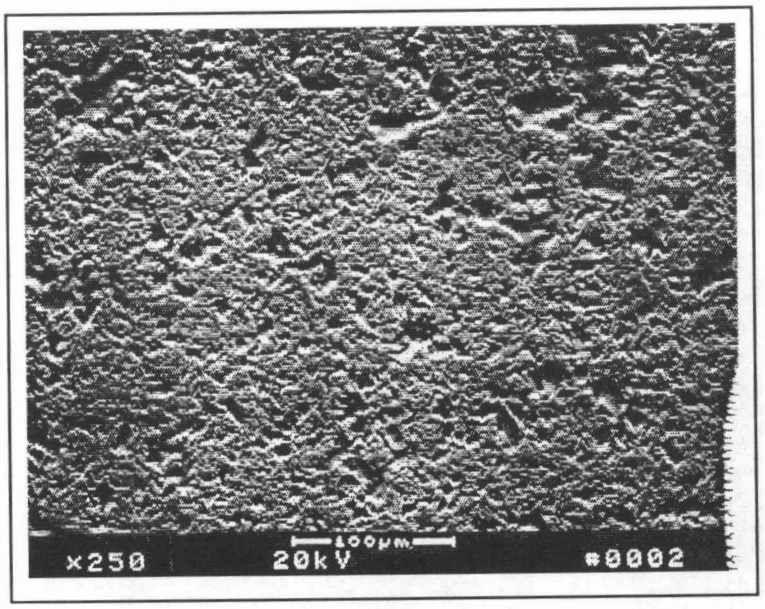

Figure 22. *Wear surface of APS ZrO_2 - TiO_2 - Y_2O_3 after sliding against grey cast iron liner for 6 hours at 200°C with fresh CE/SF lubricant.*

Conclusions

Results of piston ring - cylinder liner wear simulation tests have been described for a variety of plasma sprayed and high velocity oxy-fuel sprayed coating materials. Three categories of wear tests were conducted: (a) lubricated with a fresh CE/SF 15W40 mineral oil based lubricant, (b) with the same oil in a highly soot-loaded condition and (c) with no lubrication. Results were baselined with respect to wear coefficients measured for conventional materials (electroplated chromium rings and pearlitic grey cast iron liners). Significant improvements in wear resistance may be obtained by the use of coatings in all three categories of wear. Broadly, the greatest advantages were observed for the category (b) (highly soot-loaded) tests. HVOF cemented carbides have so far demonstrated the best combination of wear properties in all categories. Selection of an optimum ring-liner tribological system must be based on the specific engine application, which determines the relative importance of the three categories of wear, and on the relative importance of ring and liner wear protection.

Status of Milestones

1.	Develop plans for coating deposition	Oct-31-87
2.	Determine wear test conditions	Nov-30-87
3.	Procure substrate materials	Feb-28-87
4.	Develop spray parameters for Cr_2O_3 coatings	Aug-31-89
5.	Tribological evaluation of Cr_2O_3 coatings	Dec-31-89
6.	Develop spray parameters for HVOF coatings	Dec-31-89
7.	Conduct properties evaluation/wear testing of HVOF coatings	Feb-28-90
8.	Develop and test additional plasma sprayed materials	Apr-30-90
9.	Develop and test laser processed coatings	May-31-90
10.	Thermal shock and oxidation testing of coatings	Jun-30-90
11.	Develop liner counterface materials	Jul-31-90
12.	Selection of optimum ring-liner system	Jul-31-90
13.	Fabrication of test samples for ORNL	Aug-31-90

The program is on schedule.

Publications

A paper entitled "Development of Wear-Resistant Ceramic Coatings for Diesel Engine Components", by M.G.S. Naylor and M.P. Fear has been submitted for publication in the SAE proceedings of the 27th Automotive Technology Development Contractor's Coordination Meeting, Dearborn, MI, October 23 to 26, 1989.

1.4 JOINING

1.4.1 Ceramic-Metal Joints

Joining of Ceramics for Heat Engine Applications
M. L. Santella (Oak Ridge National Laboratory)

Objective/scope

The objective of this task is to develop strong reliable joints containing ceramic components for applications in advanced heat engines. Presently, this work is focused on the joining of silicon nitride by brazing. The technique of vapor coating ceramics to circumvent wetting problems that was developed for brazing zirconia at low temperatures will also be applied to brazing silicon nitride. The emphasis of this activity during FY 1990 will be on: (1) high temperature brazing of titanium-vapor-coated silicon nitride, (2) correlating braze joint microstructures with strength data to identify factors controlling joint strength, and (3) developing a method of calibrating the indentation fracture technique to determine the accuracy of residual stresses measurements in ceramic-to-metal joints.

Technical progress

Joints of Kyocera SN220 Si_3N_4 were made by brazing with a commercial Au-25Ni-25Pd wt % filler metal at 1130°C. The joint surfaces of the Si_3N_4 were left in the as-ground condition, or they were polished to a 30-μm-diamond or a 1-μm-diamond finish. Afterward, they were vapor coated with a 1-μm-thick layer of Ti before brazing. Each braze joint coupon yielded six flexure bars with nominal dimensions of 3 x 2.5 x 30 mm. The tensile faces of the bars were polished to a 1-μm-diamond finish, and the bars were tested at room temperature using a crosshead displacement rate of 0.25 mm/s. The test results were assumed to be described by a Weibull distribution function and are shown in Figs. 1-3 where the straight lines and values of m were determined by separate linear regressions. Comparison of Fig. 1 for the as-ground joint finish and Fig. 3 for the 1-μm-diamond finish indicates that because of a slightly higher average strength and less spread in the strength values, there was an advantage to using the polished joint surfaces over the as-ground surfaces. For the data sets of Figs. 1 and 3 many of the specimens actually fractured in the Si_3N_4, with the remaining specimens failing near the joint surfaces.

Comparing Fig. 2 to Figs. 1 and 3 indicates that the 30-μm-diamond joint surface finish resulted in lower joint strengths and more scatter than was found for joints with the other two joint surface finishes. All of the joints with the 30-μm finish broke near or at the interface between the Si_3N_4 and the braze layer. The erratic behavior of these joints compared to those with the the as-ground and 1-μm-diamond joint surface finishes suggests this strength data is spurious. The spurious behavior is attributed to improper cleaning of the Si_3N_4 surfaces after grinding to the 30-μm finish and before Ti vapor coating.

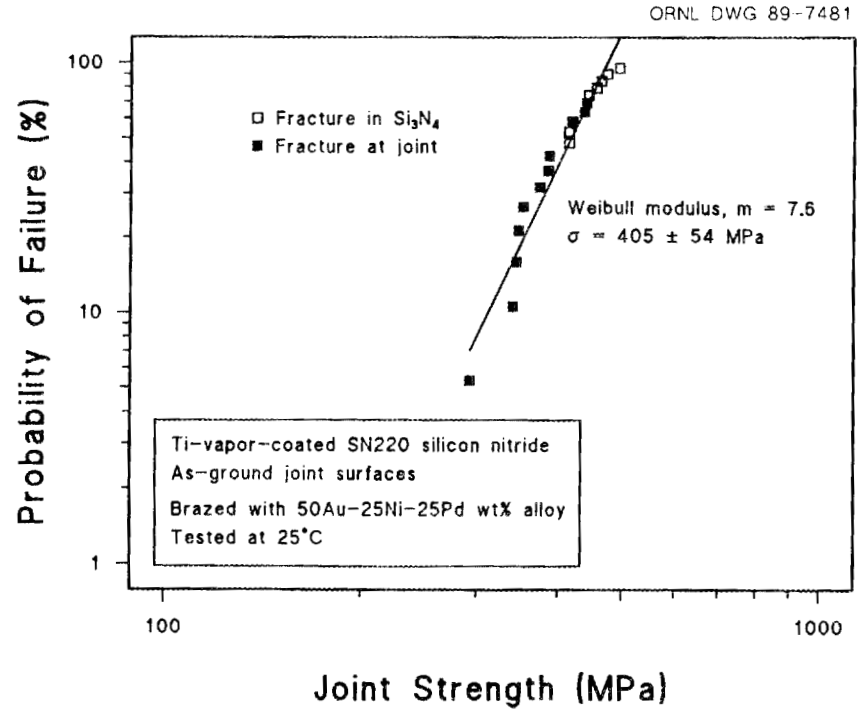

Fig. 1. Room-temperature flexure strength of Si_3N_4 braze joints that had as-ground joint surfaces.

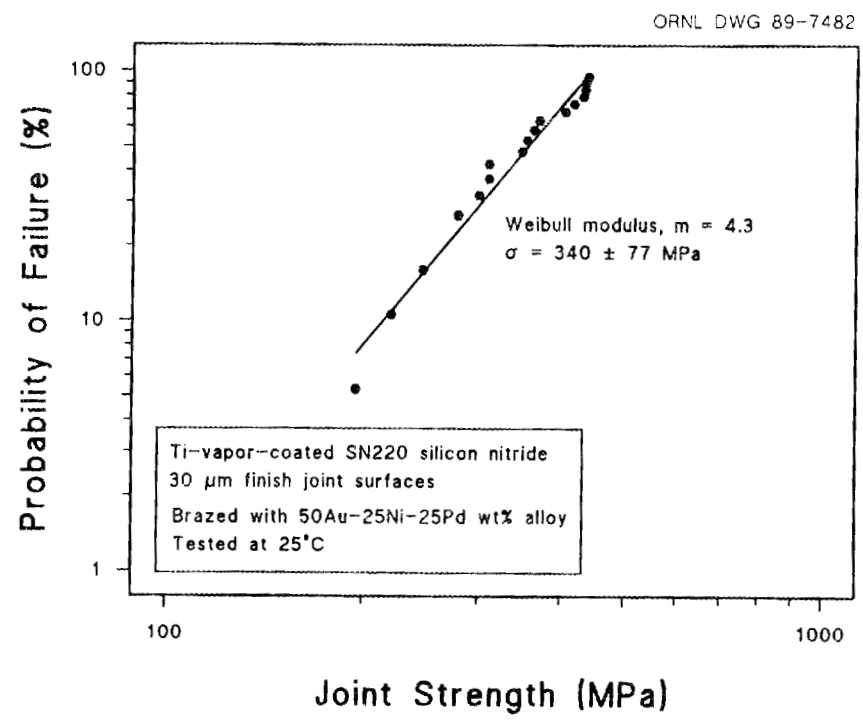

Fig. 2. Room-temperature flexure strength of Si_3N_4 braze joints that had joint surfaces ground to a 30-μm-diamond finish.

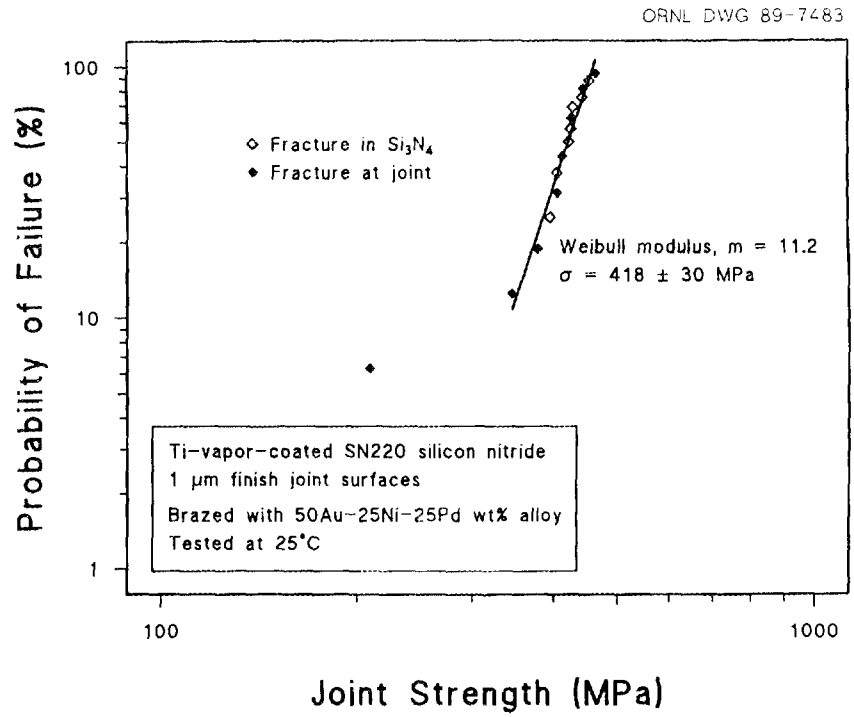

Fig. 3. Room-temperature flexure strength of Si_3N_4 braze joints that had joint surfaces ground to a 1-μm-diamond finish.

For all three finishes, when failure occurred at the joint it was always at a Si_3N_4/braze layer interface, or in the Si_3N_4 near the interface. Fracture or significant elongation of the braze filler metal layer was never observed even though the yield strength of the braze filler metal was estimated by microhardness testing to be only 265 MPa.

Analysis of the room-temperature flexure test data is continuing. Also, additional groups of flexure test bars for Kyocera SN220 Si_3N_4 brazed with Au-25Ni-25Pd wt % filler metal were prepared for testing at elevated temperature.

Several wetting experiments were also done to investigate the possibility of using the silicides $TiSi_2$ and $CrSi_2$ as materials for brazing Si_3N_4 and SiC. These two silicides were selected based on their melting temperatures (1500°C for $TiSi_2$, and 1490°C for $CrSi_2$), and because they reportedly have good oxidation resistance and have shown some promise as brazing materials in other work. Both of these silicides were supplied as -325 mesh powders. For each experiment 20-25 mg of silicide powder was mixed with a few drops of a binder and applied to the surface of a Si_3N_4 or SiC specimen. Specimens were then heated at 50°C/min to 1000°C under vacuum, and finally to 1525°C under a partial pressure (~0.5 atm) of argon. After holding at 1525°C for 10 min the specimens were cooled at 25°C/min to 500°C, and then free cooled to room temperature. The results of the wetting experiments are summarized in Table 1. For the cases where the wetting angle θ was 5° or less, spreading occurred and no well-defined droplet was formed. This condition is generally not conducive to the formation of acceptable braze joints. Well defined droplets were observed for all other cases.

Table 1. Results for wetting of Si_3N_4 and SiC by $TiSi_2$ and $CrSi_2$

Ceramic	Brazing material	Atmosphere	Wetting angle, θ
Si_3N_4	$TiSi_2$	argon	10
Si_3N_4	$TiSi_2$	vacuum	5
Si_3N_4	$CrSi_2$	argon	105
Si_3N_4	$CrSi_2$	vacuum	45
SiC	$TiSi_2$	argon	10
SiC	$TiSi_2$	vacuum	<5
SiC	$CrSi_2$	argon	45
SiC	$CrSi_2$	vacuum	15

Based on this wetting data, joints of Si_3N_4 and SiC were made using $TiSi_2$ as a brazing material for the two cases where $\theta = 10\text{-}15°$. Slips of the $TiSi_2$ powder were applied to surfaces of the dense ceramics and pressed together by hand before heating. The joints were formed by holding at 1525°C for times of either 20 min or 60 min, with melting being done under Ar at a pressure of slightly less than 1 atm. After brazing the joints were examined optically. The bond layers of the $Si_3N_4/TiSi_2$ joints contained three major phases and relatively large fraction of pores (roughly 5-10%) with a size in the range of 40 μm and less. Judging by its gold color, one of the phases in the bond layer was TiN which formed predominantly at the Si_3N_4 surfaces. Cracking of the bond layer perpendicular to the brazed Si_3N_4 surfaces was also evident. The bond layers in the $SiC/TiSi_2$ joints appeared to contain only two major phases in addition to pores at a lower fraction than that observed in the Si_3N_4 joints. The same cracking pattern was also found in these joints. There was evidence in this case that the SiC had undergone grain boundary intrusion by the $TiSi_2$, and fragments of SiC could be found throughout the bond layer.

A coupon was made for the $Si_3N_4/TiSi_2$ combination from which three bend test bars were obtained. These bars were tested in four-point loading at room temperature and had fracture strengths of 105, 100, and 116 MPa. Each bar broke through the $TiSi_2$ layer.

Status of milestones

141107 Complete initial evaluation of silicon nitride brazing

The results of initial experimental work on this subject are described in the following:

M. L. Santella, "Brazing of Titanium-Vapor-Coated Silicon Nitride," *Advanced Ceramic Materials*, 3 (1988) pp. 457-62.

M. L. Santella and L. C. Manley, "Strength and Microstructure of Titanium-Vapor-Coated Silicon Nitride Braze Joints," pp. 513-23, *Ceramic Materials and Components for Engines*, V. J. Tennery, ed., American Ceramic Society, 1989.

The second publication describes initial work on strength testing of braze joints. This work is continuing and at least one more publication on this subject is expected.

Publications

None.

Analytical and Experimental Evaluation of Joining Silicon Nitride to Metal and Silicon Carbide to Metal for Advanced Heat Engine Applications - S. Kang (GTE)

Objective/Scope

The goal of Phase I is to demonstrate analytical tools for use in designing ceramic-to-metal joints, including the strain response of joints as a function of the mechanical and physical properties of the ceramic and metal, the materials used in producing the joint, the geometry of the joint, externally imposed stresses both of a mechanical and thermal nature, temperature, and the effects of joints exposed for long times at high temperatures in an oxidizing (heat engine) atmosphere. The maximum temperature of interest for application of silicon carbide to metal and silicon nitride to metal-containing joints is 950 °C. The initial joint-fabrication work shall include "experimental" joints whose interfacial area is not less than 2 cm^2. The work shall also include demonstration of the potential for scale-up of the joint size to interfacial areas of commercial significance, applicability of the analytical joint modeling tools, and the ability to use these tools to design and predict the mechanical and thermal behavior of larger joints. These joints, referred to as "scale-up" joints, shall have an interfacial area of at least 20 cm^2.

The goal of Phase II is to optimize materials systems and joint designs, building on the results of Phase I. The anticipated environment will be oxidizing and will have joint temperatures of up to 950°C. Improved joint materials systems shall be developed to optimize the combination of competing properties which include ductility, yield strength, and creep resistance. The effect of each of these properties on joint performance shall be examined using the FEM model. Finally, a mechanical testing program shall be carried out to confirm the effectiveness of the modeling program. This shall include torsion tests, thermal and mechanical fatigue, and creep testing.

Design Criteria/Stress Analysis

The modelling and structural analysis tasks carried out centered around three items. The first was a comparison of residual stress after brazing for a single-braze system having either a Ni or Mo interlayer material. The Ni interlayer deforms much more during the brazing process than the Mo interlayer, thus significantly reducing the residual stresses in the ceramic shaft after brazing.

Two strain and temperature dependent material models (in a format acceptable for finite element input) were developed for Palniro 4 (30Au-34Pd-36Ni) and the Au-5Ni-2Pd braze alloys. These models have been added to the material model library developed to explore different systems in the ceramic-metal joint.

Lastly, two new finite element models (Figure 1 shows one of the meshes) of the ceramic-metal braze joint have been created. These new models have 1) very fine element discretization at the interface between the structural alloy and the ceramic, suitable for modifications such as increasing or decreasing the number of interlayer materials, and 2) braze layers on both sides of the current interlayer (two braze layer system), thus allowing investigations of the double-braze system.

Using the second finite element model, the residual stress state in a detailed model of the ceramic-metal braze joint was obtained. The results of this analysis were used to superimpose residual thermal deformations with the service torque loads on the joint for strength and reliability predictions.

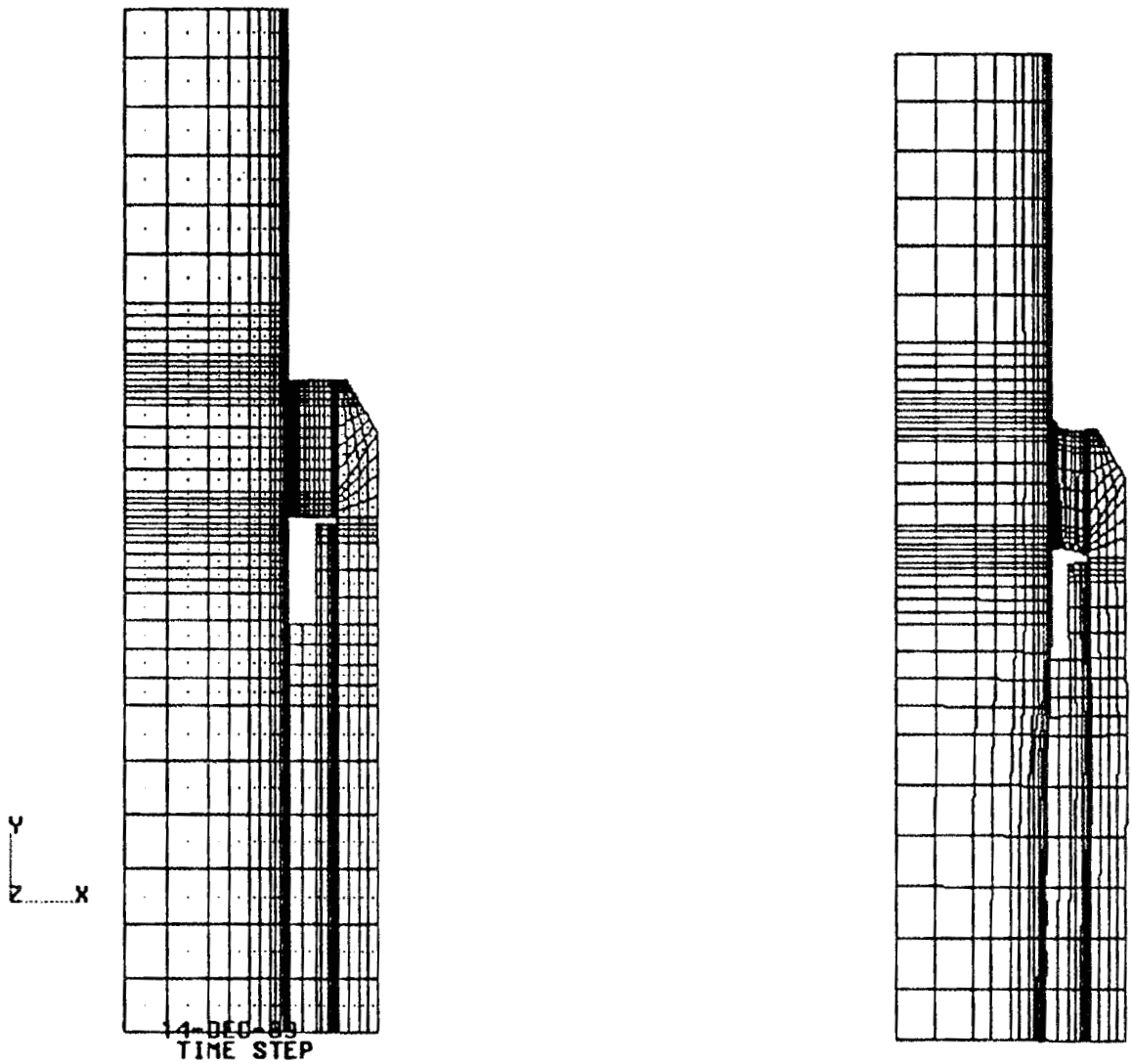

Figure 1: High-density mesh for double-braze joint system. On the left is mesh at solidus temperature of the braze (1180°C); on the right is deformed structure at room-temperature (20°C).

The temperature- and strain-dependent material properties of the components were reported previously. The following material system was selected in this analysis:

Ceramic	-	PY6
Structural Alloy	-	Incoloy 909
Interlayer	-	Ni
Braze	-	Au-5Pd-2Ni

Maximum principal stress and von Mises stress at 20°C are shown in Figures 2 and 3, respectively. Similar results for the braze joint at 650°C are shown in Figures 4 and 5. Deformation of the braze joint for 20 and 650°C was shown for the entire structure. This indicates which regions have undergone the greatest strain and permits us to select the regions of greatest deformation for further study. At both temperatures, the greatest deformation occurs in the braze region. This was expected since the braze had the lowest yield stress of the materials in the joint. The structural alloy exerts a "downward pull" on the braze. This downward motion puts the braze material at the ends of the joint region in simple shear, thus permitting large plastic deformations of the braze layers.

The deformed shapes of the model at 20 and 650°C clearly show that larger deformations existed at 20°C. Therefore, the structure does subject to larger residual strains at room temperature than at the operating temperature of the joint. Some amount of stress relaxation occurred when the joint was heated from room temperature to its operating temperature.

This relaxation phenomenon is shown in the maximum principal stress distributions at 20°C and at 650°C (Figures 2 and 4). Not only does the value of the maximum principal stress reduced from 20°C to 650°C, but the location of this maximum also changes. At 20°C, the Ni interlayer contains the maximum principal stress, thus performing its function of reducing the likelihood of ceramic fracture. The central region of the braze puts the ceramic in residual compression, away from the edges. At 650°C, however, this compression changes to positive values of σ_1 for most of the ceramic material.

The von Mises stress was concentrated in the two braze layers. The large values shown in the braze layer at 20°C emphasize the amount of deformation that these regions undergo. Similar behavior was displayed at 650°C. At 650°C the maximum values of von Mises stress were reduced, and the distribution of these maximum values was more diffuse compared to the results at 20°C, because of the relaxation which occurs at this temperature.

In summary, the braze material undergoes large deformations at both room and operating temperatures, and the interlayer provides a mechanism for ensuring that the largest maximum principal stress occurs outside of the ceramic component at room temperature. Also, some stress relaxation occurs in the structure when heated from room to operating temperature, permanent deformations notwithstanding.

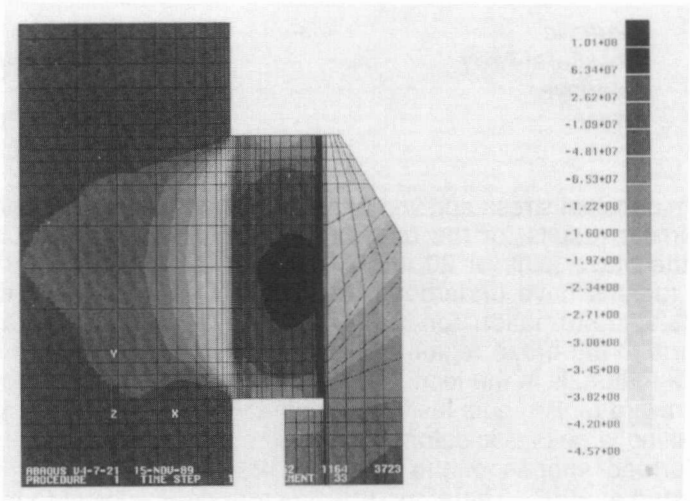

Figure 2: Contour plot of maximum principal stress (s1 in Pa) at 20°C in the vicinity of the joint.

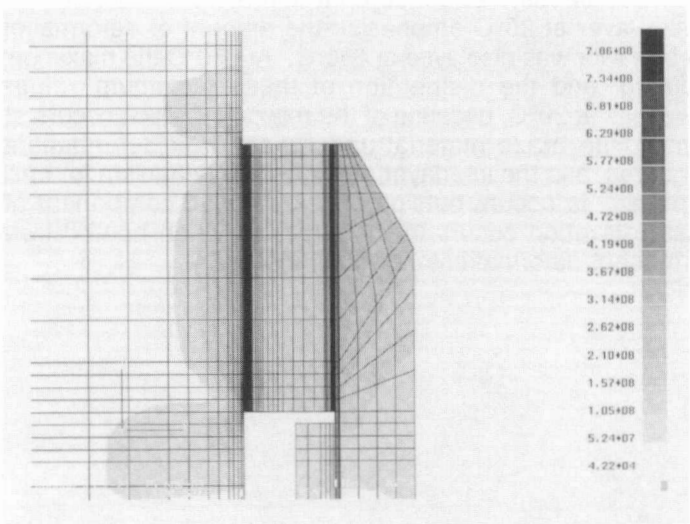

Figure 3: Contour plot of von Mises stress (Pa) at 20°C in the vicinity of the joint.

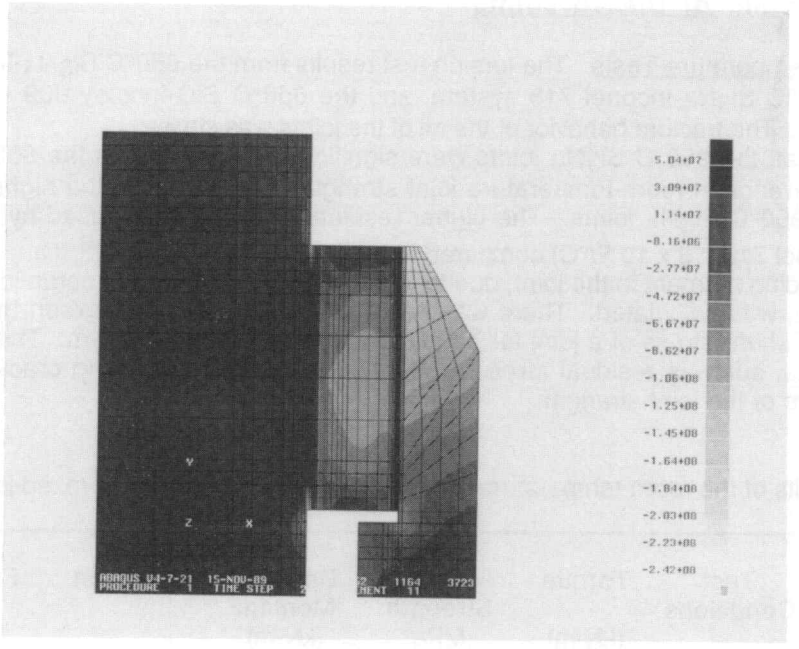

Figure 4: Contour plot of maximum principal stress (s1 in Pa) at 650°C in the vicinity of the joint.

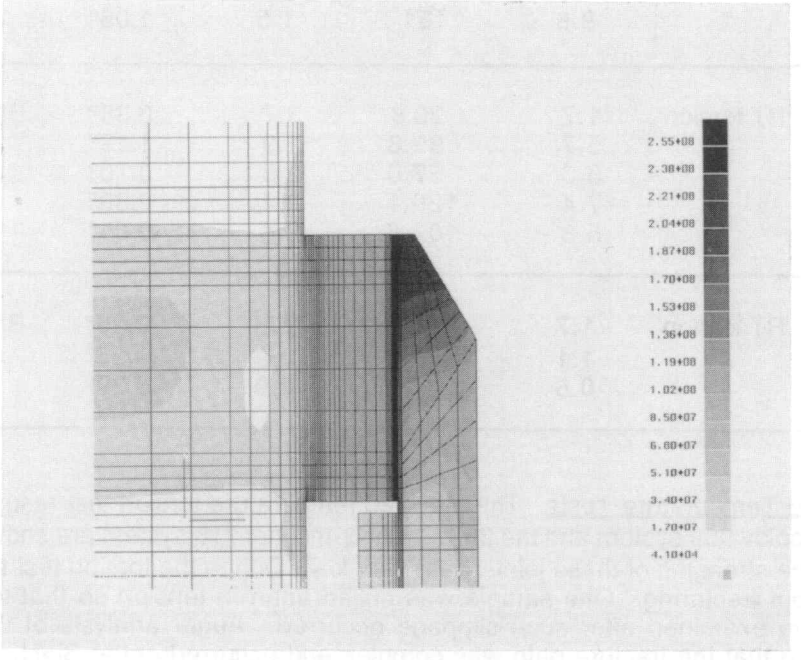

Figure 5: Contour plot of von Mises stress (Pa) at 650°C in the vicinity of the joint.

Mechanical Testing of Brazed Joints

Room Temperature Tests. The torsion test results from the 650°C Si_3N_4-Incoloy 909 system, the 950°C Si_3N_4-Inconel 718 system, and the 650°C SiC-Incoloy 909 system are shown in Table 1. The fracture behavior of the all of the joints was similar.

In general, the 950°C Si_3N_4 joints were significantly weaker than the 650°C Si_3N_4 joints. This difference in room-temperature joint strength is attributed to the higher residual stresses in the 950°C Si_3N_4 joints. The higher residual stresses are caused by the higher CTE of the Inconel 718 (18×10^{-6}/°C) compared to the Incoloy 909 (12×10^{-6}/°C).

The bending moment in the joint, due to misalignment between the ceramic and metal parts of the joint, was calculated. There was not a strong correlation between the bending moment and the shear stress of a joint for bending moments below 2.5 kN-m. This suggests that other factors, such as residual stress, unbonded area, or pre-existing cracks, are the controlling factors of the joint strength.

Table 1: Results of the room-temperature torsion tests of Si3N4 and SiC brazed joints.

Material System	Test Conditions	Torque (kN-m)	Shear Strength (MPa)	Bending Moment (kN-m)	Rotation	Fracture mode
650°C Si_3N_4	RT torsion	8.8	154	1.0	2.22°	Broke in ceramic
"	"	14.0	246	2.0	3.52°	"
"	"	7.6	134	1.6	1.98°	"
"	"	4.3	76	1.9	1.15°	"
"	"	8.6	151	1.5	1.05°	"
950°C Si_3N_4	RT torsion	1.7	30.8	3.7	0.38°	Broke in ceramic
"	"	5.7	99.8	1.9	1.19°	"
"	"	3.3	57.0	2.5	0.70°	"
"	"	7.4	129.1	2.4	0.80°	"
"	"	5.8	102.6	2.4	0.64°	"
650°C SiC*	RT torsion	1.7	30.2	2.6	0.25°	Broke in ceramic
"	"	1.1	19.9	0.9	0.25°	"
"	"	0.6	10.3	0.9	0.30°	"

Elevated Temperature Tests. The elevated temperature torsion test results from the 650°C Si_3N_4-Incoloy 909 system and the 950°C Si_3N_4-Inconel 718 system are shown in Table 2. In general, the strengths of these joints were very low. During the torsion test the ceramic would slip without fracturing. One sample was pulled apart in tension so that the fracture surface could be examined after such slippage occurred. Auger analysis of the fracture surface indicated that the fracture path was complex and occurred in the Si_3N_4, in the TiN reaction layer, and in the braze alloy.

Table 2: Results of the elevated-temperature torsion tests of the Si_3N_4 brazed joints.

Material System	Test Conditions	Torque (kN-m)	Shear Strength (MPa)	Rotation	Fracture mode
650°C Si_3N_4	650°C torsion	0.67	11.7	—	Slippage at braze/ ceramic interface
"	"	0.23	4.0	0.10°	"
"	"	1.0	17.7	—	"
"	"	0.7	12.3	0.21°	"
950°C Si_3N_4	950°C torsion	0.05	0.85	—	Slippage at braze/ ceramic interface

Performance Tests and FEA Model Predictions

The ability to compare the measured joint strength to the predicted residual stresses will allow the FEA model of the joints to be refined and will provide a tested method to aid in designing ceramic-metal joints in the future.

Linkage between the FEA predictions and mechanical testing experiments was established based on the following assumptions:

- The brazing process provides ideal joints without defects, i.e., no unbonded area.
- Alloying effects are negligible on the material properties.
- Each of the structural ceramic members has an equal probability for surface and volume defects.

While these assumptions may not be applicable to the brazed joints presently being studied, they represent a necessary assumption to make the problem tractable.

The situations with and without residual stresses are represented by the properties of the brazed joint and of the unbrazed ceramic sample, respectively. The following relationships can be established in a tension test.

$$\sigma_{fracture} = \sigma_{residual} + \sigma_{applied}, \qquad \text{Eq. 1}$$

The residual stresses in the joint are determined by FEA. The stresses σ_{zz} and $\sigma_{\theta\theta}$ are the maximum principal stresses taken from the free surface in the vicinity of the ceramic-metal joint (i.e., σ_1 and σ_3 respectively). These stresses can be converted into a maximum shearing stress for comparison with the measured joint strength by a Mohr's circle analysis.

Substituting for the residual stress quantities in Equation 1, the relationship between the residual stress in the joint and the strength of the joint, $\tau_{predicted}$, becomes

$$\sigma_{max} = \frac{\sigma_{zz} + \sigma_{\theta\theta}}{2} + \sqrt{\left(\frac{\sigma_{zz} - \sigma_{\theta\theta}}{2}\right)^2 + [\tau_{predicted}]^2} \qquad \text{Eq. 2}$$

where σ_{max} is equals τ_{max}. τ_{max} is the measured shear strength of the unbrazed ceramic from a torsion test based on the following relationship:

$$\tau_{max} = \frac{\sigma_{11} - \sigma_{33}}{2} = \frac{\sigma_{11} - (-\sigma_{11})}{2} = \sigma_{11} = \sigma_{max}. \qquad \text{Eq. 3}$$

For real, nonideal samples, Equation 2 becomes

$$\sigma_{max} = \frac{\sigma_{zz} + \sigma_{\theta\theta}}{2} + \sqrt{\left(\frac{\sigma_{zz} - \sigma_{\theta\theta}}{2}\right)^2 + [\tau_{applied} + \Delta\tau]^2} \qquad \text{Eq. 4}$$

where $\tau_{applied}$ is the shear strength for fracture measured from brazed samples. $\Delta\tau$ is the change in the principal stress due to processing, testing, and the probability factor for cracking in the ceramic material.

Therefore, a comparison can be made between the predicted values, $\tau_{predicted}$, in Equation 2 and the measured values, $\tau_{applied}$, in Equation 4, assuming that $\Delta\tau = 0$. Setting $\Delta\tau = 0$ is equivalent to assuming that the brazed joint is perfect, the ceramic has not been damaged during the brazing process, and there is no unbonded area in the joint.

Verification of FEA predictions

Comparisons between the predicted value and the measured values from torsion tests were made. The equations developed in the preceding section and testing results from the base materials and brazed joints were used in the comparison. In this analysis the strength of the base materials were treated as theoretical values and failure of the joint was assumed to occur at the maximum stress point. The residual stress state was expressed in terms of σ_{zz}, $\sigma_{\theta\theta}$, and σ_{rr}.

The values of σ_{zz} and $\sigma_{\theta\theta}$ at 20 and 650°C from the FEA study are listed in Table 3. These values were taken from the centroid of the FEA mesh element on the free surface of the ceramic. This element was immediately above the joint and did not represent the exact stress conditions, i.e., plane stress, on the surface. However, these values were taken as the principal stresses since the stress values of the third component, σ_{rr}, were significantly smaller than those of σ_{zz} and $\sigma_{\theta\theta}$.

Table 3: Comparison between FEA predictions and experimental joint strengths.

Test Temperature	FEA Prediction σ_{zz} (MPa)	FEA Prediction $\sigma_{\theta\theta}$ (MPa)	$\tau_{predicted}$* (MPa)	$\tau_{measured}$ (MPa)	$\tau_{corrected}$ (MPa)	Testing Results of Brazed Joints
20°C	188.3	166.2	448	75.6 - 246.4	128.8 - 418.6	Failed in ceramic
650°C	-77.7	- 37.8	659.4	4.2 - 17.5	—	Failed at interface

* Calculation was based on $\tau_{max} = 602$ MPa.

Using Equation 2 and 602 MPa for τ_{max}, the calculated value of $\tau_{predicted}$ at room temperature was 448 MPa while the measured values from the torsion tests were in the range of 75.6 - 246.4 MPa. The measured values change to 128.8-418.6 MPa when the stress concentration factor ($K_t = 1.7$) associated with the change in diameter at the joint (12.7 mm ceramic to 19.5 mm metal) is accounted for. The measured values are 30 - 90 % of values predicted by FEA. The relatively large scatter in the strength values of the joints should be attributed to the handling of ceramic parts and to the difference in the ideal joints modelled and the real joints tested.

The FEA values of σ_{zz} and $\sigma_{\theta\theta}$ at 650°C were obtained from the joint model which was cooled down to room temperature and heated back up to 650°C. As shown in Table 3, $\tau_{predicted}$ increased to 659.4 MPa due to the compressive principal stresses. This value exceeded the strength values of any components in the joint at 650°C and failure did not occur in the ceramic. The values of $\tau_{measured}$ (4.2-17.5 MPa) represents the strength of the weakest component, i.e., the interface region, at 650°C. In this case, the stress concentration factor was not applicable.

Brazing Alloy Development

Tensile Properties of Pd-Containing Brazes

The effects of Pd additions to the mechanical and chemical properties of Au-Ni braze alloys were studied. Six braze alloys were studied: 60Pd-40Ni, 50Au-25Pd-25Ni, 30Au-34Pd-36Ni,70Au-8Pd-22Ni, 93Au-5Pd-2Ni, and 82Au-18Ni, all in wt % (Table 4).

Pd-containing alloys mentioned above are solid solution strengthened and their application temperatures are usually limited to below 500°C. In order to establish a base line data for the development of high temperature creep resistant braze alloys, mechanical properties of thin foils of these alloys were evaluated. 82Au-18Ni was annealed at 850°C for 5 hours before tensile tests, whereas all other foils were treated at 900°C.

These alloys did not exhibit a particular pattern in strength-composition relationship. However, the highest foil strength (728 MPa yield strength) at room-temperature was observed from the 50Au-25Ni-25Pd alloy, which resulted in poorest brazing performance among the alloys studied.. Alloys 82Au-18Ni, 70Au-8Pd-22Ni, 30Au-34Pd-36Ni, 60Pd-40Ni, and 93Au-5Pd-2Ni showed 609, 588, 564, 294 and 88 MPa yield strength, respectively. Additions of Au, up to about 85%, seemed to be effective to provide high foil strength. Also, all these alloys showed significantly low modulii (28-50 GPa) compared to other Au- or Pd-based alloys (about 105 GPa), indicating excellent ductility as well as fracture toughness.

Table 4: Liquidus (TL) and brazing (TB) temperatures of the braze alloys, along with selected room-temperature mechanical properties of the braze foils, and the room-temperature coefficient of thermal expansion (CTE).

Trade Name of Braze Alloy†	Au	Pd	Ni	T_L (°C)	T_B (°C)	E (GPa)	σ_T (MPa)	σ_y (MPa)	CTE (x 10^{-6}/°C)
	(wt. pct.)								
Palni	—	60	40	1238	1290	47.3	373	292	—
Palniro 4	30	34	36	1169	1220	30.0	574	574	15.5
Palniro 1	50	25	25	1121	1170	35.0	735	728	15.5
Palniro 7	70	8	22	1037	1090	42.7	600	585	17.5
Experimental	93	5	2	1082	1180	28.7	109	88	—
Nioro	82	—	18	950	1000	49.0	760	606	17.5

† GTE WESGO, Belmont, CA.

It was found in this study that the addition of Pd to the Au-Ni system increases the high temperature capability of the alloys at the cost of strength, ductility.and more significantly, brazability. The low strength of 60Pd-40Ni, with an increased modulus of elasticity, indicates the embrittlement of this alloy. Based on this study, it seems that Au-Pd-Ni system is limited to the capacity obtainable from Au-Ni system with up to 10% of Pd addition.

Strengths of Joints Brazed with Pd-Containing Brazes

Coupons were brazed using the above alloys, Ti-coated SWN1000 Si_3N_4 and Incoloy 909. Ten coupons were brazed with each braze. Five coupons were shear tested at room temperature and 5 were shear tested at 500°C in an argon atmosphere for each braze.

The high Pd brazes, 60Pd-40Ni, 50Au-25Pd-25Ni, and 30Au-34Pd-36Ni, had very low shear strength values; all were below 35 MPa (Tables 5 and 6). Most of the coupons brazed with the high Pd-containing brazes broke during handling. Out of the 30 samples made with these brazes, only 12 survived handling and were tested. All of the samples brazed with 50Au-25Pd-25Pd braze were cracked in the Si_3N_4 on cooling and could not be tested. The cracks often propagated all-the-way through the Si_3N_4.

Table 5: Results from room-temperature and 500°C shear tests between Ni and Ti-coated Si_3N_4.

Braze Alloy Wt%			Failure Load (kN)											
			25°C Sample #						500°C Sample #					
Au	Pd	Ni	1	2	3	4	5	Ave.	1	2	3	4	5	Ave.
—	60	40	1.6	*	*	*	*	1.6	2.6	4.4	3.2	0.8	*	2.8
30	34	36	0.2	0.5	*	*	*	0.4	3.3	*	*	*	*	3.3
50	25	25	*	*	*	*	*	*	*	*	*	*	*	*
70	8	22	9.9	7.1	6.4	7.6	18.5	12.0	10.5	11.6	9.2	9.9	11.7	10.6
93	5	2	6.9	4.2	10.4	8.2	7.7	8.4	4.7	7.3	9.5	10.0	8.7	8.0
82	—	18	5.5	2.5	7.4	10.2	2.4	5.6	7.9	10.9	7.3	10.0	8.6	8.9

* indicates that the sample broke during handling and could not be tested.

Table 6: Statistics from Room Temperature and 500°C Shear Tests in Table 5.

Braze Alloy (Wt%)			Average Failure Shear Stress (MPa)			
			25°C		500°C	
Au	Pd	Ni	Mean*	Std. Dev.*	Mean*	Std. Dev.*
—	60	40	17.1†	—	29.6	16.4
30	34	36	3.7	2.3	35.7†	—
50	25	25	—	—	—	—
70	8	22	107.3	53.9	114.7	11.5
93	5	2	78.9	24.5	87.4	23.1
82	—	18	60.4	36.3	97.2	16.0

* samples which broke during handling were not included in these figures.
† no standard deviation is reported because only one sample was successfully tested.

The joints that cracked on cooling from the brazing temperature had either a high yield strength braze or were high temperature brazes and therefore were subjected to large thermal residual stresses. The coefficients of thermal expansion of these brazes are not known as a function of temperature, but they are expected to be approximately 15 x 10^{-6}/°C near room-temperature.

There was not a significant difference in the fracture mode of any of the samples (Table 7) except for the 60Pd-40Ni brazed coupons tested at 500°C. Most of the samples fractured in the ceramic (at a depth of approximately 1-2 mm) with the crack propagating parallel to the interface. The joints with the 60Pd-40Ni braze had approximately 30% unbonded area.

Table 7: Failure mode of shear coupons. C & I indicates that the crack propagated in the ceramic parallel to the interface; I indicates that the crack propagated along the braze/ceramic interface.

Braze Alloy (Wt%)			Failure Mode	
Au	Pd	Ni	25°C	500°C
—	60	40	I, C & I	I, 30% unbonded area
30	34	36	C & I	C & I
50	25	25	C & I	C & I
70	8	22	C & I	C & I
93	5	2	C & I	???, samples not completely broken
82	—	18	C & I	I, C & I

Ni-based Brazing Alloys

Two Ni-based superalloys (Inconel 600 and 625) were studied for braze alloys in ceramic-metal joints for high temperature applications. These alloys were selected based on their high-temperature performance and ductility.

These wrought products have attractive sets of mechanical properties for use as high-temperature braze alloys or interlayer materials (Table 8). The cast properties were studied, since it is the mechanical properties of re-solidified braze that concern the joint performance after brazing process. Therefore, these alloys were arc-melted for the testing. Table 8 summarizes the results of room-temperature tensile tests with cylindrical samples (4 mm dia.). In general, the remelting of the wrought alloys caused a 20-30% reduction of tensile strength, a 20-30% gain in elongation, and an insignificant change in elastic modulus, less than 15%. It is clear from the tests that the arc-melted samples still retain their attractive sets of properties.

Chemical analyses of the Inconel 600 and 625 showed no significant changes in their compositions after remelting. In addition, the wetting behavior of these alloys was found to be excellent. The wetting angles were below 10° on Ti-, Zr-, or Hf-coated SNW 1000 at 1500°C.

Table 8: Room Temperature Tensile Properties of Inconel 600 and 625.

Alloys	YS (MPa)	UTS (MPa)	Elastic Modulus (GPa)	Elongation (%)
Inconel 600 As-Received	325 339	812 809	176 187	57 58
Inconel 600 Arc-Melted	228 220 207	536 512 530	180 163 162	80 66 78
Inconel 625 As-Received	361 406 393	1029 1062 1057	191 215 221	63 65 64
Inconel 625 Arc-Melted	403 326 280	730 706 706	178 181 179	77 77 78

Status of Milestones

Phase I Milestones

Phase I completed, final report submitted.

Phase II Milestones

No milestones due this period, all milestones on schedule.

Publications

None.

References

None.

Analytical and Experimental Evaluation of Joining Ceramic Oxides to Ceramic Oxides and Ceramic Oxides to Metal for Advanced Heat Engine Applications

A. T. Hopper, J. Ahmad, A. Rosenfield, and B. Majumdar
(Battelle Columbus Division)

Objective/Scope

The objective of this project is the development of procedures necessary for the design of reliable, high strength ceramic oxide-to-ceramic oxide and ceramic oxide-to-metal joints. The research program consists of analytical and experimental tasks. Magnesia-Partially Stabilized Zirconia (PSZ) is the ceramic and nodular/ductile cast iron is the metal being used in this program. The experimental work dealing with ceramic oxide-to-metal joints was done by Dr. James Cawley and Mr. Eunsung Park of The Ohio State University and by Dr. Daniel Hauser of The Edison Welding Institute. The experimental work dealing with joining Zirconia to Zirconia was performed by Drs. S. L. Swartz and B. S. Majumdar of Battelle. Measurements of joint and constituent properties were done by Dr. B. S. Majumdar, Dr. A. R. Rosenfield, and Mr. Paul Held. Analytical modeling work was performed by Dr. Jalees Ahmad.

The goal of the analytical work is a predictive model that can be used in engineering design of ceramic joints. The model formulated represents a synergistic treatment involving applied stress, crack length, toughness, residual stress, and strength in a fundamentally sound manner. Special emphasis has been given to geometry and stress state independence, making the model concept widely applicable as a general design tool.

The experimental work was performed to provide both material property input to the design model and experimental verification of model predictions. To this end small scale and scaled up joints were fabricated to determine their mechanical behavior. Experiments included measurements of elastic constants and of stress-strain curves as a function of temperature, tensile strength, shear strength, and fracture toughness. Some experiments were also performed on specimens fabricated entirely of the interlayer materials.

Technical Progress

1.0 Analytical Efforts

The joint assessment and design model (JADM) described in the previous Semiannual Report has been incorporated into a PC computer code. It has been used to evaluate the performance of zirconia/zirconia and zirconia/cast iron joints as part of the validation calculations for large scale joints.

The model is based on elastic-plastic fracture mechanics principles, and incorporates effects associated with thermal expansion mismatch and modulus mismatch of various constituents, as well as non-linear material behavior as a function of load and temperature. Key properties of the constituents, such as those of the interlayer, reaction zone, and base material are provided as a data base; these data were measured in this program by using bulk samples. The model then uses the processing history, specimen geometry and loading conditions to evaluate the performance of the joint. The results of finite element analysis of cracked specimens have been consolidated in arriving at the engineering model, JADM.

The Joint Assessment and Design Model performs a number of functions, the two primary uses being:

(1) Evaluation of the performance of a joint with respect to the load-bearing capability of a monolithic ceramic specimen; this provides a measure of efficiency of the joint. Additionally, such relative performance is useful from a process/joint development viewpoint, since the ultimate goal is to develop a joint that has load-bearing capability at least as great as the monolithic ceramic.

(2) Evaluating the fracture load of the joint, which can then directly be used in any component design methodology.

Figure 1 is a print-out of the JADM calculations for a ZrO_2/ZrO_2 joint, fabricated using the MASZ-80 interlayer. The geometry is that of a cracked disk specimen with the crack (which is machined along the centerline of the joint) oriented at an angle of 0 degree with respect to the load axis. Thus, the material at either end of the crack experiences Mode I loading. The horizontal axis corresponds to the applied load, P, as a fraction of the critical load, P_c, for plastic collapse. The ordinate is the square root of the elastic component of the strain energy release rate, G_{el} as a fraction of the total (elastic-plastic) strain energy release rate, G_{total}, which is equal to G_c. The failure envelope is indicated by the curved line. The joint assessment vector (JAV) provides a measure of the joint's performance. For an applied load, P, of 3050 N, the JAV just intersects the failure envelope. Thus, this load corresponds to the load bearing capability of the joined disk specimen.

Figure 2 is a print-out of the JADM calculations for a ZrO_2/cast iron joint, fabricated using the active filler metal brazing process. The geometry is that of a cracked disk specimen (crack/length/diameter is 0.5), with the crack centered on the joint and rotated at an angle of 10 degrees with respect to the compressive load axis. With this loading arrangement, there is significant mixed-mode loading, i.e., the ratio of K_{II} to K_I is quite high. The JAV is calculated based on a reference load of 9541 N, which is the load needed to break a monolithic ZrO_2 specimen of identical geometry and loading arrangement. Note that the tip of the assessment vector lies well outside the failed region, indicating the load bearing capability of the joint is well below that of the monolithic ceramic specimen. In fact, by using different applied loads for calculation purposes, the calculated failure load of the joint (i.e., when the tip of JAV just touches the failure envelope) is estimated to be 6400 N. Experiments indicated that at an angle of 10 degrees, the joint failed at 6325 N. Note that the failure prediction had to take into account effects associated with mixed-mode loading.

Figure 3 provides a comparison of the predicted failure loads with measured failure loads based on experiments conducted in this project. The measured data incorporate results from cracked bend bars as well as cracked disk specimens with cracks oriented at angles up to 22.5 degrees with respect to the load axis; the angle limitation was necessitated because the crack length to diameter ratio of disk specimens was approximately 0.5, and negative K_I was intentionally avoided. The data incorporate results from monolithic ZrO_2 specimens as well ZrO_2/ZrO_2 and ZrO_2/cast iron joints. Each measured data point in Figure 3 corresponds to the average of a number of tests, so that the figure is based on a significantly large data base.

2.0 Experimental Effort

Numerous tests and experiments have been performed on specimens manufactured by joining zirconia to zirconia, by joining zirconia to cast iron and on the joint constituents; zirconia,

cast iron, braze metal, and ceramic interlayer material. In the experiments, small bend bars having dimensions 2.5 x 5.1 x 38.1mm were used in four point bend tests for load-displacement and failure stress determinations, and fracture bars having dimensions 5.1 x 5.1 x 38.1mm with a notch approximately 1.5mm deep at the joint were used for small scale fracture verification experiments. Scaled up joints used for model verification tests were in the form of disks having a diameter of 35.6mm and a thickness of 3.6mm. The advantage of the disk specimen in joint characterization is that it allows easy changeover from normal to a mixed-mode type of loading, simply by rotating the joint plane with respect to the loading axis. Mixed mode loading is extremely important in joint characterization, particularly with different substrates, because even under nominally Mode I loading, the stress-singularity has a mixed mode character.

Table 1 lists the number of tests of different types that were performed at room temperature; load-displacement data were recorded for many of the tests listed. In addition to the approximately 160 tests that are listed in Table 1, approximately 60 tests were performed early in this program; these earlier tests were conducted in the development stage of the joints, and the results were used to screen candidate joint material and joining techniques. Besides the room temperature tests, approximately 30 tests were conducted at high temperature. For the zirconia-zirconia joints and their constituents, the high temperature tests were performed at 1000 C, while, for the zirconia-cast iron joints, the high temperature tests were conducted at 400 C.

2.1 Ceramic-Ceramic Joints

Ceramic-ceramic joints were fabricated using interlayers obtained by mixing a base magnesia-alumina-silica (MAS) powder with various weight fractions of zirconia powder. The interlayers were designated MASZ-XX, where XX represents the weight fraction of zirconia in the MASZ mixture. The base MAS interlayer powder had the composition: 15 wt percent MgO, 20 percent Al_2O_3, 56 percent SiO_2, and 9 percent TiO_2. It was fabricated by milling the respective oxides and calcination at 1100 C for four hours, followed by re-milling. Differential thermal analysis confirmed that the MAS melted at a temperature close to 1300 C; joining temperatures higher than this temperature were selected.

Bulk MASZ-50, MASZ-67, and MASZ-80 interlayers material were fabricated in the form of bars using standard ceramic processing methods. PVA binder was added to the MASZ powders and bars approximately 50.8x 10.2x10.2 mm were cold isostatically pressed. After binder burnout, the bars were sintered using the identical temperature cycles that were employed during joining. Although the theoretical density of the interlayer material is unknown (because of the complicated phase constitution), the shrinkage indicated that the interlayer bars were approximately 85-90 percent dense.

Load-displacement data were monitored during many of the bend tests and fracture toughness tests. A high accuracy LVDT-type gage, calibrated to a maximum displacement of 25 to 50-microns, was used to measure displacement of the center of the bend bar with respect to the upper loading pins. Non-linearities were observed in the load-displacement records, particularly for the notched bend bars used in the fracture toughness tests. Such non-linearities may have been the result of subcritical crack growth.

Load-versus-crack opening displacements also were monitored during the fracture toughness tests using the cracked disk specimen. This specimen geometry was used for the validation experiments. Also, it provided a means to evaluate whether the analytical model was able to predict load-displacement data under mixed-mode fracture conditions. It may be noted that in actual applications, loading is generally mixed mode in character.

2.2 Ceramic-Metal Joints.

An active filler metal approach, using Incusil-ABA braze metal fabricated by GTE-Wesgo was used to braze Zirconia to modular cast iron. This material has the nominal composition : 59.2 Ag, 27.5 Cu, 12.1 In, 1.2 Ti, all in weight percent. All the large scale joints were successful using this approach.

Similar to the ceramic-ceramic joints, the constitutive response of the base zirconia, cast iron, and braze metal were determined in order to predict joint response based on stress-strain properties of the constituent materials. Tensile tests were performed on cast iron and Incusil-ABA, while bend tests were performed on the base zirconia. The temperature of testing ranged from room temperature to 400 C, the upper temperature limit for this type of joint. The strength and toughness of joints were evaluated using unnotched and notched bend bars and disk specimens.

Status of Milestones

All joints, both small scale and scaled up, have been manufactured and tested. Tests have included determination of load-displacement response of joints and their constituents, bend strength, fracture toughness, and failure loads under mixed mode conditions. An engineering joint assessment and design has been formulated, verified, and a PC computer code using the model has been written. The final report is in preparation for submittal in July, 1990.

Publications

Four papers were submitted for publication during this contract period. They were:

1. "Zirconia-Zirconia Joints - Part I, Fabrication and Microstructural Characterization", by B. S. Majumdar, S. L. Swartz, and A. T. Hopper, submitted to J. Amer. Cer. Soc.

2. "Zirconia-Zirconia Joints - Part II, Mechanical Characterization and analysis", by B. S. Majumdar, J. Ahmad, and A. R. Rosenfield, submitted to J. Amer. Cer. Soc.

3. "Fracture Toughness Evaluation of Ceramic Bonds Using a Disk Specimen", by B. S. Majumdar and A. R. Rosenfield, submitted ASTM Journal of Testing and Evaluation.

4. "Fracture Mechanics Assessment of Metal Ceramic and Ceramic-Ceramic Joints", by J. Ahmad and B. S. Majumdar, 22nd National Symposium on Fracture Mechanics, Atlanta, June 26-28, 1990.

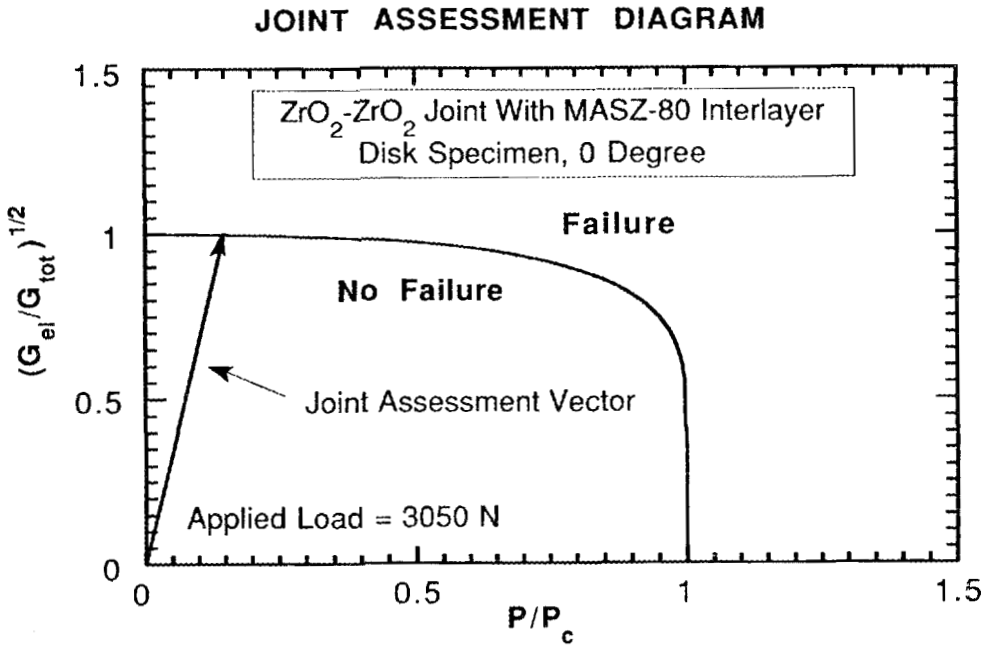

FIGURE 1. FAILURE DIAGRAM FOR ZrO_2-ZrO_2 JOINT SHOWING THE LOAD CARRYING CAPACITY OF THE JOINT.

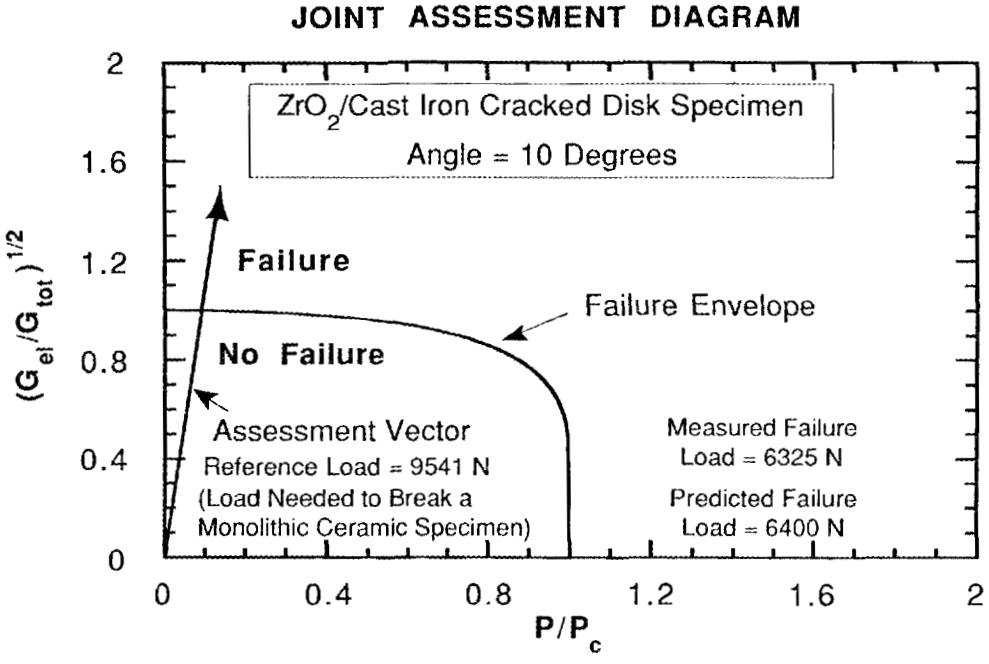

FIGURE 2. FAILURE DIAGRAM FOR A ZrO_2-CAST IRON JOINT SHOWING THE REDUCED LOAD CARRYING CAPACITY OF THE JOINT.

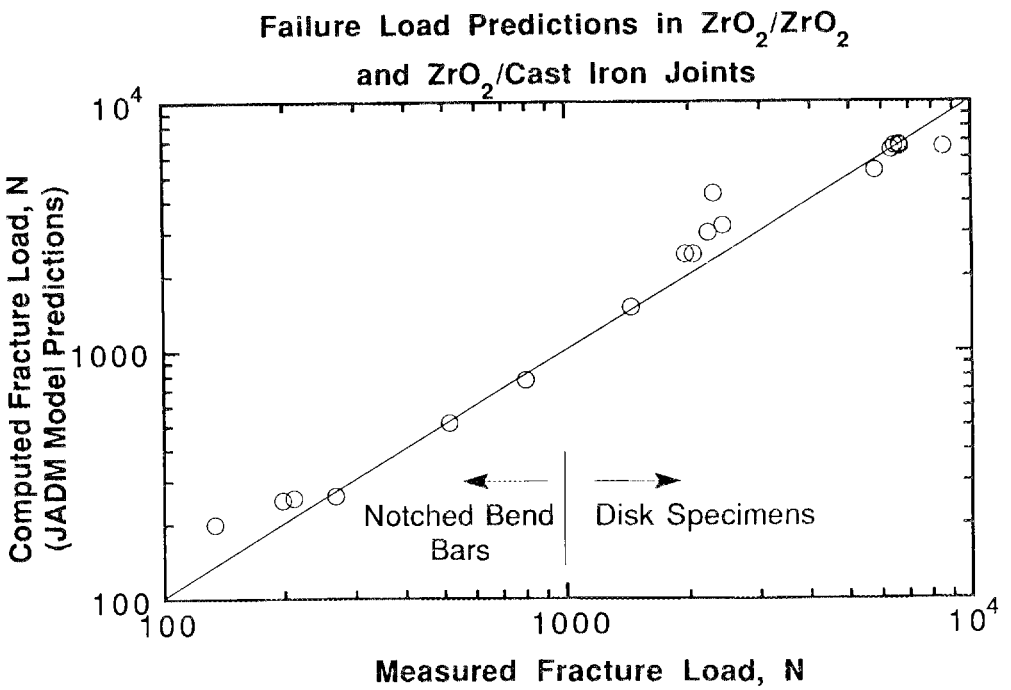

FIGURE 3. COMPARISON OF JADM CALCULATIONS AND EXPERIMENTALLY DETERMINED FRACTURE LOADS.

TABLE 1. COMPLETED TEST MATRIX FOR MECHANICAL TESTS PERFORMED AT ROOM TEMPERATURE.

Geometry	Base ZrO2 For ZrO2/CI Joint	Cast Iron	Braze Metal	ZrO2/Cast Iron Joint	MASZ-67 Interlayer	MASZ-80 Interlayer	MASZ-50 Interlayer
Bend Bar	4	2	3	27	6	6	6
Fracture Bar	2	-	-	8	3	2	1
Uncracked Disk	-	-	-	3	-	-	-
Cracked Disk	1	-	-	7	-	-	-

Geometry	ZrO2-MASZ67-ZrO2 Joint	ZrO2-MASZ80-ZrO2 Joint	ZrO2-MASZ50-ZrO2 Joint	ZrO2-MASZ67(1400C) ZrO2 Joint	ZrO2-MASZ80(1400C) ZrO2 Joint	Heat Treated ZrO2 For ZrO2/ZrO2 Joints
Bend Bar	21	10	6	6	6	10
Fracture Bar	5	3	-	2	2	2
Uncracked Disk	2	1	-	-	-	-
Cracked Disk	9	2	-	-	-	-

ZrO2-MASZ67-ZrO2 Joint implies a zirconia-zirconia joint fabricated at 1350 C, using MASZ-67 Interlayer. Similar nomenclature is used for joints with MASZ-50 and MASZ-80 Interlayers. ZrO2-MASZ67(1400C)-ZrO2 Joint implies a zirconia-zirconia joint fabricated at 1400 C, using MASZ-67 Interlayer. Similar nomenclature is used for the joint with MASZ-80 Interlayer. Heat Treated Zirconia refers to the zirconia that received a 1350 C heat treatment, similar to the thermal cycle involved in the fabrication of zirconia-zirconia joints.

Analytical and Experimental Evaluation of Joining Silicon Carbide to Silicon Carbide and Silicon Nitride to Silicon Nitride for Advanced Heat Engine Applications

G.A.Rossi, M.R.Foley, G.J.Sundberg, F.J.Wu, J.A.Wade

Norton Company

OBJECTIVE/SCOPE

The purpose of this program is to develop techniques for producing reliable ceramic-ceramic joints and analytical modeling to predict the performance of the joints under a variety of environmental and mechanical loading conditions including high temperature, oxidizing atmospheres. The ceramic materials under consideration are silicon nitride and silicon carbide. The joining approach for silicon nitride is based on the ASEA hot isostatic pressing process while the plan is to co-sinter silicon carbide green forms together. These joining methods were selected to produce joints which exhibit the minimum possible deviation in properties from those of the parent ceramic materials. Analytical models will be experimentally verified by measurements on experimental size and scale-up joints produced as part of this work.

Background

Because of their strength, oxidation resistance, and other desirable high temperature properties, silicon nitride and silicon carbide are under extensive study for use in advanced gas turbine and internal combustion engines. In both engine types there are requirements for joining the ceramics to themselves, other ceramics, and various engineering alloys. Existing bonding methods lack the high temperature capabilities required for use in advanced heat engines. Further, analytical modeling techniques to predict joint reliability and performance have not been developed. These technical needs have prevented consideration of economically fabricating large, complex ceramic engine components from smaller, less complicated segments. The current program will address these issues for silicon nitride to silicon nitride and silicon carbide to silicon carbide joints.

TECHNICAL PROGRESS

1. Mechanical Testing for Characterization (Task 1)

1.1 Fast Fracture of MOR Bars

All testing on MOR bars has been completed. Table 1 summarizes the mean strength for each specific test type and material. The fast fracture data includes the room temperature strength measured on MOR bars oxidized at high temperature and after thermal cycling.

1.2 Effect of High Temperature Oxidation on Strength

SiC joined MOR bars were tested at room temperature (RT) after oxidation treatment of 50, 100 and 200 hrs. at 1530°C in air. In all cases the average RT strength increased over that of the bars without oxidation. Si_3N_4 joined MOR bars were also tested at RT after oxidation treatments of 25, 50, and 200 hrs. at 1370°C in air. The Si_3N_4 controls were also tested at RT after exposure to 1370°C for 200 hrs. At the low exposure times of 25 and 50 hrs. the joined bars showed an increase in average strength over the value measured without oxidation. However, the strength for both joins and controls treated for 200 hrs. were lower than those measured without oxidation.

1.3 Effect of Thermal Cycling on Strength

All test bars were thermally cycled 1000 times between 1000°C and approximately 100°C in air. The time at 1000°C was 25 minutes and the time out of the furnace was 5 minutes. The strength of both materials, joined and controls, showed an increase over the MOR strength without thermal cycling.

1.4 Effect of Cyclic Fatigue on Strength

The cyclic fatigue tests were done at RT on a 5x40 mm four point bend fixture. The upper and lower stress limits were based on a percentage of the average MOR at RT. The cyclic test matrix started by cycling between 10 and 50% of the average RT strength and the sample was loaded with an initial stress of 30%. If the sample survived 1000 cycles at 1 Hertz, the upper limit was raised by 10% and the sample was cycled for another 1000 cycles. This 10% increased continued until the specimen failed. The results of these tests for both SiC and Si_3N_4, joined and controls, are reported in Table 2. The data is now being analyzed.

1.5 Stress/Strain on Cylindrical Tensile Specimens

All specimens have been machined, inspected and delivered for testing. The join in the SiC tensile rods became visible under ultraviolet light during dye penetrant inspection, whereas the join in Si_3N_4 rods was not visible. Room temperature and high temperature testing procedures are being established and testing is expected to be completed by April 30, instead of March 31, milestone date for end of characterization. The delay has been caused by several power failures and shutdowns.

1.6 Creep on "Dog-Bone" Specimens

Creep testing has begun and is continuing, but is behind schedule due to general power failures and shutdowns. Another delay was caused by the wearing out of the laser tubes that had to be replaced. Difficulties in attaining creep data on SiC, due to premature failures from inclusions or agglomerates and machining defects have also slowed down progress. The stress level required to observe creep in joined SiC specimens leaves it susceptible to early failure. In many cases such early failures were fast fracture. A complete set of data for joined Si_3N_4 at 1370°C at 3 stress levels is now available. It is expected that creep characterization will be completed by the end of April.

2. Microstructural/Chemical Characterization

Microstructural/chemical analysis of joined and control MOR bars for both SiC and Si_3N_4 was initiated to try to understand differences in mechanical behavior between joined and control samples. Due to limited funds, however, this study has not included sophisticated techniques such as Scanning Auger Spectroscopy and TEM/STEM. The results of this study are described below.

2.1 Microstructure by SEM

No significant microstructural differences between joined and control MOR bars appeared in SEM pictures, in both NCX-4500 SiC and NCX-5100 Si_3N_4. In SiC the join could be seen in most samples, whereas in Si_3N_4 was invisible, except when the join was obviously of poor quality, due to insufficient closure of the gap between adherent billets during HIP'ing.

Figs.1 through 4 were taken from a joined MOR bar of SiC at different magnifications. The interlayer thickness is about 100 μ.

Figs.5 and 6 were taken from polished joined and control MOR bars of Si_3N_4. The SEM pictures from the joined bars were taken at the center of the bar, where the join is located. However, since the join was not visible, it is possible that they do not represent the microstructure of the interlayer.

2.2 XRD of Powder from Joined and Control Bars.

For both Si_3N_4 and SiC, 3 mm thick slices were cut out of joined MOR bars at the center, so that the slice contained the interlayer region. Similar slices were obtained from control bars. The slices were ground to a powder and XRD patterns were obtained. Identical phases and polytype ratios were found in the powders from joins and controls, for both materials.

2.3 Laser Raman Spectroscopy Analysis

This analysis was performed at Rutgers University on both joined and control as-machined MOR bars for both materials. The join was not visible in the instrument monitor in either material. Eight spectra were collected for SiC and six for Si_3N_4 by performing a linear scanning across the join interlayer, which was located at the center of the bar. Each area interrogated was about 2 μ^2. No significant differences appeared in either material when different areas were analyzed in the joined specimen and when joined and control samples were compared. An attempt was made to increase the area to 10 μ^2, in order to get the result from a larger number of grains, but the sharp peaks obtained using 2 μ^2 area changed to broad bands.

In the case of SiC (see Figs. 7 and 8) a peak at about 1090 cm-1 appeared only once at the center of a joined MOR bar. All SiC spectra showed four peaks at 796, 972, 1370 and 1600 cm-1, the first two being the strongest ones. All these peaks have been reported by Japanese researchers (1) for NICALON fibers, except the 972 cm-1 peak. Since no alpha-SiC is present in the fibers, the 972 cm-1 peak in our spectrum could be due to alpha-SiC. The 1090 cm-1 peak, on the other hand, could be due to an impurity.

In the case of Si_3N_4 twelve peaks are present in the spectra (see Figs. 9 and 10) in the 100-1100 cm-1 range. These peaks have also been reported (2) except one at 520 cm-1. This peak is very likely due to free silicon, according to a recent Japanese paper (3).

2.4 Oxygen and Carbon Analysis by LECO

Oxygen and Carbon were analyzed by LECO in a 5mm slice cut out of an MOR bar. A slice was cut from a control bar, and two slices from a joined bar, one at the center containing the interlayer and the other near the end. The results are shown below.

Material	w/o O_2	w/o C	Location
Si_3N_4-J	2.34 +/-.08	0.57 +/-.02	near end
Si_3N_4-J	2.36 +/-.08	0.57 +/-.02	at join
Si_3N_4-C	2.23 +/-.08	0.39 +/-.02	
SiC-J	0.11 +/-.08	31.0 +/-.02	near end
SiC-J	0.31 +/-.08	31.0 +/-.02	at join
SiC-C	0.19 +/-.08	31.4 +/-.02	

Note: J = join; C = control

In the case of Si_3N_4 higher w/o O_2 and w/o C were found near the join. In the case of SiC more O_2 was found in the join region. Oxygen and Carbon enrichment at the join might have been caused by the binder used to prepare the aqueous slip.

2.5 Chemical Analysis by Microprobe

A joined MOR bar of Si_3N_4 was analyzed for O_2, Y and certain cation impurities using a microprobe. The measurements were taken along a straight line along the bar length, perpendicular to the joint plane, such plane being located at the center of the line. Eight measurements were made at each point, separated by a distance of about 400 μ. The area interrogated by the beam was about 80 μ^2. Figs. 11 and 12 show the results for O_2 and Y, respectively. No clear trend is apparent. The cations analyzed were Na, Ca, Al, Ti, Fe and Mg. Neither enrichment or depletion of impurities was found in the interlayer region. Microprobe analysis of impurities in a joined MOR bar of SiC is underway.

3. Analytical Modeling

Fast Fracture:

The development of modeling techniques to predict the fast fracture reliability of structural ceramics involves the implementation of finite element models to statistical and fracture mechanics analysis such as the ones found in CARES. This postprocessor developed by NASA-Lewis was recently available for ANSYS and is being evaluated under this contract. Updated versions of the program will be received shortly. Finite element MOR and tension models have been generated and will be compared with experimental results. Final results will be available in later reports.

Creep:

The Creep modeling procedure uses finite element methods to predict the time dependent deformation of structural ceramics at elevated temperatures. User-made creep subroutines using the theta projection method are under development.

STATUS OF MILESTONES

Milestones and deadlines for 1990 are reported below.

1. Complete characterization testing	Mar 31
2. Complete testing, model validation 2cm^2 joint	May 31
3. Complete 20 cm^2 joint experimental plan	Jun 30
4. Complete model development	Jun 30
5. Complete testing and model validation for 20 cm^2 joint	Aug 31
6. Delivery of final report	Oct 31

Milestone #1 is expected to be completed by April 30. The delay has been caused by power failures and shutdowns that have caused interruption of the creep and tensile tests.

Milestone #4 is also likely to be shifted to July 31, since modeling requires experimental data from characterization.

PUBLICATIONS

A paper entitled "Joining of Non-Oxide Ceramics for High Temperature Applications", co-authored by C.H.Bates, M.R.Foley, G.A.Rossi, G.J.Sundberg and F.J.Wu has been published in the March 1990 issue of the Bulletin of the American Ceramic Society.

REFERENCES

1. N. Sasaki et al. "Raman Study of SiC Fibres Made From Polycarbosilane", J. Mt. Sci., 443-448 (1987).

2. A. Takase and E. Tani, "IR Absorption and Raman Spectra of Sintered Si_3N_4 Under Pressure", Am. Ceram. Soc. Bull., 65 (12), 1590-1600 (1986).

3. A. Chino et al. "Determination of Free Silicon in Sintered Silicon Nitride by Laser Raman Spectroscopy", J. Ceram. Soc. Japan, Vol. 97, p.1466-1470 (1989)

FIGURE CAPTIONS

Fig. 1 Polished joined SiC MOR bar showing interlayer thickness of about 100 μ.

Fig. 2 Same as Fig. 1, higher magnification.

Fig. 3 Microstructure (SEM) of a joined MOR bar of SiC, polished and etched, taken at the center of the bar, within the interlayer.

Fig. 4 Microstructure (SEM) of a joined MOR bar of SiC, polished and etched, taken near the end of the bar, away from joint.

Fig. 5 Microstructure (SEM) of a joined MOR bar of Si_3N_4, polished and etched, taken at the center of the bar, where the interlayer is believed to be located.

Fig. 6 Microstructure (SEM) of a control (no join) MOR bar of Si_3N_4, polished and etched.

Fig. 7 Laser Raman pattern taken at the end of an as-machined joined SiC MOR bar, away from joint.

Fig. 8 Laser Raman pattern taken at the center of an as-machined joined SiC MOR bar, where the interlayer is believed to be located.

Fig. 9 Laser Raman pattern at the end of an as-machined joined Si_3N_4 MOR bar, away from joint.

Fig. 10 Laser Raman pattern at the center of an as-machined Si_3N_4 MOR bar, where the interlayer is believed to be located.

Fig. 11 Percent Yttrium determined by microprobe analysis as function of position on MOR bar surface, on a straight line intersecting the join plane.

Fig. 12 Percent Oxygen determined by microprobe analysis as function of position on MOR bar surface, on a straight line intersecting the joint plane.

TABLE 1

SUMMARY OF ORNL JOINING CONTRACT
CHARACTERIZATION MECHANICAL TESTS

TEST TYPE	SiC CONTROLS		SiC JOINS		Si_3N_4 CONTROLS		Si_3N_4 JOINS	
	MPa	(ksi)	MPa	(ksi)	MPa	(ksi)	MPa	(ksi)
MOR-RT	397	(57.6)	351	(50.9)	967	(140.2)	940	(136.4)
MOR-750°C	---		338	(49.0)	---		677	(98.2)
MOR-1370°C	---		---		570	(82.6)	526	(76.3)
MOR-1530°C	347	(50.3)	338	(49.0)	---		---	
OX-25 HR.	---		---		---		1019	(147.8)
OX-50 HR.	---		368	(53.4)	---		963	(139.7)
OX-100 HR.	---		394	(57.1)	---		---	
OX-200 HR.	437	(63.4)	394	(57.1)	840	(121.9)	829	(120.3)
THERMAL CYCLING	430	(62.4)	435	(63.1)	1087	(157.6)	1087	(157.7)

TABLE 2

CYCLIC FATIGUE DATA

	SiC (C)			SiC (J)		
SPECIMEN #	MPa (ksi)	% of MEAN	% OF CYCLES	MPa (ksi)	% of MEAN	# OF CYCLES
1	357 (51.8)	90	1	343 (49.8)	100	1
2	400 (58.0)	100	283	387 (56.1)	110	1
3	432 (62.7)	110	1	353 (51.3)	100	1
4	319 (46.3)	60	52	457 (66.3)	130	10
5	436 (63.3)	110	14	386 (56.0)	110	4
6	359 (52.1)	90	3	420 (60.9)	120	1
7	380 (55.1)	100	1	351 (51.0)	100	22
8	398 (57.8)	100	271	458 (66.4)	140	226
9	356 (51.6)	90	1	457 (66.3)	130	50
10	393 (57.0)	100	1	531 (77.0)	150	187

	Si_3N_4 (C)			Si_3N_4 (J)		
SPECIMEN #	MPa (ksi)	% OF MEAN	# OF CYCLES	MPa (ksi)	% OF MEAN	# OF CYCLES
1	969 (140.6)	100	103	753 (109.3)	80	875
2	969 (140.6)	100	14	942 (136.7)	100	6
3	968 (140.5)	100	774	847 (123.0)	90	471
4	969 (140.6)	100	212	971 (141.0)	100	26
5	775 (112.5)	80	18	847 (123.0)	90	832
6	873 (126.7)	90	1	847 (123.0)	90	807
7	788 (114.4)	80	642	846 (122.9)	90	52
8	969 (140.6)	100	379	847 (123.0)	90	180
9	969 (140.6)	100	77	847 (123.0)	90	683
10	872 (126.5)	90	583	829 (120.3)	90	578

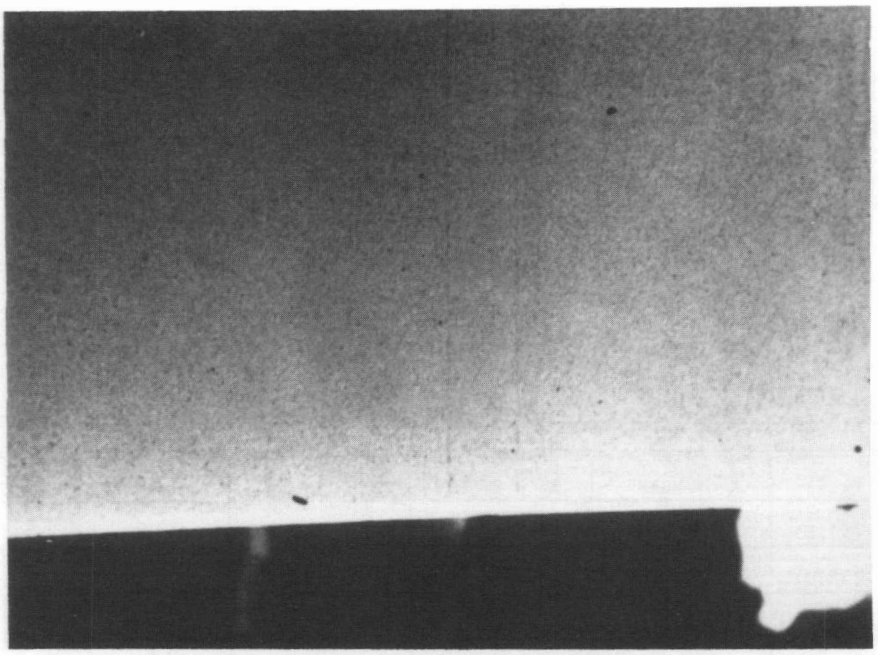

Figure 1
Polished joined SiC MOR bar showing interlayer thickness of about 100 μ.

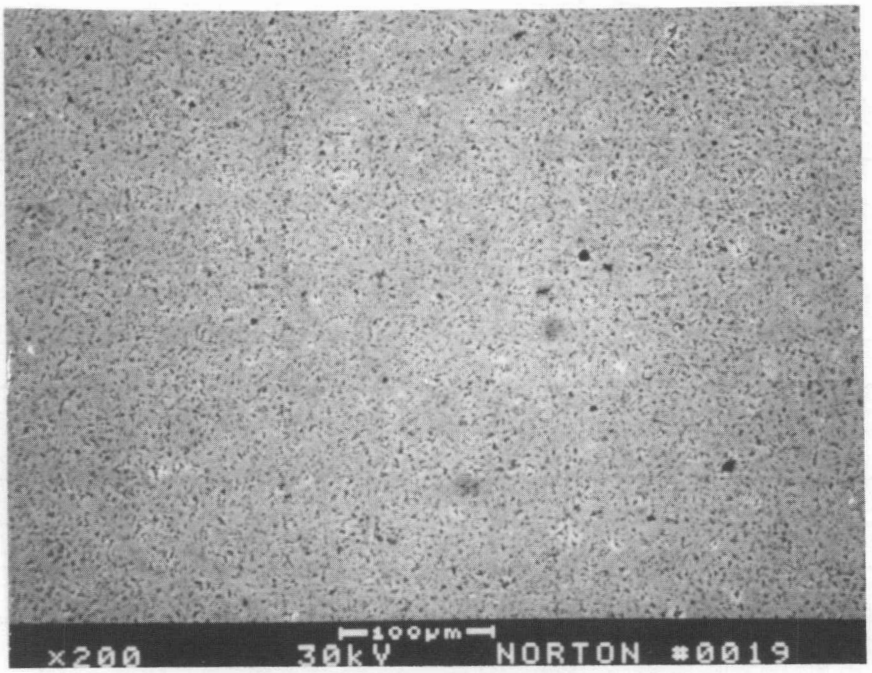

Figure 2
Same as Figure 1, higher magnification.

Figure 3
Microstructure (SEM) of a joined MOR bar of SiC, polished and etched, taken at the center of the bar, within the interlayer.

Figure 4
Microstructure (SEM) of a joined MOR bar of SiC, polished and etched, taken near the end of the bar, away from joint.

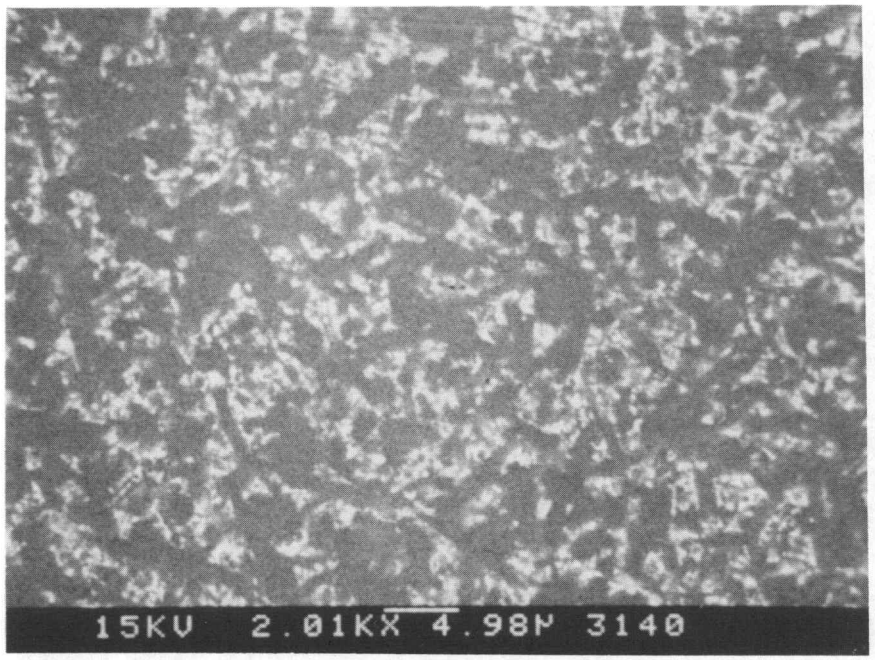

Figure 5
Microstructure (SEM) of a joined MOR bar of Si_3N_4 polished and etched, taken at the center of the bar, where the interlayer is believed to be located.

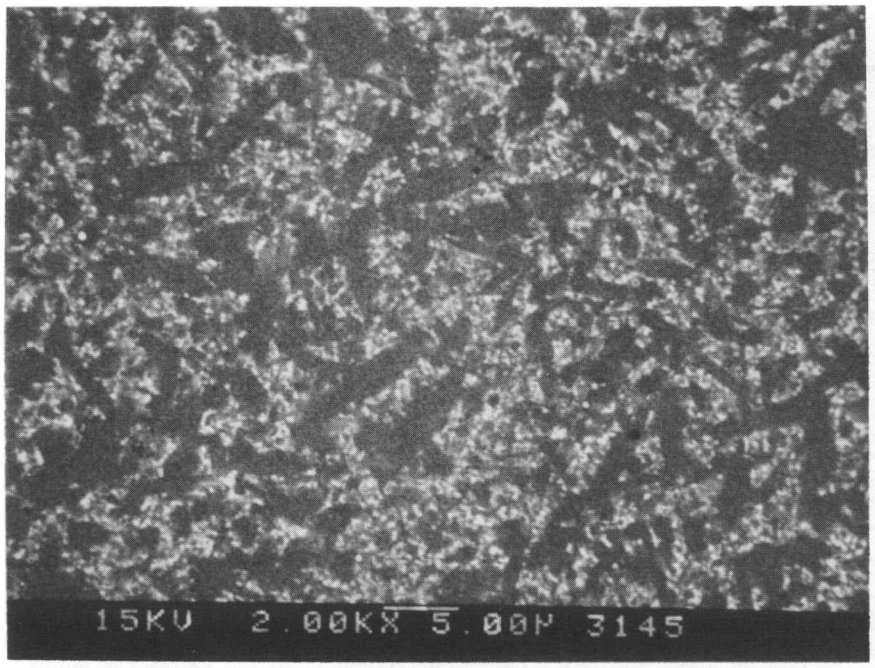

Figure 6
Microstructure (SEM) of a control (no join) MOR bar of Si_3N_4, polished and etched.

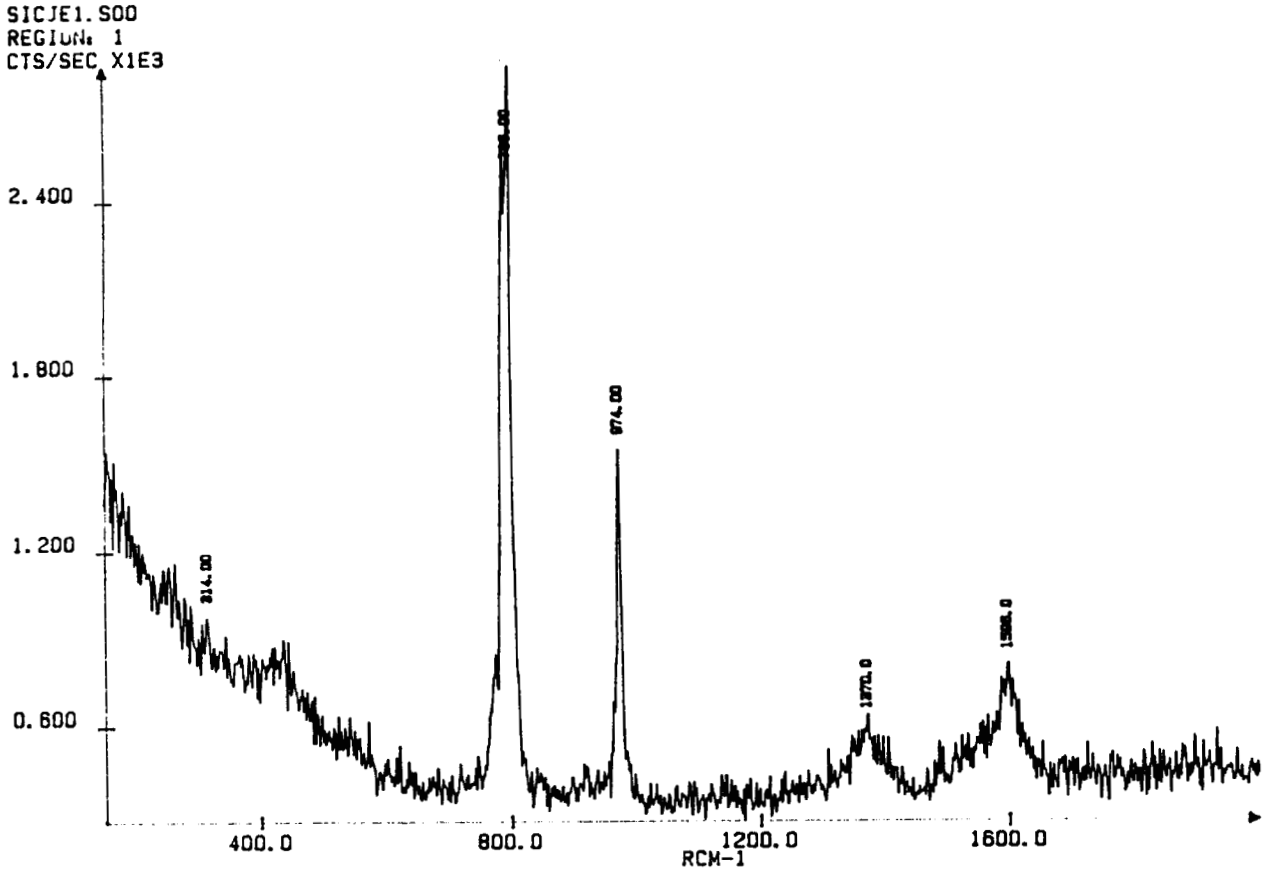

Figure 7
Laser Raman pattern taken at the end of an as-machined joined SiC MOR bar, away from joint.

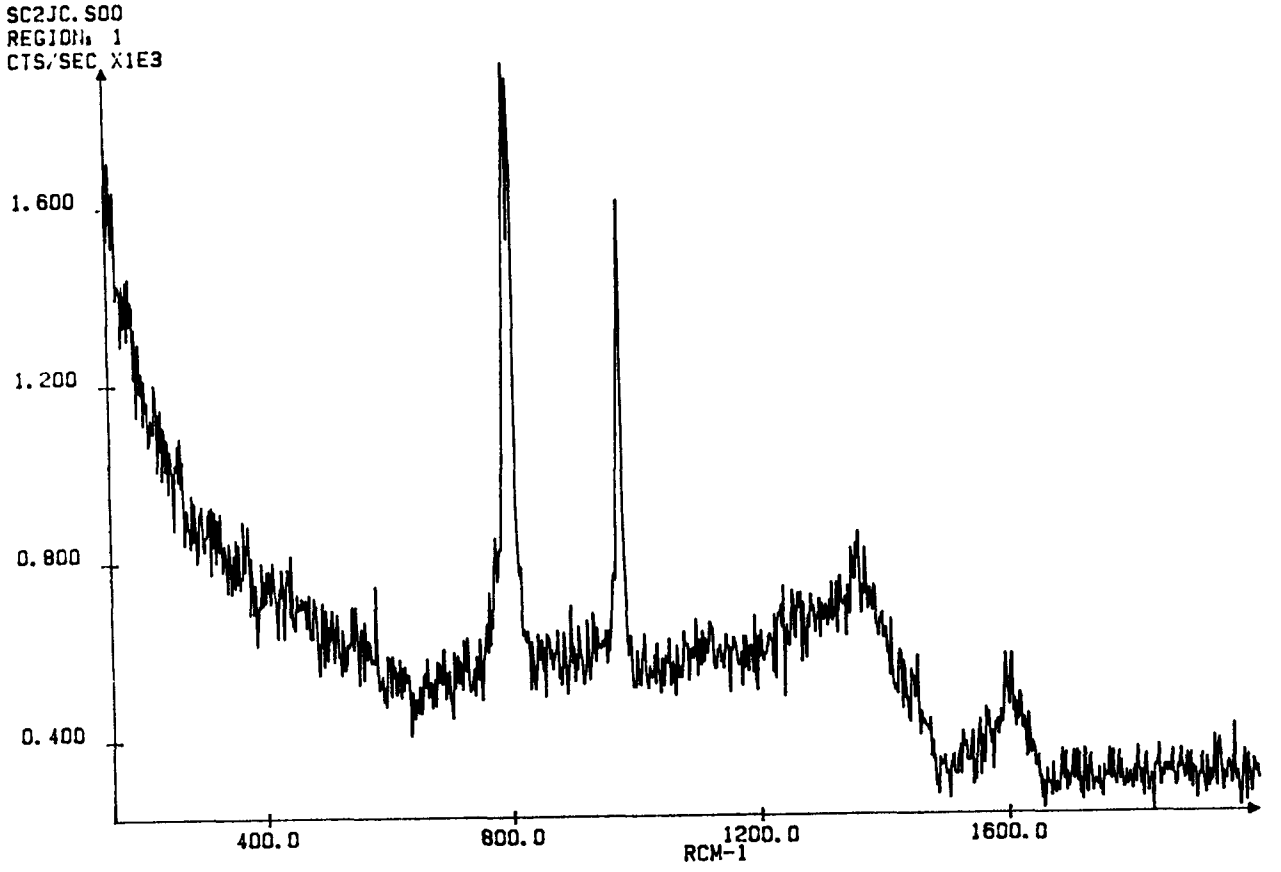

Figure 8
Laser Raman pattern taken at the center of an as-machined joined SiC MOR bar, where the interlayer is believed to be located.

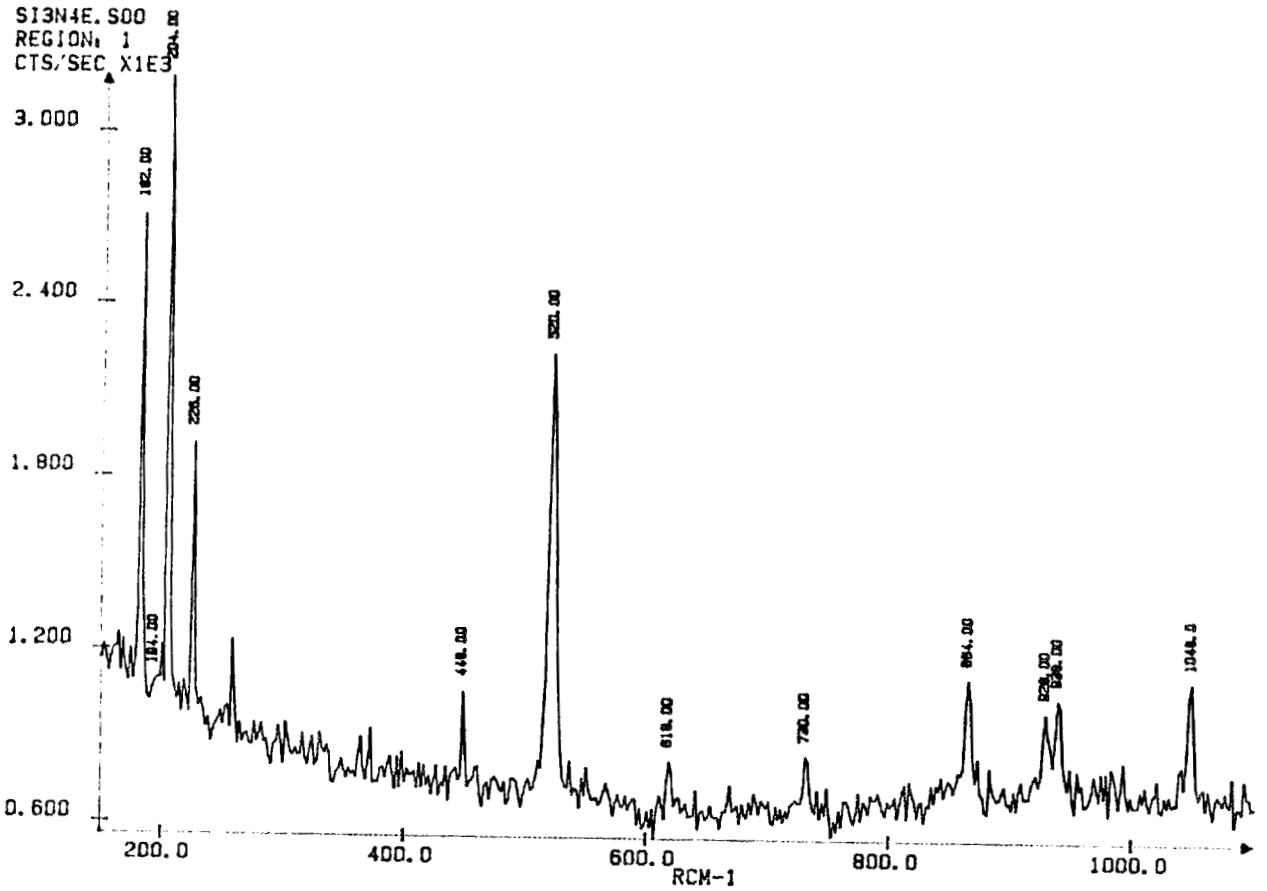

Figure 9
Laser Raman pattern at the end of an as-machined joined Si_3N_4 MOR bar, away from joint.

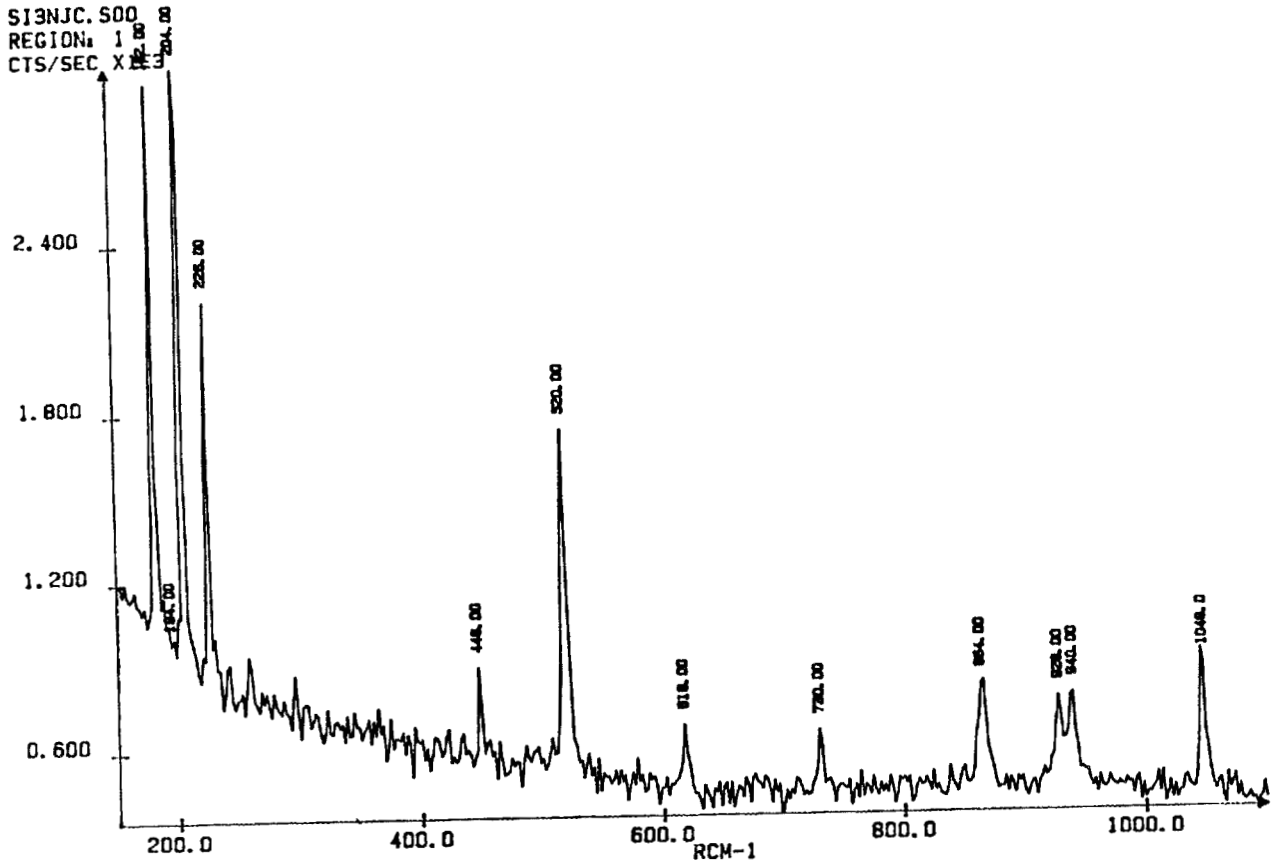

Figure 10
Laser Raman pattern at the center of an as-machined Si_3N_4 MOR bar, where the interlayer is believed to be located.

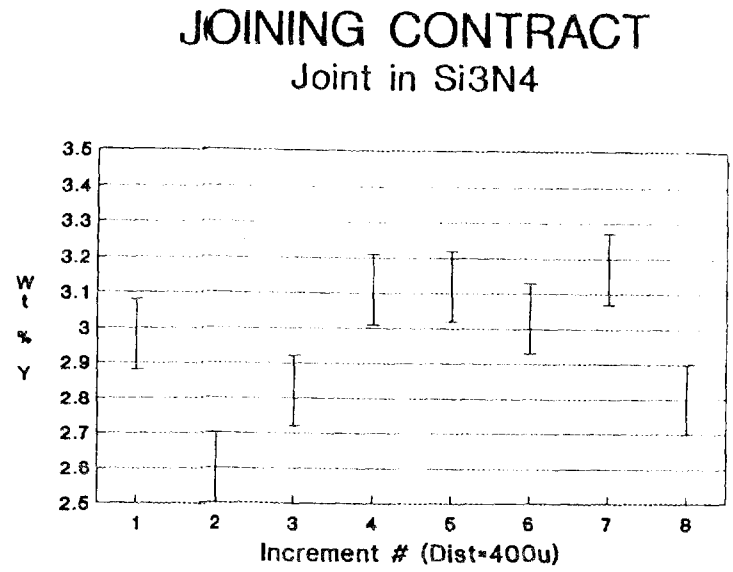

Figure 11
Percent Yttrium determined by microprobe analysis as function of position on MOR bar surface, on a straight line intersecting the joint plane.

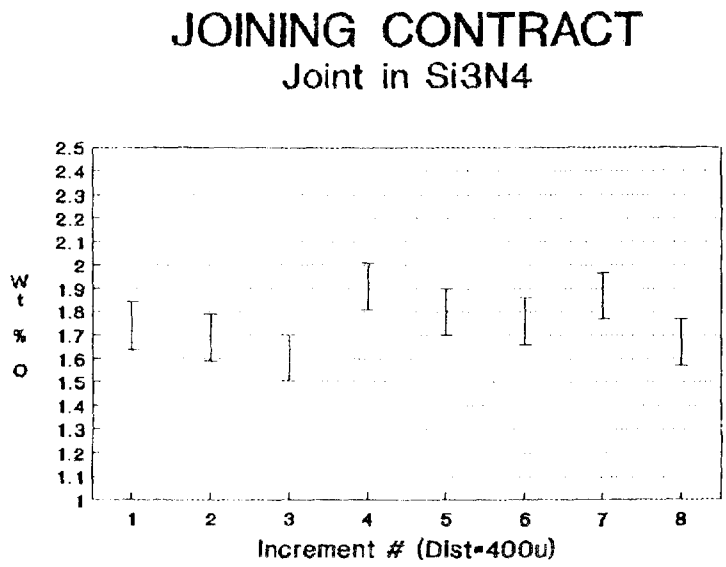

Figure 12
Percent Oxygen determined by microprobe analysis as function of position on MOR bar surface, on a straight line intersecting the joint plane.

2.0 MATERIALS DESIGN METHODOLOGY

INTRODUCTION

This portion of the project is identified as project element 2 within the work breakdown structure (WBS). It contains three subelements: (1) Three-Dimensional Modeling, (2) Contact Interfaces, and (3) New Concepts. The subelements include macromodeling and micromodeling of ceramic microstructures, properties of static and dynamic interfaces between ceramics and between ceramics and alloys, and advanced statistical and design approaches for describing mechanical behavior and for employing ceramics in structural design.

The major objectives of research in Materials Design Methodology elements include determining analytical techniques for predicting structural ceramic mechanical behavior from mechanical properties and microstructure, tribological behavior at high temperatures, and improved methods for describing the fracture statistics of structural ceramics. Success in meeting these objectives will provide U.S. companies with methods for optimizing mechanical properties through microstructural control, for predicting and controlling interfacial bonding and minimizing interfacial friction, and for developing a properly descriptive statistical data base for their structural ceramics.

2.1 MODELING

2.1.1 Modeling

Microstructural Modeling of Cracks - J.A.M. Boulet (University of Tennessee, Knoxville)

Objective/scope

The goal of the study is to develop mathematical procedures by which existing design methodology for brittle fracture could accurately account for the influence of protrusion interference on fracture of cracks with realistic geometry under arbitrary stress states. To predict likelihood of fracture in the presence of protrusion interference, a simulation will be developed. The simulation will be based on a three-dimensional model of cracks with realistic geometry under arbitrary stresses.

Technical progress

Use of the boundary element method (BEM) for analysis of cracked bodies has been explored further. As discussed in the previous semiannual report, the newer elastostatic kernels[1] have yet to be applied to multiply connected domains. Since a cracked body is a multiply connected domain, use of the newer kernels would require additional mathematical modeling before algorithm development could proceed. Because a better alternative exists (see below), the newer kernels will not be used in this project.

As discussed in the previous semiannual report, calculation of stresses near the crack is not accurate when the older elastostatic kernels[2] are used[1]. However, this "boundary layer" effect is not important for the present work. We need to calculate stress intensity factors (SIF's); as discussed below, this can be done without attempting to calculate stresses in the boundary layer. Hence, the older kernels are suitable for this project.

When straightforward application of the BEM to a body containing a closed crack is attempted, a singular linear algebra problem is found[3]. For an n-dimensional ($n = 2$ or $n = 3$) problem, evaluation of the discretized boundary integral equation (BIE) at a node yields n linear algebraic equations. Once the discretized BIE has been written for each node, the nodal equations are collected to form the overall linear algebra problem. If any two rows of the coefficient matrix in this problem are identical, the matrix is singular and the problem cannot be solved. But two adjacent nodes, one on each face of a closed crack, are mathematically at the same position. It follows that the coefficients in the nodal equations are the same for both nodes. Hence, the overall linear algebra problem is necessarily singular. (This difficulty would not occur if the crack faces were nowhere in contact.)

Singularity of the overall linear algebra problem for bodies with closed cracks can be overcome by using the multiple domain method[4, 5]. In this method, the body is separated into two regions (or subdomains) by an artificial boundary placed in its interior. The artificial boundary is arbitrary except that in each of the two regions it contains one face of the crack. The algebra problems resulting from application of the BEM to each region separately are both nonsingular. The results for the two regions can readily be combined to give the solution for the original domain.

As indicated above, SIF's can be calculated directly from BEM results without calculating stresses in the boundary layer. This is accomplished by choosing boundary elements that incorporate the stress and displacement singularities at the crack front[4, 5, 6, 7, 8].

The only feature of the present work that we have yet to consider relative to the older BEM kernels is interference (contact) of the crack faces. We plan to deal with this by iterative techniques similar to that used in previously reported two-dimensional analyses[9].

It appears that by using the multiple domain method, special boundary elements for the SIF's, iterative techniques for the contact tractions, and interference detection algorithms based on previously reported analyses[10], the three-dimensional crack-face interference problem can be analyzed using an existing BEM computer code with some modification. We are surveying the available codes and working toward acquiring one in the immediate future. If this effort is successful, development of an original code will cease.

References

1. N. Ghosh and S. Mukherjee, "A new boundary element method formulation for three dimensional problems in linear elasticity," *Acta Mech.* 67, 107-119 (1987).

2. T. A. Cruse, "Numerical solutions in three dimensional elastostatics," *Int. J. Solids Struct.* 5(12), 1259-1274 (1969).

3. T. A. Cruse, "Two-dimensional BIE fracture mechanics analysis," *Appl. Math. Modeling* 2, 287-293 (1978).

4. Z. H. Jia, D. J. Shippy and F. J. Rizzo, "Three-dimensional crack analysis using singular boundary elements," *Int. J. Numer. Methods* 28(10), 2257-2273 (1989).

5. R. Perucchio and A. R. Ingraffea, "Integrated boundary element analysis with interactive computer graphics for three-dimensional linear-elastic fracture mechanics," *Comp. Struct.* 20(1-3), 157-172 (1985).

6. A. R. Ingraffea and C. Manu, "Stress-intensity factor computation in three dimensions with quarter-point elements," *Int. J. Numer. Methods Engrg.* 15(10), 1427-1445 (1980).

7. M. L. Luchi and A. Poggialini, "Computation of 3-dimensional stress intensity factors using special boundary elements," pp. 461-470 in *Boundary Element Methods, Proc. Fifth Int. Conf. on B. E. M.*, Ed. C. A. Brebbia, Springer-Verlag, Berlin, 1983.

8. M. L. Luchi and S. Rizzuti, "Boundary elements for three-dimensional crack analysis," *Int. J. Numer. Methods Engrg.* 24(12), 2253-2271 (1987).

9. J. A. M. Boulet, *Interference of Protrusions on the Faces of a Griffith Crack in Biaxial Stress*, Final Technical Report, ESM Account No. R01-1351-37, Department of Engineering Science and Mechanics, University of Tennessee, Knoxville, Tennessee, February, 1990.

10. J. A. M. Boulet, "Microstructural Modeling of Cracks," pp. 209-11 in *CTAHE Project Bimonthly Technical Progress Report to DOE Office of Transportation Systems, August-September, 1989*, ORNL/CF-89/307, Oak Ridge National Laboratory, Oak Ridge, Tennessee, October, 1989.

Status of milestones

The recently revised milestone schedule is given below.

2111005	Represent crack faces as mathematical surfaces embedded in Euclidean space.	Jul-15-1989	Completed
2111006	Model protrusion interference kinematics.	Aug-15-1989	Completed
2111007	Solve three-dimensional protrusion interference problem.	Oct-01-1989	Terminated
2111008	Develop and implement numerical model of three-dimensional protrusion interference problem and conduct verification experiments.	Dec-31-1990	
2111009	Define and implement computer-based simulation based on numerical model.	Jul-01-1991	
2111010	Define design procedure based on computer-based simulation and identify methods for gathering required data.	Oct-01-1991	
2111011	Obtain experimental verification of design procedure.	Feb-28-1991	

2.2 CONTACT INTERFACES

2.2.1 Static Interfaces

The Elastic Properties and Adherence of Thin Films and Coatings on Ceramic Substrates - Debra L. Joslin (Department of Materials Science and Engineering, The University of Tennessee-Knoxville, Knoxville, Tennessee 37966-2200)

Objective/scope

The objective of this research is the examination of the effects of ion bombardment on the structure of thin ceramic films on ceramic substrates. The material combinations will include oxide films that have (a) no solid solubility, (b) limited solid solubility, and (c) complete solid solubility with the substrate material (also an oxide). Techniques for determination of elastic and plastic properties of thin films or coatings on ceramic substrates and for the determination of the strength of the bond between the film and substrate, which are currently being developed, will be used to determine the hardness, elastic modulus, and adherence of each material combination. The main testing techniques will be the ultra-low load micro-indentation tester (Nanoindenter) and thermal cycling tests.

Technical highlights

Implantation and analysis were performed on two specimens during the first part of this report period: (1) oxygen implanted into a chromium layer on sapphire, and (2) chromium implanted into a Ti_xO_y/Al_2O_3 multilayered structure on silicon.

For (1), it is desired that the implanted oxygen come to rest at the Cr/Al_2O_3 interface, so that the possibility of reaction to form Cr_2O_3 exists. The chromium layers deposited for system (1) were analyzed before implantation using Rutherford Backscattering Spectroscopy (RBS). From the analysis, it is known that the Cr layer already contains a small amount of oxide which may affect the implantation. After implantation with 80 keV oxygen at a fluence of 1×10^{16} ions/cm^2, RBS analysis showed no mixing effects. The Cr film will now be etched from this sample, and both the implanted and unimplanted areas will be reanalyzed using RBS to determine which area contains more chromium. Transmission Electron Microscopy (TEM) analysis will also be performed.

For (2), it is desired that the implanted chromium come to rest at a position far beyond the first four layers of the specimen (distance greater than 100 nm). A multilayer sample of crystalline Ti_xO_y and amorphous Al_2O_3 on a silicon sulbstrate was obtained for use in this study. The sample was made up of 38 repetitions of alternating layers of crystalline Ti_xO_y and amorphous Al_2O_3. In the implanted area, the thickness of each layer was approximately 190 nm. The sample was implanted with 350 KeV Cr^{2+} at room temperature. While RBS did not detect the presence of the multilayered structure either before or after implantation, TEM cross-section samples of the as-implanted specimen did show that a multilayer was indeed present. From this sample, some evidence of implantation damage could be discerned.

Other experiments involving a series of ion beam mixed copper films on sapphire substrates were performed during this reporting period. The mixed films and a control film (100-nm-thick copper, unmixed) were tested using the Nanoindenter.

Two of the films, 90 nm- and 58 nm-thick, respectively, were mixed using 1.5 MeV xenon at a fluence of 1X 10^{16} ions/cm^2. Another 50 nm-thick film was mixed with 1.5 MeV xenon at a fluence of 5 x 10^{15} ions/cm^2. The indentation test was designed so that the hardness was determined at approximately 0.5, 0.75, 1.25 and 2 times each of the respective film's thicknesses. The measured hardnesses of the mixed films were all greater than that of the unmixed film. A slight dip in hardness was noted at 0.75 times the thickness in each of the unmixed films, suggesting that irradiation produces some significant effect in the material at that depth.

An investigation of the stoichiometry of the ceramic films deposited for this project was conducted. Using an rf sputter unit, 1000 Å-thick chromium oxide and zirconium oxide films were deposited on freestanding diamond film substrates. Rutherford Backscattering (RBS) measurements were performed on an uncoated diamond film and on the coated films. The oxide films were found to be rich in oxygen. The chromium oxide is actually $Cr_2O_{4.2}$, and the zirconium oxide is $ZrO_{2.8}$. No oxygen was detected on the uncoated substrate. Within the sensitivity of RBS, the films were free from foreign contaminants.

After the stoichiometry of the films was determined, several chromium oxide and zirconium oxide films were grown on sapphire. One specimen of each oxide was implanted with 340 keV chromium ions to doses of either 1 x 10^{15} or 1 x 10^{16} ions/cm^2. These samples will now be examined using Rutherford backscattering spectrometry.

An investigation of implanted iron films on sapphire similar to the investigation of the copper films on sapphire was initiated. The films were tested on the Nanoindenter. Two of the films were implanted with 100 keV neon (one with 2 x 10^{15} ions/cm^2 and one with 2 x 10^{16} ions/cm^2). The other two films were implanted with 1.3 MeV Kr (one with 2 x 10^{16} ions/cm^2 and one with 4 x 10^{16} ions/cm^2). The data from these experiments are being processed.

Status of milestones

N/A

Publications

None

2.2.2 Dynamic Interfaces

Studies of Dynamic Contact of Ceramics and Alloys for Advanced Heat Engines.

P.A. Gaydos and K.F. Dufrane (Battelle)

Objective/Scope

The objective of the program is to develop an understanding of the friction and wear processes of ceramic interfaces based on experimental data. The supporting experiments are to be conducted at temperatures to 650 C under reciprocating sliding conditions reproducing the loads, speeds, and environment of the ring/cylinder interface of advanced engines. The test specimens are to be carefully characterized before and after testing to provide detailed input to the model. The results are intended to provide the basis for identifying solutions to the tribology problems limiting the development of these engines.

Technical Highlights

Apparatus

The apparatus developed for this program uses specimens of a simple flat-on-flat geometry, which facilitates specimen procurement, finishing, and testing. The apparatus reproduces the important operating conditions of the piston/ring interface of advanced engines. The specimen configuration and loading is shown in Figure 1. The contact surface of the ring specimen is 3.2 x 19 mm. A crown with a 32 mm radius is ground on the ring specimen to ensure uniform contact. The ring specimen holders are pivoted at their centers to provide self-alignment. A chamber surrounding the specimens is used to control the atmosphere and contains heating elements to control the temperature. The exhaust from a 4500 watt diesel engine is heated to the specimen temperature and passed through the chamber to provide an atmosphere similar to that of actual diesel engine service. A summary of the testing conditions is presented in Table 1.

Materials

Ring and Cylinder Materials

The compositions of the various materials used in the study are presented in Table 2. A variety of monolithic and coating materials were selected to represent various chemical compositions and materials with previously demonstrated successful sliding performance.

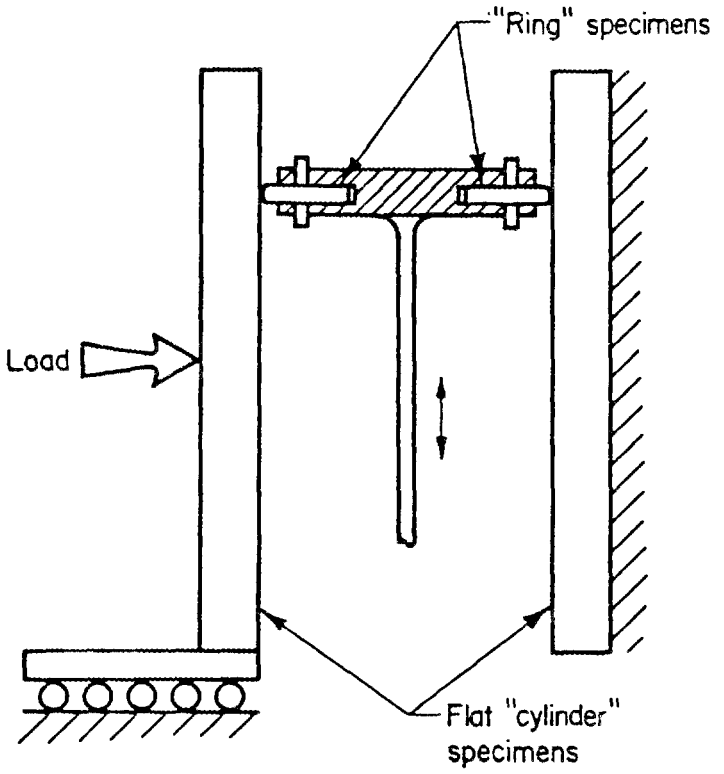

Figure 1. Test specimen configuration and loading

TABLE 1. SUMMARY OF TESTING CONDITIONS

Sliding Contact:	Dual flat-on-flat
"Cylinder" Specimens:	12.7 x 32 x 127 mm
"Ring" Specimens:	3.2 x 19 x 19 mm
"Ring" crown radius:	32 mm
Motion:	Reciprocating, 108 mm stroke
Reciprocating Speed:	500 to 1500 rpm
Average Specimen Speed:	1.8 to 5.4 m/s
Load:	to 950 N
Ring Loading:	to 50 N/mm
Atmosphere:	Diesel exhaust or other gases
Measurements:	Friction and wear (after test)

TABLE 2. MATERIALS FOR EVALUATION

Monolithic Ceramics	Coatings
YPSZ	Tribaloy 400
MPSZ	METCO 130 (13 TiO_2, 87 Al_2O_3)
ATTZ	METCO 501 (30 Mo, 12 Cr, bal Ni)
α SiC	Plasmalloy 312M ($MoSi_2$)
SiC/Al_2O_3	Cr_2O_3 (5 Cr, bal Cr_2O_3)
Sialon	Jet-Kote WC (12 Co, bal WC)
K162B (TiC - Ni/Mo)	Cr (Electroplated)
Si_3N_4	PS212 (Cr_3C_2 + BaF_2/CaF_2 + Ag)
	VR73 (WC/TaC/TiC/Co)
	VA 20 (WC/TaC/TiC/Ni)
	CA 815 (Cr_3C_2/Ni)
	Mo
	Duplex (WC and Mo)
	Ion Implanted (N in Cr_2O_3)

Wear Experiments

Previous Wear Results

In the first phase of the study the need for lubrication at the ring/cylinder interface was established by the high friction coefficients and wear rates measured during dry sliding of monolithic ceramics and ceramic coatings. With lubrication, the wear rates of ceramic coatings such as Cr_2O_3 and WC tested at 260 C were found to approach those measured in heavy duty truck engines with conventional ring/cylinder materials. With the need for lubrication, the maximum operating temperature with ceramics was found to be limited by the availability of suitable lubricants. A summary of the wear and friction data obtained under a variety of conditions is shown in Table 3.

PS212 Coating Evaluation

Further evaluation of the NASA PS212 was conducted because of encouraging results reported at the 27th Annual Automotive Technology Development Contractors' Coordination Meeting. This coating, consisting of a nickel aluminide-bonded chromium carbide with silver and Group II fluorides, was supplied by NASA Lewis Research Center. Past wear tests conducted using PS212 coatings on cylinder specimens showed poor wear results in both dry and lubricated tests. Ring wear is the parameter that is usually measured because it is a much more limiting factor than is cylinder wear. Hence very little cylinder wear data are available for comparison with the PS212 results.

For completeness and more meaningful data comparisons, ring specimens coated with PS212 were run against Cr_2O_3 coated stationary specimens within SDL-1 lubricant at 260 C. The wear was so high, however, that after the 1-hour room-temperature break-in the coating was completely removed, and no further testing could be conducted. The wear coefficients for the break-in period averaged 4.9×10^{-4} (8.3×10^{-6} $mm^3/N\text{-}mm$), and the friction coefficient ranged from 0.05 to 0.08. It appears that while this material may possess excellent friction and wear characteristics in pin-on-disk tests, more demanding tests such as those performed at Battelle show a large degeneration of those characteristics.

High Temperature Lubricant Evaluation

During this reporting period, the high temperature liquid lubricant evaluation for this phase of the program was completed. Further evaluation of Dow Chemicals experimental X-1P fluid was conducted, and Monsanto's OS-124 (polyphenyl ether) was also tested for comparison with it. In addition, the base stocks of two previously evaluated Lubrizol polyolester lubricants were tested to compare their friction and wear performance with that of their formulated versions. Lastly, a repeat test using formulated Lubrizol OS-80001H lubricant was conducted because of inconsistencies in the results from the first test. Unless otherwise stated, all of the high temperature lubricant tests were run with self-mated plasma sprayed Cr_2O_3 coatings. Tables 4 and 5 summarize the lubricants evaluated and the friction and wear results from the first part of the evaluation. A discussion of the most recent results follows.

TABLE 3. COMPARISON OF APPROXIMATE RING WEAR COEFFICIENTS

Ring Material	Cylinder Material	Lubricant	Temperature, C	Ring Loading, N/mm	Friction Coefficient	Hardness Used in Calculation, kg/mm^2	Average Ring Wear Coefficient	
							Dimensionless	$mm^3/N\text{-}m$
Cr	Cast Iron	SAE 30	100	17.5	--	975	5×10^{-9} [a]	2×10^{-10}
Cr	Cast Iron	SDL-1	100	12.3	0.03 - 0.04	975	8×10^{-8}	3×10^{-9}
WC	SiC/Al_2O_3	SDL-1	260	14.5	0.04 - 0.09	2080	3×10^{-7}	5×10^{-9}
SiC/Al_2O_3 [b]	Cr_2O_3	SDL-1	260	12.3	0.03 - 0.08	2000	5×10^{-7}	8×10^{-9}
ESA	Cr_2O_3	SDL-1	260	12.3	0.03 - 0.06	2200	6×10^{-7}	9×10^{-9}
WC	Cr_2O_3	SDL-1	260	13.9	0.03 - 0.08	2080	6×10^{-7}	1×10^{-8}
Cr_2O_3 [c]	Cr_2O_3 [c]	SDL-1	260	12.3	0.04 - 0.08	2000	1×10^{-6}	2×10^{-8}
Cr_2O_3	Cr_2O_3	SDL-1	260	13.4	0.05 - 0.08	2000	1×10^{-6}	2×10^{-8}
VR73	Cr_2O_3	SDL-1	260	12.3	0.05 - 0.09	2200	1×10^{-6}	2×10^{-8}
Cr_2O_3	SiC/Al_2O_3	SDL-1	260	15.7	0.04 - 0.08	2000	1×10^{-6}	2×10^{-8}
Si_3N_4	Si_3N_4 [d]	SDL-1	260	15.7	0.04 - 0.08	2000	1×10^{-6}	2×10^{-8}
Si_3N_4	Si_3N_4	SDL-1	260	12.3	0.05 - 0.06	2000	3×10^{-6}	5×10^{-8}
αSiC	αSiC	SAE10	20	17.0	0.04 - 0.08	2700	3×10^{-6}	4×10^{-8}
Cr_2O_3	Cr_2O_3	LB625	260	12.3	0.02 - 0.16	2000	5×10^{-6}	9×10^{-8}
Duplex	Cr_2O_3	SDL-1	260	12.3	0.04	2000	1×10^{-4}	2×10^{-6}
Cr	Cast Iron	SDL-1	260	15.7	0.07 - 0.1	975	1×10^{-5}	4×10^{-7}
Cr_3C_2	Cr_2O_3	SDL-1	260	14.0	0.13	2650	2×10^{-5}	3×10^{-7}
Cr	Si_3N_4	SDL-1	260	12.3	0.14	975	1×10^{-4}	4×10^{-6}

(a) Typical actual diesel truck engine experience
(b) CC7000
(c) Nitrogen-ion implanted
(d) Surface modified by Ceraprep process

TABLE 4. PREVIOUSLY EVALUATED HIGH TEMPERATURE LUBRICANTS

BASE STOCK	SOURCE	MANUFACTURER DESIGNATION
Polyalkylene Glycol	Union Carbide	UCON LB-625
Polyalkylene Glycol	Union Carbide	UCON LB-650X
X-1P	Dow	X-1P Fluid
Polyolester	Lubrizol	OS-80001H
Polyolester	Lubrizol	OS-75725L

TABLE 5. WEAR RATES OF Cr_2O_3 RING SPECIMENS IN VARIOUS HIGH TEMPERATURE LUBRICANTS*

Lubricant	Temperature	Run Duration min.	Friction Coefficient	Average Ring Wear Coefficient Dimensionless	$mm^3/N\text{-}m$
OS-75725L	260	60	0.07 - 0.09	1.4×10^{-6}	2.4×10^{-8}
LB-625	100	480	0.06 - 0.08	2.9×10^{-6}	4.9×10^{-8}
X-1P	460	240	0.07 - 0.10	3.0×10^{-6}	5.1×10^{-8}
OS-75725L	370	240	0.13 - 0.25	1.2×10^{-5}	2.1×10^{-7}
LB-625	260	60	0.02 - 0.08	1.6×10^{-5}	2.7×10^{-7}
LB-650X	300	120	0.02 - 0.06	1.6×10^{-5}	2.7×10^{-7}
LB-650X	260	120	0.02 - 0.06	1.9×10^{-5}	3.3×10^{-7}
OS-80001H	370	120	0.07 - 0.10	2.1×10^{-5}	3.6×10^{-7}
LB-625	300	120	0.05 - 0.13	4.5×10^{-5}	7.6×10^{-7}
OS-80001H	260	120	0.07 - 0.09	4.5×10^{-5}	7.7×10^{-7}

*Diesel exhaust environment 10.3 N/mm ring loading 500 rpm motoring speed

Further Evaluation of Dow X-1P

Another small quantity of X-1P fluid was obtained, and further characterization of its lubricating ability at high temperatures was conducted. For additional baseline data at 460 C, hard-chrome-plated ring specimens were run against cast iron cylinder specimens in X-1P fluid. A 1-hour break-in at room temperature was conducted using SDL-1 oil, and the wear coefficients averaged 6.8×10^{-8} (1.2×10^{-9} $mm^3/N\text{-}m$) with friction coefficients ranging from 0.02 to 0.06. The same specimens run at 460 C gave an average wear coefficient of 1.7×10^{-5} (2.9×10^{-7} $mm^3/N\text{-}m$) and friction coefficients between 0.23 and 0.32. More oil than usual was needed to keep the specimens lubricated, and it was necessary to reduce the ring loading during the run. Plasma sprayed Cr_2O_3 ring and cylinder specimens had five times less wear under similar conditions.

Comparison of X-1P and OS-124

Dow Chemical was pleased with the performance of its experimental X-1P fluid on Battelle's test rig and supplied some OS-124 (polyphenyl ether) lubricant to be run for comparison. Preliminary hot plate tests showed that the fluid burned off very cleanly throughout the range of possible test temperatures. Table 6 shows how the lubricant faired in tests with self-mated Cr_2O_3 coated specimens.

TABLE 6. WEAR AND FRICTION COEFFICIENTS FOR CR_2O_3 COATED SPECIMENS RUN IN X-1P AND OS-124 FLUIDS

Lubricant	Test Temp. (C)	Test Duration (min.)	Average Ring Wear Coefficient Dimensionless	$mm^3/N\text{-}m$	Friction Coefficient
X1P	460	240	3.0×10^{-6}	5.1×10^{-8}	0.07 - 0.10
OS-124	370	120	1.9×10^{-5}	3.2×10^{-7}	0.03 - 0.06
OS-124	460	30	1.3×10^{-4}	2.2×10^{-6}	0.14 - 0.19

It is readily apparent that the X-1P performed much better than the OS-124 did at 460 C. The test run with OS-124 had to be shut down after only 30 minutes because the friction was so high and the specimens required a higher than normal flow of fluid to operate quietly. Higher volatility of the OS-124, compared with the X-1P, is the most likely reason for the required increase in lubricant flow to the interface. At a lower test temperature, 370 C, the OS-124 performed fairly well. Both the wear and friction coefficients decreased significantly from the 460 C test. Testing at this temperature also required more lubricant than usual, and the test was shut down at 2 hours to conserve the fluid supply. The OS-124 burned off very cleanly during the test, but did not seem to have enough usable viscosity available at the test temperatures to lubricate the ring/cylinder interface adequately.

Evaluation of Lubrizol Base Stocks

The base stocks of two Lubrizol polyolester oils were used to lubricate self-mated Cr_2O_3 coated ring and cylinder specimens at elevated temperatures. Their formulated versions, OS-75725L and OS-80001H, could not be run higher than about 360 C because of deposit formation. By running the base stocks, it was hoped that higher test temperatures could be run without the problem of deposit formation. For convenience, the base stocks will be referred to by the last letter of the formulated oil in the following discussion.

In preliminary hot plate tests, base stock "H" burned off cleanly at the desired test temperature. While conducting actual tests, however, the fluid began leaving deposits as low as 260 C. Because of the deposit formation, the upper test temperature limit for base stock "H" was 360 C. This test temperature is no higher than the highest test temperatures with formulated OS-80001H. Base stock "L" unexpectedly left deposits in a similar hot plate test, so deposit formation during actual testing was all but certain. Since the formulated version was run to 370 C, it was decided to run the base stock at that temperature even though it would leave a large amount of deposits.

Table 7 shows the friction and wear results of the tests run with the Lubrizol base stocks. The data from the tests with the formulated versions are also presented for comparison. Both base stocks performed well at 260 C compared with the formulated versions. At 370 C, however, the OS-75725L fluid produced a wear coefficient 3 times smaller than with its base stock. Base stock "H", on the other hand, performed better than the formulated version at both 260 and 370 C. High porosity was seen in the ring coatings used for the OS-80001H tests (Figure 2), and this could be the reason their wear rates were so high.

TABLE 7. WEAR AND FRICTION COEFFICIENTS FOR CR_2O_3 COATED SPECIMENS RUN IN LUBRIZOL FLUIDS

Lubricant	Test Temp. (C)	Test Duration (min.)	Average Ring Wear Coefficient Dimensionless	$mm^3/N\text{-}m$	Friction Coefficient
Base Stock "L"	260	240	1.0×10^{-6}	1.8×10^{-8}	0.03 - 0.07
Base Stock "H"	260	240	1.1×10^{-6}	1.9×10^{-8}	0.05 - 0.08
OS-75725L	260	60	1.4×10^{-6}	2.4×10^{-8}	0.07 - 0.09
Base Stock "H"	370	120	1.1×10^{-5}	1.8×10^{-7}	0.09 - 0.18
OS-75725L	370	240	1.2×10^{-5}	2.1×10^{-7}	0.13 - 0.25
OS-80001H	370	120	2.1×10^{-5}	3.6×10^{-7}	0.07 - 0.10
Base Stock "L"	370	75	3.5×10^{-5}	6.0×10^{-7}	0.03 - 0.06
OS-80001H	260	120	4.5×10^{-5}	7.7×10^{-7}	0.07 - 0.09

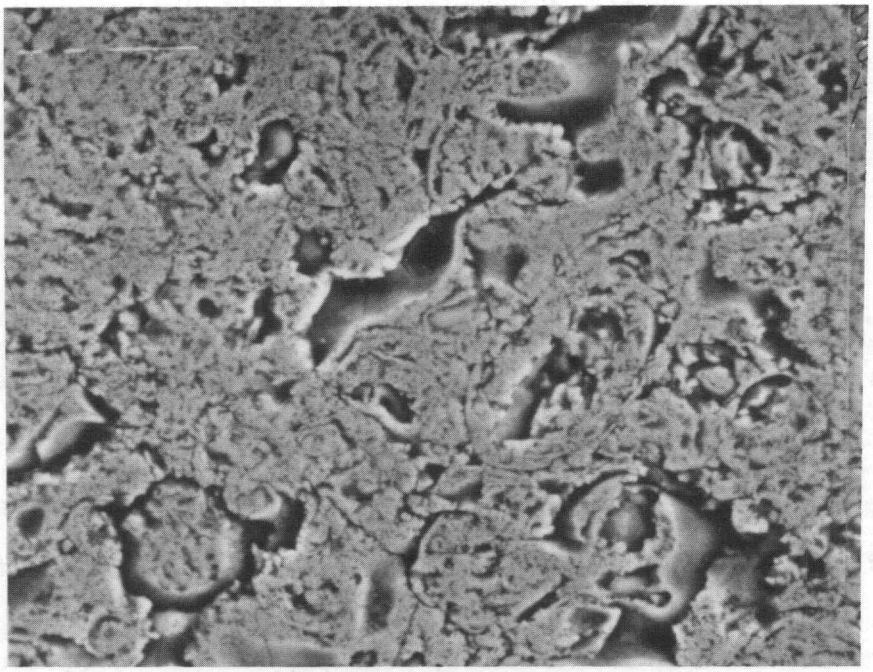

1000X 84975

a. Porous coating surface of first OS-80001H test

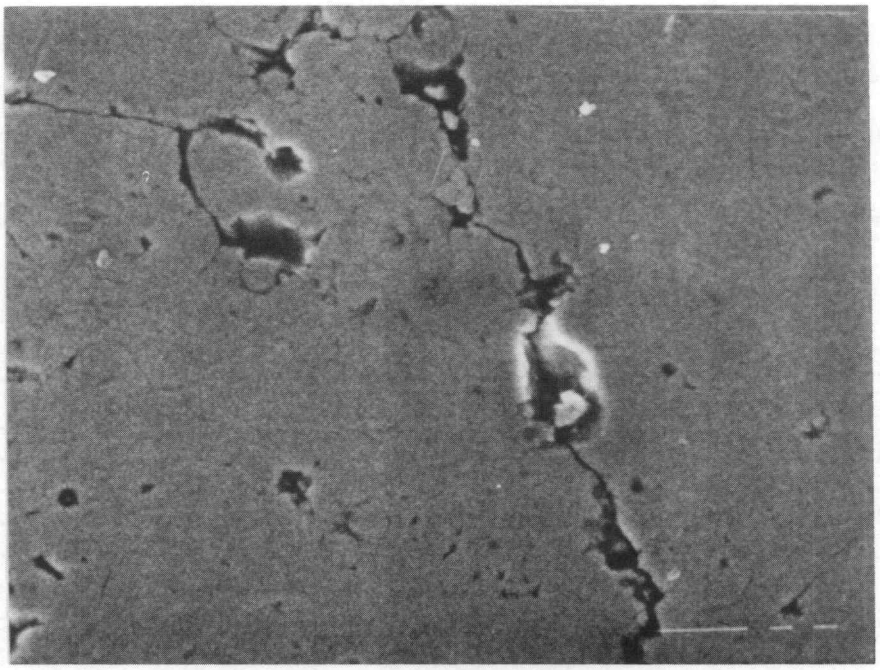

1000X 84982

b. Typical Cr_2O_3 coating surface

FIGURE 2. POROSITY OF Cr_2O_3 RING COATING WEAR SURFACES AFTER TESTING

Retest of Lubrizol OS-80001H Lubricant

An earlier test of self-mated plasma sprayed Cr_2O_3 coated specimens run with Lubrizol OS-80001H lubricant showed inconsistent results. The portion of the test running at 370 C resulted in lower wear than in the 260 C test. This result was peculiar because wear usually increases with higher temperature due to decreasing lubricant viscosity. In addition, the wear performance of the ring specimens running in this lubricant was relatively poor. The high porosity of the Cr_2O_3 ring coatings mentioned earlier was thought to be the cause of the abnormal wear.

A retest was conducted with formulated OS-80001H and plasma sprayed Cr_2O_3 coatings to try and achieve more consistent wear results. Table 8 shows the friction and wear results from the first test and the retest. The retest showed lower wear rates at both 260 and 370 C than measured in the first test by as much as ten times. The results of this test show the need for consistent coating quality.

TABLE 8. WEAR AND FRICTION COEFFICIENTS FOR CR_2O_3 COATED SPECIMENS RUN IN LUBRIZOL FLUIDS

Lubricant	Test Temp. (C)	Test Duration (min.)	Average Ring Wear Coefficient Dimensionless	$mm^3/N\text{-}m$	Friction Coefficient
OS-80001H	260	120	4.5×10^{-5}	7.7×10^{-7}	0.07 - 0.09
OS-80001H*	260	120	4.6×10^{-6}	7.8×10^{-8}	0.06 - 0.08
OS-80001H	370	120	2.1×10^{-5}	3.6×10^{-7}	0.07 - 0.10
OS-80001H*	370	120	5.6×10^{-6}	9.5×10^{-8}	0.06 - 0.10

* Repeat test

Status of Milestones

The study is progressing in accordance with the overall milestone schedule.

Publications

A paper entitled "Studies of Dynamic Contact of Ceramics and Alloys for Advanced Heat Engines" by P.A. Gaydos and K.F. Dufrane was submitted to SAE for publications as part of the 1989 CCM Proceedings.

2.3 NEW CONCEPTS

ADVANCED STATISTICAL CONCEPTS OF FRACTURE IN BRITTLE MATERIALS

C. A. Johnson and W. T. Tucker
General Electric Corporate Research and Development
Schenectady, NY 12301

Objective/Scope

The design and application of reliable load-bearing structural components from ceramic materials requires a detailed understanding of the statistical nature of fracture in brittle materials. The overall objective of this program is to advance the current understanding of fracture statistics, especially in the following four areas:

- Optimum testing plans and data analysis techniques.
- Consequences of time-dependent crack growth on the evolution of initial flaw distributions.
- Confidence and tolerance bounds on predictions that use the Weibull distribution function.
- Strength distributions in multiaxial stress fields.

The studies are being carried out largely by analytical and computer simulation techniques. Actual fracture data are then used as appropriate to confirm and demonstrate the resulting data analysis techniques.

Technical Highlights

Work performed during this reporting period included significant effort in two areas: Bias correction using bootstrap simulation and probabilistic strength analysis in multiaxial stress states. The following two sections describe recent progress in each.

1. Bias Correction using Bootstrap Simulation

Work during this reporting period included studies of bias correction through the use of information available in bootstrap analyses. Bootstrap analyses of confidence and tolerance bounds for Class IV problems (where the fracture data include specimens from multiple specimen sizes and loading geometries, while the component of interest may be of yet a different size and loading configuration) have been described in earlier semi-annual reports. Bootstrap analyses utilize estimators such as maximum likelihood and linear regression to digest a set of fracture strengths and estimate quantities such as the Weibull parameters and/or the probability of failure of a component at any quantile of interest (at any probability of failure of interest).

As with most estimators, these Weibull estimators have the property of yielding "biased" or offset estimates. The definition of bias is most easily illustrated using Figure 1 (generated during an earlier study on analysis of fracture origin positions) which

displays the variability and bias of the conventional maximum likelihood estimator of the Weibull modulus where all data are of one specimen size and loading configuration. The ratio of the estimated m to the true m is shown as a function of the number of fracture strengths being analyzed. The family of curves included on Figure 1 describes the distribution of estimates such that 1 percent of the time the ratio of m's is below the curve labelled "1"; 5 percent of the time it is below "5", etc. The curve labelled "50" then describes the median behavior where half the estimates of m's should be smaller and half should be larger. The dashed line on Figure 1 describes the arithmetic average or mean behavior.

If one considers a group of ten fracture strengths analyzed using maximum likelihood, it can be seen from Figure 1 that there is a five percent chance that the estimated m is less than 0.74 times the true m; while another five percent chance (100-95) that the estimated m is greater than 1.83 times the true m. This range of uncertainty in estimation is a natural result of sampling error that may occur due to the relatively small amount of information contained in only ten measurements of fracture strength. Since it is generally recognized that maximum likelihood is a very good method of estimation, it is disturbing in a way that neither the average nor the median behavior of this estimator properly predicts the true m. For 10 specimens, the ratio of m's for the median is 1.11 and for the average is 1.17. Therefore, the center of the distribution described by the contours of Figure 1 is shifted or biased from the preferred position (it is not centered on unity). The maximum likelihood estimator of the Weibull modulus is known as an asymptotically unbiased estimator because as one analyzes larger and larger numbers of strengths, the magnitude of the bias in estimates of m approaches zero as can be confirmed on Figure 1. As seen in the figure, the bias is even detectable with 100 specimens.

With information such as that of Figure 1, an estimate of m can be corrected for bias. If the above example of ten strength measurements yielded a maximum likelihood estimate for m of 10.0, then the unbiased estimate of the median m would be equivalent to $10.0/1.11 = 9.0$. Similar methods could be used to calculate the unbiased estimate of m at any probability of occurrence of interest. Unbiased confidence intervals would then involve a similar correction at two probabilities. The unbiased 90 percent confidence interval are estimated by calculating the bias correction to the 5 and 95 percent contours as follows: $10.0/0.74 = 13.5$; $10.0/1.83 = 5.46$. Therefore the unbiased 90 percent confidence interval on the Weibull modulus would be 5.46 to 13.5.

The Weibull modulus is not the only estimate that is susceptible to bias. The Weibull scale parameter (sigma zero) and any estimate of strength (at the same specimen size or any other) is also subject to errors due to bias. Strength estimates are particularly prone to large bias errors, especially if the strength is being estimated for a specimen or component with a much larger (or smaller) effective size than the test specimens. This large bias after size extrapolation is primarily related to bias in the estimate of m. Of course, a small error in m will lead to progressively larger errors in predicted strength as one extrapolates farther and farther from the effective size of the

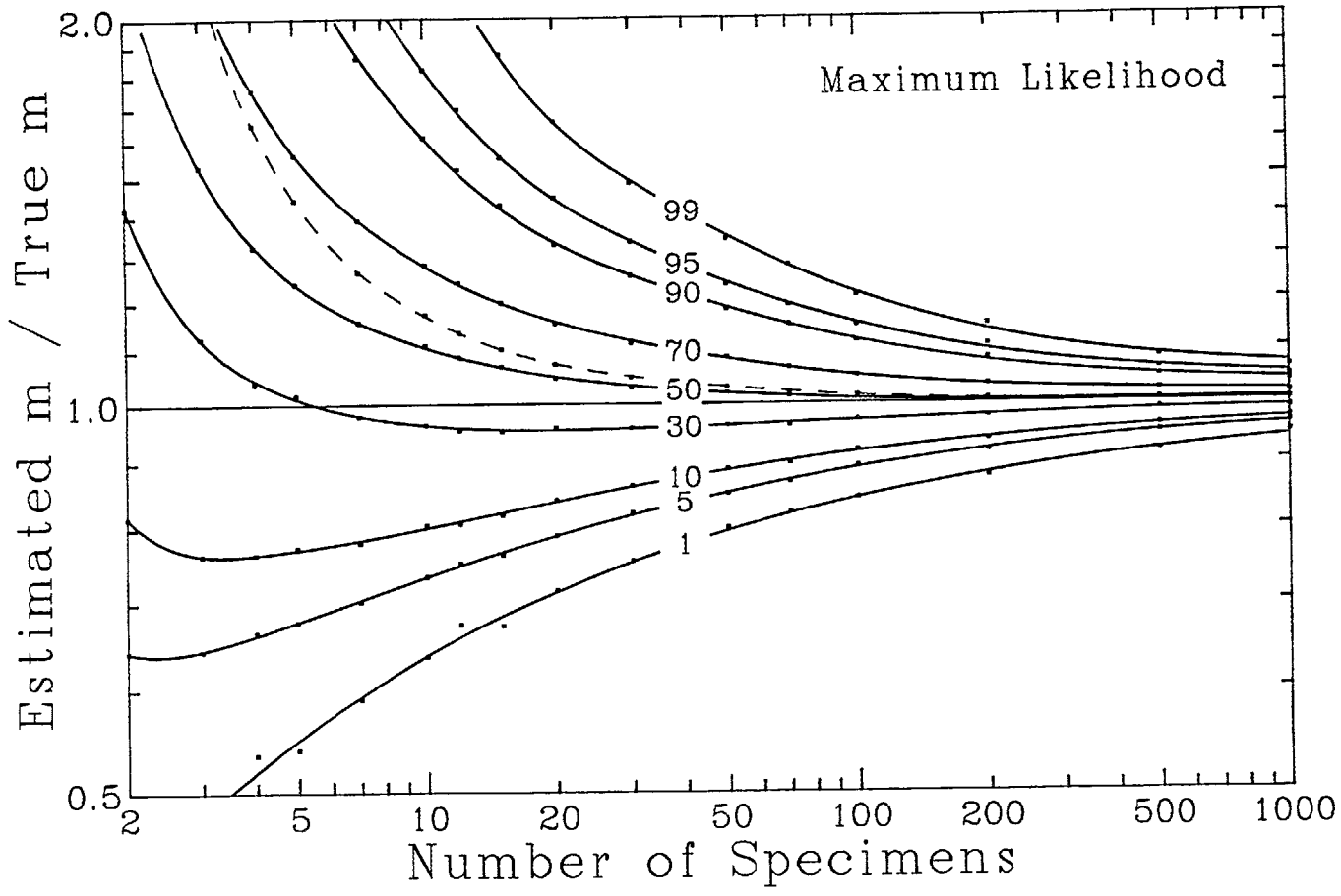
Maximum Likelihood
Estimated m / True m
2.0
1.0
0.5
99
95
90
70
50
30
10
5
1
2
5
10
20
50
100
200
500
1000
Number of Specimens

Figure 1

test specimens.

Bias can be corrected for m, sigma zero, strength estimates, etc using information such as Figure 1. In Class IV problems, however, there are many more independent variables than just the number of specimens in a single group. In addition, there are variables such as the number of specimen sizes represented in the overall data set, the relative size of each specimen, the number of specimens in each subgroup, etc. As has been pointed out in earlier reports, due to the larger number of independent variables, it is not feasible to provide information such as that of Figure 1 in advance for all combinations of Class IV problems that may become of interest.

Figure 1 was generated using Monte Carlo simulation to understand the characteristics of the maximum likelihood estimator for Class I problems. This technique involves the simulation of many computer-generated groups of failure strengths that are chosen randomly from a true Weibull distribution of strengths with a known set of Weibull parameters. By analyzing each group with the same estimator, characteristics about the variability and bias of this estimator were obtained.

The bootstrap technique for estimating confidence and tolerance bounds carries out a similar simulation, but it is performed after the problem has been defined (number of groups, sizes, etc.). Although not normally utilized, that simulation contains information about the degree of bias introduced by the estimator used in that particular bootstrap analysis. This information is now being used within the bootstrap analysis computer program to yield (practically) unbiased estimates of distribution parameters and strength estimates as well as unbiased estimates of confidence and tolerance bounds on those parameters and strength estimates.

The basic bootstrap begins with analysis of the original set of experimentally observed fracture strengths. The analysis includes at least the estimation of the distribution parameters, m and sigma zero, and may also include estimation of the strength of components at one or more component size and probability of failure that may be of interest. The bootstrap part of the analysis then involves the creation of simulated data sets that are derived from the original data set by either parametric or nonparametric methods. Each simulated data set is analyzed using the same estimator as was used on the original data set and, again, includes estimation of Weibull parameters and may include estimation of strengths at component sizes of interest. The simulation is carried out a large number of times; in this study, typically 1000 times. The distribution of m values created during the various simulation trials, then represents the variation in m values that should be expected from random sampling error. If the m's resulting from the simulations are ordered, then the range of m values from the 25th to the 975th (of 1000) is an estimate of the 95 percent confidence interval on estimates of m using this particular estimator (in 950 of 1000 trials, the estimated m value was found to fall in this interval when sampling error was the only source of error). Similar bounds can be placed on predicted strengths at a specific component size and probability of failure of interest by estimating that component strength for each of the bootstrap simulations and carrying out a similar ordering to

find the interval in strength that contains 95 percent of the estimated strength values. Of course, there is nothing magic about 95 percent intervals, so the confidence interval could be estimated in this fashion for any level of confidence that may be of interest.

Bias correction takes advantage of the fact that the "true" m and sigma zero are known for the 1000 simulated data sets, at least for parametric bootstrap methods. In the parametric bootstrap, the experimentally observed m and sigma zero are used as the true values when generating the simulated data sets (the true m is not known for the experimental data set that led to the simulation, but after choosing m and sigma zero for the simulation, those chosen parameters are, of course, known exactly). If the average m value calculated in the 1000 bootstrap simulations is not equal to the true value, then the offset or "bias" between these two values is a measure of how the whole distribution of bootstrapped m's has been shifted due to bias. Once the degree of bias is known, correction of the original estimate of m (from the experimental fracture data) as well as bias correction of the confidence intervals of interest is similar to that described above. Bias corrections can be made in a parallel manner for strength estimates and confidence intervals on strength estimates.

Bias correction of m values depends on the fact that the ratio of estimated and true m values is invariant (the distribution of the ratio is not a function of the magnitude of the true m). This invariance is reflected in the y-axis of Figure 1 as well as in details of the bias correction manipulations described above. A parallel invariant exists for strength estimates which is exact in Class I-III problems and approximate in Class IV problems (discussed in earlier semi-annual reports). This invariant of strengths is the quantity: $m \ln \hat{\sigma}/\sigma$.

The efficiency and validity of methods to correct bias in parameter and strength estimates have been evaluated by carrying out simulations of the input data to the bootstrap analysis. Since the bootstrap itself is a simulation, the check of validity in bias correction is then a simulation of a simulation; therefore, the computer execution time mushrooms quickly.

Evaluation of the validity of bias correction requires knowledge of the true distribution parameters of the experimental data set. In actual experimental data, this information clearly is not available. The problem can be approached, however, by another level of simulation where the experimental data sets are not observed by fracturing test specimens in the laboratory, but rather are created by simulation. "Simulated experimental" data sets can be created by choosing "true" distribution parameters and randomly choosing specimens from that distribution. These simulated strengths then serve as the experimental data, but in this case, the true underlying m and sigma zero are known exactly. The full bootstrap evaluation is then carried out on the "simulated experimental" data and bias corrections are made. The true m value can then be compared with the distribution of bias-corrected bootstrapped m's. For the sake of discussion, let us say that the true m fell at the 30 percentile position of the bias-corrected bootstrapped m's for this first data set. The true parameters are then

used to create a second set of simulated experimental data that, of course, contain different random sampling errors. The bootstrap analysis of this second data set will yield a similar but different distribution of bootstrapped m values. Therefore the true m might fall at say the 65 percentile position for this second analysis.

If this second level of simulation is continued for a large number of times, say 1000 times, and if the method by which the bootstrapped distribution of m's are created and bias-corrected is accurate, then the set of percentiles of the type discussed above should be uniformly distributed from zero to 100 (or if described as probabilities, they would be uniformly distributed from zero to one). A convenient method of evaluating the uniformity of distributions is by simple plots of observed probability vs expected probability where the expected probability is deduced by ranking position (similar to what is done in ranking fracture strengths and assigning associated probabilities of failure). If the points are uniformly distributed in probability from zero to one then the points should fall on a diagonal straight line from the lower left to the upper right of such a plot.

Figure 2 is such a probability vs probability plot showing the behavior of estimates of Weibull modulus from linear regression (regressing specimen size on fracture strength) for six groups of specimens with ten specimens per group. The six groups corresponded to MIL STD 1942MR specimens A, B, and C tested in both 3-point and 4-point bending (similar to the experimental data set of SiC specimens that has been described and used in several previous reports). A straight diagonal line is included on Figure 2 to illustrate the ideal behavior. The two irregular lines correspond to the behaviors of $\hat{m}$ values that in one case are uncorrected for bias and in the other are corrected. It is clear that the uncorrected $\hat{m}$ values are far from uniformly distributed about the true m, while the unbiased estimates are very uniformly distributed. There are two important implications of the non-linearity of the curve for uncorrected $\hat{m}$'s. First, estimates of m values for this type of data analyzed using this estimator contain a significant bias that consistently under-estimates the m value. Second, any confidence interval deduced from the bootstrap analysis using this estimator will contain similar bias such that the interval will be offset from the proper interval.

Often more useful than estimates of Weibull parameters are estimates of fracture strengths of components with sizes and geometries that differ from the test specimens that were measured experimentally. Information generated in the bootstrap analysis allows the calculation of unbiased estimates of strengths and confidence intervals in a parallel manner to that described above for m values. Evaluation of the need for unbiasing and the relative effectiveness of different methods of unbiasing again requires the second level of simulation. Figures 3 and 4 are probability vs probability plots for strength estimates that resulted from that simulation. Each plot contains five irregular lines corresponding to strength predictions of five different component sizes of 1, 10, 100, 1000 and 10,000 square millimeters of effective stressed area (as in the SiC fracture data, it was assumed that failure was controlled by surface-related defects, therefore area scaling was chosen). These five component sizes include both smaller and considerably larger sizes than the "simulated experimental" data that was

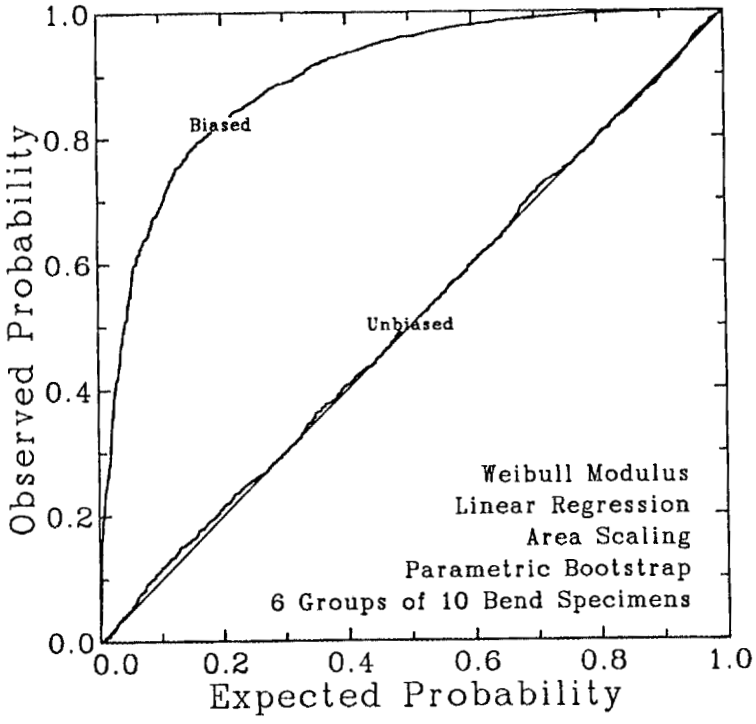

Figure 2

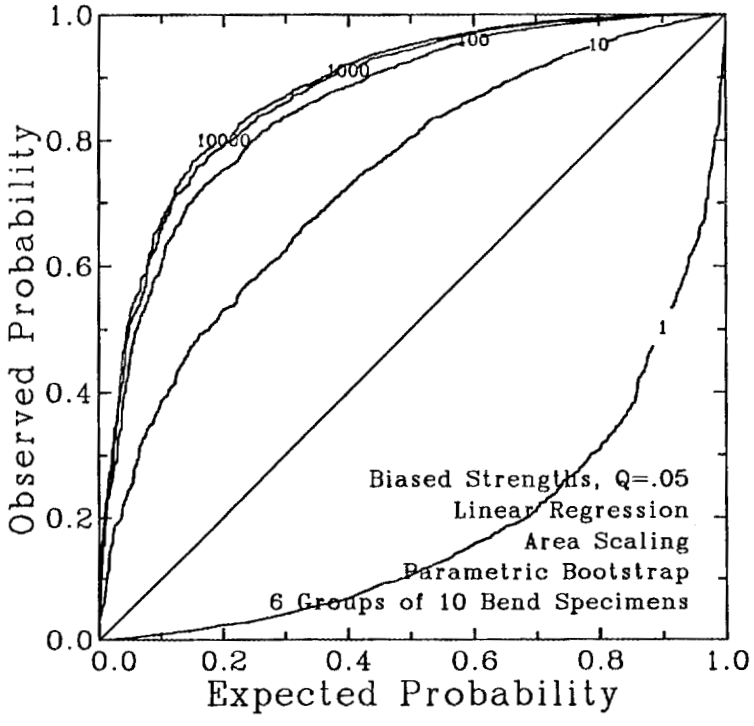

Figure 3

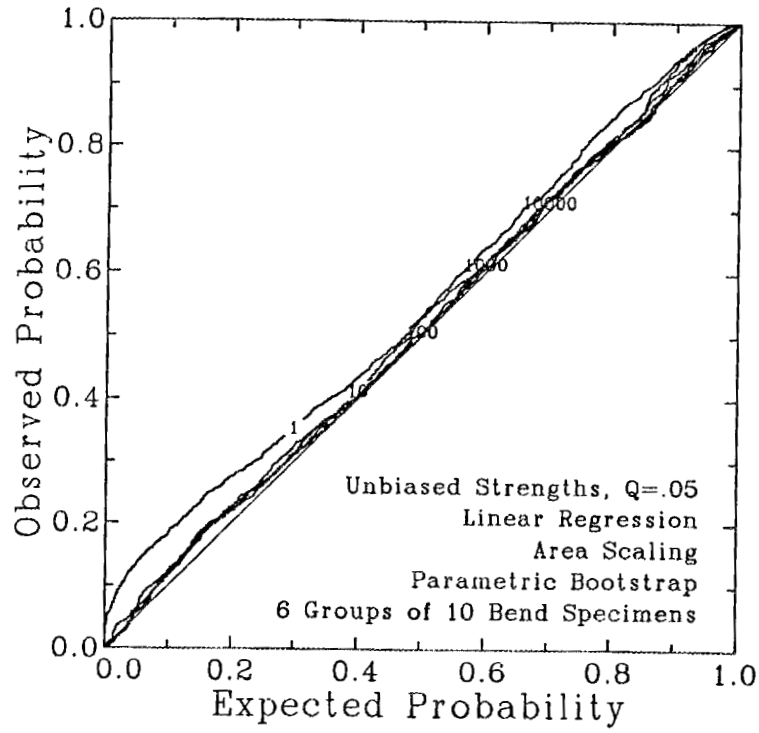
1.0
0.8
0.6
0.4
0.2
0.0
Observed Probability
0.0
0.2
0.4
0.6
0.8
1.0
Expected Probability
1
10
100
1000
10000
Unbiased Strengths, Q=.05
Linear Regression
Area Scaling
Parametric Bootstrap
6 Groups of 10 Bend Specimens

Figure 4

used to generate them, thus showing the effects of bias for size extrapolations in both directions.

Figure 3 includes the results for uncorrected strength estimates showing very strong bias that changes sign for opposite signs of size extrapolation. Figure 4 includes similar curves for unbiased strength estimates showing the effectiveness of the unbiasing technique.

The simulation-on-simulation technique is computationally intensive. The information contained in Figures 2-4 required approximately 16 hours on an IBM-PC 386 clone operating at 20 MHz with an 80387 coprocessor running NDP-386 fortran code. Similar analyses have been carried out using the maximum likelihood estimator and using non-parametric bootstrap techniques for both linear regression and maximum likelihood estimators.

2. Probabilistic Strength Analysis in Multiaxial Stress States

Also during this reporting period studies were carried out on the effects of multiaxial stress states on the probability of failure of brittle materials employed in structural applications. An important aspect of this is the error incurred in employing the PIA (principal of independent action) assumption where the three principal stresses are assumed to act as three independent uniaxial stress states. Batdorf in Ref. 1 has shown that the pure independence assumption can be either conservative or non-conservative when compared to more refined approaches. The PIA method involves the relationship:

$$P_s = P_s(\sigma_1)P_s(\sigma_2)P_s(\sigma_3),$$

where P_s gives the total probability of survival, $P_s(.)$ gives the probability of success when the effects of only one of the principle stresses are considered, and σ_1, σ_2, σ_3, are the principal stresses. Batdorf compares PIA to a more refined approach in uniaxial and equal biaxial tension in showing the nature of the conservativeness. This more refined approach is equivalent to assuming a failure criterion given by an effective stress defined by the loading and geometry of the crack. Failure of a particular crack occurs when σ_e (the effective stress) $\geq \sigma_c$, the critical stress of the crack. Here critical stress is defined as that remote stress applied normal to the crack plane that will just result in failure of that particular crack. Most writers since Weibull use these concepts in evaluating the probability of component failure by employing limiting arguments analogous to Weibull's (Ref. 2, pages 20-21) in which a "crack density" is defined. However, this approach is questionable from a mathematical viewpoint. Weibull realized this and, indeed, it was not his first approach to the problem. Weibull's original argument was in terms of the (cumulative) hazard function or what Weibull called the risk of rupture. The risk of rupture approach is based only on the assumptions of a weakest link model and statistical independence of the individual links (the independence assumption can be generalized). Also the hazard function

approach can be put into a limiting argument in a straightforward way. We shall follow this approach in our studies.

The two most promising approaches to extending Weibull to cover multiaxial conditions are:

- Batdorf's crack density, due to Batdorf and co-workers and culminating in Batdorf and Heinisch (Ref. 3), and
- Evans' elemental strength, due to Evans and co-workers as delineated in Lamon and Evans (Ref. 4) and further explained in Lamon (Ref. 5).

(Herein, the Batdorf-Heinisch approach will be referred to as the B-H approach and the Lamon-Evans as L-E.) Both of these approaches have earlier developments which are superseded by the above references; we make limited use of these earlier developments. The main difference between the two approaches is in their orientation. The B-H approach in effect calculates the fraction of cracks for a given infinitesimal critical stress range that would lead to failure based on crack orientation and the relationship to σ_e. The L-H approach in effect calculates the fraction of critical stresses for a given infinitesimal orientation range that would lead to failure based on the relationship of σ_c to σ_e. Viewed in this context, one would expect that under a common set of assumptions both would lead to the same failure probabilities.

The equivalence has been challenged by Lamon (Ref. 5) who further claims that the L-E approach is superior to the B-H approach. But, it can be shown mathematically, with an assumption of continuity on the form of σ_e, that the two approaches are identical when both employ the Weibull strength density and a common failure criterion. Moreover, the continuity assumption is met by all common failure criteria and is very reasonable on a physical basis. Thus Lamon's (Ref. 5) claim that the two approaches are not equivalent seems questionable. Lamon (Ref. 5) compared results of Shetty et al (Ref. 6) employing the B-H approach (that did not successfully extrapolate the results of 3- and 4-point bending to biaxial test specimens of the same material, failure mode, etc.) to results of analyzing the same data via the L-E approach. The L-E approach did successfully extrapolate; thus Lamon's conclusion. Initial studies aimed at finding the source of the discrepancy between the two approaches have been conducted (and further work is in progress). They should have given comparable results--not exact since the L-E approach as applied employed a different failure criterion than the shear sensitive criterion employed by Shetty et al. (Shetty et al also studied the normal stress criterion.) But the fracture criteria employed in each analysis are comparable in their shear sensitivity, so that the end results should have been more comparable. In what follows we first give a proof of the equivalence of the B-H and L-E approaches and then report on initial analytical/numerical studies aimed at resolving the discrepancy between B-H and L-E as reported by Lamon.

In the development we follow the notation common to both B-H and L-E. Thus we consider a single internal failure mode with size scaling given by the volume of

material under consideration. We begin with the L-E approach where the kernel of the hazard is given by:

$$\int_0^s g(S)dS = \int_0^s \frac{1}{2\pi} \int_0^{\pi/2} \int_0^{2\pi} g(S_E)dS_E \cos\phi d\phi d\psi \tag{1}$$

and where

$$g(S)dS = \frac{1}{2\pi} \int_0^{\pi/2} \int_0^{2\pi} g(S_E)dS_E \cos\phi d\phi d\psi \tag{2}$$

from equations (1), (7), and (10) of Ref. 4. In the hazard function approach (1) is integrated over the volume in

$$P_f = P_f(s) = 1 - \exp\left[-\int_V dv \int_0^s g(S)dS\right] \tag{3}$$

(cf. equation (1) of Ref. 4). Lamon and Evans (Ref. 4) then make assumptions that give

$$g(S_E)dS_E = mS_1^{m-1}S_0^{-m}dS_1F^m \tag{4}$$

where

$$g(S_E) = mS_E^{m-1}S_0^{-m} \tag{5}$$

with

$$S_E = S_1F\left[\frac{S_2}{S_1}, \frac{S_3}{S_1}, \phi, \psi\right] \tag{6}$$

(cf. equations 9-12 Ref. 4). (We note that the exponent, m, in (4) is given incorrectly in Ref. 4 in equation (12) as $m+1$; this situation is corrected by Lamon, in Ref. 7.) Lamon and Evans employ both Cartesian and spherical coordinate systems in which σ_1 is associated with x, σ_2 is associated with y, and σ_3 is associated with z. The angle ψ is measured from the x-axis in the (x,y)-plane and the angle ϕ is measured from the (x,y)-plane toward the z-axis. (See Fig. 3, Ref. 4) Also the strength S_i is associated with the principal stress σ_i, $i = 1,2,3$. For future reference we re-define (6) as

$$\sigma_e = \sigma_M F[\Sigma,\phi,\psi] = F[.] \tag{7}$$

where Σ (cf. Batdorf and Heinisch, Ref. 3) denotes the applied stress state throughout the elemental volume of interest and M denotes the maximum (tensile) stress occurring in that elemental volume. If we assume that any failure criterion employed is continuous, then it is always possible to define σ_e via (7); we make this assumption. Also note that in both (6) and (7), $F[.]$ is not a function of S_1 or σ_e and this allows (4) to be derived from (5) and (6). Under tensile loading (7) reduces to (6). Finally, we assume that all integrand functions are such that the order of integration can be interchanged (at will). This is clearly true for the Weibull "crack density" given by (4), and since we indicate a generalization of (4) in what follows we make the indicated assumption.

In showing the equivalence of B-H and L-E, we must show that (1) is equivalent to the corresponding hazard kernel in the B-H approach. However, before considering the B-H approach we transform (1) by interchanging the order of integration in (1) and employing (4) to give

$$\int_0^s g(S)dS = \frac{1}{2\pi}\int_0^{\pi/2}\int_0^{2\pi}(s^m/S_0^m)F^m\cos\phi\, d\phi\, d\psi$$

$$= \frac{(s^m/S_0^m)}{2\pi}\int_0^{\pi/2}\int_0^{2\pi}F^m\cos\phi\, d\phi\, d\psi. \tag{8}$$

We employ (8) for the L-E hazard kernel in what follows. The corresponding hazard kernel in the B-H approach is given by equation (3) Ref. 3 which is

$$P_f = P_f(s) = 1 - \exp\left[-\int_V dv\int_0^\infty d\sigma_c\left(\frac{dN(\sigma_c)}{d\sigma_c}\right)\frac{\Omega(\Sigma,\sigma_c)}{4\pi}\right]. \tag{9}$$

Thus in order to prove the conjecture of equivalence of B-H and L-E it must be shown that

$$\int_0^\infty d\sigma_c\left(\frac{dN(\sigma_c)}{d\sigma_c}\right)\frac{\Omega(\Sigma,\sigma_c)}{4\pi} \equiv \frac{(s^m/S_0^m)}{2\pi}\int_0^{\pi/2}\int_0^{2\pi}F^m\cos\phi\, d\phi\, d\psi. \tag{10}$$

To do this, expand Ω as

$$\Omega(\Sigma,\sigma_c) = 2\int_0^{\pi/2}\int_0^{2\pi} I(\Sigma,\sigma_c)\cos\phi\, d\phi\, d\psi \tag{11}$$

where

$$I(\Sigma,\sigma_c) = \begin{cases} 1, & \sigma_e \geq \sigma_c \text{ at the given } (\phi,\psi) \\ 0, & \text{otherwise.} \end{cases} \tag{12}$$

Equations (11) and (12) follow from the definitions given by Batdorf and Heinisch (Ref. 3) associated with their equations (1)-(4). Also note that (11) and (12) employ the spherical coordinate system of Lamon and Evans (Ref. 4). As is made clear in Batdorf and Heinisch (Ref. 3) Ω is a function of both the fracture criterion selected and the applied stress state. Thus I must be a function of both as well. This is reflected in the definition given by (12). And since the coordinate system denotes the orientation of the plane of a crack, I must be a function of (ϕ,ψ) as shown in (12). Now set

$$f(\sigma_c) = \left(\frac{dN(\sigma_c)}{d\sigma_c}\right) = m\sigma_c^{m-1}K \tag{13}$$

which follows from equation (9), Ref. 3. Then the B-H hazard kernel is given by

$$\int_0^\infty f(\sigma_c)(\Omega/4\pi)d\sigma_c = \int_0^\infty \frac{K}{2\pi}\int_0^{\pi/2}\int_0^{2\pi} m\sigma_c^{m-1} I(\Sigma,\sigma_c)d\sigma_c\cos\phi\, d\phi\, d\psi. \tag{14}$$

In (14) change the order of integration on σ_c and, prompted by (7), make the change of variable $x = \sigma_c/\sigma_M$ to obtain

$$\int_0^\infty f(\sigma_c)(\Omega/4\pi)d\sigma_c = \frac{K\sigma_M^m}{2\pi}\int_0^{\pi/2}\int_0^{2\pi}\left[\int_0^\infty mx^{m-1} I(\Sigma,\sigma_M x)dx\right]\cos\phi\, d\phi\, d\psi. \tag{15}$$

But in view of the definition of σ_e from (7), it follows that $\sigma_e \geq \sigma_c$ if and only if $F[.] \geq x$. This implies that the upper limit of integration on the inner integral of (15) is $F[.]$ and the inner integral then reduces to $\int_0^F mx^{m-1}dx$. Performing this integration gives the final result

$$\int_0^\infty f(\sigma_c)(\Omega/4\pi)d\sigma_c = \frac{K\sigma_M^m}{2\pi}\int_0^{\pi/2}\int_0^{2\pi} F^m\cos\phi\, d\phi\, d\psi. \tag{16}$$

Now (16) will be equivalent to (8) if

$$\sigma_M = s \text{ and } S_0^{-m} = K, \tag{17}$$

and F is the same in both approaches. Reversing these equalities and taking the assumption of continuity in (7), the steps that led from the definition of the B-H hazard kernel in (9) to the form given in (16) can be reversed. Thus, with these conditions, the two approaches are equivalent and (10) holds.

Now requiring that (17) hold (identically) is very reasonable; the relationships given in (17) are just notational. Also $F[.]$ just defines the failure criterion and requiring equality of the failure criterion in both approaches to yield overall equality is obvious and rational. The only questions may come with regard to the assumptions of continuity of the failure criterion and integrands that allow for the interchange of the order of integration. As to the latter, the Weibull "crack density" has this interchange property and since any $g(S)$ must be non-negative we are only requiring that some (minor) technical mathematical conditions hold for the integrands. Moreover we take the position that the continuity assumption is not unreasonable; all common failure criteria meet it. With these assumptions a more general result can be shown. Let F be such that $F' = f(\sigma_c)$ in the present situation and G be such that $G' = g(S_E)$ in the present situation. Replace the inner integral of (15), including the $K\sigma_M^m$ term, by F in the B-H approach and by G in the L-E approach. Then for general F and G it can be shown that the two approaches are equivalent if and only if $F \equiv G$ (excluding some measure-theoretical conditions). Thus in a very general sense the B-H and L-E approaches are equivalent.

The development thus far has been in terms of a hazard function approach and has been largely mathematical in nature. We now explore possible interpretations of the hazard function and the relationship to Weibull's "crack density." Without loss of generality consider the L-E approach and take as a special case a situation in which $g(S)$ is independent of V, for example, a case of uniform tensile loading. Then the hazard function is

$$H(s) = V\int_0^s g(S)dS$$

so that the hazard rate is

$$h(s) = Vg(s).$$

Now it is well known that the hazard rate (when it exists) is just a conditional probability density. Thus

$$Vg(s) = Pr(s < \text{Strength} < s + ds \mid \text{Strength} > s).$$

Therefore in the general case $g(s)$ must give the strength density per elemental volume conditional on the event that the strength is greater than s. We note that this is a strength probability density and not a crack count density and that it applies on a per elemental volume basis. Mathematically this is the only claim that we make as regards $g(s)$.

However, for practical reasons it is desirable to have a "crack density" interpretation. We do this by following Weibull's (Ref. 2, pages 20-21) "crack density" argument. The hazard kernels given in (10) are analogous to $n(\sigma)$ in Weibull's derivation. Weibull's argument requires that there be n cracks of strength σ *uniformly* (emphasis ours) distributed throughout the volume of interest. Moreover, this must hold in the limit as the total number of elemental volumes increases. This is questionable from a physical viewpoint and there is no guarantee that the mathematical limit, $n(\sigma)$, exists. All in all Weibull only gives a plausibility argument and it appears very difficult to do more than this. For example, if there is ever more than an infinitesimal number of cracks at failure risk for a particular σ, then in the limit the volume will fail with probability one. Clearly practically the only interesting cases are those in which there are a finite number of cracks present at any σ level. Then with these provisos and following Weibull, we interpret $g(s)$ as the number of cracks per unit volume which cause rupture at a stress in the range $(s, s + ds)$. This is consistent with the B-H and L-E interpretations. In any event, the hazard function approach given herein is based on the B-H and L-E approaches and thus, with a common setting, the two approaches do indeed give the same failure probabilities. This leaves us with explaining the Lamon conclusion (Ref. 5).

Initial numerical studies tend to indicate how Lamon reached his conclusion. Perusal of Lamon (Ref. 5) indicates that he employed "initial" data of Shetty et al (Ref. 8) for the shear sensitive failure mode studied. He then compared to results of Shetty et al (Ref. 8) for the Weibull approach and to Shetty et al (Ref. 6) for the B-H approach. (Apparently Lamon did not carry out any analyses in the B-H manner but just employed published results of Shetty et al.) The 3- and 4-point data appear to be the same in both the Shetty et al papers. However, the shear sensitive data are distinctly different and this difference favors Lamon's conclusion. More importantly, however, is the fact that for the shear sensitive case, Shetty et al (Ref. 6) assumed a state of equal biaxial tension throughout the pressure disk. This assumption appears to be incorrect. Employing the stress distribution equations for the pressure disk loading from Shetty et al (Ref. 8), the coplanar strain-energy-release rate failure criterion from Shetty et al (Ref. 6), and numerically integrating in the L-E manner gives a Weibull failure probability plot nearly equal to that obtained by Lamon (Ref. 5) for the L-E approach (and the L-E failure criterion). Indeed, the plot for the Shetty et al failure mode computed in this way lies between the plots for the 4- and 3-point data and not to the left of the 4-point plot as was obtained by Shetty et al (Ref. 6). As further evidence, we have analytically integrated all of the combinations of failure

criteria and loading geometries given in Ref. 6 under the Shetty et al assumptions in the L-E manner and duplicated exactly the Shetty et al results (equations 11-20 obtained in the B-H manner by Shetty et al, Ref. 6). Thus it appears that the assumption of equal biaxial tension does not properly represent the failure situation and loading geometry given by the pressure disk failure data. Work is under way to program routines to perform numerically the B-H integration for complex loading geometries (non-uniform stress states) in order to complete the comparison.

Also these studies have led to a consideration, from fundamental principles, of the general form that any failure criterion should have. Based on the assumptions that fracture does not occur in a state of equal triaxial compression and that fracture does occur for some states of compressive loading, a general form can be postulated for any acceptable failure criterion. A very mathematically simple form for σ_e meeting these requirements is

$$\sigma_e = \frac{1}{2}[\sigma + \sqrt{\sigma^2 + Q^2\tau^2}] \tag{18}$$

where σ is the stress component normal to the crack surface and τ is the shear component, and Q is a "material" constant to be determined. This form is not equivalent with fracture criteria based on strain energy concepts. The strain energy criteria so far proposed (Ref. 3, equations (4d) and (4e); Ref. 4, equation (6)) produce elliptical or similar level lines when plotted in the (σ,τ)-plane, and therefore do not meet the above requirements. For example, they allow for loading conditions in which hydrostatic compression produces failure. In contrast, the level lines of (18), given by $\sigma_e = const.$, are parabolas opening to the left in the (σ,τ)-plane. This prohibits fracture by hydrostatic compression but allows for shear sensitive fracture under general compressive loading.

Failure criteria of the form of (18) have been considered by others. Indeed, equation (4c) of Ref. 3 is a special case of (18) with $Q = 1/(1\text{-}0.5\nu)$, where ν is Poisson's ratio. This failure criterion comes from the assumption that fracture occurs when the local (tensile) stress at some point on the surface of the crack cavity reaches the ultimate strength of the material. Equation (4c) of Ref. 4 derives from results of Paul and Mirandy (Ref. 9) for a penny-shaped crack.

Also (18) can be derived from the fracture failure criterion

$$k_1/k_{1c} + (k_2/Ck_{1c})^2 = 1, \tag{19}$$

proposed by Shetty (Ref. 10) and developed and/or discussed in a series of papers by Shetty and co-workers (Ref.'s 11-13) by substituting

$$k_1 = Y_1\sigma\sqrt{a}$$
$$k_2 = Y_2\tau\sqrt{a}$$

into (18) and algebraically manipulating the result. Y_1 and Y_2 are constants associated with the geometry of the crack. Equation (18) is equivalent to (19) when

$$Q = (2Y_2)/(CY_1) \tag{20}$$

and

$$\sigma_e = k_{1c}/(Y_1\sqrt{a}).$$

In discussing (19), Ref.'s 10-13 have argued that k_{2c} is not a material constant since plots of data for k_1/k_{1c} versus k_2/k_{1c} for the same material but differing testing geometries and specimens show different intercepts for the k_2/k_{1c} axis. Clearly this should not be if k_{2c} is a material constant. However, in view of (20) and its relationship to (18) and (19) there is another possible interpretation of the results given in Ref.'s 10-13. Y_1 and/or Y_2 being incorrectly specified could also cause these results. This could come about from the presence of incorrect assumptions of flaw shape, unaccounted residual stresses in the test specimens, inadequate series expansions which determine the singular stress state in the neighborhood of the crack, etc.

Equation (18) has further interesting properties when considered as a failure criterion for an individual crack. When interpreted in this way a failure state does not occur when the Mohr's circle of the stress state associated with the particular crack just touches the failure parabola (level line of σ_e for that crack), but when the value of σ_e just equals σ_c for the particular crack. The loading defines a path in the (σ,τ)-plane; when this path just reaches the failure parabola for the first time, failure occurs. Now if $Q > 2$, then a situation can occur where a crack under uniform tension perpendicular to the crack plane is not quite at failure, but a small rotation of the crack would produce failure. This can be shown from geometric arguments involving the tangency of the Mohr's circle to the failure parabola or analytically by considering the derivative of σ_e with respect to β, the angle from the stress axis to the crack plane. Moreover, when $Q \leq 2$ this phenomenon can not occur.

This situation of a non-perpendicular crack producing a weaker specimen has occurred in other studies. Indeed, Palaniswamy and Knauss (Ref. 14), in a tour de force, examined the angled crack phenomenon analytically and numerically. Their results approximated very closely to an equation of the form of (19). Moreover, in a plot (Figure 10) of normalized critical stress versus orientation, the "dip" situation occurred, i.e., rotating the crack from normal would then produce a weakened specimen. Palaniswamy and Knauss (Ref. 14) also obtained experimental data from polyurethane specimens. It is hard to ascertain from a plot of the data (Figure 18) if

the dip phenomenon actually occurred. This is also true of experimental data obtained by a number of other authors (more concerned with determining critical stress intensity factors, etc.), for example: Williams and Ewing (Ref. 15), Sih (Ref. 16), Petrovic and Mendiratta (Ref. 17), and Shetty et al (Ref. 13). The results of Williams and Ewing tend to indicate that the dip phenomenon occurred for polymethylmethacrylate specimens (also studied by Erdogan and Sih, Ref. 18, but their results were not presented in a form that would confirm or deny the dip phenomenon). Sih presents results of Pook (Ref. 19) on DTD 5050-5 1/2% Zn aluminum that tend to show no dip phenomenon. The results of Petrovic and Mendiratta Si_3N_4 are inconclusive as are those of Shetty et al for a glass-ceramic and an alumina.

All in all, (18) appears to be a very plausible and versatile failure criterion and its study is continuing. It appears that some carefully designed experiments may determine the validity of (18) and the presence or absence of the dip phenomenon.

Status of Milestones

All milestones are on schedule.

Publications

None.

References

1. S.B. Batdorf (1977), "Some Approximate Treatments of Fracture Statistics for Polyaxial Tension," *Inter. Jour. of Fracture,* **13,** 1, 5-11.

2. W. Weibull (1939), "A Statistical Theory of the Strength of Materials," *Proceedings: The Royal Swedish Inst. for Engin. Research,* **151,** 1-45.

3. S.B. Batdorf and H.L. Heinisch (1978), "Weakest Link Theory Reformulated for Arbitrary Fracture Criterion," *J. Am. Ceram. Soc.,* **61,** 7-8, 355-58.

4. J. Lamon and A.G. Evans (1983), "Statistical Analysis of Bending Strengths for Brittle Solids: A Multiaxial Fracture Problem," *J. Am. Ceram. Soc.,* **66,** 3, 177-82.

5. J. Lamon (1988), "Statistical Approaches to Failure for Ceramic Reliability Assessment," *J. Am. Ceram. Soc.,* **71,** 2, 106-12.

6. D.K. Shetty, A.R. Rosenfield, and W.H. Duckworth (1984), "Statistical Analysis of Size and Stress State Effects on the Strength of an Alumina Ceramic," *Methods for Assessing the Structural Reliability of Brittle Materials,* **ASTM STP 844,** S.W. Freiman and C.M. Hudson, Eds., American Society for Testing Materials, Philadelphia, 57-80.

7. J. Lamon (1985), "Statistical Analysis of fracture of Silicon Nitride (RBSN) Using the Short Span Bending Technique," *Gas Turbine Conference and Exhibit,*

Houston, TX, March 18-21, **ASME,** 85-GT-151, 8 pp.

8. D.K. Shetty, A.R. Rosenfield, W.H. Duckworth, and P.R. Held (1983), "A Biaxial-Flexure Test for Evaluating Ceramic Strengths," *J. Am. Ceram. Soc.,* **66,** 1, 36-42.

9. B. Paul and L. Mirandy (1976), "An Improved Fracture Criterion for Three-Dimensional Stress States," *J. Eng. Mater. Technol., Trans. ASME,* **98,** 4, 159-63.

10. D.K. Shetty (1987), "Mixed-Mode Fracture Criteria for Reliability Analysis and Design with Structural Ceramics," *J. Eng. Gas Turb. Power., Trans. ASME,* **109,** 282-89.

11. D. Singh and D.K. Shetty (1989), "Fracture Toughness of Polycrystalline Ceramics in Combined Mode I and Mode II Loading," *J. Am. Ceram. Soc.,* **72,** 1, 78-84.

12. D.K. Shetty, A.R. Rosenfield, and W.H. Duckworth (1987), "Mixed-Mode Fracture in Biaxial Stress State: Application of the Diametral-Compression (Brazilian Disk) Test," *Eng. Fract. Mech.,* **26,** 6, 825-39.

13. D.K. Shetty, A.R. Rosenfield, and W.H. Duckworth (1986), "Mixed-Mode Fracture of Ceramics in Diametral Compression," *J. Am. Ceram. Soc.,* **69,** 6, 437-43.

14. K. Palaniswamy and W. G. Knauss (1978), "On the Problem of Crack Extension in Brittle Solids Under General Loading," *Mech. Today,* **4,** 87-148.

15. J.G. Williams and P.D. Ewing (1972), "Fracture under Complex Stress - The Angled Crack Problem," *Inter. J. Fract. Mech.,* **8,** 4, 441-46.

16. G.C. Sih (1974), "Strain-energy-density Factor Applied to Mixed Mode Crack Problems," *Inter. J. Fract.,* **10,** 3, 305-21.

17. J.J. Petrovic and M.G. Mendiratta (1976), "Mixed-Mode Fracture from Controlled Surface Flaws in Hot-Pressed Si_3N_4," *J. Am. Ceram. Soc.,* **59,** 3-4, 163-67.

18. F. Erdogan and G.C. Sih (1963), "On the Crack Extension in Plates Under Plane Loading and Transverse Shear," *J. Basic Eng., Trans. ASME,* **85,** 519-27.

19. L. P. Pook (1966), "The Effect of Crack Angle on Fracture Toughness," *J. Eng. Fract. Mech.,* **3,** 205-18.

3.0 DATA BASE AND LIFE PREDICTION

INTRODUCTION

This portion of the project is identified as project element 3 within the work breakdown structure (WBS). It contains five subelements, including (1) Structural Qualification, (2) Time-Dependent Behavior, (3) Environmental Effects, (4) Fracture Mechanics, and (5) Nondestructive Evaluation (NDE) Development. Work in the Structural Qualification subelement includes proof testing, correlations with NDE results and microstructure, and application to components. Work in the Time-Dependent Behavior subelement includes studies of fatigue and creep in structural ceramics at high temperatures. Research in the Environmental Effects subelement includes study of the long-term effects of oxidation, corrosion, and erosion on the mechanical properties and microstructures of structural ceramics. Work in the Fracture Mechanics subelement includes development of test equipment and procedures for measuring the creep behavior and strength of ceramic materials at elevated temperatures, and testing and evaluating these materials at high temperatures under uniaxial tension. Work on the NDE Development subelement involves conducting NDE development to identify approaches for quantitative determination of conditions in ceramics which affect their structural performance.

The research content of the Data Base and Life Prediction project element includes (1) experimental life testing and microstructural analysis of Si_3N_4 and SiC ceramics, (2) time-temperature strength dependence of Si_3N_4 ceramics, and (3) static fatigue behavior of PSZ ceramics.

Major objectives of research in the Data Base and Life Prediction project element are understanding and application of predictive models for structural ceramic mechanical reliability, measurement techniques for long-term mechanical property behavior in structural ceramics, and physical understanding of time-dependent mechanical failure. Success in meeting these objectives will provide U.S. companies with the tools needed for accurately predicting the mechanical reliability of ceramic heat engine components, including the effects of applied stress, time, temperature, and atmosphere on the critical ceramic properties.

3.1 STRUCTURAL QUALIFICATION

Microstructural Analysis of Structural Ceramics

B. J. Hockey, Jr. and S. M. Wiederhorn
(The National Institute of Standards and Technology)

Objective/Scope

The objective of this part of the program is to identify mechanisms of failure in structural ceramics subjected to mechanical loads at elevated test temperatures. Of particular interest is the damage that accumulates in structural ceramics as a consequence of high temperature exposure to stresses normally present in heat engines.

Design criteria for the use of ceramics at low temperature differ from those at high temperature. At low temperature ceramics are elastic and brittle; failure is controlled by a distribution of flaws arising from processing or machining operations, and the largest flaw determines the strength or lifetime of a component. By contrast, at high temperature where ceramics are viscoelastic, failure occurs as a consequence of accumulated, or distributed damage in the form of small cavities or cracks that are generated by the creep process. This damage effectively reduces the cross-section of the component and increases the stress that must be supported. Such increases in stress are autocatalytic, since they increase the rate of damage and eventually lead to failure as a consequence of loss in cross section. When this happens, the individual flaw loses its importance as a determinant of component lifetime. Lifetime now depends on the total amount of damage that has occurred as a consequence of the creep process. The total damage is now the important factor controlling lifetime.

Recent studies of high temperature failure of the non-oxide ceramics intended for use for heat engines indicates that for long term usage, damage accumulation will be the primary cause of specimen failure. Mechanical defects, if present in these materials, are healed or removed by high temperature exposure so that they have little influence on long term lifetime at elevated temperature. In this situation, lifetime can be determined by characterizing the damage and the rate of damage accumulation in the material at elevated temperatures. In ceramic materials such as silicon nitride and SiAlON, such characterization requires high resolution analyses because of the fine grain size of these materials: hence the need for transmission electron microscopy as an adjunct to the mechanical testing of ceramics for high temperature applications is apparent.

In this project, the creep and creep-rupture behavior of several ceramic materials will be correlated with microstructural damage that occurs as a function of creep strain and rupture time. Materials to be studied include: SiAlON; hot-pressed silicon nitride; sintered silicon carbide. This project will be coordinated with WBS 3.4.1.3, Tensile Creep Testing, with the ultimate goal of developing a test methodology for assuring the reliability of structural ceramics for high temperature applications.

Technical Highlights

During the past six months, a continued effort was made to characterize and compare microstructural changes that occur during the tensile creep of two-grades of hot-pressed silicon nitride, tested under Task 2. Both materials were obtained from GTE and were similarly processed using Y_2O_3 and $A\ell_2O_3$ as sintering aids; one, however was reinforced with SiC whiskers, while the other was not reinforced. The primary objective of this work is to determine the effect of whisker reinforcement on the high temperature creep and creep rupture behavior in this ceramic composite by direct comparison of microstructural changes and accumulated cavitation damage.

Experimental Technique

The bulk of the results obtained in this study were obtained by analytical transmission electron microscopy. Observations were made on both grades of material in the as-received, untested condition and after tensile testing at 1250°C. Test samples selected for examination covered the range of observed creep behavior, and included samples that failed after times ranging from ~10 to ~200 hours depending on applied stress and also samples from interrupted tests that survived for up to 2000 hours under lower applied stresses. In addition, a comparison was made of non-reinforced samples tested with and without a 500 hour pre-anneal at the test temperature. In all cases, the gauge sections of crept samples were cut parallel to the stress axis to obtain both near-surface and mid-plane sections. Prior to final TEM specimen preparation, these sections were examined optically for evidence of distributed creep cavitation or crack damage.

Results and Discussion

Microstructural analyses of the effect of tensile creep on both grades of GTE hot pressed silicon nitride, i.e., whisker reinforced and non-reinforced, has essentially been completed, and a paper entitled "Tensile Creep of Whisker-Reinforced Silicon Nitride" is currently in preparation. The following provides a summary description of the results.

Figure 1 provides representative views of the initial or as-received microstructures found in the a) SiC whisker reinforced and b) non-reinforced silicon nitride materials. Both materials exhibit a "composite-like" structure. In the reinforced material, Fig. 1a, randomly oriented α-SiC whisker, roughly 0.2 μm in dia. and 2 to 20 μm in length are interspersed within a matrix of nearly equi-axed, submicron sized silicon nitride grains, while the non-reinforced material contains a mixture of relatively large tabular and platelet ß-silicon nitride grains (with the c-axis oriented roughly along the axis of the tabular grains or normal to the "face" of the platelet grains) clustered within a matrix of more uniformly sized, equi-axed silicon nitride grains. In both grades of material, the silicon

nitride grains were predominantly ß-phase, regardless of size or shape. In the as-received condition, both grades of material also contained a continuous glassy intergranular phase of similar yttria, alumina, and silica content, but differing in that the whisker reinforced material also contained a minor concentration of calcia. This is apparently due to the limited dissolution of calcia-rich precipitates contained within the "core" region of the SiC whiskers during processing. While the bulk of this glassy phase is clearly situated within multi-grain junctions, Fig. 1, it is also found, by either diffuse dark field imaging or lattice imaging, along two-grain junctions whose separation distances range from one to roughly 200 nm.

Examination of crept samples of both grades of material revealed extensive devitrification of the glass phase occurs regardless of time at temperature. Crystallization is particularly evident within the multi-grain junctions, Fig. 2. Within these regions EDS indicates the presence of "pure" yttria silicates, i.e. the crystalline phase appears depleated of the minor constituents ($A\ell_2O_3$ and/or CaO) originally present within the glass phase. Although tested at the same temperature (1250°C), the crystallization behavior of the two materials is different. On the basis of electron diffraction, the whisker-reinforced material predominantly exhibits the monoclinic y-phase of $Y_2Si_2O_7$, which is invariably twinned on either (100) or (001), e.g. Fig. 2.

In contrast, the non-reinforced material predominantly exhibited the formation of orthorhombic, δ-phase $Y_2Si_2O_7$, although evidence for the monoclinic, x_2-phase of Y_2SiO_5 was also found within the interior regions of some creep samples (in particular, non-preannealed samples that failed rapidly). In comparing the main products of devitrification, it should be noted that the orthorhombic δ-phase found in the non-reinforced material corresponds the most stable, high temperature phase of $Y_2Si_2O_7$, while the monoclinic y-phase found in the whisker reinforced material represents a low temperature variant phase, which is conceivably metastable at temperatures above 1200°C. As such, this difference in devitrification behavior-undoubtedly a consequence of the minor but significant difference in initial glass composition - conceivably contributes to the enhanced resistance to creep exhibited by the non-reinforced material relative to the whisker-reinforced material (see previous reports, Task 2). Of greater significance to the observed differences in creep resistance, to the transient nature of creep exhibited by both materials, and to the effect of pre-annealing is the observation that devitrification is not complete, but appears to progress in a time dependent manner after an initial, rapid stage. Support for this result comes from both from observations that relatively wide glassy grain boundaries, Fig. 3, are found only in creep samples that failed rapidly (within ~20 hrs) and which had not been preannealed. It is also supported by the fact that narrow (1 to ~3 nm) glassy interfaces separate all crystalline phases (e.g. Fig. 4) even after more than 2000 hours of creep. As a consequence both materials exhibit a time dependent change in both the volume fraction and composition of retained intergranular glass phase. Since creep deformation appears to be controlled by grain boundary

sliding coupled, possibly, with diffuse processes, these changes in the amount and composition of retained glass should have a pronounced effect on creep behavior. In this regard, crystallization of principally "pure" $Y_2Si_2O_7$ should result in a yttria silicate glass riches in the minor consitutients (i.e. $A\ell_2O_3$ and/or CaO) which should tend to make it less viscous and thus less resistant to grain boundary sliding and cavitation. On the other hand, a decrease in the volume fraction of retained glass should have the effect of increasing the resistance to sliding and cavitation. The net effect of these opposing tendencies will likely depend on the applied stress and the time required to "equilibrate" the intergranular phase.

Observations on the cavitation damage produced during tensile creep indicate that at stresses sufficient for strain rates exceeding $\sim 1 \times 10^{-8}\ s^{-1}$ full fact cavitation occurs and leads to the development of creep cracks which grow stability or unstably, depending the applied stress.

In the whisker reinforced material, favorably oriented whisker interfaces Fig. 5 are found to act as preferential sites for cavity nucleation and growth, effectively forming distributed, short creep crack segments Fig. 6 which eventually link up to cause rupture. At higher stresses, the distribution of creep cracks becomes more localized, suggesting unstable, rapid crack growth after cavitation occurs along the whisker interfaces. In the non-reinforced material, cavity nucleation is also found to occur preferentially along favorably oriented interfaces bounding the larger tabular or platelet silicon nitride grains in this materials Fig. 7. Cavitated interfaces are, however, found to be widely distributed within the samples, and from Fig. 9 the cavities are typically less than full facet size and often blunted. Both optical and TEM examination of ruptured, non-reinforced samples failed to reveal distributed creep crack segments of the type found in the whisker reinforced material (Fig. 6). This results suggests that a critical stress is required for growth to full facet dimensions otherwise blunting or arrest occurs, and that continued crack growth occurs rapidly from these sites.

Since the stress required for the onset of cavitation in the whisker reinforced material is roughly one half that required for the non-reinforced material, it appears that the degradition in tensile creep behavior can be traced to the interfacial morphological and chemical changes associated with the presence of the whiskers which results in enhanced cavity nucleation and growth.

Status of Milestones

All milestones are on schedule.

Publications

1. B. J. Hockey, S. M. Wiederhorn, W. Liu, J. G. Baldoni and S.-T. Baljan, "Tensile Creep of SiC Whisker Reinforced Silicon Nitride," Proceedings of the 27th Automotive Technology Development Contractors Coordination Meeting (ATD/CCM), p-230, Dearborn, MI, October 23-26, 1989, pp. 251-264.

2. S. M. Wiederhorn and B. J. Hockey, "High Temperature Degradation of Structural Composites," Seventh Cimtec World Ceramics Congress, Montecatini Terme, Italy, June 24-30, 1990.

3. B. J. Hockey, S. M. Wiederhorn, W. Liu, J. G. Baldoni and S.-T. Baljan, "Tensile Creep of Whisker Reinforced Silicon Nitride," in preparation, to be submitted to the J. Mater. Sci.

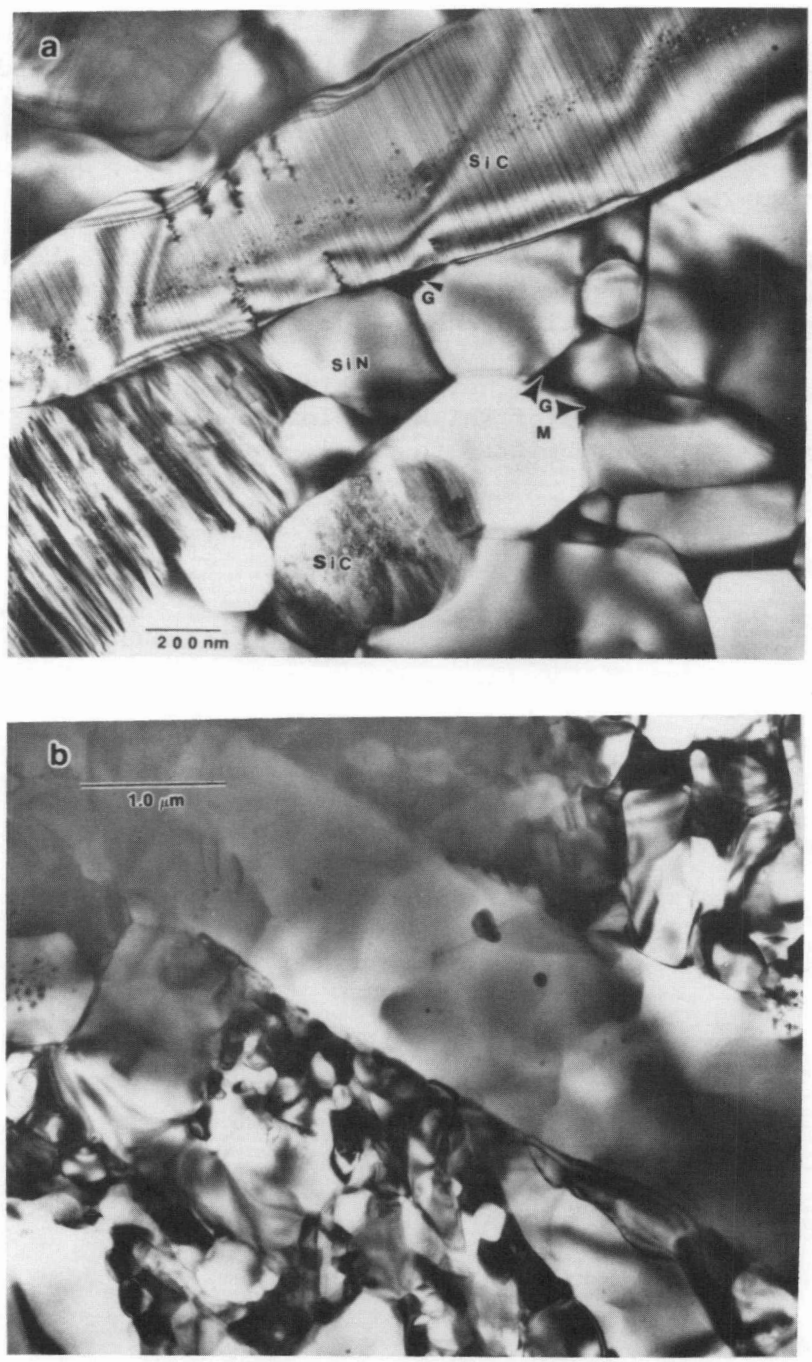

Figure 1. Representative views of as-received microstructures. a) Reinforced material, showing randomly oriented SiC whiskers within sub-micron sized silicon nitride grain matrix. The presence of glass, which forms a continuous intergranular phase is apparent at triple grain junctions. b) Non-reinforced material, illustrating presence of large, tabular ß-silicon nitride grains.

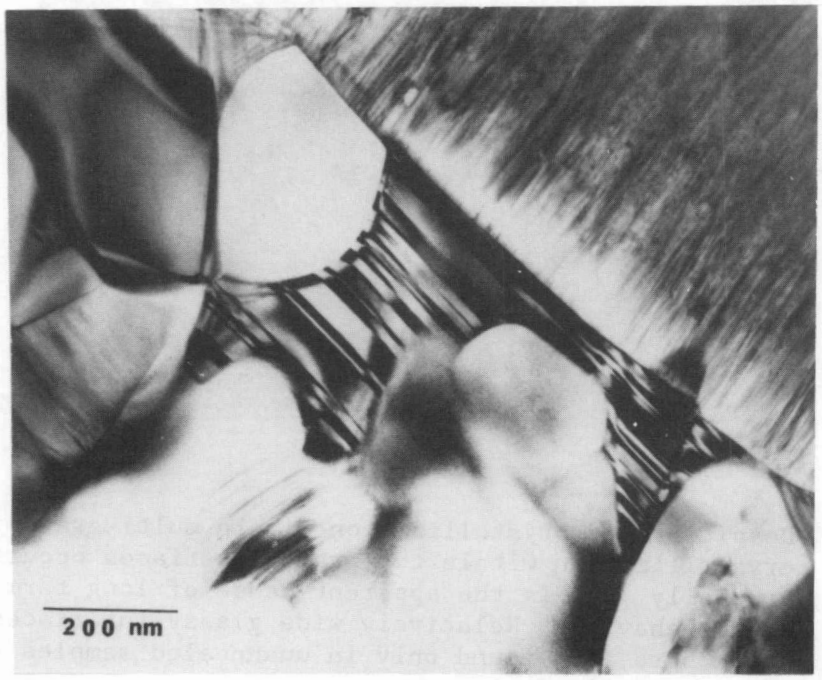

Figure 2. Testing at 1250°C results in devitrification of glass within multi-grain junctions. As shown, crystallization to twinned monoclinic, y-$Y_2Si_2O_7$ occurs in the reinforced material. Similar devitrification also occurs in the non-reinforced material, but results in the formation of the more stable orthorhombic, δ-$Y_2Si_2O_7$.

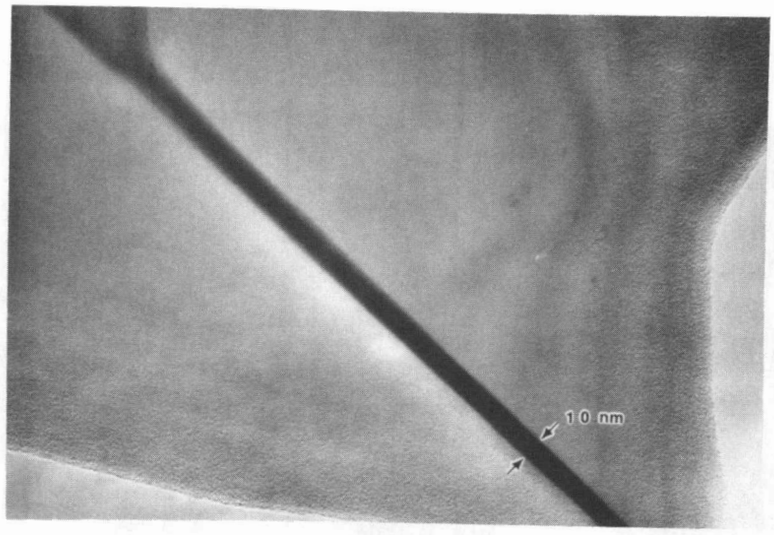

Figure 3. Despite rapid crystallization within multi-grain junctions, crystallization within two-grain interfaces occurs gradually, and is the apparent cause of long term transient creep behavior. Relatively wide glassy interfaces, as shown here, are found only in unannealed samples that failed rapidly during creep.

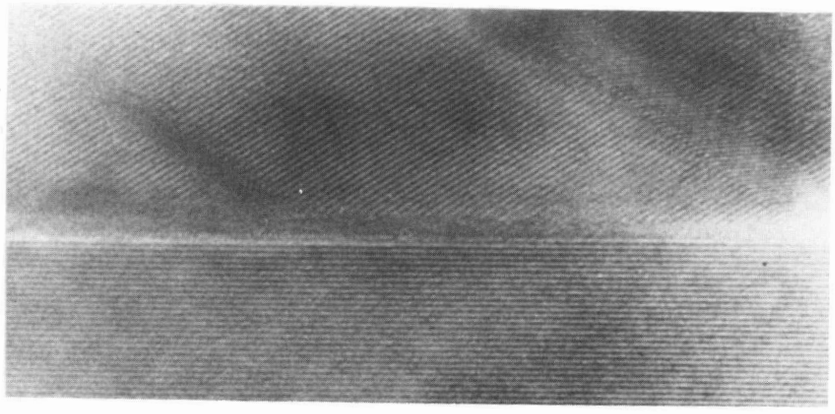

Figure 4. Even after prolonged test times of 2000 hours, all crystalline phases are separated by residual glass layers of varying thickness. Here, a glassy interface, ~3 nm thick, separates a matrix Si_3N_4 grains top from crystalline $Y_2Si_2O_7$ (bottom) that formed during creep. (Lattice fringe spacing within Si_3N_4 = 0.66 nm).

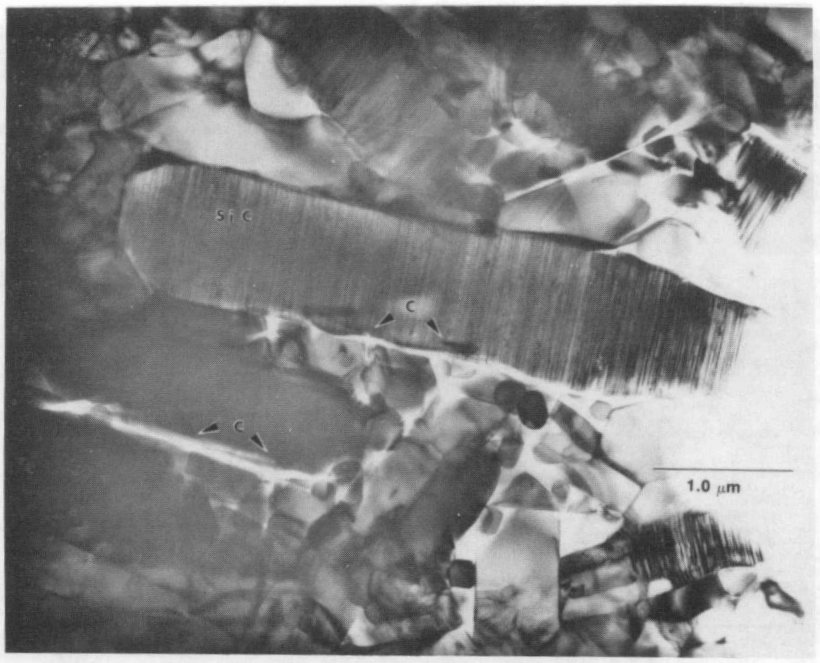

Figure 5. In whisker reinforced material, cavities nucleate preferentially within the residual glassy interfaces bounding SiC whiskers, and as shown, rapid cavity growth along the interface results in micron sized creep cracks.

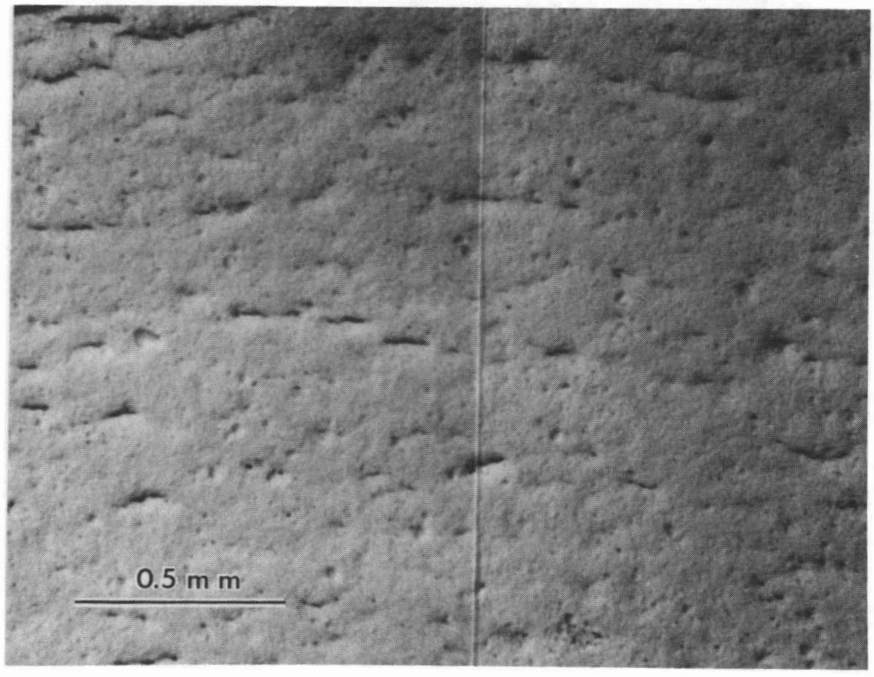

Figure 6. Polished section of whisker reinforced Si_3N_4 crept in tension showing distributed, creep crack segments. Further growth and joining of crack segments results in rupture. Similar crack distributions were not observed in the non-reinforced material.

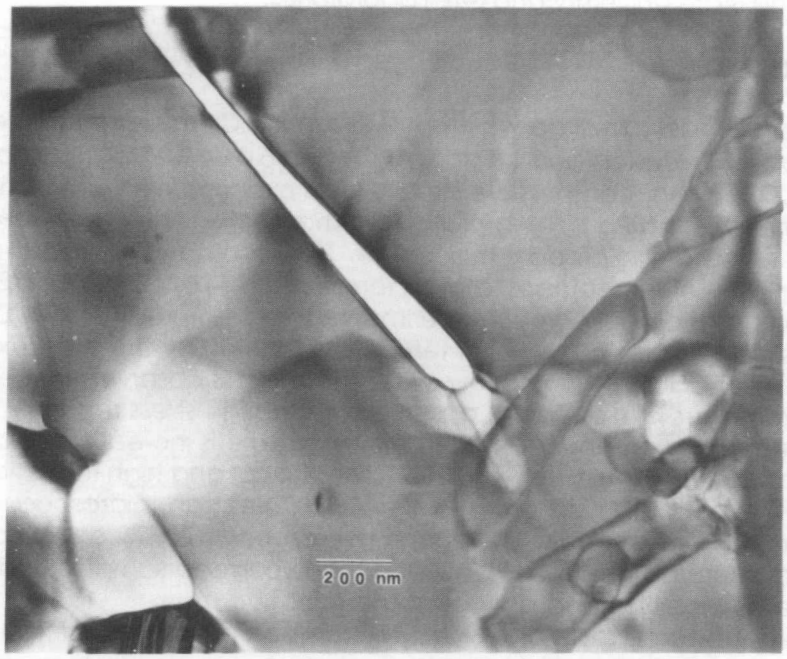

Figure 7. In the non-reinforced material, cavities tend to preferentially nucleate and grow within the residual glassy interfaces bounding the large tabular or platelet shaped grains but, as shown, often arrest and exhibit a blunted morphology.

Microstructural Characterization

Karren L. More (Oak Ridge National Laboratory)

Objective/scope

The objective of the research is to use analytical and high resolution electron microscopy to characterize the microstructure of a SiC whisker reinforced Si_3N_4 ceramic composite before and after creep deformation. This work represents a collaboration with North Carolina State University and GTE Laboratories.

Technical progress

The material under investigation is a hot-pressed SiC whisker reinforced Si_3N_4 containing 30 vol % SiC whiskers and 1.5 wt % Al_2O_3 and 6.0 wt % Y_2O_3 intentionally added as sintering aids. Constant compressive stress creep experiments were conducted in a continuously purified 0.11 MPa flowing nitrogen atmosphere. The creep specimens were initially annealed at the creep temperature. Figure 1 shows the stress exponent, **n**, for creep deformation of the composite at all temperatures tested (1470-1720 K). This work focussed on two individual creep experiments; temperatures were 1470 and 1620 K, both in the stress range 50 to 350 MPa. At temperatures >1570 K, the stress exponent exhibits a bilinear behavior in which a low stress exponent is observed in the lower stress regime and a higher stress exponent is observed in the high stress regime. This behavior becomes more pronounced as the temperature is increased. However, this behavior was not observed for creep at 1470 K. Analytical and high resolution electron microscopy (AEM and HREM), scanning transmission electron microscopy (STEM), X-ray diffraction (XRD), and scanning electron microscopy (SEM) were used to determine microstructural differences between the two creep samples and to characterize the as-received and annealed material.

In the as-hot pressed state, the SiC/Si_3N_4 composite had an amorphous grain boundary phase containing nitrogen, oxygen, aluminum, silicon, and yttrium. A TEM image of the as-received composite is shown in Fig. 2(a) along with an EDS spectrum of an amorphous grain boundary pocket (Fig. 2(b)). Prior to loading, the specimens were annealed for 4 h at the creep temperature in an attempt to "set" the microstructure. The overall microstructure remained unchanged following the anneal. The major change observed was the crystallization of the grain boundary pockets. X-ray diffraction of a bulk piece of the 4-h annealed material found two major crystalline grain boundary phases present: $Y_2Si_3N_4O_3$ and $Y_{20}Si_{12}N_4O_{48}$. It was determined by AEM that the aluminum concentration within the bulk microstructure was limited to extremely small amorphous pockets located predominantly along SiC whiskers, as shown in Fig. 3. These pockets were on the order of 10-20 nm in size. A large fraction of the aluminum was found in a glassy coating on the specimen surface. Thus, during the annealing stage alone, the aluminum present in the starting material was not only forced out of the larger grain boundary pockets by the formation of yttrium silicon oxy-nitrides into small isolated pockets next to SiC whiskers, but also to the surface of the specimen. Small, tabular yttrium silicate grains were also present on the surface.

X-ray diffraction was performed on a sample which was annealed for >20 h. The only crystalline grain boundary phase identified in this sample was γ-$Y_2Si_2O_7$, indicating that a 4-h anneal was not long enough to completely stabilize the microstructure. This did not affect the position of the break observed but did decrease the steady-state creep rates, as shown in Fig. 4.

After creep at 1620 K, the surface of the specimen appeared as shown in Fig. 5. In addition to the tabular grains found initially on the annealed surface, there were also elongated grains present on the surface of the creep cylinder (Fig. 5(a)). During the lengthy creep experiments, several of the smaller tabular shaped grains coalesced to form elongated grains on the sample surface. This is evidenced by the fact that there are no tabular grains surrounding these elongated grains (Fig. 5(b)). The composition of the glassy coating (as determined by EDS) consisted mostly of O, Al, and Si (Y is consumed by the formation of the yttrium silicate phase). To verify the structure of the crystalline phases present on the surface, a TEM specimen was prepared by backthinning the cylinder through the bulk thus preserving the surface for analysis. The elongated and tabular grains were identified by electron diffraction as β-$Y_2Si_2O_7$. Another crystalline phase, present as small rectangular grains embedded in the glassy matrix on the specimen surface, was identified by EDS and electron diffraction as cubic crystobalite.

The overall microstructure of the bulk sample following a full creep run at 1620 K was found to have changed little from that observed following the 4-h anneal. No cavitation was observed. In order to determine the reason for the break observed in the creep curve at 1620 K, a careful TEM analysis was conducted on samples taken both before the break in curve and after, and these were compared to a sample taken from the lower temperature creep run, 1470 K, where no break was observed. The microstructure representing the material before the break was obtained by allowing the material to deform at stresses of 50, 100, and 150 MPa with a final true strain of ~0.9%. The sample used to represent the microstructure after the break was deformed at stresses of 50, 100, 150, 200, 250, 300 and 350 MPa with a final true strain of ~1.5%. High resolution electron microscopy was used to examine the grain boundaries in each sample. Figure 6(a) is a HREM image of a grain boundary pocket between a Si_3N_4 grain and a SiC whisker in the sample taken before the break. The pocket was crystallized but was completely surrounded by glass (~5 nm in thickness). The corresponding EDS spectra (Fig. 6(b) and (c)) were taken from the γ-$Y_2S_2O_7$ phase and the residual Al-containing glass surrounding the crystalline pocket, respectively. An Al-containing glass was present at SiC/Si_3N_4 grain boundaries, as shown in Figure 7. In the sample taken after the break, however, there was very little of the glassy boundary phase observed, as shown in Fig. 8. The grain boundary pockets were completely crystallized and little or no glass was found at the grain boundaries between Si_3N_4 and SiC, as shown in Fig. 9. While small, isolated pockets of Al-containing glass were still found, the majority of the boundaries were glass free.

A HREM image of a grain boundary pocket in the sample crept at 1470 K is shown in Fig. 10. This image is very similar to the pocket found in the sample taken before the break; the pocket is surrounded by a relatively thick glass layer and residual glass was also observed at the boundaries. A break was not observed in the creep curve and a final true strain of less than 1% was achieved. Thus, the major difference observed in the microstructures between the three samples was the presence of residual glass surrounding grain boundary pockets and at grain boundaries in both the sample taken before the break in the creep curve at 1620 K and the sample from the creep run at 1470 K. There was a notable lack of residual glass in the sample taken after the break occurred at 1620 K.

The break in the curve at T > 1620 K appears to be due to the presence of residual glass at the boundaries. In the lower stress regime, where residual glass was present throughout the structure, **n** < 1 which is indicative of "non-steady state creep behavior."[1] As the stress is increased, a portion of the glass present at many of the interfaces migrates into isolated Al-containing pockets and out to the specimen surface. Creep of the composite in this regime (**n** > 1) occurs primarily by grain

boundary diffusion and grain boundary sliding. At the end of a creep experiment at 1620 K, there is little or no glass remaining at the interfaces. At 1470 K, even at the highest stress of 350 MPa, the temperature is too low for significant diffusion and glass remains at the boundaries.

Constant compressive stress creep experiments were also conducted in air. Preliminary results have shown that the general bilinear behavior observed for the composite crept in a nitrogen atmosphere was also observed for the composite crept in air. Figure 11 is a comparison of typical creep curves for samples crept in both air and nitrogen with the corresponding stress exponents. Higher creep rates were observed for the sample crept in air and the stress exponent was significantly higher in the high stress regime for the sample crept in air, i.e., 2.28 + 0.28 in air and 1.39 + 0.06 in nitrogen. This phenomenon is currently under investigation.

Analytical electron microscopy (AEM) was used to determine if there were any microstructural differences between the samples crept in nitrogen and air. A low magnification micrograph of the general microstructure of the sample crept in air is shown in Fig. 12. Overall, the bulk structure appeared the same in both samples. There was no cavitation observed. The grain boundary phase was crystalline and the composition was found to be very close to that determined for the sample crept in nitrogen. No aluminum was observed in the crystallized pockets. Characterization (X-ray and AEM) of the sample crept in air is ongoing.

Reference

1. B.S.B. Karunaratne and M.H. Lewis, J. *Mater. Sci.* 15, 449 (1980).

Status of milestones

On schedule.

Publications

K.L. More, D.A. Koester, and R.F. Davis, "Microstructural Characterization of a Creep-Deformed SiC Whisker-Reinforced Si_3N_4 Composite," presented at the Frontiers of Electron Microscopy in Materials Science Meeting, May 20-24, 1990, Oak Brook, Illinois. To be published in *Ultramicroscopy*.

K.L. More, D.A. Koester, and R.F. Davis, "The Role of Interfaces in the Creep-Deformation of a SiC Whisker-Reinforced Si_3N_4 Composite," presented at the International Congress for Electron Microscopy, August 17-22, 1990, Seattle, WA, published in conference proceedings.

K.L. More, D.A. Koester, and R.F. Davis, "Creep Behavior of a SiC Whisker-Reinforced Si_3N_4 Composite in Air and Nitrogen," submitted for presentation at the 2nd International Ceramic Science and Technology Congress, November 12-15, 1990, Orlando, Florida.

ORNL-DWG90-13946

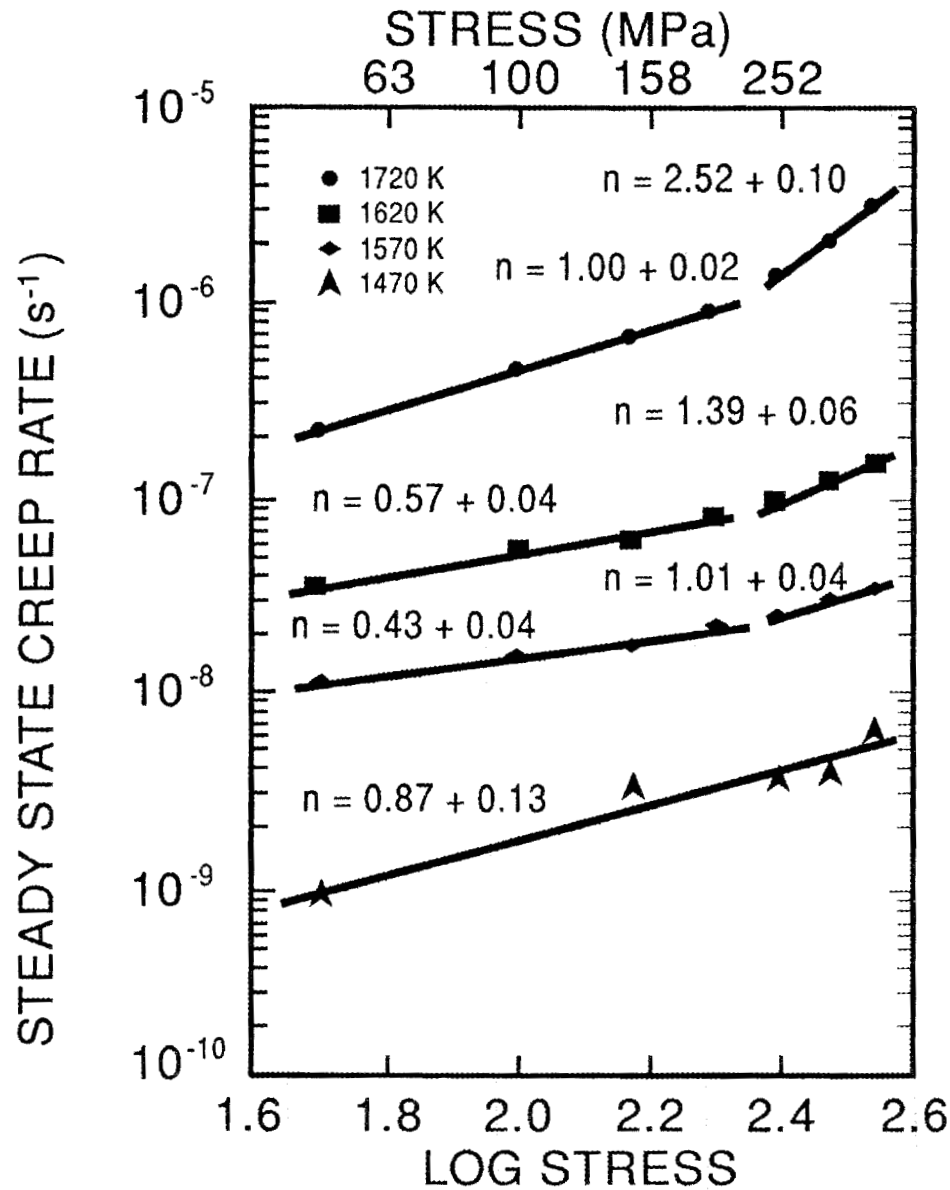

Fig. 1. Constant compressive stress creep curves for composite crept in the temperature range1470-1720 K.

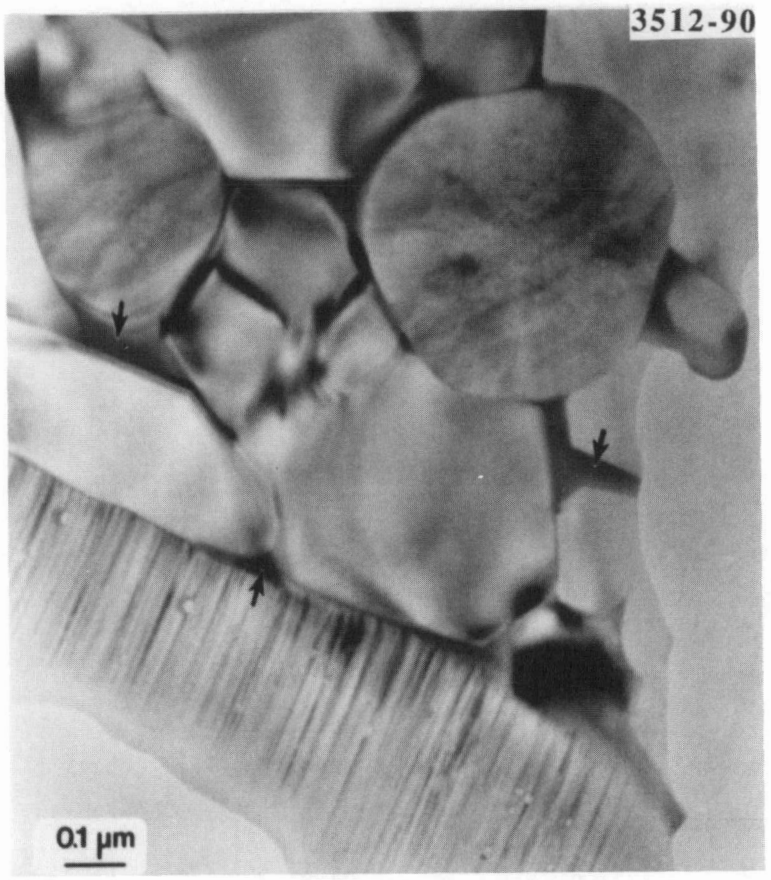

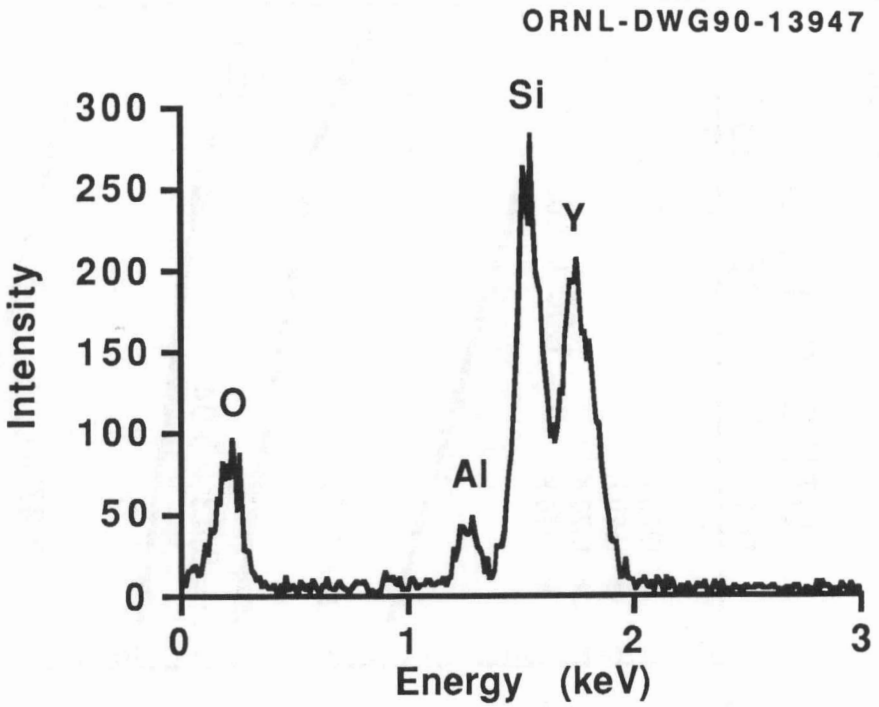

Fig. 2. (a) TEM image of as-received SiC whisker-reinforced Si_3N_4; (b) EDS spectrum from an amorphous grain boundary pocket in the as-received composite.

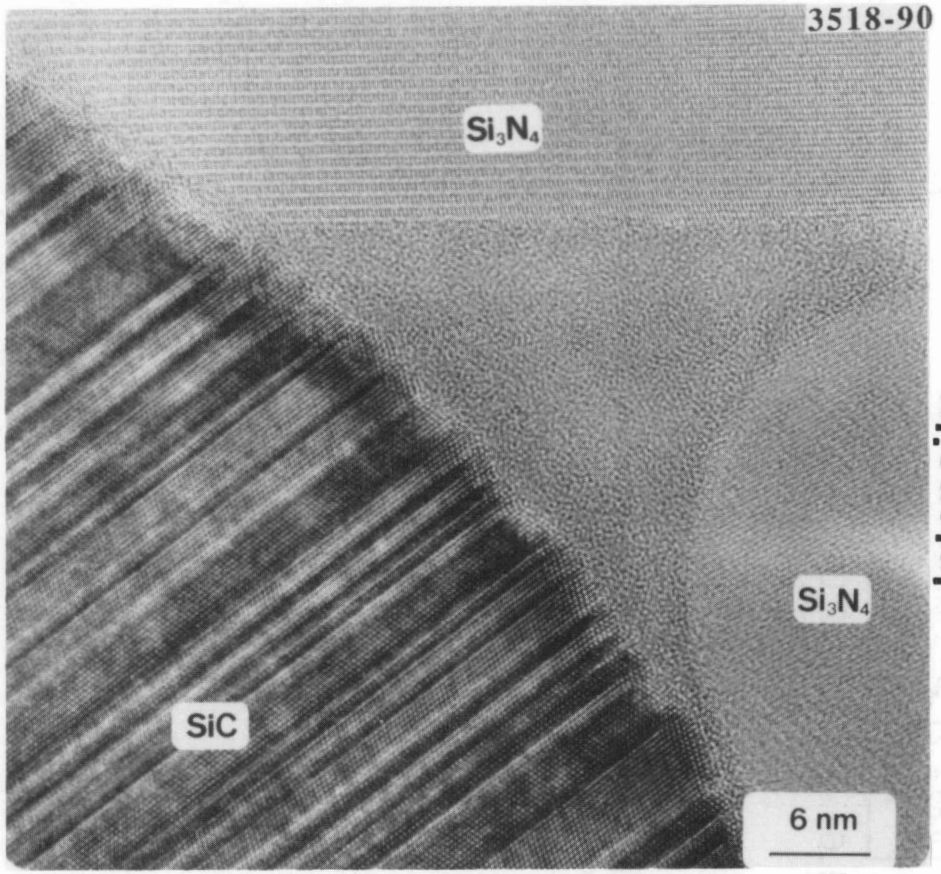

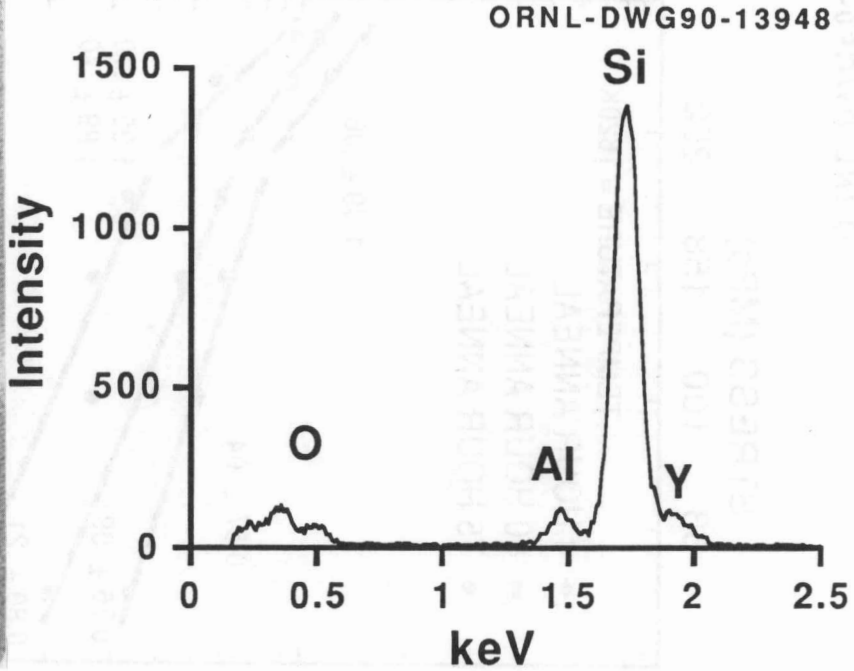

Fig. 3. (a) HREM image of a small, amorphous pocket next to a SiC whisker; (b) EDS spectrum from a small, amorphous pocket similar to that shown in (a).

ORNL-DWG90-13949

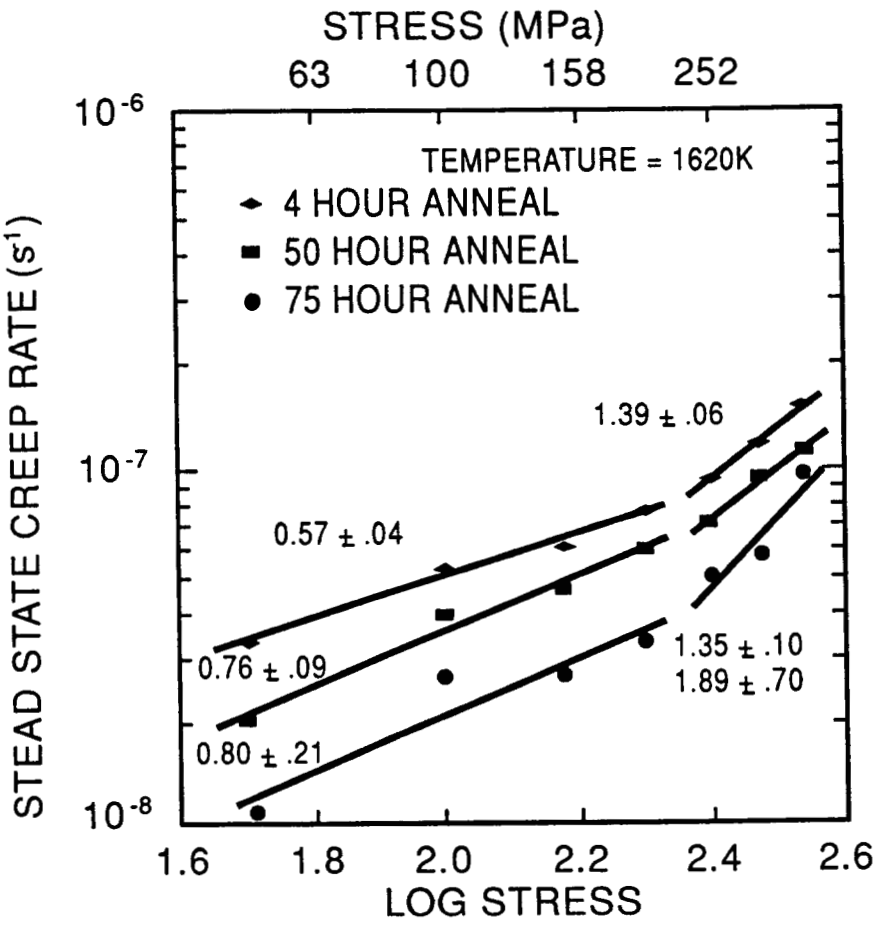

Fig. 4. Constant compressive stress creep curves for composite specimens annealed at 1620 K for 4, 50, and 75 h.

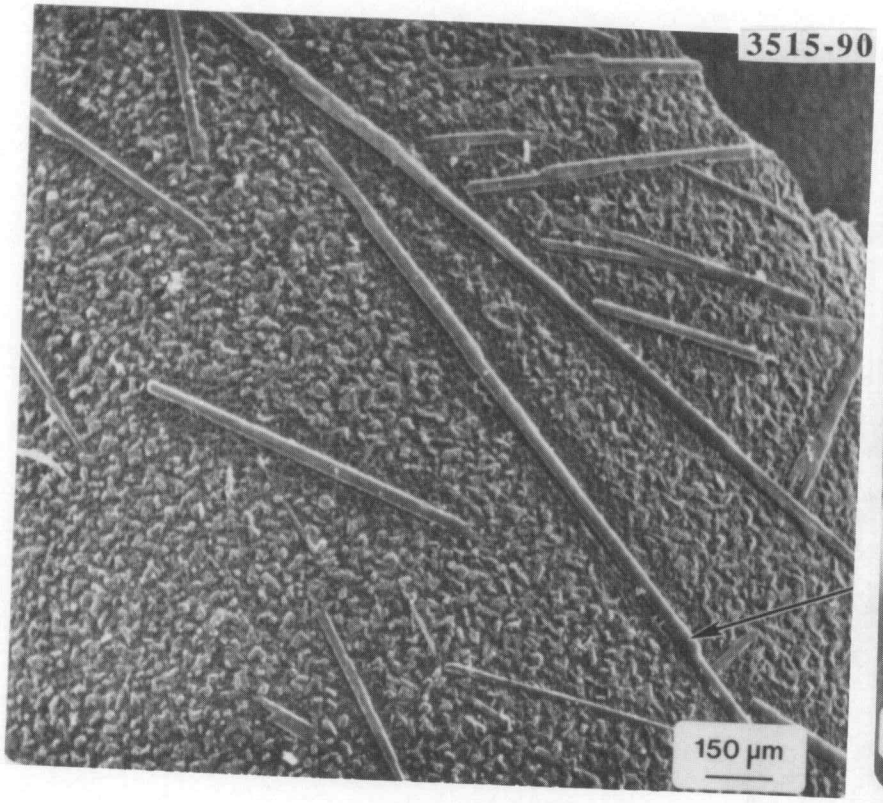

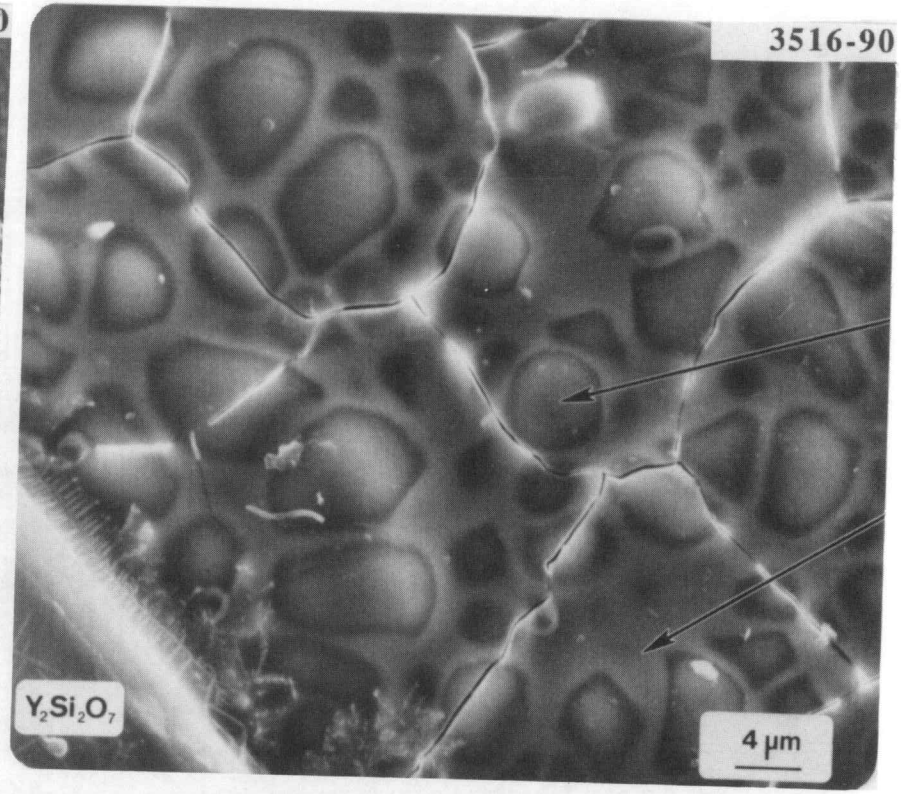

Fig. 5. (a) SEM image of the surface of a sample crept at 1620 K showing elongated β-$Y_2Si_2O_7$; (b) SEM image of a region next to an elongated β-$Y_2Si_2O_7$ grain showing SiO_2 grains embedded in a glassy matrix. Note lack of tabular yttrium silicates next to the elongated grains.

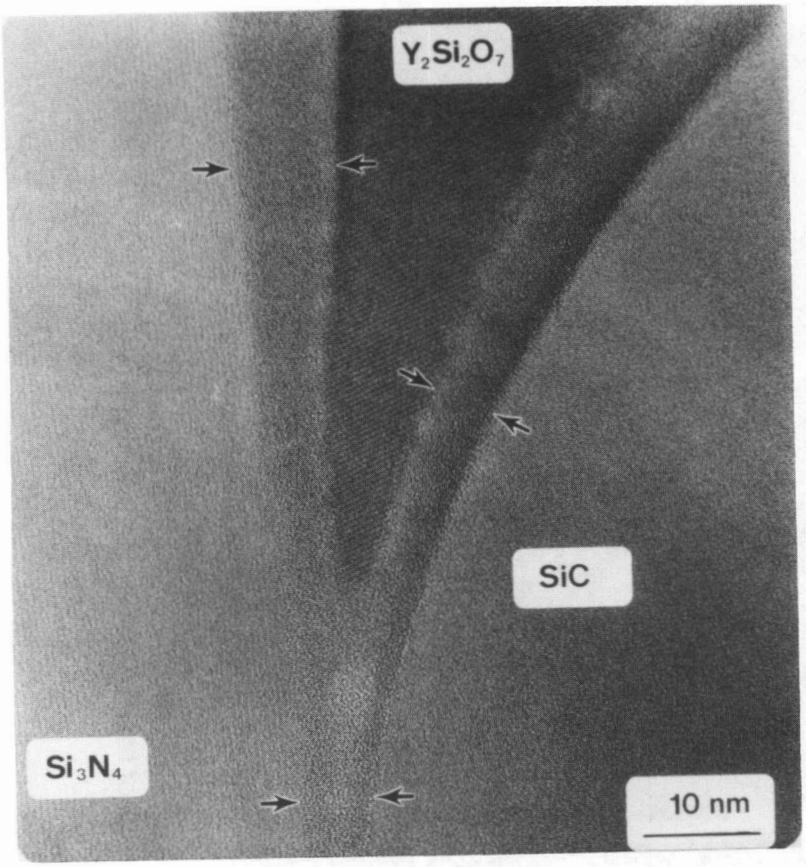

Fig. 6. (a) HREM image of a grain boundary pocket between SiC and Si_3N_4 (before the break); (b) and (c) EDS spectra from (b) γ-$Y_2Si_2O_7$ crystallized pocket and (c) glass surrounding pocket.

ORNL-DWG90-13950

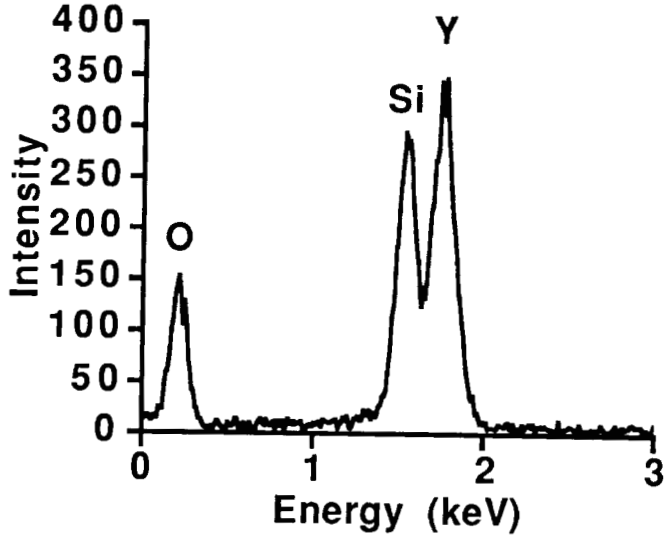

ORNL-DWG90-13951

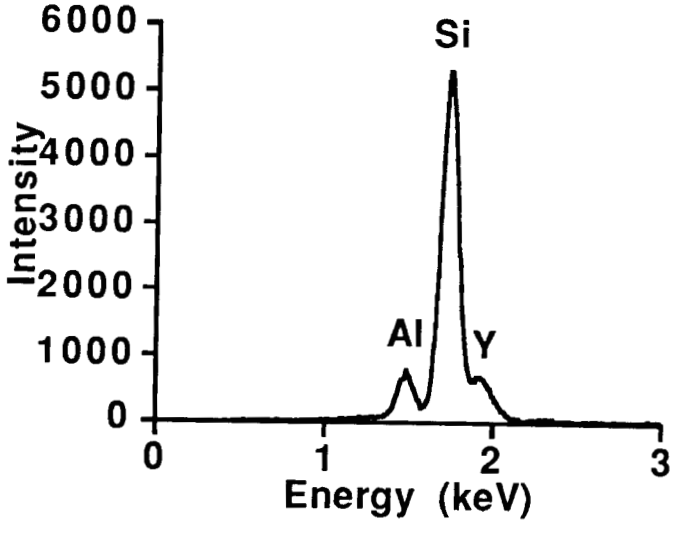

Fig. 6. Continued

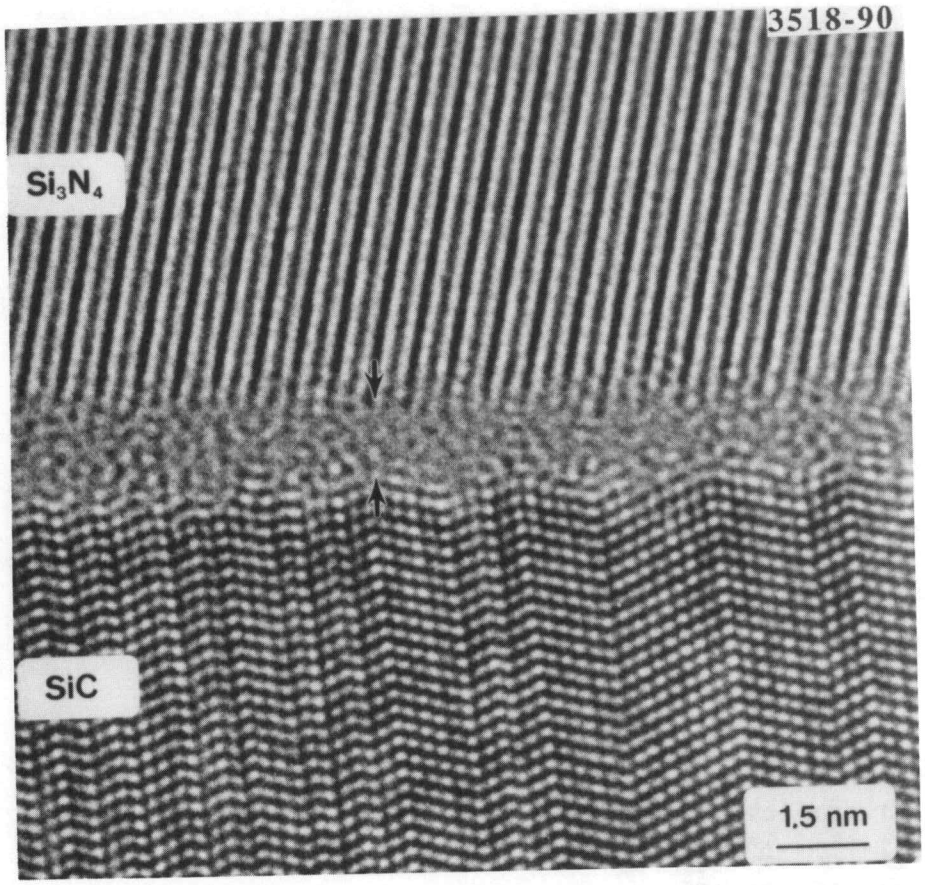

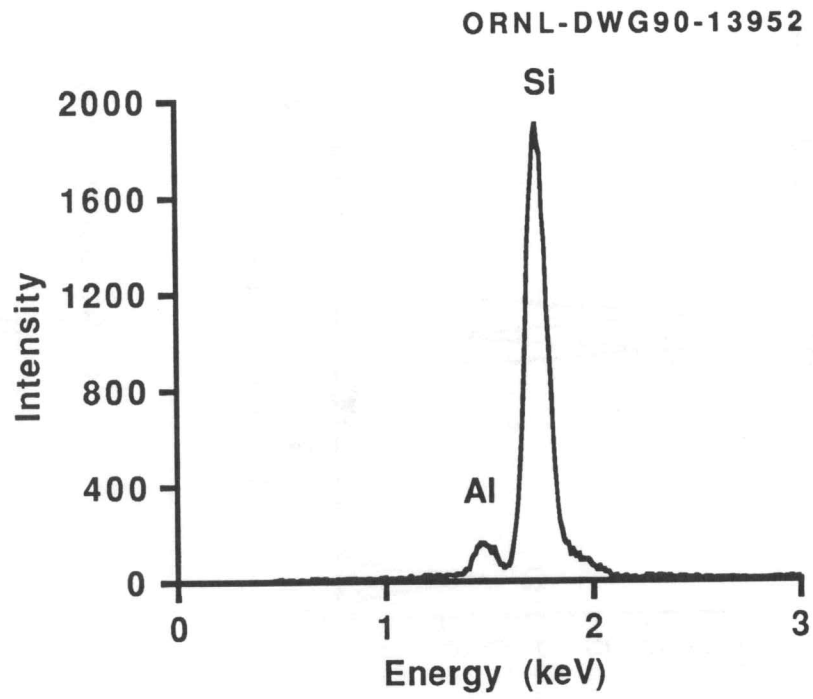

Fig. 7. (a) HREM image of a SiC/Si_3N_4 interface (before the break); (b) EDS spectrum from SiC/Si_3N_4 interface.

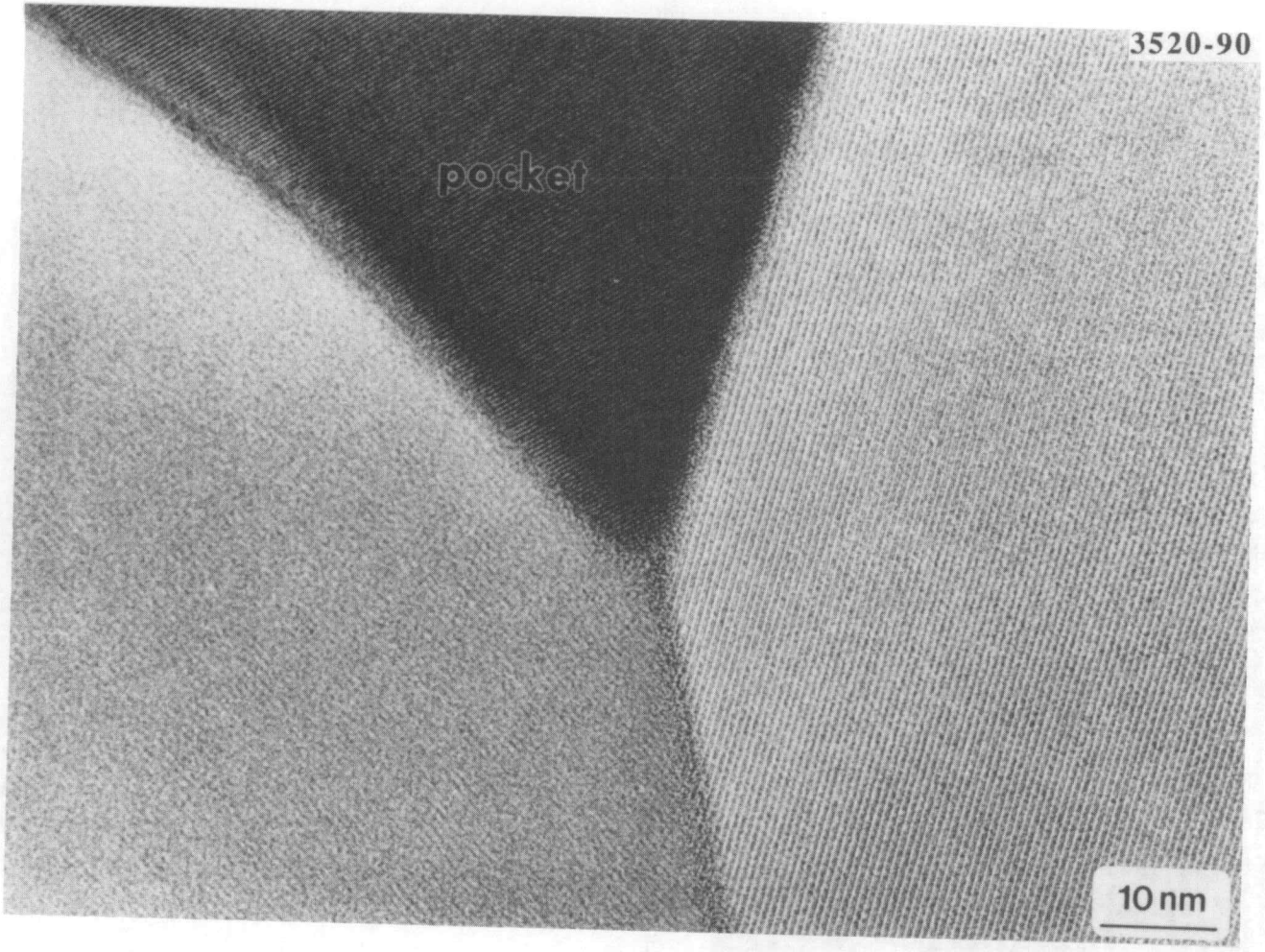

Fig. 8. HREM image of a crystallized grain boundary pocket (after the break).

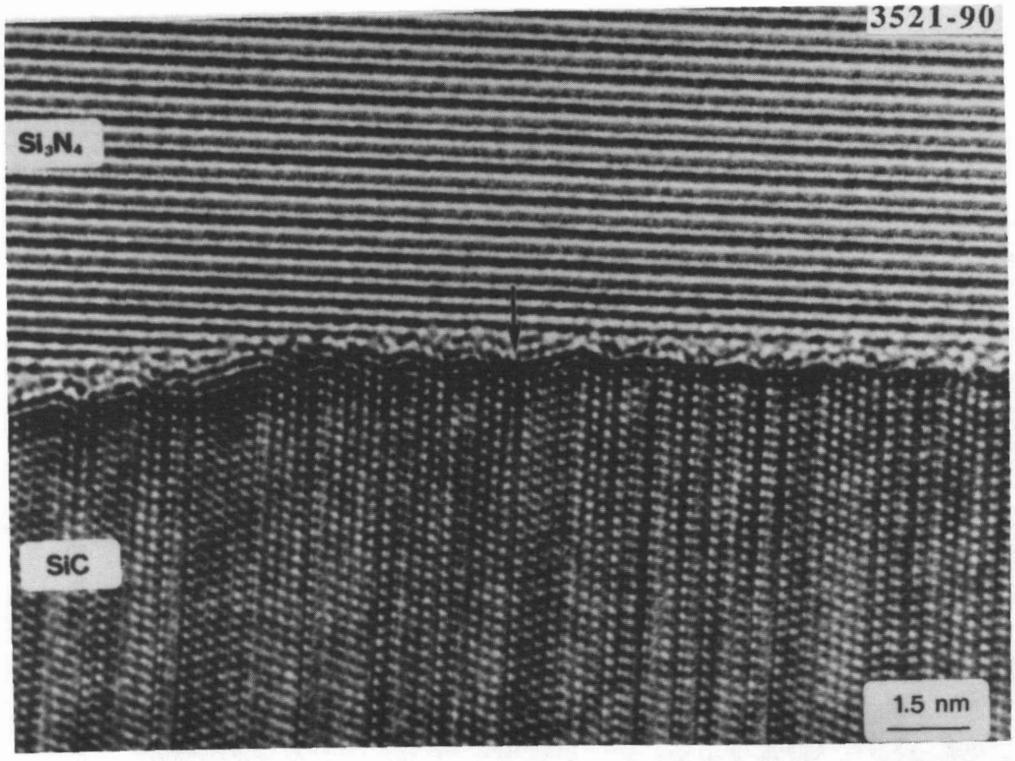

Fig. 9. HREM image of a SiC/Si_3N_4 interface showing no amorphous layer (after the break).

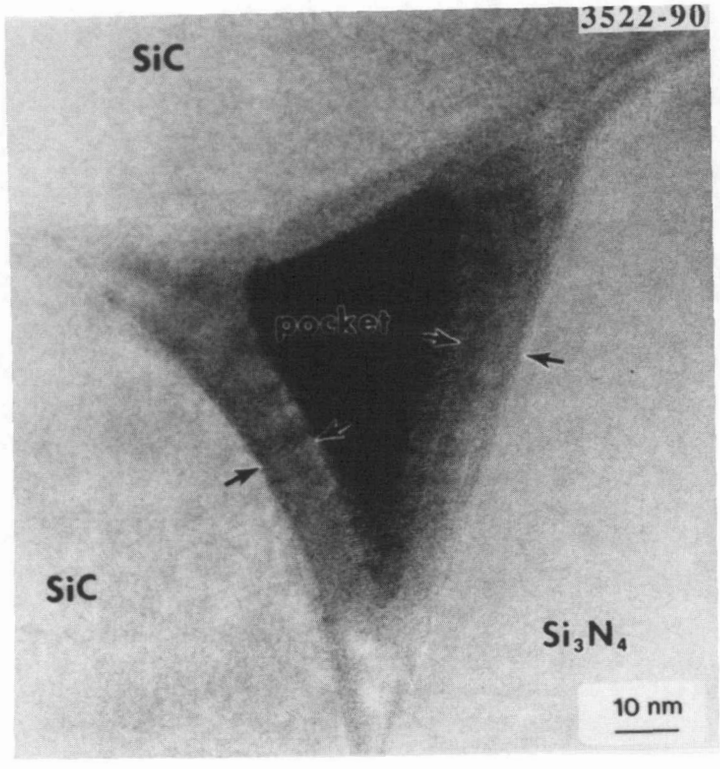

Fig. 10. HREM image of a grain boundary pocket following creep at 1470 K.

ORNL-DWG90-13953

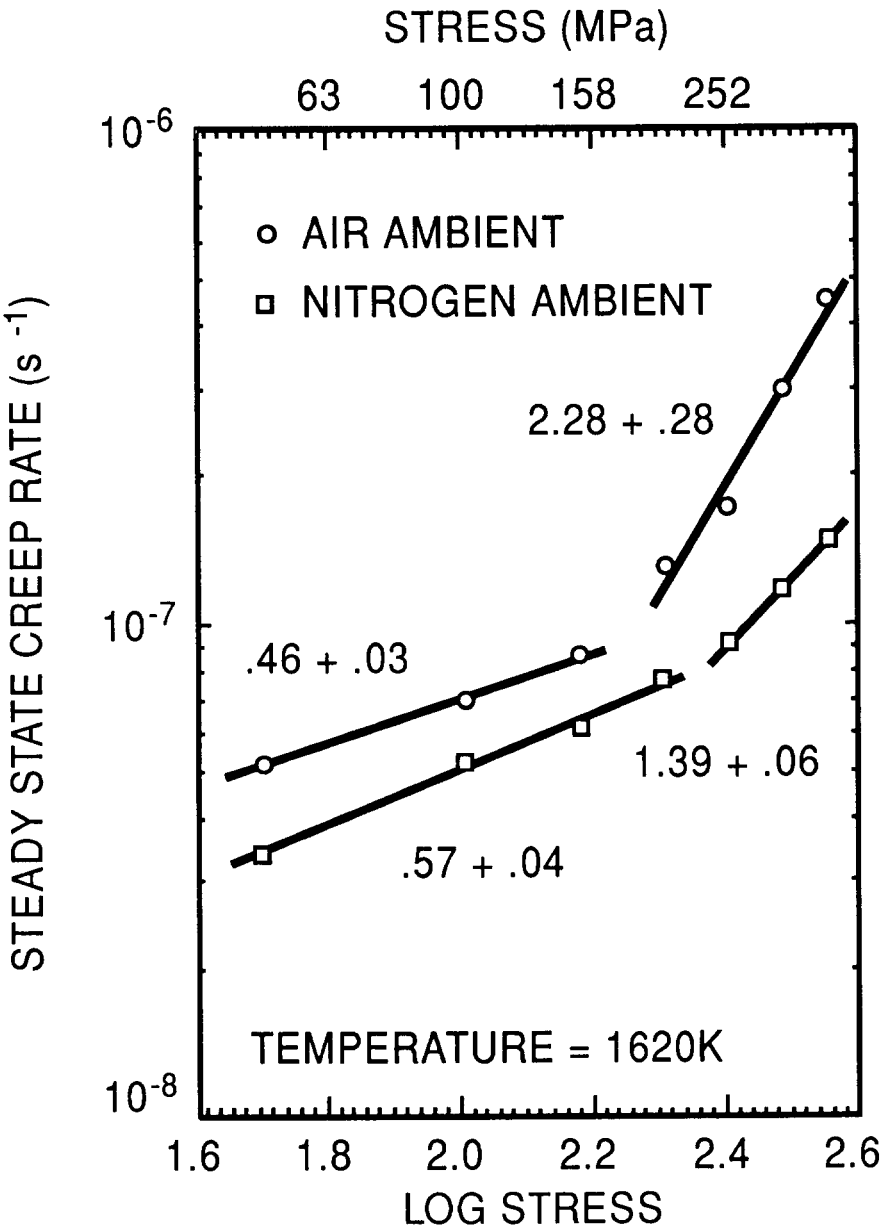

Fig. 11. Constant compressive stress creep curves comparing behavior of composite in air and nitrogen atmospheres.

Project Data Base
B. L. Keyes (Oak Ridge National Laboratory)

Objective/scope

The objective of this task is to develop a comprehensive computer data base containing the experimental data on properties of ceramic materials generated in the overall effort. This computer system is intended to provide a convenient and efficient mechanism for the compilation and dissemination of the large amounts of data involved. The data base will be made available in electronic form to all project participants. In addition, periodic hard copy summaries of the data, including graphical representation and tabulation of raw data, will be issued to provide convenient information sources for project participants.

Technical progress

The data base now contains 5497 test results on over 320 different batches of ceramic materials. Approximately 46% of these are on zirconia-based ceramics, 9% are on silicon carbides, 21% are on silicon nitrides, 5.7% are on whisker-reinforced silicon nitrides, 16.3% are on alumina-based ceramics (including whisker-reinforced aluminas and mullites), and 2% are on other ceramics. Table 1 gives a detailed breakdown, by material class, of the data stored in the system. A list of materials within a material class is available on request.

Test data from all participants in the Ceramic Technology for Advanced Heat Engines Project are needed. Data base personnel will work with anyone interested in contributing data.

A hard copy of the interim user's guide is finally complete. Intervening crises and major file restructuring caused the delay. The user's guide features file maps, field definitions, linking information, and data formats available to prospective users. The computerized user interface is scheduled for completion in the spring of 1991.

Several inconsistencies were found in some of the batch and reference codes during a routine data search, but were corrected. The cause of batch code problems were traced to a single set of data (same material, same test type, same conditions) that had been split up over several publications. Normally, each set of data presented in a report is given a different batch code if no other batch identifier is given with the data. If test results on the same batch of a material appear in different reports, then each set will be assigned a different batch code, thus leading the reader to believe the batches of material are different when that may not be the case. The reference code problem was an accidental transposition of characters. We hope to avoid such errors with automatic checking through the user interface in the future.

Storing additional notes on some test results has often been a problem in database structuring. The 24-character COMMENTS field often isn't large enough to contain everything, and a 100-character field is often too large. Since dBase IV uses fixed-length records, we simulated variable length capabilities by creating a text file with records that contain an 80-character text field for general notes, a series of codes to link the information back to the test to which it refers, and a sequence code so that several records may be used for notes on one test. This change has greatly enhanced the capabilities of the database.

The structure just described was also applied to the test background and chemistry data files. The set of linking codes are different for each of these files, but the sequenced-text structure remain the same and have proven to be more space efficient and useful. It will be a little harder to perform searches on the larger text fields, but most of this information

TABLE 1. CTAHE DATA BASE SUMMARY AS OF MARCH 31, 1990

Material Class	------ Brazed Specimens ------- MOR 4	Shear Str.	Toughness	Creep	Cyclic Fatigue	Density	Dynamic Fatigue	Elasticity	Fracture Toughness	Hardness	Interrupted Fatigue	Material Characteristics
Alumina				1	15		9	24	20			19
Alumina + reinforcing fibers						7			39			91
Alumina + Zirconia												
Mullite								2				2
Mullite + reinforcing fibers								11	16			48
Silicon Carbide						10	13	15	24	27		7
Silicon Nitride		3		27	19	28	16	24	85	112		29
Silicon Nitride + reinforcing fibers					15	2		16	31			44
Zirconia	123	58	2		51	158		92	54		239	37
Zirconia + reinforcing fibers												5
Other									3	27		
Totals	123	61	2	28	100	205	38	184	272	166	239	282

Material Class	MOR 3 Pt Bend	MOR 4 Pt Bend	Oxidation Rate	Poisson's Ratio	Shear Modulus	Tensile	Thermal Conductivity	Thermal Contraction	Thermal Diffusivity	Thermal Expansion	Thermal Shock	X-Ray Diffraction
Alumina		371				28	3			1	2	
Alumina + reinforcing fibers		144				11	34		18	4	6	
Alumina + Zirconia		7						23		21		
Mullite	1	4										
Mullite + reinforcing fibers	9	22										
Silicon Carbide		235								23		17
Silicon Nitride	10	573	1	2	1	73	9		10	44		49
Silicon Nitride + reinforcing fibers		106	3	17	16	86	9		17	14		
Zirconia		1554				50						72
Zirconia + reinforcing fibers		2				36						
Other		59										
Totals	20	3077	4	19	17	284	55	23	45	107	8	138

Total number of records on file: 5497

is presented in paragraph form as part of the material characterization or test background sections anyway. This format allows less restrictive use of the available information, so that everything that needs to be stated can be included.

It was brought to our attention that some of the terminology used in the database was inconsistent with the actual practices being used in ceramic testing. The source of the problem came from database personnel who had metallurgy backgrounds where the same terms have slightly different meanings. From now, ceramic materials joined to other materials, either ceramic or metallic, using metallic interlayers will be called brazed materials. The former WELDSHEA file is now BRAZSHER, and is joined by two more brazed-specimen files, BRAZMOR4 and BRAZTUFF. BRAZSHER contains shear test results on brazed specimens, BRAZMOR4 contains test results from modulus-of-rupture four-point bend tests on brazed specimens, while BRAZTUFF contains fracture toughness test results on brazed specimens. Our apologies to anyone who was confused by the erroneous terms.

Status of milestones

The fifth semiannual data base summary was completed through the first draft and was submitted one week late partially because of the time needed to complete the user's guide. The next semiannual report, due in September 1990, will feature an update on a variety of material test data. Work will start on the preliminary version of the computerized user's interface sometime in the late summer of 1990.

Publications

The Ceramic Technology for Advanced Heat Engines Project Database: March 1990 Summary Report and *The CTAHE Database User's Guide* are in review.

The Ceramic Technology for Advanced Heat Engines Project Database: September 1989 Summary Report is in revision.

The Ceramic Technology for Advanced Heat Engines Project Database: March 1989 Summary Report is being published.

3.2 TIME-DEPENDENT BEHAVIOR

Characterization of Transformation-Toughened Ceramics
Jeffrey J. Swab (U.S. Army Materials Technology Laboratory)

Objective/Scope:

To evaluate and characterize toughened ceramic matrix composite (CMC) materials for potential high temperature structural applications. At the present time four-point flexure testing is being used to determine the high temperature performance of these CMCs. However, a related in-house program to develop a tensile test for CMC materials is underway. Once this test has been developed and refined both techniques will be used to provide a more comprehensive characterization of CMC materials at elevated temperatures.

Technical Highlights:

Flexure Testing of CMC materials reinforced with continuous fibers has clear limitations as pointed out by a number of authors.[1-3] However, flexure testing can provide valuable information about trends and damage development, and provide qualitatively similar results to tension testing if failure is due to tensile forces.[2,3] It is also useful for material development purposes and has value in measuring the stress which initiates matrix microcracking.[2,3]

In order to insure tensile failure during flexure testing it has been shown that a long flexure span relative to the specimen thickness is necessary. Previous work[1,3] has recommended a ratio of at least 20. Although flexure testing has been shown to be more than adequate to examine this class of materials, direct tension testing would still be required to provide comprehensive structural characterization for design purposes.

A CMC material from Textron Specialty Materials, Lowell, MA was obtained in the form of as-machined bars of the following dimensions: 3 mm x 4 mm x 50 mm. The material is a Si_3N_4 matrix with 5 w/o Y_2O_3 and 1.25 w/o MgO additions; reinforced with 30 v/o SCS-6 SiC fibers. The fibers are laid up parallel to the 50 mm dimension of the bars. Although the ratio of flexure span to specimen thickness is only 13, examination of the material was carried out using four-point flexure testing in order to gain some qualitative knowledge about failures in CMC materials and provide a comparison to previous monolithic results.

Room temperature tests were performed and Figure 1 shows that there is excellent agreement with the result provided by Textron. In both instances there is an initial linear elastic region followed by a nonlinear increase in

the stress. It is this noncatastrophic failure which shows that this material has improved toughness over a monolithic material. For both specimens matrix microcracking began at ≈430 MPa. The tests run at MTL showed extensive elastic deformation and some residual permanent deformation. Examination of the fracture surfaces of the three bars tested showed that fiber pull-out and crack bridging, see Figure 2, were the dominant toughening mechanisms. As expected there was no evidence of failure origin as in monolithic materials. Fiber pull-out lengths were determined to approximately 0.9 μm.

Stepped-temperature stress-rupture (STSR) testing between 1000°C and 1400°C, see Figure 3, shows that there is no anomalous behavior in this temperature range. Preliminary examination of the fracture surfaces and the ends of the bars showed that the carbon core of the SiC fiber is no longer present. In addition, there was some oxidation of the matrix material and in several cases a white foamy substance was present towards the outer ends of the bars. The loss of the carbon core is due to oxidation. Oxidation also commonly occurs in silicon nitride after long-term exposure at elevated temperatures. The white foamy substance is probably due to burn-off of the excess binder. The ends of each fiber layer are coated with a binder to maintain the fiber spacing during processing. However, the processing is not sufficient to remove all the binder, thus it is burned off during elevated temperature tests.[4]

Failure appeared to initiate in a tensile manner then half way through the bar, approximately were the neutral axis is located, it appears to shift to a shear failure. Some of the failures initiated where fibers were exposed on the surface or at channels left behind when the fibers were removed during machining. The amount and length of fiber pull-out was much less than at room temperature. This would indicate that at these temperatures there is some increase in the fiber/matrix bond strength which would account for the reduction in fiber pull-out and the tensile type failure.

Long duration stress rupture testing was also done on this material. Five tests were carried out at various temperatures. One at 700°C, three at 900°C and one at 1200°C. The lower temperature tests were done because Textron informed us that they have seen some degradation at these temperatures. There was no evidence of any unusual degradation at either of these lower temperatures. Three of the flexure bars, the one at 700°C and two at 900°C, survived for 500+ hours under a 250 MPa applied stress without failure, but with a small amount of permanent deformation.

As was the case after the STSR tests the carbon cores of the fibers were no longer present due to oxidation, there was some oxidation of the matrix and the white foamy substance was present at the outer ends of some bars. Failures were also the same as in the STSR tests.

The flexure bar subjected to 1200°C under an applied stress of 200 MPa failed after ≈58 hours. The failure was completely brittle, since there was no fiber-pull out and the crack propagated in a perpendicular manner through the entire bar. This brittle failure indicates that at this temperature there is a strengthening of the fiber/matrix bond which reduces the likelihood of fiber pull-out or crack bridging as possible toughening/strengthening mechanisms.

References:

1. D. Lewis, C. Bulik and D. Shadwell, "Standardized Testing of Refractory Matrix/Ceramic Composites", Ceram. Sci. Eng. Proc., 6 [7-8] 507 (1985).

2. D.B. Marshall and A.G. Evans, "Failure Mechanisms in Ceramic-Fiber/Ceramic Matrix Composites", J. Am. Ceram. Soc., 68 [5] 225 (1985).

3. R.W. Davidge and J.J.R. Davies, "Ceramic Matrix Fibre Composites: Mechanical Testing and Performance", Int. J. High Tech. Ceram., [4] 341 (1988)

4. J.F. LeCostaouec, Textron Specialties Materials, personal communication to J.J. Swab, MTL, 6 Jan. 1990.

Status of Milestones:

All milestones are currently on schedule.

Communications/Visitors/Travel:

Attended the 42nd Pacific Coast Regional Meeting in Anahiem, CA and made a poster presentation at the 4th International Conference on the Science and Technology of Zirconia.

Visited Textron Specialty Materials and J.F. LeCostaouec to discuss the mechanical property results that were generated on the Textron CMC material.

Spoke with Dr. H.C. Yeh of Garrett about the availability of the toughened silicon nitride they are producing as part of a DoE contract. The material is available but FY90 DoE funding has not arrived yet.

Publications:

Swab, J.J., "High Temperature Performance of Y-TZP Materials Between 800°C and 1200°C", MTL TR 90-3, January 1990, NTIS Access No. ADA-217723.

Swab, J.J., "Low-Temperature Degradation of Y-TZP Materials", MTL TR 90-4, January 1990, NTIS Access No. ADA-218841.

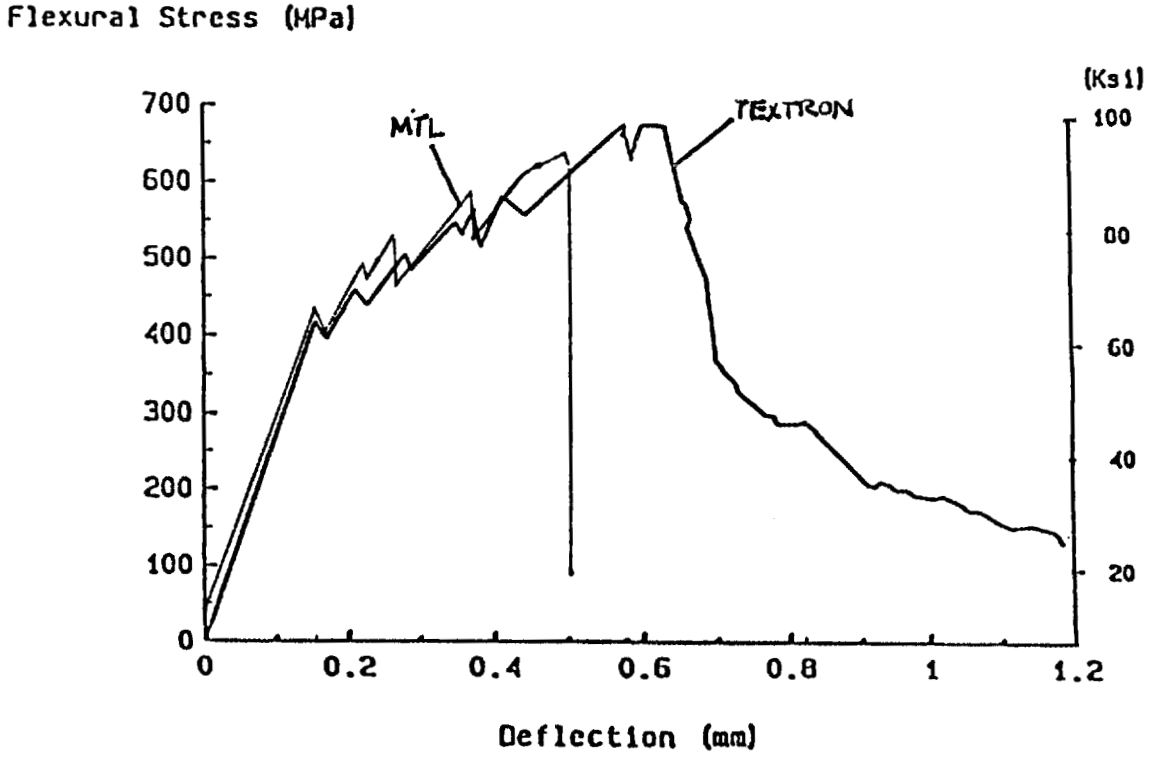

Figure 1.

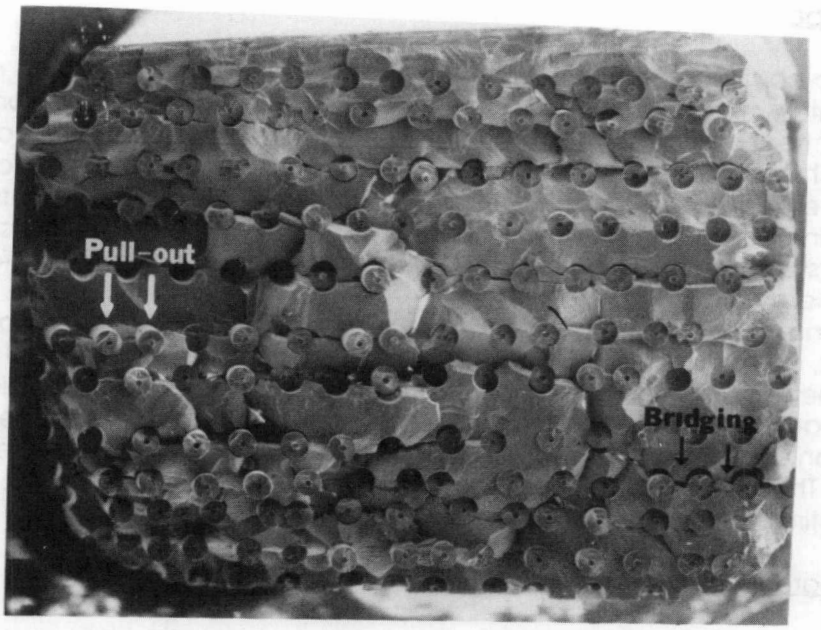

Figure 2.

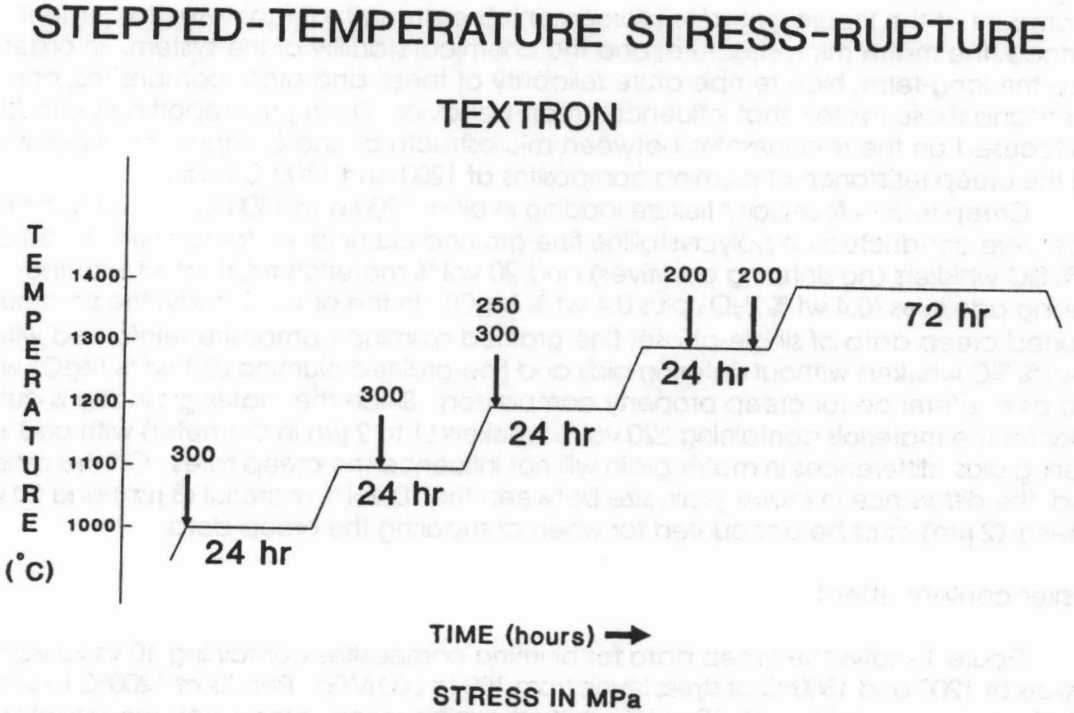

Figure 3.

Fracture Behavior of Toughened Ceramics

H. T. Lin, P. F. Becher, and W. H. Warwick (Oak Ridge National Laboratory)

Objective/scope

Ceramic composites, such as fiber and whisker-reinforced ceramics, particulate phase composites, and ceramics with elongated grain structures, offer important advantages for heat engine applications. Chief among these is the improved fracture toughness which can be achieved by appropriate design of microstructural and material parameters. Previous studies show that these materials often exhibit substantial improvements in damage, thermal shock, and slow crack growth resistances. However, design of such systems must also consider those factors influencing their performance at elevated temperatures.

In response to these needs, studies are conducted to determine the mechanical properties, e.g., creep, delayed failure, strength, and toughness at elevated temperatures for these toughened ceramics. Particular emphasis is placed on understanding how microstructure and composition influence the mechanical performance at elevated temperatures and the stability of these properties for extended periods at these temperatures. The knowledge gained from these studies provide input on how to modify materials to optimize their mechanical properties for the temperature ranges of interest.

Technical progress

Studies show that reinforcement by the incorporation of SiC whiskers significantly improve the creep resistance of polycrystalline fine-grained alumina.[1,2] This originates from the pinning of grains by the whiskers lying in and across grain interfaces which limit the creep deformation by grain boundary sliding. However, the creep properties of alumina composites reinforced with SiC whiskers in an oxidizing environment may be influenced by the amount of the incorporated reinforcement, the strength of matrix-reinforcement interface, the matrix microstructure, and the chemical stability of the system. In order to insure the long-term, high-temperature reliability of these and other composites, one must understand those factors that influence creep behavior. During this reporting period, study was focused on the relationships between microstructural and compositional parameters and the creep resistance of alumina composites at 1200 and 1300°C in air.

Creep tests in four-point flexure loading in air at 1200 and 1300°C at selected stress levels were conducted on polycrystalline fine-grained alumina reinforced with 10, 30 and 50 vol % SiC whiskers (no sintering additives) and 20 vol % materials fabricated with the sintering additives (0.4 wt % Y_2O_3 plus 0.4 wt % MgO). In the present study, the previously reported creep data of single-phase, fine-grained alumina composite reinforced with 20 vol % SiC whiskers without sintering aids and fine-grained alumina (0.1 wt % MgO) were used as a reference for creep property comparison. Since the matrix grain size is quite similar for the materials containing ≥20 vol % whiskers (1 to 2 μm in diameter) with and without sintering aids, differences in matrix grain will not influence the creep rates. On the other hand, the difference in matrix grain size between the 10 vol % material (8 μm) and 20 vol % material (2 μm) must be accounted for when comparing the creep data.

Whisker content effect

Figure 1 shows the creep data for alumina composites containing 10 vs 20 vol % SiC whiskers at 1200 and 1300°C at stress levels from 100 to 300 MPa. Results at 1200°C indicate that alumina composites with 10 vol % whiskers exhibit creep rates which are a factor of three lower than that of 20 vol % materials under the same test conditions. Also, both

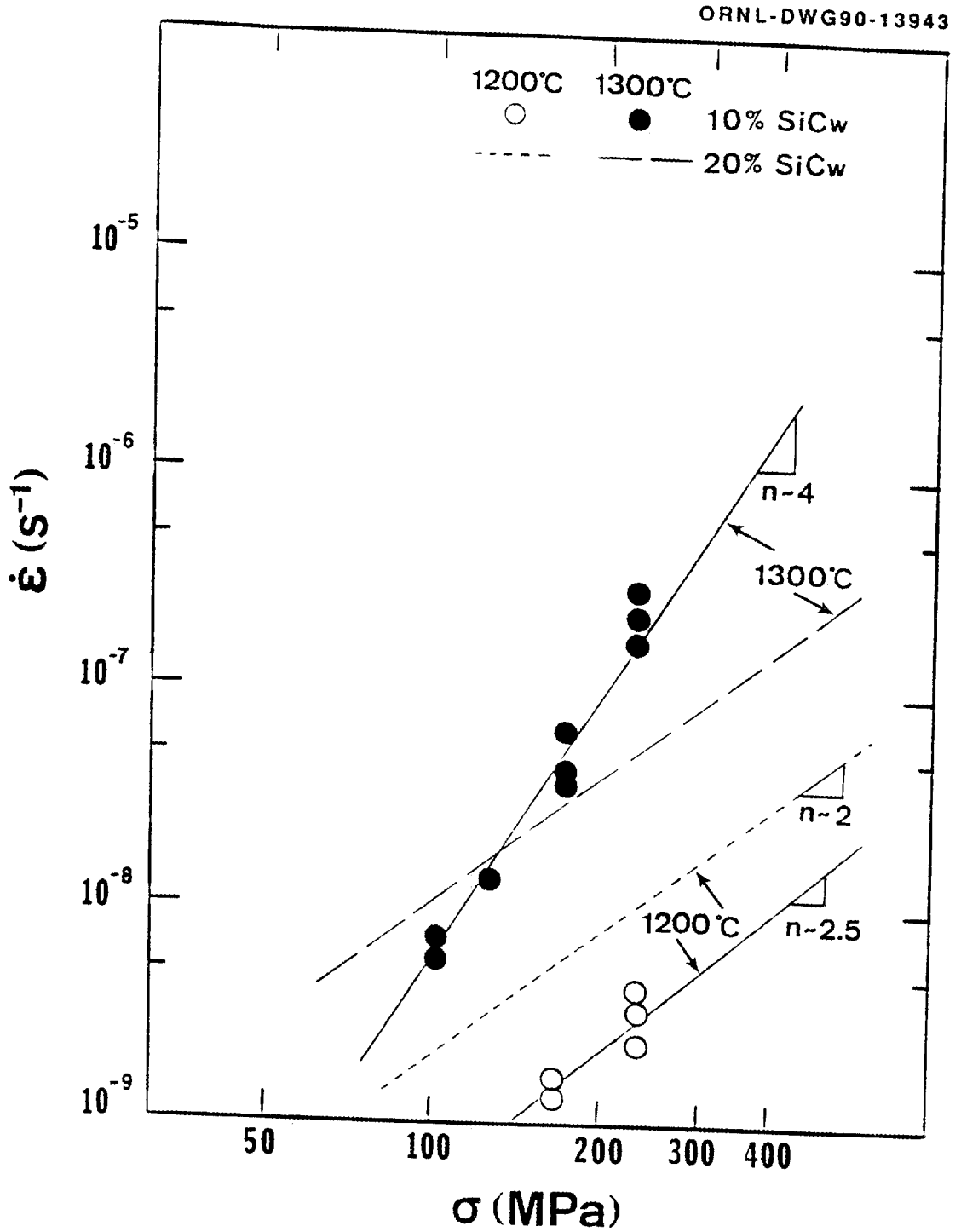

Fig. 1. Strain rate vs stress relation for creep deformation for alumina composites with 10 and 20 vol % SiC whiskers.

materials exhibit stress exponents ($n \approx 2$ to 2.5) indicative of a similar creep mechanism operating in these two materials. For the polycrystalline fine-grained alumina, a stress exponent of approximately 2 is obtained and is attributed to grain boundary sliding (GBS). At 1300°C, the composites reinforced with 10 vol % SiC whiskers become less creep resistance with respect to 20 vol % composites at stress levels greater than 125 MPa. In addition, the stress exponent of 10 vol % materials is dependent upon the test temperatures. The exponent increases from $n \approx 2.5$ at 1200°C to $n \approx 4$ at 1300°C indicating a change in rate-limiting processes. The increase in creep resistance of 10 vol % materials at 1200°C with respect to 20 vol % materials may be attributed to an increase in matrix grain size and a decrease in stress concentration sites available for creep cavitation as the whisker content is reduced. Also, an increase in matrix grain size may alter the processes for creep cavitation leading to the observation of temperature dependence of stress exponent. However, the quantitative relationship between grain size and the creep resistance of alumina composites are not fully understood at present. A study of the creep behavior for alumina composites with constant whisker content (i.e., 10 vol %) and different matrix grain sizes will be performed to evaluate the relationship between the matrix grain sizes and creep controlling mechanisms.

The creep data for the alumina composites containing 20, 30 and 50 vol % whiskers at 1200 and 1300°C for stress levels ranging from 50 to 300 MPa are shown in Fig. 2. Results show that alumina composites with 30 and 50 vol % whiskers exhibited creep rates which are higher, one to two orders in magnitude, than those with 20 vol % whiskers under the same test conditions. Also, materials with 30 and 50 vol % whiskers exhibited nearly identical creep properties at the temperature and stress ranges investigated in this study. The data for both materials at 1200 and 1300°C exhibited stress exponents ($n \approx 3$ and 6, respectively) which are greater than that of 20 vol % materials ($n \approx 2$), indicative of different rate-limiting mechanisms. At 1300°C, materials reinforced with 30 and 50 vol % SiC whiskers also exhibited a higher stress exponent ($n \approx 6$) than that at 1200° C ($n \approx 3$). The higher creep rate, plus higher stress exponent, of the 30 and 50 vol % composites is likely due to increase in strain associated with cavitation. The increase in whisker content would introduce more stress concentration sites available for cavity nucleation leading to higher number density of cavitation, hence higher cavitation strain.

Furthermore, the addition of more SiC whiskers acts to increase the amount of oxidation and reaction products at the surface. This increased oxidation-reaction process generates increasing intergranular glassy phases in the surface and subsurface region of the tensile surface enhancing the creep process. An oxidation experiment at 1300°C for periods up to 100 h in air was conducted to compare the creep data with the oxidation rates for alumina composites with 20 to 50 vol % SiC whiskers. The oxidation results revealed that the oxide scales formed on the specimen surfaces of 30 and 50 vol % materials are at least factors of three thicker than that of 20 vol % materials after 100 h. Also, the reaction rate constants at 1300°C for 30 and 50 vol % materials are threefold greater than that of 20 vol % materials. These observations support the hypothesis that the enhanced oxidation reaction is one of the key factors leading the higher creep rates and stress exponents for the alumina composites reinforced with ≥30 vol % SiC whiskers.

Sintering additive effect

Figure 3 shows the creep data for 20 vol % SiC whisker-reinforced alumina with and without sintering aids (0.4 wt % Y_2O_3 plus 0.4 wt % MgO) at temperatures of 1200 and 1300°C at applied stress ranging from 37 to 300 MPa in air. The Y_2O_3 sintering aid is used to enhance the densification rate through the formation of amorphous phases at grain boundaries and the MgO to limit grain growth of the alumina matrix. Accordingly, it is not surprising that the creep resistance of the alumina composites is decreased by approximately one to three

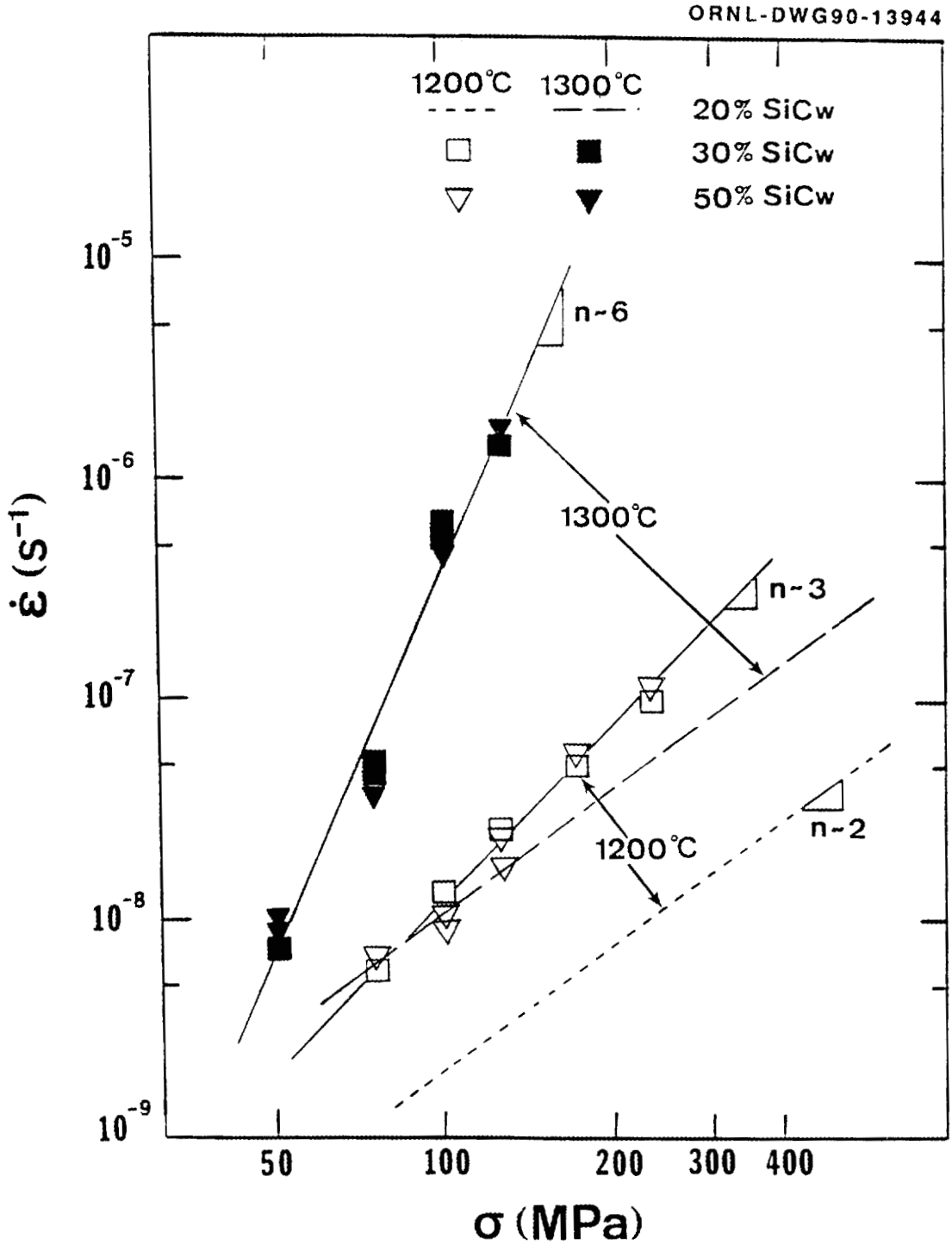

Fig. 2. Strain rate vs stress relation for creep deformation for alumina composites reinforced with 20, 30 and 50 vol % SiC whiskers.

ORNL-DWG90-13945

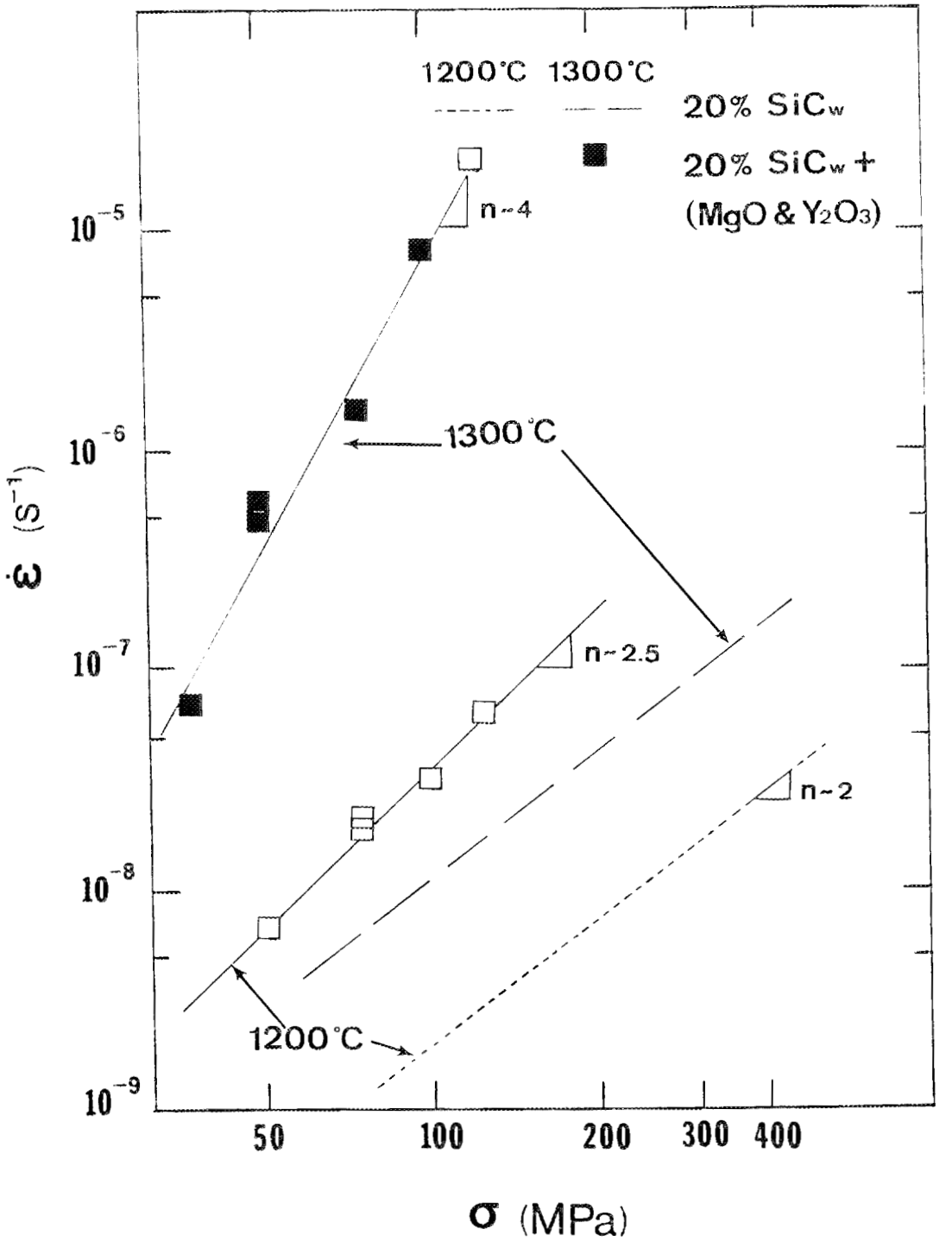

Fig. 3. Strain rate vs stress relation for creep deformation of 20 vol % SiC whisker-reinforced alumina with and without sintering aids (0.4 wt % MgO plus 0.4 wt % Y_2O_3).

orders of magnitude with the addition of this combination of sintering aids as compared to the composite without additives. At 1200°C, both materials exhibit similar stress exponent (2 and 2.5) indicative of similar creep-controlling mechanisms. Again, a stress exponent of 2 is attributed the grain boundary sliding. In addition, the composite containing sintering aids exhibits a temperature dependent stress exponent. The exponent increases from $n \approx 2.5$ at 1200°C to $n \approx 4$ at 1300°C, indicating a change in the creep process. The higher stress exponent at 1300°C for materials with sintering aids again likely results from the consequence of the more extensive cavitation than that at 1200°C. The higher creep rates found in the sintering additive containing materials are attributed to the observed substantial content of amorphous phases at grain boundaries, which contains Y, Al, Si and Ca, as compared to composites made without the sintering aids. The presence of intergranular glassy phase promotes the grain boundary sliding for creep, leading to higher creep deformation rates. In addition, the intergranular liquid phases act as a rapid diffusion path for oxidation processes, further enhancing the creep.

At elevated temperatures, the presence of intergranular amorphous phases is known to promote the creep processes of ceramic and ceramic composite systems. Higher creep rate and high stress exponent ($n \approx 4.8$) were observed in a glass-bonded, 96% alumina.[3] Also, creep is enhanced by the presence of intergranular amorphous phases in Si_3N_4 ceramics and in Si_3N_4-SiC whisker composites fabricated with sintering Y_2O_3 plus Al_2O_3 aids.[4,6] However, the creep resistance of the 96% alumina and the Si_3N_4 ceramics can be improved by a postheat treatment.[3,5] The crystallization of grain boundary phases can increase the creep resistance. Results of present study suggests that sintering aids either need to be modified or that postheat treatments be devised to crystallize the amorphous phases to achieve the optimal properties for high-temperature applications.

References

1. A. H. Chokshi and J. R. Porter, "Creep Deformation of an Alumina Matrix Composite Reinforced with Silicon Carbide Whisker," *J. Am. Ceram. Soc.* **68**(6), C-144-145 (1985).

2. H. T. Lin and P. F. Becher, "Creep Behavior of a SiC Whisker Reinforced Alumina," *J. Am. Ceram. Soc.*, in press.

3. S. M. Wiederhorn, B. J. Hocjey and R. F. Krause, Jr, "Creep and Fracture of a Vitreous-Bonded Aluminum Oxide," *J. Mater. Sci.* **21**, 810-24 (1986).

4. N. J. Tighe, S. W. Wiederhorn, T. J. Chung, and C. L. McDaniel, "Creep Cavitation and Crack Growth in Silicon Nitride," pp. 587-604 in *Mater. Sci. Res. Vol. 18: Deformation of Ceramic Materials II*, eds. R. E. Tressler and R. C. Bradt, Plenum Press, New York, 1984.

5. M. H. Lewis, G. R. Heath, S. M. Winder, and R. J. Lumby, "High Temperature Creep and Fracture of β-Si_3N_4 Ceramic Alloys," ibid. pp. 605-16 in *Mater. Sci. Res. Vol. 18: Deformation of Ceramic Materials II*, eds. R. E. Tressler and R. C. Bradt, Plenum Press, New York, 1984.

6. R. D. Nixon, S. Chevacharoenkul, M. L. Huckabee, S. T. Buljan and R. F. Davis, "Deformation Behavior of SiC Whisker-Reinforced Si_3N_4," pp. 295-302 in *Mater. Res. Soc. Proceedings Vol. 78: Advanced Structural Ceramics*, eds. P. F. Becher, M. V. Swain, and S. Somiya, MRS, Pittsburgh, 1987.

Status of milestone

On schedule.

Publications

P. F. Becher, P. Angelini, W. H. Warwick, and T. N. Tiegs, "Elevated Temperature Delayed Failure of Alumina Reinforced with 20 vol % SiC Whisker," *J. Am. Ceram. Soc.* **73**(1), 91-96 (1990).

H. T. Lin and P. F. Becher, "Creep Behavior of a SiC Whisker Reinforced Alumina," *J. Am. Ceram. Soc.*, in press (Milestone 321307).

Cyclic Fatigue of Toughened Ceramics

K. C. Liu and C. R. Brinkman (Oak Ridge National Laboratory)

Objective/scope

The objective of this task is to develop, design, fabricate, and demonstrate the capability to perform tension-tension dynamic fatigue testing on a uniaxially loaded ceramic specimen at elevated temperatures Three areas of research have been identified as the main thrust of this task: (1) design, fabrication, and demonstration of a load train column which truly aligns with the line of specimen loading; (2) development of a simple specimen grip that can effectively link the load train and test specimen without complicating the specimen geometry and, hence, minimize the cost of the test specimen; and (3) design and analysis of a specimen for tensile cyclic fatigue testing.

Technical progress

Fatigue of SiC whisker-reinforced alumina

An exploratory cyclic fatigue test at room temperature was performed on a tensile specimen made of 30% SiC whisker-reinforced alumina furnished by CERCOM of Vista, California. The specimen was cycled in tension at a stressing rate of 21,000 MPa/min, as was the test condition used in previous tests. Since little was known about the fatigue properties of this material, a cyclic stress of 330 MPa, equivalent to about 75% of its tensile fracture strength, was used as a starting point. After cycling for 111,500 cycles with no apparent indication of imminent fatigue failure, the cyclic stress amplitude was increased intermittently until the specimen finally failed in fatigue at 414 MPa in 617 cycles. The maximum peak stress was equal to about 95% of the tensile fracture strength. Test parameters, loading history, and test results are summarized in Table 1. Test data are plotted in Fig. 1 including the fatigue data of monolithic alumina tested and reported previously[1] by our laboratory.

The arrowhead attached to the open symbols, as seen in Fig. 1, indicated that specimen failure had not occurred when the intermediate cyclic loading was terminated at the indicated condition. Due to limited information, a straight line was used to approximate the fatigue behavior of the composite alumina, as shown in Fig. 1. Behavior beyond 105 cycles delineated by a broken line is somewhat speculative. Figure 1 indicates that the fatigue curve of the composite alumina was practically flat compared to that of monolithic alumina. The difference in fatigue behavior was obviously attributed to the strengthening by SiC whiskers that have effectively inhibited the slow crack growth being promoted by cyclic fatigue. The flatness of the fatigue curve implied that there was little or no fatigue-induced crack growth occurring in the specimen until the applied cyclic stress exceeded a critical value high enough to fracture the SiC whiskers. In the case of this composite material, the critical value may be in the upper 10% range of its tensile fracture strength.

Electron microscopy

Optical microscopy (OM) and scanning electron microscopy (SEM) were performed on the fracture surfaces of three specimens, specimens 1 and 2 tested in tensile fast fracture and specimen 7 tested in cyclic fatigue mode. OM and SEM micrographs of specimens 1 and 2 are illustrated in Figs. 2 and 3, respectively, and specimen 7 in Fig. 4. All the fractures were initiated from internal defects, which were either a huge single grain as large as 70 μm (Fig. 2) or a agglomerate of smaller grains (Figs. 3 and 4). X-ray analyses indicated these grains were all pure Al_2O_3. Absence of SiC whiskers inside the Al_2O_3

Table 1. Results of a cyclic fatigue test on CERCOM SiC whisker-reinforced alumina at room temperature

Loading sequence	Cyclic stress MPa (ksi)	Percent of fracture strength	Number of cycles at intermediate loading	Number of cycles to failure
1	330 (48)	75	111,500	
2	367 (53.2)	84	42,500	
3	396 (57.4)	90	33,000	
4	414 (60)	95	617	187,617

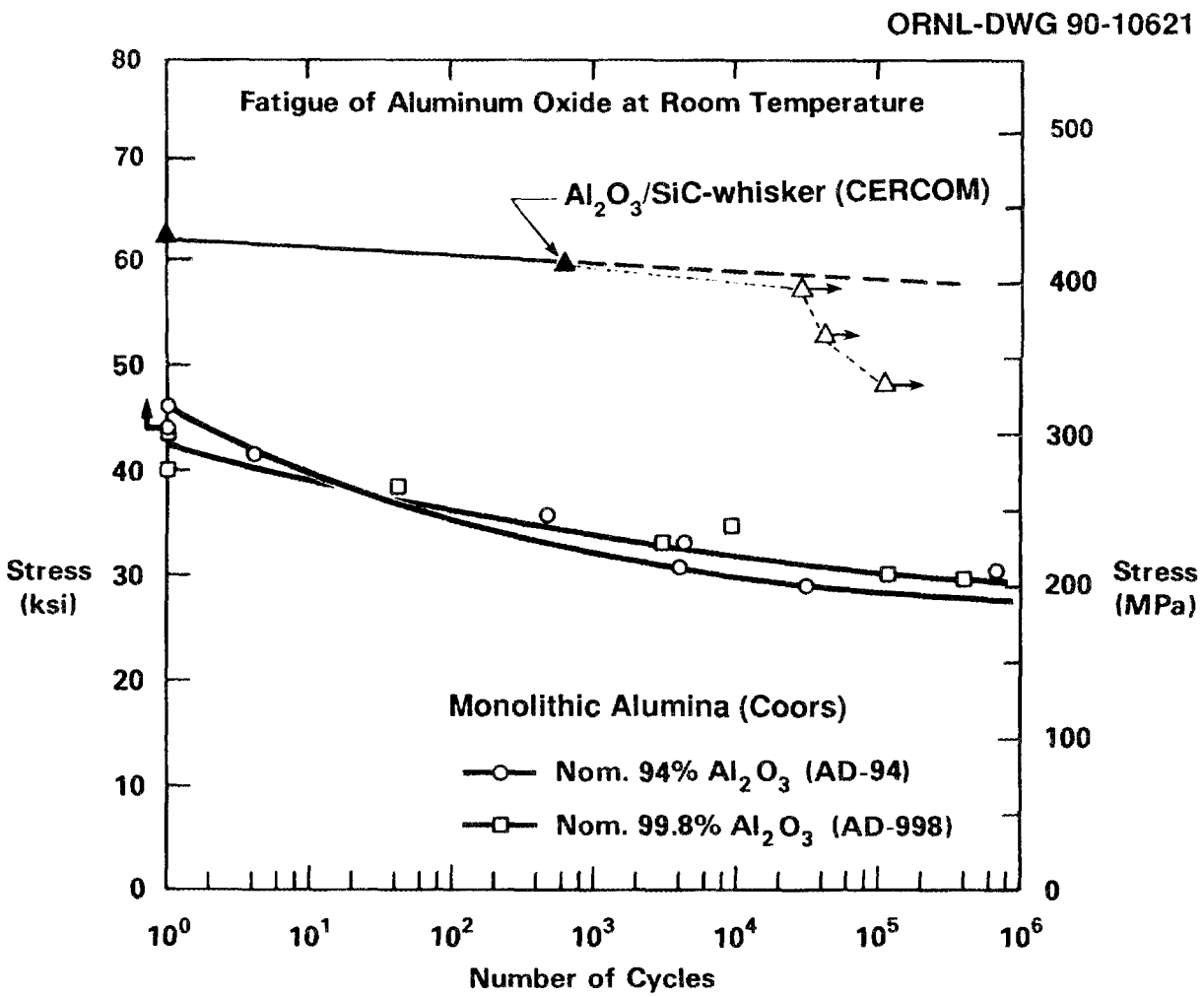

Fig. 1. Comparison of fatigue behavior of SiC-whisker reinforced alumina and that of monolithic alumina.

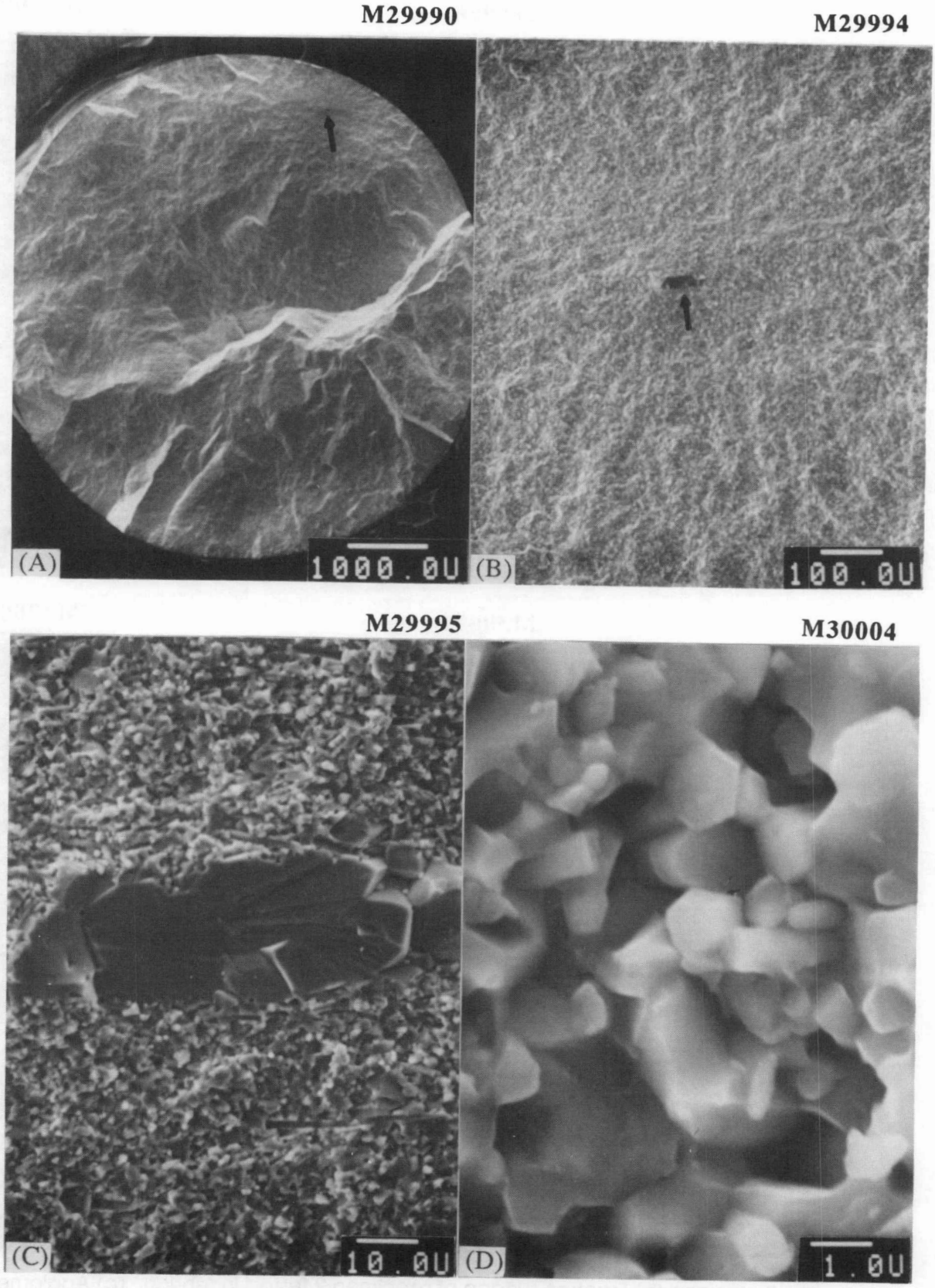

Fig. 2. (a) and (b) Fracture surface of specimen 1 tested in uniaxial tension. Arrowheads indicate the fracture initiation site. (c) An over-sized Al_2O_3 grain at the fracture origin. (d) Composite region showing little or no whisker pullouts.

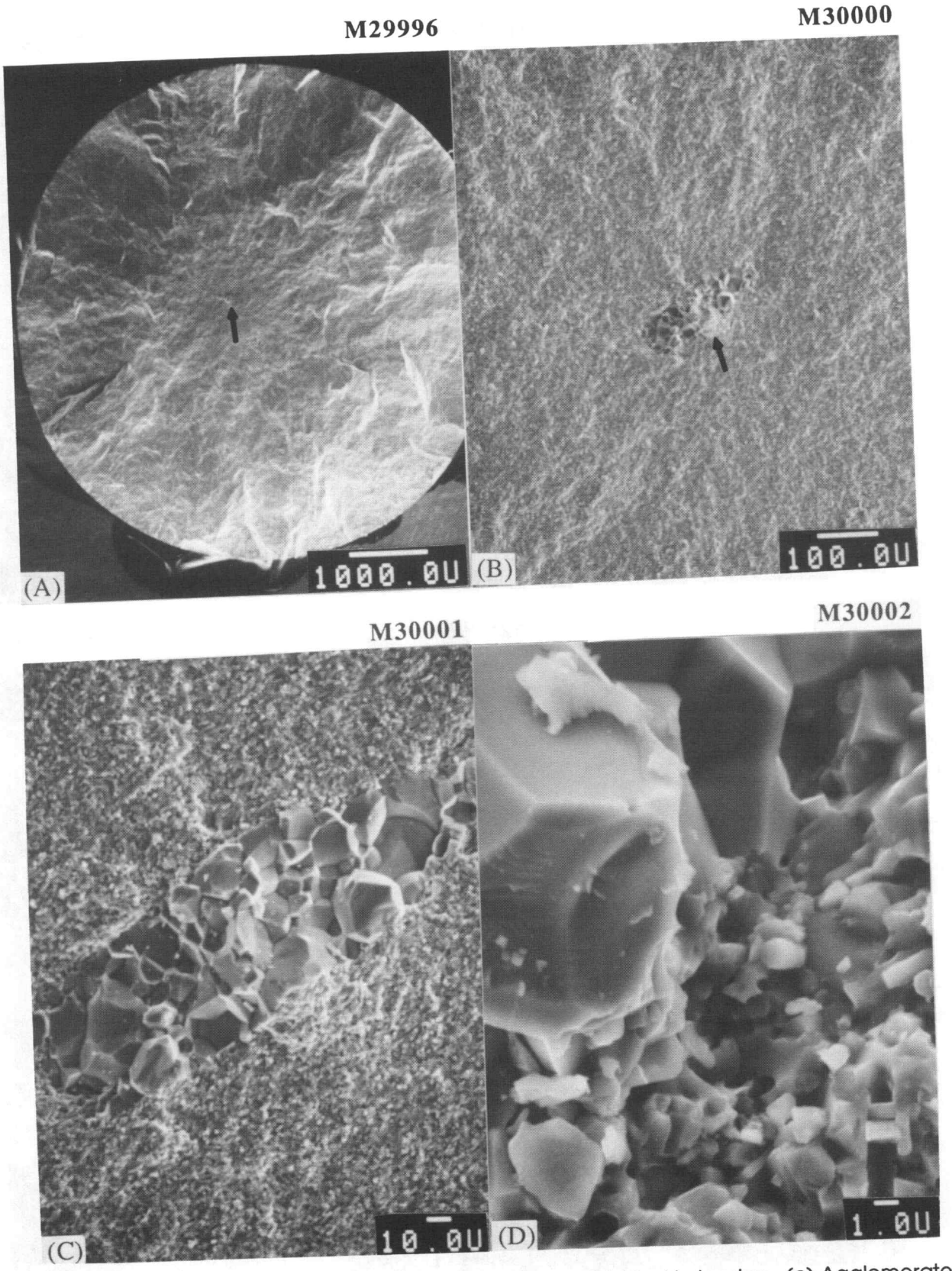

Fig. 3. (a) and (b) Fracture surface of specimen 2 tested in tension. (c) Agglomerate of Al_2O_3 grains. (d) Interface between the agglomerate and composite material.

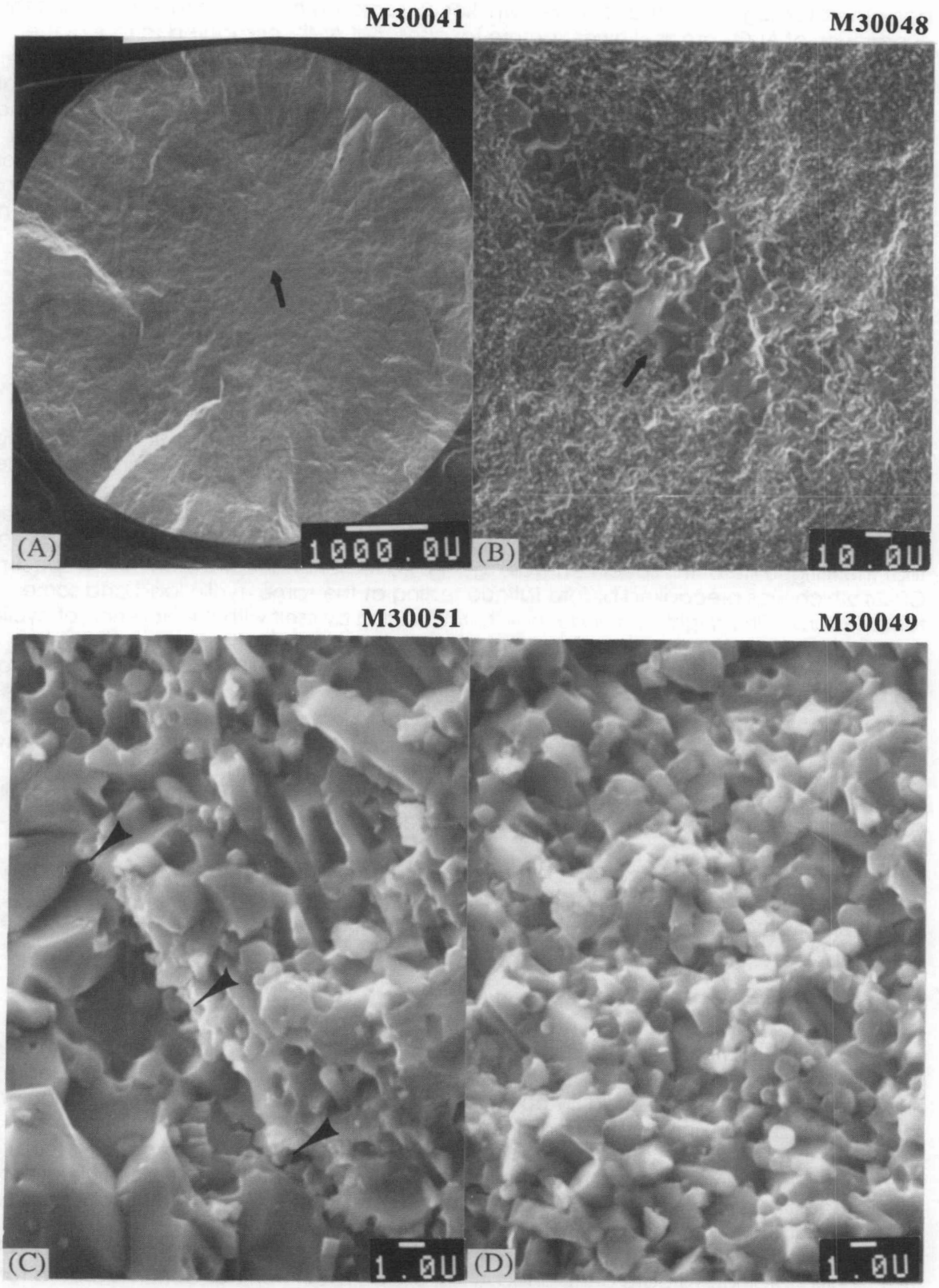

Fig. 4. (a) and (b) Fracture surface of specimen 7 tested in cyclic fatigue. (c) Microstructures at the vicinity of interface (indicated by arrowheads) between agglomerate and composite. (d) Microstructure of a region away from the fracture initiation site, showing no obvious whisker pullouts.

agglomerates suggested that poor SiC whisker dispersion in the region failed to inhibit the overgrowth of Al_2O_3 grains. Lower fracture toughness of Al_2O_3 compared to that of the composite material was an apparent reason that all the fractures were initiated from the large grain or agglomerate site. An observation indicated there was hardly any noticeable difference in fracture morphology between specimen 2 tested in tensile fast fracture and specimen 7 tested in cyclic fatigue, except that the crack mirror zone was slightly larger and well defined for the fatigue-induced fracture. This finding seems to support the theory discussed earlier in the preceding section about the outstanding fatigue performance of SiC whisker-reinforced alumina. Few whisker pullouts were observed, indicating excellent bonding between the whiskers and matrix.

Cyclic fatigue behavior of thermally aged NT-154 silicon nitride

Experimental results obtained to date on this material have consistently demonstrated that cyclic loading from low stress to high stress in intermittent steps will enhance the high-cycle fatigue life at high temperatures. This behavior is generally known as "coaxing." However, it is not known whether the strengthening mechanism is the synergistic effect of cyclic loading and temperature or merely the result of thermal aging. To investigate the effect of thermal aging on cyclic fatigue behavior, two virgin specimens were installed in creep machines with no load and aged at 1370°C for 150 h.

One of the thermally aged specimens (specimen 20-14) was then cycled to a peak stress of 243 MPa at 1370°C until failure occurred at 306,086 cycles. A comparison showed that the fatigue life of this specimen was higher by a factor of about 2 than that of specimen CP-24 which was precoaxed before fatigue testing at the same cyclic load and same temperature. One might conclude that thermal aging by itself with the absence of cyclic loading may suffice for the enhancement of cyclic fatigue life in the high-cycle regime. However, this may not be a valid comparison since the fatigue life reported for specimen CP-24 could have been higher, had it not failed prematurely due to the surface damage at pits resulting from chemical interaction between the specimen surface and probing rods of the strain extensometer. Also, considerable data scatter is inherent in the fatigue behavior of ceramics since life is governed by the size of the crack-initiating defect. To make a meaningful comparison of test data, a virgin fatigue test is currently being duplicated with a specimen selected from the same lot as specimen 20-14 as a means of eliminating lot-to-lot variations.

The second specimen (20-11) is now being remachined in the shop. The surface of its gage section was slightly pitted by some glassy substances diffusing out from the insulation of a new furnace which subsequently precipitated and caused some surface interaction.

Studies of cyclic fatigue/creep interactions

The interaction between cyclic fatigue and creep of ceramic materials is an area virtually unexplored. Although it has been demonstrated that the high-cycle fatigue life of silicon nitride can be enhanced by coaxing at high temperatures, little is known about the influence of precoaxing to the subsequent creep behavior.

To investigate the effect of initial cyclic fatigue loading (precoaxing) on creep behavior, five virgin specimens from the same lot were subjected to a series of intermittent cyclic loads for a total of about 500,000 cycles in a period of 150 h. Three specimens were precycled at 1300°C and two at 1370°C.

A precycled specimen (20-09) was then tested under an applied stress of 100 MPa. Test results obtained to date are plotted in Fig. 5. The specimen has accumulated a total strain of about 0.8% and the test is ongoing. To facilitate comparison, the creep curve of

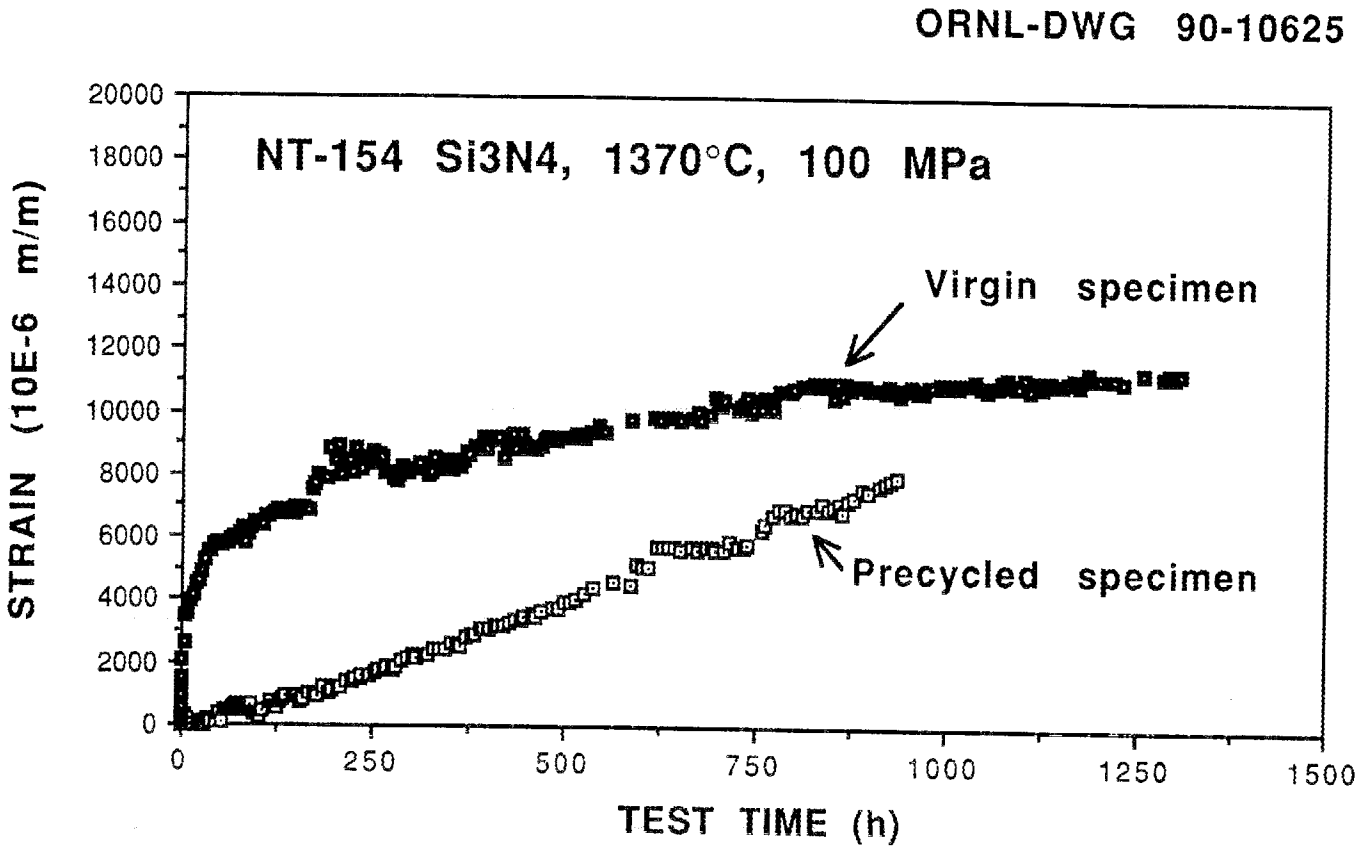

Fig. 5. Comparison of creep behavior of a virgin specimen and that of a precycled specimen tested at 1370°C.

specimen 20-07 was also given in Fig. 5. Note that specimen 20-07 was a virgin specimen and tested under the same loading condition given to the precycled specimen. The striking difference in creep behavior between the two specimens clearly suggests that precyling has modified the microstructure of the material prior to the creep testing.

Figure 6, an expanded diagram, shows the initial creep behavior of the precycled specimen. The strain recovery (or negative creep strain) occurring immediately following the initial loading and the erratic creep behavior shown in the strain-time curve were rather unconventional but appeared to be true material behavior. However, no plausible explanations can be offered at this time. As the erratic creep behavior began to subside after about 200 h of testing, the creep rate accelerated slightly as if tertiary creep had commenced. However, the material deformed steadily thereafter at a constant creep rate of 2.64×10^{-9}/s. If the creep behavior of the precycled specimen remains steady beyond the data points, it appears that the creep curve of the precycled specimen may intersect that of the virgin specimen at the point where the creep rupture occurred. Because of the uncertainty in creep behavior beyond the available data, the true effects of precycling on the creep resistance of this material remain unknown.

Uniaxial tensile creep of NT-154 silicon nitride

Exploratory creep tests were performed on tensile specimens of NT-154 silicon nitride at 1300 and 1370°C. These specimens were made from the same lot of the material, designated as CP-series, used in the cyclic fatigue tests discussed in the last progress report. Creep strain was measured using the laser diffraction strain extensometer described elsewhere.[2] Figure 7 shows the creep curves of specimens CP-28 and CP-30 tested at 1300°C under applied stress of 150 and 180 MPa, respectively. Both tests were shutdown inadvertently due to equipment adjustments. The problems have been corrected since then. Therefore, the results of the tests do not represent the creep life of the specimens. However, there were sufficient data points to delineate the essential features of the creep behavior up to the steady-state phase which was clearly definable. Both curves showed a reversed inflection at the transition between the primary and secondary creep phases, resulting in forming a bump in the otherwise smooth creep curves.

A linear relationship between the stress and strain exhibited during the initial loading is discernable in Fig. 8. The least-squares fit showed the elastic modulus was 183 GPa.

Figure 9 shows the creep curves of specimens CP-31 and CP-34 tested at 1370°C under applied stresses of 120 and 90 MPa, respectively. Unlike those obtained at 1300°C, the creep curves obtained at 1370°C were smooth. Specimen CP-31 ruptured in 47 h of testing with a total strain of about 1%. It was difficult to determine whether the test ended in the tertiary phase because of the limited data points taken after 10 h of testing, as shown in Fig. 9. The minimum creep rate was determined to be 4.25×10^{-8}/s.

The creep test on specimen CP-34 was interrupted after about 550 h of testing due to a power outage. Subsequently, the test was restarted but was shut down again by another power outage after 300 h of follow-up testing. An attempt to restart the test was not successful because the test specimen fractured during reloading. Test data as shown in Fig. 9 hint that the tertiary creep was occurring at about 800 h. Pronounced transient creep behavior exhibited immediately following the reloading was unexpected. However, the steady-state creep rates after the reloading remained about the same. The upward shifting in the second leg of the creep curve suggests that frequent unloading and reloading may accelerate creep process, i.e., enhance softening or flaw growth and shorten the creep life, if the transient creep reoccurs after every reloading.

Transient creep curves for the initial loading and subsequent reloading are compared in Fig. 10. They have been replotted so that both start at zero time to facilitate

ORNL-DWG 90-10626

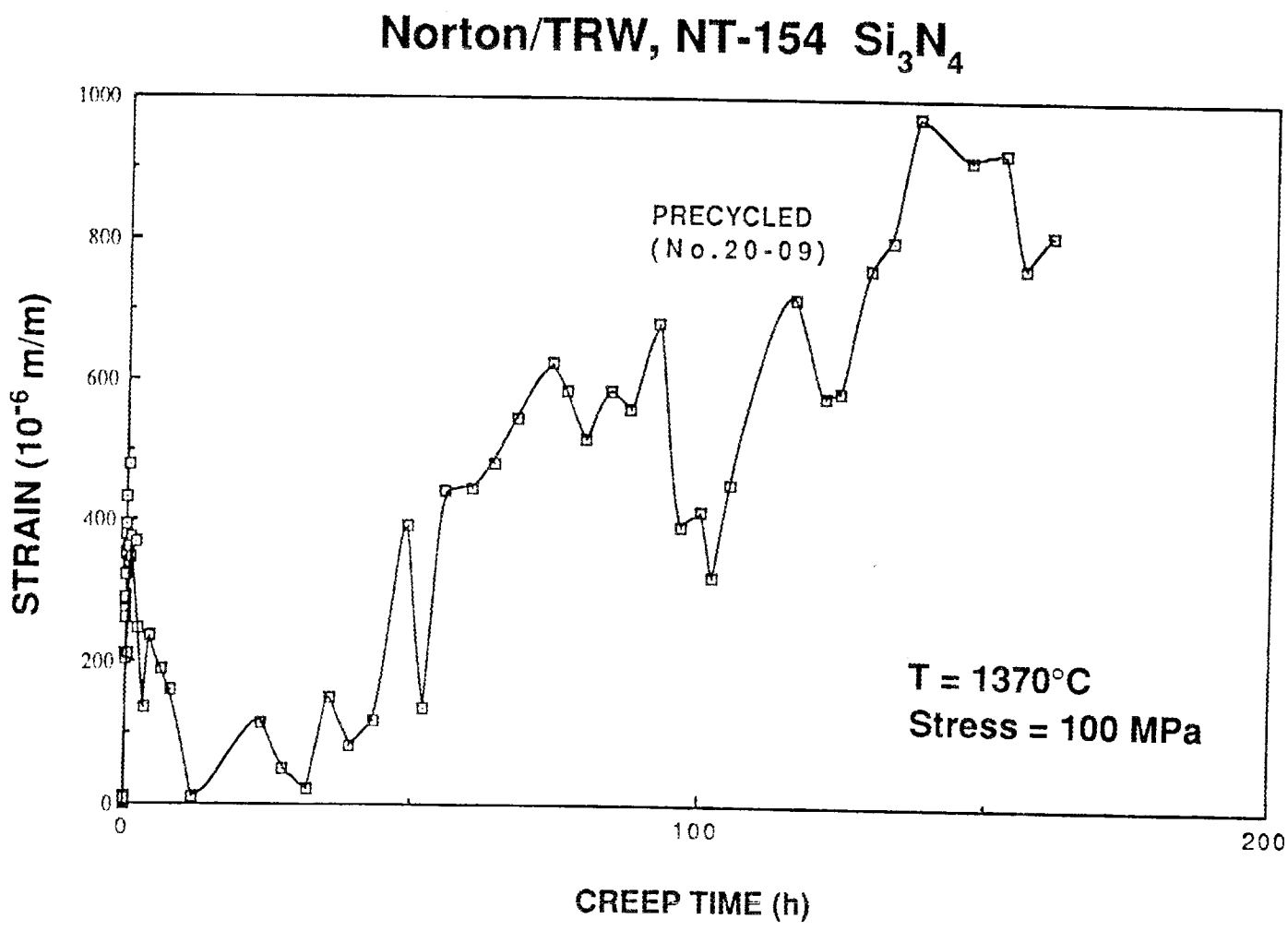

Fig. 6. Enlargement of initial creep behavior of a precycle tensile specimen (20-09) tested at 1370°C under an applied stress of 100 MPa.

ORNL-DWG 90-10622

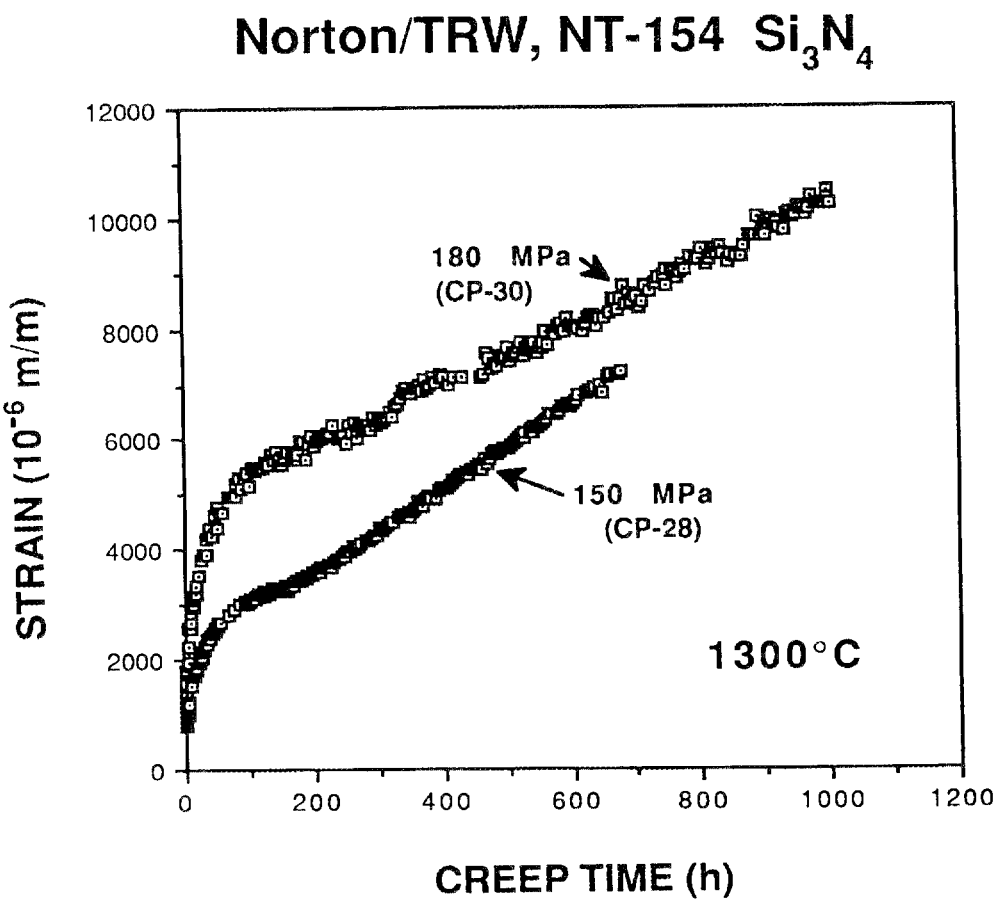

Fig. 7. Creep curves for specimens CP-28 and CP-30 tested at 1300°C under applied stresses of 150 and 180 MPa, respectively.

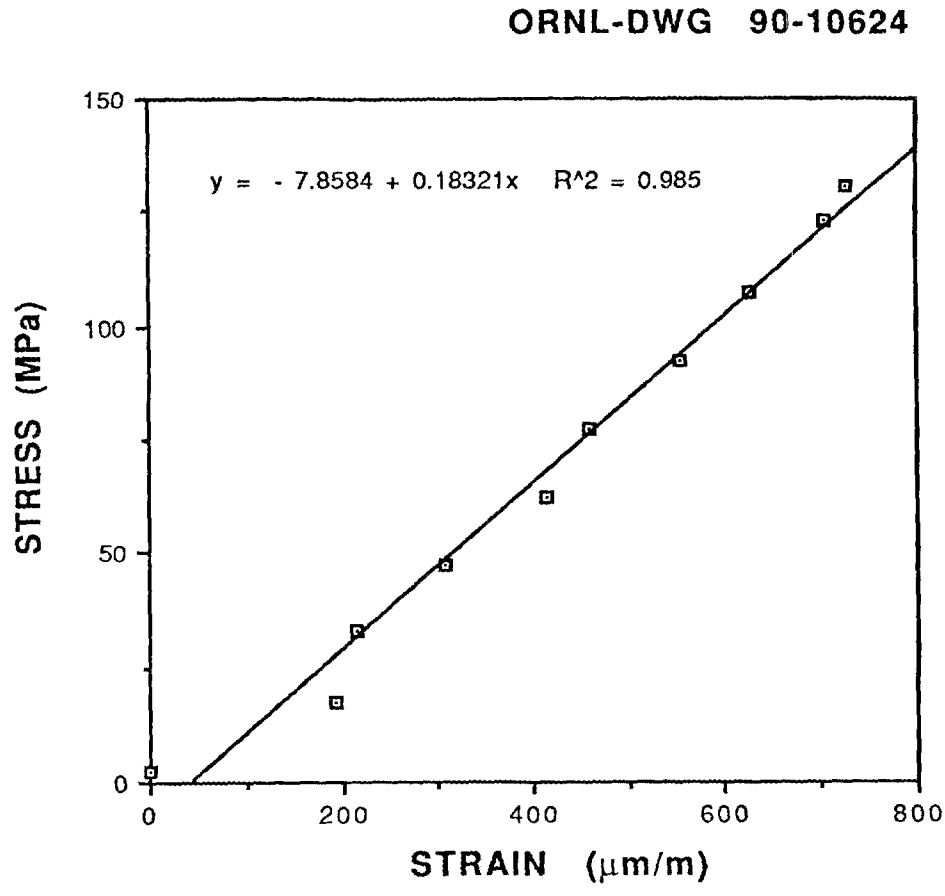

Fig. 8. A stress-strain curve of NT-154 Si_3N_4 subjected to incremental tensile loading at 1300°C.

ORNL-DWG 90-10623

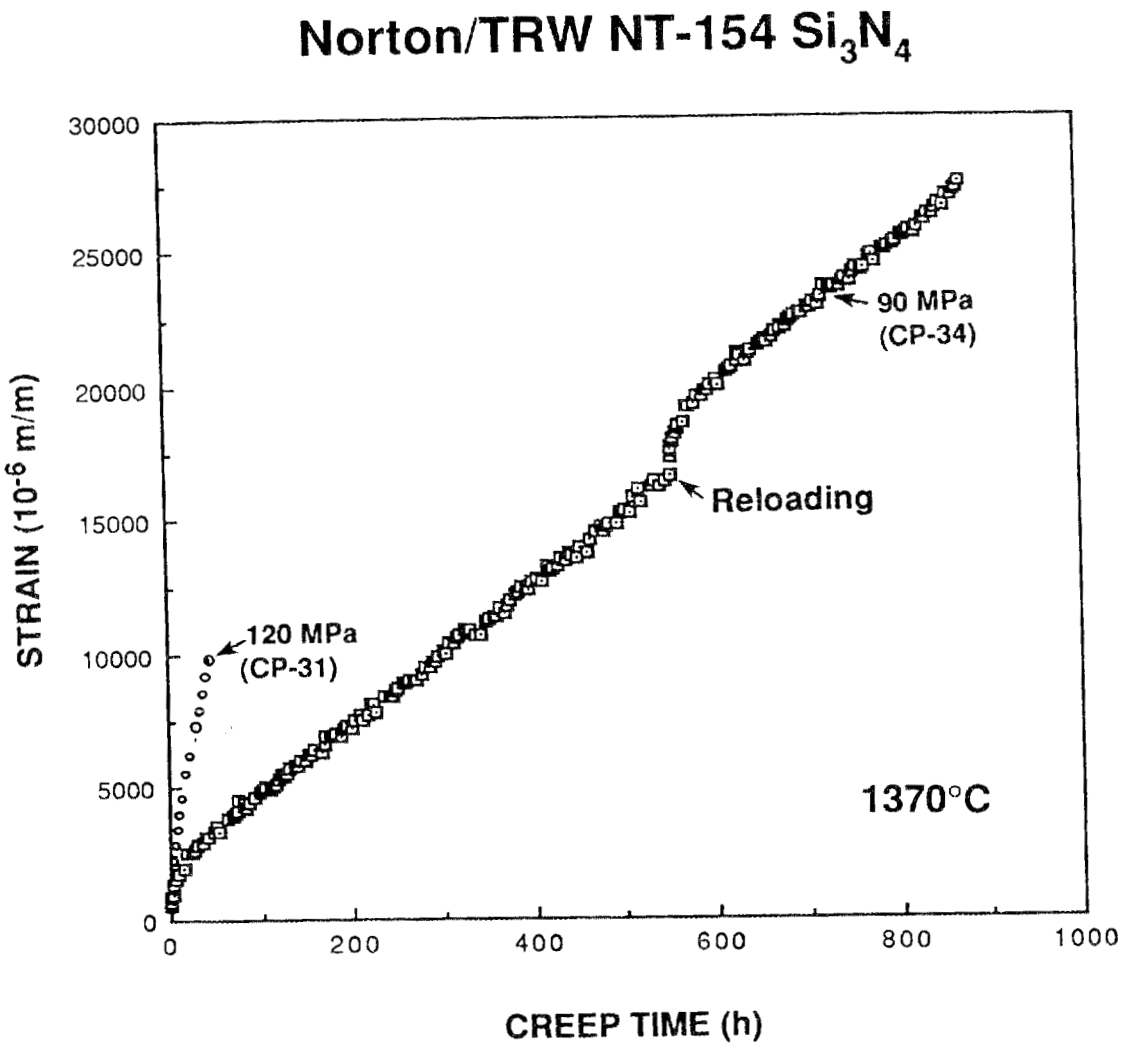

Fig. 9. Creep curves for specimens CP-31 and CP-34 tested at 1370°C under applied stresses of 120 and 90 MPa, respectively.

ORNL-DWG 90-13955

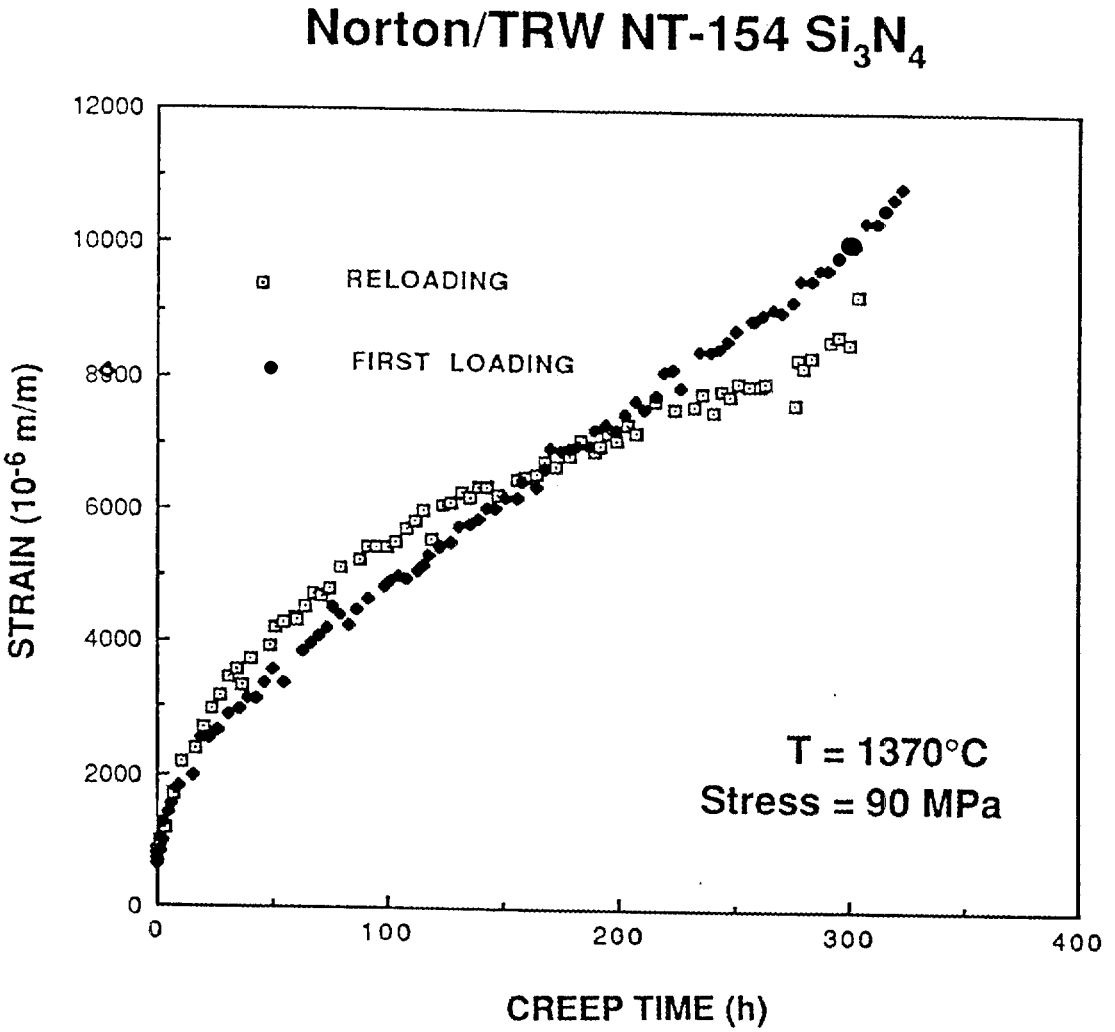

Fig. 10. Comparison of transient creep curves for initial loading and subsequent reloading under an applied stress of 90 MPa.

comparison. Both creep curves are about the same. This observation suggests that the material may have weak or no memory and behaves somewhat like a virgin material when reloaded.

Important findings and observations

1. Precycling of NT-154 Si_3N_4 at 1370°C can dramatically change the transient creep behavior. However, the high creep rate following the initial strain recovery may ultimately cancel the gain in creep resistance realized in the initial stage of creep.
2. Creep data obtained from a single interrupted creep test at high temperature suggests that recurrence of transient creep at repeated unloading and reloading may accelerate the creep process.

Status of milestones

A draft report covering results of elevated temperature tests on toughened ceramic material was completed (Milestones 321409).

Publications

K. C. Liu and C. R. Brinkman, "High Temperature Tensile and Fatigue Strengths of Si_3N_4," pp. 235-44 in *Proceedings of the 27th Automotive Technology Development Contractors Coordination Meeting*, P-230, Society of Automotive Engineers, Inc.,Warrendale, PA, April 1990.

H. Pih and K. C. Liu, "Laser Diffraction Methods For High-Temperature Strain Measurements," was submitted to *Experimental Mechanics* for review and publication.

References

1. K. C. Liu and C. R. Brinkman, "Tensile Cyclic Fatigue of Alumina at Room Temperatures," pp. 191-200 in *Proceedings of the 24th Automotive Technology Development Contractors Coordination Meeting*, Society of Automotive Engineers, Inc., Warrendale, PA, April 1989.

2. H. Pih and K. C. Liu, "Laser Diffraction Methods for High-Temperature Strain Measurements," pp. 87-93 in *Proceedings of 1989 Spring Conference of the Society for Experimental Mechanics*, Boston, MA, May 28-June 1, 1989.

Rotor Data Base Generation

M. K. Ferber and M. Jenkins (Oak Ridge National Laboratory)

Objective/scope

The goal of this task is to systematically study the tensile strength of a silicon nitride ceramic as a function of temperature and time in an air environment. Initial tests will be aimed at measuring the statistical parameters characterizing the strength distribution of three samples types (two tensile specimens and one flexure specimen). The resulting data will be used to examine the applicability of current statistical models as well as sample geometries for determining the strength distribution.

In the second phase of testing, stress rupture data will be generated by measuring fatigue life at a constant stress. The time-dependent deformation will also be monitored during testing so that the extent of high-temperature creep may be ascertained. Tested samples will be thoroughly characterized using established ceramographic, scanning, and transmission electron microscopy techniques. A major goal of this effort will be to better understand the microstructural aspects of high-temperature failure including:

(1) extent of slow crack growth;
(2) evolution of cavitation-induced damage and fracture;
(3) transition between brittle crack extension and cavitation-induced growth; and
(4) crack blunting.

The resulting stress rupture data will be used to examine the applicability of a generalized fatigue-life (slow crack growth) model. If necessary, model refinements will be implemented to account for both crack blunting and creep damage effects. Insights obtained from the characterization studies will be crucial for this modification process. Once a satisfactory model is developed, separate stress-rupture (confirmatory) experiments will be performed to examine the model's predictive capability. Consequently, the data generated in this task will not only provide a critically needed base for component utilization in automotive gas turbines, but also facilitate the development of a design methodology for high-temperature structural ceramics.

Technical progress

The evaluation of tensile collet systems was continued during this reporting period. The primary objective of this study is to gain a better understanding of the factors responsible for recent button-head failures. Particular emphasis is being placed upon evaluating the button-head strength of gageless samples fractured using both straight and tapered collets (Fig. 1). The tapered collet arrangement provided the better performance in terms of both the fracture strength and average percent bending at failure. While the use of soft copper collets in the straight-collet grips gave similar values of the button-head fracture strength, the percent bending at failure was slightly higher.

The aforementioned tests used gageless specimens so that the fracture behavior in the grip region could be directly evaluated. In order to verify the ability of the tapered collet grips to minimize button-head failures, additional strength tests of a high performance silicon nitride were initiated. Initial fast fracture tensile testing of NT-154 specimens with strain-gaged, gage sections was conducted at room temperature using the tapered collet gripping system. The tapered collets and holders were the same as those used with the alumina, straight-shank specimens in the comparison tests of the tapered and straight collet gripping systems. Additionally, other factors such as lubrication of the collet/holder

ORNL-DWG90-13956

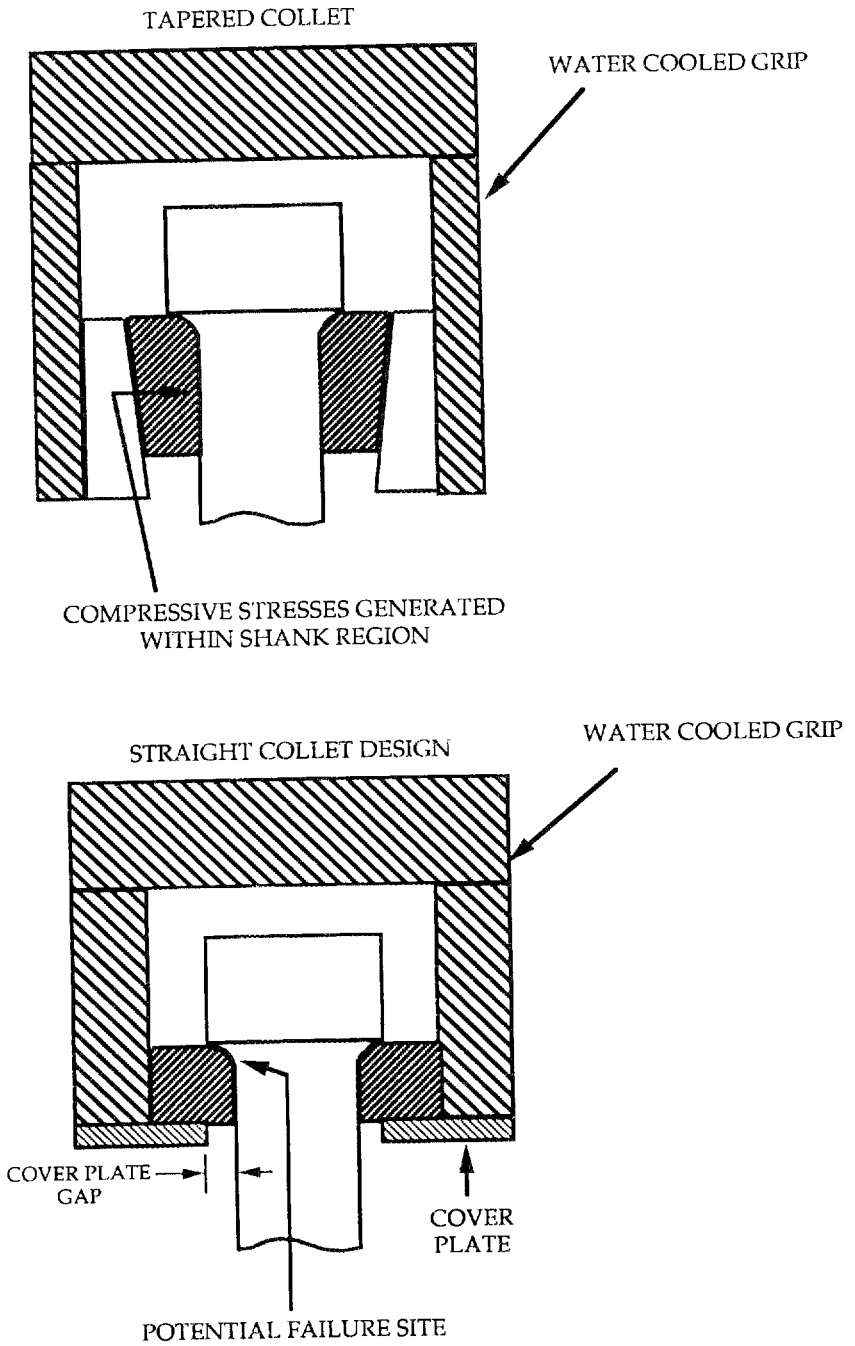

Fig. 1. Schematic illustration of two grip designs used in current tensile test equipment.

interface, stressing rate (11 MPa/s), and ambient conditions were maintained as consistently as possible with the previous tests.

During the first test, the collets were preloaded against the specimen shank by "hand-tightening" the collet holder such that the end of the specimen button-head was forced against the grip body. Thus the interaction of the taper of the collet and collet holder to applied a lateral load to the specimen shank. This preload is intended to minimize any loading into the button-head of the specimen by providing an initial normal force (and hence increased frictional load transfer) at the specimen collet interface. The first test resulted in a failure of the specimen shank which initiated at the intersection of the free surface of the shank and the collet. Failure occurred at a gage section stress of 622 MPa (19,690 N load) and 0.6% bending.

Following the unsuccessful first test, it was decided that the preloading procedure may have contributed to excessive localized loading in the specimen shank. Therefore the second test was conducted without forcing the end of the button-head against the grip body, thus allowing the "natural" movement of the tapered collet to introduce the lateral force during the longitudinal loading of the specimen. The second test resulted in a failure of the specimen shank which initiated at the intersection of the free surface of the shank and the collet. Failure occurred at a gage section stress of 765 MPa (24,250 N load) and 1.0 % bending.

Testing was suspended to investigate the cause of the two unsuccessful tests. Inspection of the failure locations indicated problems with the upper collet/holder assembly. Subsequent confirmatory tests with alumina straight-shank specimens showed failures of gripping section were still occurring in the 17,000 to 21,000 N range which had been found in the previous tests of straight-shank specimens. However, the failure locations of these confirmatory tests also indicated the following problems with the upper collet/holder assembly: (1) mismatch of the angle between the collet and holder which leads to nonuniform loading (pinching); (2) hard, superalloy collets which can cause localized surface damage to the ceramic hence initiating failure; and (3) variations in collet dimensions and/or sharp corners which can cause localized damage to the surface of the specimen. An additional concern identified is the nonoptimized angle of the taper. The present, arbitrary angle of 10° is "steeper" than the necessary, calculated angle of ~30° (for collet/specimen m = 0.6), thus causing higher than necessary lateral (normal) forces to achieve the needed frictional load transfer.

Modifications of the present, tapered collet design are under way to eliminate the three problems noted above. A procedure has been developed to fabricate, stress relieve, and "lap-in" matched sets of collets and holders to achieve a close match of the collet/holder angle. Annealed stainless steel and titanium alloy collets are being used to minimize damage to the specimen surface. Smoothing and rounding of sharp edges on the collets will be performed to minimize the possibility of localized chipping of the specimen surface.

When these modifications have been completed, a set of verification tests will be performed on straight-shank alumina specimens to confirm the efficacy of the changes in allowing failures in the gripped sections in the load range of 17,000 to 21,000 N. Upon successful completion of these verification tests, the testing of the NT-154 specimens will resume.

In addition to the empirical testing, numerical modeling efforts were also continued during this reporting period. In particular, questions concerning the acceptable level of bending stress were considered. While it is generally agreed that bending must be minimized in uniaxial tensile tests in order to minimize the scatter,[1,2] there is no general agreement as to the maximum bending allowable for any one type of tensile testing. Various reports[1,3] have been made of efforts to obtain and maintain percent bending in the range of less than 2.0. However, the American Society for Testing and Materials (ASTM)

calls for a percent bending of less than 5.0 to 10.0 for a valid tensile test depending upon the type to test being conducted.[4-7] It appears, though, that these values of percent bending are the result of attempts to maintain as low a bending as possible based on empirical observations with no formal basis for choosing the maximum allowable amount.

In this regard a limited numerical/statistical study was undertaken to evaluate the effect of bending on the determination of a material's Weibull characteristic tensile strength. This study was conducted along similar lines as Vasko and Cassenti.[8] The starting values of the Weibull statistical parameters were approximately those of the NT-154 silicon nitride at room temperature[9] (σ_o = 774 MPa, m = 7.21). In general, the Weibull distributions for the probability of failure (P_f) are:

$$P_f = 1 - \exp\left(-\int (\sigma/\sigma_o)^m \, dV/V_o\right) \tag{1}$$

for the distribution of stresses through the volume and:

$$P_f = 1 - \exp\left(-\int (\sigma/\sigma_o)^m \, dA/A_o\right) \tag{2}$$

for the distribution of stresses over the surface of the volume, where σ is the applied stress, σ_o is the Weibull characteristic tensile strength, m is the Weibull modulus, and V_o and A_o are normalizing constants for volume and surface area, respectively. The effect of the bending is assumed to make σ a linear function of position, x, which is the distance from the specimen center as shown in Fig. 2. One may write such that:

$$\sigma = \sigma_a \, (1 + bx/R) \tag{3}$$

where σ_a is the nominal applied stress, b is the bending component (percent bending divided by 100.0), and R is the radius of the gage section. The functions for the volume and surface increments are:

$$dV = dA \, dy = 2 \, (R^2 - x^2)^{1/2} \, dx \, dy \tag{4}$$

and

$$dA = dS \, dy = R \, d\Theta \, dy \tag{5}$$

where y is the longitudinal axis, A is the cross-sectional area, S is the circumferential length, and, Θ is the angle about the longitudinal axis in cylindrical coordinates (Fig. 2). R can be written in terms of Cartesian coordinates where $R = x/\sin\Theta$.

Combining Eqs. (1) through (5) yields for the distribution of stresses through the volume:

$$P_f = 1 - \exp\left(-1/V_o \int (\sigma_a \, (1 + bx/R)/\sigma_o)^m \, 2 \, (R^2 - x^2)^{1/2} \, dx \, dy\right) \tag{6}$$

for $-R \le x \le +R$ and $-l/2 \le y \le l/2$ (where l is the length of the gage section) and for the distribution of stresses along the surface:

$$P_f = 1 - \exp\left(-1/A_o \int (\sigma_a (1 + b \sin\Theta)/\sigma_o)^m \, 2 \, R \, d\Theta \, dy\right) \tag{7}$$

for $-p/2 \le \Theta \le +p/2$ and $-l/2 \le y \le l/2$. A numerical integration scheme was used to solve for Eqs. (6) and (7) for the probabilities of failure as functions of failure stress assuming constant bending in every specimen. These results were then evaluated for the effect of percent

ORNL-DWG90-13957

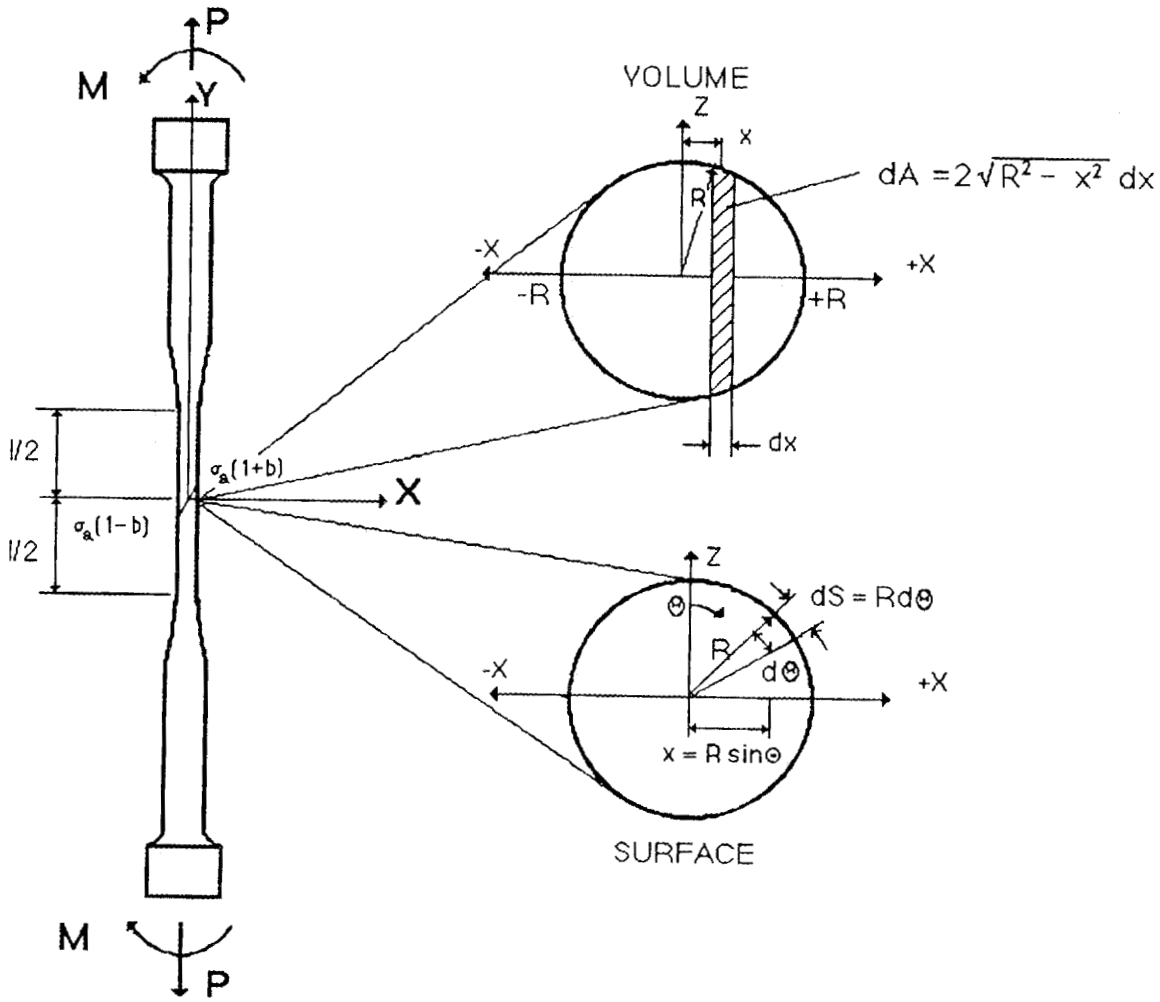

Fig. 2. Details of geometry considerations for Weibull analyses.

bending on the Weibull characteristic tensile strength (strength at $P_f = 0.632$) and the Weibull modulus.

The Weibull modulus was essentially unchanged from the starting values of 8.0 and 16.0 regardless of percent bending. However, the Weibull characteristic tensile strength, normalized to value associated with b = 0, showed large decreases for increasing percent bending (Fig. 3). Note that the decreasing strength effect was more pronounced for surface failures. However, it has been recently reported[10] that volume failures accounted for the majority (66%) of the tensile test failures in a high-performance silicon nitride at room temperature. Additionally, in that study, no correlation was found between percent bending and either calculated tensile strength or failure origin (i.e., volume or surface). In the same study, similar statistically based analyses were conducted and it was concluded that 5.0 was an acceptable maximum percent bending for tensile strength tests.

The present study concurs with the acceptance of 5.0% bending as a maximum upper limit for tensile strength tests However, the issue is more clouded for tensile stress rupture or creep tests where the effects of temperature, stress state, and creep rate may severely affect not only the material behavior but also the experimentally measured displacements or times-to-failure. Thus, at this time no upper limit for percent bending for tensile creep or stress rupture can be recommended.

The creep/fatigue studies involving a high performance silicon nitride were also initiated.* In particular, the creep strain associated with both button-head tensile samples and four-point flexure samples was measured as a function of time and stress at 1370°C. In the case of the button-head tensile samples, a direct-contact capacitance extensometer was used to monitor the displacement during constant load tests. The deflection of the specimen midspan in the flexure samples was measured with respect to the inner load points using a three-probe LVDT extensometer. Additional details of the experimental procedure are given elsewhere.[11]

The stress dependence of the steady-state creep rate is shown in Fig. 4. The high creep exponent is consistent with a diffusion-assisted cavitation process. The presence of these cavities was confirmed by SEM studies. In order to examine the fatigue behavior, all creep tests were continued until the samples failed. The resulting fatigue curve is shown in Fig. 5. The fatigue resistance determined from the button-head tests (as characterized by the fatigue exponent, n) decreased as the test time increased. At long times, n was comparable to the creep exponent. Examinations of the fracture surfaces of the corresponding test samples indicated that failure was characterized by the accumulation of creep damage. These results are consistent with a creep-constrained cavitation process in which the growth and coalescence of cavities is controlled by the creep rate of the bulk material.[12]

Status of milestones

None.

Publications

M.G. Jenkins, M.K. Ferber , and J.A. Salem, "Determination of the Stress Distributions in a Ceramic, Tensile Specimen Using Numerical Techniques," to be published in the Proceedings of the 1990 ASME International Computers in Engineering Conference and Exposition.

---

*Norton NT-154 silicon nitride.

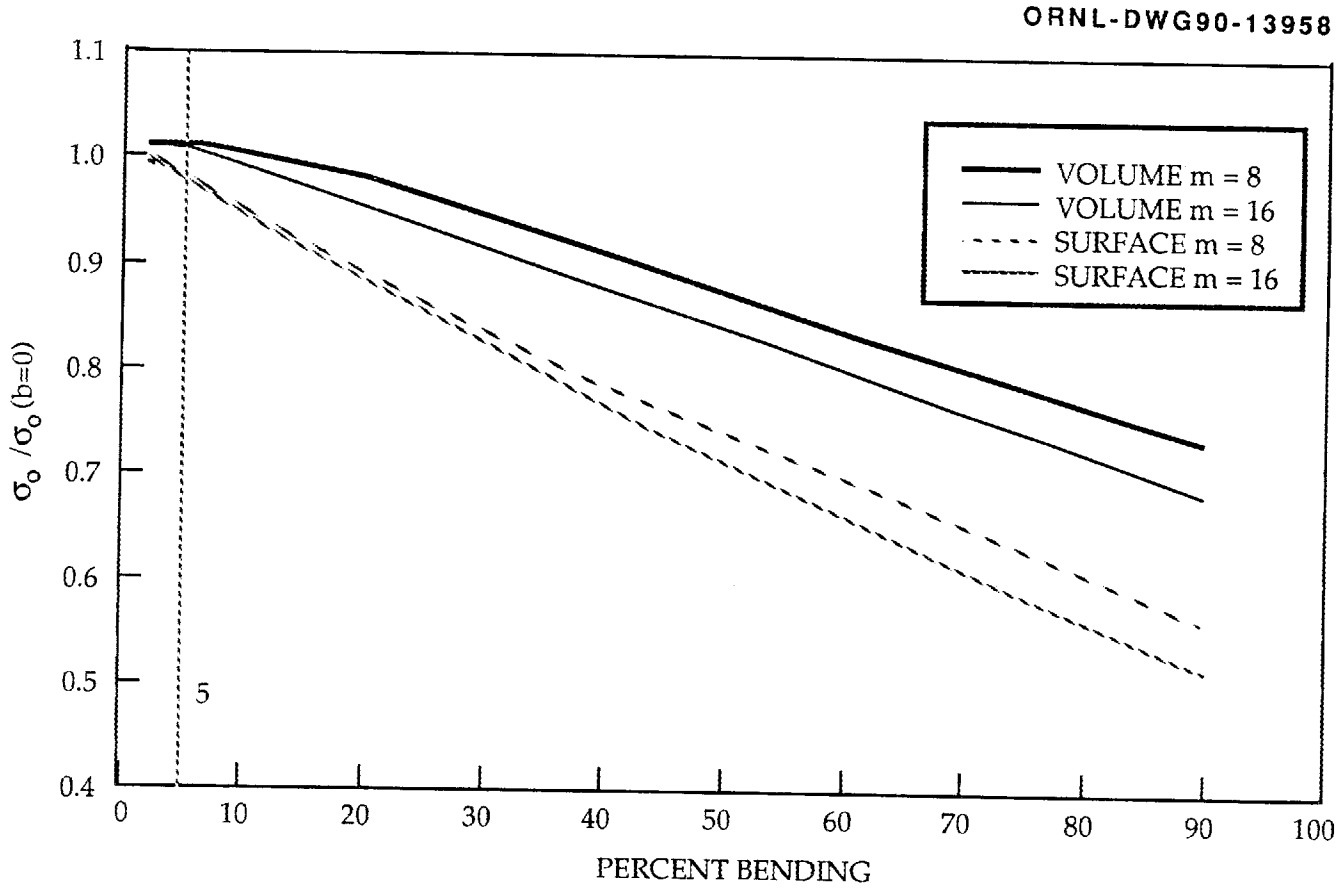

Fig. 3. Normalized Weibull characteristic tensile strength versus percent bending.

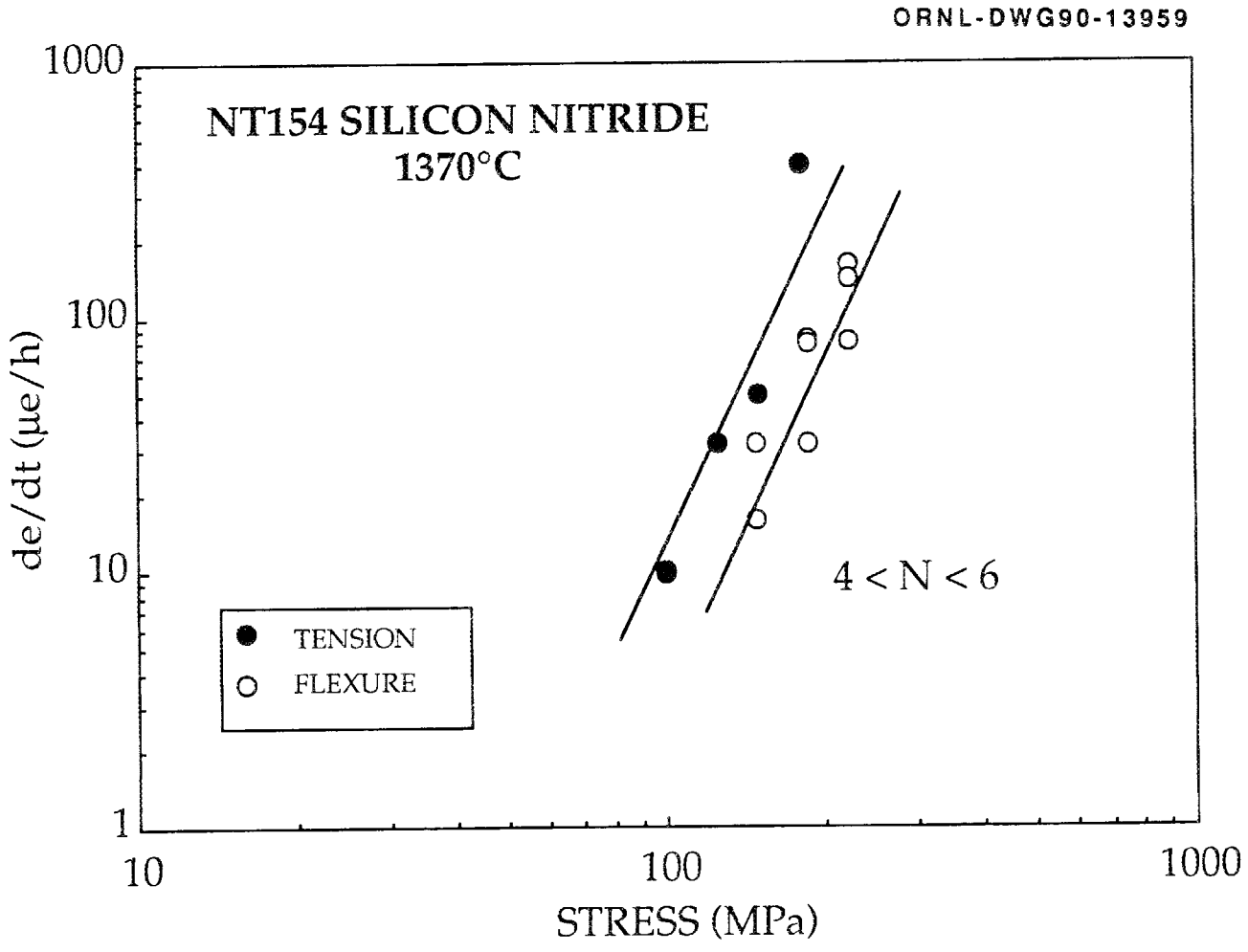

Fig. 4. Stress dependence of steady-state creep rate of silicon nitride at 1370°C.

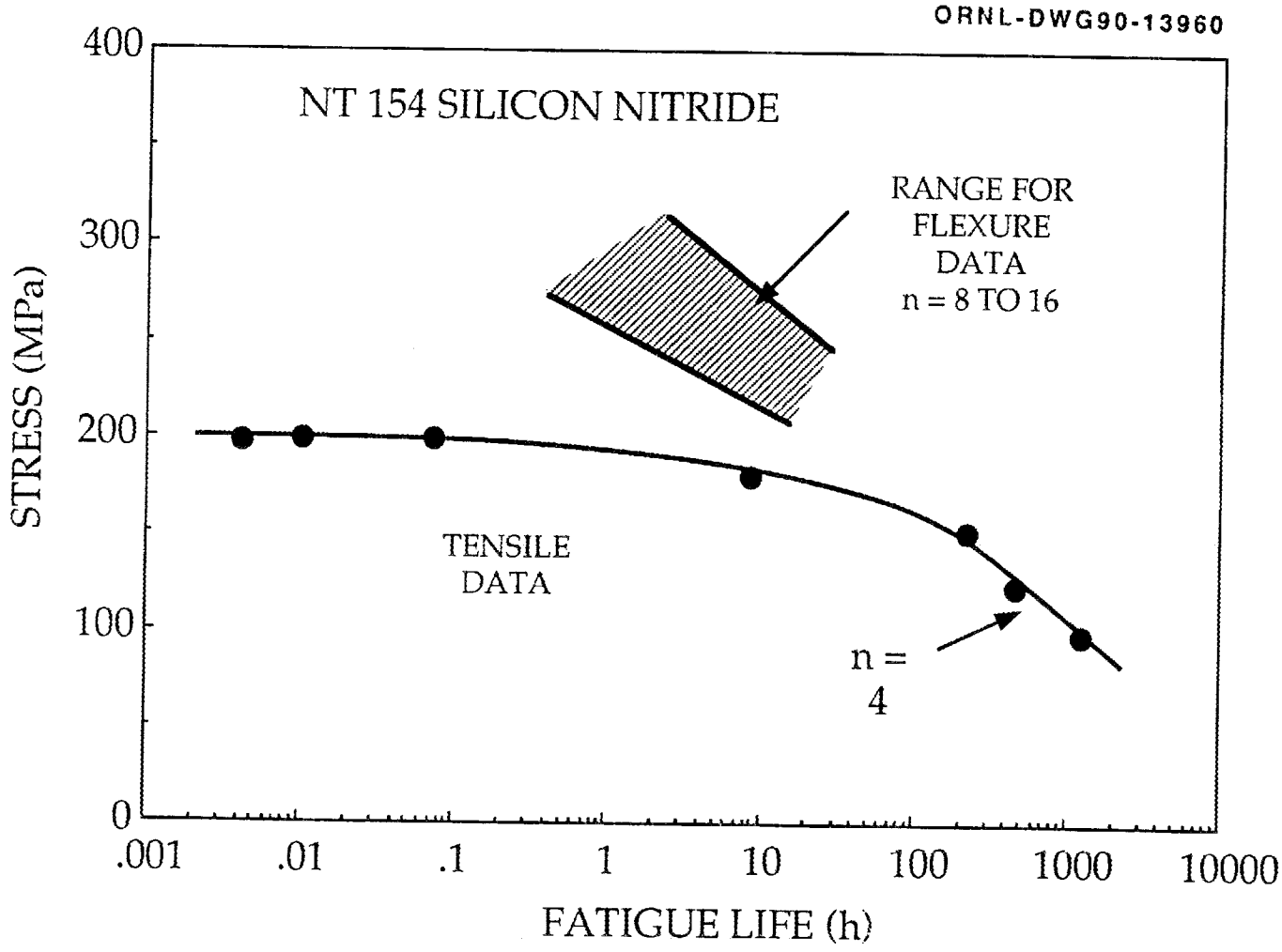

Fig. 5. Fatigue behavior of silicon nitride at 1370°C.

References

1. M. H. Jones and W. F. Brown Jr., "An Axial Loading Creep Machine," *ASTM Bull.* **211**, 53-60 (1956).

2. B. W. Christ and S. R. Swanson, "Alignment Problems in the Tensile Test," *J. Test. Eval.* **4**(6), 405-417 (1979).

3. D. Carruthers, J. Cuccio, "Button-head Failures Necessitate Tensile Specimen Redesign," presented at Biannual Advanced Turbine Technology Applications Project Meeting, Garrett Auxiliary Power Division, Phoenix, Arizona, March 29, 1989.

4. American Society for Testing and Materials, "Standard Practice for Conducting Creep, Creep-Rupture, and Stress-Rupture Tests of Metallic Materials," E139-83, *1989 Annual Book of ASTM Standards*, Vol. 03.01, p. 313.

5. American Society for Testing and Materials, "Standard Practice for Conducting Time-for-Rupture Notch Tension Tests of Materials," E292-83, *1989 Annual Book of ASTM Standards*, Vol. 03.01, pp. 418-426.

6. American Society for Testing and Materials, "Standard Practice for Conducting Constant-Amplitude Axial Fatigue Tests of Metallic Materials," E466-82, *1989 Annual Book of ASTM Standards*, Vol. 03.01, pp. 539-543.

7. American Society for Testing and Materials, "Standard Practice for Conducting Constant-Amplitude Low-Cycle Fatigue Testing," E606-80, *1989 Annual Book of ASTM Standards*, Vol. 03.01, pp. 601-613.

8. T. J. Vasko and B.N. Cassenti, "The Statistical Prediction of Failure Location in Brittle Test Specimens," United Technologies Research Center, United Technologies Corporation, East Hartford, Connecticut (1986).

9. N.L. Hecht, "Environmental Effects in Toughened Ceramics," W.B.S. Element 3.3.1.4, University of Dayton Research Institute, Ceramic Technology for Advanced Heat Engines Project, Oak Ridge National Laboratory, Oak Ridge, Tennessee (1989).

10. M. Kaji et al., "Evaluation of Techniques of Mechanical Properties," presentation given at Kyocera Central Research Laboratory, Kokubu, Japan, July 19, 1989.

11. M. K. Ferber, M. G. Jenkins, and V. J. Tennery, "Comparison of Tension, Compression, and Flexure Creep for Alumina and Silicon Nitride Ceramics," to be published in Proceedings of the 14th Annual Conference on Composites and Advanced Ceramic Materials.

12. Hermann Riedel, pp. 172-197 in *Fracture at High Temperatures*, Springer-Verlag, Berlin, Heidelburg, 1987.

TOUGHENED CERAMICS LIFE PREDICTION

J. A. Salem and S. R. Choi (NASA Lewis Research Center)

Objective/scope

The purpose of this research is to understand the room temperature and high temperature [1370°C (2500°F)] behavior of toughened ceramics, in particular SiC-whisker toughened Si_3N_4, as the basis for developing a life prediction methodology. A major objective is to understand the relationship between microstructure and the mechanical behavior within the bounds of a limited number of materials. A second major objective is to determine the behavior as a function of time and temperature. Specifically, the room temperature and elevated temperature strength and reliability, the fracture toughness, slow crack growth and the creep behavior will be determined for the as-manufactured material. The same properties will also be evaluated after long-time exposure to various high temperature isothermal and cyclic environments. These results will provide input for parallel materials development and design methodology programs. Resultant design codes will be verified.

Technical progress

The mechanical and thermal properties of an in situ toughened silicon nitride material* used to make a gas turbine combustor were experimentally measured. The location and nature of failure origins resulting from bend tests were determined with fractographic analysis. The measured Weibull parameters were used along with thermal and stress analysis to determine failure probabilities of the combustor with the CARES design code. The effects of data censoring and fracture criterion were considered in the analysis.

Test Procedures

The properties required for thermal stress analysis included Young's modulus, Poisson's ratio, thermal conductivity, thermal expansion coefficient and specific heat. The CARES analysis requires strength data (from which the Weibull parameters are calculated) and Poisson's ratio. Fracture toughness was also measured. Although this parameter is not required for the fast fracture prediction made by CARES, it is used in life-time prediction and is related to the properties used in the reliability analysis. Strength measurements, which are the basis of reliability predictions, are controlled by both the size of flaws inherent in ceramic materials and the fracture toughness. Toughness represents the ability of a material to tolerate flaws.

Young's modulus and Poisson's ratio between room temperature (RT) and 1400°C were determined by a resonance method in accordance with ASTM

---

*Kyocera SN251

C848- 76[4]. Young's modulus was also determined at room temperature by strain gaging a four-point bend specimen. Thermal expansion was measured as a function of temperature with a differential transformer. Thermal conductivity and specific heat were determined as a function of temperature via the laser flash method[5].

Test specimens for strength and fracture toughness measurements were machined from the combustor liner and heat treated in air at 1150°C for 1.5 hours to eliminate spurious residual stresses due to machining. The flexure strength was determined in four-point bending at temperatures of 25, 1000 and 1371°C. The specimens measured 3mm x 4mm in height and width and the inner and outer spans were 10mm and 30mm, respectively. Flaw type and location (connected to the surface or completely within the volume) were determined with optical microscopy or scanning electron microscopy as necessary.

Fracture toughness was determined with the single-edge-precracked-beam (SEPB)[6] and chevron-notch[6,7] methods in three-point bending. Specimens were 3x4x30mm in thickness, height and span. The SEPB specimens were tested at a stroke rate of 0.5mm/min. Chevron-notch specimens were tested at 0.005mm/min. The low stroke rate used for chevron-notch testing was required to insure stable crack extension.

Mechanical and Thermal Properties

Young's modulus, Poisson's ratio, thermal expansion, thermal conductivity and specific heat are illustrated in Figures 1, 2 and 3 as functions of temperature. Young's modulus exhibited a continuous drop with temperature. The room temperature, mechanically and sonically determined values were within 3%. Poisson's ratio was almost constant. The thermal expansion increased in a linear manner with temperature. The coefficient of thermal expansion was determined to be 3.1×10^{-6} /°C. The thermal conductivity exhibited a gradual drop with increasing temperature, while the specific heat increased gradually with temperature.

A summary of bend strength test results is given in Table 1. Both the characteristic strength (σ_θ) and Weibull modulus (m) decreased with temperature. Failure originated from either a large, 30 to 100 micrometer grain with a hexagonal cross-section, or a 15 to 70 micrometer diameter pore. Examples of failure origins are shown in Figures 4A and 4B.

The population of volume type failures observed at 25°C and 1000°C was insufficient for statistical characterization. However, nearly 50% of the specimens failed from volume flaws at 1371°C. This change from surface to volume failure indicated healing of surface connected flaws. Six specimens out of 31 tested at 25°C and three specimens out of 27 tested at 1000°C failed from processing flaws connected to the beveled edges of the specimens. These failures were analyzed as surface failures. The complete analysis of statistical parameters is discussed in the Statistical Parameters section.

Fracture toughness results are summarized in Table 2. The chevron-notch specimens exhibited nonlinear load-displacement behavior, indicating stable crack extension. Fracture toughness, calculated from maximum load and minimum stress intensity coefficient, decreased with temperature up to

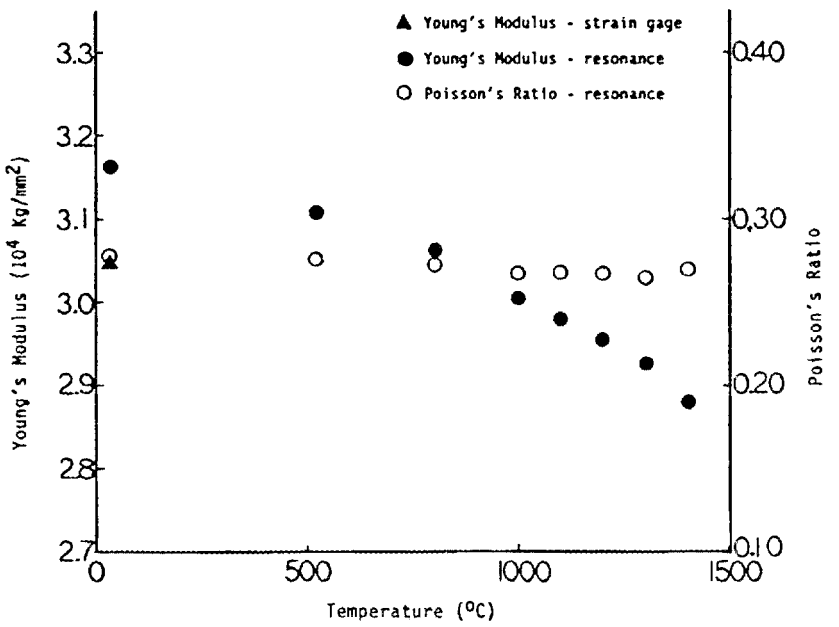

Figure 1. Young's modulus and Poisson's ratio of SN251 as a function of temperature.

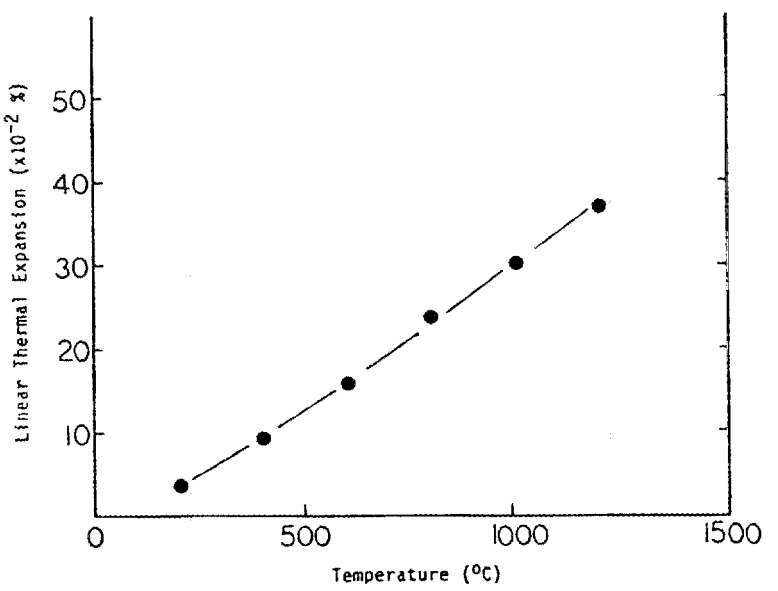

Figure 2. The linear thermal expansion of SN251 as a function of temperature.

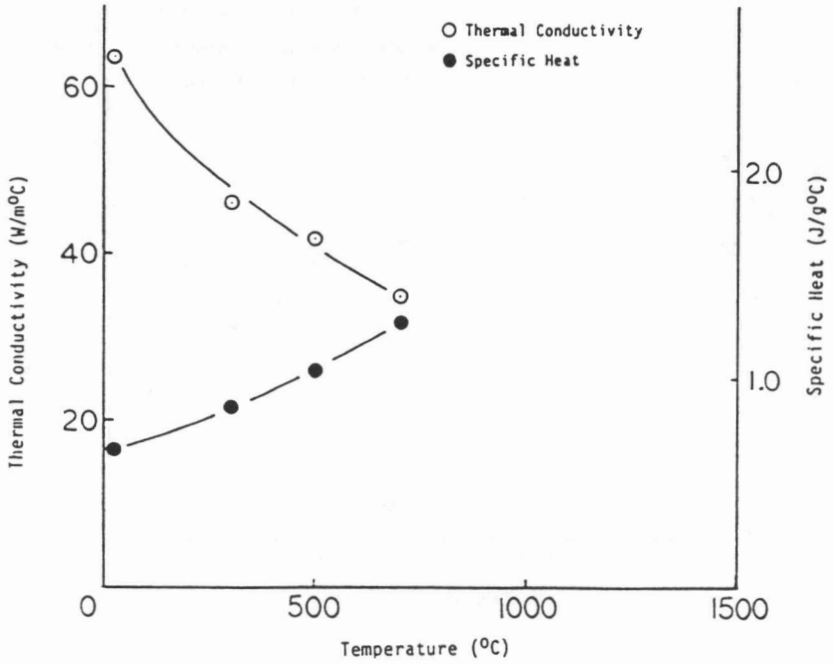

Figure 3. Thermal conductivity and specific heat of SN251 as a function of temperature.

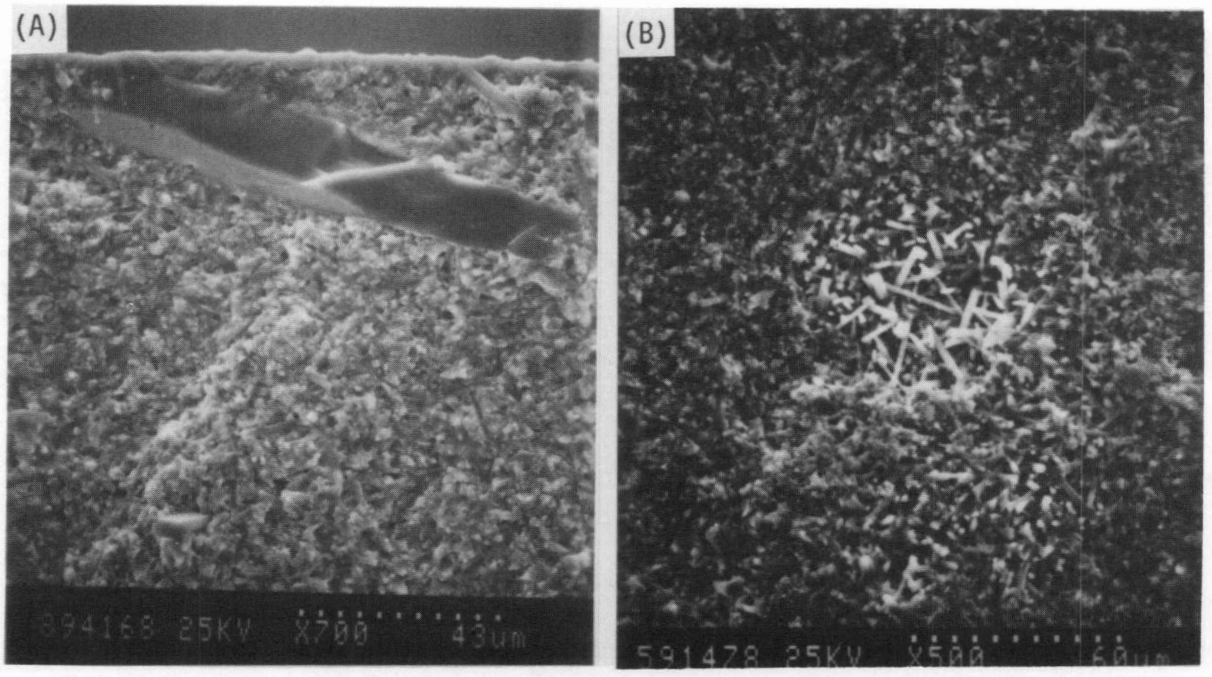

Figure 4. Failure origins: (A) large grain, and (B) volume pore.

Table 1. Bend Strength Test Results

Temp. °C	Flaw* Location	# of Specimens	Least Squares Fit σ_θ MPa	Least Squares Fit Weibull Modulus	Maximum Likelihood σ_θ MPa	Maximum Likelihood Weibull Modulus
	S	26	694	18.36	695	18.65
25	V	3	753	21.44	749	32.44
	U	2				
	S	26	592	13.78	592	13.33
1000	V	1	624+	17.00+	624+	23.80+
	U	0				
	S	29	566	10.12	575	8.86
1371	V	21	585	13.95	585	15.31
	U	0				

* S=surface flaw; V=volume flaw; U=unknown origin
\+ Interpolated values (see Statistical Parameters section)

Table 2. Fracture Toughness Data

Test Method	Temperature °C	Number of Tests	K_{IC} MPa*m$^{.5}$
Chevron Notch	25	5	7.9
	800	5	7.1
	1000	3	6.9
	1200	4	6.0
	1371	2	10.4
SEPB	25	7	7.4
	1371	4	6.1

1200°C. However, at 1371°C the load-displacement diagrams became severely nonlinear and the toughness appeared to increase substantially. Evidently, the combination of slow stroke rate and high temperature resulted in creep deformation instead of stable fracture.

Room temperature fracture toughness measured with the SEPB was comparable to that of the chevron-notch. However, measurements at 1371°C were much lower and comparable to values measured with the chevron-notch at 1200°C. The SEPB produced fast fracture at 1371°C, while the chevron-notch allowed creep deformation instead of stable fracture.

FEM Stress Analysis

Before performing the reliability evaluation with CARES, the stresses in the combustor were analyzed. Both mechanical and thermal stresses were generated in the combustor. Empirically, the critical stress of the combustor was expected to occur around the dilution port due to cooling. When an engine is shut-down, fuel is cut off and the combustor cools rapidly because of the injection of fresh air. The resulting thermal shock phenomenon produces high, transient tensile stresses on the surface. The FEM analysis was designed to simulate the worst transient thermal stress in an emergency stop.

Figure 5 shows the finite element model of the combustor. Exploiting symmetry, only 1/16 of the combustor was discretized. Table 3 shows gas temperatures and heat transfer coefficients for both steady state and transient conditions. Gas temperature during running was set at 913°C for the outside of the combustor and at 1350°C for the inside and the primary hole. The heat transfer coefficient was assumed to be the same for the steady state and transient conditions.

The highest stress at steady state was about 60 MPa located on the edge of the primary hole. The stress level was relatively low because there was less than a 70°C temperature difference in the combustor.

During the transient stage, the maximum principal stress of this part changed with time as shown in Figure 6, and reached a peak value of 163 MPa after 30 seconds. Figures 7 and 8 show the distribution of temperature and the maximum principal stress, respectively, at 30 seconds. There was almost a 200°C temperature difference between the primary hole and the bottom of the combustor. This large temperature difference resulted in the high tensile stress at the edge of the primary hole.

These results indicated relatively low stresses at steady state and higher stresses after combustor shut down. Thus, the reliability analysis concentrated on the tensile stress state at 30 seconds after shut down.

Reliability Analysis

(A) Statistical Parameters

The CARES code can estimate Weibull parameters by either maximum likelihood (ML) or least squares (LS). Since insufficient volume flaw data existed at RT and 1000°C, parameters obtained at these temperatures were neither reasonable nor consistent with each other. The volume flaw

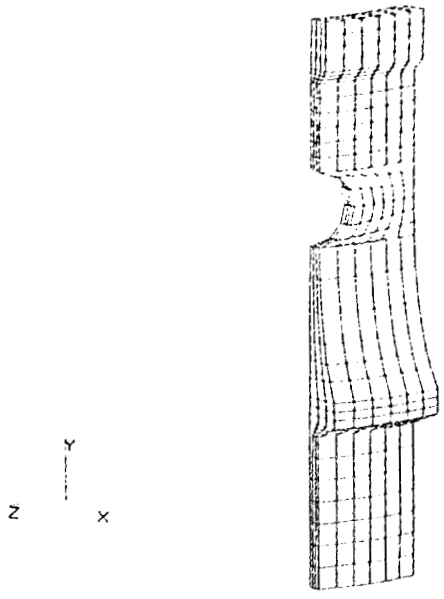

Figure 5. Finite element mesh of a 1/16 section of the combustor.

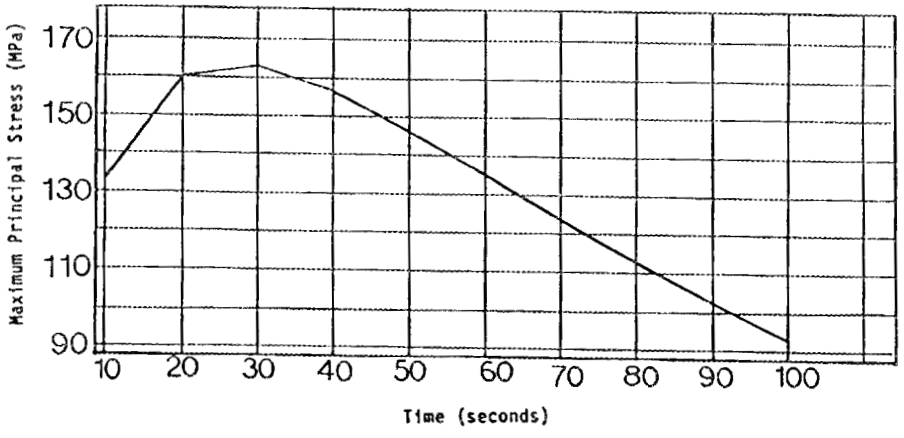

Figure 6. Maximum principal stress in the combustor as a function of time.

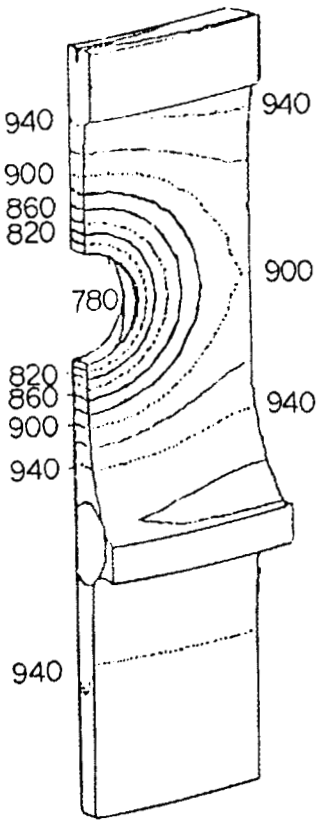

Figure 7. Temperature distribution (^{0}C) at the peak value of the maximum principal stress.

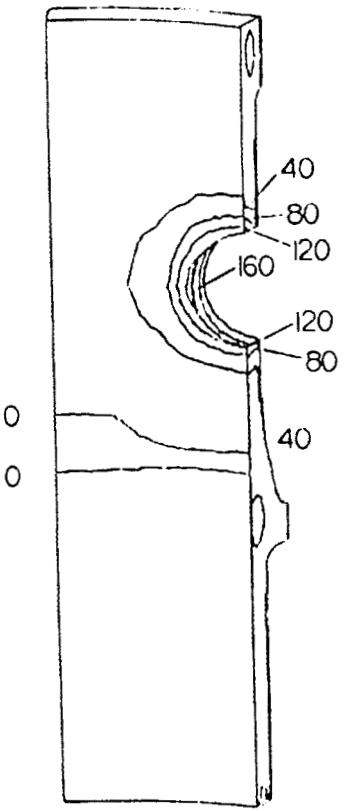

Figure 8. Maximum principal stress distribution (MPa) occurring 30 seconds after engine shut-down.

Weibull modulus was especially questionable, however, the characteristic strength appeared more consistent with surface flaw values.

The rationale to be used in the selection of material parameters for reliability calculations is not straight forward. Goodness-of-fit tests provide some indication of whether the ML or LS parameters are better suited for the data at hand. In this case, the lack of volume flaw data at RT and 1000°C caused both of these parameters to be questionable, resulting in undependable goodness-of-fit tests. The rationale used in choosing material parameters for the reliability calculations was to provide conservative values of failure probabilities. In the low failure probability regime, a lower value of the Weibull modulus results in higher failure probabilities. Failure probabilities are not strongly dependent on the characteristic strength, whereas the Weibull modulus has a much more significant effect.

Due to the lack of data, the volume-flaw characteristic strength and Weibull modulus at 1000°C were obtained by graphical interpolations of the corresponding values at RT and 1371°C as shown in Figure 9. Values obtained at 1000°C are listed in Table 1. In accordance with the aforementioned arguments, LS parameters were chosen for the analyses.

For comparison, the data was also analyzed without censoring, i.e. fracture origins were not considered. Obtained parameters are listed in Table 4.

(B) Reliability Results

Several fracture criteria were used in calculating the failure probabilities. These results are listed in Table 5. Very small failure probabilities were obtained for all criteria. The maximum failure probability was 2.463×10^{-9} for Shetty's semi-empirical case with $\overline{C}=0.82$.

Parameters obtained from the uncensored data were also used to calculate the reliability of the component. Weibull parameters are often presented without regard to the fracture origins. These parameters may be more convenient and have a larger sample size, however, differences can arise with such simplifying assumptions. For uncensored data, the estimated failure probabilities for Shetty's semi-empirical case were 1.106×10^{-13} and 2.315×10^{-12} for volume and surface analyses, respectively (see Table 6), using LS parameters. Comparing these values with the corresponding ones in Table 5, it is evident that there are large differences in the failure probabilities for censored and uncensored data. These differences emphasize the importance of separating the strength data into surface and volume flaw origins for obtaining better reliability estimates.

Additional calculations of the worst case situation were made by selecting the 90% lower confidence limits of the Weibull moduli and characteristic strengths obtained by ML. The 90% limits are not available from the CARES program for sample sizes smaller than five. For these cases the 90% lower bound was estimated using the same factors that would have been used for a sample size of five. The failure probability increased to 5.302×10^{-6} for this extreme condition, as shown in Table 6.

Table 3. Gas Temperature and Heat Transfer Coefficients

		Inside	Outside	Primary Hole
Heat Transfer Coefficient (W/m^2K)		85.5	113.3	103.2
Gas Temp. (^oC)	Steady State	1350	913	1350
	Transient State	300	300	300

Table 4. Uncensored Weibull Parameters by the Least Squares Method

Temperature (^oC)	σ_θ (MPa)	Weibull Modulus
25	691	18.92
1000	590	14.05
1371	545	11.23

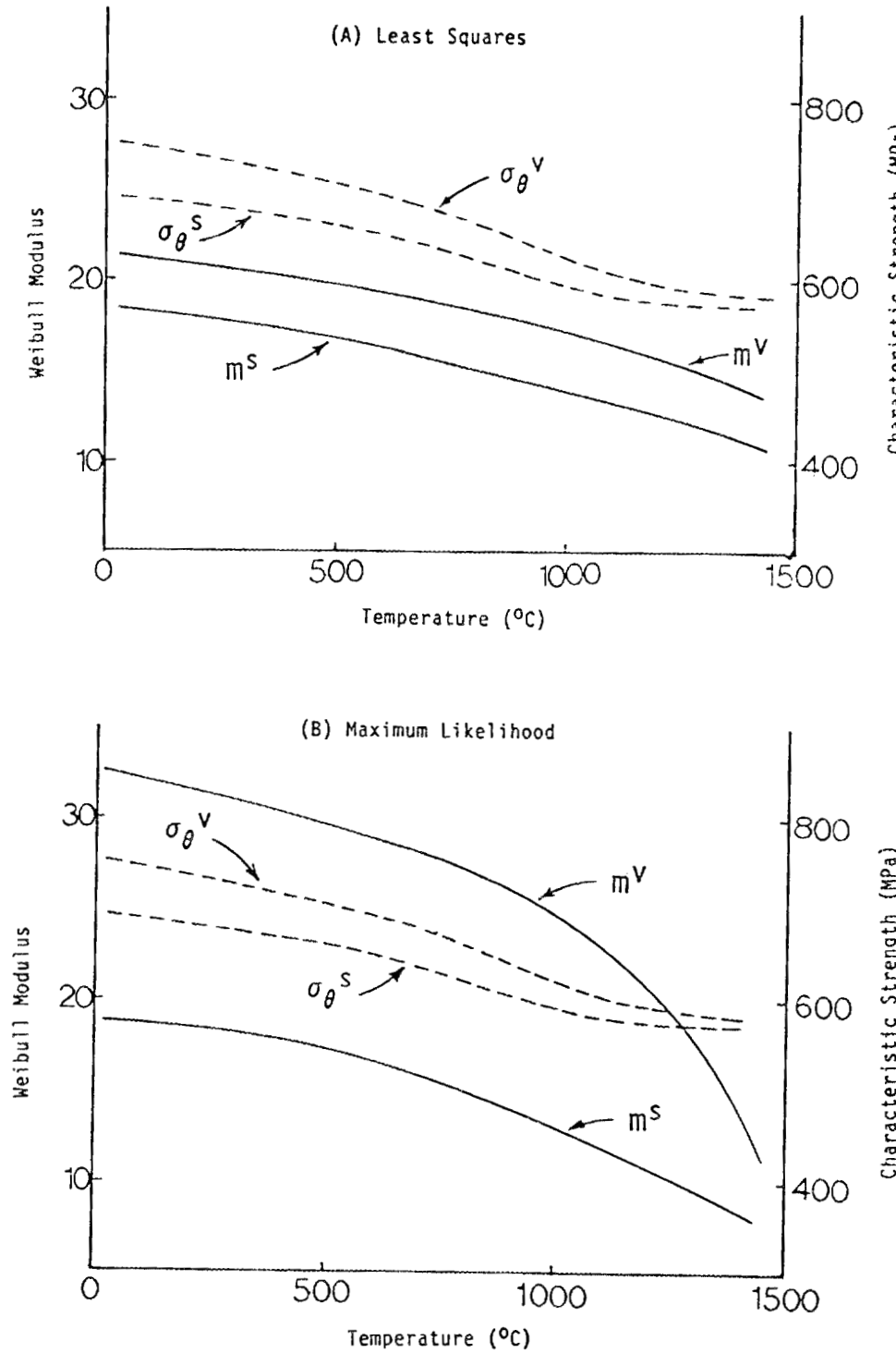

Figure 9. Weibull modulus and characteristic strength: (A) least squares fitting, and (B) maximum likelihood method.

Table 5. Failure Probability of the Combustor Predicted Using the CARES Code

Criteria	Volume	Surface	Total
Shetty's Semi-Empirical Penny Shape (Semi-Circular) Mode I Fracture	1.823×10^{-11}	2.445×10^{-9}	2.463×10^{-9}
Shetty's Semi-Empirical Penny Shape (Semi-Circular) Shear Sensitive	3.874×10^{-13}	7.719×10^{-10}	7.723×10^{-10}
Strain Energy Release Rate Penny Shape (Semi-Circular) Mode I Fracture	1.146×10^{-12}	9.929×10^{-10}	9.940×10^{-10}
Strain Energy Release Rate Penny Shape (Semi-Circular) Shear Sensitive	4.217×10^{-13}	7.050×10^{-10}	7.055×10^{-10}
Normal Stress Fracture	5.223×10^{-13}	7.001×10^{-10}	7.006×10^{-10}
Maximum Tensile Penny Shape (semi-circular)	9.954×10^{-13}	7.001×10^{-10}	7.011×10^{-10}
PIA Model	5.246×10^{-13}	6.957×10^{-10}	6.962×10^{-10}

Table 6. Failure Probabilities Predicted Using the CARES Code

Criteria : Shetty's Semi-Empirical Mode I Fracture Criterion
Penny Shape (Semi-Circular)

Condition	Volume	Surface	Total
Uncensored	1.106×10^{-13}	2.315×10^{-12}	2.426×10^{-12}
Extreme Weibull Modulus	2.888×10^{-12}	5.302×10^{-6}	5.302×10^{-6}

All of the above calculations resulted in very small failure probabilities of the combustor, even for the worst case calculation.

Conclusions

Calculations of statistical parameters and failure probabilities for a SN251 combustor were performed with the CARES computer code. The failure probabilities under extreme operating conditions were presented assuming a worst case scenario. From these calculations it was concluded that this combustor can be safely operated for the short-term under the assumed conditions. It should be emphasized that a quantitative estimate of the failure probability gives good guidance for designing ceramic components.

The importance of statistical analysis, and censoring of volume and surface flaws were demonstrated. Simple bend tests did not provide sufficient volume fracture data for this analysis. To obtain more volume fracture data, tensile testing may be required.

References

1. W. Weibull, "A Statistical Theory of the Strength of Materials," Ingeniors Vetenskaps Akademien Handlinger, No. 151, 1939.

2. J. P. Gyekenyesi, "SCARE: A Postprocessor Program to MSC/NASTRAN for Reliability Analysis of Structural Ceramic Components," *J. Eng. Gas Turbine Power* 108(3) 540 6 (1986).

3. N. Nemeth, J. Manderscheid, J. Gyekenyesi, "CARES Users and Programers Manual," NASA Technical Paper TP2916, 1990.

4. "Young's Modulus, Shear Modulus, and Poisson's Ratio for Ceramic Whitewares by Resonance," ASTM Standard Test Method C848-78. *Annual Book of ASTM Standards*, Section 15.02. Am. Soc. Testing Matls., Philadelphia, PA, 1984.

5. T. Hirai, S. Hayashi and K. Niihara, "Thermal Diffusivity, Specific Heat and Thermal Conductivity of Chemical Vapor Deposited Si_3N_4," *Ceram. Bull.* 57(12) 1126 30 (1978).

6. T. Nose and T. Fujii, "Evaluation of Fracture Toughness for Ceramic Materials by a Single-Edge-Precracked-Beam Method," *J. Am. Ceram. Soc.* 71(5) 328 33 (1988).

7. D. Munz, R. T. Bubsey and J. L. Shannon, Jr., "Fracture Toughness Determination of Al_2O_3 Using Four-Point-Bend Specimens with Straight Through and Chevron-Notches," *J. Am. Ceram. Soc.* 63(5-6) 300 5 (1980).

Status of Milestones

Milestones on time.

Communications/Visits/Travel

Attended ACS annual meeting and ASTM meeting on fracture testing of high performance ceramics.

Problems Encountered

None.

Publications

J. A. Salem "Strength and Toughness of Monolithic and Composite Silicon Nitrides," NASA Technical Memorandum 102423, NASA Lewis Research Center, Cleveland, Oh., 1990.

Life Prediction Methodology - D. L. Vaccari & P. K. Khandelwal
(Allison Gas Turbine Division of General Motors Corporation)

Objective/scope

The objective of this project is to develop and demonstrate the necessary nondestructive examination (NDE) technology, materials data base, and design methodology for predicting useful life of structural ceramic components of advanced heat engines. The analytical methodology will be demonstrated through confirmatory testing of ceramic components subject to thermal-mechanical loading conditions similar to those anticipated to occur in actual vehicular service. The project addresses fast fracture, slow crack growth, creep, and oxidation failure modes.

Technical progress

Design Methodology and Data Base Development - Effort during this reporting period addressed the development of initially proposed failure models. Failure theories dealing with slow crack growth, creep, and oxidation have been researched and the most promising ones have been identified.

Slow crack growth - The governing slow crack growth (SCG) equation applicable to the reliability analysis of ceramic components was originally developed using the Weibull principle of independent action (PIA) fast fracture model combined with classical fracture mechanics equations describing the relations between crack velocity and the stress intensity factor. By modifying the form of this SCG equation to define the degradation of the original fast fracture survivability with increasing time, both Weibull and Batdorf fast fracture methodologies, as incorporated within the CARES program, can be used to define the initial (time = 0) component reliabilities. The time dependency requires two additional material constants that are determined from statistical analysis of the fracture times of specimens with differing static loads (at a fixed temperature). Allison has programmed into CARES the capability of determining the two crack velocity constants from material testing and using this data with fast fracture data to compute component reliability at as many as six discrete time "slices". This approach incorporates both surface and volume reliability models and also can use the various Batdorf shear sensitive models as the fast fracture starting point.

Oxidation - Oxidation of a ceramic is taken to be a surface effect governed by the parabolic diffusion law and a thermal activation process of constant activation energy, with an Arrhenius type of temperature dependence. By the assuming the Griffith flaw size to be proportional to the surface oxide thickness, we can structure the

oxidation equations in a way to allow the time dependent reliability of the component to be computed within the CARES program. Three material constants must be determined from the fracture testing of oxidized specimens.

As currently planned, a number of specimens will be oxidized at a selected reference temperature and time. Room temperature, four point bend tests allow the development of the two Weibull PIA surface constants within CARES. The material constant related to activation energy is obtained by the regression analysis of room temperature fracture tests of specimens exposed to a variety of temperatures and times. In this regression, data is examined by CARES to determine if the data contains outliers (i.e. data whose normalized residual exceeds the critical value at the 10% significance level). The outliers are deleted from the data set prior to computing the activation energy constant.

One additional piece of material data required in this model is a table of critical stress intensity factors at room temperature and the component temperatures. This is currently used to determine the Weibull scale factor at temperature from room temperature data. Once the material constants are available, a component survivability may be determined at as many as six mission times.

Creep - The creep model used in CARES combines the classical Norton isothermal power law with a thermal process of constant activation energy showing the Arrhenius type of temperature dependence. Material creep data is determined by a log linear regression analysis of specimen steady state creep data determined at a variety of temperatures and stress levels. Similar to the oxidation analysis, data is examined by CARES to determine if it contains outliers. Any outliers are deleted prior to the final determination of the three material constants.

Because the creep effect may cause considerable stress redistribution in a component, the analyst must use the creep constants obtained in CARES with a finite element code (such as NASTRAN) to determine component deformation with time.

Work has continued at GTE towards the fabrication of test specimens for this program. Material has been set aside for the program and has been carefully characterized prior to the initiation of the production of deliverable specimens. A modification to the delivery schedule to allow a more desirable flow of specimen mix has been agreed upon. Injection mold tooling for MOR bars has been completed and deliveries will start shortly. Five finished isopressed tensile bar samples have been received. These bars will be tested to confirm that the geometry will produce good test results. Eighteen additional tensile bars are in final machining and another sixty are ready for HIPing. An injection mold tool for producing the plates used for the dog-bone specimens has been designed. Fifteen of these fracture plates have been HIPed and are in final NDE. An injection mold insert for circular plates has been designed and has been submitted for fabrication. Development of seeded specimens for the NDE task has also begun. Laser drilling of precision holes to simulate void-type defects was successfully accomplished on a trial basis.

Sample holes down to 20 microns in diameter were drilled. A residue observed in the holes was found to be removable through ultrasonic techniques. Hole diameter and depth were measured as repeatable within one micron. Qualified NDE reference standard MOR bars will be drilled shortly.

Analytical Tools - Work has concluded on the initial checkout of CARES, the NASA computer code for performing fast fracture analyses. Previously reported analyses addressed correlation between the predicted probability of survival from CARES and STRATA, which is Allison's in-house code. Since CARES is a public domain code, it will be used in this program. However, since Allison has extensive experience with STRATA, correlation between the two codes was first desired. Our studies have shown that the codes do indeed get the same answer for a given problem. The one item that was concluded during this reporting period dealt with the regression of material constants from raw data. Initial studies had shown differing answers from the two codes, as shown in Table 1. This has now been resolved. The two codes were handling suspended MOR tests in different fashions. Table 2 shows the regression from the two codes when suspended tests are excluded from the data set (i.e., no "suspended" surface failures were used in the volume failure regression, and vice versa). Notice that the results are similar from each code. It has been decided to use the CARES code as it currently exists. Of course, modifications will be incorporated as dictated by results of this program.

Work during this past reporting period has concentrated on developing computer code for the initially proposed failure models. The first milestone of Allison's Ceramic Life Prediction program, "Computer Implementation of Initial Failure Models" has been completed. This effort involved computer programming the initially proposed failure models for slow crack growth, creep, and oxidation. For the

Table 1. Calculation of Weibull Material Constants with Suspended Tests

Material Constant	ALLISON		CARES			
			Least Squares		Max Likelihood	
	Volume	Surface	Volume	Surface	Volume	Surface
Weibull Slope	15.72	8.39	13.24	7.51	12.79	7.95
Charact. Strength	111.0	115.3	112.2	117.2	112.3	116.9
Unit Charact. Strength	70.19	96.21	65.98	95.87	64.93	96.64

Table 2. Calculation of Weibull Material Constants without Suspended Tests

Material Constant	ALLISON Volume	ALLISON Surface	CARES Least Squares Volume	CARES Least Squares Surface
Weibull Slope	12.65	7.87	12.67	7.89
Charact. Strength	108.9	103.1	108.9	103.1
Unit Charact. Strength	62.7	85.1	62.7	85.1

most part, the code was written as modules to the CARES program. In addition to programming the failure theory, data reduction capability was also incorporated so that raw test data can be regressed into usable material constants. Although specimen testing has not yet commenced, it was desirable to develop this software now so when the test data becomes available, it can be quickly evaluated.

The proposed failure theory for slow crack growth is a probabilistic methodology based on the principles of fracture mechanics. Component failure probability starts at the fast fracture probability and deteriorates with time. In addition to the fast fracture material constants, two additional constants representing the deterioration of mean strength with time are determined from testing. The approach considers both area and volume reliabilities. The software for this task is completed and incorporated into the CARES code. The program has the ability to accept previously determined material constants and then calculate the probability of survival due to the slow crack growth failure mode. The probability of survival for up to six different "times" can be calculated with a single computer analysis. Data reduction capability has also been coded so that the appropriate material constants can be determined from the raw test data.

The proposed failure theory for oxidation is a probabilistic approach based on surface oxidation promoted by the diffusion process. The model requires four material constants. They are determined from the results of room temperature MOR tests on specimens oxidized at elevated temperature. The software for the oxidation model is completed and incorporated into the CARES code. Similar to the slow crack growth analytical capability, the code has been established to calculate the probability of survival due to oxidation for up to six

different "times" in a single computer analysis. Code also is developed for data reduction of raw test results into usable material constants.

Due to the redistribution of stresses, the evaluation of creep must be done with a finite element stress analysis code. However, a CARES module has been written for the data reduction of creep data into usable material constants. These constants can then be used in the finite element solver, such as NASTRAN.

These new modules to the CARES code are now ready. They will be used as specimen test data becomes available.

Status of Milestones

The program is currently on schedule.

Publications

None

Life Prediction Methodology for Ceramic Components of Advanced Heat Engines

A. Comfort, J. Cuccio, and H. Fang (Garrett Auxiliary Power Division, Allied-Signal Aerospace Company)

Objective/Scope

The feasibility of using ceramic components and the application of probabilistic design methods were first demonstrated by Garrett in the DARPA/Navy Ceramic Engine and DOE/NASA AGT101 programs. These programs highlighted the need for improved material properties and advanced design methods to assure adequate ceramic component life in engine use. Ceramic manufacturers are improving material properties through their own R&D efforts as well as government-funded programs in processing ceramics (e.g., DOE/ORNL Ceramic NDE/Processing program). Garrett Auxiliary Power Division (GAPD) has defined a program to develop the methodology required to adequately predict the useful life of ceramic components used in advanced heat engines.

GAPD's approach consists of materials characterization and behavior modeling, combined with component analysis and risk integration tools. Uniaxial and biaxial stress states will be evaluated to develop models for fast fracture, slow crack growth, creep deformation, and oxidation. The accuracy of the methodology will be verified by testing simulated components under stress and temperature conditions representative of gas turbine engine operation.

Technical Highlights

Material Testing and Analysis:
H. Fang

Material Testing

All test procedures are presently being reviewed to ensure their completeness and assurance of generating accurate data. The review of the flexure procedure has been completed.

A machining vendor qualification study was conducted by Norton/TRW Ceramics (NTC). The primary objective of the study was to survey and qualify machining vendors so that several machining vendors may be used to achieve lower cost, higher overall quality, and improved machining turn-around time. The study also assessed the effects of different machining procedures and post-machining heat treatments on the uniformity of mechanical properties. In addition, the amount of undesirable chamfer failures on the test bars was determined; the results will be used to select the machining vendors.

An L4 (2^3 x 4^1) Taguchi array experiment was used to investigate the effect of three processing factors and the effect of different vendors. Table 1 shows the experimental array and associated factors. A total of 480 MIL-STD 1942 Size B bars were used in the study.

TABLE 1. GRINDING VENDOR ASSESSMENT AND QUALIFICATION L4 (2^3 x 4^1) TAGUCHI EXPERIMENTAL DESIGN

Trial No.	Inside Factors			Outside Factor			
	A	B	C	D			
1	1	1	1	1	2	3	4
2	1	2	2	1	2	3	4
3	2	1	2	1	2	3	4
4	2	2	1	1	2	3	4

Inside Factors:

A = Machining Operation

Level 1 = Standard speeds and feeds. Maximum downfeed rate of 0.0001 inch per pass for a minimum of 0.0020 inch.

Level 2 = Severe speeds and feeds. More severe downfeed rate of 0.0005 ± 0.0001 inch per pass for a minimum of 0.0020 inch.

B = Grinding Orientation

Level 1 = Longitudinal
Level 2 = Transverse

C = Post-Machining Oxidation Heat Treatment

Level 1 = No Treatment
Level 2 = With Treatment

Outside Factors:

D = Machining Vendors

Level 1 = Machining Vendor A
Level 2 = Machining Vendor B
Level 3 = Machining Vendor C
Level 4 = Machining Vendor D

Fractography was performed by GAPD using a 40X microscope on all the flexure bars tested in the machining study. Special efforts were made to determine whether fractures originated from a chamfer corner of the test bars. Excessive chamfer failures during flexure testing are not acceptable, because they are not representative of failures from the tensile surface and should not be included in the life prediction analyses.

The percentage of chamfer failures from each combination of processing parameters and machining vendors are listed in Table 2. The percentage was calculated as (no. of chamfer failures/total identified failures) x 100 percent. Test bars with a damaged fracture origin were not included in the calculation. The results showed that for longitudinally machined bars, which will be typical of all the flexure bars in the program, only Vendor No. 2 demonstrated acceptable chamfer failure levels (zero and 6 percent).

TABLE 2. PERCENTAGE OF CHAMFER FAILURES ON MACHINING STUDY TEST BARS

Treatment Number	Machining Procedure	Grinding Direction	Heat Treat	Vendor			
				1	2	3	4
1	Standard	Longitudinal	No	47*	0	19	58
2	Standard	Transverse	Yes	33	11	18	21
3	Severe	Longitudinal	Yes	42	6	26	0
4	Severe	Transverse	No	0	16	0	6

*Percentage of Chamfer Failures/Total Identified Failures; Bars Flexure Tested at Room Temperature in 4-Point Loading.

Data Analysis and Methodology Developement:
J. Cuccio

Analyses were performed to provide a means of determining when ceramic flexure data is contaminated by chamfer failures that are not representative of the specimen's tensile face. Weibull size-scaling methods were used to calculate the expected percentage of chamfer failures.

The percent chamfer failures were calculated for Weibull moduli between 2 and 30, and are plotted in Figures 1 and 2; the effects of corner stress intensity and average flaw size on percent expected chamfer failures are included. The corner stress concentration was assumed to be zero percent for Figure 1, and 5 percent for Figure 2. As expected, the 5 percent corner stress concentration causes the percent of expected chamfer failures to increase with increasing Weibull modulus. This is because, as Weibull modulus increases, the material becomes more sensitive to peak stresses due to the increased stress intensity located at the chamfer.

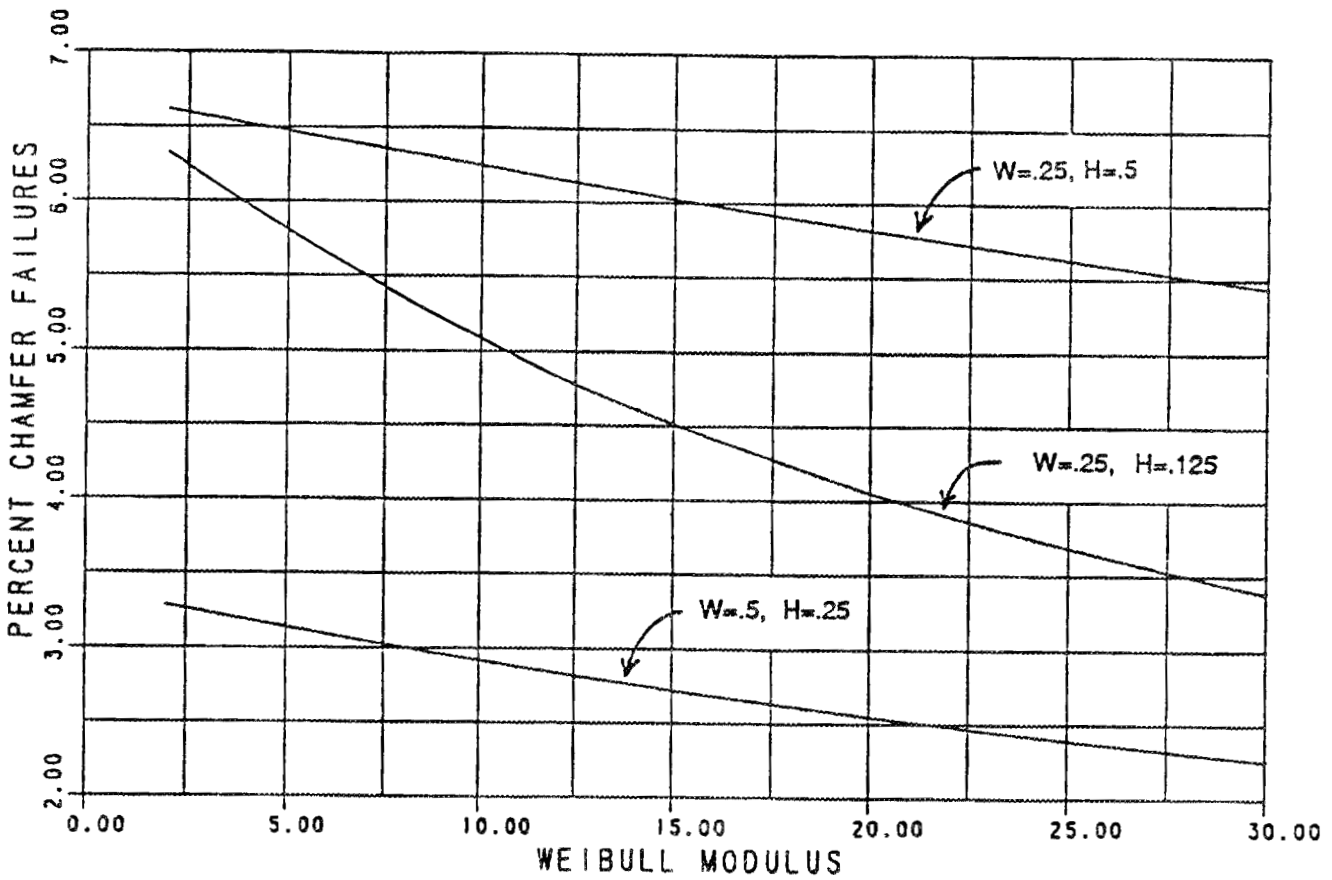

Figure 1. These Percent Chamfer Failures Should Be Observed if the Chamfer Has the Same Flaw Distributions as the Tensile Face of the Specimen. A Corner Stress Concentration of 1.00 Was Used.

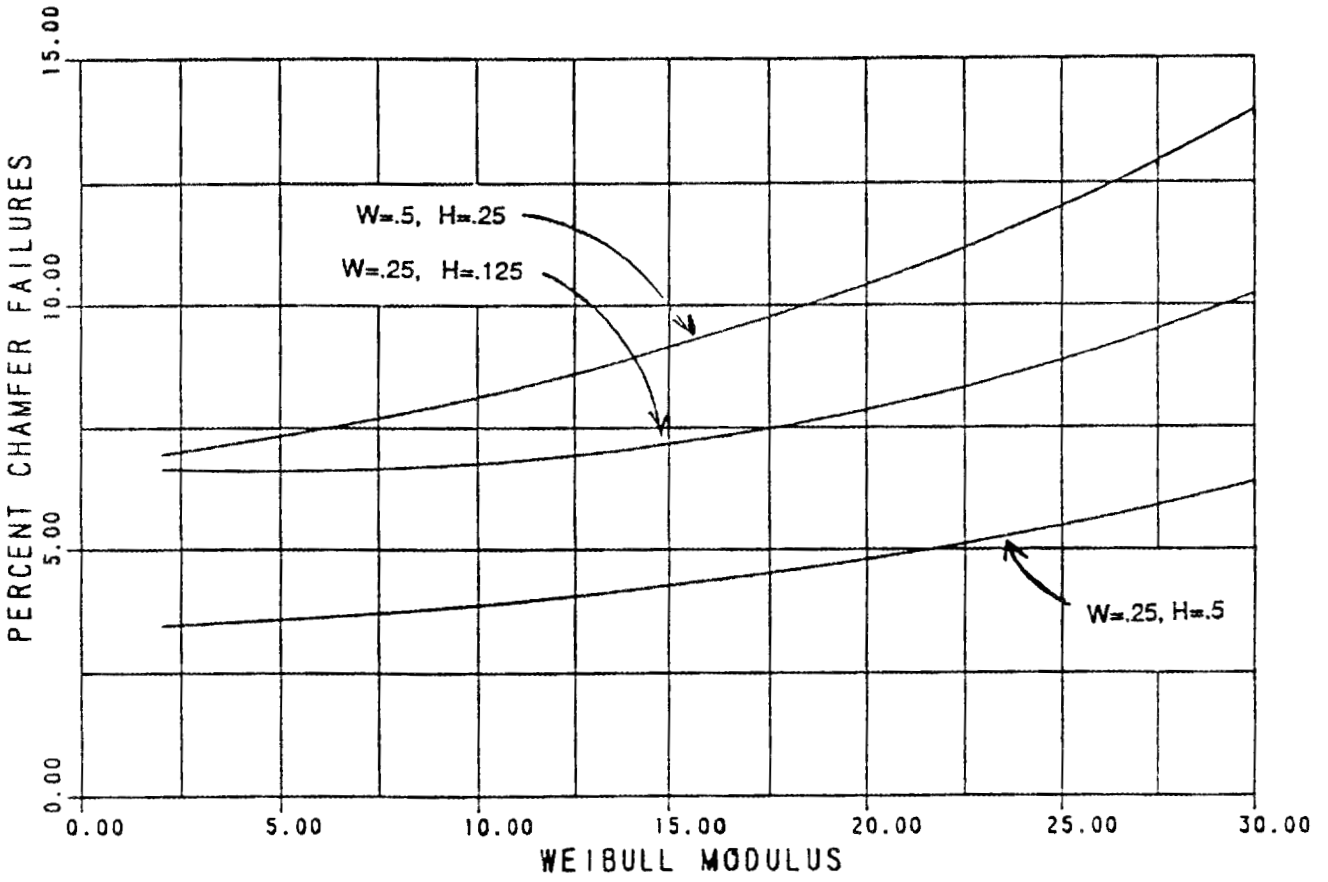

Figure 2. These Percent Chamfer Failures Should Be Observed if the Chamfer Has the Same Flaw Distributions as the Tensile Face of the Specimen. A Corner Stress Concentration of 1.05 Was Used.

General Electric Corporate Research and Development (GE-CRD) has been subcontracted to provide support in statistical methods development. Objectives and plans for the statistical methods development were discussed during the January 1990 kick-off meeting with Drs. Curtis Johnson and William Tucker. GE-CRD will provide support in three areas:

1. Statistical methods development for component life prediction.

2. Processing needs for life prediction methods development and verification.

3. Testing requirements for life prediction methods development and verification.

Planning focused on the first two areas. Testing requirements will be addressed in more detail prior to specimen delivery.

The objective of studying statistical methods for component life prediction is to develop statistically-based methods to accurately predict strength and lives, and confidence intervals for the predictions. Some key areas targeted for development include:

- Size scaling
- Multiple flaw distributions
- Multiaxial stresses
- In-service changes to flaw distributions

Considerable progress has been made in developing size scaling methods; however, statistical foundations for the other areas are lacking. As a result, confidence intervals cannot be calculated for component strength and life predictions.

Confidence intervals are essential for component strength and life prediction methods, and for methods verification in this program. Verification of the life prediction methods will be accomplished by comparing observed confirmatory specimen lives with predictions. There will be some uncertainty in the predictions, due to the size and number of specimens tested to generate the life prediction model parameters. Confidence intervals on the predictions will help quantify this uncertainty, and thereby determine (1) the expected deviation between measured and calculated lives, or (2) if the deviation is a result of modeling inaccuracies. Confidence intervals are also needed for component design to define the lower limits of reliable component operations.

Recommendations for processing Norton/TRW Ceramics NT154 silicon nitride specimens were also made during the January kickoff meeting with GE-CRD. Processing sequences and record-keeping recommendations were made, to allow processing consistency to be determined. Norton/TRW generally agreed with these requests.

Professor S. Suresh of Brown University visited GAPD in December 1989, to present recent developments in cyclic fatigue, cyclic compression fatigue pre-cracking, and mixed-mode fracture testing of ceramics. Professor Suresh will be contracted to perform mixed-mode I & III fracture toughness tests of notched cyclic compression pre-cracked tension-torsion specimens, and multiaxial strength tests on unnotched tension-torsion specimen.

These tests will provide input for mixed-mode fracture criteria, and verification of strength under multiaxial loading. Test plans and procedures were discussed, and are being finalized.

As part of the effort to verify life prediction methods, spin disk tests are planned. The spin disk design was modified during this reporting period, to increase volume failure probability. Recent analyses using NT154 tensile properties from the University of Dayton Research Institute (UDRI) showed the previous design has higher surface failure risk than volume failure risk. As a result, the disk has been redesigned, to produce higher internal failure probability. The higher volume failure probability is required to more accurately simulate rotor conditions. The new design (Figure 3) has the same volume as the previous disk; however, the disk thickness was decreased at the rim and increased at the center.

NDE Methods Development and Application
J. Minter

General Electric NDE Systems and Services has been subcontracted to provide acoustic microscopy and computed tomography inspection services, including necessary development in these two areas, for the program. A kick-off meeting for their work has been scheduled for April 3, 1990.

Acoustic emission (AE) data can be used to monitor crack growth if the AE data can be related to crack length. A preliminary study was performed, using 1/4 x 1/4 x 2 inch chevron notch specimens. Preliminary data analysis of the first several tests revealed inconsistencies in the data that are associated with transducer coupling, machine noise, and equipment threshold levels. In addition, each chevron notch specimen generated only one data set per test. Remounting the transducers for each test generated another source of error, making correlation of the data to crack growth more difficult.

Because of the multiple variables associated with the chevron notch specimens, a second study has been planned. Standard GAPD flexure bars (1/8 x 1/4 x 2 inch) will be used. Both Vicker's and spherical indentors at various loads will be used to generate cracking. Several tests per bar will be accomplished to generate multiple AE events per bar. This will reduce the error caused by setup variability; equipment parameters and machine noise will also be evaluated. After indenting the bars, the crack size will be determined destructively. The AE data will be evaluated as a function of load and crack size.

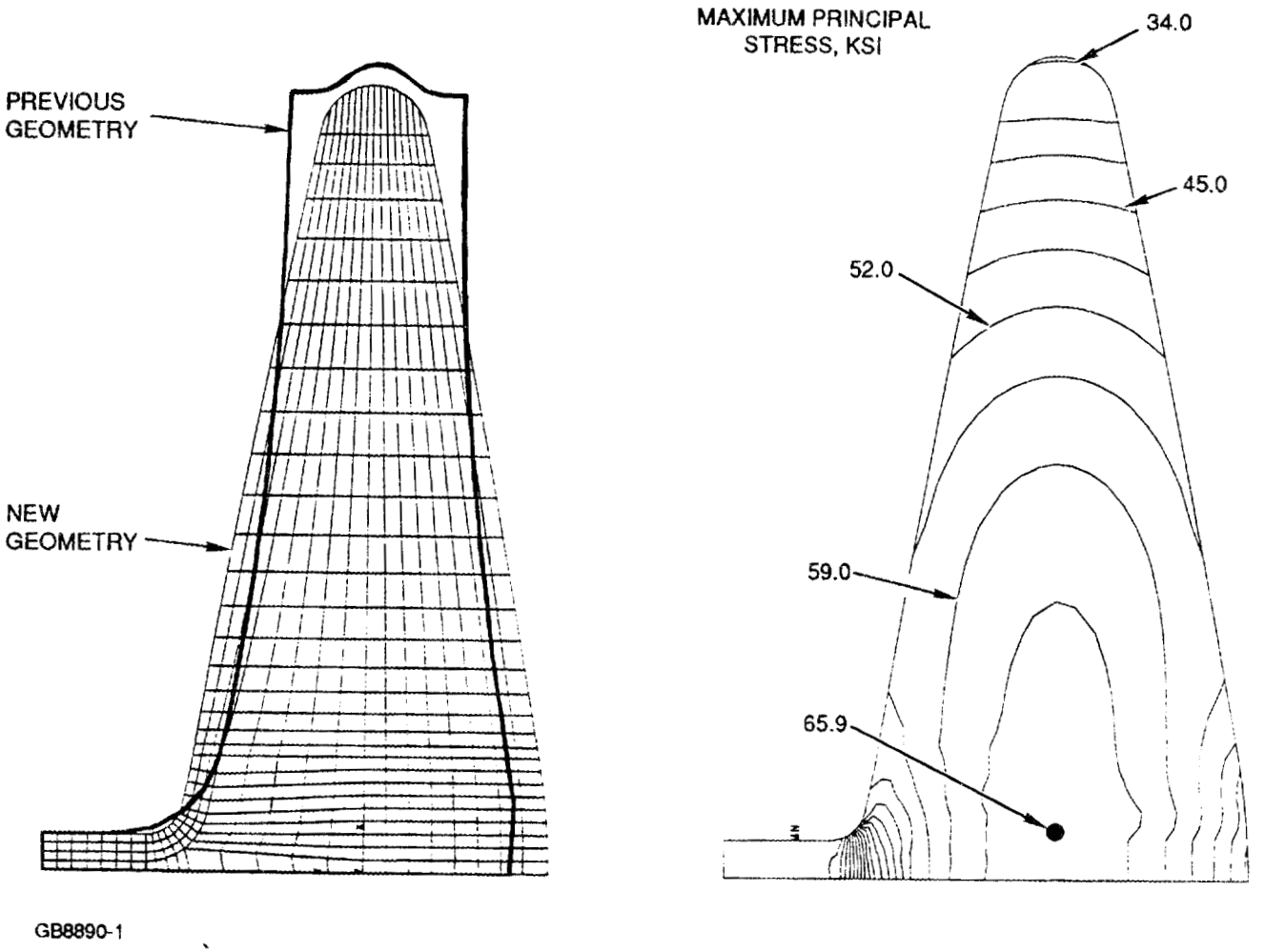

Figure 3. **Spin Disk Geometry Was Modified to Increase Maximum Volume Stress Relative to Maximum Surface Stress. Stresses Shown Are for 100,000 rpm Cold Rotation.**

An acoustic microscopy study has been designed to evaluate the effect of different surface finish conditions on the ability of acoustic microscopy to detect surface and near-surface defects. Test bars have been indented and heat-treated in accordance with the test plan (Table 3). Documentation of the test bar surface conditions has been completed and the bars have been sent to GE NDE Systems and Services for inspection.

TABLE 3. SPECIMEN TEST MATRIX FOR ACOUSTIC MICROSCOPY SURFACE FINISH STUDY

		Normal Machining	Aggressive Machining	Polished
No Heat Treatment	As Indented	X	X	X
	Indent Removed	X		X
Heat Treated After Indent		X	X	X

The first radiographs for the radiographic enhancement effort by Argonne National Laboratories have been sent to Dr. William Ellingson for enhancement. The radiographs were taken at Garrett Ceramic Components Division, as the GAPD microfocus radiography system is currently being upgraded. The upgrade will be completed by the end of April 1990 and future radiographic work will be performed at GAPD. The radiographic enhancement effort will include evaluation of various film digitization techniques, as well as the use of different enhancement routines once the radiographs are digitized. These first radiographs will be used to determine the required radiographic film type and density for optimum enhancement.

Status of Milestones

On Schedule.

Communications/Visits/Travel

Dr. Subra Suresh, of Brown University, visited GAPD in Phoenix, Arizona on December 11 and 12, 1989.

Drs. Curtis Johnson and William Tucker, from General Eleletric Corporate Research and Development, visited GAPD on January 10 and 11, 1990.

John Cuccio and Ho Fang participated in the Tensile Testing Workshop organized by Vic Tennery, discussing problems and solutions encountered during tensile testing of ceramics.

Ho Fang visited the ORNL High Temperature Material Laboratory and the Mechanical Property Laboratory to discuss tensile stress rupture, inert atmosphere

tensile testing, and indentation crack growth with Matt Feber, Ken Liu, and Christ Stevens.

Janet Minter visited Garrett Ceramic Component Division, to perform microfocus radiography inspection.

Bryan McEntire, Tony Tagalaivore, Eric Bright, Dewey Heichel, and John Holowczak, from Norton/TRW Ceramics, visited GAPD to discuss machining vendor qualification and specimen preparation status.

Problems Encountered

None.

Publications

A paper entitled "Life Prediction Methodology for Ceramic Components of Advanced Heat Engines" has been submitted to the Society of Automotive Engineers (SAE) for publication.

3.3 ENVIRONMENTAL EFFECTS

Environmental Effects in Toughened Ceramics - Norman L. Hecht (University of Dayton)

Objective/scope

Since 1985, the University of Dayton has been involved in a three-phase project to investigate the effects of environment on the mechanical behavior of commercially available ceramics being considered for heat engine applications. In the first phase of this project, the effects of environment on the mechanical behavior of transformation-toughened ZrO_2 ceramics were investigated. In the second phase, two Si_3N_4 ceramics (GTE PY6 and Norton/TRW XL144) and one SiC ceramic (Hexoloy-SA) were evaluated. In the third phase, the tensile, flexural, and fatigue strength of nine SiC and Si_3N_4 ceramics (see Table 1) are being evaluated at temperatures ranging from 20°C to 1400°C. Microstructure, chemistry, and physical properties are also investigated.

During the past six months (October 1989 to March 1990), evaluations of one SiC and two Si_3N_4 ceramics continued. The tensile strength of GTE's PY6 was measured from temperatures of 20°C to 1400°C, and the tensile stress rupture (static fatigue) behavior of Norton/TRW NT-154 and Hexoloy SA was investigated. In addition, the effect of thermal aging in air on the flexural strength of Hexoloy SA, NT-154, and PY6 was also investigated.

Experimental procedures

The tensile strength measurements of PY6 were made using button-head cylindrical specimens on an Instron Electro-Mechanical Test

Table 1. Candidate SiC and Si_3N_4 Ceramics Selected for Evaluation

Carborundum Hexoloy SA	Cold formed (injection molded or isostatic pressing) and pressureless sintered α-SiC with additions of B and C.
Carborundum Hexoloy ST	Cold formed and pressureless sintered α-SiC and TiB_2.
GTE PY6	Injection molded and HIP'ed β Si_2N_3 with additions of Y_2O_3.
Norton/TRW NT-154	Sintered and HIP'ed Si_3N_4.
CVD SiC	SiC prepared by chemical vapor deposition techniques.
Howmet SN-4	Cold formed (die pressing/isostatic pressing) sintered and HIP'ed Si_3N_4 with 10% oxide sintering aids (Al_2O_3 and Y_2O_3).
Ceradyne Ceralloy 147-3	Cold formed (isopressing/slip casting/ injection molding) sintered Si_3N_4 with additions of Y_2O_3 and Al_2O_3.
Kyocera SN-252	Cold formed (isopressed/slip cast/etc.) and sintered Si_3N_4 with additions of Yb_2O_3, Y_2O_3, and Al_2O_3 (Note: the sintering process is controlled to promote the growth of a β Si_3N_4 whisker phase in the Si_3N_4 matrix).
NTK EC-152	Gas pressure sintered Si_3N_4 with additions of Al_2O_3 and Y_2O_3.

System (Model 1361) equipped with Instron "Super-Grip" universal coupling and water-cooled holders for high-temperature tensile testing.

For high-temperature measurements an Instron high-temperature short furnace was used. Tensile strength was measured at 20°C, 1000°C, 1200°C, 1300°C, and 1400°C using a rapid loading rate (actuator speed of 0.004 cm/s). Five tensile specimens were measured

at 1000°C, 1200°C, 1300°C, and 1400°C, and 10 tensile specimens were measured at 20°C. In addition, five tensile specimens were measured at 1300°C at the slow loading rate (actuator speed of 0.00004 cm/s) to calculate dynamic fatigue at this temperature.

Tensile stress rupture was initiated to evaluate the fatigue behavior of the NT-154 and Hexoloy SA materials. These measurements were made using the Instron Electro-Mechanical Test System at temperatures from 1200°C to 1400°C. For the NT-154 Si_3N_4 tensile stress rupture was measured at 1200°C, 1250°C, and 1300°C at applied stress levels of 300 MPa and 200 MPa.

Thirty-two NT-154 tensile specimens were evaluated at temperatures from 1200°C to 1400°C. The first three specimens tested at 1400°C were to be loaded at 300 MPa for an exposure time of 100 hours. However, all three specimens failed during loading before reaching 300 MPa. As a result, an additional four tensile specimens were loaded to only 200 MPa for exposures at 1400°C up to 100 hours. At 1200°C five specimens were loaded to 300 MPa and four were loaded to 200 MPa for tensile stress rupture testing to 100 hours. The specimens that endured the 100-hour exposure were subsequently loaded to failure. In addition, five specimens were tested at 1250°C and six specimens were tested at 1300°C at 300 MPa. None of these tensile specimens survived the 100 hours. Five specimens were also loaded to 200 MPa at 1300°C for 100 hours. Fracture origins were determined by optical microscopy and SEM (JEOL/JSM-80 with EG&G Ortec System 5000 Microanalysis System).

A study investigated the effects of thermal aging in air on the flexural strength of Hexoloy SA, GTE PY6, and NT-154. Ten specimens of Hexoloy SA and PY6 were aged for 50 hours at 1000°C and for 100, 500, and 1000 hours at 1300°C in air. In addition, five specimens of NT-154 were aged for 50 hours at 1000°C and five specimens were aged for 50 hours at 1400°C. The flexural strength of all the specimens was measured after aging using two Instron Universal Testing Machines (Model 1123) following MIL-STD-1942(MR). The strength of half of the aged Hexoloy SA and PY6 specimens was measured at 20°C, and half of

the aged Hexoloy SA and PY6 specimens was measured at 1300°C. The strength of all of the aged NT-154 specimens was measured at 20°C.

The strength measurements at 1300°C are conducted in two ATS #3320 high-temperature furnaces. The test specimens used were 3 x 4 x 50 mm with the tensile surface ground and polished to a 16-microinch finish. The test specimens are loaded at a machine crosshead speed of 0.004 cm/sec. For room temperature measurements, the bend fixtures are made of steel. For measurements at 1300°C, the four-point bend fixtures are made of SiC.

Technical progress

Tensile strength of PY6

The results of the fast fracture PY6 tensile strength measurements from 20°-1400°C are summarized in Table 2 and plotted versus temperature in Figure 1. For purposes of comparison, the tensile strength values measured for NT-154 in our earlier work are also presented in Figure 1. It should be noted that the values listed for NT-154 are based on 15 test specimens/condition. During the initial tensile strength measurements, at 20°C we were plagued with 60% buttonhead failures. However, for the remaining test specimens at 20°C and for the test specimens measured at 1000°C, collets of modified design provided by GTE were used. Use of the GTE collets at the lower measurement temperature appears to have reduced the buttonhead problem.

It has been our practice to preload the tensile specimens at a crosshead speed of 0.00004 cm/s to a 455-kg (1000 lbs) load to allow the copper collets to deform around the root radius of the buttonhead. After seating for 5 minutes the specimen is loaded to failure using a crosshead speed of 0.004 cm/s. For elevated temperature strength measurements the heated furnace is placed around the preloaded specimen, which is allowed to reach the test temperature (~15 minute soak time), and then fast-loaded to failure. During the initial testing at 1400°C the first three PY6 specimens failed under preload (455 kg ~140 MPa) during the 15-minute soak time. To prevent premature

Table 2. Summary of Tensile Strength Values Measured for GTE's PY6

Temperature (°C)	Tensile Strength (MPa)	Standard Deviation (MPa)	Coefficient of Variance (%)	Fracture Initiation Site+
20	619	123	20	5 vol. incl. 1 surf. incl. 4 surf. flaw
1000	447	111	25	4 vol. incl. 1 surf. flaw
1200	310	36	12	4 vol. incl. 1 surf. flaw
1300	251	28	11	3 surf. incl. 1 vol. incl. 1 surf. flaw
1400	153	53	35	4 surf. flaw 1 surf. incl.

+vol. - volume, incl. - inclusion, surf. - surface.

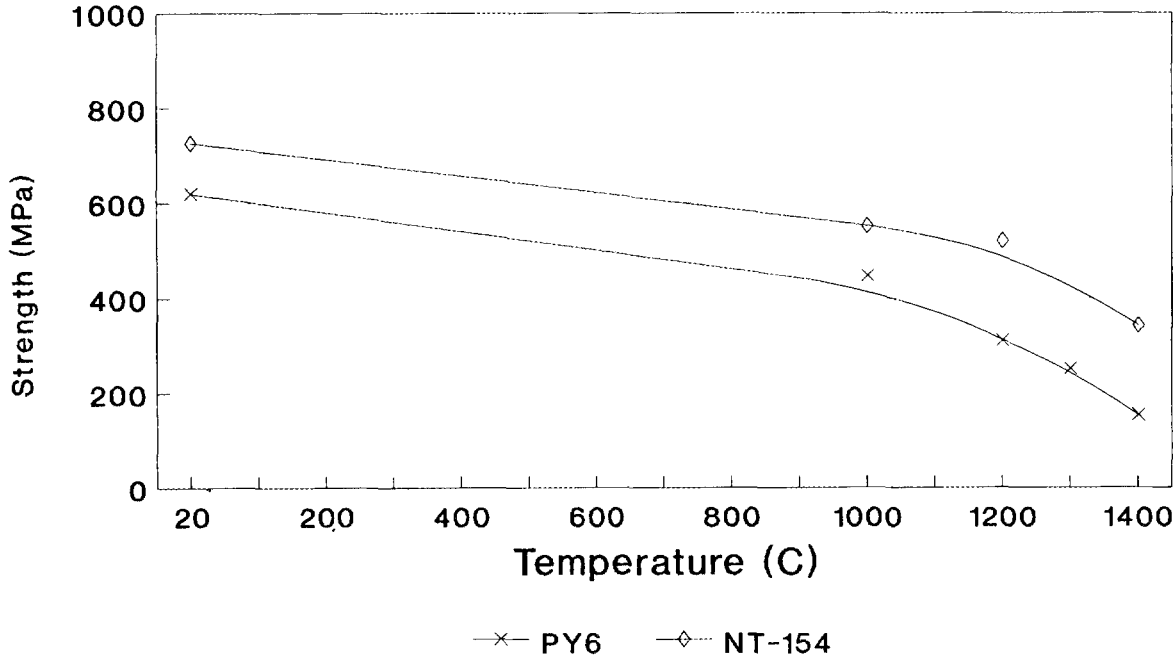

Figure 1. A comparison of the tensile strength of PY6 and NT-154 silicon nitrides.

failure we modified the preloading procedure by decreasing the hold load to 45.5 kg (100 lbs) from 455 kg for the specimen heat-up and soak time at the 1400°C, 1300°C, and 1200°C testing temperatures.

In comparing the tensile strength results obtained for PY6 with NT-154 (Figure 1) it was seen that the PY6 tensile strength is lower than the tensile strength values measured for NT-154, and the magnitude of difference increased with temperature (15% @ 20°C to 55% @ 1400°C). The PY6 Si_3N_4 has 6% Y_2O_3 sintering aid, and the NT-154 has 4% Y_2O_3 sintering aid, and it is believed that these differences account for the difference in strength observed. Preliminary examination of the fracture surfaces showed that fracture had initiated from inclusion sites in over 60% of the specimens tested. In several instances the inclusion sites were quite large (much larger than observed for NT-154). A typical volume-initiated failure is presented in Figure 2. The EDX spectrum obtained for the inclusion site is presented in Figure 3, which shows that the inclusion is predominantly iron and silicon with minor amounts of chrome.

As shown in Table 2, the fast fracture tensile strength of PY6 at 1300°C was 251 MPa with a standard deviation of 28. The slow fracture tensile strength of PY6 at 1300°C was 140 MPa with a standard deviation of 53. This represents a drop of 40% in strength due to the slower loading rate. A ln-ln plot of the strength-versus-loading rate is presented in Figure 4. The slow crack growth parameter n calculated from this ln-ln plot is 6.3, which indicates significant susceptibility to fatigue at 1300°C.

Tensile Stress Rupture of NT-154 and Hexoloy SA

The results of the tensile stress rupture tests for NT-154 at stress levels of 200 and 300 MPa are displayed in Figures 5 and 6, respectively. For an applied stress level of 300 MPa at 1250°C and 1300°C (Figure 6) the time-to-failure distribution was in two groupings approximately one order of magnitude apart. Similarly, at an applied stress level of 200 MPa at 1400°C and 1300°C (Figure 5)

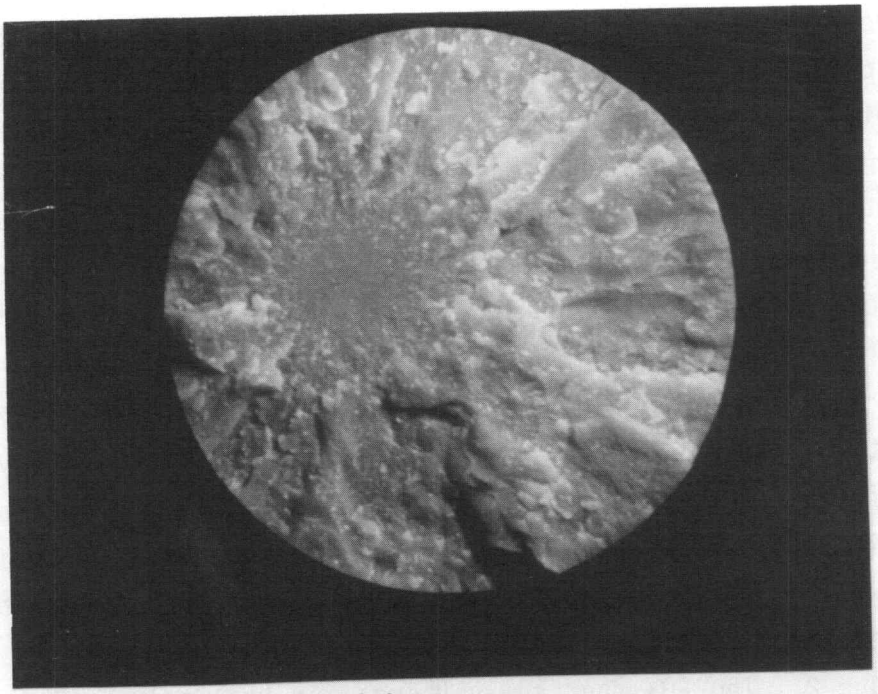

(a) at 12X

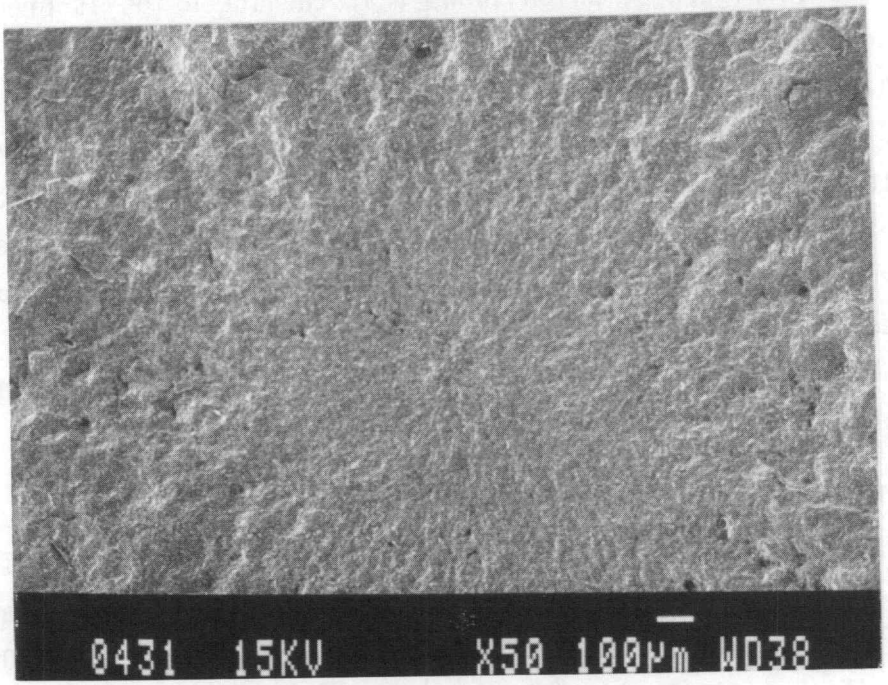

(b) at 50X

Figure 2. Micrographs of a typical PY6 fracture surface at 12X and 50X.

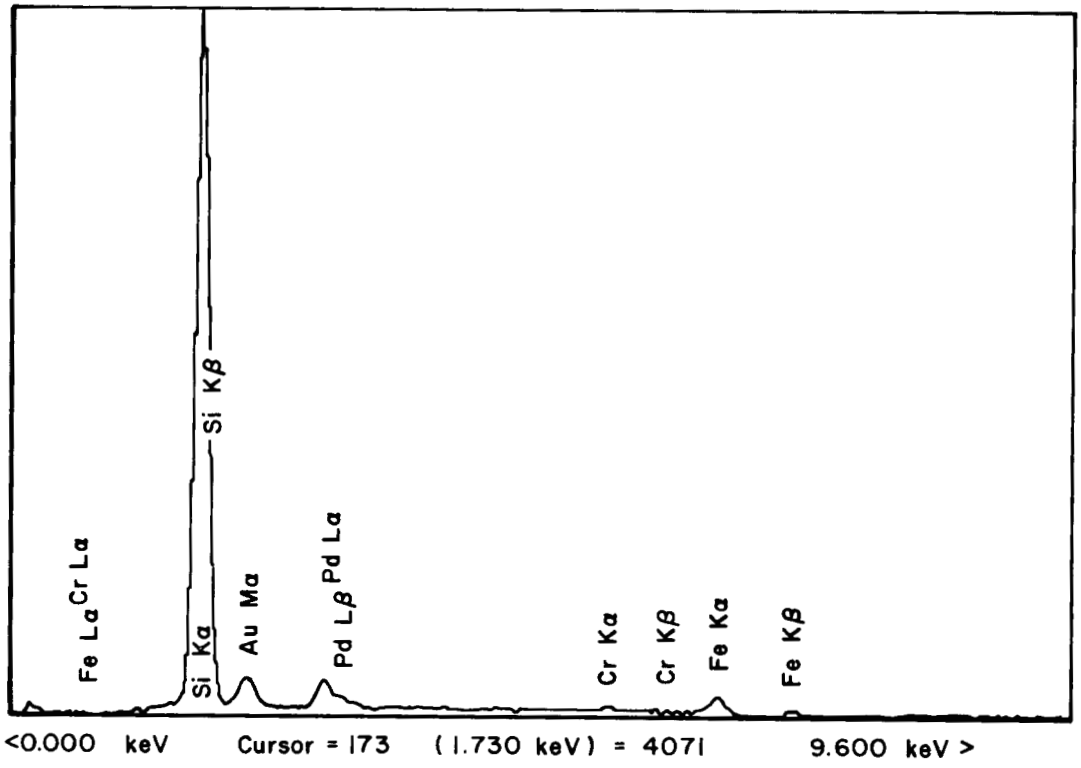

Figure 3. EDX spectrum of an inclusion site.

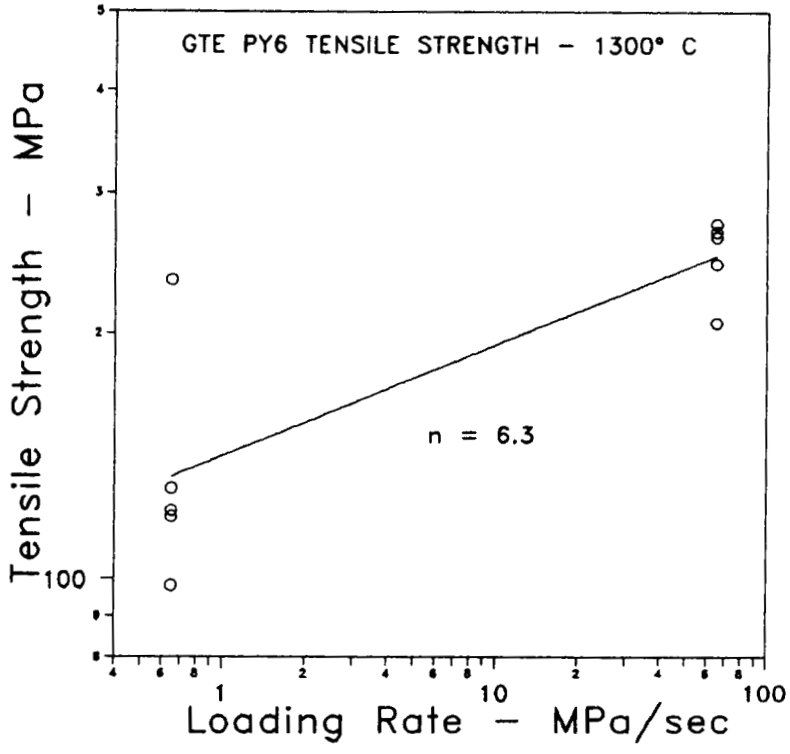

Figure 4. Ln-Ln plot of tensile strength versus loading rate for PY6 at 1300°C.

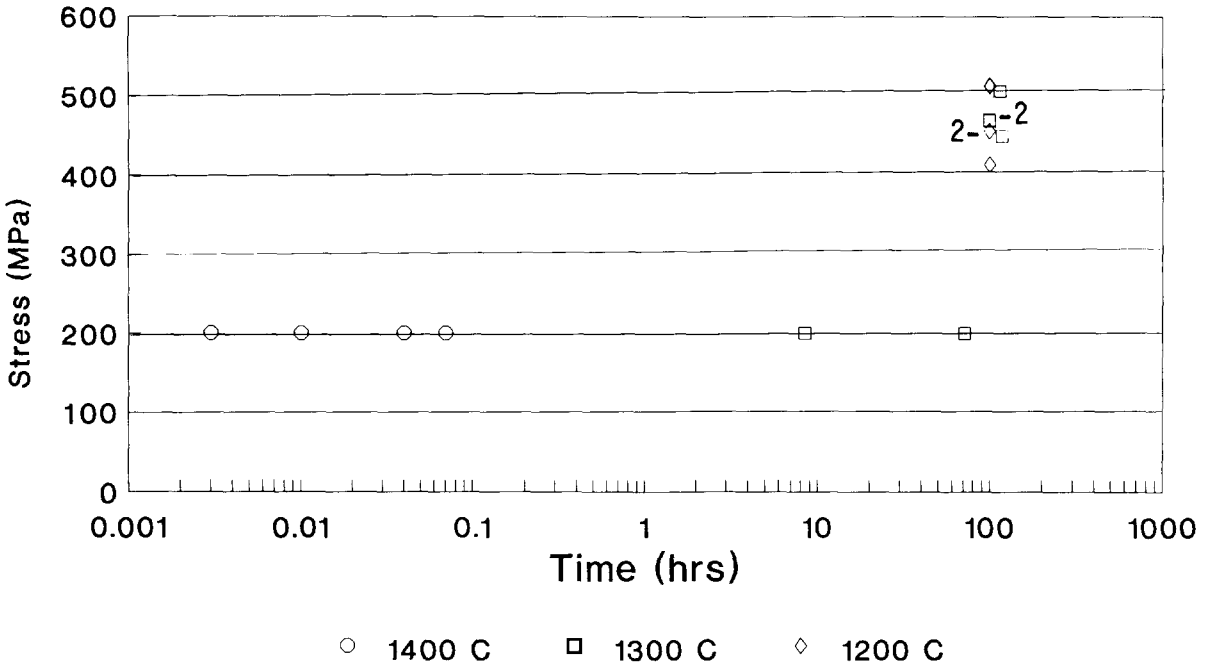

Figure 5. Tensile stress rupture behavior of NT-154 (200 MPa).

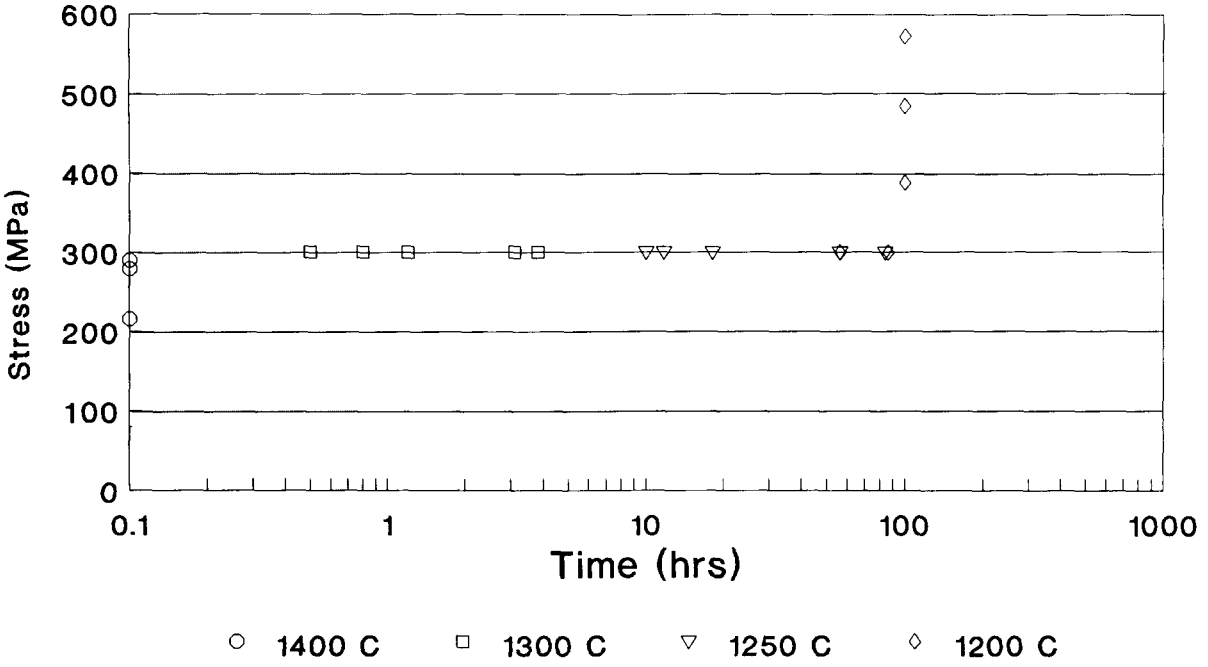

Figure 6. Tensile stress rupture behavior of NT-154 (300 MPa).

the time-to-failure was also in two groupings approximately two orders of magnitude apart.

This bimodal time-to-failure distribution (two parallel modes of failure) found at each test temperature has also been observed by Wiederhorn,[1] Quinn,[2] and Grathwohl.[3] These investigators found that the first mode of failure is due to slow crack growth or creep crack growth of pre-existing flaws, and the second mode of failure is by damage accumulation. In tensile stress rupture, damage accumulation is due to cavity nucleation, growth, and coalescence.

In the fractographic analysis, it was observed that all tensile stress rupture specimens failed from volume-initiated defects. At 1200°C for constant applied stress of 300 MPa, failures were due to strength-limiting iron-silicon inclusions. These inclusions were not seen as failure sources above 1200°C and 300 MPa applied stress. The failure mechanism above 1200°C and 300 MPa applied stress was intergranular slow crack growth and cavity nucleation (Figure 7a and b). Polished cross sections of the tensile specimens (parallel to the tensile stress axis) in the as-received and as-tested condition were prepared and are shown in Figure 8a and b. The polished sections show that a large distribution of cavities was generated during tensile stress rupture as compared to the as-received condition. Preliminary results indicate that cavities are formed where there is a lack of sintering aid, and local deformation cannot occur to accommodate the local high stress state.

Fifteen Hexoloy-SA specimens have been tested in tensile stress rupture at 1400°C. Applied stresses of 168.5, 200, 250, and 300 MPa were used. The results of the Hexoloy SA tensile stress rupture tests are summarized in Table 3 and plotted in Figure 9.

All the fractured Hexoloy SA specimens were examined at low power magnification (12X), and selected specimens were examined at higher magnification by SEM. Typical micrographs obtained for the fractured surfaces are presented in Figure 10a, b, and c. From these

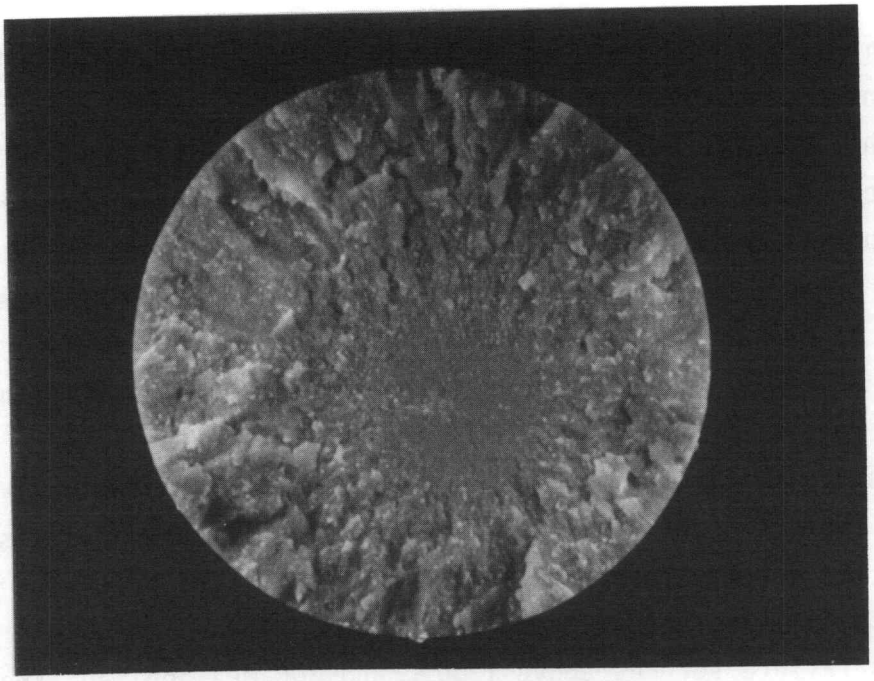

(a)

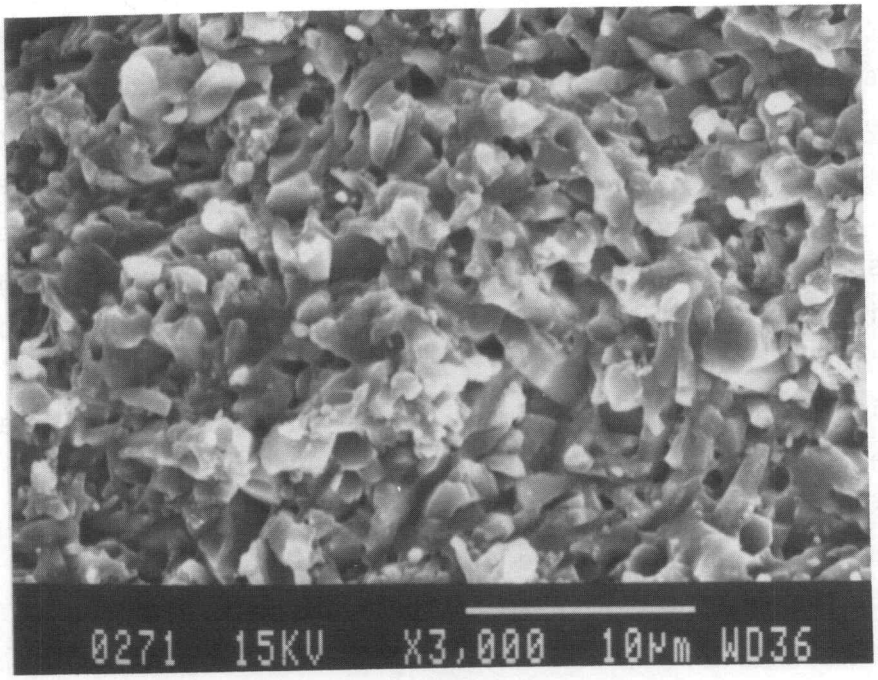

(b)

Figure 7. Fracture surface of a tensile stress rupture specimen of NT-154 at 1300°C, 300 MPa, and 0.5 sec.

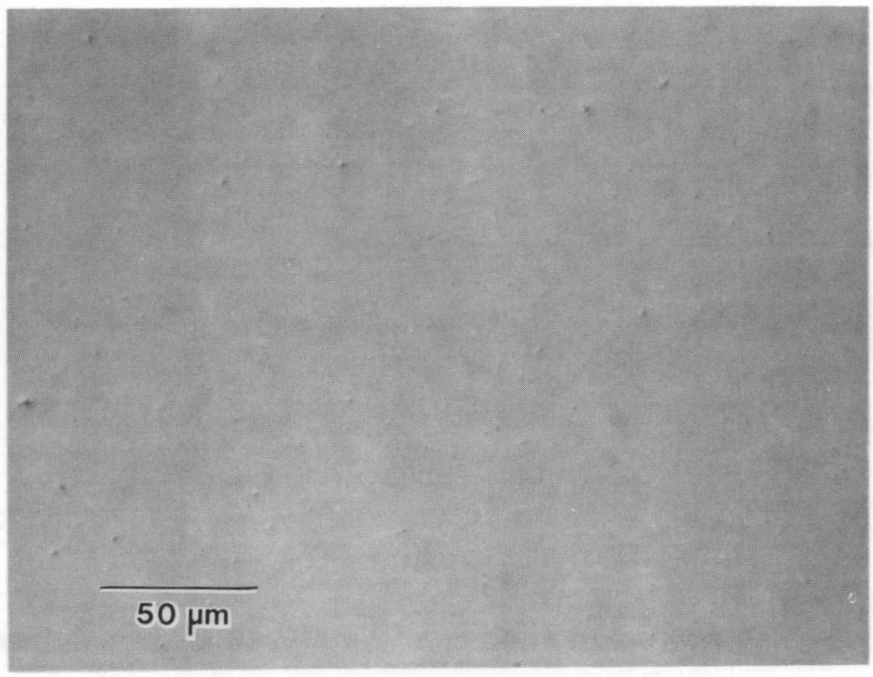

(a)

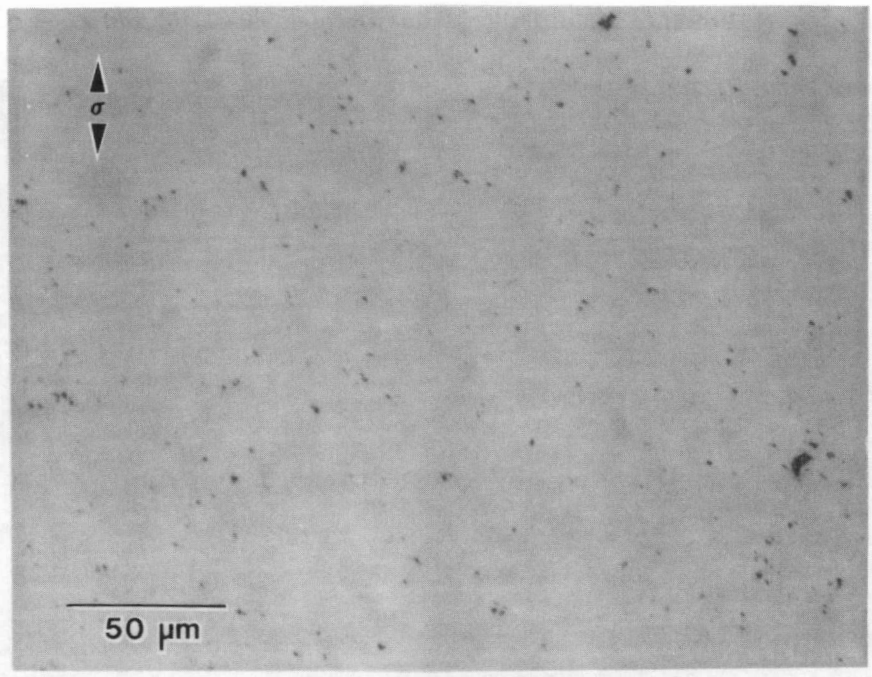

(b)

Figure 8. (a) Micrograph of a polished as-received cross section with existing microdefects, and (b) micrograph of a polished tensile stress rupture specimen that failed 3.8 hours at 300 MPa and 1300°C in air.

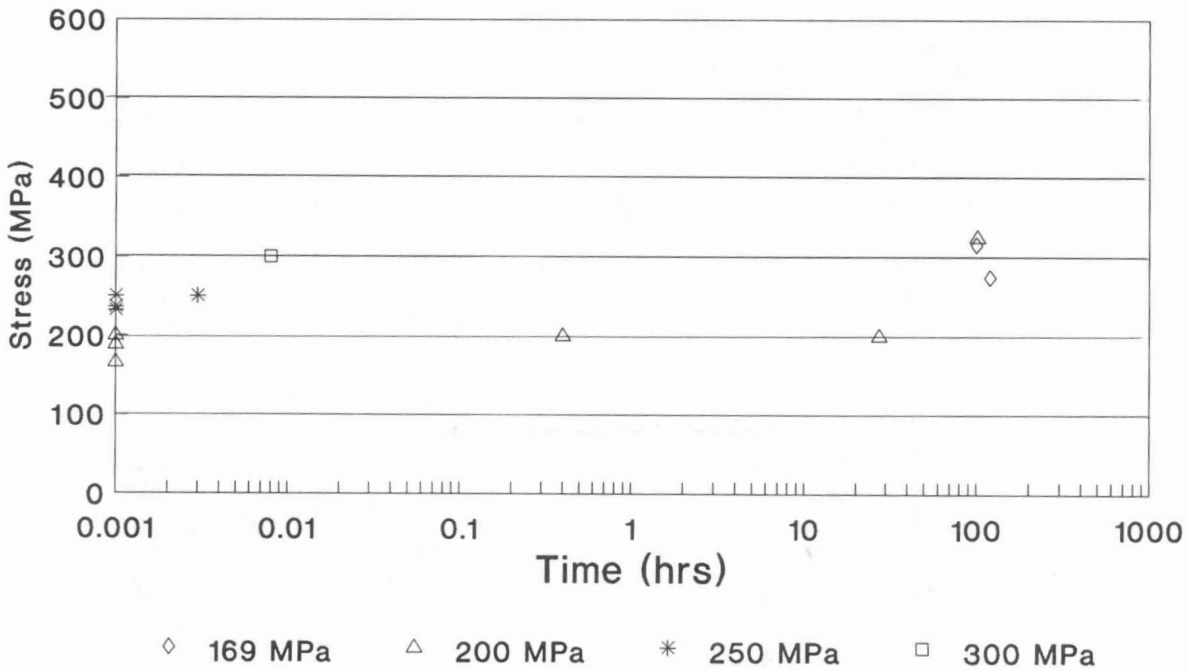

Figure 9. Tensile stress rupture behavior of Hexoloy SA tested at 1400°C.

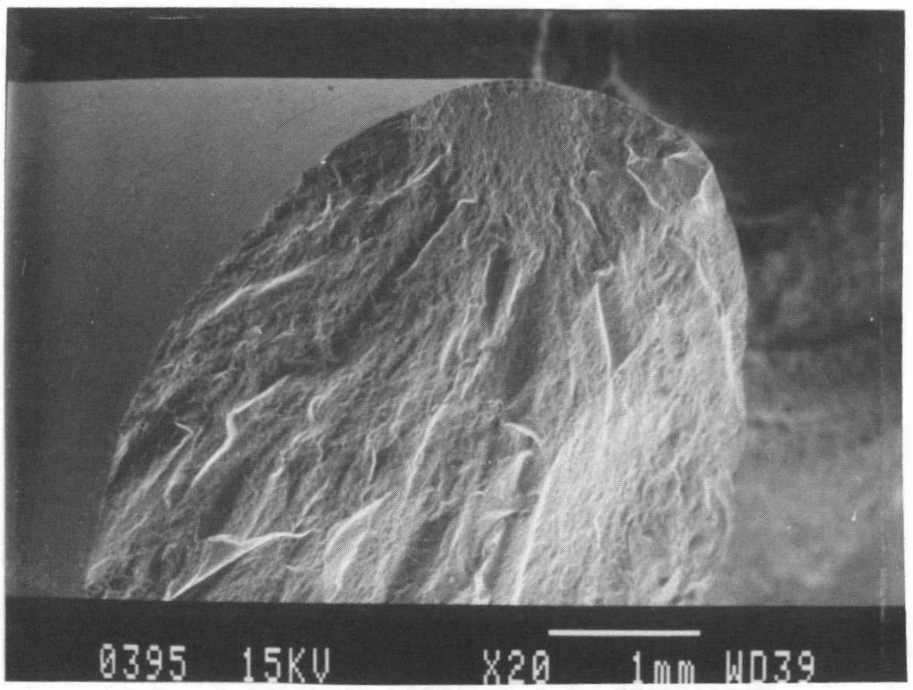

(a) at 20X

Figure 10. Typical fracture surface of Hexoloy SA tested in tensile stress rupture at 200 MPA (20X, 500X, and 2000X).

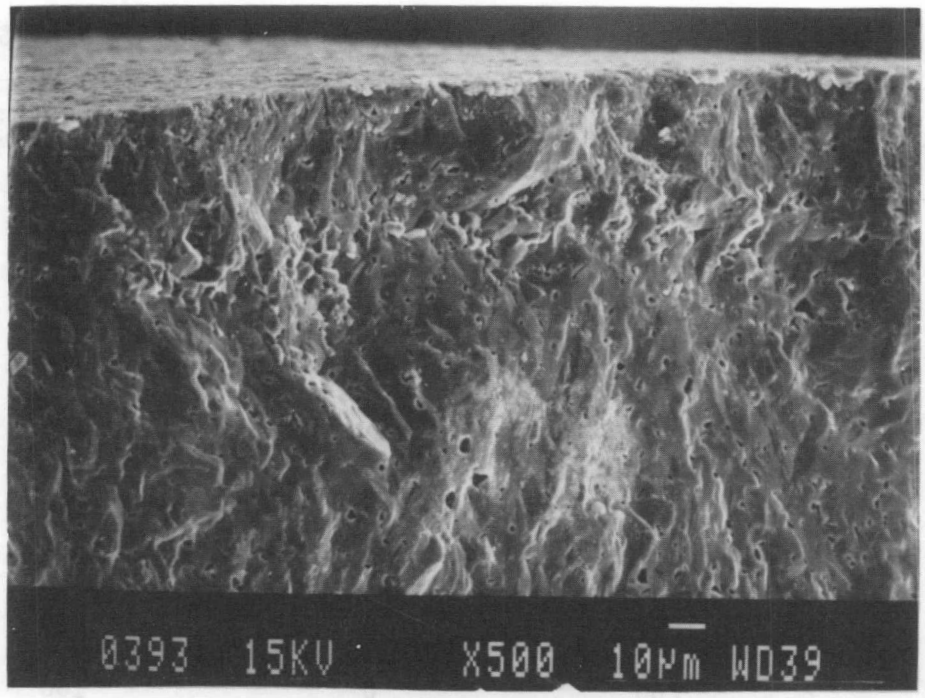

(b) at 500X

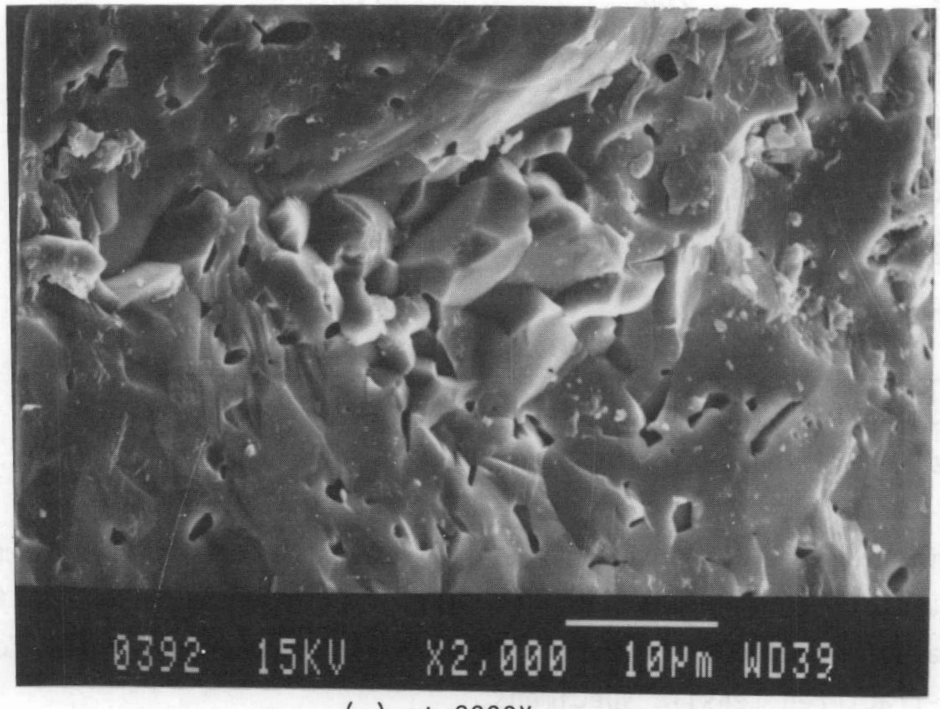

(c) at 2000X

Figure 10. Typical fracture surface of Hexoloy SA tested in tensile stress rupture at 200 MPa (20X, 500X, and 2000X) (concluded).

Table 3. Summary of Tensile Stress Rupture Tests for Hexoloy SA

Test No.	Initial Stress (MPa)	Time to Failure (hr.)	Stress at[+] Failure (MPa)
1	168.5	120	275[+]
2	168.5	100	316[+]
3	200	0.4	200
4	200	0	189[*]
5	200	101	325[+]
6	200	0	200
7	200	0	200
8	200	0	166[*]
9	200	27.3	200
10	250	0	250
11	250	0	236[*]
12	250	0	232[*]
13	250	0.003	250
14	300	0.008	300

[+]Specimen fast-loaded to failure after surviving 100 hours.
[*]Specimen failed during loading before reaching initial stress.

examinations it was observed that all the specimens failed from flaws located at, or very near, the surface. The topography of the fracture surfaces appeared to be very similar to the topography found for the fast-fractured tensile specimens.

Multimodal time-to-failure distribution may also be occurring in the Hexoloy SA subjected to tensile stress rupture (see Figure 9). However, the data are very limited, and it is premature to draw a conclusion about the failure mode for this material. Polished cross sections were prepared from the gage section (parallel to the stress axis) and the buttonhead of a Hexoloy SA tensile stress rupture specimen tested at 1400°C at a stress of 168.5 MPa for 100 hours. These sections were prepared to further investigate failure mechanisms and to determine if cavity nucleation growth and coalescence were occurring. Micrographs of the two polished sections (gage and buttonhead) are presented in Figure 11a and b. As shown in Figure 11(a and b), the density of cavities observed in the stressed (gage) and the unstressed (buttonhead) sections were the same (~6%). Cavity density in the two polished sections was determined by image analyzer to be equivalent. These observations would suggest that cavity generation and coalescence are not occurring in the Hexoloy SA during static fatigue.

It was interesting to note that the specimens which survived the 100-hour exposure time fractured at stress levels higher than the fast-fractured tensile strength measured at 1400°C. It is believed that the improved tensile strength is due to some strengthening mechanism which occurs as a result of the tensile stress and temperature exposure of the specimen in air for 100 hours (surface flaw healing, etc.).

Thermal Aging Studies

A study to investigate the effects of thermal aging in air on the flexural strength of Hexoloy SA, GTE PY6, and NT-154 was completed during this reporting period. The results of the flexural strength measurements for the Hexoloy SA specimens are presented in Table 4. Similarly, the flexural strength measurements for the PY6 aged specimens are presented in Table 5. The results of the flexural strength measurements for the NT-154 aged specimens are presented in Table 6.

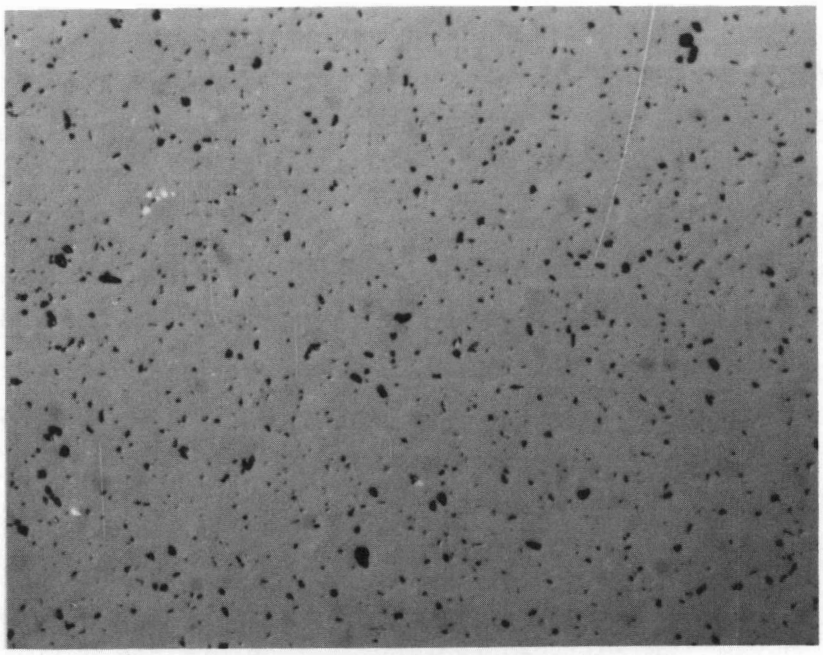

(a) Buttonhead

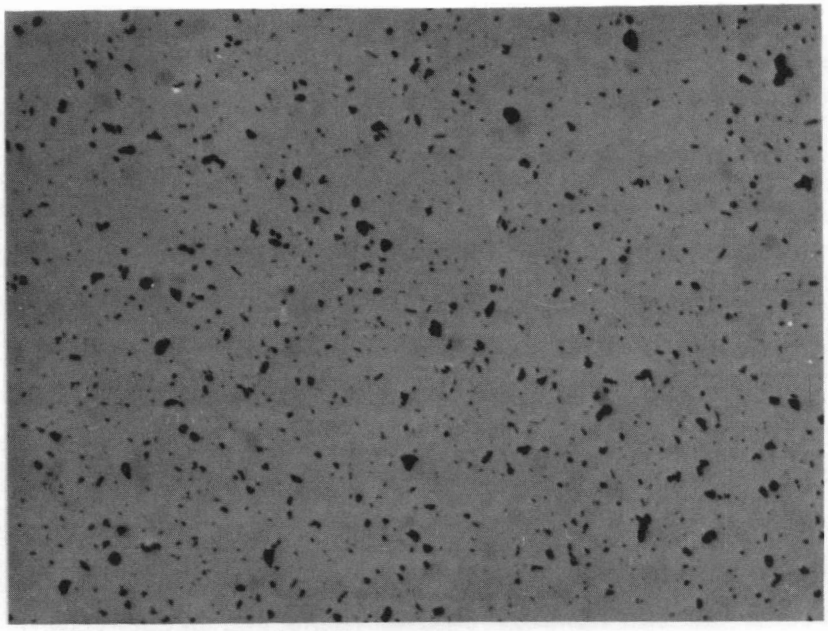

(b) 1400°C; 316 MPa after 100 hours at 169 MPa

Figure 11. Polished sections of Hexoloy SA tested in tensile stress rupture under 168.5 MPa.

Table 4. Flexural Strength Measured for Hexoloy SA Aged in Air at 1300°C

Aging Times (hrs.)	Test Temperature (°C)	Flexural Strength (MPa)	Standard Deviation (MPa)
50	1000	417	71
100	20	511	39
100	1300	419	47
500	20	462	14
500	1300	423	83
1000	20	489	32
1000	1300	416	42
As-Received	20	402	52

Table 5. Flexural Strength Measured for GTE's PY6 Aged in Air at 1300°C

Aging Times (hrs.)	Test Temperature (°C)	Flexural Strength (MPa)	Standard Deviation (MPa)
50	1000	864	89
100	20	571	87
100	1300	563	110
500	20	488	132
500	1300	624	72
1000	20	485	81
1000	1300	606	66
As-Received	20	863	86

Table 6. Flexural Strength Measured for NT-154 at 20°C

Aging Temp. (°C)	Aging Time (hrs.)	Flexural Strength (MPa) Crosshead Speed 0.004 cm/s	(Std. Dev.)	0.00004 cm/s	(Std. Dev.)
1000	50	1067	(74)	1051	(53)
1400	5	906	(31)	815	(63)
As-Received	-	907	(79)	749	(51)

The effects of the thermal aging on the flexural strength behavior of Hexoloy SA, GTE's PY6, and NT-154 are shown graphically in Figures 12, 13, and 14, respectively. As shown in Figure 12, the flexural strength of Hexoloy SA aged at 1300°C in air for 100, 500, and 1000 hours and measured at 1300°C did not vary from the unaged flexural strength (402 to 423 MPa). However, the flexural strength of Hexoloy SA aged at 1300°C and measured at 20°C showed an average improvement of 20% over the flexural strength of the unaged Hexoloy SA. The Hexoloy SA specimens aged at 1000°C for 50 hours had measured flexural strengths that were the same as the unaged material. The improved strength for the Hexoloy SA specimens aged at 1300°C and measured at 20°C is believed to be due to flaw healing effects.

As shown in Figure 13, PY6 displays a different behavior than that found for the Hexoloy SA. After thermal aging for 100 hours at 1300°C, the strength decreased about 35% for both the 20°C and 1300°C measured values. After thermal aging for 500 and 1000 hours at 1300°C the flexural strength measured at 20°C decreased an additional 10%. However, the flexural strength of the 500- and 1000-hour aged PY6 measured at 1300°C was about 5% higher than the strength measured after 100 hours aging. The higher strength values measured at 1300°C are believed due to healing of the cracks which form in the oxide surface film on cooling after thermal aging. Flexural strength of the PY6 specimens aged for 50 hours at 1000°C was the same as the flexural strength of the unaged (as-received) material.

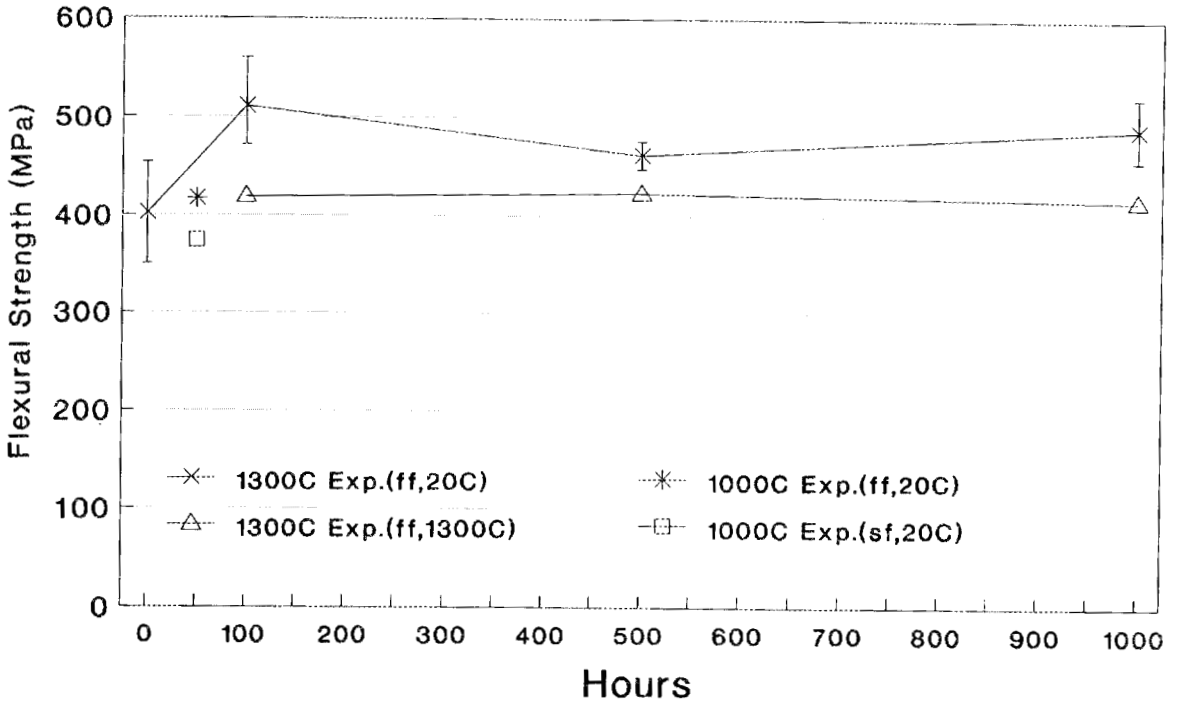

Figure 12. The effect of thermal aging on the flexural strength of Carborundum Hexoloy SA.

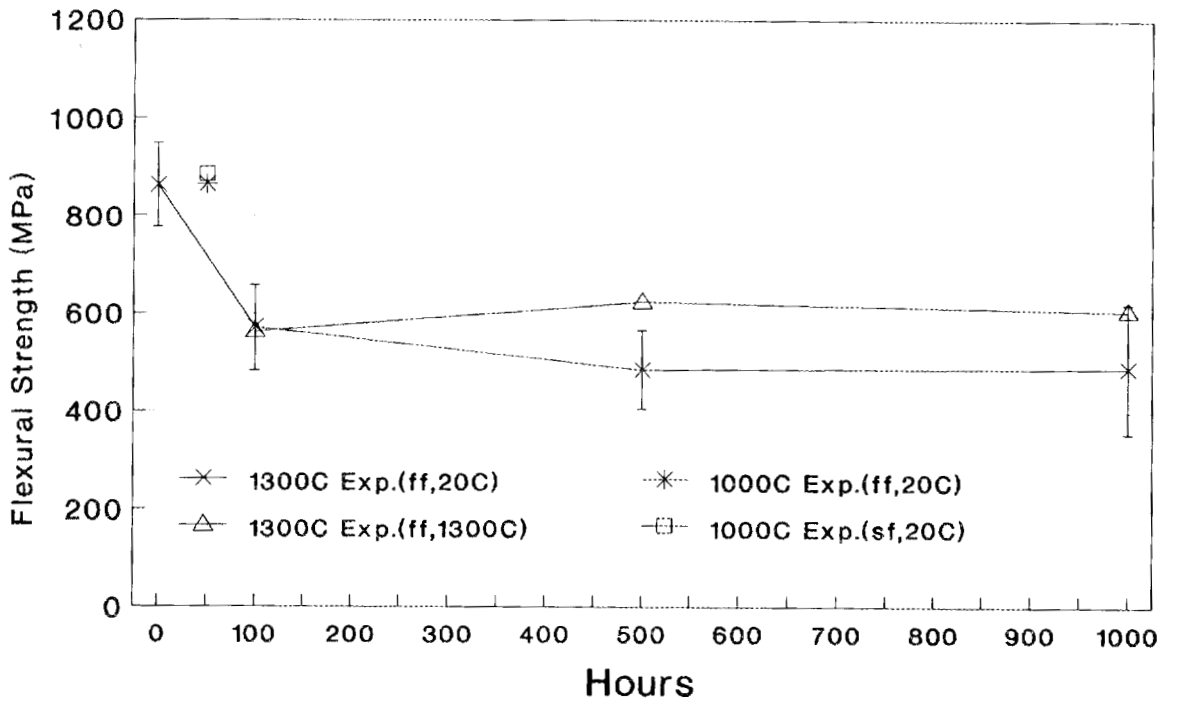

Figure 13. The effect of thermal aging on the flexural strength of GTE PY6.

As shown in Figure 14, the thermal aging of NT-154 at 1000°C for 50 hours resulted in an increase in flexural strength (18%). Thermal aging at 1400°C for 5 hours did not appear to affect the flexural strength of NT-154. It was interesting to note that the 1000°C thermal aging improved the strength of NT-154 but not the strength of PY6. Since the only known difference between the two materials is that NT-154 has a 4% Y_2O_3 sintering aid, and PY6 has a 6% Y_2O_3 sintering aid, it is difficult to explain these results.

Dynamic Fatigue Studies of Three Si_3N_4 Ceramics

During a previous reporting period, the flexural strength of five NT-154 specimens was measured at 20°C using the slow loading rate (0.00004 cm/s crosshead speed). The results of these measurements suggested the susceptibility of NT-154 to slow crack growth at 20°C ($n \sim 25$). To further evaluate this possible slow crack growth behavior in NT-154 at 20°C the flexural strength of five additional specimens was measured at the slow loading rate. The results of these measurements, combined with the earlier slow fracture measurements and the fast fracture measurements, are presented in Table 7. A ln-ln plot of strength versus loading rate is presented in Figure 15. The slow crack growth parameter n calculated from the ln-ln plot is 26. These results (Batch #3) reconfirm the earlier results (Batch #2) indicating slow crack growth susceptibility of NT-154 at 20°C.

Table 7. Flexural Strength Measurements of NT-154 at 20°C.

Batch #	Crosshead Speed cm/s	Flexural Strength	Std. Dev. (MPa)
1	0.004	907	79
2	0.00004	749	51
3	0.00004	769	95

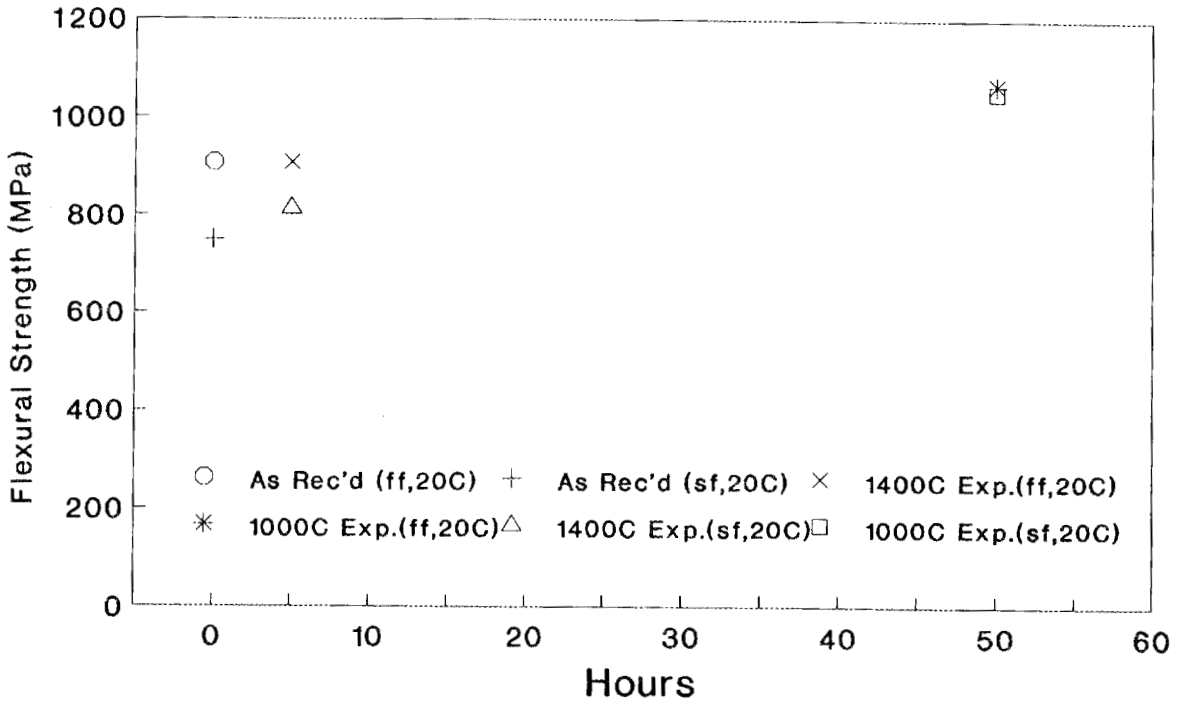

Figure 14. The effect of thermal aging on the flexural strength of Norton/TRW NT-154.

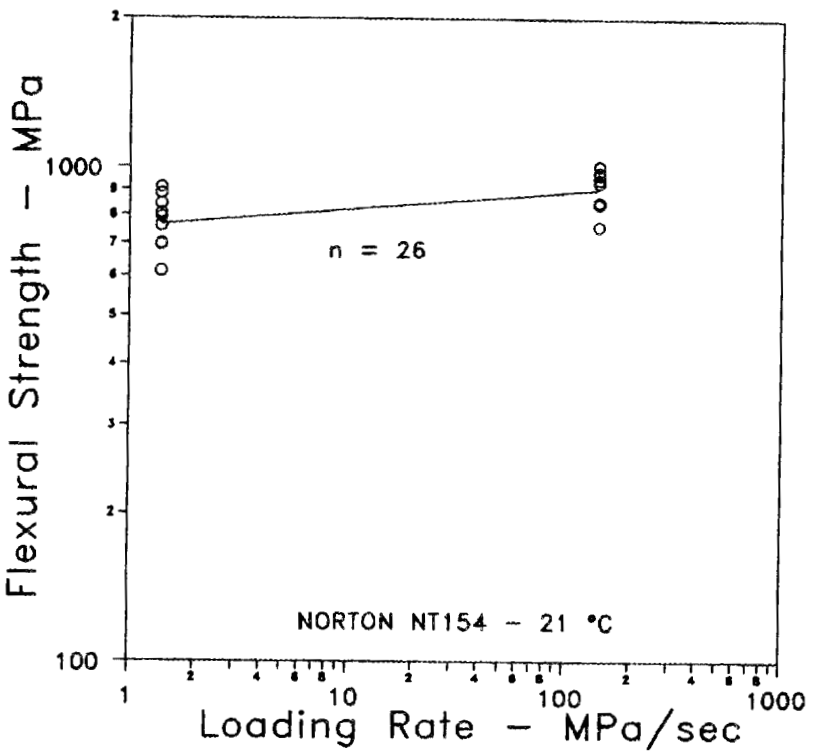

Figure 15. Ln-Ln plot of strength versus loading rate for NT-154 at 21°C.

The effect of loading rate on the room temperature flexural strength of two additional Si_3N_4 ceramics (PY6 and EC-152) was also investigated as a result of the data obtained for NT-154.

The flexural strength of NTK's EC-152 test specimens was measured following MIL-STD 1942 at 21°C (room temperature) using two different loading rates, 0.004 and 0.00004 cm/sec crosshead speeds. The results of these measurements are presented in Table 8. As shown in Table 8, the average fast loading flexural strength, 823 MPa, was higher than the slow loading flexural strength, 790 MPa. However, the difference cannot be considered significant, recognizing that the standard deviation for each loading condition was in excess of 100 MPa for the loading rate differential employed.

Table 8. Room Temperature Flexural Strength Measurements for NTK EC-152

Temperature (°C)	Crosshead Speed (cm/s)	Flexural Strength (MPa)	Standard Deviation (MPa)
20	.004	823	170
20	.00004	790	127

The flexural strength of GTE's PY6 test specimens was also measured at 21°C using the slow loading rate, 0.0004 cm/s crosshead speed. The rapid loading rate (0.004 cm/s) flexural strength for PY6 was measured earlier in this project. The results of the slow-loading-rate flexural-strength measurements are presented in Table 9. As shown in Table 9, the average slow-loading flexural strength measured for PY6 was 826 MPa with a standard deviation of 47 MPa. The average fast-loading flexural strength previously measured for PY6 at room temperature was 863 MPa with a standard deviation of 86 MPa. As with EC-152 the PY6 material had a higher average fast-loading flexural strength than the average slow-loading flexural strength; however, the difference does not appear significant.

Table 9. Room Temperature Flexural Strength Measurements for GTE PY6

Temperature (°C)	Crosshead Speed (cm/s)	Flexural Strength (MPa)	Standard Deviation (MPa)
20	.004	863	86
20	.00004	826	47

Fracture Toughness of NT-154

The fracture toughness of NT-154 is being investigated at 20°C, 1200°C, and 1400°C by the controlled surface flaw method. A Zwick hardness testing machine is used for putting a series of Vickers indents on the tensile surface of polished [MIL-STD 1942(MR) size B] flexural specimens. Indent loads of 1 to 500N were used to investigate R-curve behavior at the selected temperatures using a load displacement rate of 2.54 mm/min. The results of the fracture stress measured versus indentation load are plotted on a log-log graph in Figure 16. The slopes for the strength versus indent load plots at 20°C, 1200°C, and 1400°C are minus 0.25, 0.20, and 0.14, respectively. In the case of flat R-curve behavior the slope of the log strength versus log indent would be minus 1/3. For comparison purposes a minus 1/3 slope is included in Figure 16. This R-curve behavior can be better seen by plotting the calculated fracture resistance (K_R) versus crack length (C). This plot was prepared for the data collected at 20°C and is presented in Figure 17. As seen in Figure 17, NT-154 displays classic R-curve behavior at 20°C and readily explains the difference in K_{Ic} measured at UDRI and Norton/TRW reported in a previous progress report.

The results of the fracture toughness measurements have raised several questions that need to be further addressed:

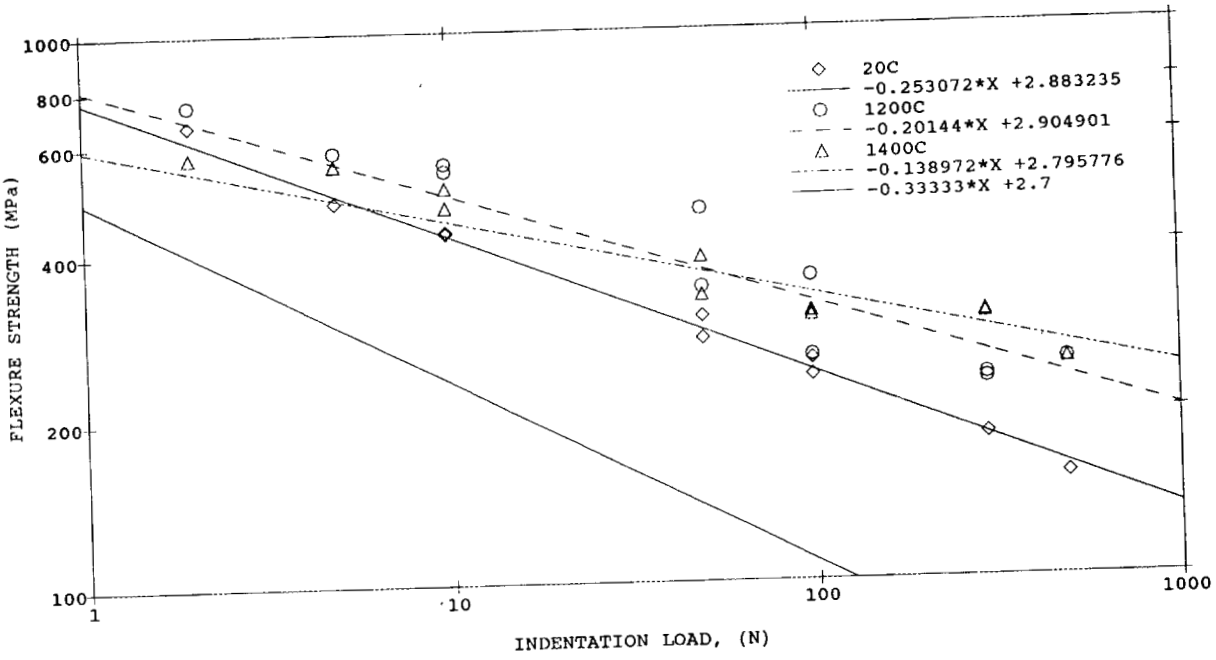

Figure 16. Log-log graph of strength versus indentation load for NT-154.

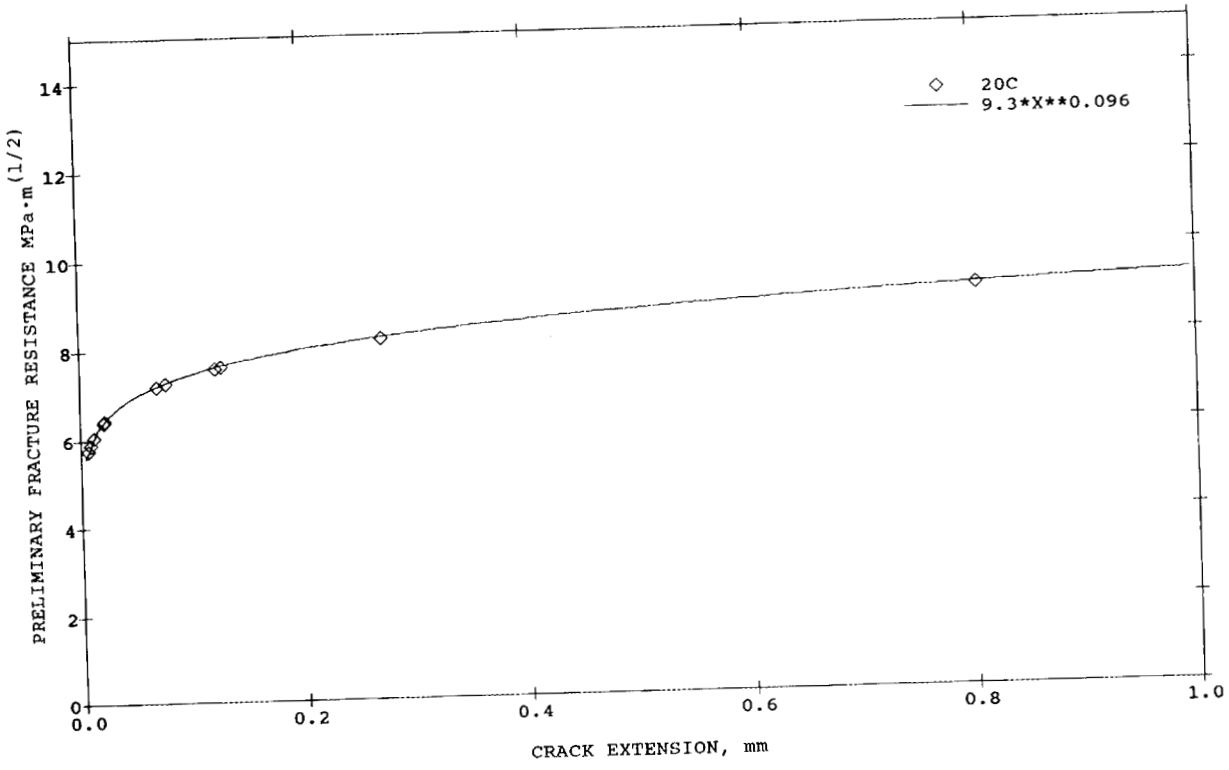

Figure 17. Fracture resistance as a function of crack extension of Norton/TRW NT-154 by controlled surface flaw at 20°C.

a) the effect of loading rate on R-curve behavior,

b) the most appropriate means to measure crack length for high-temperature measurements, and

c) the role of residual stresses from the indent on high-temperature fracture toughness values.

Status of milestones

Milestone 331409 is in progress.

Publications

1. N. L. Hecht, D. E. McCullum, S. M. Goodrich, and L. Chuck, Mechanical Properties Characterization of High Performance Ceramics, Proceedings of the 28th Automotive Technology Development Contractors' Coordination Meeting, Dearborn, MI, October 1989. Published by SAE.

2. L. Chuck, S. M. Goodrich, N. L. Hecht, and D. E. McCullum High-Temperature Tensile Strength and Tensile Stress Rupture Behavior of Norton/TRW NT-154 Silicon Nitride, Proceedings of the 14th Annual Conference on Composites and Advanced Ceramic Materials, Cocoa Beach, FL, January 1990. Published by the American Ceramic Society.

References

1. S. M. Wiederhorn, "A Probabilistic Framework for Structural Ceramics, Fracture Mechanics of Ceramics, Volume 5, edited by R. C. Bradt, A. G. Evans, D. P. H. Hasselman, F. F. Lange, Plenum Press, New York, 197-226, 1983.

2. G. Quinn, "Static Fatigue of a Sintered Silicon Nitride," U.S. Army MTL TR 84-40, Watertown, MA, 1984.

3. G. Grathwohl, "Creep and Fracture of Hot Pressed Silicon Nitride with Natural and Artificial Flaws," edited by B. Wilshire and D. R. J. Owens, Proceedings of the Second International Conference on the Creep and Fracture of Engineering Materials and Structures, Pineridge, Swansea, U.K., 565-577, April 1984.

Low Heat Rejection Diesel Coupon Test

C. R. Brinkman, R. L. Graves, B. H. West, and K. C. Liu (Oak Ridge National Laboratory)

Objective/scope

The objective of this task is to expose various structural ceramics to conditions found in small diesel engines. Commercially available ceramics, as well as new candidate monolithic and whisker-toughened ceramics, will be fabricated into small MOR bars, nondestructively examined, and exposed to a variety of operating conditions within small diesel engines. Subsequent to exposure, the bars will be nondestructively and destructively examined and the results compared to an unexposed data base.

Technical progress

Silicon nitride (Norton NT-154)

A block of silicon nitride was received and 120 MOR bar specimens were fabricated. Details of specimen geometry have been reported elsewhere.[1,2] The intent of this effort is to expose bars for 100 h in either a single- or two-cylinder engine, and to subsequently subject them to either room- or elevated-temperature four-point bend rupture testing. Rupture strengths were then compared to values obtained from unexposed bars. To date 28 bars have been exposed in either the single- or two-cylinder engine and subsequently ruptured at room temperature. Results of these tests are given in Table 1. Rupture strength comparisons given in Table 1 show no decrease in rupture strength due to engine exposure when the postexposure test temperature was approximately 25°C.

Currently, the two-cylinder engine is down for repairs. Apparently, one of the bars came loose from the grip fixture and damaged the interior of one of the cylinders. Following engine repairs, exposure of a number of bars will be continued for subsequent rupture testing at elevated temperatures.

New materials

A silicon carbide plate (1.6 x 7.6 x 17.8 cm (0.63 x 3 x 7 in.)) designated Hexaloy SA SiC was received from Carborundum Company. Approximately 150 bars have been fabricated and are currently being inspected. An alumina plate containing SiC whiskers designated "PAD" AS34W is currently on order.

References

1. C. R. Brinkman et al., "Influence of Diesel Engine Combustion on the Rupture Strength of Partially Stabilized Zirconia," *Am. Ceram. Soc. Bull.* **68**(8), 1440-45 (August 1989).

2. C. R. Brinkman et al., *Influence of Diesel Engine Exposure on the Rupture Strength of Silicon Nitride and Partially Stabilized Zirconia*, ORNL-6612, April 1990.

Table 1. Room-temperature four-point bend rupture strengths for engine-exposed and unexposed Norton NT-154 silicon nitride

No.	Exposure condition[a]	Number of specimens	Average rupture strength	Standard deviation (MPa)
1	None	40	771	80
2	Single-cylinder engine	8	836	72
3	Two-cylinder engine	20	828	67
4	Combined (single- and two-cylinder)	28	830	67

Weibull summary

	Linear regression		Maximum likelihood	
	Weibull modulus	Intercept	Weibull modulus	Intercept
1	11.6	-77.9	11.8	-78.7
2	13.6	-92.1	12.8	-86.8
3	14.9	-100.3	15.4	-103.8
4	15.0	-101.6	14.2	-96.1

[a]Engine exposure consisted of 100 h in the combustion chamber of the indicated engine. The engines were run for approximately 8 h/day.

3.4 FRACTURE MECHANICS

TESTING AND EVALUATION OF ADVANCED CERAMICS AT HIGH TEMPERATURE IN UNIAXIAL TENSION

J. Sankar, A. D. Kelkar, V. S. Avva, and Jun Gao (Department of Mechanical Engineering, North Carolina A & T State University, Greensboro, North Carolina 27411)

Objective/Scope

The purpose of this effort will be test and evaluate advanced ceramic materials at temperatures up to 1500 ^{o}C in uniaxial tension. Testing may include fast fracture strengths, stepped static fatigue strength along with analysis of fracture surfaces by scanning electron microscope. This effort will comprise of the following tasks:

Task 1. Specifications for Testing Machine and controls + (procurement)
Task 2. Identification of Test Material (s) + (procurement of specimens)
Task 3. Identification of Test specimen configuration
Task 4. Specifications for Testing grips and Extensometer + (Procurement)
Task 5. Specifications for Testing Furnace (Procurement) and controls
Task 6. Development of Test Plan
Task 7. High Temperature Tensile Testing
Task 8. Reporting (Periodic)
Task 9. Final Report

It is anticipated that this program will help in understanding the behavior of Ceramic materials at very high temperatures in uniaxial tension.

Technical Progress

During the reporting period, efforts were undertaken to develop an inhouse testing program for the creep test, which can be run on the Micro-PDP/11 computer attached to the MTS 880 Testing machine. Creep testing using the inhouse program were conducted on five SNW-1000 (Si_3N_4) specimens. For all tests the test temperature was 1200 deg.C. During the test, a deflection (elongation) versus time curve was plotted. A set of platinum flags attached to the sample along with Zygo laser system were used to measure the deflection. Figure 1 shows the deflection versus time for creep test for one of the specimens. Figure 2 shows the corresponding strains versus time for the five specimens tested. The results of the test are compiled and are given in Table 1. Figures 3 through 5 show the polished and unetched microstructure of the

creep tested specimen 1 near the edge of the circular cross section, 2 mm away from the fracture surface. It is observed that the pores are larger in size than the average pore sizes in specimens tested in tension at various temperatures previously. Further, from these photographs it can be observed that there is a strong possibility for the linkage of pores during creep testing. More work is planned to be done in this area to understand clearly this phenomenon. It may be further observed that the edges of the pores are softening and the fissures are advancing beyond the pores into the specimen (Figure 4 and 5).

Figures 6 and 7 show the images of the fracture surfaces of the same specimen. Figure 6 shows the general fracture appearance and figure 7, the fracture surface under high magnification. This indicates a failures process somewhat different from that of the pure tension failure in these samples at high temperatures. This again might be due to the softening of the grains.

Detailed studies of the microstructure and fracture surfaces of the specimens are currently underway.

Status of Milestone

Tasks 1-7 are complete.

Communications/Visitors/Travel

Dr. Sankar and Dr. Kelkar attended Twenty-Seventh Automotive Technology Development Contractors' Coordination Meeting on October 23-26, 1989 at Dearborn, Michigan

Problems Encountered

None

Publications & Presentations

None

Table 1. The results of the creep test, SNW-1000, 1200 deg. C

Specimen	Load (N)	Stress (MPa)	Duration of test (hours)	Strain Rate (1/s) (2nd stage)
1	1625	57 ($0.25\sigma_f$)	175 did not broke	5.5E-10
2	2600	92 ($0.4\sigma_f$)	560 did not broke	2.4E-9
3	3223	115 ($0.5\sigma_f$)	prograssing at current time	/
4	3858	138 ($0.6\sigma_f$)	306 broke at gage section	1.7E-8
5	4492	161 ($0.7\sigma_f$)	58.5 broke at gage section	5.4E-8

(note: σ_f is the tensile fracture stress at 1200 deg. C)

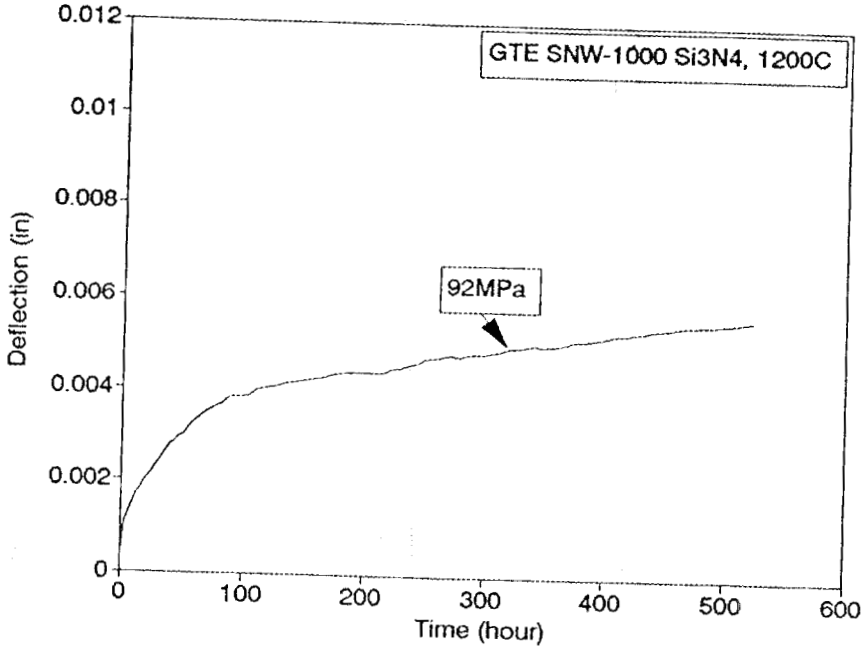

Figure 1. Deflection - time for one of the samples

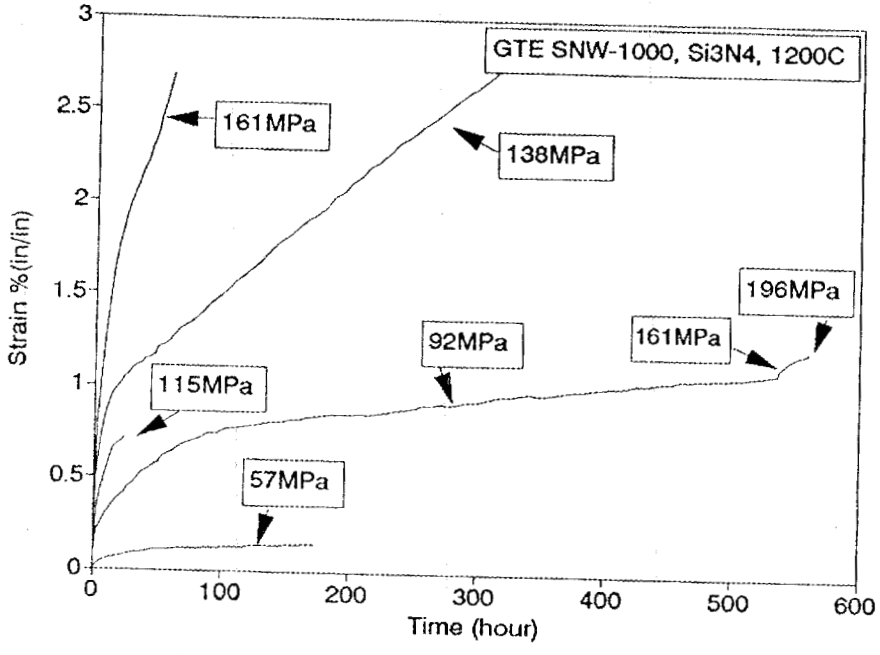

Figure 2, strains - time for the creep tests, 1200C

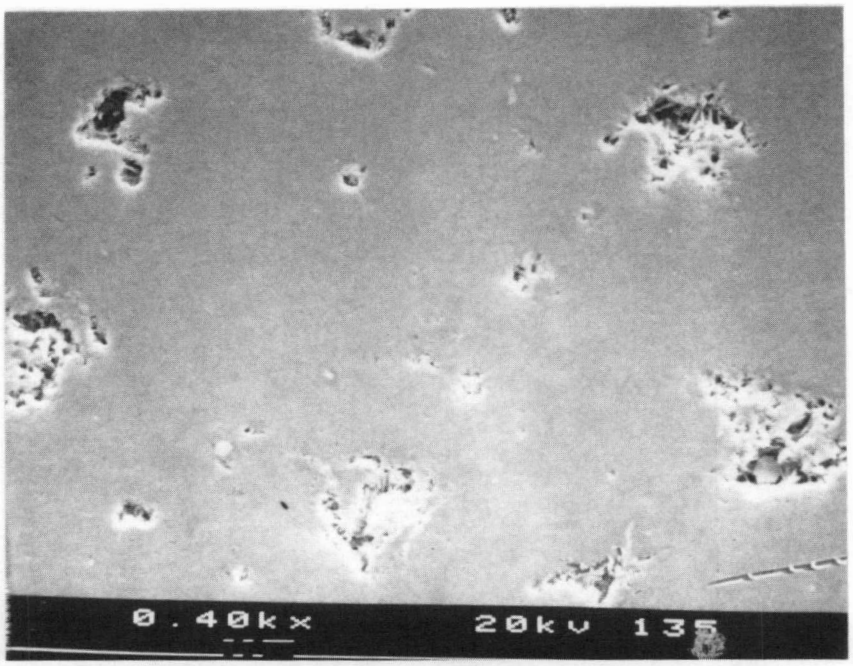

Figure 3. SEM micrograph near the edge of the gage cross-section (polished sample - creep tested)

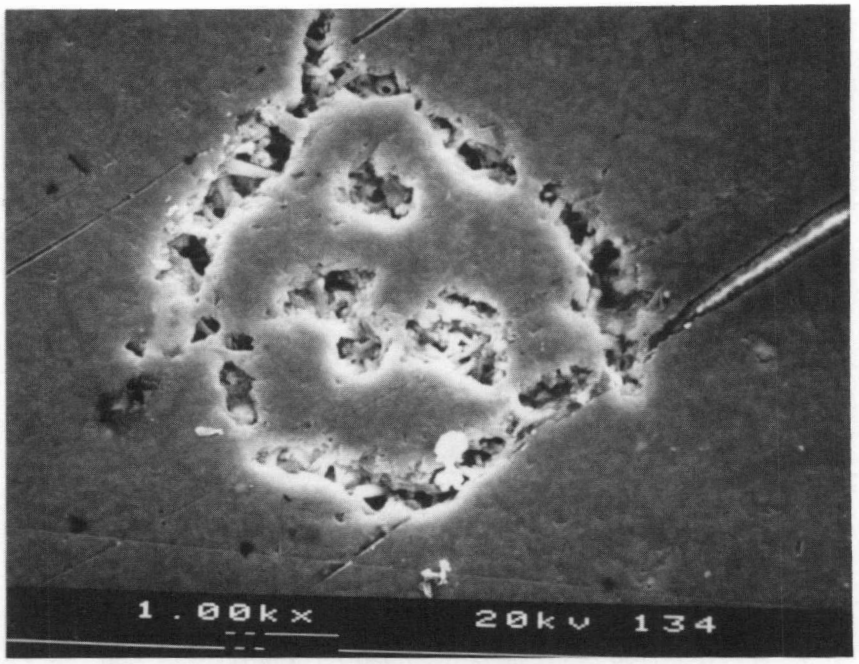

Figure 4. SEM micrograph showing a pore observed in the central area of the cross-section (same sample as in Fig 3)

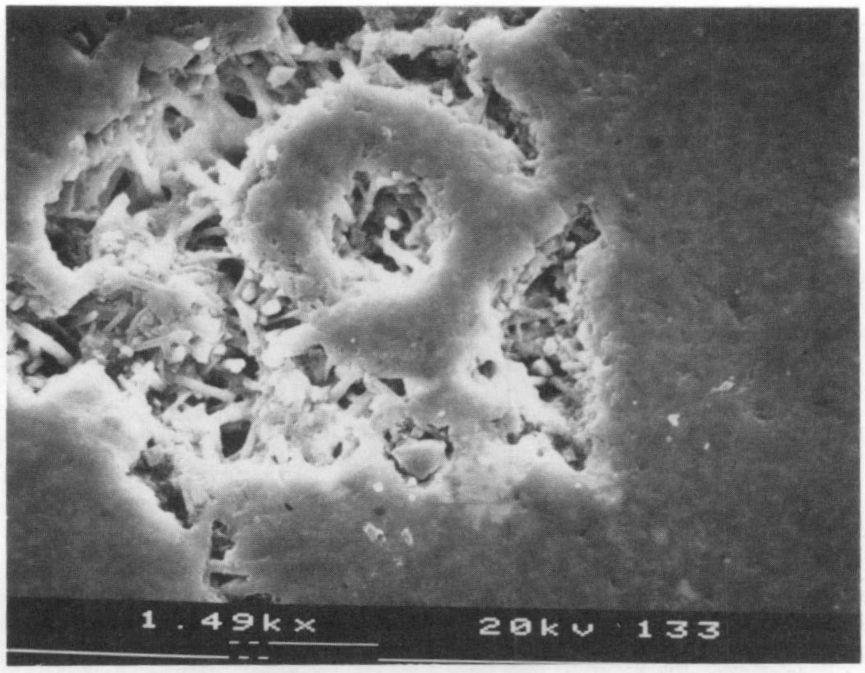

Figure 5. High magnification image of Fig 4

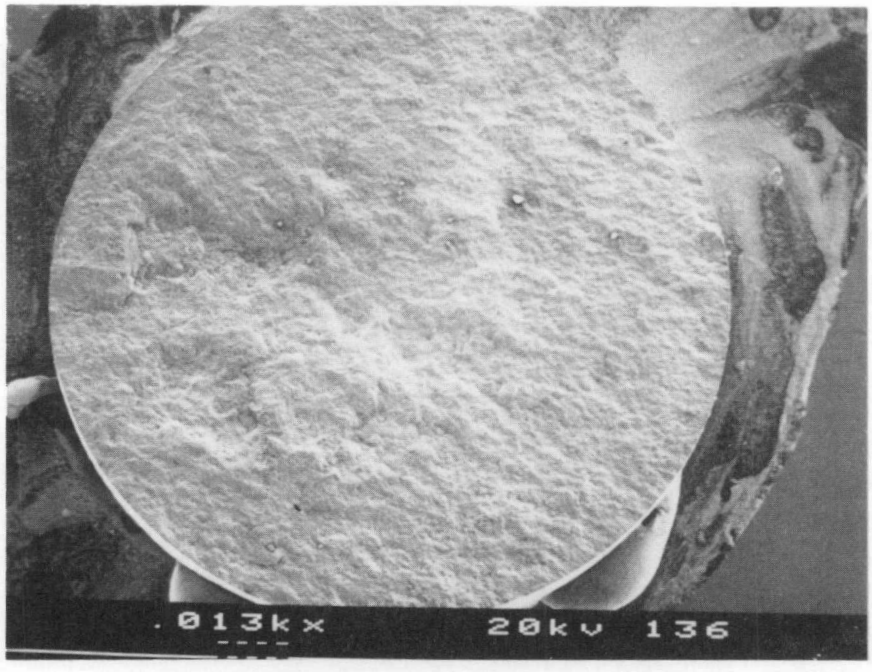

Figure 6. SEM micrograph of the general fracture appearance of the specimen (creep tested)

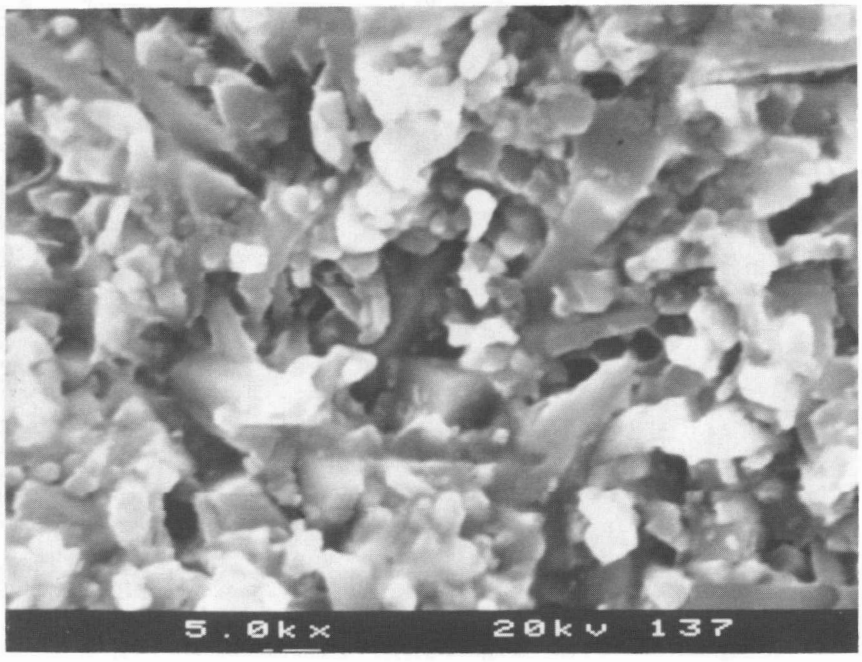

Figure 7. Fracture surface of the sample in Fig 6

Standard Tensile Test Development

S. M. Wiederhorn, D. Cranmer, D. Kauffman and D. E. Roberts
(The National Institute of Standards and Technology)

Objective/Scope:

This project is concerned with the development of test equipment and test procedures for measuring the tensile strength and creep resistance of ceramic materials at elevated temperatures. Inexpensive techniques of measuring the creep behavior and strength of structural ceramics are being developed and will be used to characterize the mechanical behavior of these materials. The test methods will use self aligning fixtures, and simple grinding techniques for specimen preparation. Creep data obtained with tensile test techniques will be compared with data obtained using flexure and compressive creep techniques. The ultimate goal of the project is to assist in the development of a data base and a test methodology for the structural design of heat engines for vehicular applications.

Technical highlights

During the past six months, the creep and creep rupture behavior of HIP-ed silicon nitride was studied as a function of applied tensile stress and temperature. Two commercial grades of material are being investigated: Norton/TRW NT154, and Allied-Signal GN10. The creep and creep rupture behavior of these materials are being characterized in tension and compression and a data base is being obtained to compare materials manufactured by different companies. This report presents data collected on the NT154. As studies have just been initiated on the GN10, data on this material will be discussed at a later date.

Experimental Technique - Dog-bone specimens, figure 1, developed as part of our tensile creep program were used in this study. To assure that failure of the test specimens occurred within the gauge section, the central section of the specimen was reduced by surface grinding with a 38 mm diameter grinding wheel. After grinding, the total thickness of the gauge section was ≈2mm. The width and length of the gauge sections were approximately 2.5mm and 10mm respectively.

Creep tests were conducted using the tensile equipment developed in an earlier phase of the project. The gauge length of the test specimen was monitored by placing small α-SiC flags on the central portion of the test specimen. The position of the flags were monitored as a function of time with a laser extensometer, which was capable of an accuracy of better than ±1μm in the measurement of distance between the two flags. This level of accuracy resulted in an precision of ±2μm in the displacement measurements during the evaluation of creep curves for each specimen. Details of the experimental apparatus were published during the current period (D.F. Carroll, S.M. Wiederhorn and D.E. Roberts, "A Technique for Tensile Creep Testing of Ceramics," J. Am. Ceram. Soc. 72[9], 1610-1614 (1989)).

In these studies, the test temperature ranged from 1300°C to 1400°C. Tests were conducted in air, with a short ≈24 hour anneal to assure thermal equilibrium within the test furnace prior to application of the stress. Most studies to date were conducted on the NT154, which is a HIP-ed grade of Si_3N_4 using Y_2O_3 as a sintering aid. The billets used were made specifically for this study, and do not relate to billets used on other parts of the DOE heat engine program. As transient effects were observed in the creep of the NT154, long-term creep measurements were conducted on two of the specimens to clarify the effect of time at temperature on the creep rate. Other specimens were loaded to a level that rupture occurred within a relatively short time,

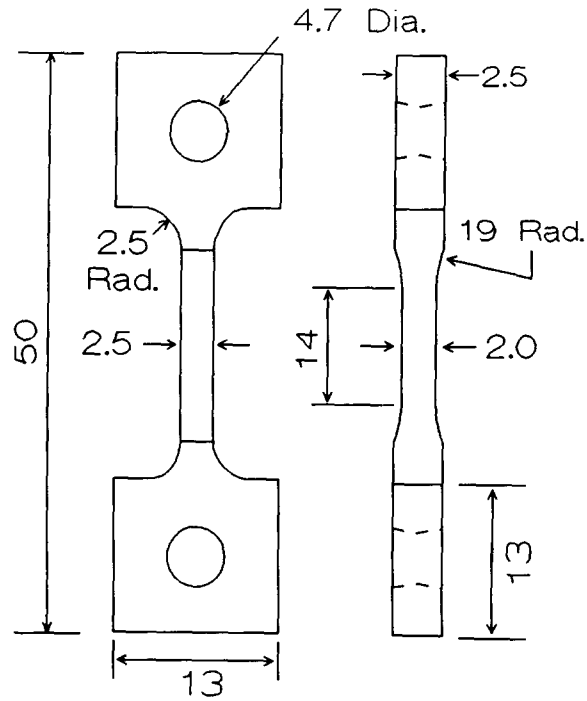

1. Specimen configuration. All dimensions are in mm. Note the double reduction in specimen gauge section. Also, the holes are tapered at an angle of ≈15°.

<250 hr. Data were then expressed in terms of a Monkman-Grant curve in which the creep rate was plotted as a function of the time to failure.

Results and Discussion - Initial tests on the NT154 indicated long term transient creep behavior for this materials. As illustrated in figure 2, in which transient creep was observed for the full 1100 hr test period, transient creep can last for extended periods in NT154. To further study transient creep, a specimen of NT154 loaded at 100 MPa was crept at a series of temperatures, ranging from 1300°C to 1400°C. The sequence of temperatures and the creep behavior at these temperatures is shown in figure 3a. The specimen was held at temperature until the creep curve appeared to approach steady state; then the next temperature was selected. Temperatures were not taken in increasing sequence; sometimes the temperature was increased between runs, sometimes the temperature was decreased. Transient creep for this material is very apparent when the minimum creep rate for each segment of the curve is plotted on an Arrhenius diagram, figure 3b. In figure 3b, the data points are numbered in the order in which they were taken. As can be seen, the sequence of points gradually approach a common line, which suggests that only after extensive periods of creep (≈1500 hr) does the material approximate a steady state behavior.

The long transient behavior, noted above, suggests that the microstructure of the material is slowly modified by exposure to elevated temperatures. Similar observations were made earlier on AY6 (made by GTE), in which case the increase in creep resistance of the material was attributed to devitrification of the glass phase at Si_3N_4 grain interfaces. The devitrification process was slow, and only effected the creep rate when the narrowest boundaries between the grains became devitrified. TEM studies on the material will be completed

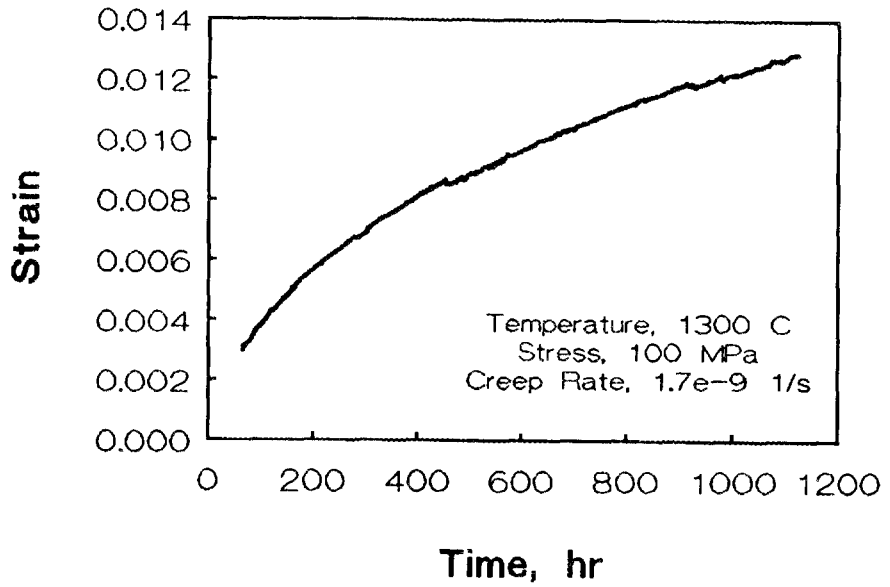

2. Extended creep curve for NT154. Note that transient creep occurs over the entire 1100 hr creep period. The minimum creep rate was determined by a least squares fit over the last 200 hr of the creep curve.

during the next 6 months to determine if the NT154 is behaving in a similar fashion.

Materials received by Dr. K. Liu at Oak Ridge National Laboratories (ORNL) exhibits the same high creep resistance as the ones that have been exposed for 1500 hr in the current tests. Also, the specimens tested by ORNL do not exhibit extensive transient creep, which suggests that the creep measurements are being affected either by minor differences in the microstructure of the two batches of materials, or by some difference in test procedure. To further study the creep process, a set of specimens are being annealed at 1350°C before being crept at high temperatures. Also, set of specimens prepared from the same billet will be tested both at ORNL and at NIST to determine if some difference in test procedure can account for the differences in creep behavior.

Because the apparent activation energy for creep, 1183 kJ/mol, is greater than the heat of formation of Si_3N_4, 744.8 kJ/mol [1], creep in this material is probably not controlled by any of the normal creep mechanisms (diffusion, climb of dislocations, etc.) used to explain the creep of ceramic materials. This high apparent activation energy may be a consequence of cavity formation in the silicon nitride, which has been reported by a number of investigators for NT154 [2, 3]. TEM studies are presently underway at NIST confirm the formation of cavities in NT154. Cavities in Si_3N_4 usually form in the glass that surrounds the Si_3N_4 grains, so the estimation of the activation energy for cavitation given here is specific for cavity formation in glass. From the work of Raj and Ashby, the activation energy for cavity formation is $16 \cdot \pi \cdot \Gamma^3 / 3 \cdot \sigma^2$, where Γ is the surface tension of the cavity, and σ is the local stress. By assuming Γ=0.3 J/m^2 (a normal value for glass at high temperature) and σ= 1 to 2 GPa (i.e. the cohesive stress of glass) an activation energy ranging from 600 to 2400 J/mol can be calculated. This range of active energies is consistent with those measured in the present experiment, tending to support our assumption that creep is a cavitation controlled process.

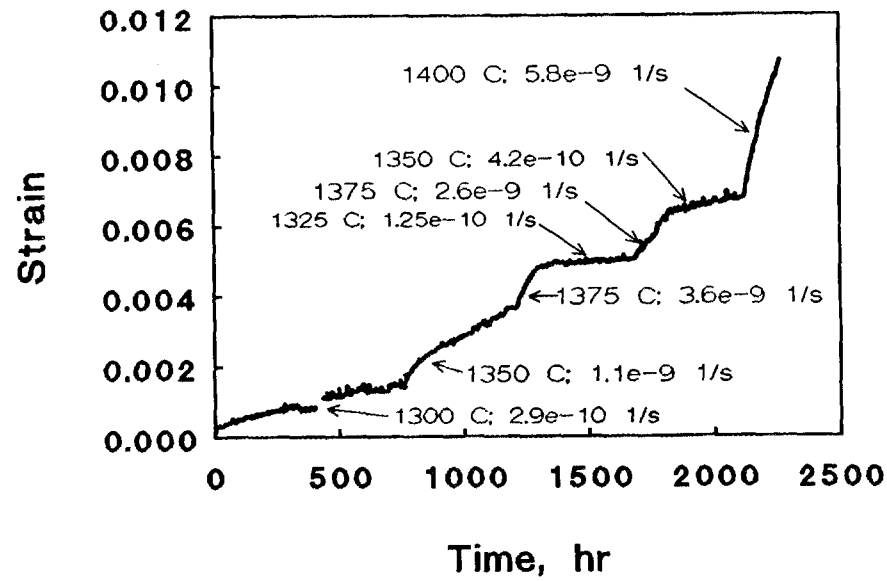

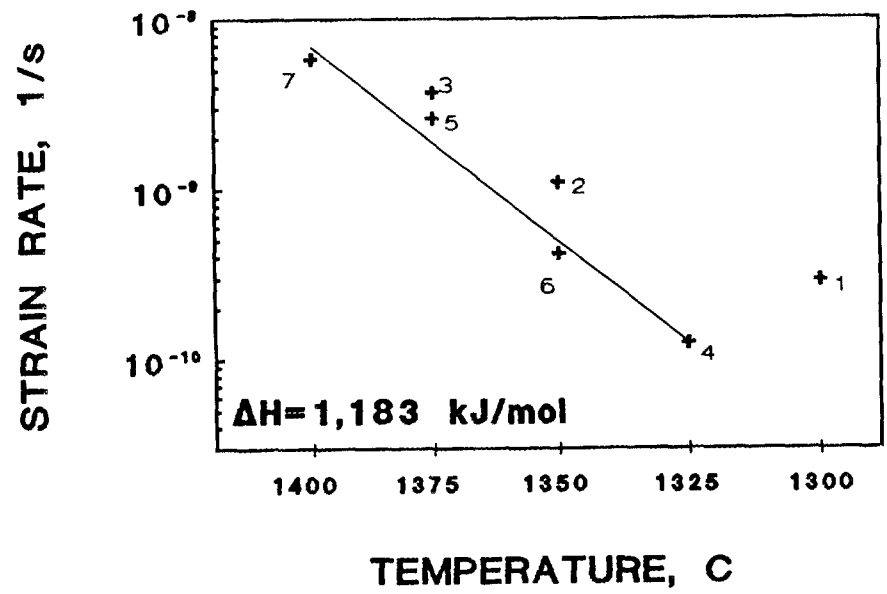

3. Effect of temperature on the creep of NT154: (a) Strain as a function of exposure time; (b) Minimum creep rate as a function of temperature. Transient creep effects are evident from the time required for the data to approach a common Arrhenius curve. Approximately 1500 hr of creep was required to approach steady state creep. Stress: 100 MPa.

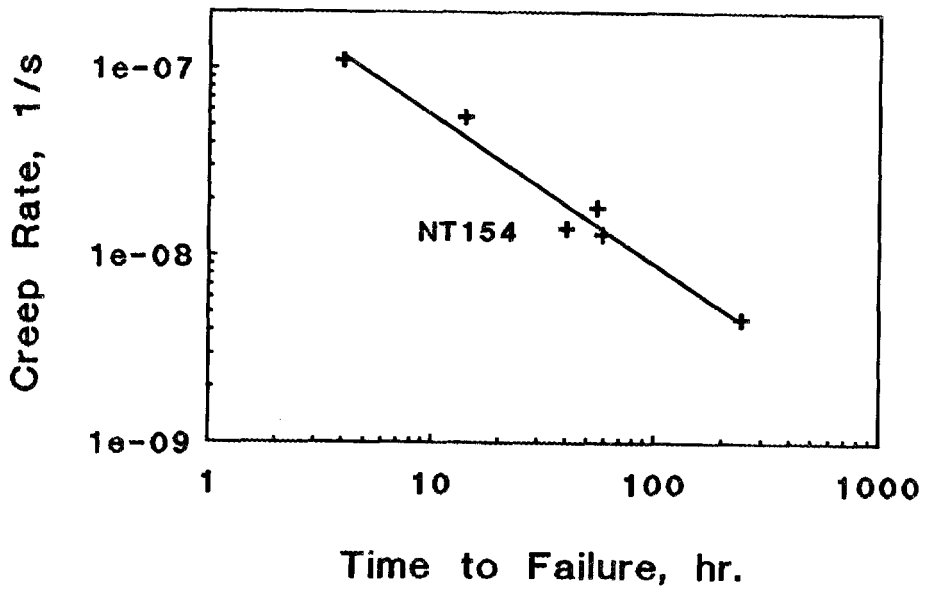

4. Creep rupture data: minimum creep rate as a function of the time to failure. Although the data set is limited, time-to-failure seems to be determined uniquely bye the rate of creep in this material, suggesting that improvement of creep rate is of paramount importance to improving lifetime.

From a practical point of view, the high apparent activation energy for creep indicates a sharp transition in the performance of this material at elevated temperatures. According to the data in figure 3, the material creeps at a rate of $\approx 1 \times 10^{-10}$ s^{-1} at 1325°C at 100 MPa, which is slow enough for a component lifetime of several years, assuming 1% strain to failure. On the same basis, the lifetime at 1400°C, is about 3 weeks. Based on other creep studies conducted at NIST on structural ceramics, the only material that has better creep behavior is α-SiC. However, this material has a lower fracture toughness ($\approx$2 MPa-$m^{\frac{1}{2}}$ for the SiC compared to $\approx$6 MPa-$m^{\frac{1}{2}}$ for the Si_3N_4), which reduces its susceptibility to thermal shock and to foreign particle damage.

To determine the susceptibility of the NT154 to stress rupture, six specimens were permitted to creep to failure. Both the time to failure and the creep rate were measured during these experiments. As can be seen in figure 4, all of the creep rupture data fall on a single curve when the creep rate is plotted as a function of the time to failure. This curve, in combination with creep curves can be used to establish stress allowables for high temperature applications. During the coming period, creep rupture data will be obtained on material that has been annealed for extended periods.

Status of Milestones

All milestones are on schedule.

Publications

1. D.F. Carroll, S.M. Wiederhorn and D.E. Roberts, "Technique for Tensile Creep Testing of Ceramics,) J. Am. Ceram. Soc. 72, 1610-14 (1989).

2. B.J. Hockey, S.M. Wiederhorn, W. Liu, J.G. Baldoni and S.-T. Baljan, "Tensile Creep of SiC Whisker Reinforced Silicon Nitride," Proceedings of the 27th Automotive Technology Development Contractors Coordination Meeting (ATD/CCM), p-230, Dearborn, MI October 23-26, 1989, pp. 251-264.

3. S.M. Wiederhorn and B.J. Hockey, "High Temperature Degradation of Structural Composites," Seventh Cimtec World Ceramics Congress, Montecatini Terme, Italy, June 24-30, 1990.

References

1. JANAF Thermochemical Tables, 2nd ed., U.S. Govt. Printing Office, Washington, DC, 1971.

2. R. Yeckley, private communication.

3. L. Chuck, private communication.

4. R. Raj and M.F. Ashby, Acta Metall., 23, 653 (1975).

5. R. Raj, Acta Metall., 26, 995 (1978).

3.5 NONDESTRUCTIVE EVALUATION DEVELOPMENT

Nondestructive Characterization
D. J. McGuire (Oak Ridge National Laboratory)

Objective/scope

The purpose of this task is to conduct nondestructive evaluation (NDE) development directed at identifying approaches for quantitative determination of conditions (including both properties and flaws) in ceramics that affect the structural performance. Those materials that have been seriously considered for application in advanced heat engines are all brittle materials with fracture affected by structural features with dimensions on the order of the dimensions of the microstructure. This work seeks to characterize those features using high-frequency ultrasonics and radiography to detect, size, and locate critical flaws and to measure nondestructively the elastic properties of the host material.

Technical progress

Ultrasonics — W. A. Simpson, Jr. and K. V. Cook

We have received and examined five silicon nitride tiles similar to those on which we have reported previously. The present samples, which will be cut up into modulus of rupture (MOR) bars, were all approximately 100 mm square and 13 to 14 mm thick. They were designated A, C, 283, 284, and 89-289-A. As before, they were fabricated by hot pressing; thus, one would not expect to find many voids larger than about 25 μm. A number of different ultrasonic tests were performed on each tile, including inspection with a 75-MHz, f/4 transducer for flaws of the order of 20 to 25 μm and larger, a back-surface echo amplitude test which is sensitive to cracks within the sample, and a high-frequency surface wave inspection which detects cracks and voids lying on or within about 120 μm of either surface. In addition, a final flaw test was performed on each tile using a 25-MHz, f/8 transducer focused near the midplane of the sample. This test was essentially an afterthought which was included for completeness but proved to be the most useful of the evaluation.

The 75-MHz flaw tests were conducted with the transducer focused about 3 mm deep in the sample, which is the maximum focal depth attainable with this unit. Using this configuration, no indications were detected within the total depth coverage of the transducer (~1 mm). All tiles were inspected from both sides. These results are consistent with those obtained on most of the earlier tiles and are characteristic of hot-pressed material.

The back-surface echo amplitude test was also performed with the 75-MHz transducer. This examination is sensitive to cracks lying anywhere within the samples, provided that they do not lie too near an edge, and to surface properties such as roughness and local changes in parallelism. It also can detect inhomogeneities such as density variations and pore clustering through changes in the effective attenuation of the material. In the present case, no cracking was detected in any of the samples, but considerable variation in the effective attenuation was indicated for all of the tiles. Most of the variation appeared to be attributable to grinding marks on the surfaces of the samples, but some of the effect was undoubtedly caused by density variations within the tiles, most of which exhibited striking visual mottling on both surfaces. Unlike previous specimens, however, there appeared to be no correlation between the ultrasonic results and the visual appearance.

The surface wave examination was performed using a 50-MHz, f/0.8 transducer which excites a radially propagating surface acoustic wave. This wave is capable of detecting voids and cracks lying on or within about 120 μm of the surface, regardless of the orientation of the latter. Experience with this transducer has indicated that it can detect extremely tight cracks such as those whose faces are held together by residual stress. Two of the current set of tiles, 284 and 89-289-A, were found to have small cracks. However, the cracks were located very near an edge, which is why they were not detected by the back-surface echo examination. The favorable location and small size of these cracks will probably not prejudice the use of these tiles since the edge zones can conveniently be removed during cutting.

A second condition, one perhaps more inimicable to the ultimate use of the tiles, was detected during the surface wave examination. All of the samples except No. A contained indications suggestive of large pores on one or both surfaces. These indications were coincident with visual white spots on the tile. A microscopic examination of these spots at 30X revealed no pores but showed what appeared to be small clusters of clear crystals approximately 1 mm in diameter. We have previously seen such crystals, which analysis proved to be silicon nitride, in a whisker-reinforced material. One of the tiles, 89-289-A, contained perhaps a score of these clusters within a 25-mm-diameter circle. For all of the affected tiles, the indications lay within a ring of visually lighter colored material near the center of the respective face.

The last examination to be applied to the tiles was, as mentioned earlier, primarily an afterthought but was the most productive in terms of locating problem areas within the samples. A flaw test was performed using a 25-MHz, f/8 transducer focused near the center of the tile. Since no flaws were found in the earlier test which interrogates down to a depth of about 3 mm, there appeared to be no a priori reason to expect flaws to occur preferentially in the center of the tile. However, the presence of possible silicon nitride crystals near the surface and our earlier experience with whisker-reinforced material suggested that we probe the central region of the current samples, even though the minimum detectable flaw size at this depth with the lower frequency transducer is perhaps 250 μm. This final flaw test revealed the presence of numerous indications in or near the midplane of each tile. The relative strength of these indications suggests a diameter of at least 375 to 500 μm for the scattering centers, if they are voids. If they are aggregates of the crystal-like material seen on the surface, they may be even larger. Tiles 283 and 284 contained the fewest midplane indications while the other three samples appeared to contain roughly equal but considerably greater numbers of indications.

We have also received and ultrasonically examined 21 silicon nitride tensile specimens. These samples are cylindrical and have a diameter of 6.4 mm in the gage section, which was the only region inspected. The evaluation was conducted using a 75-MHz, spherically focused transducer. As we have mentioned in previous reports, the sharply curved entry surface of small-diameter cylindrical specimens introduces both severe astigmatism and spherical aberration in the ultrasonic beam distribution inside the solid and limits the depth at which critical flaw sizes can be detected to a few hundred microns. Our work has indicated that this limitation could be greatly reduced by aspherical shaping of the transducer lens, but the cost of such a transducer has thus far proved prohibitive. No indications were observed in any of the specimens although we could not perform a 100% inspection on any of the rods because of equipment limitations.

A 50-MHz surface wave examination was also conducted on each sample. This evaluation is sensitive to voids and cracks lying within about one wavelength (~120 μm) of the surface and is not affected by surface curvature because of the small area of interrogation of the entry beam. As before, however, full coverage of the surface area of each specimen was not possible. No indications were detected on any of the rods.

Ultrasonically, therefore, the specimens appeared to be very homogeneous and free of voids or cracks.

We continued our studies of the possibility of using nonfocused ultrasonic waves (or at least waves which are not focused in the plane of the flaw) to detect critical flaws in ceramics at depths exceeding those accessible by conventional focused transducers. The *raison d'etre* for this work is that the time required to scan a ceramic specimen using transducers focused in or near the plane of a flaw is typically excessive for sample thicknesses of more than a millimeter or so because the volume interrogated with high sensitivity during a single pass is only a few cubic wavelengths. In order to insure detection of critical flaws at all depths in thicker materials, it is thus necessary to rescan the sample with the transducer focused at different depths, which increases the inspection time. For typical structural ceramics (alumina, silicon nitride, silicon carbide), flaws as small as 25 μm can be detected to depths of only about 3 mm because of the very high index of refraction of these materials for elastic waves and the attendant severe spherical aberration caused by propagation through the ceramic surface. If longer focal length transducers are used in an attempt to increase the depth of optimum focus, the sensitivity will inexorably decrease as the focal "spot size" increases because of physical optics limitations. It thus appears that a maximum detection depth of about 3 mm for 25-μm flaws will not likely be exceeded.

If one considers alternatives to focused transducers for detecting critical flaws in ceramics, it is readily apparent that the problem becomes one of achieving an adequate signal-to-noise ratio for the flaw size of interest. For plane-wave insonification, the power scattered by a spherical void falls off approximately as $(a/d)^2$ (ignoring beamspread in the incident wave and assuming that the wavelength is small compared to the flaw size), where a is the flaw radius and d the flaw depth. For a 25-μm-diameter void located 1 mm deep, the signal obtained using plane-wave insonification would be approximately 80 dB less than that obtained from a focused ultrasonic transducer, assuming that all of the available incident energy were scattered back to the transducer in the latter case, which of course would not be the case. Experiment shows that the ratio is nearer 50 dB, which is still a very severe loss. For a flaw lying at a depth of 3 mm, this ratio will fall by another 20 dB. However, by combining plane-wave insonification and signal processing, it may be possible to achieve sensitivities commensurate with those obtainable with conventional focused transducers. To be sure, the requirement for processing of the acquired data will add to the inspection time, but the total time may still be less than that required for focused transducer inspection. In addition, the only limitation of this approach on the maximum flaw depth (i.e., the ceramic thickness) is how small a signal-to-noise ratio may be tolerated with the processing schemes used.

In practice, even at 100 MHz, the wavelength of an ultrasonic wave is large compared to a flaw size of 25 μm, and thus a more accurate model of the differential scattering cross section is necessary. To address this problem, we have programmed the spherical scattering model of Ying and Truell,[1] with corrections for several errors in the original derivation. This model provides us with an excellent estimate of the scattered field produced by a spherical void (or inclusion) as a function of frequency, flaw size, and flaw depth.

In implementing a flaw detection technique which avoids dependence on focusing the incident energy at the desired flaw depth, several approaches are possible. In the first, plane-wave insonification is used in conjunction with temporal (and perhaps spatial) signal averaging to reduce the random noise. To this end, we have examined a 57 x 6 x 3 mm zirconia modulus of rupture bar into which an artificial flaw was placed. The flaw was a flat-bottomed hole 250 μm in diameter and lying at a depth of 2 mm. Using a conventional focused transducer, this flaw was easily detected and recorded. When insonified with a 100-MHz plane-wave transducer, however, no indication of the flaw was detected in the

raw data. When simple temporal averaging was applied, however, the flaw was readily located. This result required only minimal signal processing and, from the large signal-to-noise ratio and lateral sensitivities obtained, indicates that the entire 3 mm thickness of the sample was interrogated over an area approximately 6 mm in diameter. Only 12 transducer positions were necessary to inspect the entire sample (some overlap of the transducer positions was permitted to ensure adequate coverage of the bar). A time of 90 s, most of which are consumed by the relatively slow digitizer which we use to acquire high-frequency waveforms, were required to inspect the bar in this manner, while conventional scanning consumes almost 5 min. Computer processing time was negligible for the former case; thus, a high-speed flash digitizer would reduce the total time considerably. Applying the square-law decrease in scattered power with flaw size mentioned above, it appears that a 25-μm flaw would just be detectable at this depth using plane-wave insonification and temporal averaging.

In order to increase the detection depth, it is necessary to combine temporal averaging with some form of signal integration or spatial averaging. Using plane-wave insonification, we next acquired a series of temporally averaged records in which the transducer was moved a small distance between records. The spatial shift was small enough that no correction for signal displacement was necessary. There was a concomitant increase in signal amplitude. One advantage of this approach is that signals from all depths of the material are acquired simultaneously.

A second scheme, and one which incorporates both temporal and spatial averaging, is synthetic aperture technology. In the present case, a high-frequency transducer is focused at the surface of the specimen, thereby producing a spherically diverging wavefront inside the specimen. The sample is then scanned in a manner similar to that using conventional evaluation schemes. At each point of the scan, however, a temporally averaged record is acquired. Since the motion of the transducer is large compared to a wavelength, the signal from any given flaw undergoes a quadratic phase shift with time as the transducer position changes, as shown in Fig. 1. Actual low-frequency records of scattering from a point source are shown in Fig. 2, where the time shift of the records with transducer position is readily apparent. This shift, which varies with flaw depth, must be taken into account when processing the acquired data. A reconstruction is then obtained for any desired flaw depth using the original data set.

We have acquired scattering data from the 250-μm flaw using a nonautomated one- and two-dimensional scan. In the former case, a scan was made along a single line passing directly above the flaw. The transducer was stepped manually between data points, and the resulting data sets were processed for a range of assumed depths, as though no prior knowledge of the flaw location were available. The reconstructed flaw amplitude data peaked at the proper depth, yielding a very strong signal from the flaw. The results indicate that 25-μm flaws should be detectable at these depths.

A two-dimensional scan was also made of the 250-μm flaw. In this case the required time is much larger, since one would not have a priori knowledge of either the flaw depth or transverse position in the sample. The resulting data, processed in two dimensions (actually three, since the depth processing must also be included) yielded the correct position and depth of the flaw.

By completely automating the data acquisition and processing stages and performing all analysis on our 80386-based computer (with Weitek coprocessor support), we estimate that the total evaluation time will be less than that necessary to scan the part using conventional focused transducers, which must be focused for each depth evaluated. The ultimate depth to which we can detect critical flaws using the synthetic aperture approach is not known, but it appears that it will exceed the current 3-mm limitation. We are writing the software to do the full three-dimensional analysis and

ORNL-DWG 78-9192

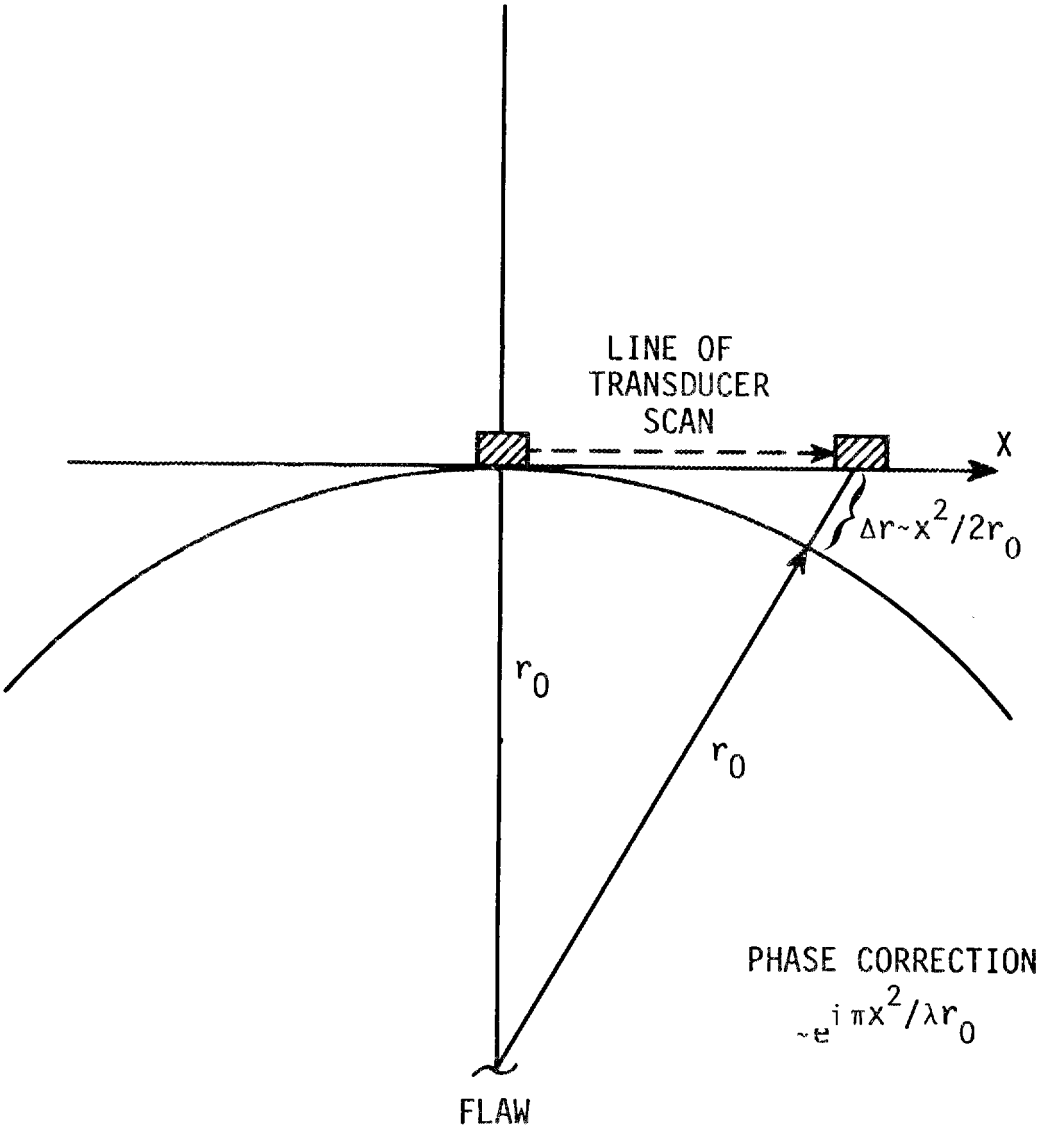

Fig. 1. Origin of quadratic phase delay during scan of a flaw.

ORNL-DWG90-13954

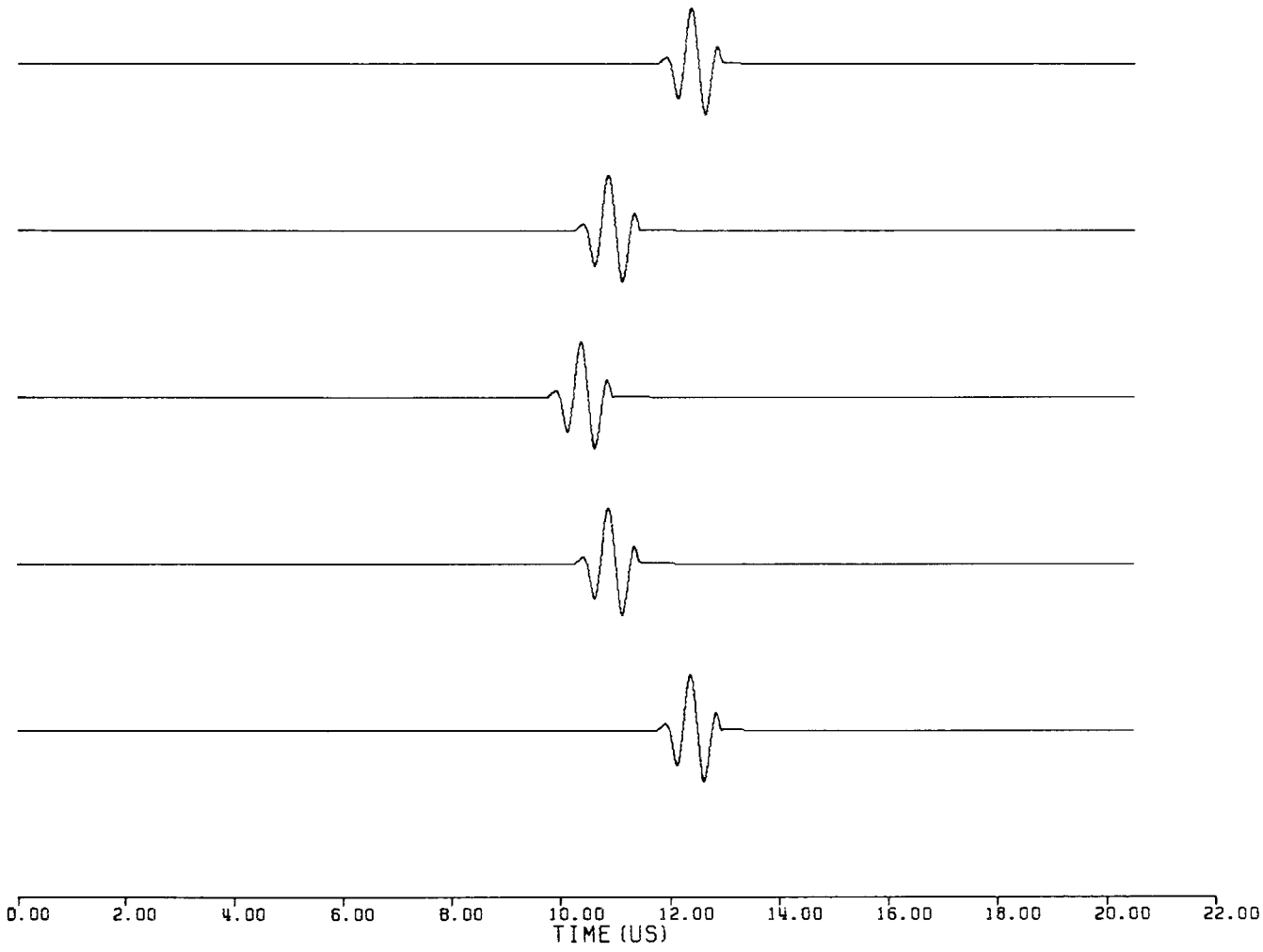

Fig. 2. Low-frequency scan of a point scatterer showing quadratic phase delay with position.

examining several approaches for controlling our present scan system with the same computer.

The above results suggest that an another excellent avenue of approach for this work would combine narrow-band insonification for good signal-to-noise characteristics with coherent detection for optimum sensitivity. While this can be accomplished with hardware, we have previously shown[2] that it may also be implemented in software. The frequency employed should be chosen to ensure that scattering from expected flaw sizes lies in the stochastic or diffuse scattering regimes. We are currently investigating this approach as well.

Radiography — B. E. Foster

Acceptance testing has been completed on the computerized X-ray tomography system that was purchased from Scientific Measurement Systems, Inc. (SMS) in Austin, Texas. The purchase agreement included several progress payment type milestones. All seven milestones have been completed. They have included a design review, approval of major item drawings, fabrication of the image processing subsystem, fabrication of the array and back projection processor, receipt of major equipment items, fabrication of the object positioning unit, specimen holder, collimator set, calibration standards, and installation and acceptance testing at ORNL with additional operator training. The X-ray units were malfunctioning intermittently thus preventing any lengthy scans and obviously preventing accomplishment of acceptance testing. Philips (the X-ray tube manufacturer) replaced the tubes, shortened the high-voltage cables, and replaced the EPROM, all to no avail. Then, at our repeated request, they replaced the negative 225-kV generator, which solved the X-ray problem. The X-ray malfunction had delayed checkout of the software. Operation of the system (after solving the X-ray problem) disclosed several bugs in the software which have been corrected. Additional software is being prepared at SMS to improve high-resolution detectability. A number of ceramic components have been obtained and are being examined for system evaluation and operator training. We are pleased with the high-resolution capability and versatility of the system inspection of complex ceramic parts and assemblies.

The 21 cylindrical ceramic tensile specimens identified in the Ultrasonics section were inspected with the CT system. Initial inspection was done utilizing digital radiography. In general, the images were quite good, and only one showed any type of discontinuity (sample 893838-2 C2). A CT slice was taken through the longitudinal center of this sample. The indication noted with digital radiography was detected. It appears to be a very low density, but small region (less than 1 mm in diameter). The area was marked with a flomaster pen for subsequent evaluation by ultrasonics but was not detected because of the difficulty in interrogating the center region of small diameter cylindrical specimens.

A total of 29 additional cylindrical silicon nitride tensile specimens have been received for inspection with the CT system. Initial inspection will be done utilizing digital radiography. Any sample showing any type of discontinuity will be further evaluated with one or more CT slices through the longitudinal center of the sample.

The high-resolution beam hardening software has been installed and is working quite well. In order to obtain optimum beam hardening corrections for the ceramic samples, a beam hardening correction wedge (triangle) fabricated of silicon nitride is needed and is being requested. The triangle should be approximately 12 mm thick with sides of 150 x 260 x 300 mm.

Additional operator training has been rescheduled from April to mid-May or June because of fabrication schedules at Scientific Measurements.

References

1. C.F. Ying and R. Truell, "Scattering of a Plane Longitudinal Wave by a Spherical Obstacle in an Elastically Isotropic Solid," *J. Appl. Phys.* 27, 1086 (1956).

2. W.A. Simpson, Jr., L. Adler, K.V. Cook, and R.W. McClung, *Ultrasonic Flaw Characterization Techniques for Stainless Steel Welds*, ORNL-6175, January 1986.

Milestones

On schedule.

Publications

Two abstracts, entitled "Spherical Wave Modeling of Transducer Beam Distributions for Ceramics Evaluation," by W. A. Simpson, Jr., and "NDE Development for the CTAHE Project," by R. W. McClung and D. R. Johnson, have been accepted for presentation at the Conference on NDE of Modern Ceramics to be held in Columbus, Ohio, July 9-12, 1990. The first abstract is also being prepared as an open-literature report. A third paper entitled "High Resolution Imaging of Ceramic Materials with Digital Radiography, Computed Laminography, and Computed Tomography," by B. E. Foster, was presented at the WaTTec Conference in Knoxville, Tennessee on February 21, 1990.

NDE Standards for Advanced Ceramics

R. W. McClung (Oak Ridge National Laboratory)

Objective/scope

The development of standards is important for the establishment of reliability and acceptance of advanced structural materials. A new committee, C-28, on Advanced Ceramics, has been organized in the American Society for Testing and Materials (ASTM) to address this issue. One of the activities of the C-28 committee is nondestructive examination (NDE). The Task Group on NDE is reviewing existing standards on NDE (primarily developed for metals) to determine potential applicability for ceramics. Use of existing or modified standards is more efficient than generation of new documents and will assure the input of a large body of NDE expertise. Close liaison has been established with ASTM Committee E-7 on Nondestructive Testing and documents are in various stages of review, recommendations for change, modification, and balloting. R. W. McClung is a member of both committees and the official liaison.

Liaison and technical support have been continued between ASTM Committees C-28 and E-7. To date, sixteen E-7 NDE standards have been reviewed in detail with recommendations made to E-7 for modifications. Successful E-7 action is complete on seven documents; E-7 balloting action is in progress on six items; the remainder require action by C-28. An advisory C-28 ballot is in progress for detailed review on five additional E-7 standards. An NDE advisory ballot is also in progress on a table of ultrasonic velocities in typical ceramic materials. When approved, this will be submitted to E-7 for incorporation in an existing NDE standard. A draft document on fabrication of seeded voids in pressureless sintered ceramics has been put into ASTM style and after a few minor additions will be ready for ballot in C-28 at the subcommittee level. A draft has been completed of a guideline document that describes available approved standards and their applicability for examination of ceramics.

X-ray Computed Tomographic Imaging – W. A. Ellingson, (Argonne National Laboratory) T. Hentea, (Purdue University, Calumet, Indiana), and P. Rizo (Visiting Scientist, CEA/Leti, Grenoble, France)

Objective/scope

The objective of this program is to develop X–ray computed tomographic (CT) imaging technology for application to structural ceramic materials. This technique has the potential for mapping short–range (<5 mm) and long–range (>5 mm) density variations (to perhaps 0.5–1%), detecting and sizing high– and low–density inclusions, and detecting and sizing (within limits) cracks in green–state and densified ceramics. CT imaging is capable of interrogating the full volume of a component and is noncontacting. It is also relatively insensitive to part shape and thus can be used to inspect components with complex shapes, such as turbocharger rotors, rotor shrouds, and large individual turbine blades.

Technical progress

During the current reporting period, we obtained data on two of the new Si_3N_4 injection-molded phantoms (turbocharger rotors) received last period, using two different 3-D algorithms for the microfocus X-ray scanner.

Density measurements

To better obtain an idea of X–ray CT sensitivity to density variations within the critical hub-blade region of a turbocharger rotor, a set of rotors was produced by Garrett Ceramic Components Division (GCC) of Allied-Signal Aerospace Corporation. Figure 1 shows the drawing from which the rotors were made. These T–25 turbocharger rotors were produced by injection-molding of Garrett's GN–10 Si_3N_4. Three insert slugs at the critical hub–blade region have 2, 4, and 6 wt.% binder differences, which resulted in an approximate 0.08 g/cm^3 mass density difference per 2 wt.% binder from a nominal 2.28 g/cm^3 base material. The slugs were inserted into the hub region so that part of the region has these known variations and part does not.

The 3-D microtomograph (Fig. 2) used in these experiments was designed and built at Argonne National Laboratory. The experimental system consists of an IRT HOMX 161 microfocus source, a Precise Optics tri-field image intensifier, a Sony XC-57 CCD (512^2) camera, a Daedal precision component-manipulation stage (X, Y, q) and an IBM/PC/AT with frame grabber and accelerator boards for data acquisition and control. Software for part manipulation and control was locally written. Reconstruction software consists of two analytical codes (Radon and Feldkamp) that reconstruct images based on circular trajectories of the X-ray source. The codes are resident in two computational environments: (a) a VAX 8700 and (b) an ALLIANT FX-8 parallel computer. Both computers are accessible from the 3-D microtomograph via a local area network.

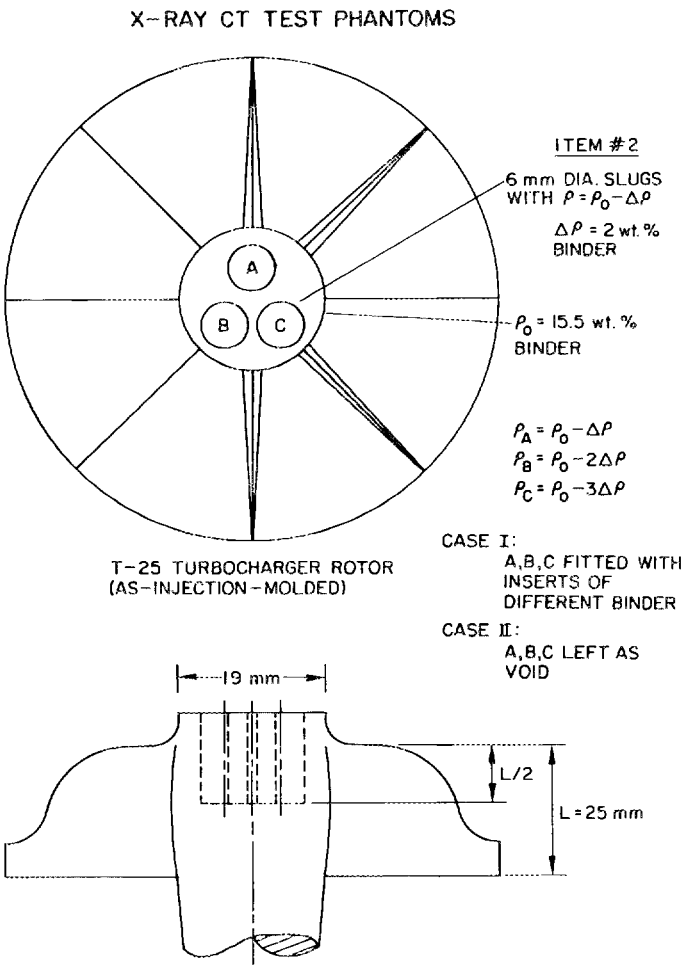

Fig. 1. Drawing of injection-molded Si_3N_4 turbocharger rotors used in the study

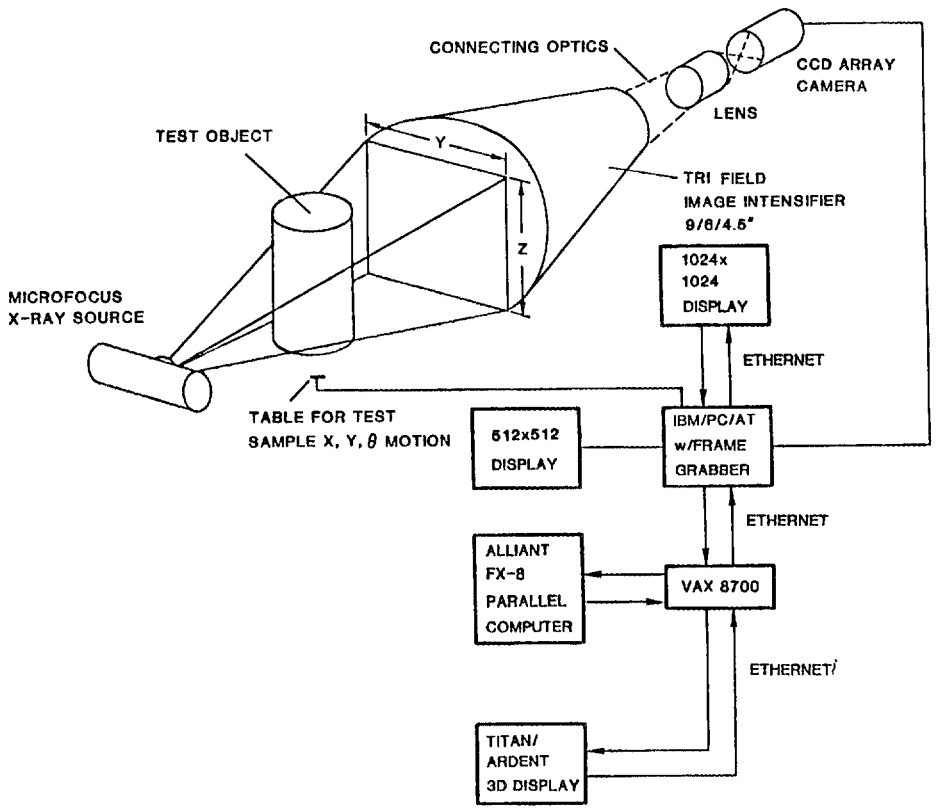

Fig. 2. Schematic diagram of 3-D X-ray microtomograph

DESCRIPTION OF THE WORK

The use of large numerical apertures (i.e., short distance between X-ray source and detector) in microtomography systems has several advantages. First, a higher flux can be achieved, which means shorter data acquisition times; second, because of higher flux, more filtration can be used, thereby providing a narrower X-ray spectrum and eliminating certain artifacts; third, higher flux allows examination of thicker and/or higher-density objects.

However, large numerical apertures also present potential problems with image reconstruction because a circular trajectory of the source has been shown to result in missing data, and the larger the numerical aperture, the more data that are missing.

For our comparison, we have employed two system geometries. The two geometries are asymmetrical in horizontal and vertical directions because of the detector area we have chosen to work with. The two geometries are (a) low numerical aperture with $\pm 3°$ vertical and $\pm 5°$ horizontal and (b) large numerical aperture with $\pm 9.5°$ vertical and $\pm 15°$ horizontal.

Low Aperture

At the low-aperture configuration, both codes show similar density (gray-scale) values. Because of the higher spatial frequency filter, the Feldkamp code better defines the edges of the blades than does the Radon code.

Large Aperture

At the large-aperture test configuration, a strong artifact is present when using the Feldkamp and Radon codes to examine the turbo rotor. This artifact is in the form of blurred blades near the extreme; phantom blades appear between the real blades. The Radon code presents this artifact at a lower gray-scale value. We suggest that the stronger artifact with Feldkamp code could be caused by asymmetric filtration. To establish the cause of this artifact, the synthesized data were modified by a look-up table simulating the image intensifier exposure. The simulation has generated the same response as real data.

This type of artifact can be further seen by examining axial sections of the turbo rotor generated from the 3-D data set, as shown in Fig. 3, and a corresponding densitometer trace (see Fig. 4) taken axially. The axial tomographic sections (Fig. 3) are approximately 1 mm thick and were taken in the positions noted in the diagram on the figure. One of the drilled holes and a part of another were also included. We noted five regions on the normalized densitometer trace (see corresponding locations on Fig. 3) that are important. Region 1 shows problems of infinite cylinder cut-off (likely a filtration problem); Regions 2 and 4 show variations in density between the codes at regions of larger numerical aperture; and Region 3 shows the typical "streak" artifact (a spike in the densitometer trace) usually observed at an abrupt geometrical feature, in this case the horizontal plane at the end of the blades. The blade artifact is more apparent with the Feldkamp code than with the Radon code for this particular example. This blade zrtifact seems to point out the critical attention needed to attenuation calibrations that, for green ceramics, is difficult because of the problems in producing high-quality green bodies. Our future

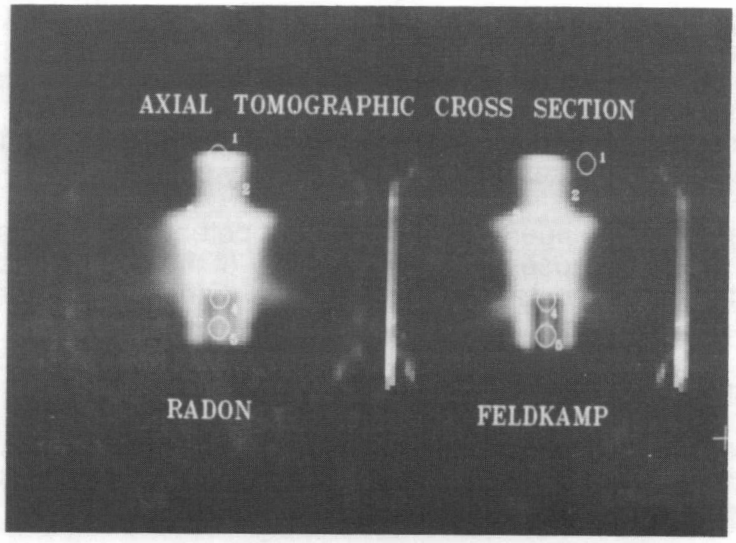

Fig. 3. Axial tomographic cross-section of Si_3N_4 injection-molded turbocharger rotor

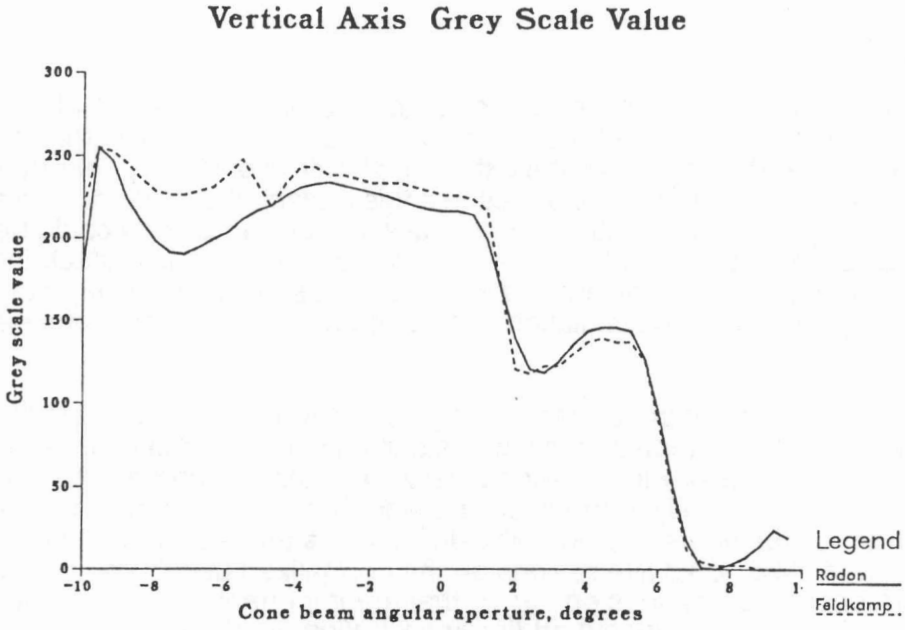

Fig. 4. Axial densitometer traces of tomographic sections shown in Fig. 3

work will concentrate on using green and dense ceramics for calibration and on attempting to assess use of alternate materials as well.

There are several considerations to be made in regard to algorithm selection. One of these is computational efficiency as it relates to the reliability of the reconstruction. We have shown that even for small reconstruction volumes, e.g., 64 x 64 x 52, there is a significant difference in computation time (9 min CPU for Feldkamp and 16 min CPU for Radon). However, as the size of the reconstructed volume increases, even more significant differences in elapsed time are likely. This leads to the need for high-speed computers.

Based on our preliminary work, we have concluded that for small numerical apertures, less than ± 3 - ± 5°, there is no significant difference in density measurements between the codes. However, because of filtration, the Feldkamp code may provide higher geometrical accuracy. At large numerical apertures, the Feldkamp code underestimates the density by 3-5 at the extreme top and bottom. In addition, we conclude that at large numerical apertures, attenuation calibration (not part of the geometrical calibrations) is a critical part of the reconstruction process. In the future, we will define appropriate calibrations for the 3-D codes.

We will also continue to compare the two algorithms on ceramic materials relative to the accuracy of both geometrical and density measurements.

Nuclear Magnetic Resonance Imaging – N. Gopalsami, S. L. Dieckman, W. A. Ellingson, and R. E. Botto (Argonne National Laboratory), and H. Yeh and J. P. Pollinger (Garrett Ceramic Components Division of Allied-Signal Aerospace Corporation)

Objectives/scope

The objectives of this program are to investigate (a) the feasibility of nuclear magnetic resonance (NMR) imaging techniques in mapping organic additive distributions in green injection-molded ceramics (experimental emphasis placed on commercial Si_3N_4 materials); (b) the potential for NMR spectroscopic techniques in determining chemical variations within or between organic additive batches that may affect process reliability; (c) the sensitivity of the NMR imaging methods to mixing and injection-molding process variables, as manifested in organic additive distribution homogeneity; and (d) the use of NMR imaging for slip-cast ceramic processing technology.

Technical progress

Work reported in this period is focused on correlation of magnetic resonance image intensities with organic binder concentrations of injection-molded Si_3N_4 ceramics.

Correlation with destructive test data

Four sets of injection-molded Si_3N_4 bars (Table 1) were produced by Garrett Ceramic Components Division of Allied-Signal Aerospace Corporation for NMR imaging tests using different values of injection mixing and molding parameters. Four test bars (one in each set, with ID Nos. 1, 21, 41, and 69) were imaged by ANL with NMR. Each bar is typically 8 mm wide, 4 mm thick, and 59 mm long. The NMR images are two-dimensional, along the width and length of the bars (x-z plane). Because the field of view of the imaging probe used was only 20 x 20 mm, each end of the bar was imaged separately, creating eight NMR images in total. The ends of the bars were labeled gate and non-gate ends, in which the gate end is the inlet side of the mold cavity.

Table 1. Fabrication Conditions for Test Bars

Bar Set	Test Bar I.D. No.	Procedure		Molding Parameter	
		Standard	Alternate	Baseline	Non-baseline
A	1–4	X	–	X	–
B	21–24	–	X	X	–
C*	41–44	–	X	–	X
D*	69–72	X	–	–	X

*Exhibited a patchy pattern on the surfaces of all bars.

Figure 1 presents NMR images of the gate end of bars 1 and 41. Bar 1 shows less uniform distribution of image intensities than bar 41. This is rather surprising because bar 1 was produced under the standard mixing and molding conditions of the Garrett process, whereas bar 41 was produced under nonstandard mixing and molding conditions. We conducted several tests to ensure that the void-like feature dominant in the image of the bar 1 is not an artifact. For example, we repeated the experiment by moving the relative position of the bar up and down inside the probe. To ensure that the image intensity was not weighted by T_1 effects, we conducted an experiment with a long pulse repetition time (2 s). There were no substantial changes in the image features of these confirmatory experiments. We also examined the X-ray images of these bars, supplied by Garrett, to check for paramagnetic inclusions (such as iron) thatwould alter the NMR signal. The X-ray images showed some nonuniform density variations in the bar, but contained no detectable features at the location of interest. It is possible, however, that there may be a minute paramagnetic inclusion that is below the detection level of X- rays but that would still be sensitive to NMR.

The NMR images of the other bars revealed no dominant features such as the void-like feature seen in bar 1. However, the image of bar 69 appeared less uniform in intensity than that of bars 41 or 21. There were no significant differences between the images of the gate and non-gate ends of the bars.

To determine the correlation between NMR image intensity and binder concentration in the test bars, a destructive evaluation was conducted. This involved cutting the sections (which had been imaged) into thin samples and then determining weight loss of each sample upon complete binder removal by heating. The bars were cut lengthwise; the thinnest sample possible was 2 mm thick and any further sectioning across the width of the sample was not practical. Because bars 1 and 69 showed some distinct image features, they were cut so that every major local feature was included in the sectioned samples. Figure 2 shows the location of the sectioned samples, with sample numbers marked for the bars 1 and 69. The other two bars were cut at 2-mm intervals from each end. A total of 54 samples were produced. These samples were heated in an air furnace to 650°C at 10°C/min, followed by a 2-h hold for binder removal. This thermal cycle was established on the base of Thermogravimetric Analysis (TGA) data. Samples were weighed before and after thermal treatment with an analytical balance accurate to 0.0002 g, thus providing weight loss or percent of organic binders in each section.

The gray-scale image intensities of the test bars were analyzed for correlation with the gravimetric data of the organic binders. Using our image processing workstation, we selected areas of interest on the test bar images corresponding to the location and size of the sectioned samples. For each area of interest, the mean and standard deviations of the gray-scale intensities were obtained. In principle, the mean gray-scale intensity of a selected image area should be proportional to the percent weight of the organics in the corresponding sectioned sample. Before such direct comparisons can be made, however, the image data must be corrected for two known experimental variations or artifacts. One of these is due to a lack of absolute scaling in displayed NMR images, so a comparison between the test bar images requires scaling the images with respect to a reference. The other artifact is due to the probe response variation relative to the location of a sample volume of interest in the probe.

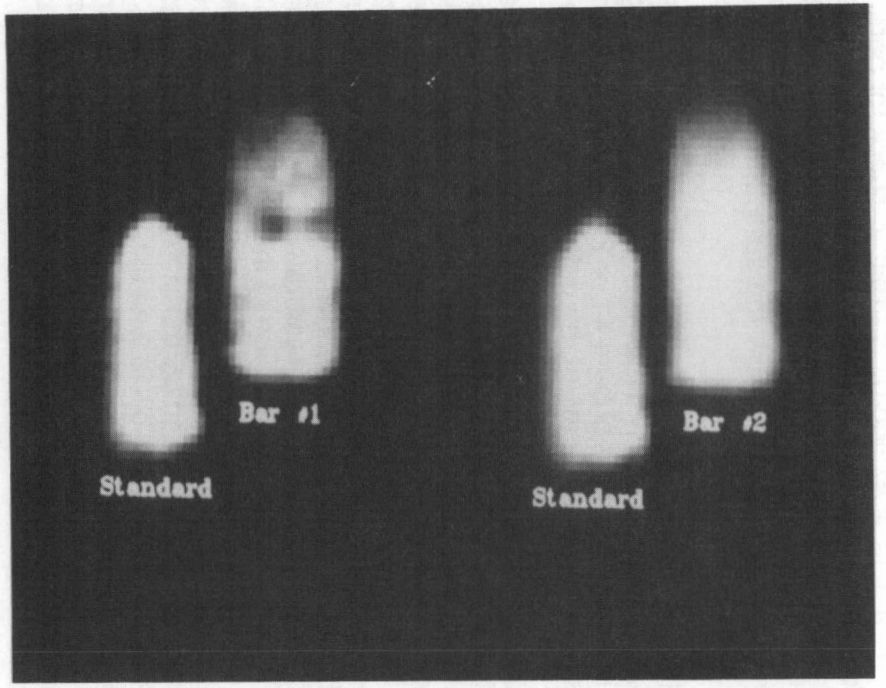

Fig. 1. Back-projection NMR images of test bars 1 and 41 (bar 1 is on the left, along with an intensity standard, and bar 41 is on the right with its intensity standard)

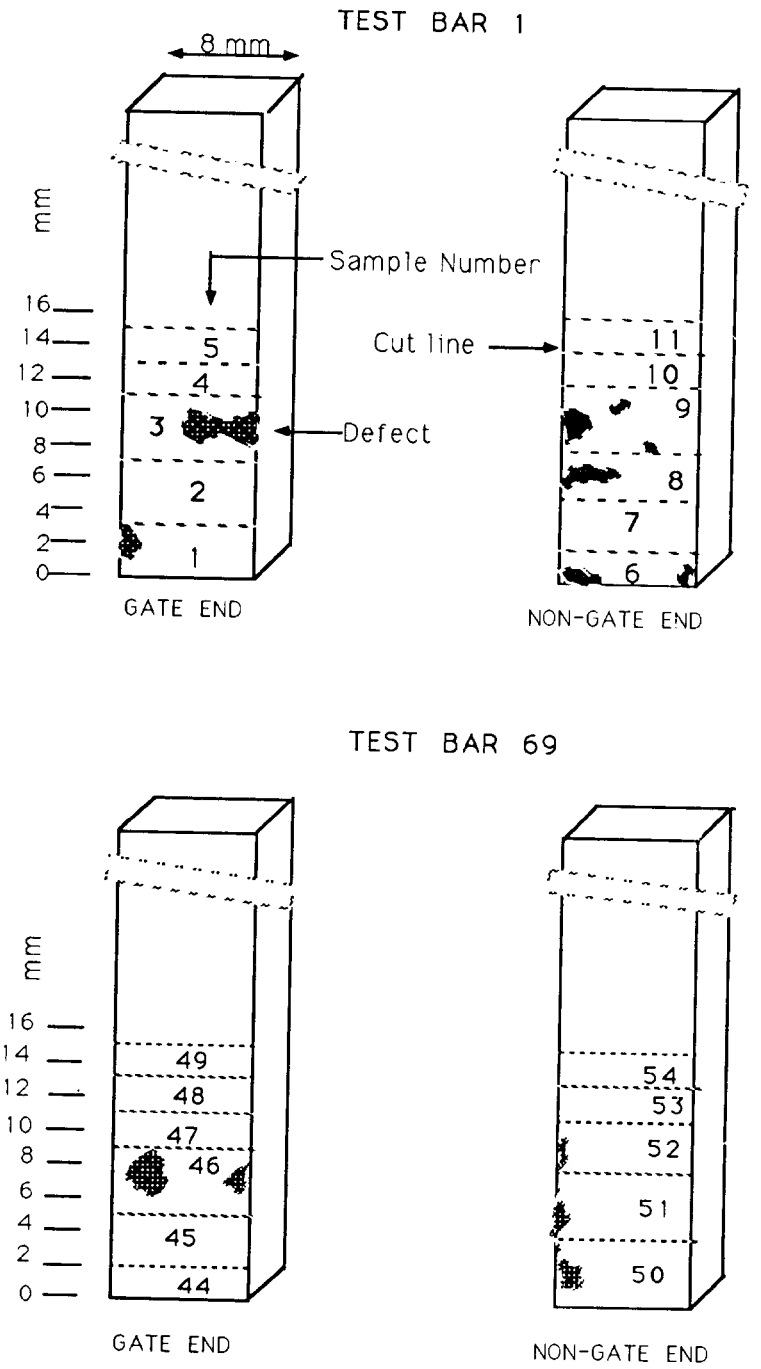

Fig. 2. Schematics showing the locations and shapes of defects detected by MRI on bars 1 and 69. Also shown are cut lines and sample I.D. numbers for destructive correlation studies

As was observed in our earlier concentration-phantom experiments, the intensity standard was found to be unreliable, due perhaps to changes in its orientation relative to the reference axis of the probe during sample mounting. Instead, the mean image intensity in the uniform field range of the probe was equated to the average weight of the organics in the corresponding section of the bar. Thus, we scaled the intensity values of all the images with respect to a reference weight.

The probe response variation with respect to sample height can be eliminated if we restrict the image field of view to the uniform field region of the RF coil of the probe, which is about 0.7 times the radius of the coil from the center. But this would reduce the data points for correlation to a statistically insignificant number since the number of sectioned slices lying in the uniform field region is small. It is possible, however, to utilize the whole field of view if the probe response can be measured or predicted with respect to the sample position. In this work, we predicted the probe response by using half of the data points, i.e., 27 data points corresponding to the non-gate ends of the bars. Because probe response is desired for a uniform binder concentration, we weight-corrected the scaled image intensities corresponding to the reference weight chosen. Thus, we have 27 intensity values corresponding to different locations of a sample for a chosen reference weight. A fourth-degree polynomial fit of the data points was used to obtain the probe response function, shown in Fig. 3. The center of the RF coil is 3.3 mm from the edge of the bar and the coil extends up to 13.3 mm in bar length. The probe response function shows an edge effect in the beginning, which is an artifact of the image reconstruction technique. The uniform field region is up to about 9 mm long in the bar, after which the intensity decreases almost linearly with length. The scaled image intensities of the bars were thus corrected for the probe response variation.

Figure 4 compares the NMR predicted weights of the organics and actual measured weights with respect to distance from each end of the bars. A fairly good correlation between the NMR and gravimetric data is seen for all the test bars. To determine the overall correlation coefficient, we plotted all 57 pairs of data in the form of a scatter plot (Fig. 5). A linear regression of the data passing through the origin was determined. If the error bar for the regression fit is chosen at one standard deviation from the fitted line, the corresponding error in the NMR data is $\pm$ 0.5 wt. %. For this case, 67% of the data are within the correlation band. Calculation of the correlation coefficient for the entire data set gives a value of about 0.1. This is a rather low value and is due not to poor correlation between the data sets but to poor signal-to-noise ratio and narrow spread of the data. When the NMR data were taken, we were limited in the amount of RF power that could be transmitted to the probe coils because of a problem with capacitor arcing. As a result, the signal-to-noise ratio of the measurement was low, and the correlation coefficient turned out to be low. The problem has since been rectified, and we believe that our newer images would show a higher correlation coefficient.

Status of Milestones

We have been delayed on some milestones because the slip-casting subcontract to the Garrett Ceramic Components Division of Allied-Signal Aerospace Corporation has not been finalized.

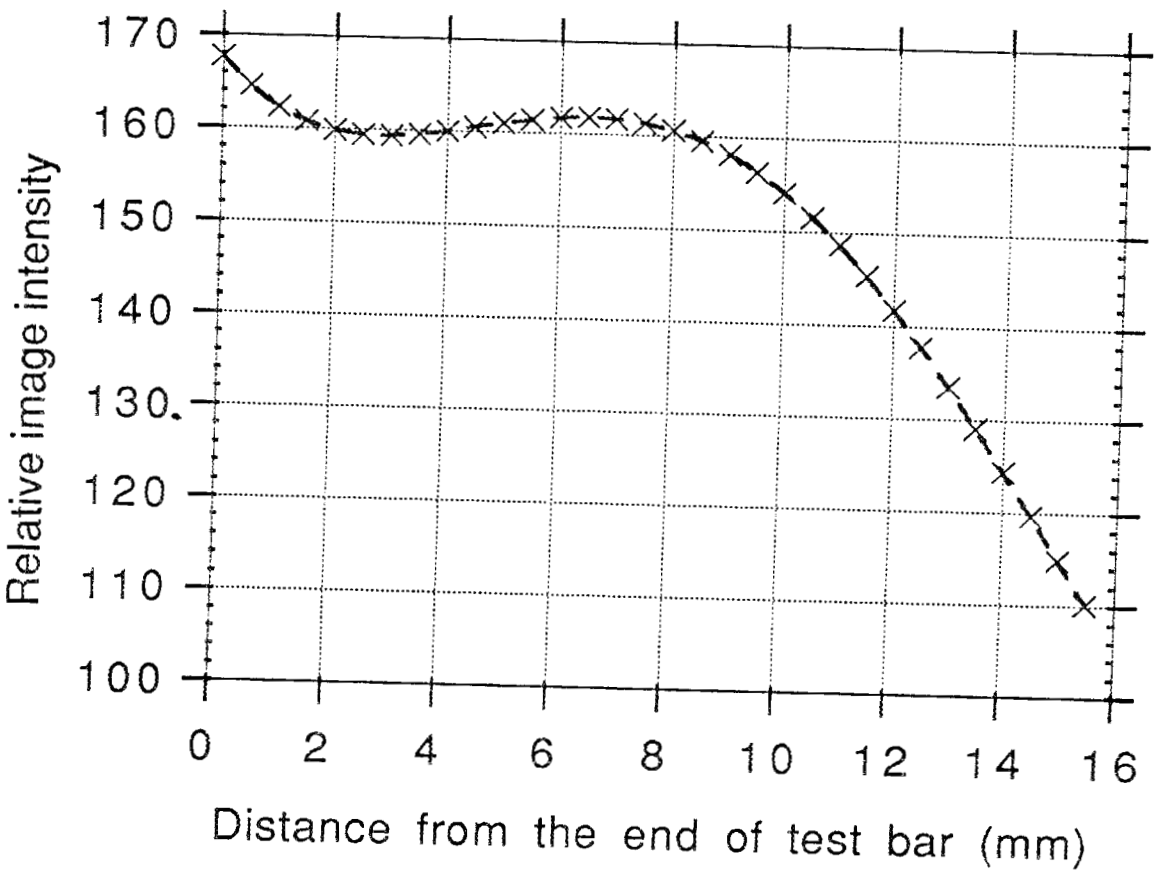

Fig. 3. Variation of probe response with sample location

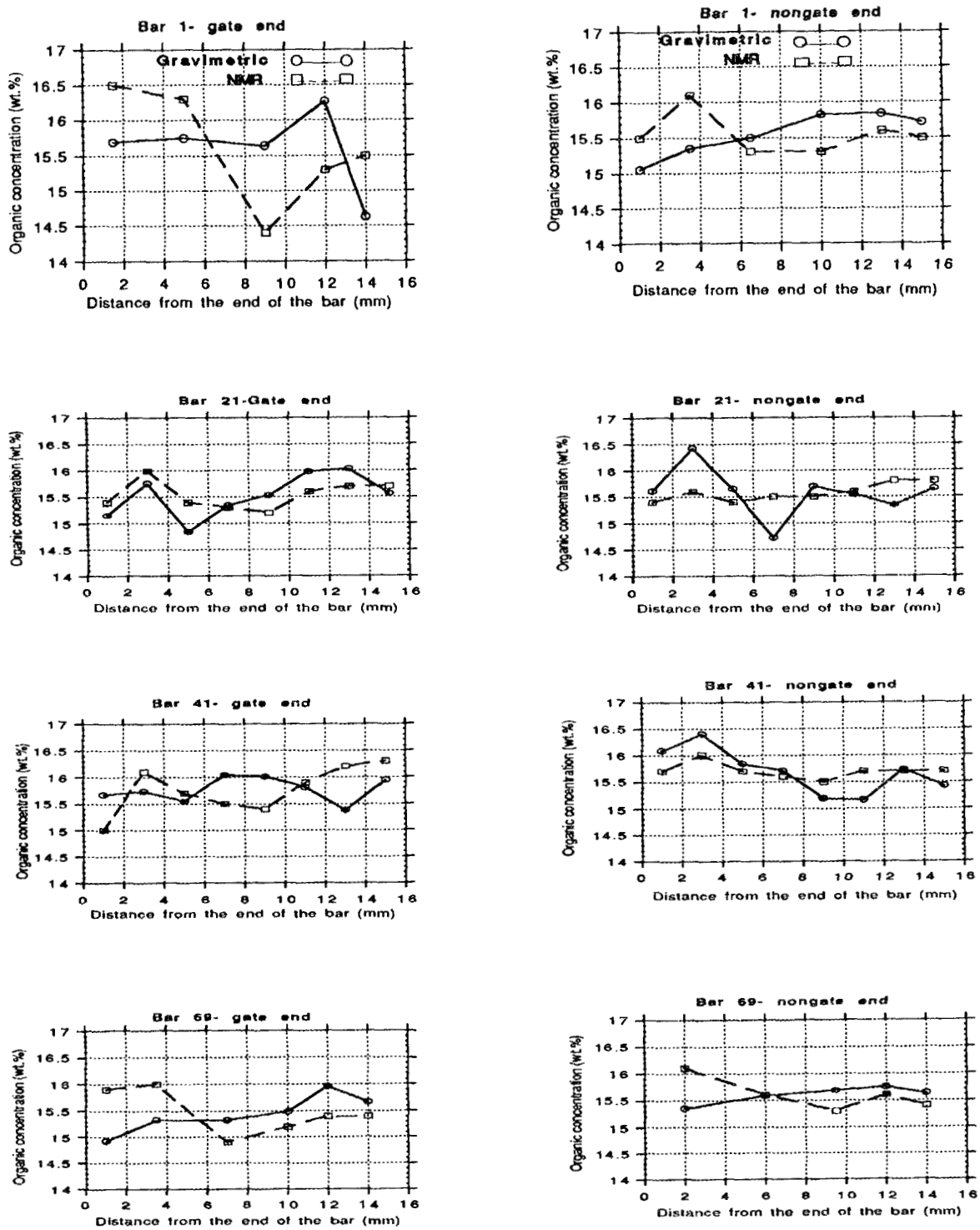

Fig. 4. Comparison of organic binder concentrations as measured by (a) □- -□ NMR and (b) destructive testing o--o in injection-molded test bars

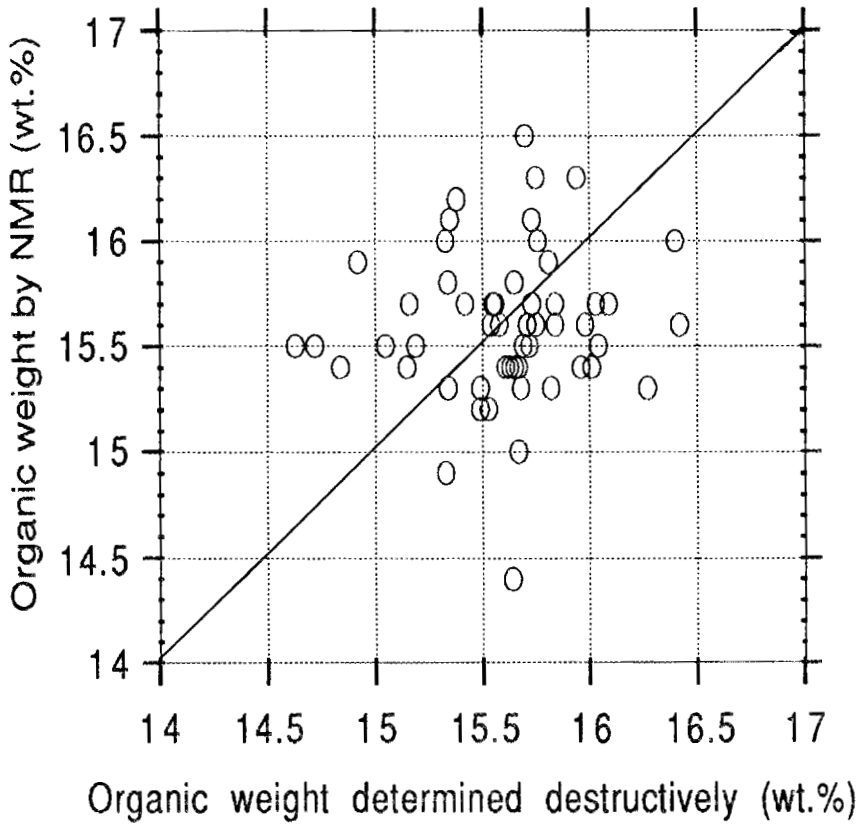

Fig. 5. Scatter plot between NMR and gravimetric data on organic concentrations

Powder Characterization
A. C. Young (Oak Ridge National Laboratory)

Objective/scope

The objectives of this task are to (1) identify those aspects of the chemistry and physics of a ceramic powder/solvent interface that control processing, (2) develop standard methods of analysis for item 1, and (3) develop procedures for writing specifications for ceramic powders to include any methods of analysis developed in this project.

Technical progress

Initial studies on two ceramic powders, RCHP-DBM alumina and Ube E-10 silicon nitride, using inverse gas-solid chromatography have been completed. The experimental results indicated that the surface characteristics of each powder changed after heat treatment in a variety of atmospheres. The shift in elution temperature and change in peak geometry of chemicals which were used to probe the ceramic surfaces were the basis of judgment.

Both powders were first isopressed at 40 to 50 MPa (6000 to 7000 psi) and screened to -40/+100 mesh for alumina and -100/+200 mesh for silicon nitride. Heat treatments of the screened powders were done at 800°C for 6 h in various atmospheres: air, Ar-4% H_2, N_2-4% H_2, and N_2. Once the powders were prepared, the experiment was performed with a Hewlett Packard gas-solid chromatograph (GSC) equipped with a flame ionized detector (FID). Packed columns which held the ceramic powder during testing were made of stainless steel tubing with 0.6 cm (0.25 in.) O.D. and 25.4 to 30.5 cm (10 to 12 in.) in length.

Table 1 lists the elution temperatures of probe chemicals for silicon nitride and alumina, respectively; the chemicals are listed in the order of injection. For each probe, the injection contained 2 µL of solution made of 50 µL solute in 10 mL of carbon disulfide. The packed column was first conditioned at 350°C for 2 h under the He carrier gas. After a 2-min soaking at 60°C, the oven temperature was increased at 8°C/min to 300°C and then allowed to soak for 4 min before being cooled down to 60°C.

The results in Table 1 indicate that the surface characteristics of these silicon nitride powders are different from one another. For example, the as-received powder was the only one that reacted weakly with Lewis base pyridine and ketones. On the other hand, all silicon nitrides except the air heat-treated one have similar elution temperatures for straight aliphatics; this implies a change of surface activity due to oxidization. The differences of the powder surfaces treated with Ar-4% H_2, N_2-4% H_2, or N_2 are real but subtle. The N_2-treated powder is more polar and acidic than the other two, showing stronger interaction with polarizable compounds (benzene, toluene,and xylene) and with Lewis base ether.

Fourier transform infrared spectroscopy (FTIR) spectra indicated that the surface layers of these ceramic particles were saturated with hydroxyls. The as-received alumina contained a relatively large amount of hydroxyl groups and a smaller amount was detected after calcination at 800°C for 6 h. The extent of dehydration during heating is not known since reduction in hydroxyl concentration may be due to powder coarsening at high temperature and rehydration of alumina can take place in a short time after cooling. For silicon nitride, the existence of hydroxyls and linear hydrocarbons on the as-received powder was revealed by the FTIR spectrum. Silicon nitride powders heat treated in N_2, N_2-4% H_2, and Ar-4% H_2 gave similar spectra with two distinctive peaks (wavenumber 3375 cm^{-1} and 3750 cm^{-1}). However, the 3375 cm^{-1} peak disappeared when calcination was carried out in air.

Table 1. Elution temperatures of probe chemicals for Si_3N_4 powders (°C)

Probe chemicals	As received	800°C, 6 h/Air	800°C, 6 h/Ar-H_2	800°C, 6 h/N_2-H_2	800°C, 6 h/N_2
Carbon disulfide	60	60	60	60	60
Benzene	95	97	96	97	113
Toluene	117	115	117	118	134
Nonane	127	104	128	128	129
Decane	145	121	145	146	147
Undecane	161	137	163	161	164
Dodecane	177	151	180	178	179
Xylene	136	138	135	135	147
Chloroform	75	60	71	70	77
Dichloromethane	60	60	60	60	61
Acetone	154	192	217	232	NE
Methyl-ethyl ketone	167	NE	NE	NE	NE
Methyl-isobutyl ketone	187	NE	NE	NE	NE
Ether	141	163	188	179	221
Benzene	97	93	93	94	103
Pyridine	255	NE	NE	NE	NE
Ethanol	NE	NE	NE	NE	NE
1-Propanol	NE	NE	NE	NE	NE
2-Propanol	NE	NE	NE	NE	NE
1-Butanol	NE	NE	NE	NE	NE
Pyridine	263	NE	NE	NE	NE
Benzene	98	91	92	90	99
Water	NE	NE	NE	NE	NE

Additional studies using a scanning electron microscope with X-ray function (SEM/X-ray) and electron spectroscopy for chemical analysis (ESCA) on the powders will be carried out. An open literature report is being prepared to summarize the results.

Milestones

On schedule.

Spectroscopic Characterization

M. A. Anderson (University of Wisconsin - Madison)

Objective/scope

This project is designed to fulfill two primary objectives:

1. characterization of the aqueous surface chemistry of silicon nitride, which also requires the development of a standard for mobility measurements and participation in a round-robin characterization of this standard; and
2. spectroscopic characterization of aqueous suspensions of silicon nitride.

Technical progress

Our efforts during this period were focused primarily on the preparation of an internal standard for use by all participants in the round robin mobility study. Three materials have been considered for use as internal standards. Red blood cells were eliminated because (1) their reported mobility values depend greatly on the buffer used to prepare the suspension and (2) the lifetime of these suspensions is relatively short. Several polystyrene latex suspensions have been tested with mixed results. Other participants will continue to characterize selected latex systems, but all latex systems suffer from the problem that they do not behave like ceramic materials when dispersed in water (e.g., the mobility of a latex does not vary with pH in aqueous suspensions except over a limited range of pH values). Consequently, we suggested the use of phosphated goethite (α-FeOOH) as a standard. Besides being a ceramic material itself, a separate study of phosphate adsorption on goethite conducted by Dr. Tejedor indicated that mobility measurements on this material correlated well with separate spectroscopic and adsorption isotherm measurements.[1] Thus, phosphated goethite may serve as an absolute mobility standard under certain conditions.

We have prepared two separate sets of aqueous suspensions of phosphated goethite at different pH values for round robin evaluation. The first set (Goethite 1) were prepared at pH 4.5, 5.1 and 6.0 in 0.01 M NaCl at a solid concentration of 1 g goethite/L. These conditions were chosen to mimic conditions described in ref. 1, and mobilities measured initially for these suspensions agreed well (within 0.2E-9 m^2/V-sec) with mobilities reported in ref. 1. Acidic suspensions were used in order to minimize pH drifts caused by CO_2 adsorption. Studies on Goethite 1 were conducted during October and November 1989. Based on these results, a more rigorous study was designed (Goethite 2) which incorporated suspensions at pH 3.5, 4.4, 5.2, 6.1 and 7.0 in 0.01 M KNO_3 at a solid concentration of 0.25 g/L. Since Goethite 2 was still being conducted in April 1990, results from this study will be presented in the next report.

Sample preparation (Goethite 1)

All samples were prepared with a phosphate loading of 100 μmol phosphate/g goethite. In more concentrated suspensions (30 g/L), addition of this level of phosphate results in almost complete adsorption of that phosphate.[1] Dilution of such a system should minimize the removal of phosphate from the surface and give more reproducible suspension characteristics. In addition, this level of phosphate loading results in an isoelectric point of about pH 5.2, so that both positive and negative mobility values could be attained without raising the pH to a point where CO_2 absorption would be a major problem. The three desired pH values were 4.5, 5.1 and 6.0, with corresponding mobilities of +1.75, +0.2 and -1.25E-8 m^2/V-sec, as measured by Dr. Tejedor.

The goethite used was a concentrated suspension prepared by the Atkinson et al. method[2], which had been washed many times with water to a constant, low conductivity and stored as an aqueous suspension in a plastic container since preparation. Although this material was not the same as that used in ref. 1, its BET surface area of 80 m^2/g, measured using N_2 adsorption, was identical to the surface area of the goethite described in ref. 1.

This suspension has a solid concentration of 157 g/L at negligible ionic strength. Three 1 L samples at a solid concentration of 1 g/L in 0.01 N NaCl, at pH 4.5, 5.1 and 6.0, were prepared. (NaCl was used as the inert electrolyte by Dr. Tejedor because it does not have any IR absorption bands.) Because Dr. Tejedor prepared her samples at 30 g solids/L for FTIR measurements and then diluted those samples for electrophoresis measurements, the Goethite 1 samples were prepared in the same manner in order to check on her mobility measurements. The actual steps in the procedure were:

1. In three 125 mL plastic containers, mix 6.3 mL of the concentrated suspension and 27.0 mL of 0.0124 N NaCl (72.5 mg solid diluted to 100 mL) to give 33.3 mL of a suspension with 30 g solid/L in 0.01 N NaCl;
2. Adjust pH in each container to within 0.2 pH units of the desired value with HCl (initial pH is about 8.4 after mixing, requiring between 0.5 and 1.0 mL of 0.1 N HCl for reaching the appropriate pH);
3. Equilibrate overnight in shaker at 25 C;
4. Check pH the next day and adjust if necessary (slight upwards drift, less than 0.10 pH unit, was observed, as expected);
5. Add 1.0 mL of 0.1 M $NaH_2PO_4.H_2O$ (138 mg undried solid diluted to 10 mL);
6. Equilibrate 1 hr in shaker;
7. Adjust pH (pH rose 4 to 4.5 units in all samples and required addition of 1.25 to 1.5 mL of 0.1 N HCl to return to desired value);
8. Equilibrate overnight in shaker at 25 C;
9. Check pH and adjust if needed (a small increase in pH was noted and required addition of 25 uL of 0.1 N HCl);
10. Dilute samples to 1 L with a solution of 0.01 N NaCl (584.5 mg solid diluted to 1 L) adjusted to the desired pH (solution pH before adjustment was about 6.0);
11. Transfer samples to 1 L plastic bottles for storage.

All plasticware used in sample preparation had been washed with a non-phosphate detergent, rinsed several times with deionized water, soaked overnight with 10% by volume nitric acid, rinsed several times with deionized water, soaked overnight with deionized water, and rinsed several times with deionized water before use. All samples were stored at room temperature. Subsamples distributed to participants were obtained by shaking the sample container and pouring out 200 mL of suspension into washed plastic bottles.

Results (Goethite 1)

Sample preparation was completed on 9/25/89, and initial measurements were obtained on 9/28/89. At this time pH values were measured as 4.36, 5.15 and 6.05. These values provide the basis for designating the samples as "Nominal pH" 4.4, 5.1 and 6.1. Table 1 lists the measurements obtained for each sample. Values of pH were obtained in stirred samples, except when two values are separated by a slash. In this case, the first value listed was obtained in a stirred sample, while the second value was obtained in a quiescent sample. Reported mobility values are averages of several measurements. A typical protocol for measuring mobility was:

1. Flush measurement cell with sample at least twice;
2. Measure mobility;
3. Let sample stand in cell for two minutes;
4. Repeat mobility measurement;
5. Let sample stand in cell another two minutes;
6. Repeat mobility measurement;
7. Load cell with fresh sample at same pH;
8. Repeat steps 2 - 6;
9. Wash measurement cell with deionized water or 0.01 N NaCl;
10. Repeat steps 2 - 8 for sample at different pH.

All University of Wisconsin (UW-M) measurements were obtained on samples taken from the 1 L stock containers, as were the first set of Rutgers (RU) measurements. All other measurements were taken using subsamples which had been dispensed into smaller plastic bottles.

Discussion (Goethite 1)

Agreement between UW-M and RU for the mobility measurements was good, although measurements at Penn State (PSU) and Oak Ridge (ORNL) were consistently low and high, respectively. This agreement is close enough to indicate that phosphated goethite may serve as an internal mobility standard for the round-robin. Measured values of pH agreed to within 0.2 pH units at all sites, which is not very good. However, these measurements may have been affected by sample aging. Several points will be discussed individually.

1.) Variations in sample properties over time.
2.) Suspension instability.
3.) Variations in pH measurements.
4.) Instrumentation problems.

TABLE 1. Round robin mobility measurements (times 1E8 m^2/V-sec) obtained for Goethite 1 mobility standards.

Nominal pH	Date (1989)	Site	Measured pH	Measured Mobility	Mobility Std. Dev.
4.4	9/28	UW-M	4.36	+ 1.68	0.10
	10/06	RU		+ 1.75	
	10/07	PSU	4.42	+ 1.1	
	10/27	UW-M	4.49/4.50	+ 1.87	0.07
	11/18	UW-M	4.46	+ 1.67	0.05
	11/18	ORNL	4.30/4.60	+ 2.30	0.20
	11/19	RU	4.33/4.35	+ 1.89	
5.1	9/28	UW-M	5.15	+ 0.33	0.02
	10/06	RU		+ 0.2	
	10/07	PSU	5.29	- 0.99	
	10/27	UW-M	5.44/5.27	+ 0.58	0.06
	11/18	UW-M	6.04	+ 0.33	0.05
	11/18	ORNL	5.06/5.25	+ 1.09	0.16
	11/19	RU	5.15/5.17	+ 0.51	
6.1	9/28	UW-M	6.05	- 1.37	0.06
	10/06	RU		- 1.25	
	10/07	PSU	6.10	- 1.6	
	10/27	UW-M	6.13/6.05	- 1.18	0.03
	11/18	UW-M	6.59	- 1.31	0.03
	11/18	ORNL	5.80/5.94	- 0.53	0.12
	11/19	RU	6.09*/6.05	- 1.26	

* A stable pH reading was not obtained. The measured values varied between 6.03 and 6.18.

(1) Sample Variation

Previous experience indicates that the long-term (over a period of several weeks) kinetics of phosphate adsorption and desorption on goethite is rather complex.[3] Some of the variations in measured properties, both pH and mobility, may be attributed to the complicated kinetic behavior of these systems.

Mobility measurements for the low pH samples at both UW-M and Rutgers may be exhibiting a slight increase over time, although these changes are small enough that they may simply be due to instrument measurement errors. The most recent UW-M measurement also does not fit this scenario, as the mobility had decreased to its original value. However, Dr. Tejedor has also

observed what appear to be periodic variations in mobility values for phosphated goethite samples as they age. If the range of these variations is limited to 0.2E-8 m^2V-sec, then this material may serve as a mobility standard even if it displays complex kinetic behavior on aging. One advantage of this material is that its pH remained relatively constant, except at PSU.

Mobility values for the high pH sample also displayed somewhat similar behavior but complicated by a significant increase in pH at some point in the aging process. This increase was noted at both PSU and UW-M, although not at the other sites. In order for mobility to remain nearly constant while pH increased, as observed at UW-M, phosphate would have to desorb from the solid.

A possible driving force for phosphate desorption could be adsorption of phosphate on the walls of the container. Although the surface area of the goethite is ca 1000 times larger than the area of the walls of the container, any microporosity, imperfections in the wall structure or leaching into the container could affect the system. One possible approach to minimize the effects of the container is to expose them to a phosphate solution before using those containers in phosphate adsorption studies.

A second possible reason for phosphate desorption could be competition between phosphate and either CO_2 or bicarbonate, depending on the system pH, for adsorption sites on the goethite. There are two reasons for discounting this hypothesis. (1) Phosphate and CO_2 do not adsorb on the same site, so no competition would be expected. (2) If phosphate and bicarbonate are adsorbing on the same site, phosphate would be expected to adsorb much more strongly because of its strong chemical bonding. Thus, phosphate should outcompete bicarbonate. However, it should be noted that the pH increase was observed at PSU only after the sample had been left open to air, while the pH increase at UW-M was obtained after the 1 L sample bottle had been opened several times to dispense subsamples. Samples at the other locations would have had less contact with air. Exposure to some component of air may affect the aging processes occurring in these samples.

The intermediate pH sample displayed larger variations in mobility as well as a fairly large pH rise, again observed only at UW-M and PSU. This rise in pH should have the same causes as the rise discussed above, while the variation in mobility values is not surprising and will be discussed next.

(2) Suspension Instability

When the samples were prepared, it was thought that the low and high pH samples would be stable suspensions with positive and negative mobilities, respectively. Based on our previous experience, these samples were expected to provide more reproducible mobility measurements than the sample at intermediate pH. The intermediate pH sample was prepared simply as a check on the behavior of a sample with a low mobility.

It was rather surprising to find that the intermediate pH samples measured at UW-M gave quite reproducible results during any one set of measurements, with reproducibility as good as or better than the reproducibility obtained for samples with higher mobilities which should have been more stable. There did not appear to be any problems due to sample settling during the UW-M

measurements. However, all other sites did indicate that sample settling was a significant problem for all the samples.

(3) Variations in pH Measurements

Differences in pH values as large as 0.3 pH units between stirred and quiescent systems were observed at both UW-M and ORNL. These measurements were performed in order to evaluate the possibility of determining pH in concentrated suspensions by allowing the particles to settle and then measuring the pH of the quiescent supernatant. It now appears that pH measurements in stirred systems are more reliable. Thus, pH measurements in concentrated suspensions can be performed by centrifuging the suspension, pouring off a sample of the supernatant, and measuring the pH of that supernatant while stirring.

There was also some variation in pH measurements among different groups for the same sample. However, it is difficult to separate variations due to sample aging from variations due to differences in measurement techniques and instrumentation. It is recommended that all groups use the same model pH electrode (Orion Model 8172BN Sure-Flow Ross combination pH electrode). Based on the results reported herein, agreement to within 0.2 units for pH values may be all that we can expect.

(4) Instrumentation Problems

If we accept that the good agreement in mobility values between Rutgers and UW-M indicates that these values are the "true" values for the samples, then measurement problems are apparent with both the ORNL and PSU instruments. The PSU instrument consistently read lower than "true", with the discrepancy being worst at the intermediate pH where sample settling problems would be most acute. On the other hand, the ORNL instrument consistently provided higher values, with the largest discrepancy occurring at the highest pH. Instrument operators at both sites mentioned that the sample instability was severe enough to significantly affect the measurement process. If the next set of samples does exhibit more suspension stability, there may be better agreement among all the instruments.

Sample Preparation (Goethite 2)

The Goethite 1 mobility round-robin proved very useful in indicating where potential problems may exist. As a result, it was decided to proceed with Goethite 2 but incorporating several changes:

a) prepare phosphated goethite samples at the same phosphate loading as used in Goethite 1 but at five pH values (3.5, 4.4, 5.2, 6.1 and 7.0);

b) pre-wash sample containers with a phosphate solution before use;

c) prepare 1 L of sample for each participant, split among five 250 mL bottles;

d) change the inert electrolyte from 0.01 M NaCl to 0.01 M KNO_3;

e) lower the solid concentration to 0.25 g/L.

Samples at five different pH values would be prepared in order to better differentiate random errors in mobility measurements from systematic errors which might indicate some systematic bias in an instrument. This procedure would also improve the measurement statistics and better define the isoelectric point. By splitting the samples among five separate sealed bottles, aging due to contact with air should be minimized. Also, it will be possible to coordinate the timing of the measurements, as was done for the last measurements in Goethite 1.

The actual steps in the procedure were:

1. To five pre-cleaned 4 L bottles, add 4 L deionized water, 1.5 mL of KH_2PO_4 solution (2.27 g/250 mL), and 4.04 g of solid KNO_3;
2. Add appropriate amounts of acid (HNO_3) or base (KOH) to obtain solutions of pH 3.5, 4.4, 5.2, 6.1 and 7.0;
3. After allowing the bottles to soak for at least two days, pour the conditioning solutions into the pre-cleaned 250 mL sample bottles;
4. In the conditioned 4 L bottles, make up the same solution as in step 1 but also add 6.35 mL of concentrated goethite suspension;
5. Again add acid or base as needed to obtain solutions at pH 3.5, 4.4, 5.2, 6.1 and 7.0;
6. After the 250 mL sample bottles have been conditioned for at least two days, replace the conditioning solution with suspension of the same pH and cap the bottle.

Because of the sample size, overnight shaking of the suspensions was not performed. Several additions of acid or base were needed to adjust the conditioning and suspension pH to the desired values. During delivery of the concentrated stock goethite suspension in step 4 above, a noticeable amount of suspension stuck to the delivery pipette (estimated at about 5% of the total solid). Thus, the actual solid concentration was somewhat less than 0.25 g/L, and the phosphate loading was correspondingly higher than 100 μmol/g. Although this problem should lower the measured isoelectric point for these samples below the value reported in ref. 1, the difference in behavior should not be significant for the purposes of the round robin. Although sonication of the suspensions might be helpful in breaking up larger particle aggregates and agglomerates, thereby giving more reproducible suspension behavior, sonication of these samples was not performed because the necessary apparatus was not available.

Samples were received by all participants at the beginning of March 1990 and round robin measurements were scheduled to be taken on or near March 10, 17 and 31 as well as April 7, with one sample held in reserve. All participants were requested to measure the sample pH and mobility of as received samples, although the actual measurement protocol (e.g., equilibration time for pH measurements and number of samples measured for mobility measurements) was not specified. These samples were then sonicated (use of a bath or probe sonicator and a sonication time were not specified), and pH and mobility measurements were repeated.

Preliminary Results and Discussion (Goethite 2)

Agreement among pH values was quite good at pH 3.5 and 4.4, but larger differences appeared as the pH increased further, with a variation of 0.5 pH units being noted for the pH 7.0 samples. This variation is likely due to CO_2 absorption in the samples which would acidify them. Generally, the UW samples at pH 5.2 and higher had a higher measured pH than the other samples, which may indicate that shaking of the samples as they were shipped to other groups introduced considerable CO_2. Samples at UW were quiescent during this period. Even at UW, absorption of CO_2 was evident, since the pH 7.0 sample had been adjusted to pH 7.1 before shipping but consistently measured pH 6.8 during the round robin.

Agreement among mobility values was reasonable, generally within 0.2 to 0.3E-8 m^2/V-sec, although larger differences would be expected at higher pH values (mobility depends on pH for oxide suspensions, and pH variations were larger at higher pH values). The largest variations in mobility occurred for the pH 5.2 samples, which are near or at the isoelectric point for this material. Before we started the round robin, we suspected that the different states of aggregation present near the isoelectric point would make mobility measurements on these samples the most problematic. Our expectations have been fulfilled.

In spite of the measurement differences, the measured isoelectric points for this material fall between pH 4.9 and 5.4. This agreement is almost as good as could be expected for an individual researcher reporting a value for an isoelectric point. Thus, measurement of isoelectric points appears to be a valid characterization technique for materials which display one.

Although sonication did cause changes in measured properties among the different groups, there does not appear to be a general effect which can be noted at this time. Differences in pH measurement techniques did not appear to be significant either.

References

1. M.I. Tejedor-Tejedor and M.A. Anderson, "Protonation of Phosphate on the Surface of Goethite As Studied by CIR-FTIR and Electrophoretic Mobility," *Langmuir* 6, 602-11 (1990).

2. R.J. Atkinson, A.M. Posner and J.P. Quirk, "Crystal Nucleation in Fe(III) Solutions and Hydroxide Gels," *J. Inorg. Nucl. Chem.* 30, 2371-81 (1968).

3. M.A. Anderson, M.I. Tejedor-Tejedor and R.R. Stanforth, "Influence of Aggregation on the Uptake Kinetics of Phosphate by Goethite," *Environ. Sci. Technol.* 19(7), 632-7 (1985).

Status of Milestones

1. Complete round robin characterization of "benchmark" colloid. Expected completion: May 31, 1990. On schedule, but may be delayed if a "Goethite 3" study is needed.

2. Complete initial round robin mobility testing of silicon nitride. Expected completion: Nov. 30, 1990. On schedule.

3. Complete round robin mobility testing of silicon nitride. Expected completion: May 31, 1991. On schedule.

4. Complete peak assignments for CIR-FTIR spectra of aqueous suspensions of silicon nitride. Expected completion: Nov. 30, 1991. On schedule.

Publications

None.

Surface Adsorption

J. H. Adair and A. Rabinovich (Pennsylvania State University)

Objective/scope

This project represents a coordinated effort among ORNL and three university laboratories (WBS Elements 3.5.1.7, 3.5.1.8, 3.1.5.9, and 3.5.2.0). The purpose of this project (WBS 3.1.5.9) is to study the surface chemical interaction of silicon nitride powders in aqueous and nonaqueous environments and to study surface chemical modification of material, and, in particular to understand the acid-base nature of the silicon nitride - solvent interface.

Background

As a heat-resistant material, silicon nitride has applications in ceramic engines, heat exchangers, turbine blades, and high frequency combustion crucibles. The variety of current and potential applications for silicon nitride require a range of forming operations to fabricate the specific components. Most of the forming processes required to achieve the range of shapes for silicon nitride components require the use of organic additives. For example, precombustion chambers for diesel engines and turbine blades are usually injection molded using highly filled thermoplastic polymers while tubular heat exchangers are extruded with less polymer as binder and usually the binder is significantly different in terms of functional groups and properties than those polymers used for injection molding.

Ceramic processing often involves the suspension of ceramic powders in an organic solvent rather than water to promote separation or dispersion of the ceramic particles during forming operations. The use of nonaqueous solvents is particularly important in the processing of nonoxide ceramics such as silicon carbide, silicon nitride, and aluminum nitride because these compounds are subject to reactions with water to form oxides or hydroxides surface groups or, in the case of aluminum nitride, uniform transformation to the hydroxide. Yet little fundamental data exist on the interaction of ceramic particle surfaces with the organic species in organic solvents. Furthermore, the role that the surface composition of the ceramic particle plays in the dispersion and interaction of particles in solvents is not well established. The current study is designed to determine the nature of the surface interactions of silicon nitride with organic solvents and solutes.

Approach

There are four participants in the overall project: ORNL and three universities, Penn State, University of Wisconsin, and Rutgers University.

The Penn State project is composed of two distinct elements:

1. A round robin characterization of electrophoretic mobility and acid-base character in aqueous suspension to be conducted by all participants.

2. Special projects at Penn State:

The Penn State workplan is based on five tasks: Task 1 to participate in round-robin particle electrophoretic mobility measurements, Task 2 to determine the nature of reactive sites on the silicon nitride surface, Task 3 to modify the chemistry of the silicon nitride interface using organic species, Task 4 to determine the rheological and dispersion properties of the nonaqueous silicon nitride suspensions, and Task 5 to ensure transfer technology to ORNL via meetings and reports. Each task is discussed in detail below.

Technical progress

FY 1989

Round robin - Electrophoresis - Goethite standards prepared at Wisconsin were evaluated as part of the Penn State participation in the round robin.

Reactions at the Silicon Nitride - Solution Interface - A study was conducted to determine the extent of aqueous reactions at the silicon nitride-water interface. It was demonstrated that up to 27 days are required to stabilize reactions at the interface as indicated by Ph and particle electrophoresis measurements. A semiautomatic titrator was also purchased and set up to utilize acid-base titrations to study the silicon nitride-solvent interface. A particular emphasis of this work will be on the nonaqueous potentiometric and conductometric titration to determine the strength of acid and base sites on the silicon nitride surface.

FY 1990

Round robin - Electrophoresis and pH measurements - The round robin electrophoresis on the goethite standards prepared at Wisconsin indicated several interesting features. The isoelectric points determined at each of the participants were similar, but measured pH values displayed considerable scatter. The suspected influence of dissolved CO_2 and adducts and methods to overcome the effect of these dissolved species are currently under investigation at Penn State.

Reactions at the silicon nitride - solution interface - The use of potentiometric titrations in nonaqueous solvents indicates that there are possibly several different kinds of acid and base sites on the silicon nitride depending on the prior environmental history of the powder. The results are generally consistent with potentiometric titrations used to evaluate the silicon dioxide surface. Future work will focus on further potentiometric as well as conductometric titrations on silicon nitride as well as model systems such as silicon dioxide.

FY 1991

Round robin - The first test of the silicon nitride powders will be completed and evaluated. A second round of tests on silicon nitride will

be performed, if necessary. The final, approved test procedure will be written. Industrial participation will be invited.

Reactions at the silicon nitride - solution Interface - The strengths of the acid and base sites at the silicon nitride surface will be estimated based on calculate relative bond strengths and the nonaqueous titrations. The surface of silicon nitride will be modified, using metal organic coatings selected to ensure both dispersion and inhibition of oxidation reactions.

Milestone schedule

The program is on schedule.

Surface Thermodynamics

R. E. Riman, D. J. Shanefield, and J.-F. Wang (Rutgers University)

Objective/scope

The purpose of this effort is to (1) identify and characterize those aspects of the chemistry and physics of the ceramic powder and powder/solvent interface that control processing, (2) develop standard methods of analysis for item (1), and (3) develop procedures for writing specifications for ceramic powders to include any methods of analysis developed in this project.

Technical progress

Microelectrophoresis is an important method for measuring surface properties of colloidal materials. In order to obtain reliable measurements, a good reference colloid must be chosen first, and both the behavior of the reference under a variety of measurement conditions and instrumental factors must be established. A good reference colloid should exhibit (a) little sedimentation and agglomeration over the course of the microelectrophoresis experiment, (b) a surface potential as insensitive to pH as possible, (c) commercial availability in a highly pure and reproducible form, and (d) resistance to environmental factors that could change its properties upon storage. Polystyrene latex fulfills most of the criteria cited above (except possibly (d)). Time-dependent, solids-loading and electrolyte concentration effects are determined below in order to establish reproducible referencing conditions. Using these referencing conditions, surface properties of silicon nitride as a function of aging time and atmosphere are studied.

Experimental

All chemicals other than those cited below were purchased from Aldrich Chemical Company, Inc. (Milwaukee, WI), were ACS reagent grade or better, and were used without further purification. Deionized water with a resistivity of 18 MΩ·cm filtered by a 0.22 μm membrane was obtained with a Milli-Q Water System (Millipore Corporation, Bedford, MA). Nitrogen with an oxygen content of less than 5 ppm was obtained from Matheson Gas Products (East Rutherford, NJ). Sulfate group-stabilized 0.5 μm polystyrene latex was purchased from Polysciences, Inc., Lot 81688 (Warrington, PA); Interfacial Dynamics Corporation (Portland, OR); and Sigma Chemical Company, Lot 98F0460 (St. Louis, MO). The former two were surfactant-free dispersions while the latter one contained 0.1-0.5 wt% surfactant. Silicon nitride powder (UBE SN-E10) was obtained from UBE Industries, Inc., Lot A810542 (New York, NY). Suspensions of polystyrene latex were prepared by diluting a concentrated commercial dispersion into a desired volume fraction with

electrolyte solution. The suspension of silicon nitride powder was prepared by dispersing the powder in solution using an ultrasonic bath. Suspension pH was adjusted by addition of either HNO_3 or KOH solution, after which suspensions were stored in sealable Falcon polypropylene containers (American Scientific Products, Edison, NJ).

Prior to characterization, each suspension was divided into two groups for electrophoretic mobility, μ, and pH measurements. A Brinkman 686 Titroprocessor with Metrohm (Switzerland) with Ag/AgCl double junction electrodes, calibrated using pH 4.00, 7.00, and 10.00 buffers, was used for pH measurements. A Malvern Zetasizer II with a Malvern System 4700c correlator at an electric field strength of 15 V/cm was used for microelectrophoresis. Since preconditioning the microelectrophoresis cell is important to obtaining reproducible measurements, a sample of the reference colloid was introduced into the cell and allowed to equilibrate for about 3 min before a second sample was introduced for actual measurement. μ and pH measurements were performed simultaneously at 25°C for each sample. At least seven measurements were made and subsequently averaged together to obtain each μ data point, except for time effect studies, which utilized a single measurement per data point.

Results and discussion

Of the three latexes described above, the Polysciences latex was selected as a reference because it displayed a high zeta potential (ζ~100 mV) and its mobility was the least sensitive to changes in pH for a given electrolyte concentration. For instance, when a 0.01 M KNO_3 electrolyte was employed over a pH range of 5.5 to 10.5 (Figure 1a), μ fell within the range of $(7.71\pm0.05)\times10^{-8}$ m^2/Vs. In contrast, for the latexes manufactured by Interfacial Dynamics and Sigma, μ varied over the

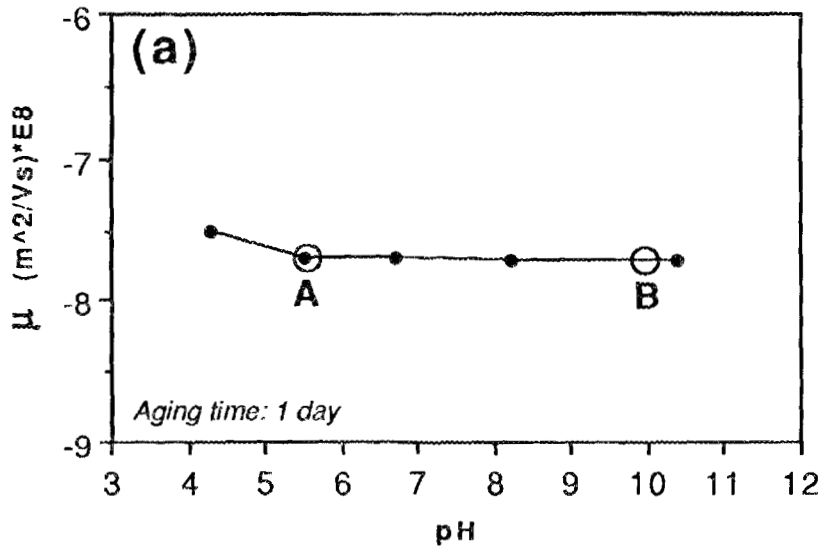

Figure 1. A 0.01 vol% polystyrene latex in 0.01 M KNO_3 solution: (a) mobility as a function of pH

ranges of (6.8±0.09) and (7.30±0.25)x10^{-8} m^2/Vs, respectively, over the same pH range.

While initial measurements for identifying sample-oriented effects made this colloid appear optimum as a reference material, additional measurements were necessary to verify the operation of the microelectrophoresis equipment. The condition of the cell and the associated optics can be examined by using the reference colloid to check the stationary layer positions of the cell. This was accomplished by varying solution pH to vary the electro-osmotic velocity[1] of the suspending solution. Using the intersection of two or more cell profiles yielded experimental stationary layer positions within 5 μm of the position determined from first principles (Figure 1b). The symmetrical μ profiles also show that there are no dimensional asymmetries present. The steepness of the μ profile increases with pH; thus, when the stationary layer position is not properly located, μ is more subject to instrumental error (Figure 1b).

Assuming the instrument is operating properly, obtaining reliable μ values for the reference colloid also depends on the sample preparation conditions. First, our studies revealed that a solids loading greater than 0.005 vol% was required before a constant μ could be obtained (Figure 2). Using different instrumentation (Pen Kem 3000), this has also been found for calcite powders[2]. A decrease in the absolute value of μ has been attributed to hydrodynamic interactions[3] and colloidal phenomena such as double layer compression. In this experiment, however, the

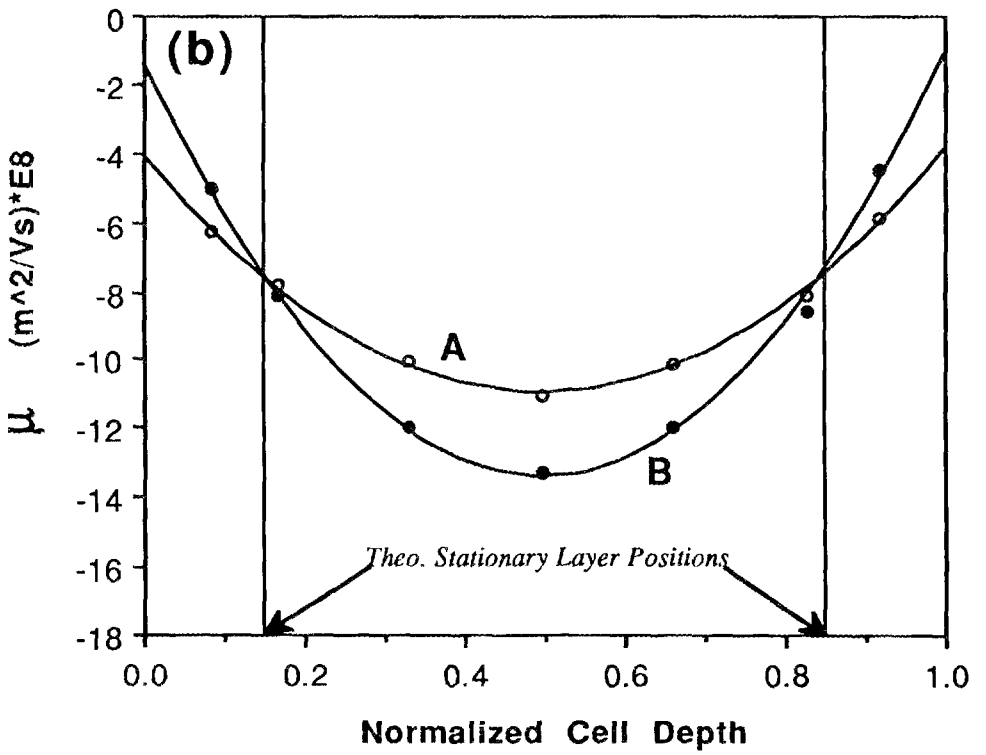

Figure 1 (Cont.). (b) cell mobility profiles as a function of pH

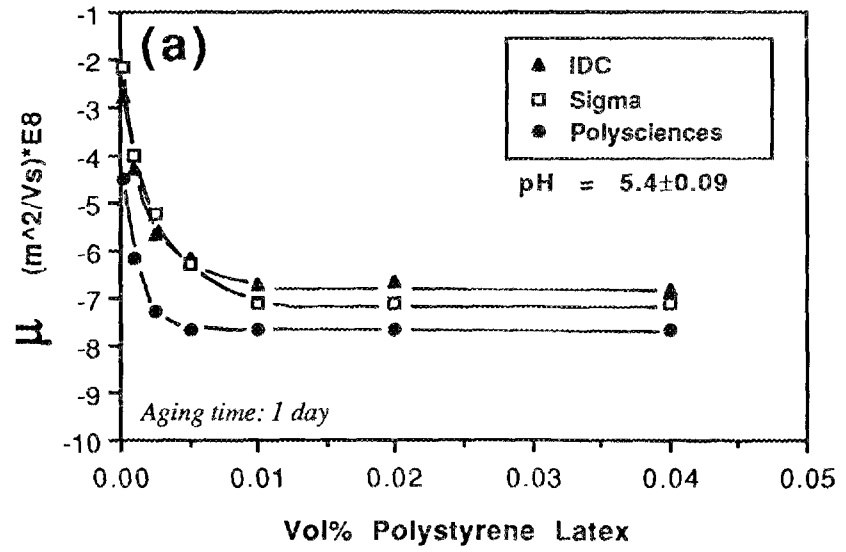

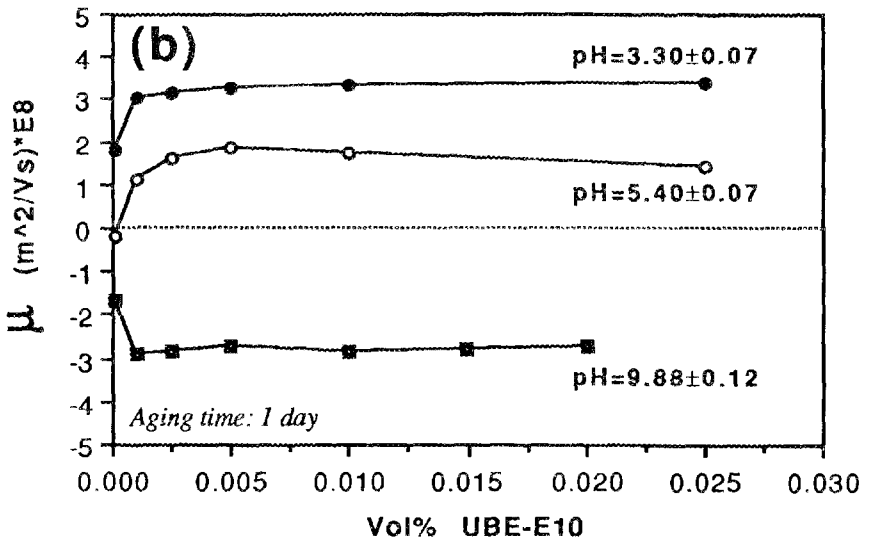

Figure 2. Electrophoretic mobility as a function of solids loading: (a) latex (b) Si_3N_4

absolute value of μ was found to increase. This difference could have been caused by insufficient particle population in the sampling volume for laser Doppler velocimetry. Second, the mobility was found to vary with the time elapsed after introducing the sample into the microelectrophoresis cell, which also varied with the

type and concentration of electrolyte (Figure 3). Therefore, all the measurements were performed immediately after injection into the conditioned sample cell (~2s). This overall approach led to the collection of reproducible μ data. For instance, in a pH range of 5.5 to 10.5 and under the conditions summarized in Figure 1a, the average μ taken from μ plateaus measured 6 months apart differed by as little as 3.4×10^{-9} m^2/Vs.

After using the above reference colloid to check our instrument, μ studies on silicon nitride were conducted. In general, neither time dependency nor electrolyte

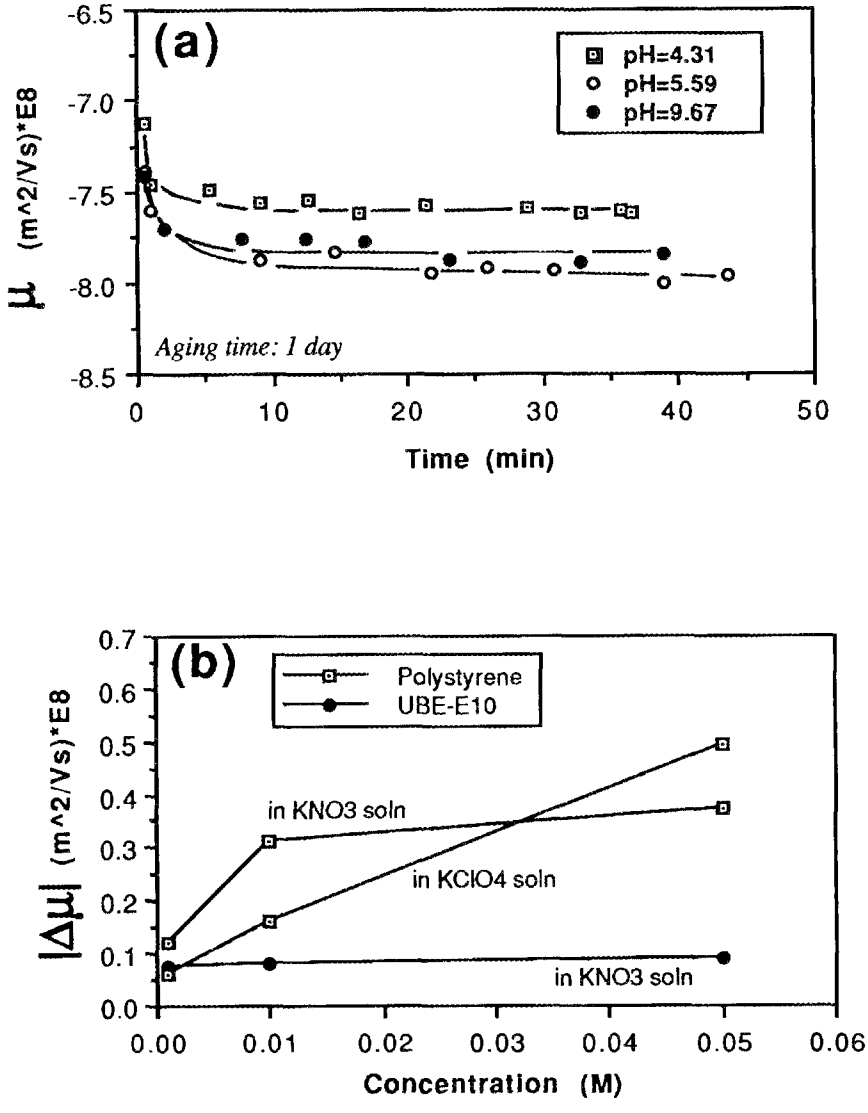

Figure 3. (a) mobility of 0.01 vol% polystyrene latex in 0.01 M KNO_3 solution as a function of time elaped after sample introduction (b) mobility shift of colloid as a function of electrolyte concentration and type

effects were observed for this powder (Figure 3b). However, as with polystyrene latex, solids loading was found to strongly influence the μ (Figure 2b). Thus, in order to obtain reproducible μ measurements, slightly higher solids loadings (>0.01 vol%) are recommended for this powder. To examine μ as a function of aging time and environment, 0.01vol% solids loading suspensions were either exposed to ambient air, stored under air in a sealed container, or stored under nitrogen in a sealed container for a period of 1 to 30 days. The IEP of 0.01 vol% UBE powder in 0.01 M KNO_3 solution shifted from 7.4 to 8.8 as it was aged 1 to 3 days (Figures 4a & 4b). Aging in ambient air for 1 day increased μ greatly in the pH 7 to 8 range,

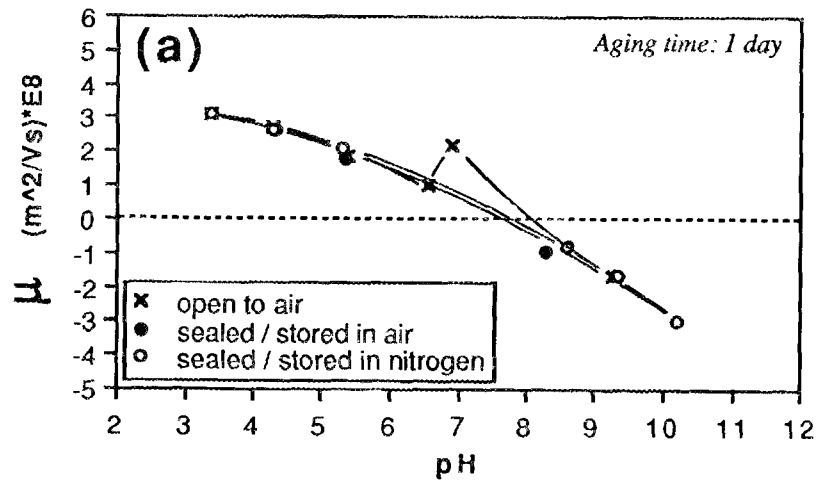

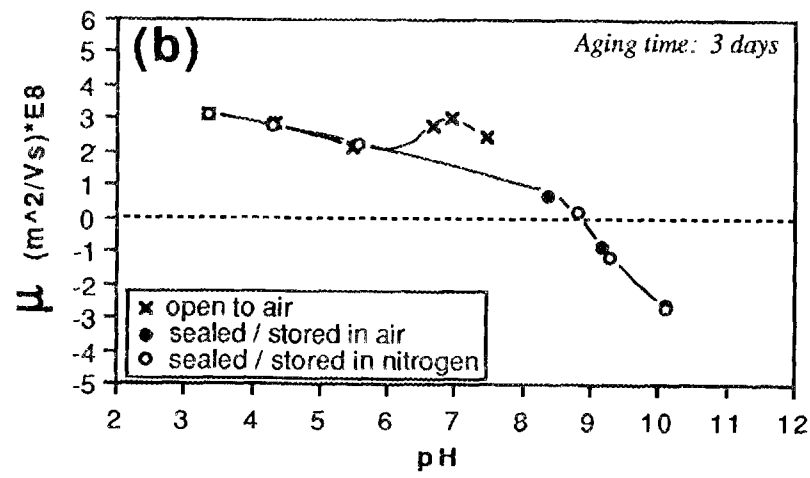

Figure 4. Electrophoretic mobility of silicon nitride powder (0.01 vol% in 0.01 M KNO_3) as a function of aging time and atmosphere: (a) 1 day (b) 3 days

while aging in the other two closed systems did not. At aging times greater than 3 days, the behaviors of different aging environments appear to converge (Figures 4c & 4d). However, at these long aging times, at any pH value below the IEP, the magnitude of μ is greater than at shorter times regardless of the aging environment. The above results can be interpreted in terms of silicon nitride surface chemistry and its chemical interaction with water. This work will be presented in a future publication.

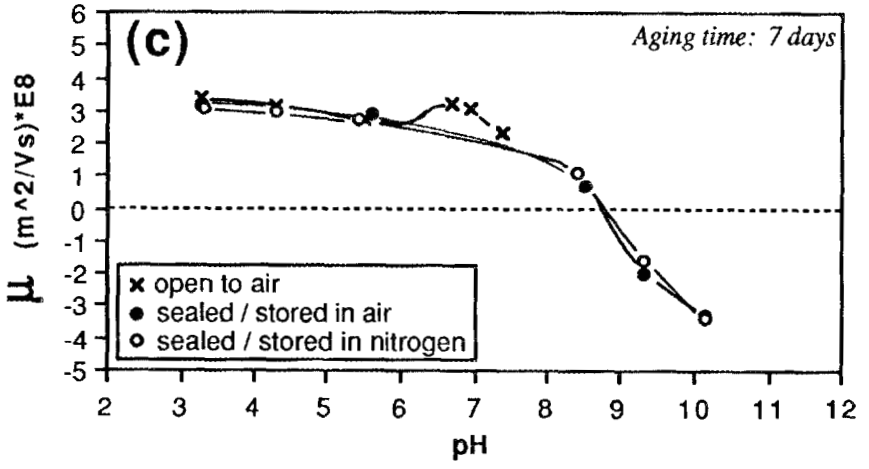

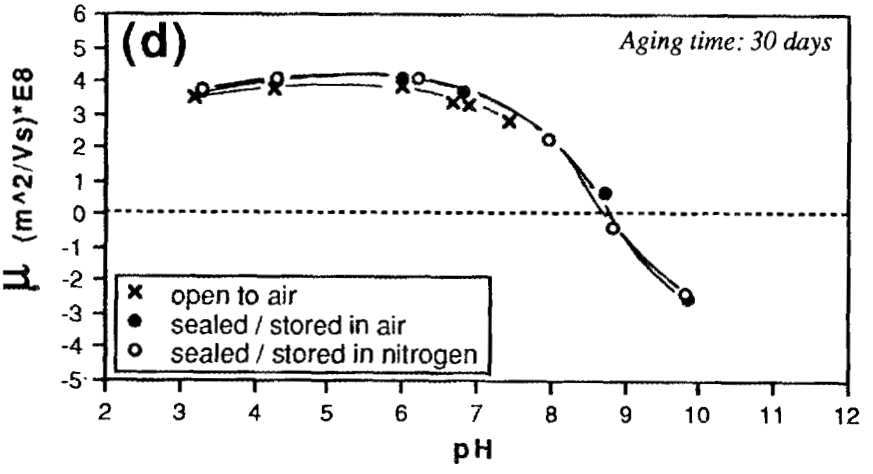

Figure 4 (Cont.). (c) 7 days (d) 30 days

Conclusion

Based on criteria cited earlier, polystyrene latex has been identified as a good reference colloid for establishing the proper operation of a microelectrophoresis apparatus. However, the effects of solids loading, electrolyte concentration, and time on μ must be determined before reference μ values can be established for the colloid. Similar studies should be undertaken when examining any unknown material. When this is done, long-term time-dependent studies can be accomplished with minimal experimental error.

Status of milestones

Milestone 351702---Complete round robin mobility testing of "benchmark" colloid---is expected to be completed before the next Progress Meeting.

Publications

J.-F. Wang, R. E. Riman, and D. J. Shanefield, "Reliable Electrokinetic Characterization Procedures for Ceramic Powders," Presented at Materials Research Society Meeting, San Francisco, Calif., April 16, 1990.

References

1. P. C. Hiemenz, *Principles of Colloid and Surface Chemistry,* 2nd ed., Marcel Dekker, Inc., New York, 1986.

2. B. Siffert and P. Fimbel, "Parameters Affecting the Sign and the Magnitude of the Electrokinetic Potential of Calcite," *Colloids and Surfaces* 11, 377-89 (1984).

3. J. L. Anderson, "Concentration Dependence of Electrophoretic Mobility," *J. Colloid & Interface Sci.* 82(1), 248-50 (1981).

4.0 TECHNOLOGY TRANSFER

4.1 TECHNOLOGY TRANSFER

4.1.1 Technology Transfer

Technology Transfer
D. R. Johnson (Oak Ridge National Laboratory)

Technology transfer in the Ceramic Technology Project is accomplished by a number of mechanisms including the following:

Trade Shows - A portable display describing the program has been built and has been used at numerous national and international trade shows and technical meetings.

Newsletter - A Ceramic Technology Newsletter is published regularly and sent to a large distribution.

Reports - Semiannual technical reports, which include contributions by all participants in the program, are published and sent to a large distribution. Informal bimonthly management and technical reports are distributed to the participants in the program. Open-literature reports are required of all research and development participants.

Direct Assistance - Direct assistance is provided to subcontractors in the program via access to unique characterization and testing facilities at the Oak Ridge National Laboratory.

Workshops - Topical workshops are held on subjects of vital concern to the ceramics community.

International Cooperation - This program is actively involved in and supportive of the cooperative work being done by researchers in West Germany, Sweden, and the United States under an agreement with the International Energy Agency. That work, ultimately aimed at development of international standards includes physical, morphological, and microstructural characterization of ceramic powders and dense ceramic bodies, and mechanical characterization of dense ceramics. Japan is expected to participate in Subtask 6, a new powder characterization research subtask.

IEA Annex II Management
V. J. Tennery (Oak Ridge National Laboratory)

Objective/scope

The purpose of this task is to organize, assist, and facilitate international research cooperation on the characterization of advanced structural ceramic materials. A major objective of this research is the evolution of measurement standards. This task, which is managed in the United States by ORNL, now includes a formal IEA Annex agreement identified as Annex II between the United States, the Federal Republic of Germany, Sweden, and Japan. The original annex included four subtasks, including: (1) information exchange, (2) ceramic powder characterization, (3) ceramic chemical and physical characterization, and (4) ceramic mechanical property measurements. In the United States, a total of 13 industrial and government laboratories have participated and contributed their resources to this research. The research in Subtasks 2, 3, and 4 is now completed. The last report to be published is for Subtask 2, and the master copy was received at ORNL from National Institute of Standards and Technology (NIST) on March 19. The new mechanical strength research is included in a new Subtask 5, while new ceramic powder characterization research is included in a new Subtask 6. An Executive Committee meeting was held on October 24 in Dearborn, Michigan, at which the research plans for Germany, Sweden, and the United States were adopted and that of Japan for Subtask 5 was adopted contingent upon Japan providing a research plan on powders for Subtask 6. We received notification from Japan on December 22 that Japan would be participating in Subtask 6. We also received the names of the tentative technical leaders in Japan for both Subtasks 5 and 6 during December. For Subtask 5, the United States has selected GN-10 silicon nitride for the research to be conducted on mechanical properties. The next Executive Committee meeting is now scheduled to be held in Italy in June. A formal IEA audit of our Annex II research was conducted recently, with Mr. T. Ohji of the Government Industrial Research Institute, Nagoya, Japan, being the program reviewer. A detailed review was conducted at ORNL by Mr. Ohji on October 20. Prior to the meeting, Dr. V. J. Tennery was required to complete an extensive questionnaire on the research participation of industrial research laboratories. The final report on the project which was submitted to the IEA in Paris, France, was very favorable.

Technical progress

Subtask 2 - Ceramic Powder Characterization--A verbal report was received from NIST regarding status of the data analysis report on ceramic powders on November 30. It was expected that the report would be received at ORNL for publication by the end of December.

The final report on ceramic powder characterization and analysis was received from NIST on January 22 in the form of mats ready for reproduction. The report numbered 569 pages. Suggestions were provided to NIST for shortening the report, and NIST agreed to revise the report. Additional mats and the original camera-ready copy were returned to NIST on February 2.

The final report on ceramic powder characterization and analysis was received from NIST on March 19. The report is scheduled for publication by the end of April.

This completes all research activity for Subtask 2.

Subtask 3 - Ceramic Chemical and Structural Characterization--We received preliminary copies of the report (Subtask 3) from reproduction at ORNL on October 18. This report concerns chemical and structural characterization of the sintered ceramics studied

in Subtask 4. Final copies of the report were received from reproduction on November 10. The copies were mailed with the Subtask 4 report on December 8.

Copies of the report entitled "Characterization of Sintered Silicon Nitride and Silicon Carbide Structural Ceramics," prepared by Mr. M. E. Hatcher of KemaNord Industrikemi in Sweden and printed at ORNL, were distributed to all participants on December 8.

This completes all research activity for Subtask 3.

Subtask 4 - Mechanical Properties of Ceramics--A final copy of a report prepared in Germany, entitled "Analysis of Error Sources in Four Point Flexure Strength Measurements of Structural Ceramics," by A. Brückner-Foit, K. Hofacker, and D. Munz of the KFA, Universität Karlsruhe and printed at ORNL, was provided to us at the Executive Committee meeting on October 24. This report was placed upon mats and was sent to reproduction November 11, 1989. The finished reports were received from reproduction on December 1, 1989. They were sent to the participants in the United States and to the representatives for distribution in Germany and Sweden on December 8.

The distribution of this report concludes all of the research work planned in this subtask.

Subtask 5, Flexural and Tensile Properties of Ceramics--On October 2, V. J. Tennery sent a letter to U.S. participants in this subtask providing information on the recent developments in the annex. On October 11, a copy of communication from Mr. A. Chesnes, USDOE, to Mr. Soichi Nagamatsu, Director for Development Program, Moonlight Project Promotion Office of Ministry of International Trade and Industry (MITI) in Japan, was received regarding details of research plans and in reply to certain concerns regarding funding of the research from the Japanese side. A formal communication was provided to the IEA in Paris by L. Boesch, and received at ORNL on October 16, 1989, regarding research content of the new Subtask 5.

Eight plates of GN-10 were sent for machining on October 13 to Bomas Machine Specialties, Inc. Machined specimens were scheduled for shipment on December 4. We sent an additional three plates to Bomas in late November. These plates provide the 450 flexure specimens required for this research in the United States, in addition to the archive specimens. The purchase order for the rods from which tensile specimens of GN-10 silicon nitride will be prepared was placed, with the first partial delivery made in mid-December. Including shipments received on December 20, 1989, and January 29, 1990, we received the entire complement of 668 machined GN-10 flexure bars from Bomas. These specimens are being used for the flexure strength measurements being conducted in this subtask. Dimensioning, repackaging, and randomizing of the 668 specimens were completed. A total of 30 bars will be tested at room temperature and 15 bars will be tested at high temperature by 9 U.S. laboratories and ORNL. Randomizing of the 668 flexure bars of GN-10 silicon nitride was completed in March, and the specimen sets for the room temperature and high-temperature strength measurements were prepared for distribution. Final checks on the steel room-temperature flexure fixtures were completed and the fixtures packed for shipment to the nine participating laboratories (in addition to ORNL). On March 8, letters were sent to all U.S. participants, with a description of the status of the flexure fixtures and specimens. On March 30, instructions for use of the flexure fixtures and a request for a time schedule for the measurements were sent to all U.S. participating laboratories.

Machining of the tensile specimens to be used in the United States plus the five specimens to be provided to Germany and Sweden, and perhaps Japan will start in April and is planned to be completed by the end of August. In addition, on December 28, we received a partial shipment of GN-10 Si_3N_4 cylindrical rods (47 of 160) from Garrett Ceramic Components Division. On February 23, we received 95 of the 160 rod blanks required for preparation of the tensile specimens. On March 22, we were authorized to order an

additional 50 rod blanks of GN-10 for this purpose. On March 29, we received the final shipment of 18 rod blanks of the initial order of 160 for tensile specimen preparation. Based upon the conclusions of an industrial workshop meeting on tensile testing of structural ceramics held on March 5 in the HTML at ORNL, and a consensus of the U.S. industrial participants in this subtask, it was decided to include a critical comparison of the tensile strengths measured using both straight and tapered collet grips and specimens.

A formal IEA audit of our Annex II research was conducted during this period, with Mr. T. Ohji of the Government Industrial Research Institute, Nagoya, being the program reviewer. A detailed review was conducted at ORNL by Mr. Ohji on October 20. Prior to the meeting, V. J. Tennery was required to complete an extensive questionnaire on the research participation of industrial research laboratories.

V. J. Tennery presented a summary of research plans for Germany, Sweden, Japan, and the United States to the Executive Committee on October 24. Representatives of each country then elaborated on their planning for the research participation in this new subtask. The Executive Committee agreed that if Japan will agree to also participate in Subtask 6 on ceramic powders, then Japan will become a participating member of Annex II. It was agreed that this detail would be resolved by the end of calendar year 1989.

On March 23, the final minutes of the Executive Committee meeting from June 1989 in Maastricht were received.

The following scheduled events have been selected to complete this research by approximately the end of calendar year 1991.

1. Initiate strain gauged flexural specimen strength measurements in participating industrial laboratories, by April 30, 1990.
2. Complete flexure strength measurements in U.S. laboratories by January 31, 1991. Complete tensile strength measurements in U.S. laboratories by September 30, 1991.
3. Complete data analysis and preparation of report draft of research results on Mechanical Properties of Ceramics by December 31, 1991.

Subtask 6, Advanced Ceramic Powder Characterization--On October 12, a proposed description of the new research to be conducted on ceramic powders in this new subtask was received from Dr. S. Malghan of NIST.

Dr. S. Hsu reviewed the research plans for this subtask at the Executive Committee meeting on October 24.

Plans were completed for Dr. S. Malghan and Dr. S. Hsu to visit Japan in February to finalize the ceramic powder characterization plans with our Japanese colleagues.

The following scheduled events have been selected to complete this research by approximately the end of calendar year 1991.

1. Complete 25% of data compilation for five ceramic powders at NIST, and start data analysis by March 30, 1991.
2. Complete powder data analysis, at NIST, by December 31, 1991, including preparation of report draft.

Status of milestones

The milestone is on schedule.

Publications

A. Brückner-Foit, K. Hofacker, and D. Munz, "Analysis of Error Sources in Four Point Flexure Strength Measurements of Structural Ceramics," IEA Report, ORNL, December 1989.

M. E. Hatcher, "Characterization of Sintered Silicon Nitride and Silicon Carbide Structural Ceramics," IEA Report, ORNL, October 1989.

M. K. Ferber and V. J. Tennery, "Fractographic Study of a Silicon Nitride Ceramic," *Euro-Ceramics, Vol. 3, Engineering Ceramics*, pp. 3.120-3.125, Elsevier Applied Science, New York, 1989.

Standard Reference Materials

S. G. Malghan, L. S. Lum, D. B. Minor, J. F. Kelly, and J. P. Cline
(National Institute of Standards and Technology)

Objective/Scope

Ceramics have been successfully employed in engines on a demonstration basis. The successful manufacture and use of ceramics in advanced engines depends on the development of reliable materials that will withstand high, rapidly varying thermal stress loads. Improvement in the characterization of ceramic starting powders is a critical factor in achieving reliable ceramic materials for engine applications. The production and utilization of such powders require characterization methods and property standards for quality assurance.

The objectives of the NIST program are (1) to assist with the division and distribution of five ceramic starting powders for an international round-robin on powder characterization; (2) to provide reliable data on physical (dimensional), chemical and phase characteristics of powders; and (3) to conduct statistical assessment, analysis and modeling of round-robin data. This program is directed toward a critical assessment of powder characterization methodology and toward establishment of a basis for the evaluation of fine powder precursors for ceramic processing. This work will examine and compare by a variety of statistical means the various measurement methodologies employed in the round-robin and the correlations among the various parameters and characteristics evaluated. The results of the round-robin are expected to provide the basis for identifying measurements for which Standard Reference Materials are needed and to provide property and statistical data which will serve the development of internationally accepted standards.

Technical Progress

The technical progress covered in this report includes descriptions of work on preparation of final report on IEA Annex II Subtask 2 activities, start-up activities of Subtask 6, and preparation of samples for interlaboratory comparison study.

Final Report on Subtask 2 Activities. The final report containing data, technical analysis, procedures, statistical analysis of data, and recommendations was sent to ORNL for publication in March 1990. The copies of this report will be sent to participants of Subtask 2 in May 1990.

Subtask 6 Start-up. The Subtask 6 start-up activities are primarily devoted to define: 1) technical scope in terms of powder properties to be studied; 2) inclusion of powders; 3) inclusion of Japan as a participating country 4) tightening of procedures 5) preparation of samples for the interlaboratory study.

Powder Properties. Based on the recommendations of Subtask 2 study and subsequent discussions with the participants, a technical plan was developed. The properties to be studied in Subtask 6 are divided into 3 groups -- physical, bulk chemical and surface chemical properties. A total of 26 properties are included for measurement. The physical and bulk chemical measurements will be carried out using tightened procedures; whereas, the surface chemical measurements will be obtained using the procedures of participants choice. The overall purpose of the Subtask 6 (Group 1 and 2) is to determine variability in the method of powder analysis with respect to the laboratory, when all the labs. are following the same procedure. The properties in the Group 3 are considered to be of exploratory nature.

Inclusion of Powders. Following the discussions with participants, five powders are included in this study:

1. Silicon nitride, Ube SNE-10
2. Silicon carbide, Starck
3. Zirconia - 4% Yttria, TOSOH
4. Silicon nitride, Starck LC-10
5. Aluminum nitride, Dow

The first two powders are considered to be primary; while the remaining are optional. The participants will analyze primary powders plus one of the optional powders.

Japan's Participation. In March 1990, Japan joined the Subtask 6 program as a fourth participant. Fourteen participants have elected to join from Japan. The list includes most of the major ceramic companies and national labs. With the inclusion of Japan the total number of participants in Subtask 6 has increased to 44.

Tightening of Procedures. This activity has been in progress since December 1989. The first step was to collect procedures from all the participants. The compiled procedures were studied by the participants. Finally, for each method, a recommended procedure (incorporating technical improvements) was developed by the participants. The same process was carried out in each of the participating countries. Currently, these procedures are subjected to ruggedness testing.

Preparation of Samples. The preparation of powder samples for the interlaboratory comparison study has begun. Of the five powders, we have only one powder for which, a sufficient number of samples are available. The remaining powders are ready for splitting. All the necessary equipment is being prepared to start the powder blending and splitting process.

Status of Milestones

On target

Publications

1. S. G. Malghan, A. L. Dragoo, S. M. Hsu, H. Hausner, R. Pompe, "Physical and Chemical Characterization of Ceramic Powders in an International Interlaboratory Comparison Program" Accepted for publication in the proceedings of World Ceramics Congress, 7th CIMTEC, June 1990.

2. S. M. Hsu, A. L. Dragoo, H. Hausner, R. Pompe, S. G. Malghan, "Characterization of Ceramic Powders-IEA/Annex II Subtask 2-Final Report". To be Published by DoE-ORNL, May 1990.

Visits

S. M. Hsu and S. G. Malghan visited Japan in February 1990 to assist Japan in joining the IEA Subtask 6 activity.

INTERNAL DISTRIBUTION

1-2. Central Research Library
3. Document Reference Section
4-5. Laboratory Records Department
6. Laboratory Records, ORNL RC
7. ORNL Patent Section
8-10. M&C Records Office
11. L. F. Allard, Jr.
12. B. R. Appleton
13. R. L. Beatty
14. P. F. Becher
15. T. M. Besmann
16. P. J. Blau
17. A. Bleier
18. E. E. Bloom
19. K. W. Boling
20. R. A. Bradley
21. C. R. Brinkman
22. V. R. Bullington
23. R. S. Carlsmith
24. P. T. Carlson
25. G. M. Caton
26. R. H. Cooper, Jr.
27. S. A. David
28. J. H. DeVan
29. J. I. Federer
30. M. K. Ferber
31. W. Fulkerson
32. R. L. Graves
33. D. L. Greene
34. M. A. Janney
35-39. D. R. Johnson
40. R. R. Judkins
41. M. A. Karnitz
42. H. D. Kimrey, Jr.
43. T. G. Kollie
44. T. B. Lindemer
45. K. C. Liu
46. E. L. Long, Jr.
47. W. D. Manly
48. R. W. McClung
49. D. L. McElroy
50. J. R. Merriman
51. A. J. Moorhead
52. T. A. Nolan
53. J. L. Rich
54. C. R. Richmond
55. J M Robbins
56. M. Rohr
57. M. W. Rosenthal
58. M. L. Santella
59. A. C. Schaffhauser
60. G. M. Slaughter
61. W. B. Snyder, Jr.
62. E. J. Soderstrom
63. D. P. Stinton
64. R. W. Swindeman
65. V. J. Tennery
66. T. N. Tiegs
67. J. R. Weir, Jr.
68. F. W. Wiffen
69. R. K. Williams
70. S. G. Winslow
71. C. S. Yust

EXTERNAL DISTRIBUTION

72. Donald F. Adams
University of Wyoming
Mechanical Engineering
Department
Laramie, WY 82071

73. Jane W. Adams
Corning Glass Works
SP-DV-21
Corning, NY 14831

74. J. Ahmad
Battelle Columbus
Laboratories
Engineering Mechanics
Department
505 King Avenue
Columbus, OH 43201-2693

75. Richard L. Allor
Ford Motor Company
Material Systems
Reliability Division
20000 Rotunda Drive
Post Office Box 2053
Dearborn, MI 48121-2053

76. Richard T. Alpaugh
U.S. Department of Energy
Office of Transportation
Technologies
1000 Independence Avenue, SW
Forrestal Building CE-322
Washington, DC 20585

77. Norman C. Anderson
Ceradyne, Inc.
Ceramic-to-Metal Division
3169 Redhill Avenue
Costa Mesa, CA 92626

78. H. Arbabi
Brunel University
Department of Materials
Technology
Uxbridge Middlesex UB8 3PH
UNITED KINGDOM

79. V. S. Avva
NC A&T State University
Department of Mechanical
Engineering
Greensboro, NC 27411

80. Michel Badia
Embassy of France
4101 Reservoir Road, S.W.
Washington, DC 20007-2176

81. Kirit J. Bahnsali
U.S. Army Materials
Technology Laboratory
SLCMT-EMM
405 Arsenal Street
Watertown, MA 02172

82. John M. Bailey
Caterpillar Inc.
Research Department
Technical Center
Building L
Post Office Box 1875
Peoria, IL 61656-1875

83. Murray Bailey
NASA Lewis Research Center
21000 Brookpark Road
MS:77-6
Cleveland, OH 44135

84. R. R. Baker
Ceradyne, Inc.
3169 Red Hill Avenue
Costa Mesa, CA 92626

85. J. Gary Baldoni
GTE Laboratories Inc.
40 Sylvan Road
Waltham, MA 02254

86. P. M. Barnard
Ruston Gas Turbines Limited
New Products Division
Firth Road
Lincoln LN6 7AA
ENGLAND

87. A. L. Bement, Jr.
TRW, Inc.
23555 Euclid Avenue
Cleveland, OH 44117

88. M. Bentele
Xamag, Inc.
259 Melville Avenue
Fairfield, CT 06430

89. Clifton G. Bergeron
University of Illinois
Department of Ceramic Engineering
105 South Goodwin Avenue
204 Ceramic Building
Urbana, IL 61801

90. Deane I. Biehler
Caterpillar Inc.
Engineering and Research Materials
Technical Center, Building E
Post Office Box 1875
Peoria, IL 61656-1875

91. William D. Bjorndahl
TRW, Inc.
Materials Characterization and Chemical Analysis Department
One Space Park
Building 01, Room 2060
Redondo Beach, CA 90278

92. Dan Blake
Solar Energy Research Institute
1617 Cole Boulevard
Golden, CO 80401

93. Keith Blandford
Boride Products, Inc.
2879 Aero Park Drive
Traverse City, MI 49684

94. Paul N. Blumberg
Ricardo-ITI
415 East Plaza Drive
Westmont, IL 60559

95. Tibor Bornemisza
Sundstrand Turbomach
Division of Sundstrand Corporation
4400 Ruffin Road
Post Office Box 85757
San Diego, CA 92138-5757

96. Han Juergen Bossmeyer
BMW Technologies, Inc.
Watermill Center
800 South Street
Waltham, MA 02154

97. J. A. M. Boulet
University of Tennessee
310 Perkins Hall
Knoxville, TN 37996

98. Les J. Bowen
GTE Laboratories, Inc.
40 Sylvan Road
Waltham, MA 02254

99. Steve Bradley
Signal UOP Research Center
50 UOP Plaza
Des Plaines, IL 60016-6187

100. Raymond J. Bratton
Westinghouse Electric Corporation
R&D Center
1310 Beulah Road
Pittsburgh, PA 15235

101. Catherine E. Brown
E. I. DuPont de Nemours & Company, Inc.
Experimental Station Information Center
E302/301
Wilmington, DE 19898

102. J. J. Brown
Virginia Polytechnic Institute and State University
Department of Materials Engineering
Blacksburg, VA 24061

103. S. L. Bruner
Ceramatec, Inc.
2425 South 900 West
Salt Lake City, UT 84119

104. W. Bryzik
U.S. Army Tank Automotive Command
R&D Center
Propulsion Systems Division
Warren, MI 48090

105. S. T. Buljan
GTE Laboratories Inc.
40 Sylvan Road
Waltham, MA 02254

106. John M. Byrne, Jr.
PPG Industries, Inc.
Corporate Development Department
One PPG Place
Pittsburgh, PA 15272

107. Donald J. Campbell
Air Force Wright Aeronautical Laboratory
AFWAL/POX
Wright-Patterson AFB, OH 45433

108. Roger Cannon
Rutgers University
Department of Ceramics
Bowser Road
Post Office Box 909
Piscataway, NJ 08855-0909

109. Harry W. Carpenter
19945 Acre Street
Northridge, CA 91324

110. David Carruthers
Allied-Signal Aerospace Company
Garrett Auxiliary Power Division
2739 East Washington Street
Post Office Box 5227
Phoenix, AZ 85010

111. Jere G. Castor
J. C. Enterprise
5078 North 83rd Street
Scottsdale, AZ 85253

112. En-sheng Chen
B&C Engineering Research
13906 Dentwood Drive
Houston, TX 77014

113. Albert A. Chesnes
U.S. Department of Energy
Office of Transportation Technologies
1000 Independence Avenue, S.W.
Forrestal Building CE-30, 5G-048
Washington, DC 20585

114. Frank Childs
EG&G, Inc.
Idaho National Engineering Laboratory
Post Office Box 1625
Idaho Falls, ID 83415

115. Gilbert Y. Chin
Bell Telephone Laboratories
R&D
Murray Hill, NJ 07974

116. Melvin H. Chiogioji
U.S. Department of Energy
Office of Transportation Technologies
1000 Independence Avenue, S.W.
Forrestal Building CE-22
Washington, DC 20585

117. William J. Chmura
Torrington Company
Corporate Research
59 Field Street
Torrington, CT 06790

118. Eugene V. Clark
Turbine Metal Technology, Inc.
7327 Elmo Street
Tujunga, CA 91042-2204

119. William L. Cleary
ORI, Inc.
1375 Piccard Drive
Rockville, MD 20850

120. W. J. Clegg
ICI Advanced Materials
Post Office Box 11
The Heath, Runcorn Chesire
WA7 4QE
ENGLAND

121. Jack L. Clem
J. M. Huber Corporation
Carbon Black Division
Post Office Box 2831
Borger, TX 79008-2831

122. Harry E. Cook
Chrysler Motors Corporation
Automotive Research
and Technical Planning
1200 Chrysler Drive
Highland Park, MI 48288-1118

123. Stephen Copley
University of Southern
California
Materials Science Department
Los Angeles, CA 90089-0241

124. John A. Coppola
Carborundum Company
Post Office Box 1054
Niagara Falls, NY 14302

125. Normand D. Corbin
Norton Company
Advanced Ceramics
Goddard Road
Northboro, MA 01532-1545

126. Charles H. Craig
Defense Technology Security
400 Army-Navy Drive,
Suite 300
Arlington, VA 22202

127. William J. Croft
U.S. Army Materials
Technology Laboratory
405 Arsenal Street
Watertown, MA 02172

128. Gary M. Crosbie
1430 Culver Avenue
Dearborn, MI 48121

129. Floyd W. Crouse, Jr.
U.S. Department of Energy
Morgantown Energy
Technology Center
Collins Ferry Road
Post Office Box 880
Morgantown, WV 26505

130. Raymond Cutler
Ceramatec, Inc.
2425 South 900 West
Salt Lake City, UT 84119

131. David A. Dalman
Dow Chemical Company
Central Research, Organic
Specialties
1776 Building
Midland, MI 48674

132. James I. Dalton
Reynolds Metals Company
Metallurgy Laboratory
Fourth and Canal Streets
Post Office Box 27003
Richmond, VA 23219

133. Stephen C. Danforth
Rutgers University
Bowser Road
Post Office Box 909
Piscataway, NJ 08854

134. Robert F. Davis
North Carolina State University
Materials Engineering
Department
232 Riddick Laboratory
Post Office Box 7907
Raleigh, NC 27695

135. Evelyn M. DeLiso
Corning Glass Works
Corning, NY 14831

136. J. Franklyn DeRidder
Omni Electro Motive, Inc.
12 Seely Hill Road
Newfield, NY 14867

137. Keith F. Dufrane
Battelle Columbus
Laboratories
505 King Avenue
Columbus, OH 43201

138. Edmund M. Dunn
Texel Company
21 Eire Street
Cambridge, MA 02139

139. Jeremy D. Dunning
Indiana University
Industrial Research
Liaison Program
Bloomington, IN 47405

140. Sunil Dutta
NASA Lewis Research Center
21000 Brookpark Road
MS:49-3
Cleveland, OH 44135

141. Paul N. Dyer
Air Products and Chemicals,
Inc.
Post Office Box 538
Allentown, PA 18105

142. Robert J. Eagan
Sandia National Laboratories
Department 1840
Post Office Box 5800
Albuquerque, NM 87185

143. Christopher A. Ebel
Norton Company
Advanced Ceramics
Goddard Road
Northboro, MA 01532-1545

144. J. J. Eberhardt
U.S. Department of Energy
Office of Advanced
Transportation Materials
1000 Independence Avenue, S.W.
Forrestal Building CE-12
Washington, DC 20585

145. William A. Ellingson
Argonne National Laboratory
9700 South Cass Avenue
Argonne, IL 60439

146. Charles D. Estes
U.S. Senate
Committee on Appropriations
SD-152 Dirksen Senate
Office Building
Washington, DC 20510

147. John N. Eustis
U.S. Department of Energy
Office of Industrial
Technologies
1000 Independence Avenue, S.W.
Forrestal Building CE-221
Washington, DC 20585

148. Peggy Evanich
National Aeronautics
and Space Administration
Energy Systems Office
Washington, DC 20546

149. Anthony G. Evans
University of California
College of Engineering
Santa Barbara, CA 93106

150. Robert C. Evans
NASA Lewis Research Center
Vehicular Gas Turbine and
Diesel Project Office
21000 Brookpark Road
MS:77-6
Cleveland, OH 44135

151. Katherine T. Faber
Ohio State University
Ceramic Engineering Department
2041 College Road
Columbus, OH 43210

152. John W. Fairbanks
U.S. Department of Energy
Office of Transportation Technologies
1000 Independence Avenue, SW
Forrestal Building CE-151, 5G-042
Washington, DC 20585

153. Larry Farrell
Babcock and Wilcox
Old Forrest Road
Lynchburg, VA 24505

154. Rolf Fasth
Chem Systems, Inc.
303 South Broadway
Tarrytown, NY 10591

155. H. W. Foglesong
Dow Corning Corporation
3901 South Saginaw Road
Midland, MI 48686

156. Thomas F. Foltz
Avco Corporation
Special Materials Division
Two Industrial Avenue
Lowell, MA 01851

157. Robert G. Frank
Technology Assessment Group
10793 Bentley Pass Lane
Cincinnati, OH 45140

158. Douglas W. Freitag
LVT Missiles and Electronics Group
Post Office Box 650003
Dallas, TX 75265-0003

159. P. A. Gaydos
Battelle Columbus Laboratories
505 King Avenue
Columbus, OH 43201

160. George E. Gazza
U.S. Army Materials Technology Laboratory
Ceramics Research Division
405 Arsenal Street
Watertown, MA 02172-0001

161. Bruce W. Gerhold
Phillips Petroleum Company
Engineering Materials, R&D
91-G, PRC
Bartlesville, OK 74004

162. Charles M. Gilmore
George Washington University
Civil, Mechanical, and Environmental Engineering
Washington, DC 20052

163. Paul Glance
Concept Analysis
R&D
950 Stephenson Highway
Dupont Automotive Development Building
Troy, MI 48007-7013

164. Fred M. Glaser
U.S. Department of Energy
Office of Fossil Energy
FE-14 GTN
Germantown, MD 20585

165. Joseph W. Glatz
Naval Air Propulsion Test Center
Systems Technology Division
Post Office Box 7176, PE 34
Trenton, NJ 08628

166. W. M. GoldbergerSuperior Graphite Company
R&D
2175 East Broad Street
Columbus, OH 43209

167. Stephen T. Gonczy
Signal UOP Research Center
Materials Science Department
50 UOP Plaza
Des Plaines, IL 60016-6187

168. Robert J. Gottschall
U.S. Department of Energy
Office of Material Sciences
ER-131 GTN, MS:G-256
Germantown, MD 20585

169. Earl Graham
Cleveland State University
Department of Chemical Engineering
Euclid Avenue at East 24th Street
Cleveland, OH 44115

170. Kenneth Green
Coors Ceramics Company
17750 West 32nd Street
Golden, CO 80401

171. Robert E. Green, Jr.
Johns Hopkins University
Center for Nondestructive Evaluation
Maryland Hall 107
Baltimore, MD 21218

172. Lance E. Groseclose
General Motors Corporation
Allison Gas Turbine Division
Post Office Box 420
Indianapolis, IN 46206-0420

173. P. Ulf Gummeson
Hoeganaes
R&D
River Road and Taylors Lane
Riverton, NJ 08077

174. Bimleshwar P. Gupta
Solar Energy Research Institute
Solar Heat Research Division
1617 Cole Boulevard
Golden, CO 80401

175. M. D. Gurney
NIPER
Post Office Box 2128
Bartlesville, OK 74005

176. John P. Gyekenyesi
NASA Lewis Research Center
21000 Brookpark Road
MS:49-7
Cleveland, OH 44135

177. J. J. Habeeb
Esso Petroleum Canada
Research Division
Post Office Box 3022
Sarina Ontario N7T 7MI
CANADA

178. H. T. Hahn
Pennsylvania State University
ESM Department
227 Hammond Building
University Park, PA 16802

179. Nabil S. Hakim
Detroit Diesel Corporation
13400 West Outer Drive West
Detroit, MI 48239

180. Friedrich Harbach
Asea Brown Boveri AG
Department of Functional Ceramics
Eppelheimer Strasse 82
D-6900 Heidelberg 1
WEST GERMANY

181. Kay Hardman-Rhyne
DARPA
1400 Wilson Boulevard
Arlington, VA 22209

182. R. A. Harmon
25 Schalren Drive
Latham, NY 12110

183. Stephen D. Hartline
Norton Company
Advanced Ceramics
Goddard Road
Northboro, MA 01532-1545

184. Michael H. Haselkorn
Caterpillar Inc.
Engineering Research
Materials
Technical Center, Building E
Post Office Box 1875
Peoria, IL 61656-1875

185. Willard E. Hauth
Dow Corning Corporation
Composite Development
Ceramics Program
3901 South Saginaw Road
Midland, MI 48640

186. Kevin L. Haynes
McDonnell Douglas
Astronautics Company
Post Office Box 516, MS:107/1
St. Louis, MO 63166

187. Norman L. Hecht
University of Dayton Research
Institute
300 College Park
Dayton, OH 45469-0001

188. S. S. Hecker
Los Alamos National
Laboratory
Material Science and
Technology Division, G-756
Post Office Box 1663
Los Alamos, NM 87545

189. Peter W. Heitman
General Motors Corporation
Allison Gas Turbine Division
Post Office Box 420, W-5
Indianapolis, IN 46206-0420

190. Richard L. Helferich
The Duriron Company, Inc.
Post Office Box 1145
Dayton, OH 45401

191. H. E. Helms
General Motors Corporation
Allison Gas Turbine Division
Post Office Box 420
Indianapolis, IN 46206-0420

192. Thomas L. Henson
GTE Products Corporation
Chemical & Metallurgical
Division
Hawes Street
Towanda, PA 18848-0504

193. Thomas P. Herbell
NASA Lewis Research Center
21000 Brookpark Road
MS:49-3
Cleveland, OH 44135

194. Hendrik Heystek
Bureau of Mines
Tuscaloosa Research Center
Post Office Box L
University, AL 35486

195. Robert V. Hillery
General Electric Company
One Neumann Way
Post Office Box 156301
Cincinnati, OH 45215

196. Jonathan W. Hinton
Carborundum Company
Structural Ceramics Division
Post Office Box 1054
Niagara Falls, NY 14302

197. Joe Homeny
University of Illinois
Department of Materials Science
and Engineering
105 South Goodwin Avenue
Ceramics Building
Urbana, IL 61801

198. A. T. Hopper
Battelle Columbus Laboratories
Engineering Mechanics
Department
505 King Avenue
Columbus, OH 43201-2693

199. George Hsu
Jet Propulsion Laboratory
4800 Oak Grove Drive
MS:512-103
Pasadena, CA 91109

200. Shih Hsu
Digital Equipment Corporation
77 Reed Road
MS:HL02-1/L8
Hudson, MA 01749-2895

201. Stephen M. Hsu
National Institute of Standards and Technology
Institute for Materials Science and Engineering
Gaithersburg, MD 20899

202. Harold A. Huckins
Princeton Advanced Technology, Inc.
56 Finley Road
Princeton, NJ 08540

203. Fred Huettic
Advanced Ceramic Technology, Inc.
17 Deerfield Road
East Brunswick, NJ 08816

204. O. Richard Hughes
Celanese Research Company
86 Morris Avenue
Summit, NJ 07901

205. Joseph E. Hunter, Jr.
General Motors Corporation
Research Labs
Metallurgy Department
12 Mile and Mound Roads
Warren, MI 48090-9055

206. Louis C. Ianniello
U.S. Department of Energy
Office of Material Sciences
ER-13 GTN
Germantown, MD 20585

207. Robert H. Insley
Champion Spark Plug Company
Ceramic Division
20000 Conner Avenue
Detroit, MI 48234

208. Curtis A. Johnson
General Electric Company
Ceramics Branch, Physical Chemistry
Post Office Box 8, K1/3C7
Schenectady, NY 12301

209. Larry Johnson
Argonne National Laboratory
Center for Transportation Research
9700 South Cass Avenue, Bldg. 362
Argonne, IL 60439

210. L. A. Joo
Great Lakes Research Corporation
Post Office Box 1031
Elizabethton, TN 37643

211. A. David Joseph
Sealed Power Corporation
R&D
100 Terrace Plaza
Muskegon, MI 49443

212. Debra Joslin
University of Tennessee
Metallurgical Engineering Department
Knoxville, TN 37996

213. Adam Jostsons
Australian Nuclear Science & Technology Organisation
Lucas Heights Research Laboratories
New Illawarra Road
Lucas Heights, New South Wales
AUSTRALIA

214. Roy Kamo
Adiabatics, Inc.
630 South Mapleton
Columbus, IN 47201

215. Allan Katz
Air Force Wright Aeronautical Laboratory
Metals and Ceramics Division
Materials Laboratory
AFWAL/MLLM
Wright-Patterson AFB, OH 45433

216. R. N. Katz
U.S. Army Materials Technology Laboratory
405 Arsenal Street
Watertown, MA 02172

217. Ted Kawaguchi
Tokai Carbon
375 Park Avenue, Suite 3802
New York, NY 10152

218. Frederick L. Kennard, III
General Motors Corporation
AC Spark Plug Division
Department 32-24
1300 North Dort Highway
Flint, MI 48556

219. J. R. Kidwell
Allied-Signal Aerospace Company
Garrett Auxiliary Power Division
2739 East Washington Street
Post Office Box 5227
Phoenix, AZ 85010

220. Max Klein
Gas Research Institute
8600 West Bryn Mawr Avenue
Chicago, IL 60631

221. C. E. Knapp
Norton Research Corporation
8001 Daly Street
Niagara Falls, Ontario
L2G 6S2 CANADA

222. A. S. Kobayashi
University of Washington
Department of Mechanical Engineering
MS:FU10
Seattle, WA 98195

223. Wolfgang Kollenberg
Projektleitung Material-Rohstofforschung - PLR
Kernforschungsanlage Juelich GmbH
Postfach 1913
D-5170 Juelich
WEST GERMANY

224. David M. Kotchick
Allied-Signal Aerospace Company
AiResearch Los Angeles Division
2525 West 190th Street
Torrance, CA 90509

225. Joseph A. Kovach
Eaton Corporation
Manufacturing Technologies Center
32500 Charvon Road
Willoughby Hills, OH 44094

226. Saunders B. Kramer
U.S. Department of Energy
Office of Transportation Technologies
1000 Independence Avenue, S.W.
Forrestal Building CE-151
Washington, DC 20585

227. Dan M. Kreiner
Allied-Signal Aerospace Company
Garrett Auxillary Power Division
Post Office Box 5227
Phoenix, AZ 85010

228. A. S. Krieger
Radiation Science, Inc.
Post Office Box 293
Belmont, MA 02178

229. Pieter Krijgsman
Ceramic Design Int. Hold., Ltd.
Post Office Box 68
8050 AB Hattem
THE NETHERLANDS

230. Jack H. L'Amoreux
11346 Gates Mill Drive
Knoxville, TN 37922

231. W. J. Lackey
Georgia Tech Research Institute
Energy and Materials Sciences
Georgia Institute of Technology
Atlanta, GA 30332

232. Everett A. Lake
Air Force Wright Aeronautical Laboratory
AFWAL/POSL
Wright-Patterson AFB, OH 45433-6563

233. Hari S. Lamba
General Motors Corporation
Electro-Motive Division
LaGrange, IL 60525

234. Manfred Langer
Volkswagen AG
Forschung-Neue Technologien Werkstofftechnologie
D-3180 Wolfsburg 1
WEST GERMANY

235. James Lankford
Southwest Research Institute
Department of Materials Sciences
6220 Culebra Road
Post Office Drawer 28510
San Antonio, TX 78284

236. David C. Larsen
Corning Glass Works
Materials Research Department
Sullivan Park, FR-51
Corning, NY 14831

237. S. K. Lau
Carborundum Company
Technology Division
Post Office Box 832
Niagara Falls, NY 14302

238. Harry A. Lawler
Carborundum Company
Niagara Falls R&D Center
Post Office Box 832
Niagara Falls, NY 14302

239. Alan Lawley
Drexel University
Materials Engineering
Philadelphia, PA 19104

240. Daniel Lee
Temescon
2850 7th Street
Berkeley, CA 94710

241. June-Gunn Lee
Korea Advanced Institute of Science and Technology
Post Office Box 131
Dong Dac Mun Seoul
KOREA

242. E. M. Lenoe
Air Force Office of Scientific Research
Office of Naval Research
Liaison Office, Far East
APO San Francisco, CA 96503-0110

243. Stanley R. Levine
NASA Lewis Research Center
21000 Brookpark Road
Cleveland, OH 44135

244. David Lewis
Naval Research Laboratory
Materials Science and Technology
4555 Overlook Avenue, S.W.
Code 63-70
Washington, DC 20375

245. Bill Long
Babcock and Wilcox
Post Office Box 1260
Lynchburg, VA 24505

246. L. A. Lott
EG&G, Inc.
Idaho National Engineering Laboratory
Post Office Box 1625
Idaho Falls, ID 83415

247. Raouf O. Loutfy
Materials and Electrochemical Research Corporation
7960 South Kolb Road
Tucson, AZ 85706

248. Bryan K. Luftglass
Chem Systems, Inc.
303 South Broadway
Tarrytown, NY 10591

249. Robert Lundberg
Swedish Institute for Silicate Research
Box 5403
S-402 29 Gothenburg
SWEDEN

250. Michael J. Lynch
General Electric Company
Medical Systems Group
Post Office Box 414, 7B-36
Milwaukee, WI 53201

251. Vincent L. Magnotta
Air Products and Chemicals, Inc.
Technical Diversification R&D
Post Office Box 538
Allentown, PA 18105

252. Tai-il Mah
Universal Energy Systems
Ceramics and Composites Research
4401 Dayton-Xenia Road
Dayton, OH 45432

253. L. Manes
Commission of the European Communities
Joint Research Centre
Ispra Establishment
1-21020 Ispra (Varese)
ITALY

254. Giel Marijnissen
Interturbine R&D
Post Office Box 4339
5944 ZG Arcen
THE NETHERLANDS

255. Gerald R. Martin
Fleetguard, Inc.
Cookeville, TN 38501

256. J. W. McCauley
U.S. Army Materials Technology Laboratory
SLCMT-OMM
405 Arsenal Street
Watertown, MA 02172-0001

257. Bryan J. McEntire
Norton Company, TRW Ceramics
Goddard Road
Northboro, MA 01532-1545

258. Thomas D. McGee
Iowa State University
Department of Materials Science and Engineering
Ames, IA 50011

259. H. Christopher McGowan
Advanced Ceramic Technology, Inc.
17 Deerfield Road
East Brunswick, NJ 08816

260. Malcolm G. McLaren
Rutgers University
Department of Ceramics
Bowser Road
Busch Campus
Post Office Box 909
Piscataway, NJ 08854

261. Arthur F. McLean
6225 North Camino Almonte
Tucson, AZ 85718

262. Brian L. Mehosky
British Petroleum
440 Warrensville, Center Rd.
Cleveland, OH 44128

263. Joseph J. Meindl
Reynolds International, Inc.
6603 West Broad Street
Post Office Box 27002
Richmond, VA 23230

264. D. Messier
U.S. Army Materials
Technology Laboratory
DRXMR-MC
405 Arsenal Street
Watertown, MA 02172

265. Brad Miller
Norton Company
Advanced Ceramics
Goddard Road
Northboro, MA 01532-1545

266. Amar Mishra
Engelhard Corporation
R&D
Menlo Park, CN-28
Edison, NJ 08818

267. Bill Moehle
Ethyl Corporation
R&D Laboratories
Post Office Box 341
Baton Rouge, LA 70821

268. Helen Moeller
Babcock and Wilcox
Post Office Box 11165
Lynchburg, VA 24506-1165

269. Peter E. D. Morgan
Rockwell International
Science Center
1049 Camino Dos Rios
Post Office Box 1085
Thousand Oaks, CA 91360

270. Lawrence M. Murphy
Manager
Solar Energy Research Institute
Thermal Systems Research Branch
1617 Cole Boulevard
Golden, CO 80401

271. Solomon Musikant
General Electric Company
Space Systems Division
Post Office Box 8555, MS:U-1219
Philadelphia, PA 19101

272. Pero Nannelli
Pennwalt Corporation
900 First Avenue
Post Office Box C
King of Prussia, PA 19406-0018

273. William D. Nix
Stanford University
Department of Materials Science
and Engineering
Stanford, CA 94305

274. Richard D. Nixdorf
ReMaxCo Technologies, Inc.
231 Sherway Rd
Knoxville, TN 37922

275. S. D. Nunn
University of Michigan
Materials Science and
Engineering
Ann Arbor, MI 48109-2136

276. Brian M. O'Connor
Lubrizol Corporation
Tribology Section
29400 Lakeland Boulevard
Wickliffe, OH 44092

277. W. Richard Ott
Alfred University
Center for Advanced Ceramic
Technology
Alfred, NY 14802

278. William C. Owen
Sundstrand Turbomach
Division of Sundstrand Corporation
4400 Ruffin Road
Post Office Box 85757
San Diego, CA 92138-5757

279. Muktesh Paliwal
GTE Products Corporation
Hawes Street
Towanda, PA 18848-0504

280. Joseph E. Palko
General Electric Company
Gas Turbine Division
TTD Building, 55-113
Schenectady, NY 12345

281. Hayne Palmour, III
North Carolina State University
Engineering Research Services Division
2158 Burlington Engineering Labs
Post Office Box 5995
Raleigh, NC 27607

282. Joseph N. Panzarino
Norton Company
Advanced Ceramics
Goddard Road
Northboro, MA 01532-1545

283. Pellegrino Papa
Corning Glass Works
Corning Technical Products Division
Corning, NY 14831

284. R. H. Parrish
Vanderbilt University
Post Office Box 1621, Station B
Nashville, TN 37235

285. James G. Paschal
Reynolds Metals Company
Post Office Box 76154
Atlanta, GA 30358

286. Arvid E. Pasto
GTE Laboratories Inc.
40 Sylvan Road
Waltham, MA 02254

287. James W. Patten
Cummins Engine Company, Inc.
Box 3005, Mail Code 50183
Columbus, IN 47202-3005

288. Robert A. Penty
Eastman Kodak Company
Manufacturing Technology Department
Apparatus Division
901 Elmgrove Road
Rochester, NY 14650

289. Gary R. Peterson
U.S. Department of Energy
Idaho Operations Office
785 D.O.E. Place
Idaho Falls, ID 83402

290. R. Byron Pipes
University of Delaware
Center for Composite Materials
2001 Spencer Laboratory
Newark, DE 19716

291. Bruce J. Pletka
Michigan Technological University
Department of Metallurgical Engineering
Houghton, MI 49931

292. Robert C. Pohanka
Office of Naval Research
800 North Quincy Street
Code 431
Arlington, VA 22217

293. J. P. Pollinger
Allied-Signal Aerospace Company
Garrett Ceramic Components Division
19800 South Van Ness Avenue
Torrance, CA 90509

294. Stephen C. Pred
ICD Group, Inc.
1100 Valley Brook Avenue
Lyndhurst, NJ 07071

295. Karl M. Prewo
United Technologies Corporation
Research Center
Silver Lane , MS:24
East Hartford, CT 06108

296. Hubert B. Probst
NASA Lewis Research Center
Materials Division
21000 Brookpark Road
MS:49-1
Cleveland, OH 44135

297. Joseph M. Proud
GTE Laboratories Inc.
Materials Science Laboratory
40 Sylvan Road
Waltham, MA 02254

298. D. W. Prouse
Ceramatec, Inc.
2425 South 900 West
Salt Lake City, UT 84119

299. Carr Lane Quackenbush
Norton Company
Advanced Ceramics
Goddard Road
Northboro, MA 01532-1545

300. Brian Quigy
National Aeronautics and Space Administration
Energy Systems Office
Washington, DC 20546

301. George Quinn
U.S. Army Materials Technology Laboratory
405 Arsenal Street
Watertown, MA 02172

302. Dennis T. Quinto
Kennametal, Inc.
Phillip M. McKenna Laboratory
Post Office Box 639
Greensburg, PA 15601

303. Dennis W. Readey
Ohio State University
2041 College Road
Columbus, OG 43210

304. Michael J. Readey
Coors Ceramics Company
R&D
17750 West 32nd Street
Golden, CO 80401

305. Robert R. Reeber
U.S. Army Research Office
Post Office Box 12211
Research Triangle Park, NC 27709

306. K. L. Reifsnider
Virginia Polytechnic Institute and State University
Department of Engineering Science and Mechanics
Blacksburg, VA 24061

307. Paul E. Rempes
McDonnell Douglass Missile Systems Company
Department E-467
Building 107, Level 1
Post Office Box 516
Mail Code 1066086
St. Louis, MO 63166-0516

308. Theresa M. Resetar
U.S. Army Materials Technology Laboratory
Materials Characterization Center
405 Arsenal Street
SLCMT-OMM
Watertown, MA 02172

309. K. T. Rhee
Rutgers University
College of Engineering
Bowser Road
Post Office Box 909
Piscataway, NJ 08854

310. Roy W. Rice
W. R. Grace and Company
7379 Route 32
Columbus, MD 21044

311. David W. Richerson
Ceramatec, Inc.
2425 South 900 West
Salt Lake City, UT 84119

312. Scott L. Richlen
U.S. Department of Energy
Office of Industrial Programs
1000 Independence Avenue, SW
Forrestal Building CE-141
Washington, DC 20585

313. Paul Rieth
Ferro Corporation
661 Willet Road
Buffalo, NY 14218-9990

314. Michael A. Rigdon
Institute for Defense Analyses
1801 Beauregard Street
Alexandria, VA 22311

315. John E. Ritter, Jr.
University of Massachusetts
Mechanical Engineering Department
Amherst, MA 01003

316. Giulio A. Rossi
Norton Company
Advanced Ceramics
Goddard Road
Northboro, MA 01532-1545

317. Barry R. Rossing
Lanxide Corporation
Tralee Industrial Park
Newark, DE 19711

318. Bruce Rubinger
Gobal
50 Milk Street, 15th Floor
Boston, MA 02109

319. Robert Ruh
Air Force Wright Aeronautical Laboratory
Metals and Ceramics Division
AFWAL/MLLM
Wright-Patterson AFB, OH 45433

320. Robert J. Russell, Sr.
Norton Company
Advanced Ceramics
Goddard Road
Northboro, MA 015332-1545

321. George P. Safol
Westinghose Electric Corporation
R&D Center
1310 Beulah Road
Pittsburgh, PA 15235

322. J. A. Salem
NASA Lewis Research Center
21000 Brookpark Center
Cleveland, OH 44135

323. J. Sankar
North Carolina A&T State University
Mechanical Engineering Dept.
Greensboro, NC 27411

324. Vin K. Sarin
Boston University
Department of Manufacturing Engineering
44 Cummington Street
Boston, MA 02215

325. Maxine L. Savitz
Allied-Signal Aerospace Company
Garrett Ceramic Components Division
19800 South Van Ness Avenue
Torrance, CA 90509

326. Ashok Saxena
Georgia Institute of Technology
Materials Engineering
Atlanta, GA 30332-0245

327. Richard Schapery
Texas A&M University
Civil Engineering Department
College Station, TX 77843

328. Jim Schienle
Allied-Signal Aerospace Company
Garrett Auxiliary Power Division
2739 East Washington Street
Post Office Box 5227, MS:1302-2P
Phoenix, AZ 85010

329. Liselotte J. Schioler
Air Force Office of Scientific Research
Bolling AFB
Washington, DC 20332-6448

330. Richard A. Schmidt
Battelle Columbus Laboratories
Mechanics Section
505 King Avenue
Columbus, OH 43201-2693

331. Arnie Schneck
Deere & Company Technical Center
Post Office Box 128
Wood-Ridge, NJ 07075

332. Matthew Schreiner
ALANX Products L.P.
101 Lake Drive
Newark, DE 19702

333. John Schuldies
Industrial Ceramic Technology, Inc.
37 Enterprise Drive
Ann Arbor, MI 48103

334. R. B. Schulz
U.S. Department of Energy
Office of Transportation Technologies
1000 Independence Avenue, S.W.
Forrestal Building CE-34, 5G-046
Washington, DC 20585

335. Wesley J. C. Schuster
Thermo Electron Corporation
Metals Division
115 Eames Street
Post Office Box 340
Wilmington, MA 01887

336. Murray A. Schwartz
Bureau of Mines
30 Orchard Way, North
Potomac, MD 20854

337. Douglas B. Schwarz
Dow Chemical Company
52 Building
Midland, MI 48674

338. Thomas M. Sebestyen
U.S. Army Tank Automotive Command
AMSTA-RGRT
Warren, MI 48397-5000

339. Brian Seegmiller
Coors Ceramics Company
17750 West 32nd Street
Golden, CO 80401

340. Peter T. B. Shaffer
Advanced Refractory Technologies, Inc.
699 Hertel Avenue
Buffalo, NY 14207

341. Laurel M. Sheppard
Advanced Materials and Processes
Route 87
Metals Park, OH 44073

342. Dinesh K. Shetty
University of Utah
Department of Materials Science and Engineering
Salt Lake City, UT 84112

343. Jack D. Sibold
Coors Ceramics Company
17750 West 32nd Street
Golden, CO 80401

344. Neal Sigmon
U.S. House of Representatives
Subcommittee on Interior and Related Events
Rayburn Building, Room B308
Washington, DC 20515

345. Richard Silberglitt
Quest Research Corporation
7600 Leesburg Pike #A
Falls Church, VA 22043

346. A. Sinha
North Carolina A&T State University
Department of Mechanical Engineering
Greensboro, NC 27411

347. Maurice J. Sinnott
University of Michigan
Chemical and Metallurgical Engineering
438 West Engineering Building
Ann Arbor, MI 48109-2136

348. S. R. Skaggs
Los Alamos National Laboratory
Program Office
Post Office Box 1663, MS:F-682
Los Alamos, NM 87545

349. Jay R. Smyth
Allied-Signal Aerospace Company
Garrett Auxillary Power Division
Post Office Box 5227
MS:93-172/1302-2K
Phoenix, AX 85010

350. Rafal Sobotowski
British Petroleum
R&D
3092 Broadway Avenue
Cleveland, OH 44115

351. E. Solidum
Allied-Signal Aerospace Company
Garrett Ceramic Components Division
19800 South Van Ness Avenue
Torrance, CA 90509

352. Thomas M. Sopko
Lubrizol Enterprises, Inc.
29400 Lakeland Boulevard
Wickliffe, OH 44092

353. Richard M. Spriggs
Alfred University
Center for Advanced Ceramic Technology
Alfred, NY 14802

354. Charles Spuckler
NASA Lewis Research Center
2100 Brookpard Road
Cleveland, OH 44135

355. M. Srinivasan
Materials Solutions
Post Office Box 663
Grand Island, NY 14702-0663

356. Gordon L. Starr
Cummins Engine Company, Inc.
Metallic/Ceramic Materials Department
Post Office Box 3005
Mail Code 50183
Columbus, IN 47202-3005

357. L. Brian Starling
ICI Advanced Ceramics
2055 East Technology Circle
Tempe, AZ 85284

358. Harold L. Stocker
General Motors Corporation
Allison Gas Turbine Division
2001 South Tibbs Avenue
Post Office Box 420, T-23
Indianapolis, IN 46206-0420

359. Paul D. Stone
Dow Chemical Company
1801 Building
Midland, MI 48674

360. Roger Storm
Carborundum Company
Niagara Falls R&D Center
Post Office Box 337
Niagara Falls, NY 14302

361. E. E. Strain
Allied-Signal Aerospace Company
Garrett Auxiliary Power Division
Department 76-50
2739 East Washington Street
Building 1302-1N
Post Office Box 5227, MS:301-2N
Phoenix, AZ 85010

362. Thomas N. Strom
NASA Lewis Research Center
21000 Brookpark Road, 77-6
Cleveland, OH 44135

363. Jerry Strong
Albright & Wilson
Post Office Box 26229
Richmond, VA 23260

364. Richard Suddeth
Boeing Motor Airplane Company
Post Office Box 7730, MS:K-76-67
Wichita, KS 67277

365. Paul Sutor
Midwest Research Institute
425 Volker Boulevard
Kansas City, MO 64116

366. P. L. Sutton
U.S. Department of Energy
Office of Transportation Technologies
1000 Independence Avenue, S.W.
Forrestal Building CE-322
Washington, DC 20585

367. J. J. Swab
U.S. Army Materials Technology Laboratory
Ceramics Research Division
SLCMT-EMC
405 Arsenal Street
Watertown, MA 02172

368. John W. Swain, Jr.
Kollmorgen Corporation
PCK Technology Division
15424 Garrison Lane
Southgate, MI 48195

369. Lewis Swank
Ford Motor Company
Material Systems Reliability Department
20000 Rotunda Drive
Building SRL, Room S-2023
Post Office Box 2053
Dearborn, MI 48121-2053

370. Chris Tarry
GTE Products Corporation
Hawes Street
Towanda, PA 18848

371. Anthony C. Taylor
U.S. House of Representatives
Committee on Science and Technology
Rayburn Building, Room 2321
Washington, DC 20515

372. Monika O. Ten Eyck
Carborundum Company
Technology Division
Post Office Box 337
Niagara Falls, NY 14302

373. John K. Tien
Columbia University
Center for Strategic Materials
1137 S.W. Mudd Building
New York, NY 10027

374. T. Y. Tien
University of Michigan
Materials and Metallurgical Engineering
Dow Building
Ann Arbor, MI 48109-2136

375. Julian M. Tishkoff
Air Force Office of Scientific Research
(AFOSR/WC) Bolling AFB
Washington, DC 20332

376. Louis E. Toth
National Science Foundation
Division of Materials Research
1800 "G" Street, N.W.
Washington, DC 20550

377. Richard E. Tressler
Pennsylvania State University
Ceramic Science and Engineering
201 Steidle Building
University Park, PA 16802

378. W. T. Tucker
General Electric Company
Research Laboratory
Post Office Box 8
Schenectady, NY 12301

379. Donald L. Vaccari
General Motors Corporation
Allison Gas Turbine Division
2001 South Tibbs Avenue
Post Office Box 420
Speed Code T10B
Indianapolis, IN 46241

380. O. Van Der Biest
Katholieke Universiteit Leuven
Departement Metaalkunde en Toegepaste
de Croylaan 2
B-3030 Leuven
BELGIUM

381. Edward C. Van Reuth
Technology Strategies, Inc.
10722 Shingle Oak Court
Burke, VA 22015

382. Mark Van Roode
Solar Turbines, Inc.
2200 Pacific Highway
Mail Zone R-1
San Diego, CA 92138

383. V. Venkateswaran
Carborundum Company
Niagara Falls R&D Center
Post Office Box 832
Niagara Falls, NY 14302

384. Ted Vojnovich
U.S. Department of Energy
Office of Transportation Technologies
1000 Independence Avenue, S.W.
Forrestal Building CE-151
Washington, DC 20585

385. K. E. Voss
Engelhard Corporation
Research Department
Menlo Park, CN-28
Edison, NJ 08818

386. John B. Wachtman, Jr.
Rutgers University
College of Engineering
Bowser Road
Post Office Box 909
Piscataway, NJ 08855-0909

387. Harlan L. Watson
U.S. House of Representatives
Committee on Science and Technology
Rayburn Building, Suite 2321
Washington, DC 20515

388. John D. Watson
Broken Hill Proprietary Co., Ltd.
Melbourne Research Laboratories
245 Wellington Road
Mulgrave 3170 Victoria
AUSTRALIA

389. Karen E. Weber
Detroit Diesel Corporation
13400 West Outer Drive
Detroit, MI 48239

390. C. David Weiss
Caterpillar Inc.
Technical Center, Building E
Post Office Box 1875
Peoria, IL 61656-1875

391. Albert R. C. Westwood
Martin Marietta Laboratories
R&D
1450 South Rolling Road
Baltimore, MD 21227

392. Thomas J. Whalen
Ford Motor Company
Material Systems Reliability Department
20000 Rotunda Drive
Building SRL, Room S-2023
Post Office Box 2053
Dearborn, MI 48121-2053

393. Sheldon M. Wiederhorn
National Institute of Standards and Technology
Inorganic Materials Division
Gaithersburg, MD 20899

394. James C. Williams
General Electric Company
Engineering Materials Technology Labs
One Neumann Way
Cincinnati, OH 45215-6301

395. Janette R. Williams
Kollmorgen Corporation
PCK Technology Division
322 L.I.E. South Service Road
Melville, NY 11747

396. Craig A. Willkens
Norton Company
Advanced Ceramics
Goddard Road
Northboro, MA 01532-1545

397. Roger R. Wills
TRW, Inc.
Valve Division
1455 East 185th Street
Cleveland, OH 44110

398. J. M. Wimmer
Allied-Signal Aerospace Company
Garrett Auxiliary Power Division
2739 East Washington Street
Post Office Box 5227, MS:1302-2P
Phoenix, AZ 85010

399. David Wirth
Coors Ceramics Company
Technical Operations and Engineering
17750 West 32nd Street
Golden, CO 80401

400. Thomas J. Wissing
Eaton Corporation
Engineering & Research Center
26201 Northwestern Highway
Post Office Box 766
Southfield, MI 48037

401. Dale Wittmer
Southern Illinois University at Carbondale
Department of Mechanical Engineering
Carbondale, IL 62901

402. Stanley M. Wolf
U.S. Department of Energy
Office of Industrial Technologies
1000 Independence Avenue, SW
Forrestal Building CE-232
Washington, DC 20585

403. George W. Wolter
Howmet Turbine Components Corporation
Technical Center
699 Benston Road
Whitehall, MI 49461

404. James C. Wood
NASA Lewis Research Center
21000 Brookpark Road
MS:500-210
Cleveland, OH 44135

405. Roger P. Worthen
Eaton Corporation
Engineering and Research Center
26201 Northwestern Highway
Post Office Box 766
Southfield, MI 48076

406. J. C. Wurm
Commission of the European Communities
Advanced Materials Research Programme
Rue de la Loi 200
B-1049 Brussels
BELGIUM

407. John Yamanias
Allied-Signal, Inc.
Metals and Ceramics Lab
Post Office Box 1021R
Morristown, NJ 07960-1021

408. Harry C. Yeh
Allied-Signal Aerospace Company
Garrett Ceramic Components Division
19800 South Van Ness Avenue
Torrance, CA 90509

409. Thomas M. Yonushonis
Cummins Engine Company, Inc.
Post Office Box 3005
Mail Code 50183
Columbus, IN 47202-3005

410. Don Zabierek
Air Force Wright Aeronautical Laboratory
AFWAL/POTC
Wright-Patterson AFB, OH 45433

411. Charles Zeh
U.S. Department of Energy
Morgantown Energy Technology Center
Post Office Box 880
Morgantown, WV 26505

412. Anne Marie Zerega
U.S. Department of Energy
Office of Transportation Technologies
1000 Independence Avenue, S.W.
Forrestal Building CE-30
Washington, DC 20585

413. Martin Zlotnick
Nichols Research Corporation
8618 Westwood Center Drive
Suite 200
Vienna, VA 22180-2222

414. Klaus M. Zwilsky
National Research Council
National Materials Advisory Board
2101 Constitution Avenue
Washington, DC 20418

415. Department of Energy
Oak Ridge Operations Office
Deputy Assistant Manager for
Energy Research and
Development
Post Office Box 2001
Oak Ridge, TN 37831-8600

416-425. Department of Energy
Office of Scientific and
Technical Information
Office of Information
Services
Post Office 62
Oak Ridge, TN 37831

For distribution by
microfiche as shown in
DOE/OSTI-4500,Distribution
Category UC-332
(Ceramics/Advanced Materials)

CRL(A)